



**BODIPY copolymers as potential
triplet photosensitisers for the
photocatalytic generation of hydrogen
and enhanced antimicrobial activity**

Aoibhín Cullen B. Sc. (Hons)

A thesis submitted in partial fulfilment for the degree of Ph.D.

Supervisor: Dr. Mary Pryce

School of Chemical Sciences,

Dublin City University

February 2021

Declaration

I hereby certify that this material, which I now submit for assessment on the programme of study leading to the award of Doctor of Philosophy (PhD) is entirely my own work, and that I have exercised reasonable care to ensure that the work is original, and does not to the best of my knowledge breach any copyright, and has not been taken from the work of others save and to the extent that such work has been cited and acknowledged within the text of my work.

Signature: A. Cullen ID number: 13106538 Date: 08 Feb 2021

Dedicated to my parents, for all their love and support.

Acknowledgements

To my supervisor, Dr. Mary Pryce – how you manage to remain calm in the midst of chaos, will forever be a mystery to me. Thank you for allowing me to learn, to be creative and for sharing your positivity with me. Thank you for building a research group where we are all so supportive and cooperative. To Prof. Conor Long, thank you for sharing your expertise on the latest few publications – I admire your outstanding ability to apply fundamental chemistry concepts to what seems like the most complicated systems and you have taught me above all else, that there's clarity in simplicity.

To the technicians and the entire staff in the School of Chemical Sciences – I know how much work you put in to keep all the instrumentation running smoothly and the laboratories fully stocked – we are so lucky to have you. To the wider university staff including the ample student support services available, thank you for helping me along this journey.

My working group past and present: Jen, Liam, Laura, Tony, Michael, Ahmed, Kaithi, Martin, Puia, Florian, Ashwene, Jessica, Lauren, Stephen, and Ross. I'm so lucky to have been a part of this group – an environment where everyone shares their new ideas and supports each other. I'm so proud of the kindness, friendship and helpfulness we've shown each other – especially over the last year, which has been more challenging than others. Ashwene – thank you for all your antimicrobial work and help with photocatalysis. Puia – thank you for constantly sharing new literature and chemistry ideas. Michael – thank you for explaining electrochemistry concepts (you're an excellent teacher) and thank you for your work recently on the electrochemistry of the polymers. Martin, thank you for your constant support both in and out of the laboratory – I've never met someone who can talk for hours and not even touch their Big Mac[®]! Equally, I've never met someone with quite so much excellent advice – both for synthetic chemistry and real-life scenarios. You let me follow in your footsteps when you joined the group and I'm so appreciative of that. To the DCU crew – cheers to all the memories, the laughs, the rants over countless coffee breaks and Nubar drinks on payday.

Mam and Dad – having you two as parents will be the biggest privilege I’ll ever know, certainly in this life, and the next and the next. Mam, thank you for constantly telling me I’m strong and believing in me that I can persevere – even when I didn’t think I could myself. Thank you for listening to all my problems and turning around with a plan of what “we” are going to do. Thank you for being approachable and a bright, bubbly role-model for me. Dad, thank you for going out of your way to take care of me in so many ways, the jobs you do behind the scenes do not go unnoticed and your chats keep me going every day. Thank you for showing me not to take life too seriously. Granny and Grandad, my earliest memories of education and homework are in your house. Granny, I remember you teaching me how to correctly hold a pen! I’m so grateful for you teaching me the value of learning and education. Your amazement at my success only makes realise how far I’ve come.

Eoghan and Niamh – thank you for putting up with my stringent requests for a quiet “study-friendly” household. You two are my rocks. Laoise and Lauren – thank you for listening to all of my dilemmas (I can be so dramatic!), thank you for reminding me that this will all be worth it. Now, there’s a roof-top pool in Dubai calling our names? Daisy (I know you can’t read yet!) – but thank you for those walks on the beach (especially during the lockdown months) and showing me how fast you can chase after all the birdies! Those walks mean the world to me.

And last, but by no means least, thank you to my best friend and my wonderful fiancé Brian, who’s taught me that it’s okay to dance to the beat of your own drum. You’ve been nothing but flexible on this journey of madness with me. Thank you for answering every phone call, for going on endless walks, for watching as many Disney movies as it took, I owe you a few action movies now! Thank you for constantly making me laugh til my ribs hurt, even when all I wanted to do was cry – here’s to a lifetime of laughter with you.

“She has no fear of failure, not because she has never failed, but because failure has only ever been a detour, a small diversion, on a journey that has ultimately led to success”

Research Output

Publications

Pryce, Mary T, Cullen, Aoibhin A.; O'Reilly, Laura, Heintz, Katharina; Long, C.; Heise, A.; Murphy, R.; Gibson, E. A.; Karlsson, Joshua; Towrie, Michael; Greetham, G. M. *Front. Chem.* **2020**, *8*, 1-14. DOI: 10.3389/fchem.2020.584060.

Cullen, A.; Rajagopal, A.; Heintz, K.; Heise, A.; Murphy, R.; Sazanovich, I. V; Greetham, G. M.; Towrie, M.; Long, C.; Fitzgerald-Hughes, D.; Pryce, M. T. *J. Phys. Chem. B* **2021**, *125*, 1550-1557. DOI: 10.1021/acs.jpcc.0c09634.

Kaufmann, M.; Müller, C.; Cullen, A. A.; Brandon, M. P.; Dietzek, B.; Pryce, M. T. *Inorg. Chem.* **2021**, *60*, 760–773. DOI: 10.1021/acs.inorgchem.0c02765.

Cullen, A. A.; Long, C.; Pryce, M. T. *J. Photochem. Photobiol. A Chem.* **2021**, *410*, 113169. DOI: 10.1016/j.jphotochem.2021.113169.

Scientific talks

‘Light absorbing polymers for Hydrogen Evolution’ at Chemistry Day, Dublin City University, 5th June 2020.

Posters

‘BODIPY copolymer for antimicrobial photodynamic therapy’. Aoibhín A. Cullen, Ashwene Rajagopal, Deirdre Fitzgerald-Hughes, Mary Pryce. Institute of Chemistry of Ireland (ICI) Postgraduate Chemistry Research Symposium, 9th September 2020.

Awards

Awarded 2nd place poster prize at Institute of Chemistry of Ireland’s Postgraduate Chemistry Research Symposium, 9th September 2020.

Aims of Research

Solar energy is widely considered to be one of the most promising avenues towards the development of new environmentally friendly energy sources of the future. The development of visible light absorbing chromophores that are both stable under solar irradiation and have high quantum yields for hydrogen generation is imperative if society is to establish a viable scale-up option for hydrogen fuel. The main objective of this research was to synthesise visible light absorbing copolymers and assess their ability for hydrogen evolution under a range of experimental conditions. On the basis of previous publications reporting broad absorption of BODIPY-based copolymers in the visible region, this thesis focuses on BODIPY-based copolymers incorporating a series of BODIPY dyes into the polymeric backbone, which are known for their high molar absorption coefficients. A central aim was to evaluate the performance of these BODIPY copolymers for photocatalytic hydrogen evolution. Photolysis in solution was to be optimised in terms of choice of catalyst, sacrificial agent, and reaction parameters to fully comprehend both the stability and catalytic ability of the copolymers. Comprehending electron transfer processes and the mechanism of triplet state population in photosensitisers for photocatalytic hydrogen evolution is paramount to the progression of the catalytic efficiency of the system. The foremost efforts this research was to elucidate the excited state dynamics of the novel BODIPY copolymers. This was achieved by using a combination of time-resolved techniques including transient absorption spectroscopy, time resolved infrared spectroscopy and time correlated single photon counting. The latter sections of this thesis focus on ruthenium(II) polypyridyl complexes and uses a combination of electrochemistry, photophysical measurements, DFT calculations and time-resolved spectroscopies to probe their excited state dynamics. An in-depth understanding of the behaviours of these inorganic complexes upon their interaction with light is key towards their optimisation in photodriven applications.

Thesis outline

Chapter 1

This chapter gives an overview of hydrogen (H₂) as a potential candidate for solar fuel production. The main principles of photocatalytic hydrogen generation are described. Furthermore, this chapter provides an overview of the fundamentals of photophysics. Singlet fission is introduced, specifically regarding intramolecular singlet fission in conjugated copolymers. An overview of the time-resolved techniques used in this research project are summarised. Relevant examples of conjugated polymers for photocatalytic hydrogen evolution in solution-based studies are reviewed and examined. BODIPY copolymers are introduced with specific focus on the photophysical properties reported to date.

Chapter 2

This chapter describes the full synthesis and characterisation of a novel BODIPY-copolymer containing a BODIPY chromophore (substituted with 3-(trimethylsilyl)ethynyl at the *meso* position) and an ethynylbenzene linker moiety. Efficient hydrogen evolution is evident under visible light irradiation ($\lambda > 420$ nm) when the copolymer is irradiated in conjunction with a cobalt cobaloxime catalyst and ascorbic acid as the sacrificial agent. The copolymer shows efficient triplet state formation (high singlet oxygen quantum yield $\Phi_{\Delta} = 0.77$) and a long-lived triplet state (61 μ s) (determined using transient absorption spectroscopy). Time-resolved techniques including transient absorption (TA) spectroscopy and time-resolved infrared spectroscopy (TRIR) are depicted on the ps-ns timescale and kinetic analysis aids to understand the excited state photodynamics of this polymer using several solvents of varying solvent polarity.

Chapter 3

This chapter describes a novel BODIPY copolymer containing 4-hydroxymethylphenyl at the *meso* position of the BODIPY core. A high singlet oxygen quantum yield (Φ_{Δ}) motivated additional studies to assess antimicrobial activity of the polymer. Successful killing of both gram-negative and gram-positive

bacteria is reported both in solution and on a surface under visible light irradiation (> 500 nm). Ultrafast time resolved studies including TA and TRIR reveal an insight into the photophysical properties of both the copolymer and monomeric precursors. In the case of the copolymer, experimental evidence suggests that the triplet state generation may occur via a singlet fission mechanism.

Chapter 4

This chapter particularly focuses on unveiling the mechanism of triplet state population in a novel BODIPY copolymer (containing an anthracenyl moiety in the *meso* position). The body of this work illustrates how BODIPY copolymer can undergo intramolecular singlet fission (iSF) through the separation of the correlated triplet pair along the polymeric backbone. The copolymer displays high hydrogen evolution rates when used in solution with ascorbic acid and Pt | TiO₂ nanoparticles.

Chapter 5

This chapter describes the synthesis and characterisation of two novel Ru(II) polypyridyl-type complexes based on π -extended dipyrrophenazine ligands containing a 4-hydroxythiazole unit. Two different substituents of different donor strengths are covalently attached to the 4-position of the thiazole unit. TA spectroscopy on both ps- and ns- timescale combined with DFT calculations and electrochemical measurements reveals information about the excited state dynamics of both complexes, particularly giving insight into the population of ¹MLCT, ³ILCT and ³MLCT states and their corresponding lifetimes.

Chapter 6

This chapter examines the photophysics of a well-established ruthenium complex, [Ru(phen)₂dppz]²⁺ and aims to extrapolate a mechanism of radiative/non-radiative decay pathways to ultimately explain the renowned *light-switch effect*. The effects of hydrogen-bonded water interaction with the phenazine unit plays a key role in the ground state properties of [Ru(phen)₂dppz]²⁺ and [Ru(phen)₂dppz]²⁺•2H₂O, and this is studied using UV-visible absorption spectroscopy.

Thesis publications

Chapter	Title	Publication status*	Authors	Contribution
2	A time-resolved spectroscopic investigation of a novel BODIPY copolymer and its potential use as a photosensitiser for hydrogen evolution	<i>Front. Chem.</i> 2020 , <i>8</i> , 1-14. DOI: 10.3389/fchem.2020.584060	Cullen, A., Heintz, K., O'Reilly, L., Long, C., Heise, A., Murphy, R., Karlsson, J., Gibson, E., Greetham, G., Towrie, M., Pryce, M.	Manuscript primary author. Primary contributor to experimental design and execution.
3	Exploiting a neutral BODIPY copolymer as an effective agent for photodynamic antimicrobial inactivation	<i>J. Phys. Chem. B.</i> 2021 , <i>125</i> , 1550-1557. DOI: 10.1021/acs.jpcc.0c09634	Cullen, A., Rajagopal, A., Heintz, K., Long, C., Heise, A., Murphy, R., Sazanovich, I. V., Greetham, G., Towrie, M., Fitzgerald-Hughes, D., Pryce, M.	Co-author of manuscript. Synthesis and characterisation of compounds. Conducted all photophysical studies.
4	Singlet fission in a diethynylbenzene-BODIPY copolymer; a time resolved spectroscopic, TD-DFT, electrochemical and hydrogen evolution study	Manuscript submitted.	Cullen, A., Brandon, M., Rajagopal, A., Brannigan, R., Karlsson, J., Sazanovich, I. V., Greetham, G., Heise, Gibson, E., Long, C., D., Pryce, M.	Manuscript primary author. Primary contributor to experimental design and execution.
5	Photophysics of Ruthenium (II) complexes with thiazole π -extended dipyrrophenazine ligands	<i>Inorg. Chem.</i> 2021 , <i>60</i> , 760-773. DOI: 10.1021/acs.inorgchem.0c02765	Kaufmann, M., Müller, C., Cullen, A., Brandon, M., Dietzek, B., Pryce, M.	Named author of manuscript with contribution to emission and lifetime studies.
6	Explaining the role of water in the "light-switch" probe for DNA intercalation: modelling water loss from $[\text{Ru}(\text{phen})_2(\text{dppz})]^{2+} \cdot 2\text{H}_2\text{O}$ using DFT and TD-DFT methods	<i>J. Photochem. Photobiol. A.</i> 2021 , <i>410</i> , 113169. DOI: 10.1016/j.jphotochem.2021.113169	Cullen, A., Long, C., D., Pryce, M.	Manuscript primary author. Primary contributor to experimental execution.

*for example, 'published'/'in press'/'accepted'/'returned for revision'/'submitted'

Signed:



Candidate



Principal Supervisor

08 Feb 2021

Date

11/2/2021

Date

Table of Contents

Declaration	i
Acknowledgements	iii
Research Output	v
Publications	v
Scientific talks	v
Posters	v
Awards	v
Aims of Research	vi
Thesis outline	vii
Chapter 1	vii
Chapter 2	vii
Chapter 3	vii
Chapter 4	viii
Chapter 5	viii
Chapter 6	viii
Thesis publications.....	ix
Table of Contents.....	x
Table of Figures	xviii
Table of Schemes	xliv
Table of Tables.....	xlvi
Table of Equations	xlix
Abbreviations	l
Units of measurement and symbols	liii
Thesis Abstract.....	liv
Chapter 1	
Introduction	1

1.1 Abstract	2
1.2 Hydrogen fuel to combat the current energy crisis	3
1.2.1 The current energy crisis	3
1.2.2 A move towards renewable energy vectors	5
1.2.3 Hydrogen (H ₂) fuel	7
1.3 Solar to chemical energy conversion	10
1.3.1 Natural Photosynthesis.....	10
1.3.2 Artificial Photosynthesis	12
1.3.3 Fundamentals of photocatalytic water splitting	13
1.3.4 Photocatalytic hydrogen evolution.....	14
1.4 Principles of photophysics	24
1.4.1 The fundamentals of photophysics.....	24
1.4.2 Singlet excited state vs. triplet excited state	26
1.5 Singlet Fission.....	28
1.5.1 Singlet Fission in BODIPY dimers	30
1.5.2 Singlet Fission in conjugated copolymers	31
1.6 Time-resolved techniques	38
1.6.1 Time correlated single photon counting	38
1.6.2 Transient absorption spectroscopy	39
1.6.3 Time resolved infrared spectroscopy	42
1.7 Conjugated polymers for photocatalytic hydrogen evolution.....	43
1.7.1 Polymers for hydrogen generation	43
1.7.2 Soluble conjugated polymers in solution for hydrogen evolution	46
1.7.3 Insoluble conjugated polymers in solution for hydrogen evolution.....	48
1.7.4 Structural influences of polymers for hydrogen evolution	62
1.8 BODIPY chromophores	64
1.8.1 The BODIPY chromophore	64
1.8.2 Synthesis	64
1.8.3 Photophysics and optical properties of the BODIPY dye.....	67
1.8.4 Homogeneous photocatalytic hydrogen evolution using BODIPY dyes	67
1.8.5 Heterogeneous hydrogen evolution using BODIPY dyes	71
1.9 BODIPY copolymers	75
1.9.1 Ethynyl linked BODIPY copolymers.....	75
1.9.2 Non-ethynyl linked BODIPY copolymers	87
1.9.3 Other BODIPY containing polymers	98
1.10 Photodynamic therapy (PDT)	103

1.10.1 Singlet oxygen ($^1\text{O}_2$) generation	103
1.11 Conclusion	106
1.12 Bibliography.....	108

Chapter 2

A time-resolved spectroscopic investigation of a novel BODIPY copolymer and its potential use as a photosensitiser for hydrogen evolution

2.1 Abstract	123
2.2 Introduction.....	124
2.3 Materials and Methods.....	127
2.4 Results and Discussion.....	131
2.4.1 Synthesis.....	131
2.4.2 UV-visible and emission spectroscopy	131
2.4.3 Lifetime analysis using TCSPC.....	134
2.4.4 Transient absorption spectroscopy	136
2.4.5 Time resolved infrared spectroscopy	139
2.4.6 Photocatalytic hydrogen generation studies	141
2.5 Conclusion	146
2.6 Supporting information.....	146
2.7 Bibliography	147

Chapter 3

Exploiting a neutral BODIPY copolymer as an effective agent for photodynamic antimicrobial inactivation

3.1 Abstract	156
3.2 Introduction.....	157
3.3 Results and Discussion.....	160
3.3.1 Synthesis.....	160
3.3.2 Photophysical properties.....	160
3.3.3 Picosecond transient absorption (ps-TA).....	162
3.3.4 Nanosecond transient absorption (ns-TA)	164
3.3.5 Time resolved infrared spectroscopy	165
3.3.6 Antimicrobial photodynamic inactivation.....	167
3.4 Conclusion	171
3.5 Supporting information.....	171
3.6 Bibliography	172

Chapter 4

Singlet fission in a diethynylbenzene-BODIPY copolymer; a time resolved spectroscopic, TD-DFT, electrochemical and hydrogen evolution study	179
4.1 Abstract	180
4.2 Introduction.....	181
4.3 Results and Discussion.....	184
4.3.1 Synthesis and characterisation	184
4.3.2 Photophysical properties.....	185
4.3.3 The photophysical properties of M1	187
4.3.4 The photophysical properties of M2	190
4.3.5 The photophysical properties of P1	191
4.3.6 Explanation of the bimodal character of the UV-visible absorption and emission of P1	199
4.3.7 Nanosecond transient absorption studies and singlet oxygen quantum yields 201	
4.3.8 Electrochemistry	202
4.3.9 Photocatalytic hydrogen studies	203
4.4 Experimental	208
4.4.1 Materials and Equipment.....	208
4.4.2 DFT calculations	209
4.4.3 Synthesis.....	209
4.5 Conclusion	211
4.6 Supporting information.....	211
4.7 Bibliography	212

Chapter 5

Photophysics of Ruthenium(II) Complexes with thiazole π-extended dipyrrophenazine ligands.....	222
5.1 Preface	223
5.2 Abstract	224
5.3 Introduction	225
5.4 Experimental Section.....	229
5.5 Results and Discussion.....	233
5.5.1 Synthesis.....	233
5.5.2 Electrochemical properties	234

5.5.3	Ground-state absorption properties.....	236
5.5.4	Photoinduced dynamics.....	238
5.6	Conclusion.....	248
5.7	Supporting information.....	249
5.8	Bibliography.....	250
 Chapter 6		
Explaining the role of water in the “light-switch” probe for DNA intercalation; modelling water loss from [Ru(phen)₂(dppz)]²⁺•2H₂O using DFT and TD-DFT methods.....		
		264
6.1	Abstract.....	265
6.2	Introduction.....	266
6.3	Experimental.....	269
6.4	Results.....	270
6.4.1	UV/visible spectrum of [Ru(phen) ₂ (dppz)] ²⁺ ; Does the ground state engage in hydrogen bonding to water?.....	270
6.4.2	Modelling the UV/visible spectrum of [Ru(phen) ₂ (dppz)] ²⁺ and [Ru(phen) ₂ (dppz)] ²⁺ •2H ₂ O.....	271
6.4.3	Water-loss reaction coordinates.....	274
6.4.4	Excited state Dynamics; Identifying “Drain-Pipe” States.....	276
6.5	Discussion.....	280
6.6	Conclusion.....	285
6.7	Supporting information.....	285
6.8	Bibliography.....	286
 Appendices A - E		
Appendix A.....		296
S2.1.	Synthetic procedure.....	296
S2.2.	NMR spectra.....	300
S2.3.	Mass Spectroscopy.....	303
S2.4.	Size Exclusion Chromatography (SEC).....	304
S2.5.	FTIR spectra.....	305
S2.6.	Absorption Spectra.....	306
S2.7.	Excitation Spectra.....	307

S2.8.	Emission Spectra.....	309
S2.9.	Emission map experiments.....	311
S2.10.	Singlet oxygen measurements.....	314
S2.11.	Lifetime measurements.....	315
S2.12.	Optical gap determination.....	318
S2.13.	Steady state UV-visible absorption and emission spectra.....	319
S2.14.	Transient absorption spectra (ps-timescale).....	320
S2.15.	Transient absorption spectra (ns-timescale).....	322
S2.16.	Time resolved Infrared Spectroscopy (ps-timescale).....	323
S2.17.	Summary of photophysical properties.....	326
S2.18.	Photocatalytic hydrogen evolution experiments in solution.....	327
S2.19.	Photoelectrochemical hydrogen evolution using NiO photocathodes.....	330
S2.20.	Literature review of organic-based polymers for hydrogen evolution.....	334
S2.21.	Compounds in solution.....	336
S2.22.	Bibliography.....	337
Appendix B.....		339
S3.1.	Experimental section.....	339
S3.1.1.	Instrumentation.....	339
S3.1.2.	Experimental Methods.....	340
S3.2.	Synthesis.....	343
S3.3.	Characterisation.....	346
S3.3.1.	NMR spectra.....	346
S3.3.2.	Mass spectroscopy.....	347
S3.3.3.	Size exclusion chromatography.....	348
S3.3.4.	Stability of drop coated copolymer surface.....	349
S3.4.	Absorption and emission spectra.....	350
S3.5.	Lifetime measurements (TCSPC measurements).....	351
S3.6.	Singlet oxygen measurements.....	352

S3.7.	Transient absorption (TA) spectroscopy	353
S3.7.1.	Picosecond transient absorption.....	353
S3.7.2.	Nanosecond transient absorption	355
S3.8.	FTIR spectra.....	356
S3.9.	Time resolved infrared spectroscopy (TRIR)	357
S3.10.	Antimicrobial Evaluation.....	360
S3.11.	Cytotoxic study using MTT assay.....	363
S3.12.	Bibliography	365
Appendix C	366
S4.1.	Experimental Methods	366
S4.1.1.	Fluorescence quantum yield calculation	366
S4.1.2.	Singlet oxygen quantum yield calculation	366
S4.1.3.	Electrochemical characterisation	367
S4.1.4.	Time correlated single photon counting (TCSPC)	368
S4.1.5.	Time resolved spectroscopy.....	368
S4.1.6.	Homogeneous photocatalytic hydrogen generation	368
S4.1.7.	Photodeposition of Pt on TiO ₂	369
S4.1.8.	Photocatalytic hydrogen evolution using Pt TiO ₂	369
S4.2.	Synthesis	371
S4.3.	NMR spectra	375
S4.4.	Size exclusion chromatography (SEC).....	377
S4.5.	FTIR spectra.....	378
S4.6.	UV-visible absorption and emission spectra	379
S4.7.	Excitation spectra	382
S4.8.	Singlet oxygen NIR emission spectra.....	384
S4.9.	Time correlated single photon counting (TCSPC).....	385
S4.10.	Quantum chemical calculations	389
S4.11.	Transient absorption measurements (ps-ns)	395
S4.12.	Transient absorption measurements (ns-μs).....	397

S4.13.	Electrochemistry	399
S4.14.	Optical gap determination	400
S4.15.	Photocatalytic hydrogen evolution.....	401
S4.16.	SEM-EDX	403
S4.17.	Bibliography	404
Appendix D.....		405
S5.1.	Synthetic procedure.....	405
S5.2.	Steady-state experiments	411
S5.2.1.	Electrochemical measurements	411
S5.2.2.	Ground-state absorption properties.....	412
S5.2.3.	Steady-state emission properties	414
S5.3.	Transient absorption and emission spectroscopy.....	415
S5.3.1.	Photoexcitation at 403 nm (fs-TA) and 410 nm (ns-TA, ns-Em) in acetonitrile.....	415
S5.3.2.	Photoexcitation at 470 nm (fs-TA, ns-TA, ns-Em) in acetonitrile	417
S5.3.3.	Photoexcitation at 470 nm (fs-TA, ns-TA, ns-Em) in dichloromethane ...	418
S5.4.	NMR spectra	419
S5.5.	Bibliography	429
Appendix E.....		430
S6.1.	Materials, Instrumental techniques, and methods.....	448
S6.1.1.	Complex synthesis.....	448
S6.2.	Bibliography	450

Table of Figures

Figure 1.1. Primary energy usage in Ireland 2008-2018 showing the energy consumption categorised by fuel source. Data obtained from SEAI 2019 report. ³	3
Figure 1.2. Ireland's total GHG emissions by sector (left), Ireland's energy-related emissions by sector (right). Data obtained from EPA report 2018. ⁴	4
Figure 1.3. Earth's global surface temperature changes over time. From left to right 1910-1913, 1984-1988, and 2014-2018. Legend showing temperature change in °C. Adapted from reference. ⁵	4
Figure 1.4. Renewable energy in Ireland 2008-2018 split by source. Data shown in non-normalised to accurately depict the annual variation. Adapted from SEAI, 2019 report. ⁸	5
Figure 1.5. Current energy sources across three areas – electricity, heat, and transport. Fossil fuel use shown in grey. Renewable energy shown in coloured section for electricity (blue), heat (green) and transport (purple). ⁸	6
Figure 1.6. Grey, blue, and green routes for hydrogen production showing a transition from a hydrocarbon to a carbon- neutral society. Figure adapted from literature. ¹⁸	9
Figure 1.7. Hydrogen generating systems, showing a) three, b) two and c) one component assemblies, where PS = photosensitiser, ER = electron relay, CAT = catalytic centre, and SA = sacrificial agent.....	15
Figure 1.8. Intermolecular inorganic-based complexes used as PS used in homogeneous photocatalysis. PF6 – counter anions omitted for clarity. ³⁶	17
Figure 1.9. Intermolecular organic-based chromophores used as PS used in homogeneous photocatalysis. ^{39,40}	18
Figure 1.10. Intramolecular photocatalytic systems containing PS covalently bound to CAT – organic based PS moiety (left), inorganic based PS moiety (right). ^{41,42}	19
Figure 1.11. A series of five novel perylene monoimide (PMI) dyes showing different anchoring groups (R) for attachment to the surface of TiO ₂ semiconductor. ⁴⁹	22
Figure 1.12. Simplified frontier energy diagram i) showing types of electronic transitions in organic molecules ii) showing transitions typical of metal-ligand photosensitisers. LC – ligand charger transfer, MLCT – metal to ligand charge transfer, HOMO – highest occupied molecular orbital. Figure adapted from literature. ⁴³	24
Figure 1.13. Jablonski diagram showing molecular electronic states and the various excitation and relaxation processes that occur upon photoexcitation. Associated rate constants for each transition is denoted, k. Solid arrow – radiative process, curly arrow – non radiative process. Figure adapted from the literature. ⁴³	25

Figure 1.14. a) Structure of BODIPY dimer, b) TA spectra of BODIPY dimer in CHCl ₃ solution following 509 nm excitation at various time delays, c) Proposed SF mechanism after excitation in polar solvents, VR – vibrational relaxation. Figure adapted from literature. ⁵⁷	30
Figure 1.15. Molecular structures of D-A copolymers studied by Busby et al. for intramolecular singlet fission (iSF). Acceptor unit (thiophene-1,1-dioxide) shown in red. Donor unit (benzodithiophene) shown in black. ⁶²	32
Figure 1.16. a) UV-visible absorption spectrum of PBTDO1 in dilute chloroform (CHCl ₃) solution, b) Transient absorption spectra of PBTDO1 ($\lambda_{exc} = 800$ nm) in CHCl ₃ , c) kinetic decay trace of singlet induced absorption (> 750 nm) (black circles) and kinetic formation of triplet induced absorption at ~ 675 nm (red circles), d) population concentration versus time for S ₁ (black solid line), T ₁ (red solid line) and CS (blue solid line) excited states. ⁶²	33
Figure 1.17. Molecular structure of D-A copolymer and schematic showing iSF in A-D-A repeating unit. ⁶⁰	34
Figure 1.18. Direct, mediated, and delayed pathways for iSF. ⁶⁰	35
Figure 1.19. a) Time resolved photoluminescence spectra of PBTDO1 in diluted 1,2-dichlorobenzene solution, showing various time delays, b) spectral deconvolution of the data obtained in (a) to show two distinct emissive species labelled S ₁ (black) and ¹ TT (red) and c) decay kinetics obtained for both S ₁ (black) and ¹ TT (red) over 100 ps. ⁶⁴ .	36
Figure 1.20. Deconvoluted emission spectra of PBTDO1 in different solvents showing S ₁ emission contribution (top) and ¹ TT emission contribution (bottom). Solvents XYL – p-xylene, CLB – chlorobenzene, DCB – 1,2-dichlorobenzene, DCM - dichloromethane. ⁶⁴	37
Figure 1.21. An example of a TA spectrum showing general spectroscopic features observed shown using change in absorption of sample (ΔA) and wavelength (nm). Figure adapted from literature. ⁶⁷	41
Figure 1.22. An example of a TRIR spectrum showing ESA and GSB features at different time delays shown in the legend. Time resolved data displayed in the IR region (wavenumber, cm ⁻¹). Figure adapted from literature. ⁶⁹	42
Figure 1.23. Number of publications in the last 10 years, per year from literature research using keywords "water splitting" and "polymers" (data source ISI Web of Science). .	43
Figure 1.24. Iridium-based polymethacrylate polymer for hydrogen generation under 470 nm. TEGMA - tri-ethylene glycol methyl ether methacrylate. Colloidal Pt generated in situ from K ₂ PtCl ₄ . ⁷⁹	46

Figure 1.25. Homogenous photocatalytic system containing poly(fluorene- <i>co</i> -phenylene) (PFP), EDTA as the sacrificial agent (SA) and DuBois NiP as catalyst (CAT). PS – photosensitiser in 0.1 M EDTA solution at pH 6. ⁸⁰	47
Figure 1.26. Polymer dots containing water soluble polymer (PS-PEG-COOH) and water insoluble polymer (PFBT) - fabrication of polymer dots to form homogeneous solution. Wavy line represents soluble side chain. ⁸¹	48
Figure 1.27. Graphitic carbon nitride units showing s-triazine unit (left) and tri-s-triazine unit (right). ⁷⁷	49
Figure 1.28. (a) g-C ₃ N ₄ as a semiconducting material for overall water splitting. CB – conduction band, VB – valence band, E _g – band gap of polymeric semiconductor. (b) UV-visible diffuse reflectance spectrum of g-C ₃ N ₄ , inset showing polymer powder. Figure adapted from literature. ⁸³	50
Figure 1.29. PPP used for first polymeric hydrogen evolution reaction; consisting of terminal 4-bromophenyl units and repeating unit of n = 13. ⁹⁰	51
Figure 1.30. Planarised conjugated polymers synthesised showed a decrease in optical band gap; which was shown to produce more H ₂ than their non-fused equivalents. ⁹¹	52
Figure 1.31. Conjugated polymers containing no (PFT), two (PF2T) and three (PF3T) fused thiophene rings (blue structures) linked with fluorene units (black structures). ⁹³	53
Figure 1.32. A series of CMP synthesis containing varying ratio of monomer units to tune the optical band gap of CMPs. ⁷⁶	55
Figure 1.33. Polybenzothiadazole polymers synthesised for hydrogen evolution. Left: linear polymer series. Right: 3-D polymer series consisting of 1,2,4, 1,3,5, and 1,2,4,5 substituted phenyl comonomer units. ⁹⁵	56
Figure 1.34. Conjugated microporous polymers synthesised for testing donor- π -acceptor moieties effect on hydrogen evolution. Blue – pyrene (donor); orange – benzene (π crosslinker); red – benzothiadiazole (acceptor). ⁹⁶	57
Figure 1.35. A linear series and porous series of donor-acceptor (D-A) polymers. Polymers differed in substituent on the acceptor benzothiadiazole unit (H, F, OCH ₃). ¹⁰¹	58
Figure 1.36. Covalent organic framework (COF) containing hydrazone groups with a pore size of 3.8 nm. ¹⁰³	60
Figure 1.37. Covalent-triazine frameworks (CTFs) used in hydrogen evolution. ^{106,107}	61
Figure 1.38. Structural influences of ethynyl linker between two conjugated polymers for hydrogen evolution. ¹⁰⁰	63
Figure 1.39. BODIPY core scaffold indicating the IUPAC numbering system. ^{113,114}	64

Figure 1.40. Multicomponent hydrogen evolution system comprising cobaloxime (2.5×10^{-3} M), a BODIPY PS (1.0×10^{-4} M), and ascorbic acid (0.1 M) as the SA in acidic homogenous solution pH 5 $\text{CH}_3\text{CN}/\text{H}_2\text{O}$, 1:1 (v/v). ¹²³	69
Figure 1.41. Intramolecular PS-CAT assemblies for hydrogen generation based on BODIPY-cobaloxime assemblies. ⁴¹	70
Figure 1.42. BODIPY-cobaloxime intramolecular assemblies for electrocatalytic hydrogen evolution. ¹²⁴	71
Figure 1.43. A series of BODIPY monomers and halogenated monomers for use as photosensitisers in hydrogen evolution. ¹²²	72
Figure 1.44. Dye for heterogenous catalysis on NiO containing donor (triphenylamine) and acceptor (BODIPY) moieties with carboxylic acid anchoring group. ¹²⁵	73
Figure 1.45. Heterogeneous catalysis showing a BODIPY dye and phenothiazine assembly on a TiO_2 surface, where AA is ascorbic acid used as the sacrificial agent. ¹²⁶	74
Figure 1.46. a) Molecular structure of BODIPY monomeric unit used as the organic linker in MOF, b) Proposed mechanism of BODIPY-based MOF for photocatalytic hydrogen evolution. Figure adapted from literature. ¹²⁷	74
Figure 1.47. BODIPY polymers reported with tunable optical properties. ¹³⁰	76
Figure 1.48. Homopolymers (polymer A and polymer B) and copolymers (polymers C, D, E) synthesised via Sonogashira polymerisation. All absorption spectra were recorded in CH_2Cl_2 at room temperature. ¹³¹	77
Figure 1.49. BODIPY oligomers with repeating unit varied from $n = 0 - 4$. ¹³³	77
Figure 1.50. Deep red emissive polymers differing in the number of dodecyl substituents on the phenyl ring in the meso position of the BODIPY core. ¹³⁵	78
Figure 1.51. BODIPY alternating donor-acceptor copolymers. Qx - quinoxaline, BzT - 2,1,3-benzothiadiazole, NDI - N,N'-di(2'ethyl)hexyl-3,4,7,8-naphthalenetetracarboxylic diimide, PDI - N,N'-di(2'ethyl)hexyl-3,4,9,10-perylene tetracarboxylic diimide. Showing donor unit (BODIPY) in black, and acceptor units in blue. ¹³⁶	79
Figure 1.52. Alternating donor-acceptor copolymers. BODIPY unit as donor (black), acceptor units (blue). ¹³⁷	80
Figure 1.53. Absorption spectra of BODIPY monomers and polymers in 2-MeTHF. Monomer 1 (orange), Monomer 2 (purple), Polymer 1 (blue), Polymer 2 (green) - each colour corresponding compound to absorption spectra. ¹³⁸	81
Figure 1.54. BODIPY copolymer (donor material) and carbazole-diketopyrrolopyrrole unit (acceptor material) used in BHJ solar cells. ¹⁴⁰	82
Figure 1.55. CMP synthesised incorporating the BODIPY chromophore for visible light photocatalysis. BODIPY chromophore (red), phenyl acetyl linker (black). ¹⁴²	83

Figure 1.56. Anthracene containing BODIPY CPP synthesised for lithium-ion storage. ¹⁴³	84
Figure 1.57. Molecular structure of BODIPY monomer MD1, MD2 and BODIPY conjugated microporous polymer (CMPBDP) studied by Douhal and co-workers. ¹⁴⁴	85
Figure 1.58. a) The absorption (black solid line) of MD2 and CMPBDP in DCM solution and the excitation spectra of each compound (blue solid line, red dashed line) showing emission detection wavelength for each, b) The emission decay at 560 nm ($\lambda_{exc} = 371$ nm) in DCM solution for MD2 (left) and CMPBDP (right), c) the lifetime data obtained using exponential fitting to the decay curves in DCM solution shown in (b) including % decay of each lifetime component. ¹⁴⁴	86
Figure 1.59. BODIPY based polyfluorene monomers, iodo monomers and copolymers. ¹⁴⁸	88
Figure 1.60. BODIPY polymers synthesised showing homopolymer (left) and copolymer with a benzene linker (right). ¹⁴⁹	89
Figure 1.61. BODIPY-based conducting polymer bearing EDOT copolymeric unit. ¹⁵⁰	90
Figure 1.62. Water soluble NIR emissive BODIPYs polymers, polymer A and polymer B. ¹⁵²	91
Figure 1.63. Conjugated polymers with different band gaps synthesised via Stille polymerisation. All polymerisation reactions were synthesised in the presence of $[Pd_2(dba)_3]$ (2 mol%), $[(o-Tol)_3P]$ (8 mol%) in toluene at <i>ca.</i> 110 °C for 24 hours. Inset shows absorption maxima for each polymer in chloroform solution. ¹⁵³	93
Figure 1.64. Molecular structure of the BODIPY copolymer (P-BODIPY) used as a heterogeneous photocatalyst in the oxidation reaction. ¹⁵⁴	93
Figure 1.65. BODIPY copolymers P1, P2 and P3, containing BODIPY (permanent dipole) and DPP (quadrupole) units. ¹⁵⁵	94
Figure 1.66. BODIPY-benzodithiophene copolymers a) α -linked (coiled geometry) and b) β -linked (linear geometry). Inset showing emission maxima ($\lambda_{exc} = 669$ nm) in chloroform solution and respective lifetime. ¹⁵⁶	95
Figure 1.67. A series of BODIPY-fluorene copolymers P1 (α -linked units) and P2 (β -linked units). Corresponding monomeric precursors shown above (M1 and M2). Photophysical properties of monomers and polymers shown in inset. ¹⁵⁷	96
Figure 1.68. A series of donor-acceptor BODIPY copolymers (P1 – P3) synthesised using Stille polycondensation reaction. BODIPY unit (black), fluorene (purple), BDT (red) and DPP (blue). ¹⁵⁸	97
Figure 1.69. Examples of BODIPY polymers reported in the literature (examples show BODIPY polymers that are not linking the BODIPY chromophore by the 2 and 6 position). ¹⁶²	98
Figure 1.70. BODIPY copolymers containing different aromatic linking units. ¹⁶³	99

Figure 1.71. Novel BODIPY fluorene alternating copolymers, showing EWG (CF ₃ , blue circle), EDG (OCH ₃ , green circle) and fluorine atoms unsubstituted (red circle). ¹⁶⁴	100
Figure 1.72. Random BODIPY copolymer showing BODIPY monomer (green circle) as pendant side chain and styrene (grey circle) used as spacer along polymeric backbone. ¹⁶⁵	101
Figure 1.73. a) Synthesis of BODIPY copolymer (p-2I-BDP) using AIBN as an initiator in radical copolymerisation reaction and b) Solid UV-vis absorption spectrum of p-2I-BDP (solid black line), prompt photoluminescence spectrum (red solid line) and delayed photoluminescence spectrum (blue solid line). ¹⁶⁶	101
Figure 1.74. Synthesis of polystyrene polymer supported BODIPY resins using benzoyl chloride resin intermediate in a continuous flow procedure. DMAP – 4-dimethylaminopyridine. ¹⁶⁷ Inset displays starting material resins (A) and BODIPY functionalised resins (B) both under ambient conditions (top image) and under UV light (bottom image).	102
Figure 1.75. Pyrene-BODIPY BODIPY dyad for heavy-atom free PS for singlet oxygen generation. i) PeT to form a CT state from donor to acceptor, ii) photophysical processes that can occur to form triplet state iii) singlet oxygen yields in both polar and non-polar solvent for selected donor-acceptor dyads. SOCT-ISC: spin orbit charge transfer intersystem crossing, RP-ISC: radical pair intersystem crossing, CR: charge recombination, BODIPY = BDP. ¹⁷⁰	104
Figure 1.76. Cationic BODIPY compounds show singlet oxygen generation and antimicrobial activity. ¹⁷¹	105
Figure 1.77. Range of BODIPY-based PS reported as singlet oxygen generating PS. ^{172,173}	105
Figure 2.1. a) BODIPY core scaffold (4,4-difluoro-4-bora-3a,4a-diaza-s-indacene) showing IUPAC numbering system and b) 3-TMS polymer reported in this study (red bonds showing the BODIPY unit in the polymeric backbone).	125
Figure 2.2. Synthesis of 3-TMS polymer. <i>Reagents and conditions</i> i) TFA, DDQ, BF ₃ OEt ₂ , TEA, dry CH ₂ Cl ₂ , N ₂ , RT, 3 days; ii) I ₂ , HIO ₃ , EtOH, r.t. overnight; iii) Pd(PPh ₃) ₂ Cl ₂ , PPh ₃ , CuI, THF/Diisopropylamine, reflux, 3 days.	131
Figure 2.3. Normalised absorption spectra for monomer (solid red), polymer (solid blue) and normalised emission spectra for monomer (dashed red) and polymer (dashed blue). CH ₂ Cl ₂ , 298 K.	132
Figure 2.4. a) Emission spectra of the polymer in acetonitrile (red), chloroform (blue), dichloromethane (green), dimethylformamide (black), dimethyl sulfoxide (orange) and tetrahydrofuran (purple) following excitation at 530 nm, b) 3-D Emission map of	

polymer in dichloromethane, recorded at room temperature. Fixed wavelength axis indicates the various excitation wavelengths used. All spectra recorded in at room temperature.....	134
Figure 2.5. a) Emission decay of polymer in CH ₂ Cl ₂ and b) DMF obtained using FLS1000 Photoluminescence spectrometer $\lambda_{exc} = 510$ nm. All solutions purged with N ₂ for 20 minutes prior to sample measurement.	135
Figure 2.6. a) Transient absorption spectra of polymer in CD ₃ CN following excitation using 525 nm, b) Transient absorption spectra of polymer corresponding to indicated time delays, grey lines indicate kinetic traces analysed, c) Temporal evolution of the spectra at wavelengths indicated by grey broken lines in (b) together with the exponential best fit line (b) and d) Normalised Decay Associated Spectra (DAS) corresponding to the lifetimes extracted from modelling of the TA spectra in CD ₃ CN.	136
Figure 2.7. Transient absorption spectroscopy of polymer in CH ₃ CN, shown at different time delays, ($\lambda_{exc} = 355$ nm) and corresponding decay at ESA and GSB shown in inset at stated wavelength: 445 nm (black squares) and 525 nm (red circles) with red line showing monoexponential fitting to obtain triplet lifetime. Grey shaded curve represents the ground state absorption spectra of polymer in same solvent. All samples were prepared using freeze-pump thawed to degas.	139
Figure 2.8. a) TRIR spectra following excitation at 525 nm of the polymer in CD ₃ CN in the fingerprint region and b) TRIR spectra following excitation at 525 nm of the polymer dissolved in chloroform the triple bond region. Blue spectra indicating initial time delays (ps), red spectra indicated final time delays (ps).....	140
Figure 2.9. Photocatalytic results following irradiation at $\lambda > 420$ nm, cobaloxime as the catalyst (2.5 mM), ascorbic acid as the SA (0.1 M, which was adjusted to pH 5 prior to sample preparation using the appropriate amount of 2M NaOH), polymer as PS (0.06 mg/mL). Hydrogen evolution curve displayed for different solvent ratios: THF/H ₂ O, 1:1 (v/v) (blue squares, solid line) or CH ₃ CN/H ₂ O, 1:1 (v/v) (red squares, solid line). Hydrogen turnover frequency displayed for each solvent system in $\mu\text{mol h}^{-1} \text{g}^{-1}$: THF/H ₂ O, 1:1 (v/v) (blue triangles, dashed line) and CH ₃ CN/H ₂ O, 1:1 (v/v) (red triangles, dashed line). All samples were degassed using three freeze-pump thaw cycles prior to irradiation.	142
Figure 2.10. Photocatalytic results following irradiation at $\lambda > 420$ nm, cobaloxime as the catalyst (2.5 mM), ascorbic acid as the SA (0.1 M, which was adjusted to pH 5 prior to sample preparation using the appropriate amount of 2M NaOH), solvent ratio THF/H ₂ O, 1:1 (v/v) and polymer as PS (0.25 mg/mL; blue squares, solid line) or (0.06 mg/mL; red squares, solid line). Hydrogen turnover frequency displayed for each polymer	

concentration analysed in $\mu\text{mol h}^{-1} \text{g}^{-1}$: 0.25 mg/mL (blue triangles, dashed line) and 0.06 mg/mL (red triangles, dashed line). All samples were degassed using three freeze-pump thaw cycles prior to irradiation. 143

Figure 3.1. a) Chemical structure of 2,6-diiodo-8-(4-hydroxymethylphenyl)-4,4'-difluoro-1,3,5,7-tetramethyl-4-bora-3a,4a-diaza-s-indacene (BODIPY-2I), (b) 8-(4-hydroxymethylphenyl)-4,4'-difluoro-1,3,5,7-tetramethyl-4-bora-3a,4a-diaza-s-indacene (BODIPY-2H), and (c) the repeat unit of the copolymer. 160

Figure 3.2. Normalised UV-visible absorption spectra of BODIPY-2H (orange solid line), copolymer (purple solid line) and normalized emission spectra of BODIPY-2H (orange dashed line) and copolymer (purple dashed line). Excitation wavelength corresponding to the maxima of the lowest energy absorption band for both systems. All spectra recorded in CH_2Cl_2 at room temperature. 161

Figure 3.3. a) Transient absorption (TA) spectra of the copolymer in acetonitrile, and b) EAS in acetonitrile. $\lambda_{\text{exc}} = 525 \text{ nm}$ (0.4 $\mu\text{J}/\text{pulse}$) (the gap in the TA plots corresponds to the excitation wavelength which is masked by a narrow band pass filter). 163

Figure 3.4. TA spectra of the copolymer in CH_3CN at different time delays (< 1 μs - 68 μs). Sample was degassed using three freeze-pump-thaw cycles. Grey dashed line on TA spectra indicates the wavelengths chosen for the kinetic traces shown in the inset which were used to determine the decay lifetimes. 165

Figure 3.5. a) TRIR spectra of the copolymer in CD_3CN in the spectral window of 1610 – 1250 cm^{-1} at various time delays following excitation at 525 nm and b) and the corresponding EAS. 166

Figure 3.6. TRIR spectra of the copolymer in CHCl_3 following pulsed photolysis ($\lambda_{\text{exc}} = 525 \text{ nm}$) in the triple bond region recorded at various time delays, with arrows indicating the time dependent behaviour of the spectral features. FTIR of copolymer displayed in the same IR region (grey solid line) for reference. 167

Figure 3.7. Antimicrobial activity of the copolymer under irradiation and non-irradiation conditions, with *S. aureus* (ATCC 25923 and ATCC 43300 (MRSA)) and *E. coli* (ATCC 25922 and CL11 (ESBL)), [copolymer] for *S. aureus*: 1 $\mu\text{g}/\text{mL}$, [copolymer] for *E. coli*: 5 $\mu\text{g}/\text{mL}$, time of irradiation: 15 minutes, wavelength of light for irradiation $\lambda \sim 525 \text{ nm}$. Data represent percentage killing (CFU/mL relative to controls) and are the mean \pm SEM of three assays carried out in triplicate. 168

Figure 3.8. Comparison of the antimicrobial activity of drop coated copolymer on 96-well plate under irradiation and non-irradiation conditions for (a) *S. aureus* (ATCC 25923),

(b) MRSA (ATCC 43300), (c) *E.coli* (ATCC 25922), (d) ESBL (CL11), [copolymer]:
 40 µg/mL, varied irradiation time, wavelength of light for irradiation $\lambda \sim 525$ nm.... 170

Figure 4.1. a) Molecular structure of BODIPY core, b) Donor-acceptor (D-A) dyad BODIPY derivative,²⁵ c) BODIPY dimer derivative.²⁴ Triplet lifetimes (τ_T) of each BODIPY derivative previously reported displayed below molecular structure (μs)..... 183

Figure 4.2. Molecular structures of M1, M2 and P1..... 184

Figure 4.3. a) The normalised UV-visible absorption spectrum of P1 in THF and DMSO with the spectrum of M1 in THF (dashed) and b) the normalised emission spectra of P1 in THF and DMSO following excitation at 550 nm..... 186

Figure 4.4. a) The optimised molecular structure of M1 showing the anthracenyl substituent towards the top, light grey hydrogen, dark grey carbon, blue nitrogen, pink boron, and green fluorine atoms; (b) the electron density difference map (EDDM) for the T_1 excited state of M1 (i.e. the lowest energy triplet excited state) (c) the EDDM for T_2 showing the anthracenyl-centred nature of this excited state and (d) the EDDM for the S_1 state (red volumes indicate regions where the electron density is greater in the excited state compared to the ground-state, and blue volumes are the regions where the electron density is less in the excited state compared to the ground-state, iso value 0.004). ... 188

Figure 4.5. The difference spectra obtained following 525 nm photolysis of M1 in CD_3CN , a) the early times showing the growth of S_1 , b) the TA spectra at later times showing the decay of features of S_1 and formation of weak features of the triplet species (up arrow with asterisk), c) early time TRIR spectra including the singlet spectrum from global analysis (red dashed) and d) late time TRIR spectra showing decay of the singlet features and the formation of the triplet with the triplet spectrum obtained from global analysis (blue dashed), the inset shows the time-dependent concentrations of singlet (red) and triplet (blue) components..... 189

Figure 4.6. a) The TA difference spectra obtained following photolysis of M2 in CD_3CN showing the formation of a singlet excited state and its evolution associated spectrum obtained from an global analysis (red dashed); b) the longer time spectroscopic changes showing the decay of the singlet state and formation of a triplet state with its evolution associated spectrum from global analysis (blue dashed) and the kinetic data obtained using a sequential model in the inset; c) the TRIR spectra showing the formation of a singlet excited state (the red dashed spectrum is the evolution associated spectrum from global analysis; and d) the longer time scale changes showing the formation of a persistent triplet state with the evolution associated spectrum (blue dashed) and the inset

- displays the time dependent concentration plot indicating a quantum yield of 1.0 for the formation of the triplet species. 190
- Figure 4.7. The EDDMs of the lowest energy singlet excited states of the three BODIPY oligomers a) the two-BODIPY, b) the four BODIPY, and c) the six BODIPY oligomers, blue volumes represent regions where the electron density is reduced compared to the ground state (donor) and red volumes represent regions where the electron density in the excited state is greater than the ground state (acceptor). 192
- Figure 4.8. The time-resolved changes observed following photolysis of P1 at 525 nm in CD₃CN; a) the TA spectra showing the depletion of the parent and formation of a singlet and triplet excited states; b) the evolution adjusted difference spectra for an initially formed species (black) which reacts in 4ps to form the singlet (red) which in turn forms a triplet (blue) excited states, (the inset shows the kinetics of the reaction sequence indicating a lifetime for the singlet species of 165 ps; c) the TRIR spectra showing the decay (down arrows) of the initially produced singlet excited state and formation of the triplet excited state (up arrows), and d) the evolution associated difference spectra for the Franck-Condon species (black), singlet (red), and spin coherent triplet (blue) and spatially discrete triplet pair (green), the inset shows the kinetic behaviour of these components. 194
- Figure 4.9. a) The EDDM for the two lowest energy (and almost degenerate) triplet states (T₁ and T₂; 1.37 and 1.38 eV respectively) in the optimised 2-BODIPY oligomer where the BODIPY units are coplanar, this represents a spin-correlated triplet pair ¹(TT) (iso value 0.004), b) the EDDM for the degenerate T₁ and T₂ states (1.27 eV) for the 2-BODIPY oligomer where the BODIPY units are set to be orthogonal showing two degenerate spatially discrete triplets with spin density located separately on each BODIPY unit. 195
- Figure 4.10. The energy levels for the optically accessible singlet state (S₁; red) of the 6-BODIPY oligomer and the lower energy triplet states (blue) which form two bands of energetically close states, the upper band consist of spin-correlated triplet states ¹(TT) and the lower band comprise spatially discrete triplets (T) (blue dashed) with lower two EDDMs representing two spatially discrete triplets at the extremes of the oligomer and the upper EDDM showing a typical spin-correlated triplet, expanded regions highlight the involvement or otherwise of the diethynylbenzene links which confirm a reduced charge-transfer character for the spatially discrete triplets compared to the spin correlated triplets. 196
- Figure 4.11. a) The TRIR spectra obtained in the -C≡C- region in CHCl₃ showing the ground-state bleach (GSB) at 2215 cm⁻¹ and the greatly enhanced excited state feature(s) at 2070

cm ⁻¹ ; and b) global analysis of the time dependent behaviour of spectra inset showing the decay of the singlet (red) and formation of triplet (blue) species.	197
Figure 4.12. Different rotational conformations along the polymeric backbone showing <i>anti</i> and <i>syn</i> possible conformations.	199
Figure 4.13. The variation in the energies of the ground state and excited states up to the lowest energy singlet excited state against the sequential twist angle in the 6-BODIPY oligomer, the inset shows the relative change in the ground-state and S ₁ energies.	201
Figure 4.14. Photocatalytic activity of polymer, P1 when irradiated using a Xe Arc lamp, $\lambda > 420$ nm in combination with TiO ₂ Pt nanoparticles (6 mg), 0.1 M ascorbic acid as sacrificial agent in a 4 mL 1:1 (v/v) THF:H ₂ O solution. Activity shown above in mmol H ₂ g ⁻¹ (based on mass of polymer in photocatalytic solution). Various experiments studied the effect of different polymer concentration where 0.1 mM (purple dash), 0.2 mM (grey dash), 0.4 mM (green dash), 0.8 mM (red dash) and 1.2 mM (blue dash). Concentration of polymer, P1 (in mM) in solution calculated based on the monomeric repeating unit of the polymer.....	205
Figure 5.1. General structural formula of Ru1 and Ru2. The photophysically important moieties, namely the phenanthroline- (phen), phenazine- (phz) and thiazole-unit (tz), are highlighted.....	228
Figure 5.2. UV-vis spectra of the Ruthenium complexes Ru1 and Ru2 (b) and the corresponding dppz-ligands L1 and L2 (a) in acetonitrile. TD-DFT simulated absorption spectra (dashed grey lines) of Ru1 and Ru2 (solid lines in (c) and (d) and charge density differences of MLCT _{phz} and ILCT _{tz/phz} states. The character of the predicted states is highlighted in blue (ILCT), green (MLCT) and black ($\pi\pi^*$), respectively.....	236
Figure 5.3. Nanosecond time-resolved emission (a) and transient absorption spectra (d) and their corresponding decay associated spectra (ns-Em: (c), ns-TA: (e)) of Ru1 (22 μ M) following excitation at 410 nm (3.0 mW, OD at $\lambda_{exc} = 0.44$), in acetonitrile. The steady-state emission (solid, grey line) together with the lifetime weighted transient emission spectrum (solid, green line) recorded following excitation at 410 nm are compared in (b). The inset in figure (e) displays the emission decay signal at 680 nm (dark green) compared to the transient absorption kinetic trace at 680 nm (green). The solid grey lines in figure (c) and (e) represent the steady-state emission spectrum and TA of the long-lived ³ MLCT _{phen} state of Ru0, respectively.....	239
Figure 5.4. Transient absorption (a) and decay associated spectra (b) Ru1 (90 μ M) following excitation at 403 nm (0.5 mW, OD at $\lambda_{exc} = 0.16$) in acetonitrile. TD-DFT simulated	

absorption spectra of the optimized S_0 ($^1\text{Ru1}$, singlet-singlet excitations, solid, green line) and T_1 ($^3\text{Ru1}$, triplet-triplet-excitation, dotted, dark green line) geometries of Ru1. The vertical transition energies and their corresponding oscillator strength are shown by bars (c, d), which were broadened using Gaussian functions (c, full-width half-maximum of 0.30 eV). Comparison of the decay associated spectra (normalized at 550 nm) of τ_4 (grey marks) and τ_5 (black marks) to the simulated difference spectrum (solid, green line) for an $^1\text{Ru1}$ to $^3\text{Ru1}$ excitation and spin density distribution of Ru1 in the lowest triplet state (d)..... 240

Figure 5.5. Nanosecond (a) and picosecond time-resolved transient absorption spectra (b) with their respective decay associated spectra (c) of Ru2 upon excitation at 410 nm (ns-TA, 3.0 mW, OD at $\lambda_{\text{exc}} = 0.4$) or 403 nm (fs-TA, 0.5 mW, OD at $\lambda_{\text{exc}} = 0.2$) in acetonitrile. 242

Figure 5.6. Jablonski diagram for the formation of the long-lived $^3\text{MLCT}$ and $^3\text{ILCT}$ states (right side) and the short-lived phz-centered $^3\text{MLCT}$ state ($^3\text{MLCT}_{\text{phz}}$, left side) upon photoexcitation of Ru1 and Ru2 at 400 and 470 nm. The relative population density in the $^3\text{MLCT}$ manifold is depicted by the green-blue-coloured box, indicating a higher population density of $^3\text{MLCT}_{\text{phz}}$ states upon excitation in the red-flank of the absorption band (470 nm, green shading) or the proximal $^3\text{MLCT}$ states upon 400 nm excitation (blue, shading). The colours in the schematically shown ground-state structure (S_0) depict the origin of the excess electron density, which is either from the tz-unit (ILCT character: orange) or the Ru(II) center (MLCT character: violet). In the sketches of the excited-state geometries the colours highlight the localization of the excess electron density either in the $^3\text{MLCT}$ (violet) or $^3\text{ILCT}$ sphere (orange). The numbers associated with the dotted arrows are the first order rate constants associated with the respective processes in acetonitrile..... 243

Figure 5.7. Time-resolved spectra of Ru1 (top row, green) and Ru2 (bottom row, blue) upon 470 nm excitation in acetonitrile: Ultrafast transient absorption spectra (a – b, 0.2 mW, OD at $\lambda_{\text{exc}} = 0.3 – 0.5$) and the corresponding decay associated spectra (c – d) and transient emission spectra (e – f, 3.5 mW, OD at $\lambda_{\text{exc}} = 0.1 – 0.3$) and corresponding decay associated spectra (g – h). The solid grey lines in figures g – h show the steady-state emission spectrum of Ru0. For reasons of comparability the decay associated spectra obtained upon 403 nm (410 nm) excitation are represented in figures c – d and g – h (dashed lines)..... 244

Figure 5.8. Time-resolved spectra of Ru2 upon 470 nm excitation in dichloromethane: Ultrafast transient absorption spectra (a), 0.2 mW, OD at $\lambda_{\text{exc}} = 0.3$) and the corresponding decay associated spectra (b) and transient emission spectra (c), 3.5 mW,

OD at $\lambda_{exc} = 0.3$) and corresponding decay associated spectra (d). For comparison the decay associated spectra obtained upon 470 nm excitation in acetonitrile are represented in figure (b) (dashed lines). The solid grey line in figure (e) shows the steady-state emission spectrum of Ru0 compared to the normalized decay-associated spectra shown in panel (d). 246

Figure 6.1. A representation of the molecular structure of $[\text{Ru}(\text{phen})_2\text{dppz}]^{2+}$ 266

Figure 6.2. The UV-visible absorption spectrum of $[\text{Ru}(\text{phen})_2(\text{dppz})]^{2+} \cdot 2(\text{PF}_6^-)$ in dry acetonitrile (red $1.12 \times 10^{-5} \text{ M dm}^{-3}$, 2.5 mL solution volume) and acetonitrile containing water (blue + 160 μL ; orange +360 μL ; green + 1000 μL of H_2O respectively) normalised at 450 nm, showing the relative increase in the extinction of the features close to 360 nm with respect to the broad feature centred at 450 nm..... 271

Figure 6.3. a) The calculated vertical transitions for for $[\text{Ru}(\text{phen})_2(\text{dppz})]^{2+}$ and the experimental UV/visible spectrum (red) of $[\text{Ru}(\text{phen})_2(\text{dppz})]^{2+}$ intercalated with poly[d(AT)₂] which removes the effects of hydrogen bonded water and the counterion, this spectrum was obtained from reference [18] and b) the calculated vertical transitions of $[\text{Ru}(\text{phen})_2(\text{dppz})]^{2+} \cdot 2\text{H}_2\text{O}$ (the magnitude of the transitions are represented by the height of the lines); red lines represent dppz-centred excited states, blue lines represent phen-based excited states, and dashed lines represent excited states involving both phen and dppz ligands..... 273

Figure 6.4. The molecular structure of $[\text{Ru}(\text{phen})_2(\text{dppz})]^{2+} \cdot 2\text{H}_2\text{O}$ showing the two hydrogen bonding water molecules and the location of the ruthenium atom which is obscured by the ancillary phen ligands in this orientation. 274

Figure 6.5. a) The structural change along the reaction coordinate 1 (RC1), modelling the loss of two hydrogen-bonded water molecules; (b) the structural changes along reaction coordinate 2 (RC2); the red arrows indicate the trajectory of the oxygen nuclei. 276

Figure 6.6. The energy change along RC2 for the lowest three triplet excited states (ES1 to ES4), showing that ES1 mirrors the ground state in being slightly attractive to hydrogen bond formation with water (red indicates a dppz-based state and blue the phen-based states..... 277

Figure 6.7. Selective energy profiles along RC2 (a) highlighting the behaviour of the lowest energy triplet “drain-pipe” state (ES14) with the early data showing a small energy barrier highlighted (excited states below 2.5 eV are removed for clarity) while (b) highlights the lowest energy singlet drain-pipe state at an energy not accessible to 400 nm excitation; the electron density difference maps indicate the regions of reduced

electron density in blue, and the regions of increased electron density in red (iso value set at 0.001).	278
Figure 6.8. An expanded view of an adiabatic description of the excited state energies along RC1 highlighting the lowest energy drain-pipe state, the electron density difference maps for the extremes of the drain-pipe and the electron density difference map for the lowest energy triplet excited state resulting from internal conversion at the extreme of the reaction coordinate.	279
Figure 6.9. Historical energy level diagram describing the photophysics of [Ru(phen) ₂ (dppz)] ²⁺ in (a) water or (b) acetonitrile derived from E. J. C. Olson, D. Hu, A. Hormann, A. M. Jonkman, M. R. Arkin, E. D. A. Stemp, J. K. Barton and P. F. Barbara, <i>J. Am. Chem. Soc.</i> , 1997, 119, 11458-11467.	280
Figure 6.10. a) A schematic energy level diagram for the photophysics of [Ru(phen) ₂ (dppz)] ²⁺ in acetonitrile and b) A schematic energy level diagram describing the development of the excited states following excitation of [Ru(phen) ₂ (dppz)] ²⁺ •2H ₂ O showing the greater population of dppz-centred triplet states and the deactivation by expulsion of water producing a “dry” dark state and its subsequent reaction with bulk water.	282
Figure 6.11. a) The molecular structure showing the orientation used for the e-density maps including the location of the ruthenium atom, b) the electron density difference map for the 14 th excited state (triplet drain-pipe) showing both the metal-to-dppz and n-to-π* character of this state (iso value 0.001), c) the electron density difference map for the 6 th excited state (triplet, drain-pipe at its extreme) for a N-H distance of 3.1 Å showing the dppz-centred nature of this excited state, and d) the lowest energy triplet excited state for a N-H distance of 3.1 Å; blue regions have reduced electron density relative to the ground state, and red region have increased electron density relative to the ground state, carbon atoms are coloured grey, hydrogens light grey, and nitrogen atoms are blue and oxygen atoms red.	283
Figure 6.12. An expanded view of the energy changes (adiabatic) to ES13 and ES14 (“drain-pipe”) in the early stages of RC1 showing a very small (0.2 kJ mol ⁻¹) barrier to progression of ES14 along this reaction coordinate.	284
Figure S2.1. ¹ H NMR spectra of monomer. CDCl ₃ as calibration standard, δ = 7.26 ppm.	300
Figure S2.2. ¹³ C NMR spectra of monomer. CDCl ₃ as calibration standard, δ = 77.16 ppm.	300
Figure S2.3. ¹ H NMR spectra of diiodo monomer. CDCl ₃ as calibration standard, δ = 7.26 ppm.	301

Figure S2.4. ^{13}C NMR spectra of diiodo monomer. CDCl_3 as calibration standard, $\delta = 17.16$ ppm.	301
Figure S2.5. ^1H NMR spectra of polymer. CDCl_3 as calibration standard, $\delta = 7.26$ ppm... ..	302
Figure S2.6. MS spectra $[\text{M}+\text{H}]$ for 3-TMS BODIPY monomer.	303
Figure S2.7. MS spectra for $[\text{M}+]$ for 3-TMS diiodo BODIPY monomer.....	303
Figure S2.8. SEC results obtained for polymer showing molecular weight distribution of the polymer.	304
Figure S2.9. FTIR spectra of 1,4-diethynylbenzene (red spectra, top) and polymer (black spectra, bottom), recorded in a solution cell in spectrophotometric grade dichloromethane. Structures inserted below each IR spectra. Inset showing details between $2400 - 2000 \text{ cm}^{-1}$	305
Figure S2.10. Normalised absorption spectra of monomer in acetonitrile (red), chloroform (dark blue), THF (black), toluene (light blue) and acetone (green), dichloromethane (orange). Recorded at room temperature.	306
Figure S2.11. Normalised absorption spectra of polymer in THF (black), DMSO (red), DMF (green), dichloromethane (dark blue), chloroform (light blue). Recorded at room temperature.....	306
Figure S2.12. Excitation spectra of monomer in CH_2Cl_2 . Recorded at the emission maxima.	307
Figure S2.13. Excitation spectra of polymer in CH_2Cl_2 . Recorded at the emission maxima.	307
Figure S2.14. Excitation spectra of monomer (red) and polymer (blue) in CH_2Cl_2 . Recorded at each emission maxima respectively.	308
Figure S2.15. Emission spectra monomer in CH_2Cl_2 . λ_{exc} corresponding to lowest energy absorption band.	309
Figure S2.16. Emission spectra polymer in CH_2Cl_2 . λ_{exc} corresponding to lowest energy absorption band.	309
Figure S2.17. Emission spectra monomer (red) and 3-TMS polymer (blue) in CH_2Cl_2 . λ_{exc} corresponding to lowest energy absorption band.....	310
Figure S2.18. Emission map of polymer in dichloromethane, recorded at room temperature. Excitation wavelengths shown in inset: 350 nm (black squares), 390 nm (red circles), 420 nm (green triangles), 440 nm (olive triangles), 500 nm (magenta squares), 520 nm (cyan triangles), 540 nm (navy triangles), 550 nm (grey circles).....	311
Figure S2.19. Excitation Emission contour map of polymer in dichloromethane, recorded at room temperature. Emission spectra shown at the bottom using $\lambda_{\text{exc}} = 360 \text{ nm}$ (blue) and $\lambda_{\text{exc}} = 540 \text{ nm}$ (red).	311

Figure S2.20. Emission map of polymer in dichloromethane, recorded at room temperature. Fixed wavelength axis shows varying excitation wavelengths used.	312
Figure S2.21. Emission map of monomer in dichloromethane, recorded at room temperature. Excitation wavelengths shown in inset: 350 nm (red circles), 400 nm (magenta triangles), 430 nm (green circles), 460 nm (cyan squares), 480 nm (violet circles), 490 nm (blue squares), 500 nm (grey triangles).	312
Figure S2.22. Excitation Emission contour map of monomer in dichloromethane, recorded at room temperature. Emission spectra shown at the bottom using $\lambda_{exc} = 360$ nm (blue) and $\lambda_{exc} = 500$ nm (red).	313
Figure S2.23. 3-D Emission map of monomer in dichloromethane, recorded at room temperature. Fixed wavelength axis shows varying excitation wavelengths used.	313
Figure S2.24. NIR Singlet oxygen emission spectra of monomer (grey spectra) and 3-TMS polymer (red spectra) in $CHCl_3$ using $\lambda_{exc} 530$ nm. Φ_{Δ} displayed in Table S2.2.....	314
Figure S2.25. Emission decay of monomer in dichloromethane, $\lambda_{exc} = 510$ nm. Solution purged with N_2 for 20 minutes prior to sample measurement. Red line showing exponential fit.	315
Figure S2.26. Emission decay of polymer in THF, $\lambda_{exc} = 510$ nm. Solution purged with N_2 for 20 minutes prior to sample measurement. Red line showing biexponential fit.	315
Figure S2.27. Emission decay of polymer in $CHCl_3$, $\lambda_{exc} = 510$ nm. Solution purged with N_2 for 20 minutes prior to sample measurement. Red line showing biexponential fit.....	316
Figure S2.28. Emission decay of polymer in CH_3CN , $\lambda_{exc} = 510$ nm. Solution purged with N_2 for 20 minutes prior to sample measurement. Red line showing biexponential fit.....	316
Figure S2.29. Emission decay of polymer in DMSO, $\lambda_{exc} = 510$ nm. Solution purged with N_2 for 20 minutes prior to sample measurement. Red line showing biexponential fit.....	317
Figure S2.30. UV- visible absorption spectra of polymer in CH_2Cl_2 . Inset showing Tauc Plot used to calculate the optical gap from the onset of absorption. ^{3,4}	318
Figure S2.31. Normalised UV-visible absorption and emission spectra for monomer absorption (solid red), emission (dashed red), diiodo monomer absorption (solid blue) and emission (dashed blue). Recorded in $CHCl_3$	319
Figure S2.32. Transient absorption spectra of polymer in a) CD_3CN , b) DMSO, c) chloroform and d) dichloromethane. Time delays indicated in inset. $\lambda_{exc} = 525$ nm.	320
Figure S2.33. Exponential fitting (red curve) of polymer TA spectra at stated wavelengths in a) CD_3CN , b) DMSO, c) chloroform and d) dichloromethane. Red line indicates exponential decay.	320

Figure S2.34. Transient absorption spectra of a) monomer in CD ₃ CN at random time delays. Notch in graph where excitation wavelength occurred, grey dashed lines indicate the kinetic traces analysis and b) kinetic traces at stated wavelength, red lines indicate the exponential fit used, $\lambda_{\text{exc}} = 525$ nm.....	321
Figure S2.35. Transient absorption spectra of a) diiodo monomer in CD ₃ CN at random time delays. Notch in graph where excitation wavelength occurred, grey dashed lines indicate the kinetic traces analysis and b) kinetic traces at stated wavelength, $\lambda_{\text{exc}} = 525$ nm.	321
Figure S2.36. Transient absorption decays at stated wavelengths for 3-TMS polymer in CH ₃ CN at stated wavelengths: 445 nm (black squares) and 525 nm (red circles). $\lambda_{\text{exc}} = 355$ nm. Red lines indicate exponential fit.....	322
Figure S2.37. TRIR spectra of 3-TMS polymer in a) CD ₂ Cl ₂ (top), b) CD ₃ CN (centre) and c) DMSO (bottom) in the IR spectral window of 1750 cm ⁻¹ - 1250 cm ⁻¹ . Blue spectra indicating initial time delays (ps), red spectra indicating final time delays (ps), $\lambda_{\text{exc}} = 525$ nm.	323
Figure S2.38. TRIR of 3-TMS diiodo monomer in CD ₃ CN showing the spectral window of 1750 cm ⁻¹ – 1300 cm ⁻¹ in the IR region. Blue spectra indicating initial time delays (ps), red spectra indicating final time delays (ps), $\lambda_{\text{exc}} = 525$ nm.	324
Figure S2.39. TRIR spectra of 3-TMS monomer in CH ₃ CN showing the spectral window of 1750 cm ⁻¹ – 1300 cm ⁻¹ approximately in the IR region. Blue spectra indicating initial time delays (ps), red spectra indicating final time delays (ps), $\lambda_{\text{exc}} = 525$ nm.....	324
Figure S2.40. TRIR spectra of a) 3-TMS monomer, b) 3-TMS diiodo monomer and c) 3-TMS polymer in CHCl ₃ , showing the spectral window of 2300 cm ⁻¹ – 1930 cm ⁻¹ in the IR region. Blue spectra indicating initial time delays (ps), red spectra indicating final time delays (ps), $\lambda_{\text{exc}} = 525$ nm.....	325
Figure S2.41. a) Hydrogen evolution of the polymer over 24 hours and b) corresponding turnover frequencies. Conditions summarised in Table S2.3 for 1-5.	328
Figure S2.42. Ascorbic acid showing multiple deprotonation steps and monooxidation step in different pH environments. ⁹	329
Figure S2.43. Reaction scheme for synthesis of (4'4-dicarboxy-2'2'-bipyridine)dichloroplatinum(II).	330
Figure S2.44. Photoelectrocatalysis cell block exploded view and photo of the device.	331
Figure S2.45. Steady-state absorption spectra of sensitised NiO films.....	332
Figure S2.46. SEM image of the dye-sensitized NiO surface containing 3-TMS BODIPY polymer and Pt-bipy catalyst.	332

Figure S2.47. Linear sweep (in the dark) for a NiO film sensitized with 3-TMS BODIPY polymer and Pt-bipy catalyst in pH 5 phthalate buffer vs Ag/AgCl. Scan speed 0.05 V/s.	333
Figure S2.48. Chronoamperometry measurement of NiO sensitized with 3-TMS BODIPY polymer and Pt-bipy, in pH 5 phthalate buffer with an applied potential of -0.3 V vs Ag/AgCl. A period of equilibration in the dark takes place till AM 1.5 1 sun illumination is introduced at approximately 380 seconds.	333
Figure S2.49. Control chronoamperometry experiment with bare NiO in pH 5 phthalate buffer with an applied potential of -0.3 V vs Ag/AgCl under 1 sun illumination. Chopping the light output had no impact on the current.	333
Figure S2.50. Quartz cuvettes showing monomer (left), diiodo monomer (centre) and polymer (right) in CH ₂ Cl ₂ , aerated solution.	336
Figure S3.1. ¹ H NMR (600 MHz) of BODIPY-2H in CDCl ₃	346
Figure S3.2. ¹ H NMR (600 MHz) of BODIPY-2I in CDCl ₃	346
Figure S3.3. Mass spectra for [M ⁺] for BODIPY-2I, diiodo monomer.	347
Figure S3.4. Size exclusion chromatography (SEC) trace of copolymer (dRI detection, PMMA standards).	348
Figure S3.5. a) UV-visible spectra of OH copolymer drop coated onto a cuvette surface, b) SEM image representing the morphology of the OH copolymer when drop coated on a surface.	349
Figure S3.6. a) UV-visible absorption spectra of copolymer in a range of solvents; dichloromethane (solid magenta), DMSO (solid blue), THF (solid red), toluene (solid cyan), acetone (solid violet), acetonitrile (solid black), chloroform (solid green) and b) Emission spectra of copolymer in the same range of solvents, λ _{exc} = 560 nm, 15 nm slit width. Inset shows normalised emission spectra of copolymer. All spectra recorded at room temperature in aerated solution.	350
Figure S3.7. Emission decay profiles for a) BODIPY-2H in CH ₂ Cl ₂ , b) copolymer in CH ₂ Cl ₂ , c) copolymer in CH ₃ CN and d) copolymer in DMSO. The λ _{exc} = 510 nm for all samples, and a detection wavelength of 520 nm for BODIPY-2H and 610 for the copolymer. All emission decays recorded at room temperature in aerated solution.	351
Figure S3.8. NIR singlet oxygen emission spectrum of Rose Bengal (red), copolymer (purple), BODIPY-2H (orange) in CH ₃ CN, following excitation at 525 nm.	352
Figure S3.9. a) TA spectra of diiodo monomer (BODIPY-2I) in CD ₃ CN shown at indicated time decays in ps and b) corresponding kinetic traces at 430 nm (blue) and 473 nm (red).	

The red line corresponding to the kinetic trace at 473 nm shows the monoexponential fit used to obtain S_1 lifetime of halogenated species. As the signal at 473nm decays ($\tau = 146$ ps), an additional species grows in at 430 nm ($\tau = 137$ ps). These are assigned to the decay of the BODIPY singlet state and formation of the triplet state which persists beyond the time frame of the experimental set-up. The grey dashed lines on the TA spectra correspond to kinetic traces on the right. The asterisk indicates the isosbestic point at 463 nm. $\lambda_{exc} = 525$ nm (0.4 μ J/pulse)..... 353

Figure S3.10. Transient absorption (TA) spectra of the copolymer and corresponding EAS spectra in (A) d_3 -acetonitrile, (B) d_6 -DMSO and (C) d_2 -dichloromethane, following excitation ($\lambda_{exc} = 525$ nm (0.4 μ J/pulse) (the gap in the TA plots corresponds to the excitation wavelength which is masked by a narrow band pass filter)..... 354

Figure S3.11. a) TA spectra of H-monomer (BODIPY-2H) in CH_3CN and b) corresponding kinetic traces at 431 nm (red) and 545 nm (grey). The grey dashed lines on the TA spectra correspond to kinetic traces on the right which do not decay to the baseline within the timeframe of the experiment. $\lambda_{exc} = 525$ nm (0.4 μ J/pulse)..... 355

Figure S3.12. FTIR spectra of 1,4-diethynylbenzene (black), BODIPY-2H (blue), BODIPY-2I (red) and copolymer (green) recorded in dichloromethane solution. Inset displays triple bond region $2400 - 2000$ cm^{-1} 356

Figure S3.13. a) TRIR spectra of the copolymer in CD_3CN in the spectral window of $1610 - 1290$ cm^{-1} at various time delays following excitation at 525 nm, and b) the corresponding EAS..... 357

Figure S3.14. TRIR spectra of copolymer in DMSO in the spectral window of $1610 - 1290$ cm^{-1} at various time delays following excitation at 525 nm. Arrows display spectral changes observed throughout the course of the experiment..... 357

Figure S3.15. TRIR spectra of BODIPY-2I in CD_3CN in the spectral window of $1610 - 1290$ cm^{-1} at various time delays following excitation at 525 nm. Arrows display spectral changes observed throughout the course of the experiment..... 358

Figure S3.16. TRIR spectra of BODIPY-2H in CD_3CN in the spectral window of $1610 - 1290$ cm^{-1} at various time delays following excitation at 525 nm. Arrows display spectral changes observed throughout the course of the experiment..... 358

Figure S3.17. TRIR spectra of the copolymer in $CHCl_3$ following pulsed photolysis ($\lambda_{exc} = 525$ nm) in the triple bond spectral region, recorded at various time delays, with arrows indicating the time dependent behaviour of the spectral features. Inset displays the kinetic traces at both $2103cm^{-1}$ and $2073cm^{-1}$ (corresponding to both red and blue dashed lines on spectra) and the biexponential fit (solid red and solid blue line) to obtain the decay lifetimes..... 359

Figure S3.18. UV-visible absorption spectra of copolymer in a range of solvents; especially depicting the stability of the compound in a DMSO/PBS solvent mixture (cyan colour).	361
Figure S3.19. Comparison on the photoactivated bactericidal activity of copolymer and its BODIPY-2H, Conditions: Bacterial strains Staphylococcus aureus (MSSA, ATCC 25923), methicillin-resistant S.aureus (MRSA, ATCC 43300), Esherichia.coli (E.coli, ATCC 25922) and an extended spectrum β -lactamase (ESBL) producing E.coli (CL11), [copolymer/BODIPY-2H] for gram-positive bacteria: 1 μ g/ml, [copolymer/monomer] for gram-negative bacteria: 5 μ g/ml, time of irradiation: 15 minutes, wavelength of light for irradiation λ ~525 nm.....	362
Figure S3.20. The half maximal inhibitory concentration (IC ₅₀) curve of OH copolymer under varied concentration on the keratinocyte HaCaT cells.....	364
Figure S4.1. ¹ H NMR spectra of M1. CDCl ₃ as a calibration standard, δ = 7.26 ppm.....	375
Figure S4.2. ¹³ C NMR spectra of M1. CDCl ₃ as a calibration standard, δ = 77.16 ppm.....	375
Figure S4.3. ¹ H NMR spectra of M2. CDCl ₃ as a calibration standard, δ = 7.26 ppm.....	376
Figure S4.4. ¹³ C NMR spectra of M2. CDCl ₃ as a calibration standard, δ = 77.16 ppm.....	376
Figure S4.5. SEC results of P1 showing the molecular weight distribution (g/mol) of the copolymeric chain for batch 1 (blue solid line) and batch 2 (green solid line). Both synthetic procedures for the synthesis of the polymer were carried out under identical experimental conditions, as per synthetic method described.	377
Figure S4.6. FTIR spectra of 1,4-diethynylbenzene, M1, M2 and P1 in CH ₂ Cl ₂ showing the molecular structure of each compound in inset. The assignment of vibrational bands are shown for C \equiv C at 2109 cm ⁻¹ (cyan dashed line) and for terminal C \equiv C-H at 3297cm ⁻¹ (blue dashed line) for 1,4-diethynylbezne and at 2203cm ⁻¹ for C \equiv C of P1 (magenta dashed line).	378
Figure S4.7. UV-visible absorption spectra of P1 in toluene (black solid line), THF (red solid line), CHCl ₃ (cyan solid line), DMSO (violet solid line), CH ₂ Cl ₂ (olive solid line), DMF (green solid line) and CH ₃ CN (magenta solid line).	379
Figure S4.8. a) Photoluminescence spectra of P1 in toluene (black circles), THF (red triangles), CHCl ₃ (cyan circles), DMSO (violet triangles), CH ₂ Cl ₂ (olive triangles), DMF (green circles) and CH ₃ CN (magenta circles), recorded using 1.0 nm slit width, λ_{exc} = 540 nm and (b) normalised spectra in the same solvents, λ_{exc} = 540 nm.	379
Figure S4.9. Photoluminescence spectra of M1 (red dashed line), M2 (green dashed line) and P1 (purple dashed line) using 490 nm excitation and 0.6 nm slit width for both the	

excitation and emission beam. Samples were isoabsorptive at the excitation wavelength. All samples recorded at room temperature in CH ₂ Cl ₂ . Inset displays zoomed part of the spectra between 540 – 700 nm.....	380
Figure S4.10. CIE diagram of the luminescence of M1 (blue), M2 (red) and P1 (black) each showing x and y co-ordinates in brackets.	381
Figure S4.11. Normalised absorption (grey dashed spectra) and excitation spectra (solid red and solid black line) of P1 in (a) toluene, (b) THF, (c) CHCl ₃ (inset showing zoomed part of spectra from 520 – 580 nm) and (d) CH ₂ Cl ₂ . Emission detection wavelengths used for each excitation spectra are shown in the legend.....	382
Figure S4.12. Normalised absorption (grey dashed spectra) and excitation spectra (solid red, solid green, and solid black line) of P1 in (a) DMSO and (b) DMF. Insets showing zoomed part of spectra from 525 – 565 nm. Emission detection wavelengths used for each excitation spectra are shown in the legend.	382
Figure S4.13. Normalised absorption spectra (blue solid line) and excitation spectra (red dashed line) of M1 in CHCl ₃ . The excitation spectrum is observed at 530 nm.	383
Figure S4.14. a) Singlet oxygen NIR emission of P1 (red solid line) and M2 (green solid line) following 530 nm excitation and b) singlet oxygen NIR emission of M1 (blue solid line) following 505 nm excitation. The purple spectra in (a) and (b) represent the standard, diiodo BODIPY monomer ($\Phi_{\Delta} = 0.87$), IBDP. ² All samples were recorded in aerated dichloromethane solution at room temperature.....	384
Figure S4.15. Emission decay of P1 in toluene using a) 375 nm LED as excitation source and b) 510 nm LED as excitation source. $\lambda_{\text{det}} = 622$ nm. Inset shows biexponential lifetimes obtained (τ_1 and τ_2 (ns)), the percentage contribution of each lifetime component in brackets (%) and the goodness of fit (χ^2). The sum of residuals is shown below each emission decay curve.....	385
Figure S4.16. Emission decay of P1 in THF using a) 375 nm LED as excitation source and b) 510 nm LED as excitation source. $\lambda_{\text{det}} = 622$ nm. Inset shows biexponential lifetimes obtained (τ_1 and τ_2 (ns)) and the percentage contribution of each lifetime component in brackets (%) and the goodness of fit (χ^2). The sum of residuals is shown below each emission decay curve.....	385
Figure S4.17. Emission decay of P1 in CHCl ₃ using a) 375 nm LED as excitation source and b) 510 nm LED as excitation source. $\lambda_{\text{det}} = 622$ nm. Inset shows biexponential lifetimes obtained (τ_1 and τ_2 (ns)) and the percentage contribution of each lifetime component in brackets (%) and the goodness of fit (χ^2). The sum of residuals is shown below each emission decay curve.....	386

Figure S4.18. Emission decay of P1 in CH ₂ Cl ₂ using a) 375 nm LED as excitation source and b) 510 nm LED as excitation source. $\lambda_{\text{det}} = 622$ nm. Inset shows biexponential lifetimes obtained (τ_1 and τ_2 (ns)) and the percentage contribution of each lifetime component in brackets (%) and the goodness of fit (χ^2). The sum of residuals is shown below each emission decay curve.....	386
Figure S4.19. Emission decay of P1 in DMSO using a) 375 nm LED as excitation source and b) 510 nm LED as excitation source. $\lambda_{\text{det}} = 590$ nm. Inset shows biexponential lifetimes obtained (τ_1 and τ_2 (ns)) and the percentage contribution of each lifetime component in brackets (%) and the goodness of fit (χ^2). The sum of residuals is shown below each emission decay curve.....	387
Figure S4.20. Emission decay of P1 in DMF using a) 375 nm LED as excitation source and b) 510 nm LED as excitation source. $\lambda_{\text{det}} = 590$ nm. Inset shows biexponential lifetimes obtained (τ_1 and τ_2 (ns)) and the percentage contribution of each lifetime component in brackets (%) and the goodness of fit (χ^2). The sum of residuals is shown below each emission decay curve.....	387
Figure S4.21. Emission decay of P1 in CH ₃ CN using a) 375 nm LED as excitation source and b) 510 nm LED as excitation source. $\lambda_{\text{det}} = 590$ nm. Inset shows biexponential lifetimes obtained (τ_1 and τ_2 (ns)) and the percentage contribution of each lifetime component in brackets (%) and the goodness of fit (χ^2). The sum of residuals is shown below each emission decay curve.....	388
Figure S4.22. a) The optimised molecular structure of M2 with the two iodine atoms indicated in purple and the anthracenyl substituents towards the top of the molecule, b) the EDDM for the lowest energy triplet state T ₁ , c) the T ₂ state which is an anthracenyl-based state, d) and e) are nearly degenerate anthracenyl-to-BODIPY charge-transfer states (T ₃ and S ₁) white f) and g) are BODIPY-centred states where (g) can be optically populated (i.e., the S ₂ state) (red boxes indicate triplet and blue represent singlet states).	389
Figure S4.23. The energy variation of the ground-state and all excited states up to and including the lowest energy singlet excited state against dihedral angle between BODIPY units in the 2-BODIPY oligomer.	393
Figure S4.24. The evolution adjusted difference spectra of the TA spectra following photolysis of P1 at 525 nm in CD ₃ CN displaying an initially formed species (black) which reacts in 4 ps to form the singlet (red) which forms a spin-coherent triplet (blue) excited state which in turn forms the spatially discrete triplet pair (green) (the inset shows the kinetics of the reaction sequence).	395

Figure S4.25. a) The evolution difference spectra of the TRIR spectra following photolysis of P1 at 525 nm in CD ₃ CN displaying a Franck-Codon state (black), singlet (red) and spin coherent triplet (blue) and spatially discrete triplet (green) (the inset shows the kinetics of the reaction sequence showing singlet decay (red) and spin coherent triplet decay (blue) and production of the spatially discrete triplet (green) over the course of the experiment); b) the difference spectra generated by subtracting the evolution adjusted difference spectrum of the spin-coherent triplet from the equivalent spectrum of the spatially discrete triplet in CDCl ₃ (red), DCM (green) and ACN (blue).	396
Figure S4.26. a) Transient absorption spectra of polymer P1 in THF solution at 32 μs, 47 μs, 86 μs, 125 μs and 242 μs following excitation with pump laser 355 nm. Sample degassed using three freeze-pump-thaw-cycles. Arrows indicate the depletion of features during measurement, b) Kinetic traces at 445 nm (dotted blue) and 545 nm (dotted red). Monoexponential fit lines at 445 nm (solid blue) and 545 nm (solid red). Inset displays triplet lifetime obtained in μs.....	397
Figure S4.27. a) Transient absorption spectra of diiodo BODIPY monomer (M2) in deoxygenated THF solution measured at 15 μs, 24 μs, 44 μs, 63 μs, 122 μs and 190 μs after laser excitation ($\lambda_{exc} = 355$ nm). Sample degassed using three freeze-pump-thaw cycles, b) Kinetic decay traces at 445 nm (dotted blue) and 525 nm (dotted red). Monoexponential fit lines at 445 nm (solid blue) and 525 nm (solid red). Inset triplet lifetime obtained in microseconds (μs).....	397
Figure S4.28. a) Transient absorption spectra of BODIPY monomer (M1) in deoxygenated THF solution measured at 6 μs, 9 μs, 12 μs, 14 μs, 15 μs, 19 μs and 30 μs after laser excitation ($\lambda_{exc} = 355$ nm). Sample degassed using three freeze-pump-thaw cycles and b) Kinetic decay traces at 420 nm (dotted blue) and 520 nm (dotted red). Monoexponential fit lines at 420 nm (solid blue) and 520 nm (solid red). Inset triplet lifetime obtained in microseconds (μs).....	398
Figure S4.29. Cyclic voltammograms of a bare glassy carbon (GC) electrode (a), a GC electrode coated with a film of M1 (b), and a GC electrode coated with a film of P1 (c). All voltammograms were recorded initially negative sweep direction at a scan rate of 100 mV.s ⁻¹ at room temperature in a deoxygenated 0.1 M TBAPF ₆ /acetonitrile electrolyte solution.	399
Figure S4.30. UV-visible absorption spectra of M1 on a thin film (green solid line). Inset showing Tauc Plot used to calculate the optical band gap energy by the onset of absorption. Band gap energy (E_g) shown in blue.	400

Figure S4.31. UV-visible absorption spectra of P1 on a thin film (red solid line). Inset showing Tauc Plot used to calculate the optical band gap energy by the onset of absorption. Band gap energy (E_g) shown in blue.	400
Figure S4.32. Photocatalytic activity of polymer, P1 (0.1, 0.2, 0.4, 0.8 and 1.2 mM) using TiO ₂ Pt nanoparticles (6 mg) and 0.1 M ascorbic acid in a 4 mL 1:1 THF/H ₂ O (v/v) under 300 W Xe arc lamp irradiation, $\lambda > 420$ nm. Graph displaying hydrogen generation ($\mu\text{mol g}^{-1}$).	401
Figure S4.33. a) Photocatalytic activity of polymer, P1 (0.4 mM) using TiO ₂ Pt nanoparticles in a 1:1 THF/H ₂ O (v/v) solution and either TEOA (10 vol%) – grey dashed column or ascorbic acid (0.1 M) – blue dashed column. Hydrogen evolution displayed in $\mu\text{mol H}_2 \text{g}^{-1}$ based on mass of P1. Inset shows colour change of photocatalytic solution after 6 hr irradiation (300 W Xe arc lamp, $\lambda > 420$ nm) using TEOA (10 vol%) as SA. (b) UV-visible absorption spectra of P1 in 0.1 M AA solution before irradiation (blue solid), after 6 hours irradiation (blue dash) and P1 in TEOA solution (10 vol%) before irradiation (grey solid) and after 6 hours irradiation (grey dash). Green arrow shows growth of new band at 506 nm.	402
Figure S4.34. Energy level diagram (eV) showing the TiO ₂ conduction band (CB) edge, the P1 HOMO (-5.45 eV) and LUMO (-3.63 eV) band edge (calculated with the data extracted from the CV experiments). Red arrows indicate direction of electron transfer mechanisms during photocatalysis. Purple arrow shows the proton reduction reaction to liberate hydrogen gas at the Pt ⁰ particles catalytic site.....	402
Figure S4.35. EDX spectrum of Pt TiO ₂ nanoparticles. Signals for Pt are detected.	403
Figure S4.36. Scanning electron micrograph elemental mapping image of Pt TiO ₂ nanoparticles showing Pt detection (grey particles) on TiO ₂ surface (dark background).	403
Figure S5.1. (TD)-DFT simulated iso-density surface ($\rho = \pm 0.002$) of the spin density distribution of singly oxidized (<i>top row</i>) and singly reduced Ru1 (<i>right</i>) and Ru2 (<i>left</i>).	411
Figure S5.2. Cyclic voltammograms of solutions of Ru1 and Ru2 at room temperature in acetonitrile (scan rate: 0.2 V·s ⁻¹ , supporting electrolyte: 0.1 M ⁿ Bu ₄ PF ₆). The peak potentials are referenced vs. the Fc ⁺ /Fc redox couple.	411
Figure S5.3. Mean molar extinction coefficients of the Ruthenium complexes Ru1 and Ru2 (a) and the corresponding dppz-ligands L1 and L2 (d) in acetonitrile. TD-DFT simulated absorption spectra (dashed grey lines) of Ru1 (b), Ru2 (c), L3 (e) and L2 (f) and charge	

density differences of MLCT_{phz} and $\text{ILCT}_{\text{tz/phz}}$ states. The states of $\text{ILCT}_{\text{tz/phz}}$, MLCT , $\pi\pi^*_{\text{dppz}}$ and $\pi\pi^*_{\text{carb}}$ character are highlighted in blue, green, black and orange, respectively.....	412
Figure S5.4. <i>Left</i> : Normalized UV-vis absorption spectra of the Ru(II) complexes – Ru1 and Ru2 – and their corresponding ligands – L1 and L2 – in acetonitrile. <i>Right</i> : Normalized absorption spectra of Ru1 (a) and Ru2 (b) in dichloromethane (DCM) and acetonitrile (ACN).....	412
Figure S5.5. Steady-state emission spectra of Ru1 and Ru2 in acetonitrile upon excitation at 420 nm.....	414
Figure S5.6. Ultrafast transient absorption spectra, decay associated spectra and kinetic traces at some selected probe wavelengths (as indicated by vertical lines in the transient spectra) of Ru1 at 403 nm excitation (0.5 mW, OD at $\lambda_{\text{exc}} = 0.16$) in acetonitrile.	415
Figure S5.7. Ultrafast transient absorption spectra, decay associated spectra and kinetic traces at some selected probe wavelengths (as indicated by vertical lines in the transient spectra) of Ru2 at 403 nm excitation (0.5 mW, OD at $\lambda_{\text{exc}} = 0.20$) in acetonitrile.	415
Figure S5.8. Time-resolved data of Ru2 in acetonitrile at delay times up to 10 ns (a, b) and on a sub- μs timescale (e-i): Ultrafast transient absorption spectra (a) and decay associated spectra (b) at 403 nm excitation (0.5 mW, OD at $\lambda_{\text{exc}} = 0.20$). Nanosecond transient absorption (e) and emission spectra (h) and their corresponding decay associated spectra (ns-TA: f, ns-Em: i) at 410 nm excitation (3.0 mW, OD at $\lambda_{\text{exc}} = 0.12$). TD-DFT simulated absorption spectra of $^1\text{Ru2}$ (solid, orange line) and $^3\text{Ru2}$ (dotted, dark orange line). The vertical transition energies and their corresponding oscillator strength are shown by bars (c, d), which were broadened using Gaussian functions (c, full-width half-maximum of 0.30 eV). Comparison of the decay associated spectra of τ_4 (grey marks) and τ_5 (black marks) to the simulated difference spectrum (solid, orange line) for an $^1\text{Ru2}$ to $^3\text{Ru2}$ excitation and spin density distribution of Ru2 in the lowest triplet state (d). Comparison of the steady-state and transient emission spectrum (j) recorded upon excitation at 410 nm (ns-Em spectrum at a delay time of 100 ns). The inset figure g shows the emission decay kinetic at 680 nm (filled marks) compared to the transient absorption kinetic trace at 680 nm (empty marks). The kinetic traces are normalized at 30 ns. The solid grey lines in figure f and i represent the steady-state emission spectrum and TA of the long-lived $^3\text{MLCT}_{\text{phen}}$ state of Ru0, respectively.....	416
Figure S5.9. Ultrafast transient absorption spectra, decay associated spectra and kinetic traces at some selected probe wavelengths (as indicated by vertical lines in the transient spectra) of Ru1 at 470 nm excitation (0.15 mW, OD at $\lambda_{\text{exc}} = 0.30$) in acetonitrile. ..	417

Figure S5.10. Ultrafast transient absorption spectra, decay associated spectra and kinetic traces at some selected probe wavelengths (as indicated by vertical lines in the transient spectra) of Ru2 at 470 nm excitation (0.15 mW, OD at $\lambda_{exc} = 0.15$) in acetonitrile. ..	417
Figure S5.11. Time-resolved spectra of Ru1 upon 470 nm excitation in dichloromethane: Ultrafast transient absorption spectra (a, 0.2 mW, OD at $\lambda_{exc} = 0.3$) and the corresponding decay associated spectra (b) and transient emission spectra (c, 3.5 mW, OD at $\lambda_{exc} = 0.3$) and corresponding decay associated spectra (d). The solid grey line in figure d shows the steady-state emission spectrum of Ru0.....	418
Figure S5.12. Ultrafast transient absorption spectra, decay associated spectra and kinetic traces at some selected probe wavelengths (as indicated by vertical lines in the transient spectra) of Ru1 at 470 nm excitation (0.15 mW, OD at $\lambda_{exc} = 0.3$) in DCM.	418
Figure S5.13. Ultrafast transient absorption spectra, decay associated spectra and kinetic traces at some selected probe wavelengths (as indicated by vertical lines in the transient spectra) of Ru2 at 470 nm excitation (0.15 mW, OD at $\lambda_{exc} = 0.15$) in DCM.	418
Figure S5.14. ^1H NMR spectrum of 2 in CDCl_3	419
Figure S5.15. ^{13}C NMR spectrum of 2 in CDCl_3	419
Figure S5.16. ^1H NMR spectrum of 3 in d_6 -DMSO.	420
Figure S5.17. ^1H NMR spectrum of L1 in CDCl_3	420
Figure S5.18. ^1H NMR spectrum of 4 in CDCl_3	421
Figure S5.19. ^{13}C NMR spectrum of 4 in CDCl_3	421
Figure S5.20. ^1H NMR spectrum of 5 in d_6 -DMSO.	422
Figure S5.21. ^{13}C NMR spectrum of 5 in d_6 -DMSO.	422
Figure S5.22. ^1H NMR spectrum of 6 in d_6 -DMSO.	423
Figure S5.23. ^1H NMR spectrum of 7 in CDCl_3	423
Figure S5.24. ^{13}C NMR spectrum of 7 in CDCl_3	424
Figure S5.25. ^1H NMR spectrum of 8 in CDCl_3	424
Figure S5.26. ^{13}C NMR spectrum of 8 in CDCl_3	425
Figure S5.27. ^1H NMR spectrum of L2 in CDCl_3	425
Figure S5.28. ^{13}C NMR spectrum of L2 in CDCl_3	426
Figure S5.29. ^1H NMR spectrum of Ru1 in d_3 -ACN.....	426
Figure S5.30. ^1H NMR spectrum of Ru2 in d_6 -acetone.	427
Figure S5.31. High resolution MS of Ru2.....	427
Figure S5.32. High resolution MS of Ru1.....	428

Table of Schemes

Scheme 1.1. Mechanistic steps of natural photosynthesis occurring in chlorophyll of plants. Figure adapted from Llobet et al. 2014. ²¹	11
Scheme 1.2. Reductive quenching (left) and oxidative quenching (right) mechanisms for photocatalytic hydrogen evolution. PS shown in red. Adapted from literature. ²⁸	16
Scheme 1.3. A schematic representation of photocatalytic hydrogen evolution using dye sensitised TiO ₂ semiconductor nanoparticles. VB – valence band, CB – conduction band. Adapted from literature. ³⁰	22
Scheme 1.4. Dexter energy transfer process to from ground state PS and excited state CAT. ⁵¹	26
Scheme 1.5. Förster energy transfer process to form ground state PS and excited state CAT. ⁵¹	27
Scheme 1.6. Simplified spin diagram schematic for the electronic processes that occur during singlet fission. ⁵⁴	28
Scheme 1.7. Photoexcitation of the ground state (GS) A-D-A repeating unit to populate a low-lying singlet excited state with significant charge transfer (S ₁ /CT) character to finally populate a correlated triplet pair (¹ TT). Question mark denotes the possibility of three distinct mechanisms that can occur to populate the ¹ TT state – direct, mediated and delayed mechanisms. ⁶⁰	35
Scheme 1.8. Schematic of the instrumental set-up in a typical TCSPC spectrometer. ⁶⁵	38
Scheme 1.9. Schematic displaying a simplified experimental set-up for "pump-probe" technique for ultrafast TA spectroscopy experiments. Adapted from literature reference. ⁶⁶	40
Scheme 1.10. Reactions employed in polymer synthesis. Dashed bond represents polymer chain. Adapted from reference. ⁷⁵	44
Scheme 1.11. Synthetic route in the overall synthesis of the BODIPY core, carried out at room temperature in anhydrous CH ₂ Cl ₂ solution. ¹¹⁷	65
Scheme 1.12. Sonogashira Pd catalysed cross-coupling catalytic cycle including Cu cycle as co-catalyst (below).	66
Scheme 1.13. Oxidative condensation reaction of benzylamine (1 mmol) with 2-aminothiophenol (2 mmol) under aerated conditions, using visible light ($\lambda > 385$ nm) and P-BODIPY on silica (1 mol%) as the photocatalyst. ¹⁵⁴	94
Scheme 5.1. Synthetic route of the ligands L1 and L2.	234

Scheme S4.1. Synthetic outline of M1, M2 and P1. Reaction conditions a) i) TFA, ii) DDQ, iii) BF_3OEt_2 , TEA in dry CH_2Cl_2 under flow of N_2 , 2 days at room temperature, b) HIO_3 , I_2 in EtOH/ H_2O under flow of N_2 , 2 hours at 60 °C, c) $[\text{Pd}(\text{PPh}_3)_4]$, CuI, dry THF/Diisopropylamine, 1:1 (v/v) under flow of N_2 , 3 days at 80 °C..... 371

Table of Tables

Table 1.1. A brief summary of BODIPYs for hydrogen evolution obtained in homogenous photocatalysis. PS – photosensitiser, CAT – catalyst, sol – solvent mixture, SA – sacrificial agent, TON – turnover number, ref – reference, THF – tetrahydrofuran, TEA – triethylamine, TEOA – triethanolamine.....	68
Table 1.2. Photophysical properties of BODIPY compounds as shown in Figure 1.59. All measurements recorded in dichloromethane solution.	89
Table 1.3. Photophysical properties of water soluble BODIPY compounds. Note absorption and emission spectra were recorded in CH_2Cl_2 . ¹⁵² Structures shown in Figure 1.62....	92
Table 2.1. Photophysical properties of the monomer and polymer. All spectra were recorded in CH_2Cl_2 at room temperature.	133
Table 2.2. Fluorescence decay lifetimes of the monomer and polymer using 510 nm LED diode. %rel of each lifetime decay represents the relative contribution of each lifetime decay (%).	134
Table 2.3. Summary of the lifetimes in the TAS experiments for the ESA feature at ~ 445 nm (using a biexponential function) following excitation at 525 nm.	137
Table 3.1. Photophysical properties of BODIPY 2-H and copolymer carried out in CH_2Cl_2	162
Table 3.2. Summary of lifetimes obtained using global analysis from psTAS experiments in different solvents following excitation at 525 nm. The Reichardt parameter $E_T(30)$ is shown to indicate solvent polarity. ⁷⁷	164
Table 4.1. The photophysical properties of M1, M2 and polymer, P1 recorded in CH_2Cl_2 at 298 K. ^a Fluorescence quantum yields were calculated using 3-pyridine BODIPY as a std ($\Phi_{\text{std}} = 0.62$, $\lambda_{\text{exc}} = 490$ nm in CH_2Cl_2). ⁷³ ^b Fluorescence lifetimes were calculated using TCSPC ($\lambda_{\text{exc}} = 510$ nm in degassed CH_2Cl_2 solution). ^c Singlet oxygen quantum yield	

(Φ_{Δ}), diiodobodipy used as a standard ($\Phi_{\Delta} = 0.87$ in CH_2Cl_2). ⁷⁴ $^{\text{e}}$ 530 nm excitation. For full experimental details see Appendix C.	186
Table 4.2. Summary of emission decay lifetimes of the polymer, P1 obtained using both 375 nm and 510 nm excitation sources. Luminescence decay recorded at 622 nm for toluene, THF, CHCl_3 , CH_2Cl_2 and 590 nm for DMSO, DMF and CH_3CN . The percentage contribution of each radiative lifetime component (amplitude) is shown as a percentage of each lifetime (%). The Reichardt parameter, E_T is shown to indicate the variance in solvent polarity. ⁷⁵	187
Table 4.3. A summary of TA spectral features for M1, M2 and polymer P1 following 355 nm excitation (in freeze pumped thawed THF solutions). Triplet lifetime (τ_T) values were obtained using mono-exponential decay fittings.	202
Table 4.4. Summary of electrochemical results obtained for glassy carbon electrodes coated with thin films of M1 and P1 – see Appendix C, Figure S4.29.....	203
Table 5.1. Summary of the photophysical and electrochemical properties of Ru1 and Ru2. As a reference to compare the literature known compound Ru0 ($[\text{Ru}(\text{bpy})_2\text{dppz}]^{2+}$) was added to the table. values taken from: (a) Ref. ⁶¹ , (b) Ref. ⁶³ , (c) depicted potentials are peak potentials, corrected against $E_{1/2} \text{Fc/Fc}^+$	236
Table 6.1. The orbital energies for orbitals close to the valence level with the contributions of molecular fragments to those orbitals	273
Table S2.1. Summary of photophysical properties monomer and diiodo monomer in CHCl_3	319
Table S2.2. Summary of photophysical properties of 3-TMS monomer and 3-TMS polymer.	326
Table S2.3. Summary of experimental parameters using polymer as PS and cobalt cobaloxime as catalyst, irradiation Xe arc lamp, $\lambda > 420$ nm. SA – sacrificial agent, TEA – triethylamine, AA – ascorbic acid. A parameter altered in every subsequent experiment is shown in red.....	328
Table S2.4. Comparison of photocatalytic experimental conditions and hydrogen evolution rate (HER) of organic polymeric photocatalysts reported in the literature. COF – covalent organic framework, CMP – conjugated microporous polymer.	334

Table S3.1. Summary of photophysical properties of copolymer analysed in a range of solvents – dichloromethane, dimethyl sulfoxide, THF, toluene, acetone, acetonitrile and chloroform. The Reichardt parameter $E_T(30)$ (kcal mol ⁻¹) is shown beside each solvent in brackets to indicate solvent polarity. ⁷ All spectra recorded at room temperature in aerated solution. 560 nm excitation wavelength was used for emission spectra with 15.0 nm slit width. All samples were isoabsorptive at the excitation wavelength.	350
Table S3.2. Fluorescence decay lifetimes (τ) including margin of error associated with each lifetime, % relativity of each component (B_i) for BODIPY-2H in CH ₂ Cl ₂ and copolymer in CH ₂ Cl ₂ , CH ₃ CN and DMSO. $\lambda_{exc} = 510$ nm using FLS1000 photoluminescence spectrometer.	351
Table S3.3. Lifetimes obtained (ps) for the species observed in the diiodo monomer at 472 and 430 nm, corresponding to decay of the singlet, and formation of the triplet state.	353
Table S3.4. Summary of lifetimes obtained (μ s) of the copolymer from a monoexponential fit of both the ESA feature (446 nm) and GSB feature (524 nm).	355
Table S4.1. SEC results of P1 showing the number average molecular weight of the polymer (M_n), the weight average molecular weight (M_w) and the polydispersity of the polymer (D_M), calculated by M_w/M_n . The different batches of polymer indicate separate synthetic reactions under identical experimental conditions.	377
Table S4.2. Summary of absorption and emission maxima for P1 in toluene, THF, CHCl ₃ , DMSO, CH ₂ Cl ₂ , DMF and CH ₃ CN. Reichardt parameter (E_T) is shown to indicate the solvent polarity. ¹⁰ Emission spectra were collected following 540 nm excitation wavelength with 1.0 nm slit width for all samples. All samples recorded at room temperature.	380
Table S4.3. The energy (eV), multiplicity, oscillator strength and electron density difference maps for M2 (red volumes are regions where the electron density is greater in the excited state compared to the ground state and blue volumes are regions where the electron density in the excited state is less than that of the ground state).	390
Table S4.4. The multiplicity, energy (eV) and electron density difference maps (iso value 0.0002) for the twelve lowest energy excited states of the 6-BODIPY oligomer (cam-B3LYP/6-31G(d,p) (red volumes are regions where the electron density is greater in the excited state compared to the ground state and blue volumes are regions where the electron density in the excited state is less than that in the ground state).	392

Table S4.5. The vertical excitation energies to the lowest energy singlet state, and equivalent wavelengths as the dihedral angle between the BODIPY units in the 2-BODIPY oligomer was varied.	394
Table S4.6. The calculated absorption (based on the energy difference between the ground-state and S ₁ state) and emission based on the energy difference between the ¹ (TT) states and the ground-state) wavelengths for various sequential twist angles for the 6-BODIPY oligomer.	394
Table S4.7. Table of experimental parameters and resulting hydrogen evolution of the polymer under various photocatalytic conditions. Conditions remaining constant – TiO ₂ Pt nanoparticles (6 mg), ascorbic acid (0.10 M) in 1:1 (v/v) THF: H ₂ O solution (4 mL total volume). Concentration of polymer, P1 described in table. Irradiation with Xe arc lamp, λ > 420 nm.	401
Table S5.1. Change density differences (CDD, TD-B3LYP/TZVP) of some singlet states involved in the photoexcitation of Ru1 and Ru2. Excitation occurs from blue to yellow (ρ = ±0.0015).	413
Table S6.1. The valence and low-lying singlet virtual orbitals, principle transitions for [Ru(phen) ₂ (dppz)] ²⁺ calculated in vacuo, with their energies (photon equivalent) and oscillator strengths with fragment contributions (Ru, dppz, and phen)); red highlighting represents dppz-based transitions, blue phen-based and yellow transitions with both phen and dppz contributions (L3 = all three ligands).	430
Table S6.2. The valence and low-lying virtual orbitals, principle transitions for [Ru(phen) ₂ (dppz)] ²⁺ •2H ₂ O calculated in vacuo, with their energies (photon equivalent) and oscillator strengths with fragment contributions (Ru, dppz, phen, and water); red highlighting represents dppz-based transitions, blue phen-based and yellow transitions with both phen and dppz contributions (L3 = all three ligands).	431
Table S6.3. The orbital assignments of the optically accessible excited states of [Ru(phen) ₂ (dppz)] ²⁺ (in vacuo) UB3LYP/LanL2DZ.	438
Table S6.4. The Orbital Assignments of the Optically Accessible Excited States of [Ru(phen) ₂ (dppz)] ²⁺ •2H ₂ O (in vacuo) UB3LYP/LanL2DZ.	442
Table S6.5. Representations of the valence molecular orbitals of [Ru(Phen) ₂ (dppz)] ²⁺ and [Ru(phen) ₂ (dppz)] ²⁺ •2H ₂ O (iso value 0.02) with their energies (eV) and orbital designation number.	447

Table of Equations

Equation 1.1. Steam-methane reformation equation to generate hydrogen	8
Equation 1.2. Conversion of carbon monoxide to hydrogen	8
Equation 1.3. Overall photosynthesis reaction using solar energy to generate glucose, oxygen, and water.	10
Equation 1.4. Photocatalytic splitting of water to generate hydrogen and oxygen	13
Equation 1.5. Oxidation of water to form oxygen	13
Equation 1.6. Reduction of protons to form hydrogen	13
Equation 1.7. Photoexcitation of the photosensitising dye to produce dye*	20
Equation 1.8. Electron injection into the conduction band of TiO ₂ to form a charge separated state.	20
Equation 1.9. Regeneration of the ground state dye by the sacrificial agent (SA)	20
Equation 1.10. Proton reduction at the platinum (Pt) centre following charge migration to the surface.	20
Equation 1.11. Deactivation of the excitation state dye (dye*) via radiative loss.	21
Equation 1.12. Deactivation of the charge separation state via charge recombination.	21
Equation 1.13. Energy transfer equation between PS (D) and CAT (A).	26
Equation 1.14. Transient absorption data displayed as a change in optical density detected from sample.	40
Equation 1.15. Formation of the triplet excited state of the PS.	103
Equation 1.16. Generation of singlet oxygen via an energy transfer mechanism.	103

Abbreviations

AA	Ascorbic acid
ACN	Acetonitrile
AIBN	2,2'-azobis(2-methylpropionitrile)
AQY	Apparent quantum yield
BODIPY	4,4-difluoro-4-bora-3a,4a-diaza-s-indacene
Bpy	2,2'-bipyridine
CAT	Catalyst
CB	Conduction band
CMPs	Conjugated microporous polymers
COFs	Covalent organic frameworks
CSS	Charge separated state
CT	Charge transfer
CTFs	Covalent triazine frameworks
CV	Cyclic voltammetry
D-A	Donor-acceptor
DAS	Decay associated spectra
DCM	Dichloromethane
DDQ	2,3-dichloro-5,6-dicyano-1,4-benzoquinone
DMSO	Dimethylsulfoxide
dppz	Dipyrido[3,2- <i>a</i> :2'3'- <i>c</i>]phenazine
EA	electron affinity
EDDM	Electron density difference map
EDG	Electron donating group
EPA	Environmental protection agency
ER	Electron relay
ESA	Excited state absorption
EU	European Union
EWG	Electron withdrawing group
GHG	Greenhouse gas
GPC	Gel permeation chromatography
GS	Ground state
GSB	Ground state bleach

HEC	Hydrogen evolution catalyst
HER	Hydrogen evolution rate
HOMO	Highest occupied molecular orbital
ICP-MS	Inductively coupled plasma mass spectrometry
ICT	Intramolecular charge transfer
IR	Infrared
ISC	Intersystem crossing
iSF	Intramolecular singlet fission
LED	Light emitting diode
LOH	Liquid organic hydride
LUMO	Lowest unoccupied molecular orbital
MLCT	Metal-to-ligand charge transfer
MOF	Metal organic framework
MEG	Multiple exciton generation
NADPH	Nicotinamide adenine dinucleotide phosphate
NDP	National development plan
NHE	Normal hydrogen electrode
OD	Optical density
OEC	Oxygen evolution catalyst
PCE	Power conversion efficiency
PDT	Photodynamic therapy
PEC	Photoelectrochemical cells
POPs	Porous organic polymers
PS	Photosensitiser
PSI	Photosystem one
PSII	Photosystem two
RAL	Rutherford Appleton laboratory
RED	Renewable energy directive
ROS	Reactive oxygen species
SA	Sacrificial agent
SAR	Structure activity relationship
SE	Stimulated emission
SEAI	Sustainable energy authority of Ireland
SEC	Size exclusion chromatography

SF	Singlet Fission
SHE	Standard hydrogen electrode
TA	Transient absorption
TAC	Time-to-amplitude
TAS	Transient absorption spectroscopy
TCSPC	Time correlate single photon counting
TEA	Triethylamine
TEOA	Triethanolamine
TGA	Thermogravimetric analysis
THF	Tetrahydrofuran
TICT	Twisted intramolecular charge transfer
TMS	Trimethylsilyl
TOF	Turnover frequency
TON	Turnover number
TRIR	Time resolved infrared spectroscopy
TW	Terawatts
UV	Ultraviolet
VB	Valence band

Units of measurement and symbols

λ	Wavelength
τ	Lifetime
ε	Molar absorption coefficient
μL	Microlitre
μs	Microsecond
$E_{\text{g}}^{\text{chem}}$	Electrochemical band gap
$E_{\text{g}}^{\text{opt}}$	Optical band gap
ΔA	Change in absorption
ΔG°	Gibbs free energy
cm^{-1}	Reciprocal wavelength
eV	Electron volts
fs	Femtosecond
g	Gram
hr	Hour(s)
K	Kelvin
L	Litre
M	Molar
mg	Milligram
MHz	Megahertz
min	Minute
mL	Millilitre
mM	Millimolar
mol	Mole
nm	Nanometre
ns	Nanosecond
$^{\circ}\text{C}$	Degrees Celsius
ps	Picosecond
v/v	Volume per volume
W	Watt
Φ_{Δ}	Singlet oxygen quantum yield
Φ_{fl}	Fluorescence quantum yield

Thesis Abstract

Development of efficient and robust organic-based systems for light-driven hydrogen evolution is crucial to the progression of cost-effective green hydrogen production as an alternative to the burning of fossil fuels. Conjugated organic polymers offer potential for advancement in this area mainly fuelled by their tunability, low-cost and availability of starting materials. The main objective this research was to incorporate boron-dipyrromethene (BODIPY) chromophores into a polymeric backbone and investigate the activity of a series of BODIPY polymers for hydrogen generation. Although extensive research has been carried out on inorganic complexes for hydrogen evolution, many studies utilise ultraviolet (UV) light to drive these reactions and their activity using visible light is very poor. This project aims to surmount this limitation in the development of BODIPY polymers that absorb in the visible region of the solar spectrum. Furthermore, existing research on inorganic photocatalysts require the use of expensive and rare metals in their overall synthesis – the polymers reported in this project are comprised of fully organic-based molecular architectures and their activity for hydrogen evolution was studied in conjugation with an earth-abundant cobalt-based molecular catalyst. The novel BODIPY polymers were characterised using ^1H , ^{13}C NMR spectroscopy, gel permeation chromatography, UV-visible absorption, and photoluminescence spectroscopy. Little is known about the mechanism of polymeric photocatalysts and their activity that leads to enhancement in hydrogen evolution. The experimental work presented here provides one of the first investigations into the photodynamic properties of the polymers in solution-based studies. This was carried out using both transient absorption (TA) and time-resolved infrared (TRIR) spectroscopies spanning the early picosecond (ps) to microsecond (μs) timescale, including measurement of a triplet-state lifetime (μs timescale), which is an important photophysical property of the polymer required to advance the efficiency of the system.

Although this study focuses on the novel BODIPY polymers for hydrogen evolution, the findings were hypothesised to have bearing on antimicrobial applications as they possess the desired properties of a successful photodynamic therapy (PDT) agent (i.e. long-lived triplet lifetime and absorptivity in the visible region of the spectrum). Hence, the copolymers were also assessed for their ability to generate singlet oxygen

as a potential for use in antimicrobial applications and were successful both in solution and when absorbed onto a surface for killing both gram-negative and gram-positive bacteria.

Inorganic complexes are well established in the field of photocatalytic hydrogen evolution. Their activity for hydrogen evolution, combined with their superior photostability make them ideal candidates for viable scale-up options. However, poor absorptivity in the visible light region of the solar spectrum has limited the application of inorganic complexes such as ruthenium(II) polypyridyl complexes. A main objective of the research on novel Ru(II) complexes in this thesis was to extend the visible light absorptivity of these inorganic complexes through π -extended ligands and addition of ligands with different donor strengths. The investigation of the photophysics of these complexes is imperative to gain an understanding of the excited state dynamics and hence optimise these complexes for solar-driven applications.

Chapter 1

Introduction

1.1 Abstract

Chapter 1 provides a general introduction to the project including an insight into the current energy crisis and the hydrogen economy. The principles and approaches to hydrogen evolution are described, with a focus on photocatalytic hydrogen evolution with a brief overview of inorganic and organic systems previously reported. The fundamentals of the photophysical processes involved are described including the importance of triplet state population in the chosen photosensitiser and the design principles for singlet fission. The main techniques used throughout this investigation are discussed with a focus on time-resolved spectroscopy. Polymeric materials for hydrogen evolution are introduced and the rationale for the incorporation of polymers into photocatalytic hydrogen generating systems is summarised. BODIPY copolymers are introduced as potential photosensitising agents for the photocatalytic generation of hydrogen. Furthermore, photodynamic therapy (PDT) requiring visible-light absorbing triplet photosensitisers is mentioned with an overview of the role of singlet oxygen generation ($^1\text{O}_2$).

1.2 Hydrogen fuel to combat the current energy crisis

1.2.1 The current energy crisis

The development of a clean and renewable energy source is one of the most urgent challenges of our time. The increase in global energy demand has resulted in increased consumption of fossil fuels, leading to detrimental air pollution and global warming.^{1,2} In addition, the limited supply of fossil fuels has caused great concern for future energy supplies. Ireland relies heavily on fossil fuels particularly oil (48.8 % of energy used in 2019) and natural gas (30.6 % of energy used in 2019) across all energy sectors, (according to a national survey published in the Sustainable Energy Authority of Ireland (SEAI)).³ **Figure 1.1** displays the primary energy consumption by fuel in kilo tonnes of energy (ktoe) in Ireland from 2008 to 2018 wherein the primary energy refers to the total amount of energy used including the energy loss encountered during energy transformation processes such as oil refining. In 2018, over 89% of all energy consumption in the country was from the burning of fossil fuels, with a 4.5% increase in final energy demand by end-users (showing an increase in all sectors).

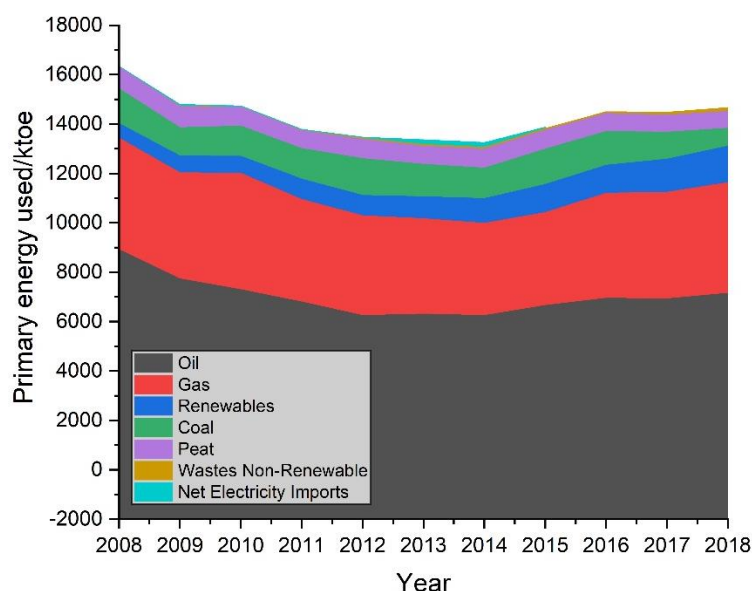


Figure 1.1. Primary energy usage in Ireland 2008-2018 showing the energy consumption categorised by fuel source. Data obtained from SEAI 2019 report.³

According to the Environmental protection agency (EPA), Ireland's greenhouse gas (GHG) emissions in 2018 were attributed to 59% from energy-related emissions (areas

such as transport (40%) and residential (24%)) and 34% from the agricultural sector, particularly methane (CH₄) emissions from agricultural livestock (**Figure 1.2**).

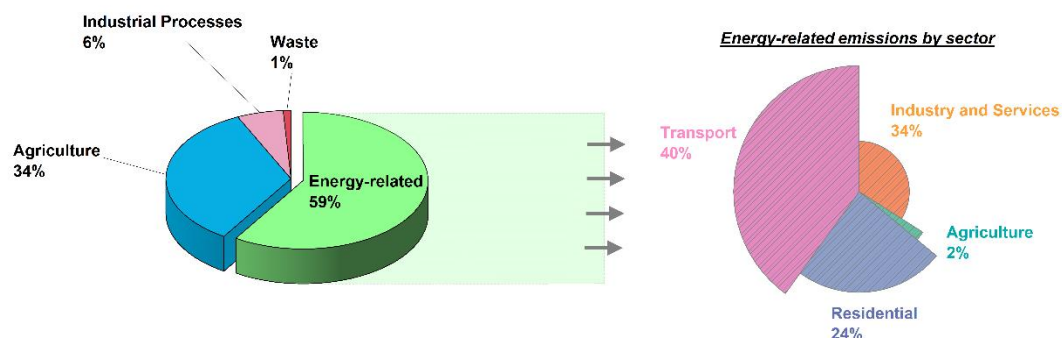


Figure 1.2. Ireland's total GHG emissions by sector (left), Ireland's energy-related emissions by sector (right). Data obtained from EPA report 2018.⁴

While there has been a national decrease in energy-related carbon dioxide (CO₂) emissions (-2.1%) in 2018, Ireland has 20% higher CO₂ emission intensity on an EU average and is ranked among the top three largest GHG emissions contributor per capita, where all GHG emissions (e.g., CO₂, CH₄, nitrous oxide (N₂O), hydrofluorocarbons) are collectively expressed as CO₂ equivalents.

An increase in GHG emissions liberated upon the combustion of fossil fuels has resulted in warming of the earth's temperature – commonly referred to as anthropogenic climate change. The global rise in temperature can be seen in **Figure 1.3**, displaying an alarming increase since the industrial revolution. Notably, the warmest years recorded in the last 35 years, have all been since 2010.⁵

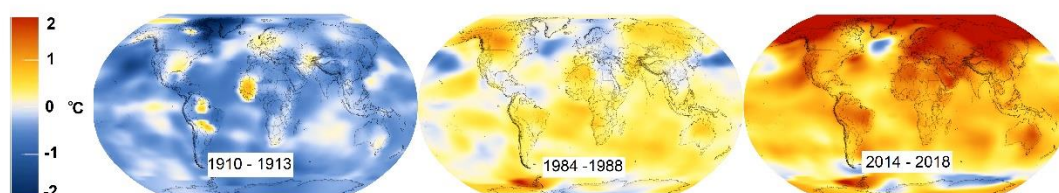


Figure 1.3. Earth's global surface temperature changes over time. From left to right 1910-1913, 1984-1988, and 2014-2018. Legend showing temperature change in °C. Adapted from reference.⁵

This increase in temperature has many effects including; rising sea levels (~ 20 cm in the last century), shrinking of ice sheets (e.g. Greenland ice sheet has lost 286 billion tons of mass every year between 1993-2016), loss of biodiversity, ocean acidification,

glacial retreats and extreme weather events such as high levels of precipitation and flooding.⁶ In addition, human health has also been negatively impacted as a result of the increase in pollutants in the atmosphere.⁷

In order to cease the damaging consequences of GHG emissions, we must transition to a clean, renewable energy source as our primary energy vector. In addition to the effects of global warming described above, the dwindling supply of fossil fuels is further motivation to find an alternative energy solution. Fossil fuels, such as coal and petroleum products are close to depletion, and if continued to be used at the same rate, are estimated to be fully depleted within 50 years.

1.2.2 A move towards renewable energy vectors

Many routes towards renewable energy sources, have been investigated, including wind, hydro, geothermal, biomass and solar. Of the aforementioned sources, solar energy is one of the most abundant in nature and hence offers huge potential for future development. All renewable energy sources convert one form of energy into another e.g., wind turbines convert kinetic energy into electric. **Figure 1.4** displays the different sources of renewable energies implemented in Ireland – most notably wind energy is predominant (52% all renewable energy in Ireland in 2017).

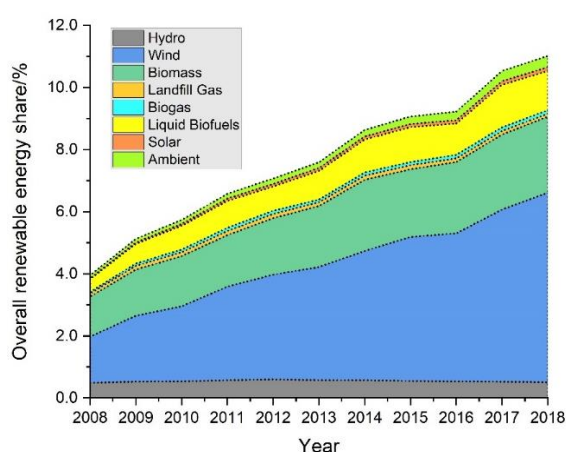


Figure 1.4. Renewable energy in Ireland 2008-2018 split by source. Data shown in non-normalised to accurately depict the annual variation. Adapted from SEAI, 2019 report.⁸

The renewable energy directive (RED) published by the European Union (EU) set a goal for Ireland to achieve a mandatory target of an overall renewable energy share (RES) of 16% by 2020.⁹ Earlier this year, the SEAI published a report stating Ireland

has already failed to meet these targets, with a final RES of 11%. In steps towards accomplishing these goals, the new national development plan (NDP) of Ireland for 2018-2027 states that for a transition to a low-carbon and climate resilient society, €21.8 billion will be invested in renewable energy development for the country.¹⁰ This national capital investment is essential if we are to comply with international commitments, such as those made by the United Nations in the Paris agreement, 2015.¹¹

In 2018, wind power generated 28% of all electricity in Ireland. Incidentally, Ireland was reported to have the second largest share of wind energy in the EU. However, as can be seen in **Figure 1.5**, there is still a considerable amount of energy generated from the burning of fossil fuels (grey area).

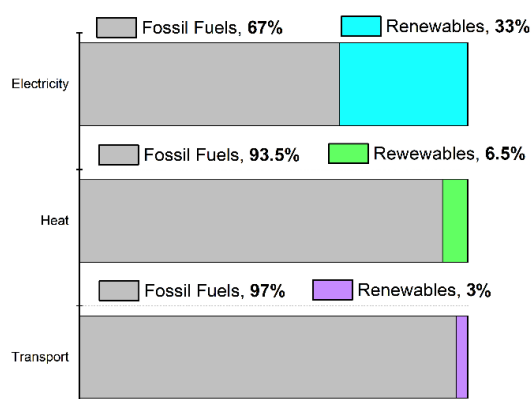


Figure 1.5. Current energy sources across three areas – electricity, heat, and transport. Fossil fuel use shown in grey. Renewable energy shown in coloured section for electricity (blue), heat (green) and transport (purple).⁸

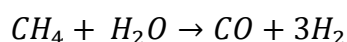
Although there has been significant progress in the renewable energy sector in Ireland, particularly using wind power, the intermittency of this energy source is a challenge.¹² For example, wind speed must be above 3.5 m/s to generate electricity using a wind turbine, but below 25 m/s to avoid damage to the turbine. It is clear from the challenges associated with each type of clean energy source, that one energy source alone is not sufficient to overcome this energy crisis, and it will more than likely be an accumulation of different types of energy vectors to tackle this problem.

1.2.3 Hydrogen (H₂) fuel

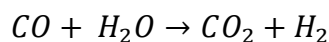
Of all the renewable energy options displayed in **Figure 1.4**, solar energy is the most abundant, yet it is significantly underdeveloped. Solar energy has attracted much attention, specifically due to the large amount of energy it supplies to the earth annually. A range of 100,000 – 120,000 TW of solar energy hits the earth's surface every year (global energy consumption annually is ~ 18 TW).¹² Unfortunately, solar energy is also an intermittent energy source and therefore results in unpredictable power generation. A proposed solution is to transform the incident solar energy into chemical energy as a storage reservoir, commonly referred to as “solar fuels”

Hydrogen (H₂) fuel offers a unique energy storage solution and it is often considered crucial to develop solar fuels if we are to fully exploit the benefits of solar energy.^{7,13} Hydrogen is a non-toxic, colourless, odourless and tasteless element. It is the most abundant element in the universe and can potentially be extracted from an array of different materials. H₂ has a high energy per mass content of 143 MJ kg⁻¹, which is over three times larger than petrol 46.4 MJ kg⁻¹.¹⁴ Hence, H₂ can potentially replace the use of fossil fuels for energy generation, especially in the transport sector, where H₂ powered transportation such as commercial airliners and cars are already in operation in some cities.¹⁵ H₂ fuel also offers attractive potential for localised hydrogen production (eliminating the high cost of large power plants). Upon combustion of H₂, only H₂O is liberated, thus eliminating the issues associated with the combustion of fossil fuels.

While H₂ is currently being produced predominantly for industrial applications, it is estimated that 95% of H₂ production is produced via steam reformation (e.g. steam-methane reforming) and gasification.⁷ The overall conversion of methane to hydrogen is displayed in **Equation 1.1**, and is carried out using at high temperatures of 700 – 1100 °C and a pressure of 3-25 atm.⁷ Furthermore, to maximise the H₂ generated in the overall reformation process, the liberated carbon monoxide from **Equation 1.1** is further reacted with steam (**Equation 1.2**) and the liberation of carbon dioxide (CO₂) occurs in this process which adds to the increase in GHG emissions in the atmosphere.



Equation 1.1. Steam-methane reformation equation to generate hydrogen.



Equation 1.2. Conversion of carbon monoxide to hydrogen.

In order to create a sustainable and renewable procedure for hydrogen fuel generation, the process must be driven using renewable energy as the energy input. Utilising sunlight to drive this chemical conversion can be carried out using a photocatalytic reaction, which will be described in Section 1.3.3.

The term ‘hydrogen economy’ refers to the infrastructure used to support the generation of clean H₂ using renewable energy, the storage, distribution and use of H₂ fuel in society.^{7,16} In addition to considering the clean production of H₂, a limiting factor to the development of H₂ is the large amount of space it occupies in its gaseous form. Storage solutions have been developed to overcome this challenge, and the most conventional way to store H₂ fuel is using pressurised tanks.¹⁴ However, it has a lower storage density compared to other storage solutions. Liquification of H₂ fuel has also been explored as it has a high energy density (of H₂) and can be transported under low pressures. The process of converting H₂ gas into liquid occurs at temperatures below –250 °C.¹⁴ H₂ fuel has also been stored in solid materials, such as metal hydrides, wherein a combination of insertion/removal of H₂ stores H₂ fuel at atmospheric pressure.¹⁷ There have been issues with the stability of the metal hydrides in this approach, referred to as hydrogen embrittlement, observed when the metal hydride becomes brittle after constant exposure to pure H₂.^{7,14} Liquid organic hydrides (LOHs) are also a promising form of chemical storage for H₂ involving an unsaturated (hydrogen poor) and a saturated (hydrogen rich) form of the molecule.¹⁶ Dehydrogenation reactions liberate the H₂ fuel when required. Unfortunately, all storage methods described above require an additional energy input to modify the H₂ gas and hence these processes add to the production power demand (30% in the case of liquification). Technology development for efficient storage of hydrogen is still underway and it is crucial to the realisation of a hydrogen economy.

With increasing efforts working towards a carbon-free society, the hydrogen economy is split into three stages: the current stage, the mid-term stage, and the long-term stage, often referred to as grey, blue and green hydrogen production, respectively. As can be seen in **Figure 1.6**, grey hydrogen production using fossil fuels is currently the predominant process for generating H_2 .

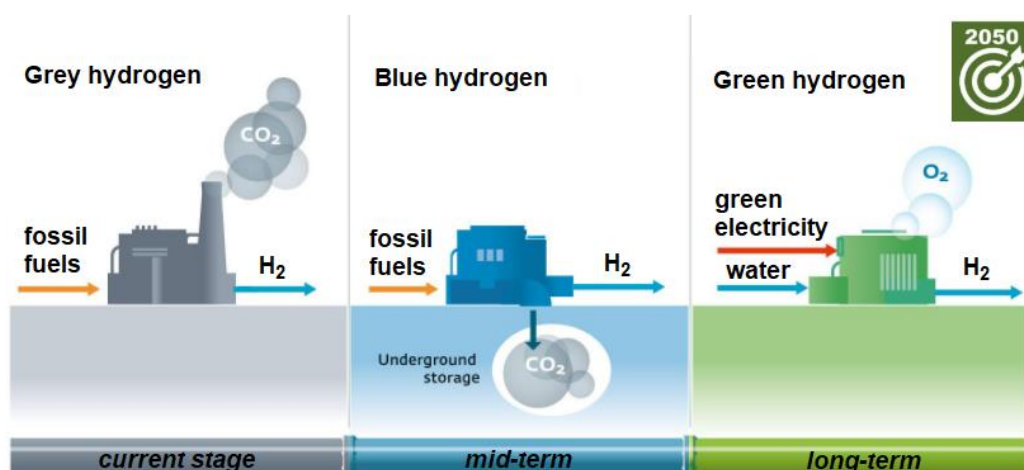


Figure 1.6. Grey, blue, and green routes for hydrogen production showing a transition from a hydrocarbon to a carbon- neutral society. Figure adapted from literature.¹⁸

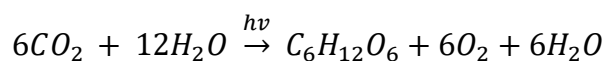
Blue hydrogen production is envisaged as the next step in the H_2 pipeline as it implements carbon capture technologies to prevent liberation of CO_2 emissions. By contrast, green hydrogen production uses renewable energy to generate hydrogen fuel and O_2 is the only by-product of the manufacturing process. Some methods of hydrogen production today using renewable energy sources include thermochemical splitting of water, water electrolysis, photocatalytic water splitting and photoelectrochemical water splitting.^{7,17} The methods for generating blue and green hydrogen are underdeveloped in comparison to the grey hydrogen production methods and hence the efficiency of these processes needs to be drastically improved to fully implement a green hydrogen economy.

1.3 Solar to chemical energy conversion

The use of solar energy to create efficient and sustainable technologies for the generation of solar fuels is a promising option to meet the current and future energy demands. A well-established technology to produce hydrogen (and oxygen) is the photocatalytic splitting of water using solar energy to drive the photochemical conversion and ultimately eliminating little to no GHG emissions.¹⁹

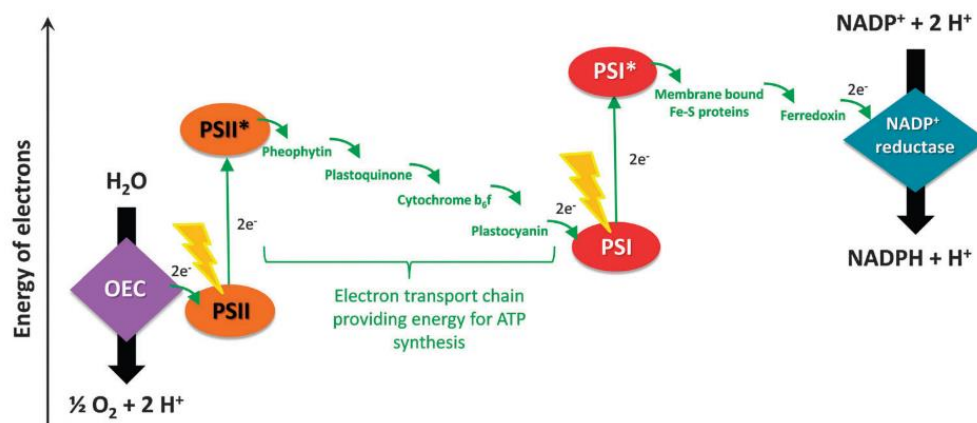
1.3.1 Natural Photosynthesis

Natural photosynthesis occurs in green plants (and in some micro-organisms) using chlorophyll to efficiently harvest solar energy to synthesise glucose, i.e., solar to chemical energy conversion (**Equation 1.3**):



Equation 1.3. Overall photosynthesis reaction using solar energy to generate glucose, oxygen, and water.

Small organic molecules produced during photosynthesis are the building blocks of all living organisms.²⁰ In addition, all fossil fuels used today are the product of millions of years of photosynthetic activity. A mechanistic insight into this process has been the subject of much research, with aims to mimic the basic steps and apply this to solar fuel technologies. The term ‘artificial photosynthesis’ is hence given to all photocatalytic water splitting processes that aim to harvest solar energy in a similar way.¹⁹ The mechanistic steps occurring in photosynthesis, commonly referred to as the “Z-scheme” are depicted in **Scheme 1.1**.



Scheme 1.1. Mechanistic steps of natural photosynthesis occurring in chlorophyll of plants. Figure adapted from Llobet et al. 2014.²¹

In this process, PSII is irradiated with solar light to produce an excited PSII* state. The oxygen evolution catalyst (OEC) is crucial in this process, as the MnCaO₅ cluster co-ordinates to the water molecule and splits it into ½O₂ and 2H⁺. PSII is also known as P680 (Mg-porphyrin compound), a name attributed to the λ_{max} of the pigment at 680 nm. From here, a cascade of energy transfer processes occurs using surrounding electron acceptors to transfer this acquired energy to PSI. Another light-induced energy transfer process also occurs, and PSI is excited to PSI*. PSI absorbs light at 700 nm and thus is also called P700. PSI* is the most powerful reducing agent in the Z-scheme and the excited state electron is transferred to ferredoxin (which has a core structure of iron-sulfur cluster). The reduced ferredoxin then catalyses the reduction of NADP⁺ to NADPH in the presence of protons.²²

The efficiency of photosynthesis can be attributed to a number of key points; first, the energy of the excited state in PS680* is efficiently transferred to the ground state of PS700, which eliminates thermal loss of energy. Secondly, the OEC and HEC are highly effective for each half reaction, operating with accelerated kinetics to inhibit charge recombination. Third, the Z-scheme migration of electrons is ideal for the charge transfer between PS680 and PS700. Insight into photosynthesis, helps us to design molecular assemblies that perform in a similar manner. For example, design principles involve a two electron transport chains (like PSII and PSI) or efficient water oxidation catalysts that accelerate this half-reaction on the surface of the semiconductor and inhibit charge recombination.

1.3.2 Artificial Photosynthesis

Artificial photosynthesis is inspired by natural photosynthesis that occurs in the chlorophyll of plants wherein solar energy is converted into chemical energy and stored in chemical bonds. Photosynthesis has been an area of intense research for decades and scientists have developed an in-depth knowledge of natural photosynthetic light harvesting systems and attempted to mimic this using various molecular components, electron donors and acceptors, and light driven charge separation processes. However, these artificial designs are still not as efficient or robust to result in a viable scale-up option.

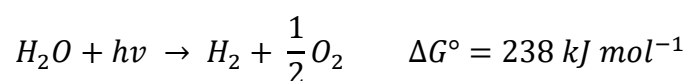
Artificial photosynthesis is an uphill thermodynamic reaction and to ensure a viable photocatalytic process, some key components must be considered: i) a light-harvesting moiety, ii) charge separation and iii) the catalytic centre to allow the reduction reaction to occur (one or multi electron processes), with the incorporation of two components - both an OEC (similar to PSII) and a HEC (similar to PSI).²³ In this instance, the two half reactions (oxygen and hydrogen production) occur separately and combine to make up the overall water splitting reaction, known as the Z-scheme. In many systems, an electron relay, such as methylviologen (MV^{2+}), is added to facilitate the charge separation requirement for successful water splitting.²⁴ Furthermore, it is critical to ensure the system has appropriate excited state energies and redox potentials to drive proton reduction. The prevailing challenge is the molecular design which will simultaneously use the captured light to form the dioxygen bond to form oxygen and also have sufficient reduction potential to reduce protons to hydrogen. While there has been some success using semiconductors, high energy UV light irradiation is required for water splitting.²⁰

Despite the huge effort in the advancement of solar-to-hydrogen conversion, there are obstacles remaining which require innovative solutions. For example, many of the systems reported require UV light to drive the formation of hydrogen. A crucial design consideration of these molecular assemblies is to have a visible light driven system, as nearly half (*ca.* 48%) of the solar energy incident on the Earth's surface is in this region (400 nm – 800 nm).²⁵ The most challenging areas to date have been engineering

of appropriate optical gaps in photosensitising materials, promoting charge separation by acceleration of surface catalytic reactions, efficient charge mobilities and inhibiting charge recombination.²²

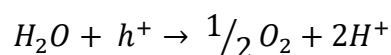
1.3.3 Fundamentals of photocatalytic water splitting

The fundamental concept of water splitting using sunlight is a multi-electron process involving a light-absorbing molecule (chromophore) and a catalyst. Upon irradiation of the aqueous system, the chromophore absorbs the light energy and forms an excited state. From this excited state, the chromophore undergoes energy transfer to the catalyst, where water splitting occurs as per the following **Equation 1.4**:²⁶

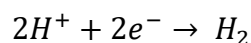


Equation 1.4. Photocatalytic splitting of water to generate hydrogen and oxygen.

The positive Gibbs free energy (ΔG°) indicates that this is a non-spontaneous, endothermic process. This equation shown above is the equivalent of $\Delta E^\circ = 1.23 \text{ eV}$ (calculated using $\Delta G^\circ = -nF \Delta E^\circ$, where $F = 96485.3365 \text{ C mol}^{-1}$, Faraday's constant). This overall water splitting reaction can be further broken down into two half reactions – the reduction reaction to liberate hydrogen, and the oxidation reaction to form oxygen.



Equation 1.5. Oxidation of water to form oxygen.



Equation 1.6. Reduction of protons to form hydrogen.

In order to solely develop hydrogen generating systems, the majority of photocatalytically active systems for hydrogen evolution incorporate a sacrificial agent to replace the water oxidation half reaction. For the purposes of this study, we will solely focus on optimisation of the reduction half reaction (**Equation 1.6**), as hydrogen evolution is the primary goal.

1.3.4 Photocatalytic hydrogen evolution

Artificial photosynthesis has been successfully applied to the hydrogen evolution half reaction using several methods, the most common are homogeneous photocatalysis using either a single component or multi component systems and semiconductor-based devices or photoelectrochemical cells (PEC). For the purpose of this thesis, homogeneous photocatalysis will be the focus for the development of a novel multicomponent hydrogen producing system.

1.3.4.1 Homogeneous photocatalytic hydrogen evolution

Homogeneous photocatalytic systems include all components of the reaction solution dissolved in solution or in the same phase during irradiation. These components consist of a **photosensitiser**, a **catalyst** and a **sacrificial agent** under various experimental conditions. Understanding these three main components in photocatalysis is essential, as it is the design of these components that can enhance hydrogen evolution and increased stability. Homogenous catalysis can provide mechanistic insights into light-driven processes, that can aid in the development of heterogeneous photocatalytic systems, or photoelectrocatalytic systems.²⁴

Displayed in **Figure 1.7** is an overview of three different photocatalytic systems involving a three (a), two (b) and one (c) component(s) assembly that are commonly employed in homogeneous hydrogen generating systems.^{27,28} In all systems shown above, the first step is light absorption by the photosensitiser (PS), wherein an electron is promoted from the ground state (GS) or highest occupied molecular orbital (HOMO) to the excited state or lowest unoccupied molecular orbital (LUMO), to produce a photoexcited species, denoted PS*, provided the incident irradiation has energy equal to or greater than the optical gap of the dye. The optical gap is defined as the lowest energy (longest wavelength) that is required to promote an electron to the excited state (HOMO – LUMO transition) and is often calculated using the onset absorption spectrum of the photosensitiser.²⁹ The PS* then undergoes electron transfer/acceptor reactions to form a charge separated state (CSS), which then has sufficient thermodynamic driving force for proton reduction. In the case of the three-component system (**Figure 1.7** (a)), the electron relay (ER) accepts electrons from the

PS* and transfers them to the catalytic centre. An ER can be used to enhance charge separation from the PS to the CAT and hence avoid undesired charge recombination.²⁴ The two-component system (**Figure 1.7 (b)**), contains a PS and CAT in solution and electron transfer occurs from the PS* to the CAT. This process is often referred to as an intermolecular assembly as the PS and the CAT are not covalently bound. Lastly, the single-component system displayed in **Figure 1.7 (c)** contains a PS unit covalently bound to the CAT centre through the use of a conjugated molecular bridge. Intramolecular systems using this molecular design are synthesised as such to control the electron transfer process, aiming to drive the direction of electron transfer from the PS to the CAT and avoid detrimental charge recombination or back electron transfer.²² A great deal of chromophores have been discovered for use as light absorbing units in the three photocatalytic assemblies described, most notably – metal free organic dyes,^{30–32} metal complexes^{12,28,33} and metal-organic frameworks (MOFs).^{34,35}

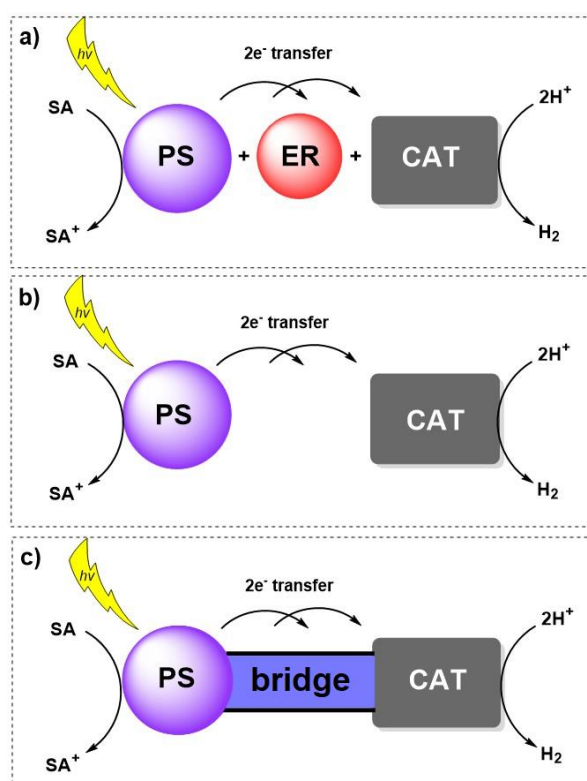


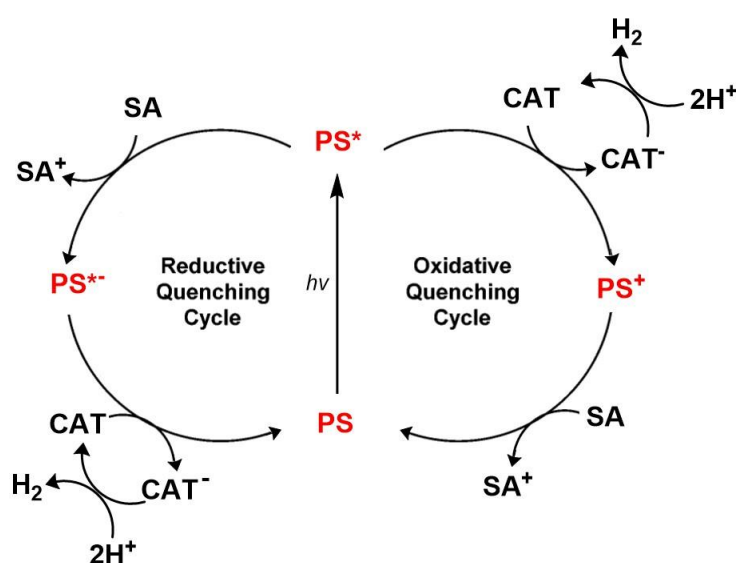
Figure 1.7. Hydrogen generating systems, showing a) three, b) two and c) one component assemblies, where PS = photosensitiser, ER = electron relay, CAT = catalytic centre, and SA = sacrificial agent.

Following photoexcitation of the chromophore and population of an excited state, PS^* , hydrogen may be generated via two mechanisms:

- i) Reductive quenching
- ii) Oxidative quenching

These two processes are depicted in **Scheme 1.2**. In the case of reductive quenching, the PS^* is quenched by an electron donor (the sacrificial agent, SA) which reduces the PS^* to form PS^- (resulting in an oxidised form of the SA, i.e., SA^+). From here, the reduced PS transfers electrons to the CAT, which subsequently reduces the protons to hydrogen. This step is often the rate-limiting step of the reaction and a short-lived PS^* can result in photo-relaxation to the ground state (via thermal loss or fluorescence/phosphorescence) without partaking in energy transfer to the SA or CAT.

Alternatively, the PS^* is oxidised by the CAT and thus loses an electron to form PS^+ , while the CAT gains an electron to form CAT^- respectively. The oxidised PS is replenished by the SA in solution to reform the ground state PS and an oxidised form of the SA, SA^+ . In both cases the PS is returned to the electronic ground state, PS, and the cycle is repeated. The catalyst used must drive the reduction of protons to liberate hydrogen gas, H_2 .



Scheme 1.2. Reductive quenching (left) and oxidative quenching (right) mechanisms for photocatalytic hydrogen evolution. PS shown in red. Adapted from literature.²⁸

The first intermolecular system reported was over 40 years ago, and involved the well-renowned $[\text{Ru}(\text{bpy})_3]^{2+}$ (**Figure 1.8**) as the photosensitiser, methylene viologen, MV^{2+} , as the electron mediator, TEOA as the electron donor and a colloidal catalyst.³⁶

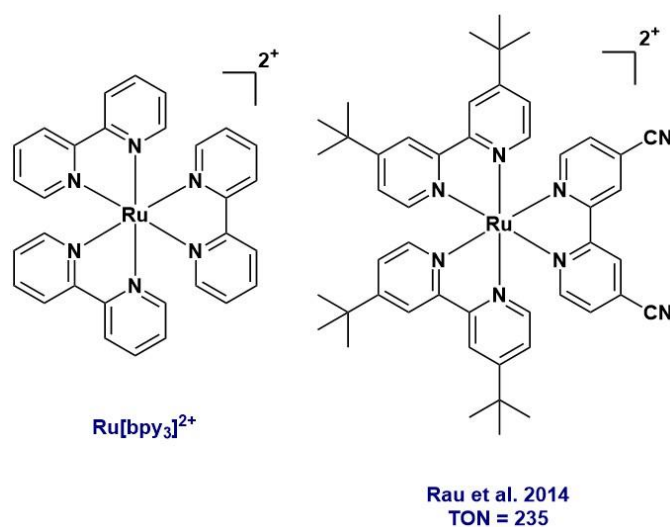


Figure 1.8. Intermolecular inorganic-based complexes used as PS used in homogeneous photocatalysis. PF_6^- counter anions omitted for clarity.³⁶

Displayed in **Figure 1.8** is a heteroleptic ruthenium polypyridyl complex reported by Rau et al. in 2014, where the Ru complex is the photosensitiser, a cobalt complex $[\text{Co}(\text{dmgH})_2]$ was used as the catalyst and TEA as the sacrificial electron donor in a MeOH/water solvent mixture. Aerobic conditions gave the best hydrogen turnover numbers of approximately 235 after 20 h irradiation using a 470 nm LED stick (51.1 ± 1.0 mW).³⁷ Recent efforts have been made to enhance the absorption of inorganic complexes in the visible region of the spectrum through numerous synthetic variations including π -extension of the peripheral ligands and covalent attachment of organic based chromophores. In 2019, a broadband visible light Ir(III) complex containing both coumarin PS and BODIPY PS showed absorption over *ca.* 50% of the visible light region compared to only UV-light absorption of the unsubstituted Ir(III) complex prior to synthetic modification.³⁸

Organic-based photosensitisers have also been used without the incorporation of an inorganic complex into the molecular structure, albeit the efficiencies of these systems are not on a par to those reported for inorganic systems. However, the elimination of precious metals in organic-based photosensitisers offers a cheaper alternative and is

hence a more attractive and viable route for future scale-up. The photophysical properties of organic-based photosensitisers can be fine-tuned at a molecular level by incorporation of different functional groups, adding more diversity into the design of multi-component photocatalytic systems. Eisenberg et al. used xanthene dyes and the same cobalt catalyst, and observed that changing the heteroatom from S to Se yielded higher turnover number (TON) for intermolecular systems (**Figure 1.9**).³⁹ Weinstein et al. studied zinc porphyrin dyes (**Figure 1.9**) in conjugation with a cobalt cobaloxime (hereafter referred to as cobaloxime) catalyst in ACN/H₂O solution with TEOA 5% (v/v) solution. TON of over 280 were observed using visible light source $\lambda > 440$ nm.⁴⁰ Boron-dipyrromethene (BODIPY) dyes are a hot topic in the field of organic dyes and will be introduced later in this chapter as it is the photosensitiser chosen in this project.

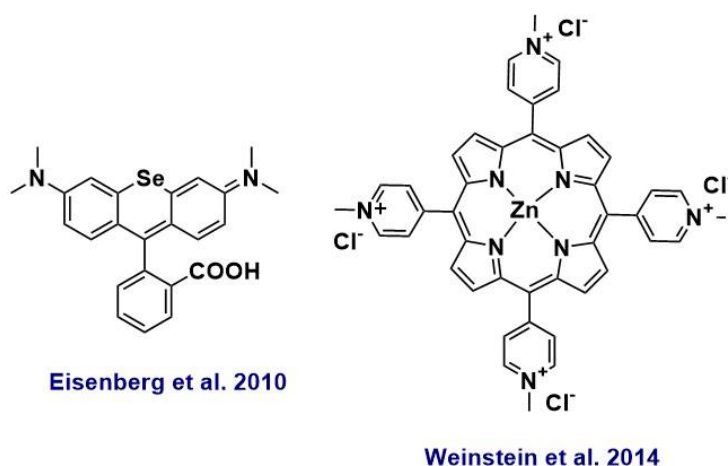


Figure 1.9. Intermolecular organic-based chromophores used as PS used in homogeneous photocatalysis.^{39,40}

Intramolecular assemblies have a covalent bond or bridging ligand between the CAT and the PS which aims to improve the electron transfer from the excited state PS to the CAT. This covalent link eliminates the requirement for the diffusion of reactants in homogeneous photocatalytic solutions and improves the electron transfer kinetics.²⁴ Intramolecular systems published include cobaloxime catalysts covalently bound to BODIPY dyes and Ru complexes bound to a Pt centre via a bridging ligand (**Figure 1.10**).^{41,42} These systems report a higher TON of hydrogen evolution when compared to their equivalent system containing the untethered counterparts.

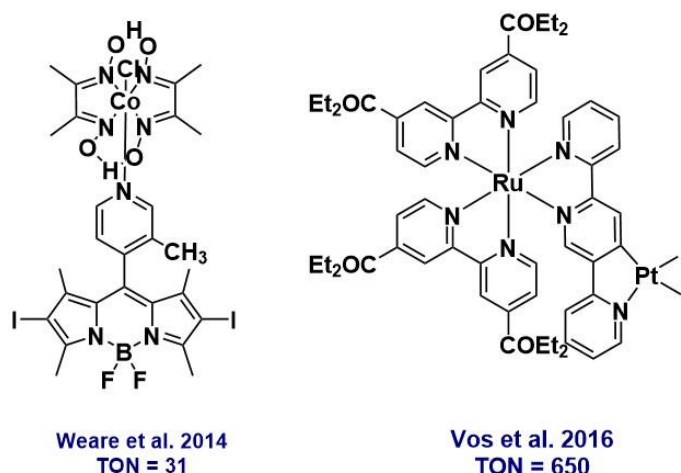


Figure 1.10. Intramolecular photocatalytic systems containing PS covalently bound to CAT – organic based PS moiety (left), inorganic based PS moiety (right).^{41,42}

Choice of photosensitiser

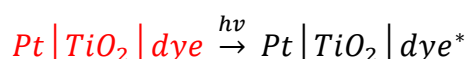
Ideally, a photosensitiser will be highly absorbing in the visible-region of the spectrum (typically $\epsilon > 10^4 \text{ M}^{-1} \text{ cm}^{-1}$). Many synthetic designs aim to modify the photosensitiser to aim for a bathochromic absorption shift in the UV-vis spectrum i.e., shifting the absorption of the molecule to a lower energy to allow for a greater region of the solar spectrum to be absorbed. Once excited, an energy transfer process is more likely to occur if the excited photosensitiser is long-lived to allow for good charge separation to occur, thus giving more time for proton reduction. The population of a long-lived triplet state is ideal for a PS and can be accomplished through methods such as enhanced spin-orbit coupling. Phosphorescence or nonradiative decay from the triplet state is undesirable, as the energy transfer process ceases with energy loss in the transition from the excited state to the ground state, inhibiting further photocatalytic processes. The PS must also be stable under irradiative conditions to inhibit photodecomposition of the system and allow for many catalytic cycles. Reproducibility is often a central concern in molecular artificial photosynthesis.⁴³ Lastly, an effective PS must have a suitable redox potential to carry out the proton reduction reaction wherein a redox couple with a more positive reduction potential than $\text{H}_2\text{O}/\text{H}_2 = -0.41 \text{ V vs. NHE}$ at $\text{pH} = 7$, can thermodynamically reduce protons to hydrogen in the bielectron reduction reaction.²¹

A range of experimental factors need to be considered about the photocatalytic system in order to improve the hydrogen evolution efficiency and hence result in a high quantum yield efficiency under solar irradiation of the system. These factors include choice of sacrificial agent, reactor used, irradiation wavelength and intensity, pH of solution, choice of sacrificial agents, and addition of cocatalysts.¹⁹

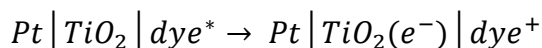
1.3.4.2 Photocatalytic hydrogen evolution using sensitised semiconductor suspensions

Since the initial discovery of the Honda-Fujishima effect in the 1972 that displayed photo-driven water splitting using n-type TiO₂ photoanode semiconductor in a photoelectrochemical (PEC) cell, the use of semiconductor materials in both photocatalytic and photoelectrochemical systems has vastly expanded.⁴⁴⁻⁴⁶ In the case of photocatalytic hydrogen production, semiconductors such as TiO₂ are often sensitised with a light-absorbing molecule due to the poor visible light absorption of the bare TiO₂ nanoparticle (band gap 2.96 – 3.20 eV depending on the type of polymorph).

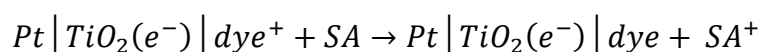
The mechanistic steps of a typical photocatalytic system using a dye sensitised Pt|TiO₂ nanoparticle are shown below (**Equation 1.7 - Equation 1.12**):^{26,30,47}



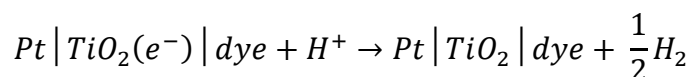
Equation 1.7. Photoexcitation of the photosensitising dye to produce dye*.



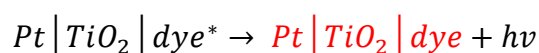
Equation 1.8. Electron injection into the conduction band of TiO₂ to form a charge separated state.



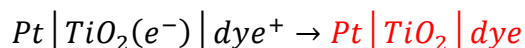
Equation 1.9. Regeneration of the ground state dye by the sacrificial agent (SA).



Equation 1.10. Proton reduction at the platinum (Pt) centre following charge migration to the surface.



Equation 1.11. Deactivation of the excitation state dye (dye*) via radiative loss.

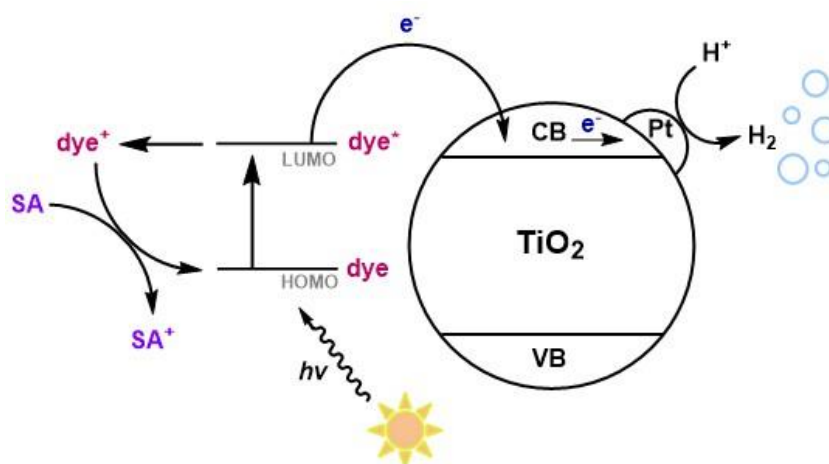


Equation 1.12. Deactivation of the charge separation state via charge recombination.

Initially, the dye is irradiated with a wavelength of light that has significant overlap with the absorption spectra of the dye, to produce an excited state of the dye, denoted dye* (**Equation 1.7**). This excited state injects an electron into the conduction band (CB) of the TiO₂ nanoparticle to form a charge separated electron-hole pair displayed as TiO₂ (e⁻) and dye⁺ in step (**Equation 1.8**). The sacrificial agent (SA) in solution then reduces dye⁺ to regenerate the ground state dye molecule and the SA itself gets oxidised in this process to form SA⁺ (**Equation 1.9**). Charge migration of the electrons in the TiO₂ CB to the surface of the nanoparticle allows for the Pt⁰ particles embedded on the surface of the nanoparticle to trap these electrons, and reduce the protons to molecular hydrogen, H₂ in a surface catalytic reaction (**Equation 1.10**). The majority of dye sensitised TiO₂ photocatalytic systems deposit Pt⁰ particles to act as a co-catalyst on the surface of the nanoparticle to trap electrons on the surface of the material and avoid undesired back-electron transfer. This functionalisation method is typically carried out using a photodecomposition method wherein H₂PtCl₆ is stirred in solution with TiO₂ nanoparticles under UV light irradiation. The addition of a co-catalyst on the surface of the semiconductor has been shown to significantly increase the amount of hydrogen generated and this has been attributed to the increased reaction rate between the co-catalyst and the charges that have migrated to the surface of the semiconductor (thus suppressing the back electron transfer pathway) and also the provision of a reaction site for the reduction half reaction, thus lowering the activation energy and pushing the forward reaction.^{47,48}

Equation 1.11 and **Equation 1.12** displayed above exhibit destructive processes to hydrogen evolution including excited state deactivation of the dye with radiative loss (**Equation 1.11**) and charge recombination of the photogenerated electron-hole (e⁻/h⁺) pair (**Equation 1.12**).

A schematic for this category of energy production is displayed in **Scheme 1.3**.



Scheme 1.3. A schematic representation of photocatalytic hydrogen evolution using dye sensitised TiO_2 semiconductor nanoparticles. VB – valence band, CB – conduction band. Adapted from literature.³⁰

In 2019, Reisner et al. reported efficient hydrogen evolution using dye-sensitised photocatalysis for a series of five novel perylene monoimide (PMI) dyes containing either carboxylic acid (**PMI-CO₂H**), acetylacetonate (**PMI-Acac**), phosphonic acid (**PMI-PO₃H₂**), hydroxyquinoline (**PMI-HQui**) or dipicolinic acid (**PMI-DPA**) as anchoring groups for attachment onto the surface of TiO_2 (**Figure 1.11**).⁴⁹

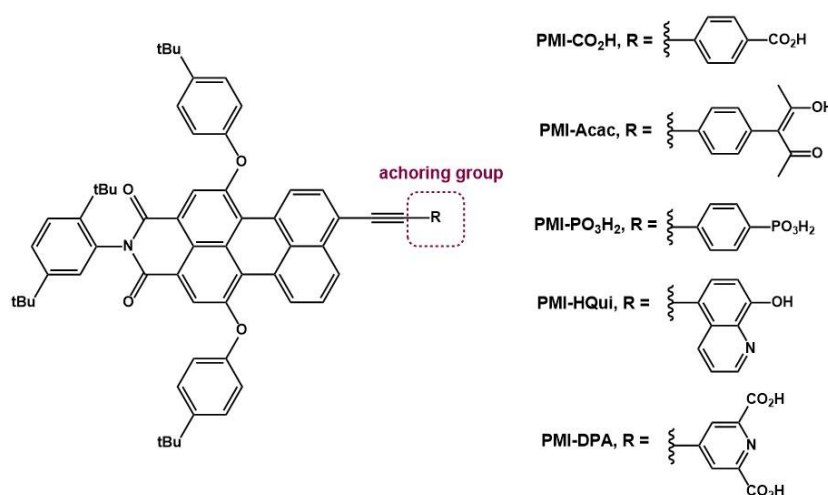


Figure 1.11. A series of five novel perylene monoimide (PMI) dyes showing different anchoring groups (R) for attachment to the surface of TiO_2 semiconductor.⁴⁹

All PMI dyes showed strong absorption in the visible region with λ_{abs} ranging from 536 – 545 nm. Photocatalytic experiments were carried out by dispersion of 1.25 mg of PMI | TiO_2 | Pt in 3 mL aqueous sacrificial agent solution containing either ascorbic acid (AA, 0.1 M, pH 4.5) or TEOA solution (0.1 M, pH 7.0. or 0.1 M, pH 8.5). The

solution was purged with N₂ and then sonicated for 15 minutes to disperse the nanoparticles in the reaction flask before irradiating the solution using a 300 W Xe arc lamp, $\lambda > 420$ nm for 24 hours. The highest activity for H₂ ($\text{TON}_{\text{PMI-CO}_2\text{H}} = 6461 \pm 749$) was generated by using **PMI-CO₂H** in an AA solution, pH 4.5. This system also displayed high stability over a long-term experiment of 72 hours ($\text{TON}_{\text{PMI-CO}_2\text{H}} \sim 1.1 \times 10^4$), which is the highest activity reported to date for an organic dye in an aqueous semiconductor-based system. However, the pH of the solution is shown to be a crucial parameter as $\text{TON}_{\text{PMI-CO}_2\text{H}} = 490 \pm 170$, using TEOA as the sacrificial agent, pH 8.5. This was attributed to detachment from the TiO₂ surface in an alkaline environment.

1.4 Principles of photophysics

1.4.1 The fundamentals of photophysics

Photochemistry is the discipline that studies the electronic transitions that occur as a result of the absorption of a photon of radiation ($h\nu$). This irradiation allows transitions to occur that might not have occurred thermally. Excitation or electronic transitions can occur in chromophores upon irradiation with a light equivalent to a wavelength of which they absorb. This absorbed energy can then result in a population of an excited state. For this electronic transition to occur, the energy of the light must be at greater than or equal to the highest occupied molecular orbital (HOMO) and the lowest unoccupied molecular orbital (LUMO). **Figure 1.12** i) displays the electronic transitions that can occur in organic chromophores, e.g. $\pi - \pi^*$ transition is typical of molecules with double bonds from the bonding to anti-bonding orbital. **Figure 1.12** ii) focuses on molecular orbitals usually found in metal-containing photosensitisers with organic ligands co-ordinated to the metal centre. In this instance, there are filled π orbitals representing electrons in the ligand HOMO and filled $d\pi$ orbitals representing electrons on the metal HOMO. Absorption of light of an appropriate wavelength can result in a $\pi - \pi^*$ ligand-centred (LC) transition or a $d\pi - \pi^*$ metal-to-ligand charge transfer (MLCT) transition.⁴³

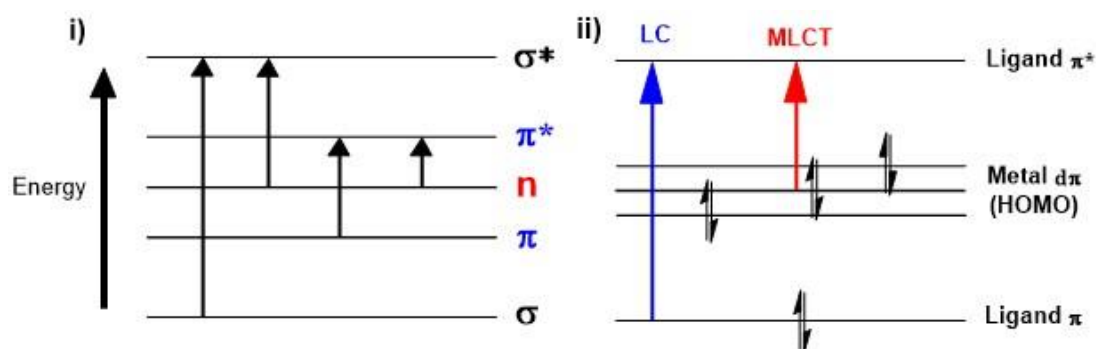


Figure 1.12. Simplified frontier energy diagram i) showing types of electronic transitions in organic molecules ii) showing transitions typical of metal-ligand photosensitisers. LC – ligand charger transfer, MLCT – metal to ligand charge transfer, HOMO – highest occupied molecular orbital. Figure adapted from literature.⁴³

The electronic transitions shown in the figure above can be displayed on a state diagram known as the Jablonski diagram, displaying electronic transitions that a chromophore can undergo when it absorbs light (**Figure 1.13**). Upon photoexcitation,

an electron moves from the singlet ground state (S_0) to the singlet excited state (S_1). This transition follows Wigner's spin conversion rule, wherein the spin flip of the electron is maintained (spin allowed process). However, there can also be intersystem crossing (ISC) from the singlet excited state to the triplet excited state (T_1). This process changes the spin of electrons to be spin parallel (high energy configuration) and hence is a spin forbidden process.⁴³ Although ISC is a spin-forbidden process, there are many examples of ISC in both organic and inorganic chromophores which is facilitated due to spin-orbit coupling which will be discussed in section 1.8.3.

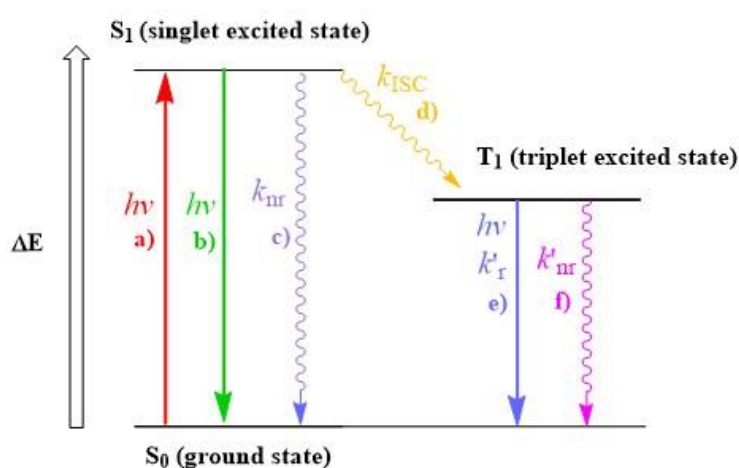


Figure 1.13. Jablonski diagram showing molecular electronic states and the various excitation and relaxation processes that occur upon photoexcitation. Associated rate constants for each transition is denoted, k . Solid arrow – radiative process, curly arrow – non radiative process. Figure adapted from the literature.⁴³

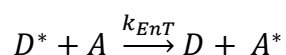
From the excited state, the electron can follow two major relaxation pathways to the ground state; i) radiative decay (light is emitted, known as luminescence) or ii) non radiative decay (energy lost as heat). The processes as per labelled in **Figure 1.13** are as follows:

- a) Excitation ($S_0 \rightarrow S_1$)
- b) Fluorescence (luminescence with retention of spin)
- c) Non-radiative decay
- d) Intersystem crossing
- e) Phosphorescence (luminescence without retention of spin)
- f) Triplet-state non radiative decay

In photocatalytic processes developed using metal-ligand based photosensitisers (**Figure 1.8**) it is common that the rate of intersystem crossing from the singlet excited state to the triplet excited state is quite fast and the rate of decay from the triplet state is not favoured, such that $k_{ISC} \gg k_r, k_{nr}$. Allowing the triplet excited state to be populated with near 100% efficiency. As the triplet excited state is of keen interest (excited state from which further processes can occur), it is not surprising that metal-based PS have been popular for use in photocatalytic systems.

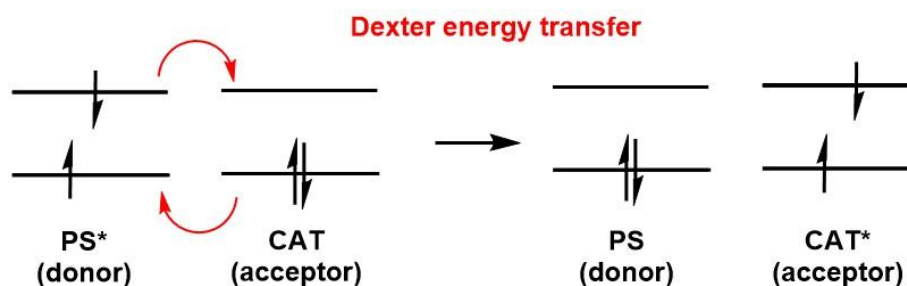
1.4.2 Singlet excited state vs. triplet excited state

After population of the triplet excited state, the chromophore has a longer-excited state lifetime, due to formation of an excited state via a spin forbidden process (decay to the ground state at microsecond timescale).⁵⁰ This longer lifetime is important as it allows time for energy transfer from the PS (donor, D) to the CAT (acceptor, A); without undesirable charge recombination; according to the following equation;



Equation 1.13. Energy transfer equation between PS (D) and CAT (A).

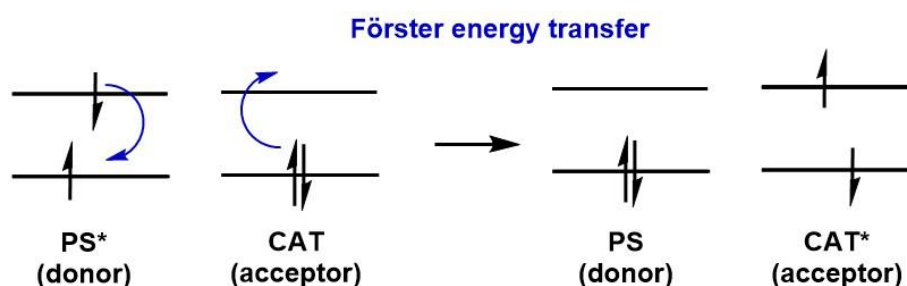
This non-radiative energy transfer mechanism can occur either via Dexter (through-bond) or Förster (through space) energy transfer mechanisms (**Scheme 1.4**, **Scheme 1.5**) from the LUMO of the excited state photosensitiser, denoted PS*. Both of these processes generate a ground state PS (donor) and an excited state catalyst (acceptor).⁵¹



Scheme 1.4. Dexter energy transfer process to from ground state PS and excited state CAT.⁵¹

The Dexter energy transfer process (also known as the electron exchange mechanism) depicted above in **Scheme 1.4**, transfers an electron from the excited state LUMO of PS* to the LUMO of the CAT. At the same time, an electron is transferred from the

HOMO of the CAT to the HOMO of the PS. The “through-bond” nature of this mechanism means that an orbital overlap between the donor and acceptor species is required. Furthermore, in order for the Dexter energy transfer to be thermodynamically feasible, the energy of the LUMO of the PS* must be higher than the LUMO of the CAT i.e., electron transfer must be exergonic.



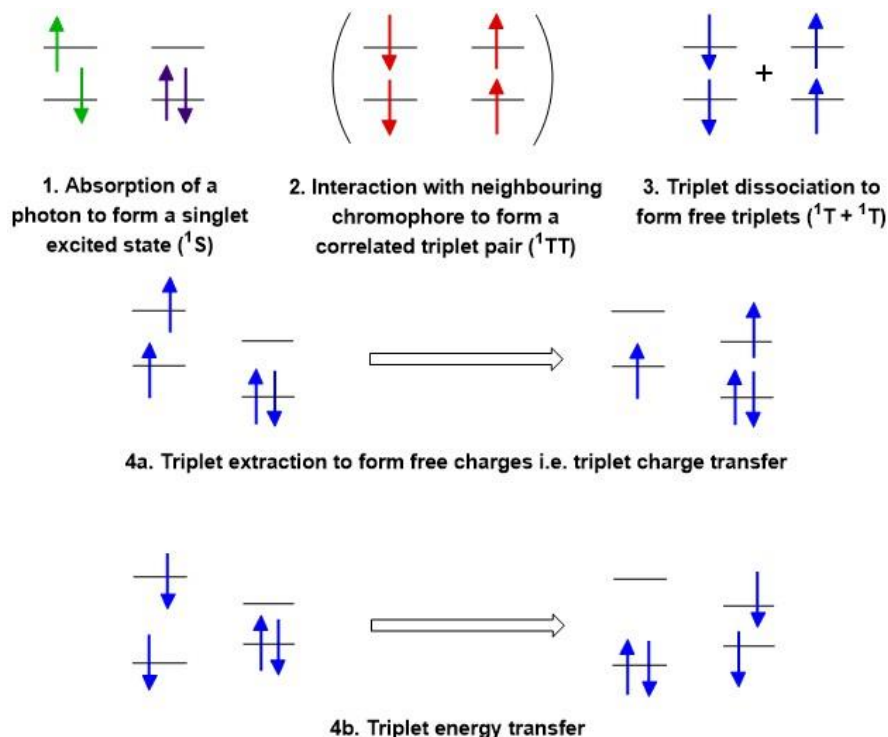
Scheme 1.5. Förster energy transfer process to form ground state PS and excited state CAT.⁵¹

The “through space” or dipole-dipole mechanism of Förster energy transfer process (**Scheme 1.5**) allows the coupling of transition monomer dipole of the donor to the transition moment dipole of the acceptor, without need for orbital overlap. In this case, the deactivation of the excited state PS* (donor) produces an electric field or transition dipole, which promotes an electron from the HOMO to the LUMO in the CAT (acceptor). The distance limitation for this mechanism to occur is typically 10 – 100 Å.⁵¹ For an energy-transfer process to occur via Förster energy transfer process, there needs to be an overlap between the emission spectra of the donor and absorption spectra of the acceptor; hence this process is also referred to as fluorescence resonance energy transfer (FRET).

Energy transfer typically occurs via a non-radiative process as described above. However, there are some systems known as “trivial” systems; wherein the emission from the donor, results in absorption of this emitted light by the acceptor, in a radiative energy transfer process.⁵¹

1.5 Singlet Fission

Singlet fission (SF) is a process whereby the population of one singlet state (1S) results in the formation of two triplet states ($2 \times ^1T$) and was first discovered over 50 years ago. In recent years there has been a flurry of activity based on singlet fission with aims to increase the efficiency of solar cells.^{52,53} The spin-allowed process of singlet fission initiates with the absorption of a photon and excitation to a singlet excited state (Step 1, **Scheme 1.6**). The energy of the photon absorbed is approximately twice that of the triplet state such that: $E(S_1) \geq 2E(T_1)$. This singlet state populated then interacts with a neighbouring molecule to form a correlated triplet pair (Step 2, **Scheme 1.6**) – this interaction can be either through space (e.g. in crystals), or through covalent bonds such as dimers/polymers. Each triplet state in this case has half the energy of the original singlet excited state and maintains a net singlet spin.^{54,55} Step 3 involves the formation of free triplet states, the mechanistic steps of which remain unclear in the literature. These free triplets then undergo further charge/energy transfer to acceptor molecules (Steps 4a and 4b, **Scheme 1.6**).⁵⁴



Scheme 1.6. Simplified spin diagram schematic for the electronic processes that occur during singlet fission.⁵⁴

From this schematic described above, it is evident that in order facilitate multiple exciton generation (MEG) through SF, the organic chromophore must fulfil some critical requirements.⁵⁶ Michel et al. proposed a few essential prerequisites for SF:

- i) SF does not occur in single chromophores as at least two excitation sites are needed, hence multi-chromophoric systems are essential,
- ii) Favourable energies must be obtained i.e., the initial singlet excited state must be at least double that of the later triplets in order to have the subsequent steps energetically favourable,
- iii) The interaction between the chromophores is critical and it has been observed that orthogonal chromophores are more likely to undergo SF than their linear equivalents (initially excited chromophore shares its excitation energy with neighbouring chromophore),
- iv) The triplet excited states produced must undergo charge transfer sufficiently and independently in order for power conversion efficiency (PCE) to be enhanced,
- v) Strong absorption of chromophore in the visible region,
- vi) fast singlet fission occurrence, approximately ps or even sub-ps timescale (so other decay processes such as intersystem crossing and internal conversion are not favoured), and fast charge/energy transfer from the dissociated triplet states in order to harvest the energy of the two triplet states.

If all of these requirements are fulfilled, singlet fission may occur, and this can give lead to the formation of triplet states with a yield in excess of 100%. Most importantly, the formation of the two triplet states is not enough to increase PCE alone, it is also imperative that the energy generated is transferred efficiently to the photocatalytic system.⁵² It has been observed that SF occurrence is strongly dependant on chromophore structure and geometries, as this dictates the interchromophore coupling.⁵⁴ Although there has been significant process made in the area of SF, the repertoire of chromophores known to undergo SF is scarce and thus an understanding of the design principles governing efficient SF in chromophores is limited.

1.5.1 Singlet Fission in BODIPY dimers

Intramolecular SF (iSF) has been reported to occur in an orthogonal BODIPY dimer (**Figure 1.14** (a)) wherein two BODIPY units are in orthogonal geometry with respect to each other (restricted by rotation due to the methyl groups at the 1 and 3 positions, **Figure 1.39**). DFT calculations confirmed that the energetic requirements for the singlet and triplet states were satisfied i.e. $E(S_1) \geq 2E(T_1)$.⁵⁷

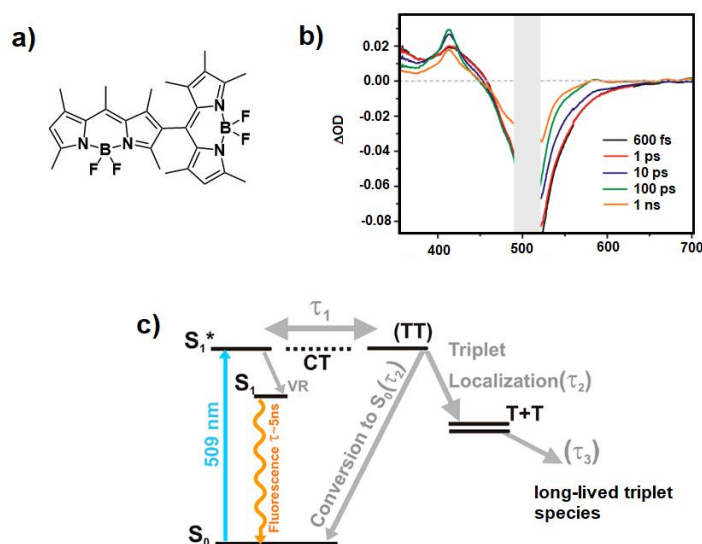


Figure 1.14. a) Structure of BODIPY dimer, b) TA spectra of BODIPY dimer in CHCl_3 solution following 509 nm excitation at various time delays, c) Proposed SF mechanism after excitation in polar solvents, VR – vibrational relaxation. Figure adapted from literature.⁵⁷

TA spectra of the dimer in CHCl_3 following 509 nm excitation is displayed **Figure 1.14** (b) and analysis of the decay kinetics revealed a triexponential decay of $\tau_1 = 16.2 \pm 0.2$ ps, $\tau_2 = 391 \pm 10$ ps and $\tau_3 \gg 1$ ns. Decay associated spectra (DAS) were used to assign these excited state species, with the first lifetime component (τ_1) attributed to a build-up of the correlated triplet pair (^1TT) at 413 nm within 16 ps. The second lifetime component (τ_2) was ascribed to decay from the ^1TT state in combination with a recovery of the parent band at 503 nm indicating a direct conversion from the ^1TT excited state to the electronic ground state of the chromophore. The DAS spectra of the third lifetime component (τ_3) also showed a positive feature at 413 nm (corresponding to a transient of triplet nature) that indicated that despite the population

decay from the ^1TT species, some excited state species did not decay to the ground state. The authors ascribed this feature to two individual triplet states that have dissociated ($^1\text{T} + ^1\text{T}$) and use this spectral observation to explain the high singlet oxygen quantum yield obtained for the dimer in CHCl_3 ($\Phi_{\Delta} = 0.75$).⁵⁸ TA spectroscopy was carried out on a longer timescale to measure the triplet lifetime of the dimer in CHCl_3 solution (386 μs) and to confirm the assignment of the band at 413 nm to that of triplet nature. In these studies, the correlated triplet pair (^1TT) was calculated to be 132% ($\Phi_{\text{TT}} = 1.32$ in CHCl_3).

In this study, the formation rate of the triplet was found to be strongly solvent dependent, and this indicated that the iSF mechanism occurs through a mediated charge-transfer state. For example, using the same principles as described above, TA spectra of the dimer in CH_3CN solution confirmed the ^1TT state yield to be 160% ($\Phi_{\text{TT}} = 1.60$ in CH_3CN). However, TA spectra of the dimer in cyclohexane solution displayed no spectral features of a triplet species and hence could not be measured at longer timescales. In addition, no singlet oxygen was observed for the dimer in cyclohexane. This supports the argument of an intermediate CT state prior to population of the correlated triplet pair (^1TT).

1.5.2 Singlet Fission in conjugated copolymers

SF in conjugated polymers, particularly donor-acceptor (D-A) copolymers offer great potential in comparison to homo/hetero dimers typically reported to undergo SF. Foremost, D-A copolymers can be tuned at a molecular level by choosing the D-A monomeric units, they have ease of processability in solution and they display good charge transfer mobilities along the polymeric backbone.⁵⁹ A particularly attractive aspect of exploring these polymers is that two acceptor units on the polymeric backbone enables spatial separation of the correlated triplet pair (^1TT) into individual triplets ($^1\text{T} + ^1\text{T}$), thus avoiding detrimental triplet-triplet recombination.⁶⁰ Furthermore, as intramolecular singlet fission (iSF) is an intrinsic property of D-A copolymers it thus eliminates the precise molecular orientation required of two chromophores in intermolecular SF and hence this unpredictable geometry is no longer a critical consideration in iSF.⁶¹

Pioneering work by Busby et al. reported D-A copolymers capable of iSF and emphasised the importance of strong D-A interactions along the polymeric backbone. For comparison, two copolymers (**PBTDO1** and **PBTDO2**) were synthesised containing an electron-rich donor unit benzodithiophene (B) and either mono- or bi-thiophene-1,1-dioxide (TDO) as the electron acceptor unit (**Figure 1.15**).⁶²

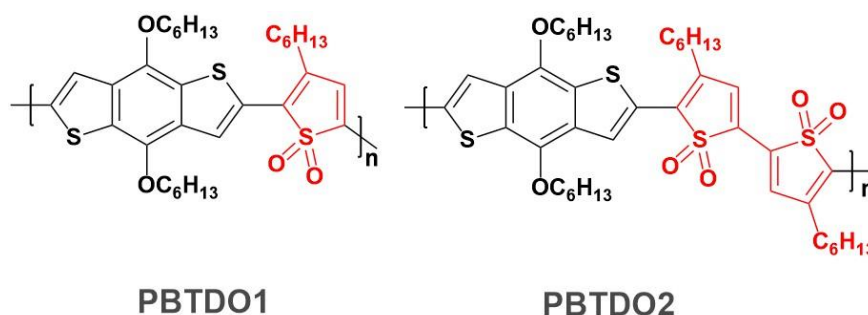


Figure 1.15. Molecular structures of D-A copolymers studied by Busby et al. for intramolecular singlet fission (iSF). Acceptor unit (thiophene-1,1-dioxide) shown in red. Donor unit (benzodithiophene) shown in black.⁶²

PBTDO1 displayed broad absorption features extending into the red region of the solar spectrum (**Figure 1.16** (a)) and a narrowing of the bandgap upon polymerisation (1.79 eV) as measured using cyclic voltammetry. The absorption properties of the copolymer show additional excitonic structures which are typical of D-A copolymers and indicate a feature with strong CT character. The population of excited CT states was a central focus in this paper, as coupling between a CT state and a T_1 state is stronger than that between a S_1 state and a T_1 state, thus mediating the population transfer to the triplet species during SF.

Transient absorption (TA) measurements of **PBTDO1** following 800 nm excitation were obtained to get an insight into the iSF mechanism (polymer was kept in a dilute CHCl_3 solution to avoid bimolecular interactions). **Figure 1.16** (b) displays the TA spectra over time (in ps), which initially produces an excited singlet absorption (> 750 nm) of high charge transfer character. This singlet absorption feature rapidly decays with a lifetime $\tau = 7$ ps (**Figure 1.16** (c), black circles) and simultaneously an additional transient at ~ 675 nm is formed, assigned to the absorption of the triplet exciton ((**Figure 1.16** (c), red circles). The formation of the triplet excited state on the ultrafast timescale is considered characteristic of the SF mechanism and has been reported for other systems that undergo SF. As can be seen in **Figure 1.16** (d), the

decay of this triplet species occurs with a time constant of $\tau = 70$ ps. A weak positive absorption feature spanning the visible region is then evident – this feature has been attributed to a charge-separated state (CSS), which persists after the decay of the triplet species and subsequently decays (> 1 ns). Using global analysis in combination with the TA data shown below, a study of the population evolution over time revealed that $\Phi_T = 170\%$.

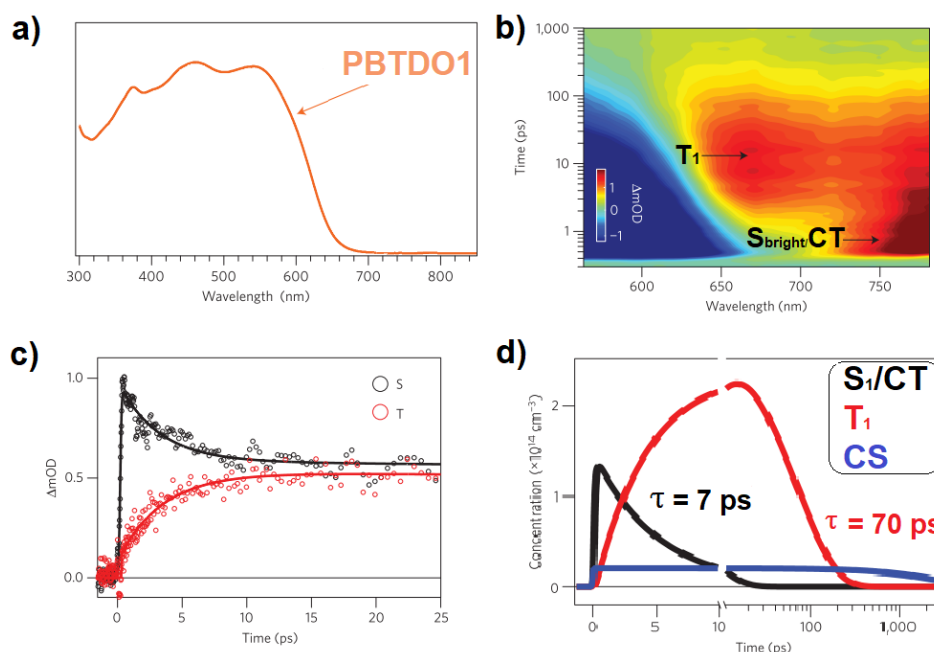


Figure 1.16. a) UV-visible absorption spectrum of **PBTD01** in dilute chloroform (CHCl_3) solution, b) Transient absorption spectra of **PBTD01** ($\lambda_{\text{exc}} = 800$ nm) in CHCl_3 , c) kinetic decay trace of singlet induced absorption (> 750 nm) (black circles) and kinetic formation of triplet induced absorption at ~ 675 nm (red circles), d) population concentration versus time for S_1 (black solid line), T_1 (red solid line) and CS (blue solid line) excited states.⁶²

While the triplet lifetime ($\tau_T = 70$ ps) obtained in this work is very short (as most often triplet lifetimes are in the μs - us range), the authors have attributed this to rapid recombination. They further stated that the short-lived nature of the triplet species reaffirms iSF as the predominant mechanism for population of the triplet state in the copolymer. It is declared that recombination of the triplet pair to the ground state can occur via spin-allowed triplet-triplet annihilation (opposed to the more commonly reported slower spin-forbidden recombination process of lone triplet excited states).

A valuable theoretical insight on iSF in D-A copolymers was reported recently by Corminboeuf and Fumanal wherein they described the involvement of three molecular

repeating units (A-D-A unit) along the polymeric backbone using poly(benzodithiophene-*alt*-thiophene-1,1-dioxide) (**Figure 1.17**).⁶⁰

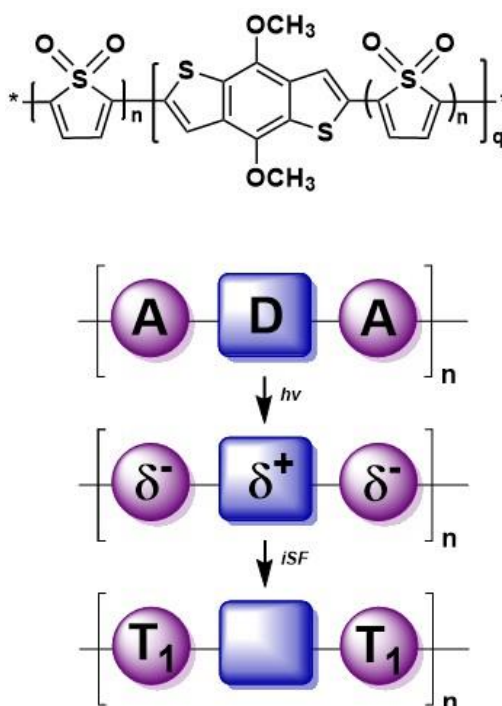
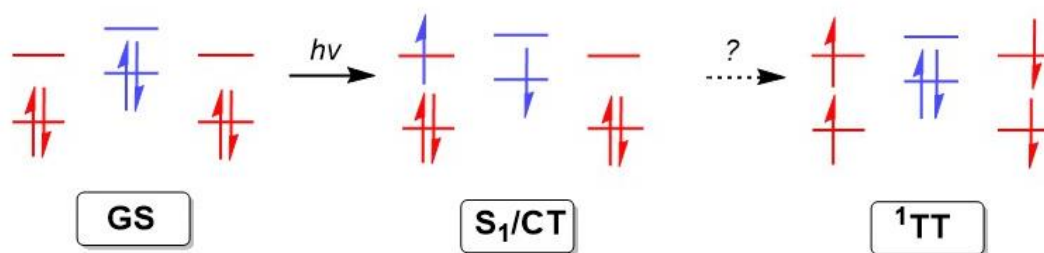


Figure 1.17. Molecular structure of D-A copolymer and schematic showing iSF in A-D-A repeating unit.⁶⁰

As can be seen in the diagram below (**Scheme 1.7**), photoexcitation of the ground state (GS) polymer results in population of an S_1 singlet excited state with significant CT character from the donor unit to the acceptor units. This then results in formation of the triplet correlated pair (1TT), followed by formation of individual triplets ($^1T + ^1T$) wherein the triplet states are located on the two acceptor units. The mechanism of iSF in D-A copolymers therefore must be distinct from that of homo/heterodimers previously reported only based on the involvement of two chromophore units.

A-D-A copolymer

Scheme 1.7. Photoexcitation of the ground state (GS) A-D-A repeating unit to populate a low-lying singlet excited state with significant charge transfer (S_1/CT) character to finally populate a correlated triplet pair (1TT). Question mark denotes the possibility of three distinct mechanisms that can occur to populate the 1TT state – direct, mediated and delayed mechanisms.⁶⁰

Three mechanisms possible for the $S_1 \rightarrow ^1TT$ splitting were summarised as direct, mediated, and delayed iSF and are shown in **Figure 1.18** including the energy levels of each energetic state.

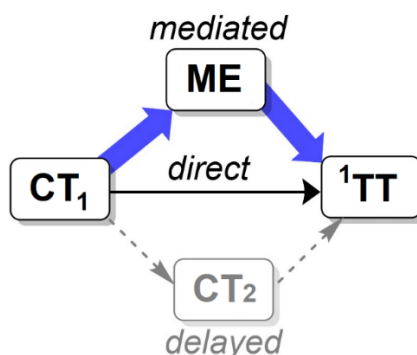


Figure 1.18. Direct, mediated, and delayed pathways for iSF.⁶⁰

For direct iSF to occur, the coupling between the S_1/CT (CT_1) state and the 1TT upper state must be significantly large. Alternatively, for mediated iSF to occur an upper CT state can be populated, followed by electron transfer to the strong vibronically coupled 1TT state. The delayed pathway shows population of a low-lying CT state which results in ultrafast population decay to the ground state species and hence inhibits population of 1TT state. Three factors which are central to iSF include: (1) energetics, (2) coupling and (3) separation, based on these mechanistic insights.⁶³

Moving from a theoretical study to an experimental study on poly(benzodithiophene-*alt*-thiophene-1,1-dioxide (**Figure 1.15**, PBTDO1), Busby et al. reported the influence of solvent polarity on the dynamics of the 1TT state.⁶⁴ The ground state absorption

spectra of the polymer dissolved in solvents with varying polarity, showed little to no spectral difference. Thus, despite the CT character associated with the singlet excited state in the D-A copolymer, the ground state properties of the S_1 state were found to be relatively insensitive to a change in solvent polarity.

The time resolved photoluminescence spectra of the polymer in all solvents (p-xylene, chlorobenzene, 1,2-dichlorobenzene, dichloromethane) showed a red-shift in the main emission band over the course of the experiment (100 ps) (**Figure 1.19** (a)). Spectral deconvolution revealed at least two species contributing to the observed emission (S_1 and 1TT , **Figure 1.19** (b)). The former contribution was attributed to fluorescence from S_1 with a time *ca.* 5 ps and the latter emission from 1TT with a decay time *ca.* 50 ps (**Figure 1.19** (c)). These time constants were consistent with kinetics extracted from TA spectra in earlier reports. The photoluminescence spectra of the polymer in all solvents used thus include both emission from the S_1 state and the longer-lived correlated triplet pair, 1TT .

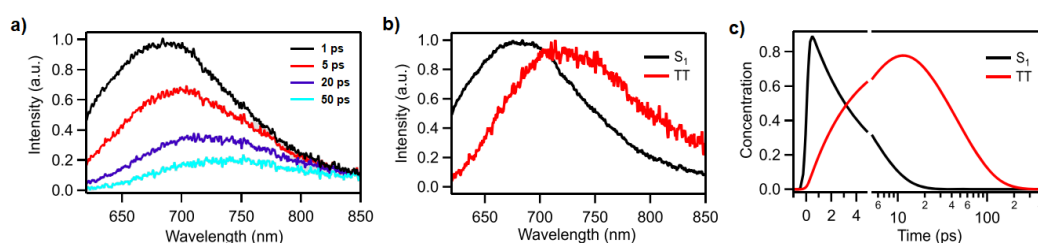


Figure 1.19. a) Time resolved photoluminescence spectra of **PBTD01** in diluted 1,2-dichlorobenzene solution, showing various time delays, b) spectral deconvolution of the data obtained in (a) to show two distinct emissive species labelled S_1 (black) and 1TT (red) and c) decay kinetics obtained for both S_1 (black) and 1TT (red) over 100 ps.⁶⁴

The deconvoluted emission spectra of **PBTD01** in these four different solvents shows a red shift of the 1TT emission band in more polar solvents (**Figure 1.20**, bottom spectra). As can be seen from these two sets of spectra, the emission from S_1 is solvent independent, while the emission from 1TT is somewhat solvent dependent, with a lower energy emission observed in solvents with higher polarity (e.g., 1.76 eV in non-polar solvents versus 1.66 eV in more polar solvents) showing the high CT character of the 1TT state. Despite the energy differences observed between S_1 and 1TT states,

this was not found to significantly influence the overall rate of iSF (presumably due to several other energetic and environmental factors at play).

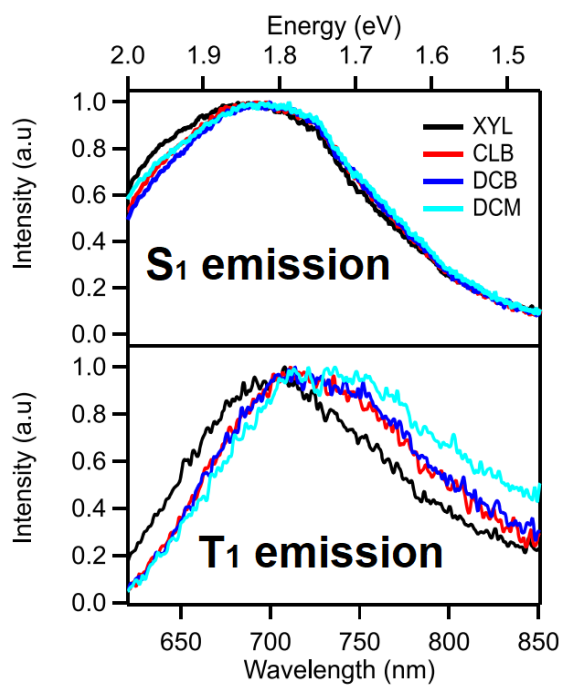


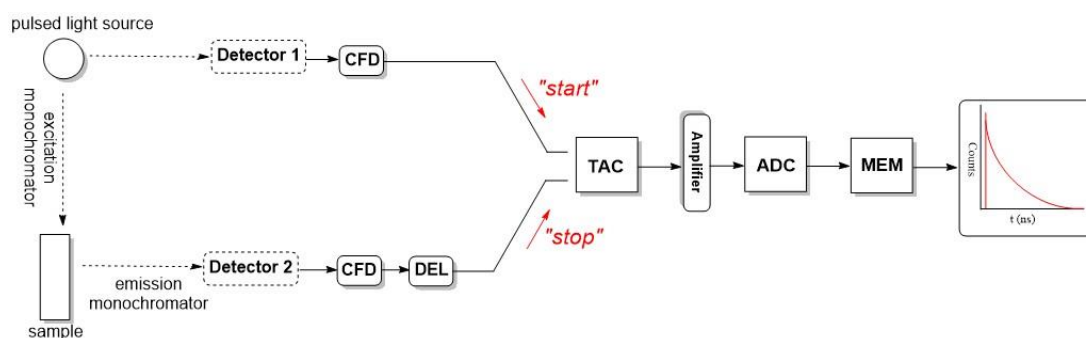
Figure 1.20. Deconvoluted emission spectra of **PBTDO1** in different solvents showing S_1 emission contribution (top) and 1TT emission contribution (bottom). Solvents XYL – p-xylene, CLB – chlorobenzene, DCB – 1,2-dichlorobenzene, DCM - dichloromethane.⁶⁴

1.6 Time-resolved techniques

The photophysical properties of photosensitisers can be further studied using time-resolved techniques to gain insight into the excited state dynamics of the PS in question and reveal key properties such as emission lifetimes (τ_{fl}) and electron transfer rates such as the rate of ISC onto the triplet surface.

1.6.1 Time correlated single photon counting

Time correlated single photon counting (TCSPC) is a technique used to measure photoluminescence lifetimes (τ_{PL}) of emitting molecules or more specifically to measure the precise amount of time it takes for an excited state molecule to emit photons. This is a powerful technique that employs a laser source with a high repetition rate to excite the sample (picosecond pulsed laser), followed by detection of a single photon from the radiative decay using a photomultiplier positioned at a right angle to the excitation beam. The experimental set up is displayed in **Scheme 1.8** illustrating the main components of the spectrometer set up – the light source, the excitation monochromator, the sample chamber, the emission monochromator, the detector and the computer for data accumulation and processing.



Scheme 1.8. Schematic of the instrumental set-up in a typical TCSPC spectrometer.⁶⁵

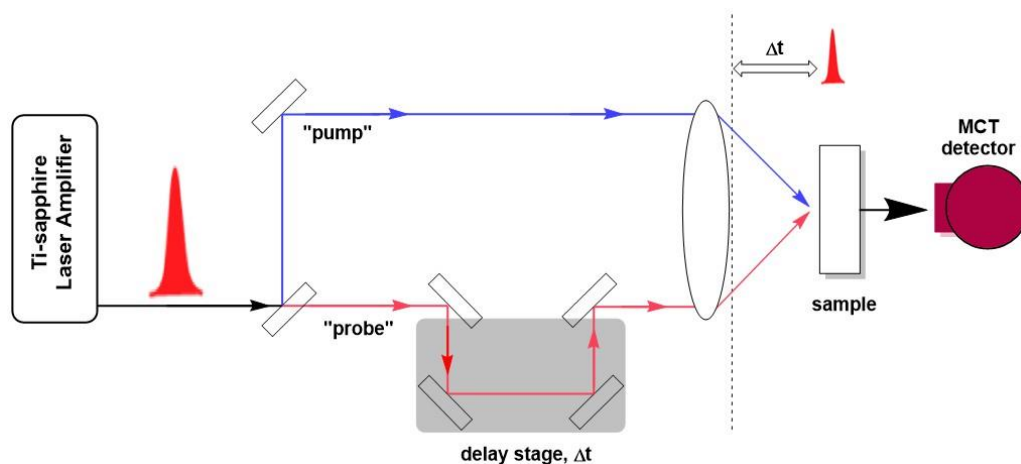
During a TCSPC experiment, the pulsed laser excitation source is triggered in order to generate an excited state chromophore, which subsequently emits after a certain time (ps-ns timescale for fluorescent processes). Following excitation of the sample using a single laser pulse, multiple molecules in the sample are excited at slightly different times, which results in a rate of radiative decay, measured using a decay curve.

Part of the laser excitation source is directed onto detector 1, **Scheme 1.8** which is thus measured as a “start” signal pulse and builds up charge as a voltage. The second beam from the laser excitation source is used to excite the sample prior to sample emission. Detection of a single emissive photon from detector 2 results in a “stop” signal pulse to be generated. After these start-stop signals are detected, a signal is sent to the time-to-amplitude (TAC) converter which will cease the increase of the voltage building up (which was initiated from the “start” signal). The constant fraction discriminator (CFD) is used to elucidate precise timing of the pulses. The experimental set-up includes an electrical delay (DEL) which can delay the signal transmission to the TAC converter if required. Hence, the TAC signal is initiated once a signal reaches it from the emission of the sample i.e., an output pulse is generated from the TAC after one start-stop sequence. This signal is amplified and sent to an analogue to digital converter (ADC) and digital memory (MEM). This process is repeated to build up the time correlation consisting of multiple start-stop sequences. The accumulation of the data and the various time intervals are recorded on a histogram to construct a decay profile of the emission of the chromophore. Deconvolution methods are carried out using either monoexponential or multiexponential fit function(s) to obtain the lifetime of the chromophore with a corresponding standard error associated with the measurement and a chi-squared value (χ^2). The high repetition rate of the pulse laser excitation source is crucial in this technique, as it allows picosecond accuracy for detection of the emissive photon of the sample and thus enables measurement of lifetimes on the early picosecond to nanosecond timescale. It is imperative that the excitation beam successfully populates an excited state of the chromophore in question and this is ensured by choosing a wavelength corresponding to ground state absorption bands of the chromophore.

1.6.2 Transient absorption spectroscopy

Transient absorption spectroscopy (TAS) can provide valuable insights into the excited state dynamics of molecules. TAS works using a pump-probe experimental set-up (**Scheme 1.9**). Also known as laser flash photolysis, this process involves excitation of a ground state sample with a short but intense laser pulse (known as the “pump”) to populate either singlet or triplet excited state species. The rapid generation

of these laser pulses of the “pump” allows for ultrafast dynamics of excited states to be measured (ps-ns timescales) as typically the “pump” must be significantly shorter than the photophysical processes being measured. A broadband white light pulse known as the “probe” is then sent through the sample with a specific delay time, Δt , before being measured by the detector.^{66–68}



Scheme 1.9. Schematic displaying a simplified experimental set-up for “pump-probe” technique for ultrafast TA spectroscopy experiments. Adapted from literature reference.⁶⁶

The TA data is interpreted using a difference spectrum i.e., the absorption spectra of the transient species minus the ground state absorption spectrum (ΔA). To obtain a range of delay times in an experiment, the delay time, Δt , between the pump and probe is varied to obtain a range of spectra ΔA at different time delays i.e., ($\Delta A(\lambda, \tau)$). This is often reported as a change in optical density (OD) as per the following **Equation 1.14**.⁶⁶

$$\Delta OD(\lambda, \tau) = \log \frac{I_{00}}{I(\lambda, \tau)}$$

Equation 1.14. Transient absorption data displayed as a change in optical density detected from sample.

Where I_{00} is the intensity of the pump light source before transient species are formed and $I(\lambda, \tau)$ is the intensity measured from the sample after transient species are formed (and at varying delay times). An advantage of TA spectroscopy is the ability to observe the photodynamics of non-emissive states.

Displayed in **Figure 1.21** is an example of a typical TA spectrum.⁶⁷ A ground state bleach (GSB) feature appears as a negative absorption band due to the decrease in concentration of ground state molecules as a result of population of the excited state species. The ground state (S_0) absorption spectrum (dashed line) demonstrates that the GSB feature is observed at approximately the same wavelength as the absorption maxima of the ground state absorption. In this example, stimulated emission (SE) (dotted line) occurs when the excited state species returns to the ground state after the probe pulse passes through the sample (the probe induces emission). The SE feature typically corresponds to the fluorescence spectrum of the parent compound and hence is more prominent in shorter timescale experiments that are collected within the same timeframe as the emissive processes occurs. In the case of chromophores with a small Stokes shift, SE overlaps with the GSB and may not be spectrally resolved in the TA spectrum. The positive feature in **Figure 1.21** is referred to as an excited state absorption (ESA) feature resulting from the initial formation of excited state species after excitation with the pump laser, followed by further population of further excited states of the molecule and these appear as positive features in the spectrum. Another feature that can be observed in a TA spectrum is a product absorption, wherein the transient species formed can react to form different species such as radical anions and cations that can appear at different wavelengths to the initially formed ESA feature. The lifetime of the excited state species can be obtained and (depending on the timescale of the experimental set-up) this can provide knowledge of singlet lifetimes (τ_S), triplet lifetimes (τ_T) or identify any excited state intermediates such as CSS.

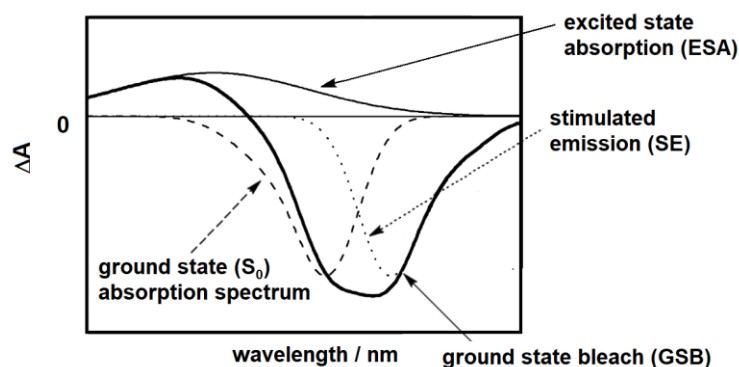


Figure 1.21. An example of a TA spectrum showing general spectroscopic features observed shown using change in absorption of sample (ΔA) and wavelength (nm). Figure adapted from literature.⁶⁷

1.6.3 Time resolved infrared spectroscopy

Time-resolved infrared (TRIR) spectroscopy operates using the same principles as those described in TA spectroscopy, however, an infrared probe is monitored as a function of time (i.e., transient species are monitored using IR detection). A typical TRIR spectrum is shown in **Figure 1.22** displaying both GSB and ESA features in the IR region (wavenumber (cm^{-1})).^{69,70}

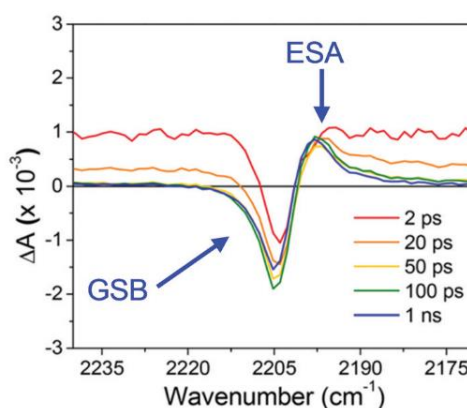


Figure 1.22. An example of a TRIR spectrum showing ESA and GSB features at different time delays shown in the legend. Time resolved data displayed in the IR region (wavenumber, cm^{-1}). Figure adapted from literature.⁶⁹

TRIR spectroscopy provides structural information pertinent to the chromophore and functional groups such as $\nu(\text{CO})$ and $\nu(\text{CN})$ with strong and characteristic vibrational bands in the IR spectrum are very susceptible to molecular structural changes, and these type of functional groups are referred to as reporter ligands.⁷¹ For example, in metal carbonyl complexes such as $(\eta^6\text{-benzene})\text{Cr}(\text{CO})_3$ can be monitored closely using TRIR by observed of the spectrally unique carbonyl (CO) bands at 1984 cm^{-1} and 1916 cm^{-1} .⁷² TRIR spectroscopy has also been used more recently to investigate intermediate excited states in the process of singlet fission (which will be discussed in more detail in Chapter 4).⁶⁹ The picosecond-to early nanosecond (ps-ns) time resolved studies reported in this work was carried out using the ULTRA Laser system at the Central Laser Facility in Rutherford Appleton Laboratory (RAL) using ultrafast (~ 50 fs) pump lasers allowing for early-time kinetics of both TA and TRIR spectra to be recorded.⁶⁸

1.7 Conjugated polymers for photocatalytic hydrogen evolution

1.7.1 Polymers for hydrogen generation

As shown in **Figure 1.23**, polymeric photocatalysis for hydrogen evolution has developed rapidly over the past decade with the discovery of many active materials. This includes linear conjugated polymers, planarised polymers, conjugated microporous polymers (CMPs), covalent triazine frameworks (CTFs), covalent organic frameworks (COFs), carbon nitrides (g-C₃N₄) and polymer dots.⁷³ For the purposes of this literature survey, there is a focus on polymers used for photocatalytic hydrogen evolution in solution based studies (including both soluble polymers and insoluble polymers).

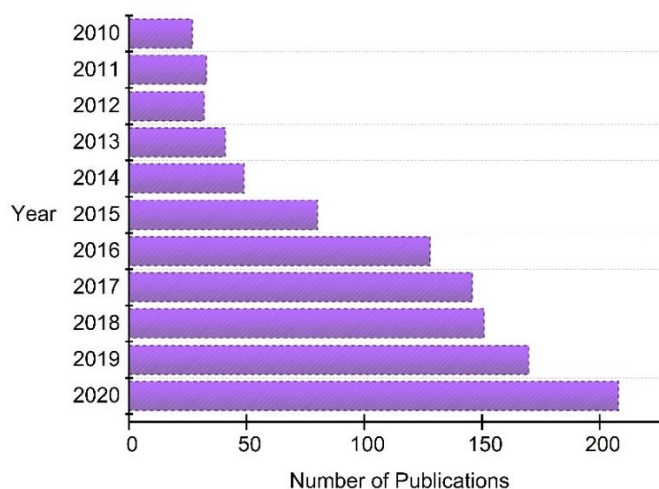
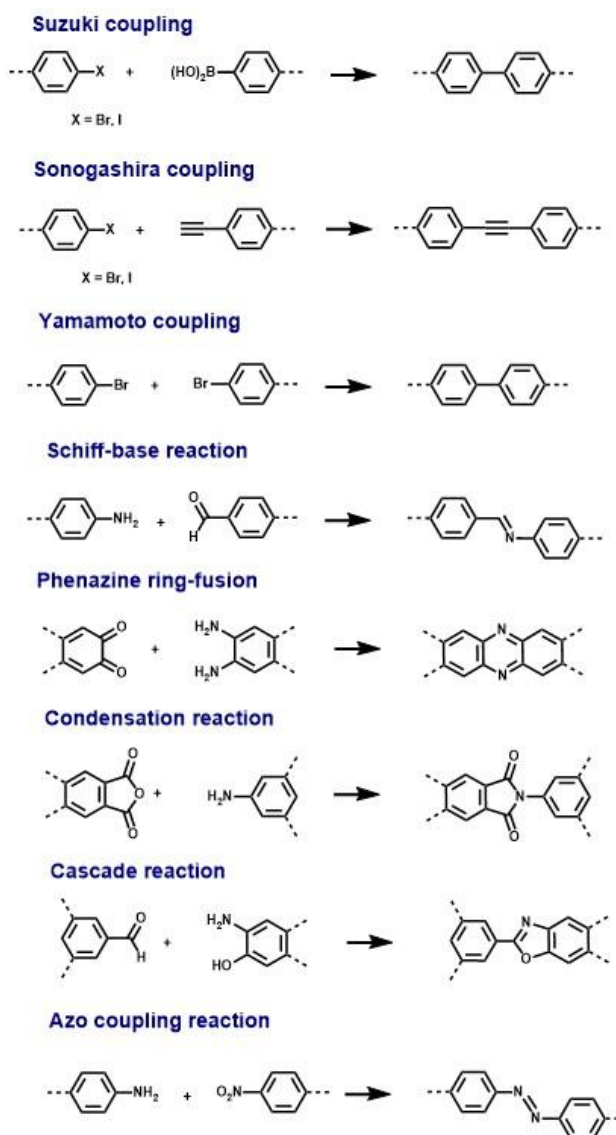


Figure 1.23. Number of publications in the last 10 years, per year from literature research using keywords "water splitting" and "polymers" (data source ISI Web of Science).

Conjugated polymers present advantages compared to previously investigated inorganic metal oxide semiconductors, such as robustness and non-toxicity. The building blocks for these polymers consist mainly of C, H and N atoms – which are both cheap and abundant in nature.⁷⁴ Cross-coupling between two different monomers with di-functionalised end-groups has allowed for the synthesis of a wide range of polymeric materials using different building blocks (**Scheme 1.10**), which has facilitated structure-activity relationships in hydrogen generating systems.^{75,29} Inorganic semiconductors have been widely used in the past, however the d⁰ and d¹⁰ electronic configurations of these inorganic metal oxides results in limited

properties.⁷⁴ However, it is possible to manipulate the optical gap in conjugated polymers by varying the monomer composition.^{29,76,77}



Scheme 1.10. Reactions employed in polymer synthesis. Dashed bond represents polymer chain. Adapted from reference.⁷⁵

Upon polymerisation of the corresponding monomeric units, an increase in π -conjugation results in an increase electron transport ability along the polymer backbone (this improve charge separation).⁷⁷ The π -stacking between 2D polymer backbones has led to strong interplanar interactions, which has been shown to give way to additional charge migration processes such as charge hopping. This increase in electron migration conclusively provides more photogenerated charges for the catalyst to carry out the necessary reduction reaction to liberate hydrogen.⁷⁴ Furthermore, a red

shift upon polymerisation is often evident (due to enhanced conjugation) thus pushing the absorption of the polymers into the visible region of the solar spectrum.

While there is ambiguity regarding the mechanism of photocatalytic activity of the polymers reported to date for hydrogen evolution, there is a limited understanding of their activity to date. The fundamentals of light absorption in polymeric materials are similar to that previously described in section 1.3.4.1 for organic chromophores. In brief, upon absorption of light, an excited electron-hole pair (exciton) is formed, which then undergoes charge separation to form the corresponding free charges; subsequently driving the proton reduction half reaction in hydrogen generation. A crucial consideration in the photocatalytic experimental design is to ensure the incident light is equal to or greater than the optical gap of the polymer i.e., the irradiation wavelength chosen must have considerable overlap with the absorption spectra of the polymer to successfully generate excitons and thus free charges. In organic-based polymeric materials, Frenkel excitons are usually generated which possess a high binding energy (E_b typically > 100 meV) and often make exciton dissociation into free charges difficult. These tightly bound excitons often lead to deactivation through pathways including radiative and thermal pathways to the electronic ground state of the polymer. Excitons that are formed must also migrate to the surface of the polymer at the polymer-solution interface, where a free charge carrier that has separated from the exciton binding force, can be used in the reduction reaction.²⁹ Recently, Wang et al. reported a decrease in exciton binding energy in a donor-acceptor polymer based on a dibenzothiophene-*S,S*-dioxide acceptor and a diphenyl donor. A low-lying charge transfer state was shown to promote electron transfer from the donor to the acceptor, thus boosting charge migration and leading to enhancement in photocatalytic performance.⁷⁸

Furthermore, the free electron must be able to thermodynamically drive the proton half reaction and thus the electron affinity (EA) of the polymer must be more negative than the potential of the proton reduction half-reaction ($H^+_{(aq)} + e^- \rightarrow \frac{1}{2} H_{2(g)}$, $E = -0.41$ V versus SHE at pH 7).²⁹

The majority of literature reported to date using conjugated polymers for hydrogen evolution describes the polymers during the photocatalytic experiments as ‘powder suspensions’, as conjugated polymers maybe insoluble in either aqueous or organic solutions. Thus, there are only a few reports of conjugated polymers fully dissolved (soluble) during photocatalytic experiments. Both soluble and insoluble polymers (as heterogeneous particles) in solution will be summarised in this chapter.

1.7.2 Soluble conjugated polymers in solution for hydrogen evolution

Rau and co-workers studied novel polymethacrylate iridium-based polymers for hydrogen generation. This approach comprised of an “all-in-one” polymeric assembly containing the PS, a viologen electron mediator and a tri-ethylene glycol methyl ether methacrylate (TEGMA) solubilising moiety along attached via a methacrylate polymer backbone (**Figure 1.24**).⁷⁹ This rationale for this design was to enhance energy transfer processes and inhibit back electron transfer. Photocatalytic experimental conditions use TEA as a sacrificial donor, colloidal Pt as a catalyst (*in situ* from K_2PtCl_4) and an LED of $\lambda = 470$ nm, yielding a TON of 139 following irradiation for 7 hr.



Figure 1.24. Iridium-based polymethacrylate polymer for hydrogen generation under 470 nm. TEGMA - tri-ethylene glycol methyl ether methacrylate. Colloidal Pt generated *in situ* from K_2PtCl_4 .⁷⁹

In efforts to move away from precious metal-based photosensitisers, incorporating Ru or Ir, organic based polymers such as poly(flourene-*co*-phenylene) (**PFP**) was used as

a photosensitiser (PS) in combination with a DuBois-type NiP catalyst in a 0.1 M solution of ethylenediaminetetraacetic acid (EDTA) as SA at pH 6 (**Figure 1.25**).⁸⁰

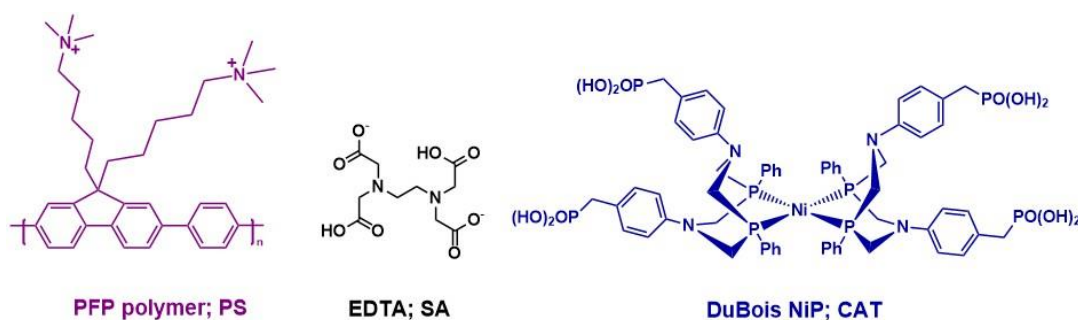


Figure 1.25. Homogenous photocatalytic system containing poly(flourene-*co*-phenylene) (**PFP**), EDTA as the sacrificial agent (SA) and DuBois NiP as catalyst (CAT). PS – photosensitiser in 0.1 M EDTA solution at pH 6.⁸⁰

Hydrogen evolution was moderate over 4 hr obtaining 6.2 $\mu\text{mol H}_2$ and an AQY = 0.64% using Xe arc lamp $\lambda > 320$ nm. In the design of **PFP** as a PS, charged alkyl groups were incorporated to enhance the solubility of the polymer. Time resolved studies provided insights into the photocatalytic cycle. An insight into the excited state behaviour using time-resolved techniques is much more difficult with insoluble polymers (which will be mentioned in the subsequent sections) and this is a major drawback of insoluble polymers used as heterogenous nanoparticles for hydrogen generation.

Tian et al. reported polymer dots for photocatalytic splitting of water by incorporating a water-soluble polystyrene polymer with a carboxyl group (**PS-PEG-COOH**) and [(9,9'-dioctylfluorenyl-2,7-diyl)-*co*-(1,4-benzo-{2',1,3} thiadiazole)] (**PFBT**) in an organic-free solvent system. Formation of these micelles was carried out by first dissolving the **PFBT** in THF, adding it to a water solution containing **PS-PEG-COOH** and purging off the THF solvent under ultrasonication to yield a homogeneous green solution of the polymer dots (**Figure 1.26**).⁸¹

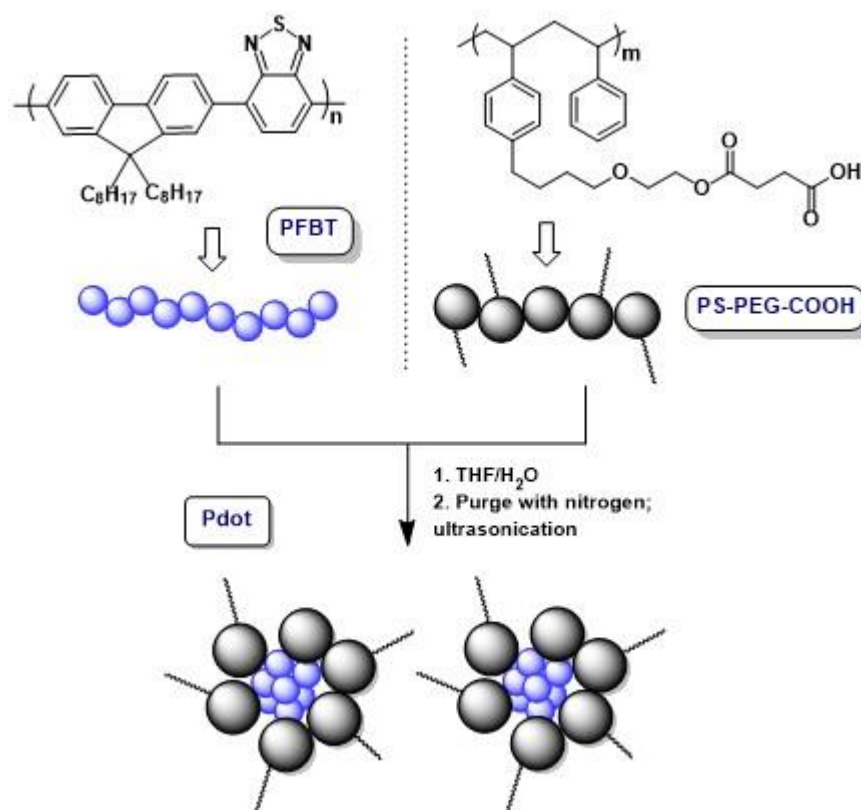


Figure 1.26. Polymer dots containing water soluble polymer (PS-PEG-COOH) and water insoluble polymer (PFBT) - fabrication of polymer dots to form homogeneous solution. Wavy line represents soluble side chain.⁸¹

The polymer dots obtained showed a red shift of ~ 20 nm in the UV-visible absorption spectrum compared to the **PFBT** polymer in THF solution, and this was attributed to the J aggregation of the polymer dots in solution. Hydrogen experiments carried out using ascorbic acid as a SA produced a moderate amount of hydrogen ($8.3 \text{ mmol h}^{-1} \text{ g}^{-1}$) with an AQY = 0.5%. However, deactivation of the system after one hour was observed due to aggregate formation and it is clear that the long-term stability of the system needs to be improved. Addition of a co-catalyst and/or increasing the concentration of polymer dots in solution were suggested to improve the photocatalytic activity.

1.7.3 Insoluble conjugated polymers in solution for hydrogen evolution

The emerging field of polymers for photocatalytic hydrogen generation has been dominated by heterogeneous catalysis. Under this terminology, the conjugated polymers are added to the photocatalytic solution as powder suspensions and the solution is mixed throughout irradiation. Due to the insolubility of these polymer

materials in both aqueous and organic solvents, the polymers are sonicated until a ubiquitous dispersion of powder particles form and are then used for photocatalytic experiments.

1.7.3.1 Carbon nitride (g-C₃N₄) polymers

Carbon nitride (g-C₃N₄) has received a lot of attention due to the attractive properties it has for overall water splitting.^{82–84} Carbon nitride polymer structures consist of *s*-triazine and tri-*s*-triazine units (heptazine/melon) (**Figure 1.27**).⁷⁷ The majority of carbon nitride polymers are synthesised using the tri-*s*-triazine unit as it is energetically favoured, more stable and easier to purify than the *s*-triazine unit.⁸²

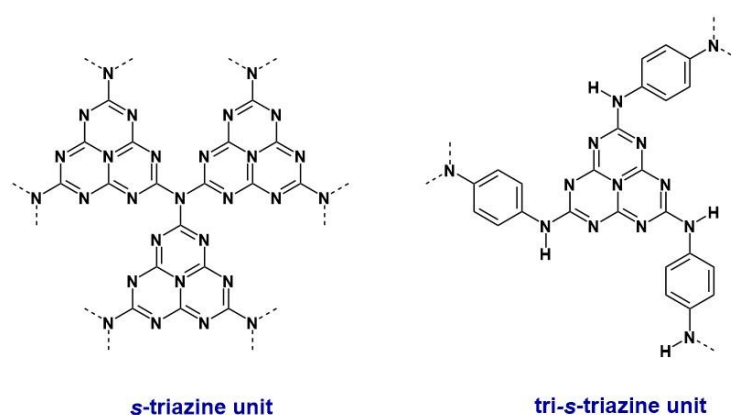


Figure 1.27. Graphitic carbon nitride units showing *s*-triazine unit (left) and tri-*s*-triazine unit (right).⁷⁷

In 2009, Wang et al. who demonstrated the overall water splitting ability of carbon nitride polymers based on tri-*s*-triazine units. These 2D graphitic planar polymers are insoluble in organic solvents and aqueous solutions (in addition to both acidic and basic aqueous solutions). Preliminary hydrogen experiments were carried out using the g-C₃N₄ powder suspended in aqueous solution containing 10% TEOA as a sacrificial agent. While a moderate amount of hydrogen was observed (~ 4 μmol h⁻¹), more activity was observed using 3.0 wt.% Pt-deposited g-C₃N₄ to obtain 770 μmol after 72 hr irradiation, displaying high stability during irradiation.⁸⁵

Factors that contribute to the superiority of carbon nitride as a polymer for overall water splitting include remarkable thermal stability (thermogravimetric analysis shows decomposition only above 600 °C), exceptional chemical stability (van der

Waals interaction between polymer sheets increases stability) and optical properties suitable for water splitting (band gap ~ 2.7 eV, **Figure 1.28** (a)).^{86,87}

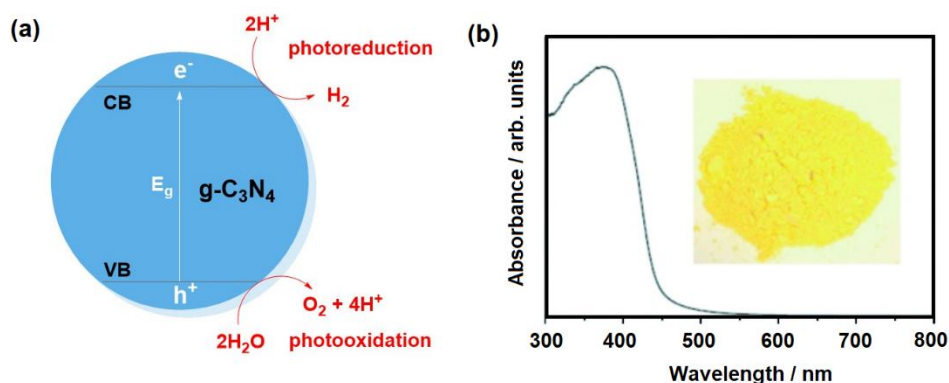


Figure 1.28. (a) $g\text{-C}_3\text{N}_4$ as a semiconducting material for overall water splitting. CB – conduction band, VB – valence band, E_g – band gap of polymeric semiconductor. (b) UV-visible diffuse reflectance spectrum of $g\text{-C}_3\text{N}_4$, inset showing polymer powder. Figure adapted from literature.⁸³

While the interest in $g\text{-C}_3\text{N}_4$ as a photocatalyst for hydrogen evolution has surged since this publication, there are still some drawbacks associated with this polymeric material. A lack of chemical diversity of the starting materials (triazine, heptazine units), has hindered the synthetic flexibility regarding possible $g\text{-C}_3\text{N}_4$ functionalised polymers. Harsh synthetic conditions are also required for the synthetic procedure of $g\text{-C}_3\text{N}_4$ (some thermal polycondensation preparation methods require over 500 °C).^{85,73} Furthermore, $g\text{-C}_3\text{N}_4$ has limited light absorption in the visible region ($\lambda > 470$ nm) as shown by the solid-state absorption spectrum in **Figure 1.28** (b).⁸³ Modification of $g\text{-C}_3\text{N}_4$ by sensitisation with a visible-light absorbing chromophore (Eosin Y) has proved successful for extending the optical absorption of $g\text{-C}_3\text{N}_4$ up to 600 nm and an AQY for hydrogen evolution of 19.4% was obtained at 550 nm using this strategy.⁸⁸ Eosin Y adsorbed onto the $g\text{-C}_3\text{N}_4$ surface is photoexcited and an electron moves from the HOMO to the LUMO of the dye. From here, electron injection occurs from the LUMO of the dye into the CB of the $g\text{-C}_3\text{N}_4$, which prevents undesirable charge recombination.⁸²

The irregular composition of bulk $g\text{-C}_3\text{N}_4$ polymer is also considered an intrinsic drawback of the material as it results in slow charge transfer of generated charges to the surface. A recent summary of strategies for surface engineering of $g\text{-C}_3\text{N}_4$ material

highlight the importance of surface regulation, surface functionalisation and surface assembly as routes to improve the overall activity of $g\text{-C}_3\text{N}_4$, all aiming to tackle the challenges associated with the polymeric material.^{84,89}

1.7.3.2 Linear conjugated polymers

The pioneering report of polymers for hydrogen evolution can be traced back to 1985, when Yanagida et al. reported a linear polymer, poly-p-phenylene (**PPP**) with a band gap of 2.9 eV for water splitting in an aqueous solution of diethylamine under irradiation $\lambda > 290$ nm (**Figure 1.29**).⁹⁰

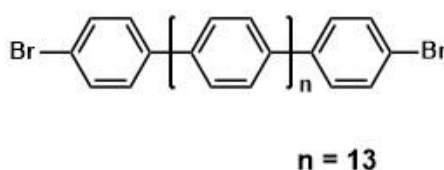


Figure 1.29. **PPP** used for first polymeric hydrogen evolution reaction; consisting of terminal 4-bromophenyl units and repeating unit of $n = 13$.⁹⁰

After 40 hours of irradiation approximately $8.3 \mu\text{mol h}^{-1}$ of H_2 was detected. While this is a low value and would not be sustainable for scale-up; it paved the way for future work in the area. When the **PPP** polymer containing $n = 6$ monomer units was used – no hydrogen was observed. This could indicate that a certain degree of π -conjugation is required for successful water splitting. Although this research can be deemed quite preliminary, it presented the potential of conjugated polymers for hydrogen evolution.

1.7.3.3 Planarised linear conjugated polymers

Almost two decades later, this work was expanded by Cooper et al., who investigated planarised polymers for hydrogen generation. This was carried out by the addition of a methylene bridge into the polymeric backbone of a linear polymer (**Figure 1.30**).⁹¹

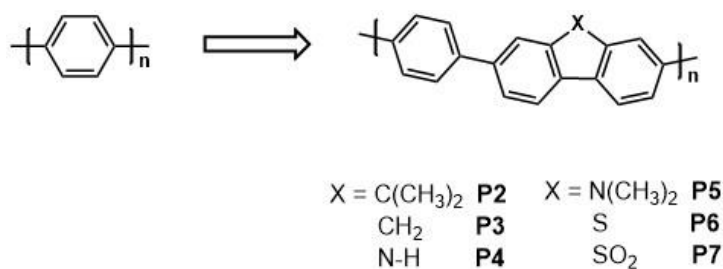


Figure 1.30. Planarised conjugated polymers synthesised showed a decrease in optical band gap; which was shown to produce more H₂ than their non-fused equivalents.⁹¹

In this study, addition of the methylene bridge to form the planarised polymer, resulted in increased rigidity and lowered the torsional angle. Increase in conjugation subsequently results in a larger area for electron/hole oscillation, leading to a large charge separation.⁹² Consequently, creation of these novel polymers in extended dimensions decreased the optical gaps, thus allowing the capture of more photons for photocatalysis. Furthermore, longer charge carrier lifetimes were observed, which can contribute further to the higher hydrogen evolution rates observed with the planarised polymers compared to the linear counterparts (**Figure 1.30**).⁹¹ Photocatalytic experiments were carried out by dispersion of 25 mg of the polymer in a water/TEA/MeOH mix and irradiation using a Xe arc lamp with i) $\lambda > 295$ nm and ii) $\lambda > 420$ nm. These conditions produced 92 $\mu\text{mol h}^{-1}$ (**P7**, **Figure 1.30**), without a co-catalyst, and 118 $\mu\text{mol h}^{-1}$ when a co-catalyst was added. No solubilising groups were added to these polymers, resulting in limited characterisation and photocatalytic experiments conducted using the polymer dispersion.

An investigation into the effect of fused rings in conjugated polymers for hydrogen evolution has expanded in this research field and the majority of reports conclude that incorporation of a fused ring structure into the polymer significantly boosts the hydrogen evolution efficiency. For example, a comparative study on the effect of fused thiophene rings with fluorene as a linker unit (**PFT**, **PF2T** and **PF3T**, **Figure 1.31**) was carried out to investigate the effect of increasing the fused rings along the polymeric backbone on photocatalytic hydrogen evolution.⁹³ The photophysical properties, specifically the UV-visible absorption maxima of the three polymers varied showing a stronger red shift for **PF3T** (**PF3T**: $\lambda_{\text{abs}} = 448$ nm, **PFT**: $\lambda_{\text{abs}} = 428$ nm) attributed to the increase in π -conjugation due to the fused thiophene units.

Interestingly, the fluorescence lifetimes of the three polymers were almost identical when excited with 420 nm in dilute CH_2Cl_2 solution (**PFT**: $\tau_{\text{fl}} = 0.73$ ns, **PF2T**: $\tau_{\text{fl}} = 0.70$ ns and **PF3T**: $\tau_{\text{fl}} = 0.71$ ns). **PF3T** displayed the highest hydrogen evolution efficiency of $1095 \mu\text{mol h}^{-1} \text{g}^{-1}$ when irradiated (350 W Xe arc lamp, $\lambda > 420$ nm) in a 1:1:1 solution TEA:H₂O:MeOH. Under identical conditions, **PF2T** which contained only two fused thiophene units, showed activity of $655 \mu\text{mol h}^{-1} \text{g}^{-1}$ after 6 hours of irradiation.

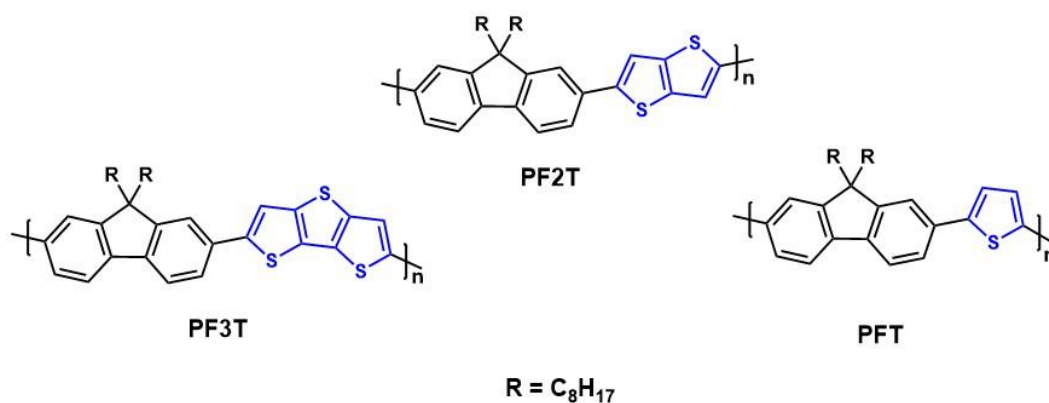


Figure 1.31. Conjugated polymers containing no (**PFT**), two (**PF2T**) and three (**PF3T**) fused thiophene rings (blue structures) linked with fluorene units (black structures).⁹³

1.7.3.4 Porous organic polymers

Well-known for their high surface area and porosity, porous organic polymers (POPs) offer a promising new class of materials for this application. POPs consist of covalently linked monomer units, with defined pore size and diameter. It is thought that these pores can facilitate photocatalytic processes such as those involved with electron-hole dynamics by increasing the surface area of electron/hole pairs at the surface. The organic building blocks available for synthesis of POPs allows tunability of polymers by variation of linker unit, hence variation of pore size and other properties.⁹⁴ POPs are divided into three main families – conjugated microporous polymers (CMPs), covalent organic frameworks (COFs) and covalent-triazine frameworks (CTFs).

1.7.3.4.1 Conjugated microporous polymers (CMPs)

Conjugated microporous polymers (CMP's) are distinguished from other polymers by both their porous nature i.e., they do not have a defined lattice structure such as those found in crystalline solids. Similarly to many polymers discussed in this section, CMPs have a π -conjugated molecular architecture, a high surface area and hence a large area of delocalised electrons.⁷⁵ CMPs offer great potential for effective catalytic conversions as their confined pores can act as active sites for the interplay between photons, electron-hole pairs and free electrons. The large electron delocalised network of the CMPs can enhance the charge carrier transportation of these generated free electrons.⁹⁴ As with previous polymers discussed in this section, CMP's reported to date are insoluble; and hence hydrogen generation reported has been for heterogenous mixtures i.e. powdered catalyst used for photocatalysis, in conjugation with a sacrificial agent in aqueous solution.

In 2015, the pioneering work of Cooper et al. received much attention in the area of CMPs as it was the first example of systematically tuning the optical gap of a series of polymers and measuring the correlation between optical gap of the polymers and the photocatalytic performance. A range of pyrene-containing polymers were synthesised by varying both the molar ratio and monomer composition (x, y, z and a, **Figure 1.32**).⁷⁶ Variation of the monomer composition allowed tuning of the optical band gap between 1.94 – 2.95 eV, which in turn affected the hydrogen evolution ability of the polymer photocatalysis (note – porosity of polymers were also varied by a change in monomer composition). For example, **CP-CMP1** with an optical band gap of 2.95 eV produced 5 $\mu\text{mol H}_2$ after 6 hr irradiation (300 W Xe Arc lamp, H_2O /diethylamine mix), whereas **CP-CMP10** with an optical band gap of 2.33 eV produced 100 $\mu\text{mol H}_2$ under identical experimental conditions. However, as the pyrene content in the CMPs increased along the series from **CP-CMP10** (33% pyrene content, $E_g^{\text{opt}} = 2.33$ eV) to **CP-CMP15** (100% pyrene content, $E_g^{\text{opt}} = 1.94$ eV) the photocatalytic hydrogen evolution rate decreased dramatically from 100 $\mu\text{mol H}_2$ to <1 $\mu\text{mol H}_2$, respectively. The authors note that they unsure of how to explain this observation but suggest that there is an increase in dark non-radiative decay of the

excited electrons to the ground state in CMP containing a higher pyrene content, thus decreasing the photocatalytic performance. It was postulated that these systems containing exclusively donor moieties, resulted in low hydrogen TON due to insufficient charge separation (no push-pull system for enhancing electron migration to the surface). As a result, future work focused on CMPs incorporating both donor and acceptor monomers into their architecture.

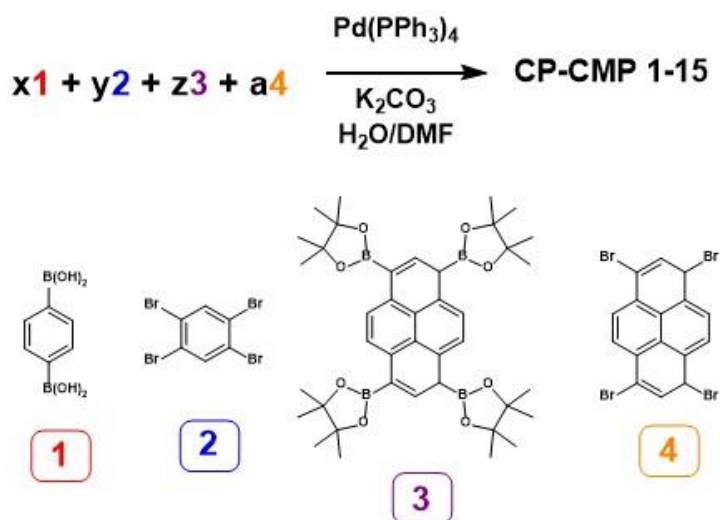


Figure 1.32. A series of CMP synthesis containing varying ratio of monomer units to tune the optical band gap of CMPs.⁷⁶

Benzothiadiazole (acceptor unit/electron withdrawing unit) moieties have been incorporated into different positions along polymer backbones and reported for their evolution of hydrogen under photocatalytic conditions by Wang et al.⁹⁵ Herein, both 1D and 3D architectures were fabricated and a range of band gaps between 2.17 – 2.29 eV were obtained (**Figure 1.33**).⁹⁵ All polymers are insoluble in organic solvents and were tested for hydrogen production by charging 50 mg of the polymer powder in an aqueous solution containing 10% vol TEOA as the SA. Low hydrogen activity was observed for polymers without the addition of a co-catalyst. The co-catalyst employed in this study were Pt, Rh and Pd which were deposited on the surface of the polymer *in situ* using either H_2PtCl_6 , RhCl_3 or PdCl_2 respectively.

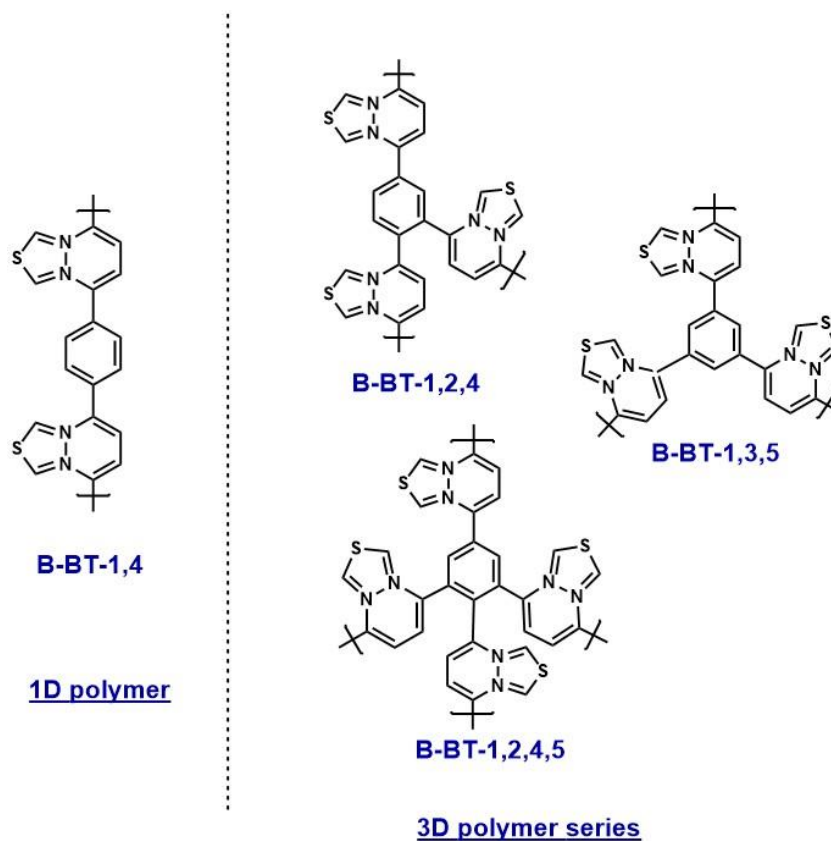


Figure 1.33. Polybenzothiadazole polymers synthesised for hydrogen evolution. Left: linear polymer series. Right: 3-D polymer series consisting of 1,2,4, 1,3,5, and 1,2,4,5 substituted phenyl comonomer units.⁹⁵

This paper reports that the linear polymer produced the most hydrogen with $116 \mu\text{mol h}^{-1}$ using TEOA 3.0 wt.% Pt co-catalyst irradiated with a 300 W Xe arc lamp. Despite the lower band gaps obtained for the 3D polymers, it was found that upon the introduction of the 3D crosslinker to the polymer backbone, a decrease in hydrogen generation was observed. The suggested reason for this observation was attributed to the enhanced charge carrier mobility, charge transfer and hence charge separation of the linear conjugated polymers. Inductively coupled plasma mass spectrometry (ICP-MS) measurements were carried out on both polymer series to test for residual Pd in the polymers (which could act as a catalyst and add to an increased hydrogen activity of the system) and polymers were found to contain residual Pd (e.g., 24.6 ppm for **B-BT-1,4**, **Figure 1.33**) and this was not accounted for in the hydrogen TON calculations.

As previously mentioned, incorporation of both donor and acceptor moieties into a polymer backbone is thought to enhance the ‘push-pull’ characteristics and hence

promote charge separation. Jiang et al. reported a series of D- π -A copolymers using pyrene as the donor, benzothiadiazole as the acceptor and either a benzene or biphenyl as the π -linker (**Figure 1.34**).⁹⁶ By varying the donor/acceptor ratio a series of copolymers were synthesised and tested for hydrogen evolution using 100 mg of polymer in 20 vol% TEOA solution and irradiated using UV light, $\lambda > 300$ nm. The highest activity for hydrogen evolution was observed for a 9:2 molar ratio of donor: acceptor (**PyBt₂**, **Figure 1.34**) of $106.2 \mu\text{mol h}^{-1}$ obtained using 3.0 wt.% Pt co-catalyst in H₂O/TEOA (20 vol%) irradiated with Xe arc lamp $\lambda > 300$ nm. A decrease in hydrogen evolution was observed when either the π -linker substituent or the acceptor moiety was eliminated from the copolymeric structure (under the same experimental conditions, a D-A polymer obtained $9.6 \mu\text{mol h}^{-1}$ and D- π -D polymer obtained $37.4 \mu\text{mol h}^{-1}$) indicating that all three donor, acceptor and π -linker play significant roles in the hydrogen generation.

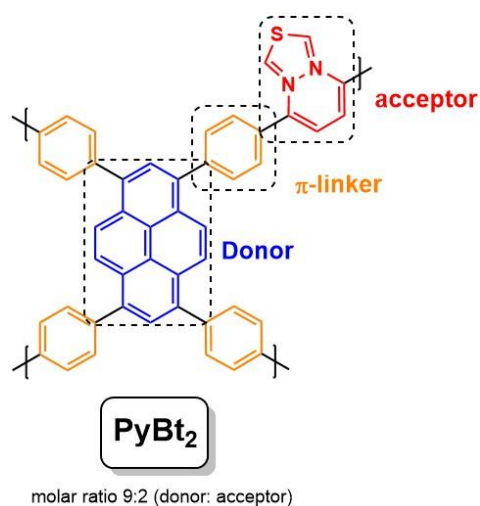


Figure 1.34. Conjugated microporous polymers synthesised for testing donor- π -acceptor moieties effect on hydrogen evolution. Blue – pyrene (donor); orange – benzene (π crosslinker); red – benzothiadiazole (acceptor).⁹⁶

However, identical experiments using **PyBt₂** (**Figure 1.34**) without the co-catalyst resulted in $52.6 \mu\text{mol h}^{-1}$ ($\lambda > 300$ nm) and only $29.6 \mu\text{mol h}^{-1}$ when visible light was used for irradiation ($\lambda > 420$ nm). Further improvements with these CMP systems are required in order to produce as system that is both active under visible light and does not require the addition of a co-catalyst to improve catalytic performance. Despite the lower activity under visible light irradiation, this work highlighted the importance of

incorporating all three – donor, acceptor and π -linker unit into the CMP in order to increase the catalytic performance of the polymer material. Enhancement in hydrogen evolution activity has also been reported by other groups by changing a donor-containing conjugated polymer, to a donor-acceptor copolymer.^{97, 98, 99}

In addition to the D- π -A polymers discussed above, Zhang and co-workers established the benefit of including alkynyl groups as linking bonds in a previously reported linear polymer backbone. It was determined that incorporation of the alkynyl group lowered the LUMO level, resulting in narrowing of the band gap. This bathochromic shift in the UV (to ~ 750 nm) allows more photoabsorption and hence enhances activity.¹⁰⁰

This theory was later applied to CMPs by Xiang et al. who synthesised a linear and a porous series of CMPs containing alkynyl linker groups to test the effect of addition of an electronegative fluorine atom to the acceptor unit to enhance the electron acceptor ability (**Figure 1.35**).¹⁰¹

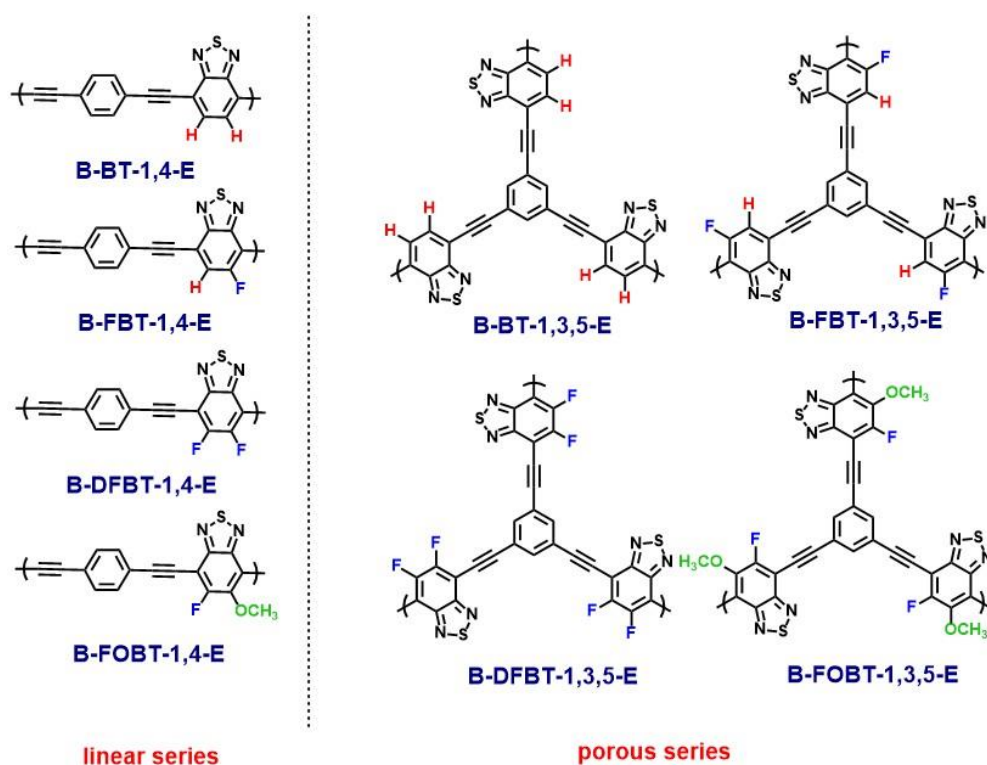


Figure 1.35. A linear series and porous series of donor-acceptor (D-A) polymers. Polymers differed in substituent on the acceptor benzothiadiazole unit (H, F, OCH₃).¹⁰¹

In this study, it was observed that addition of fluorine atoms enhances hydrogen evolution and that upon fluorination the HOMO and LUMO levels decrease in energy (e.g., LUMO level of **B-BT-1,4-E** = - 3.73 eV, **B-DFBT-1,4-E** = - 3.95 eV). Hydrogen evolution rates were highest for the linear polymer **B-FOBT-1,4-E** with 399 $\mu\text{mol H}_2$ generated compared to 128 $\mu\text{mol H}_2$ produced from the corresponding **B-BT-1,4-E** without the electronegative substituents (photocatalytic conditions including dispersion of polymer in TEOA/H₂O mix, $\lambda > 420$ nm). Interestingly, the porous polymer was not as active for hydrogen as the linear equivalent, which liberated 288 $\mu\text{mol H}_2$ for **B-FOBF-1,3,5-E** (also showed an increase in activity with addition of F and OCH₃). The reason for the superiority of the linear polymers tested under these conditions is not mentioned, but perhaps the electron charge carrier mobility is enhanced in linear polymers, inhibiting charge recombination and promoting charge separation.

From the above examples of CMPs, it is clear to see that by changing the monomer(s) unit, one can easily tune the polymer properties, as well as changing the comonomer ratio to fine tune the donor-acceptor ratio required for optimum hydrogen evolution rates. Organic-based polymers as such, offer an advantage in their abundance of starting materials available allowing a wide range of choice of monomer starting materials. The geometry, and length of the linker plays a key role in determining the porosity of the CMP's.⁷⁵ Also, π -delocalisation (which is enhanced in these polymers) has been shown to increase electron transport to the surface of the polymer, to allow the electron to participate in the necessary redox reactions required in overall water splitting reactions.

1.7.3.4.2 Covalent organic frameworks (COFs)

Another category of CMPs are covalent organic frameworks (COFs). These polymers differ from the previous two as they are crystalline-like, with a high degree of uniformity and order in the connectivity of the monomeric units. Chemical and thermal stability is an extensive advantage, and this has been exploited in other applications such as optoelectricity and catalysis.¹⁰²

Lotsch et al. published a paper that has gained much attention in the area of COFs for hydrogen evolution. This hydrazone-based COF was synthesised using a Schiff-base reaction and contains mesopores of 3.8 nm diameter with a high surface area (**Figure 1.36**).¹⁰³ Hydrogen evolution reactions were carried out using Pt-doped polymer and Pt as the proton reduction catalyst and sodium ascorbate as the sacrificial agent. Hydrogen evolution of 97.2 μmol was obtained after 52 hr of heterogeneous photocatalysis and stability of up to three catalytic cycles was observed. When the sacrificial agent was changed to TEOA, a higher hydrogen evolution was observed initially, but the system was not as stable as it was when sodium ascorbate was employed in prior photocatalytic experiments.

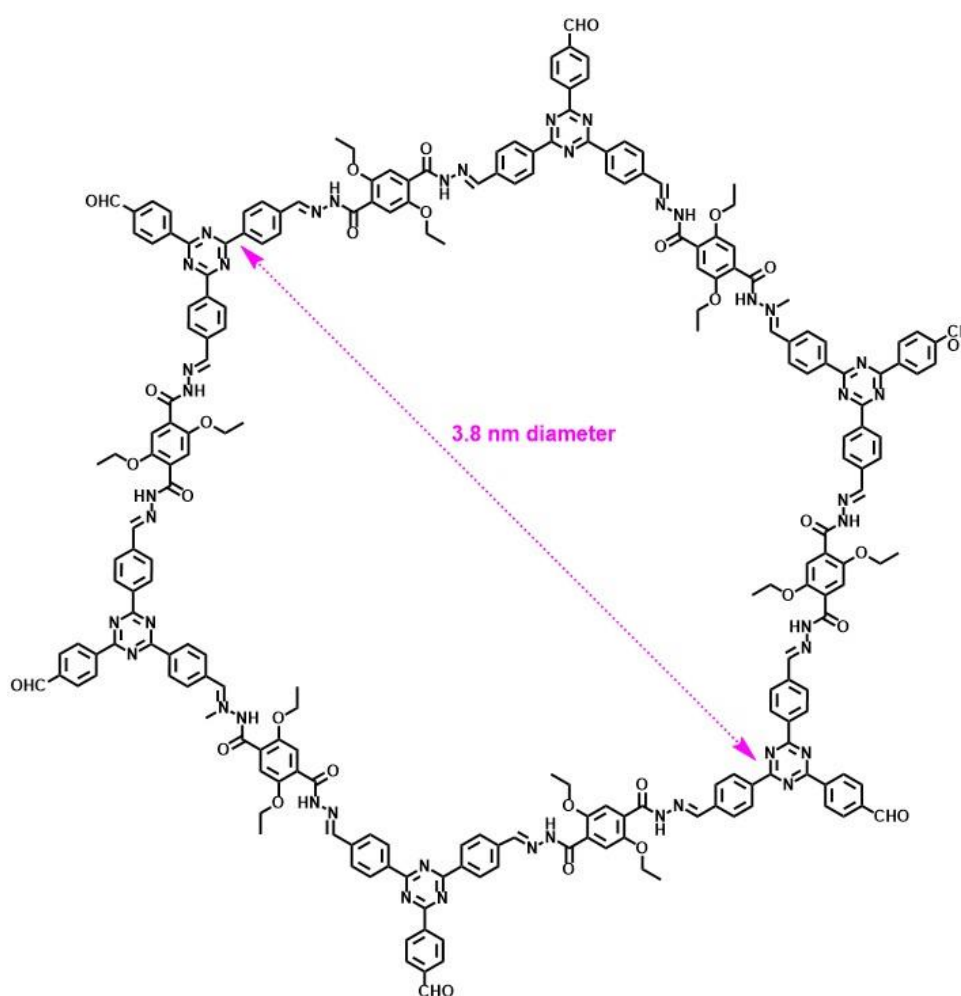


Figure 1.36. Covalent organic framework (COF) containing hydrazone groups with a pore size of 3.8 nm.¹⁰³

In trend with CMPs previously introduced, it was reported that incorporation of an alkynyl moiety increased hydrogen evolution rates owed to broadening of visible light

absorption and lowering energy of the LUMO. Thomas et al. determined that diacetylene units produced more hydrogen than their monoacetylated equivalents.¹⁰⁴ Incorporation of a triple bond into the polymer backbone will be a central focus throughout this project and it is thought, that similar to the aforementioned work, the alkynyl group will increase conjugation and hence visible light absorption.

Hydrogen evolution with COFs has recently been shown to have higher HER when a cobaloxime catalyst was used instead of a Pt catalyst.¹⁰⁵ Cobaloxime is used as the catalyst in photocatalytic hydrogen producing system reported in chapter 2 of this thesis.

1.7.3.4.3 Covalent-triazine frameworks (CTFs).

Covalent-triazine frameworks (CTFs) contain an electron-withdrawing triazine unit, which may cause an increase in hydrogen evolution acting as a redox active site for catalysis. Synthesis of CTFs can result in carbonisation if reaction temperatures are too high, hence reaction is usually carried out at low temperature using trifluoromethanesulfonic acid (TfOH) to catalyse the trimerisation of nitriles. CTFs show high chemical and thermal stability and have been used both in photocatalytic and photoelectrochemical hydrogen evolution reactions (**Figure 1.37**).^{106,107} It is thought that the triazine unit allows for π -stacking of aromatic groups enabling exciton separation upon photoabsorption and charge transport from conjugated electrons.

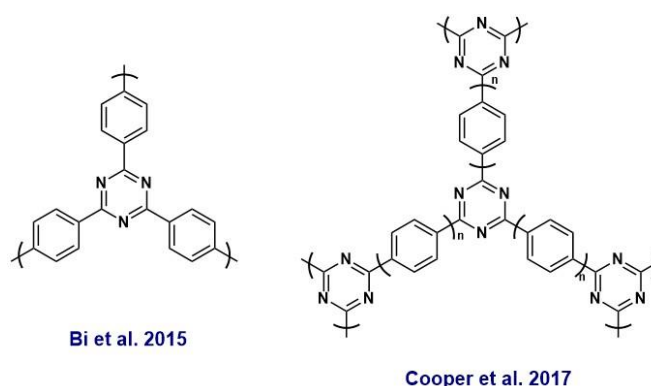


Figure 1.37. Covalent-triazine frameworks (CTFs) used in hydrogen evolution.^{106,107}

1.7.4 Structural influences of polymers for hydrogen evolution

From this overview given on polymers for hydrogen evolution; it is clear to see that there is an abundance of structures of polymers, a variety of hydrogen AQYs obtained and various different experimental approaches employing these polymers. As with any PS utilised for solar fuel production, it's critically important to establish a structure activity relationship (SAR). SAR determination strives to develop an understanding of the photocatalytic cycle at a molecular level and grants further optimisation of the molecular architecture.

Of the research work conducted thus far, a few fundamentals of polymer design are evident. First and foremost, structural features of the polymer that largely effect the polymer properties are i) the polymer backbone, ii) the side chains on the polymer and iii) the substituents. Side chains on the polymer backbone control features such as molecular weight, solubility and processability. These side chains can also lead to detrimental outcomes in the polymer performance, such as causing an insulating effect and dilute the effect of the chromophore, or even disturbing the π - π stacking along the polymer backbone and hence reduce the charge carrier mobility. The polymer backbone is the most prominent feature of the polymer, controlling overall polymer properties such as optical gap, energy levels, inter/intra molecular interactions. The type of polymer synthesised depends on the monomeric repeating unit(s) chosen for the synthesis and can form homopolymers, donor-acceptor polymers, quinoid polymers or other polymers containing novel spacer units.¹⁰⁸

Donor-acceptor copolymers have an extreme advantage in optical gap manipulation as the energy levels can be easily tuned through modification of the donor/acceptor units, and hence the optical gap lowered. Reduction of the optical gap in polymeric materials augments the light harvesting ability of the polymer and is often found to increase the hydrogen evolution rate (HER).²⁹ This is specifically evident when a “weak donor” and a “strong acceptor” is utilised in the construction of the polymer backbone. The weak donor has been shown to lower the HOMO of the polymer, while the strong acceptor has been shown to reduce the optical gap via internal charge transfer.¹⁰⁹ However, in contrast to this understanding, the pyrene-copolymers

published by Cooper et al. reported that the polymer with the narrowest optical gap did not display the highest HER.⁷⁶

Important structural considerations that have been highlighted in the literature include the incorporation of ethynyl linkers into the polymer backbone. Chen et al. studied the difference in hydrogen production of a series of 1,4 benzene linker polymers compared to their equivalent 1,4-ethynylbenzene linked conjugated polymers (**Figure 1.38**). **P7E** had an absorption edge bathochromically shifted by 150 nm and a negative LUMO shift upon addition of an ethynyl linker, compared to **P7**. The AQY of **P7E** is calculated to be 4.2% at 420 nm without addition of a co-catalyst and 7.2% when 3.0 wt.% Pt is added.¹⁰⁰

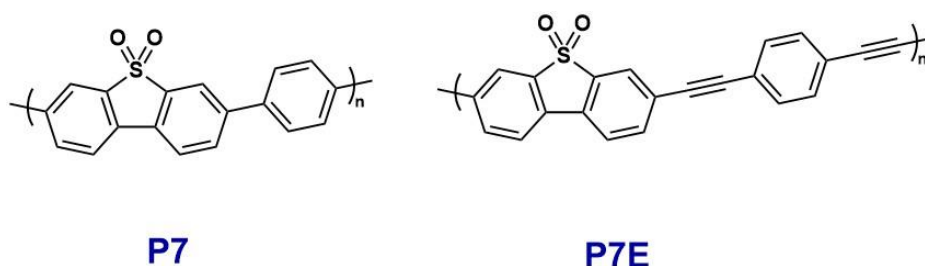


Figure 1.38. Structural influences of ethynyl linker between two conjugated polymers for hydrogen evolution.¹⁰⁰

Other structural influences for increase photocatalytic activity that have become apparent are linear polymers having higher activity than either 3D equivalents,⁹⁵ planarisation of linear polymers,⁹¹ reduction in particle size,⁸¹ effect of the linking pattern on conjugated polymers,¹¹⁰ and porosity of conjugated polymers.¹¹¹ Recent literature has also been published that aims to shed light onto the SAR for the hydrogen evolution ability of polymers in photocatalytic routes for hydrogen generation. This study suggests that the local environment of the polymer backbone can play a crucial role in charge transfer processes, such as the hydrophilic environment around a sulfone group in a polymer backbone during photocatalysis.¹¹²

1.8 BODIPY chromophores

1.8.1 The BODIPY chromophore

4,4-Difluoro-4-bora-3a,4a-diaza-*s*-indacene (BODIPY) dyes were first synthesised by Treibs and Kreuzer in 1968 and have since been used for a variety of applications such as cellular imaging, laser dyes, labelling proteins/DNA, and fluorescent switches.^{113,114} Displayed below is the BODIPY core and its IUPAC numbering system (**Figure 1.39**).

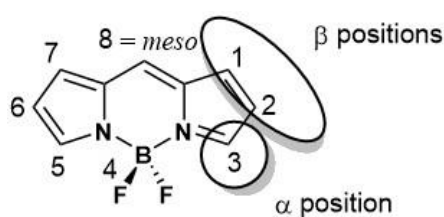


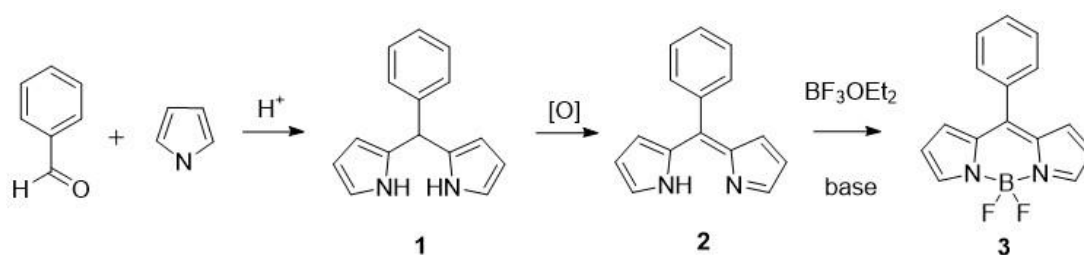
Figure 1.39. BODIPY core scaffold indicating the IUPAC numbering system.^{113,114}

BODIPY compounds are based on a half-porphyrin structural design and are a rigid structure owing to the linking difluoroboron moiety.¹¹⁵ Advantages of these compounds include ease of synthesis, low cost starting materials, high molar extinction coefficients, strong UV absorbance, sharp emission bands, and ability to modify the excited state properties. Formation of the excited triplet state can be persuaded by the addition of a heavy-atom (such as iodine or bromine) into the 2,6 positions of the BODIPY core - enhances spin-orbit coupling and hence ISC to the triplet state (i.e., synthetic modification allows tunability of BODIPY properties). Additional advantages include their relative stability under a variety of pH conditions and in a variety of polarities.

1.8.2 Synthesis

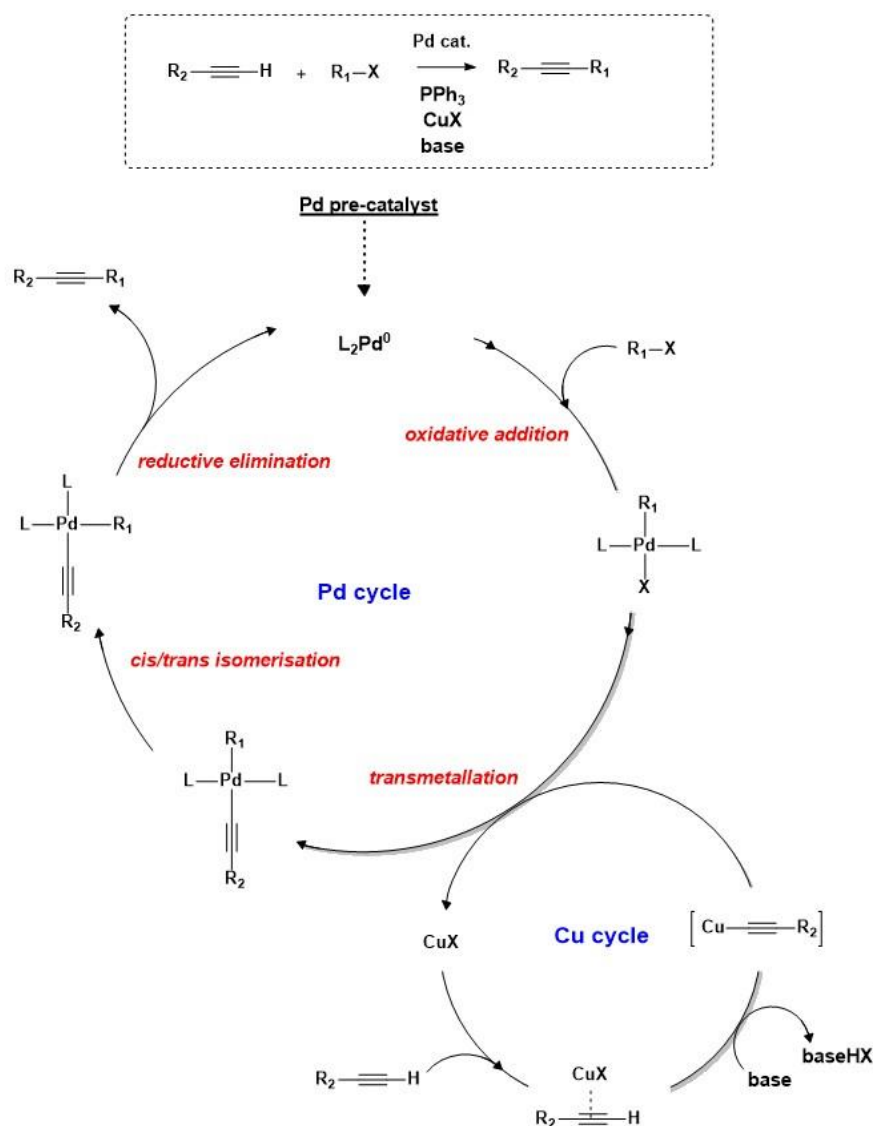
Condensation between a pyrrole and an aldehyde is well established as the synthetic method of choice for the synthesis of the BODIPY core.¹¹⁶ A diverse range of BODIPY dyes can be synthesised using this method, by changing either/both the starting aldehyde and/or pyrrole. The synthesis for the BODIPY core is based on chemistry of the porphyrin structure, using a 1:2 molar ratio of aldehyde to pyrrole respectively.¹¹⁷ **Scheme 1.11** displays the synthetic steps for the overall synthesis of

the BODIPY core in dichloromethane (CH_2Cl_2). The initial step in the reaction sequence involves an acid catalysed condensation of an aromatic aldehyde and a pyrrole to yield a dipyrromethane (**1**). This intermediate is quite unstable, reacts readily with air and is not stable under light. Oxidation with either p-chloranil or 2,3-dichloro-5,6-dicyano-1,4-benzoquinone (DDQ) yields the corresponding dipyrromethene (**2**). Harsher conditions result from the use of DDQ. Finally, addition of the boron under basic conditions results in complexation of N atoms with the boron to form the final BODIPY molecule (**3**). The development of a one-pot synthesis allows for the formation of the final product *in situ* i.e., direct conversion from the dipyrromethene to the BODIPY core.



Scheme 1.11. Synthetic route in the overall synthesis of the BODIPY core, carried out at room temperature in anhydrous CH_2Cl_2 solution.¹¹⁷

Iodination of the BODIPY core occurs via an electrophilic aromatic substitution reaction which proceeds rapidly at room temperature using iodic acid and iodine in tandem with ethanol as a solvent. Polymerisation of the BODIPY core is carried out using Sonogashira polycondensation reaction. This is a type of cross-coupling chemistry; wherein an aryl or vinyl halide reacts with a terminal alkyne under Pd catalysed and Cu co-catalytic conditions to form a new $\text{sp}^2\text{-sp}$ carbon-carbon bond.¹¹⁸ Typically, the reaction requires anhydrous conditions (such as dry solvents) and proceeds under anaerobic conditions. In this case, the monomers are difunctional, meaning that both sides of the monomer can cross-couple to another monomer, resulting in a polymerisation reaction.¹¹⁹ Sonogashira cross-coupling occurs via the catalytic cycle shown below (**Scheme 1.12**).



Scheme 1.12. Sonogashira Pd catalysed cross-coupling catalytic cycle including Cu cycle as co-catalyst (below).

As shown in this scheme, initially the active Pd catalyst (Pd^0) is formed *in situ* from Pd^{II} via ligand dissociation from the metal centre to form the active catalyst. As seen below, the phenyl/vinyl halide inserts into the metal centre in oxidative addition. This step is the rate-limiting step. The copper halide co-catalyst reacts with the terminal alkyne, eliminating the terminal proton to form a copper acetylide intermediate. This intermediate then undergoes transmetallation with the L_2Pd^{II} (R_1X) intermediate to form Pd centre bound to two R groups, and regeneration of the copper catalyst. This complex then undergoes cis/trans isomerisation to form a resulting complex wherein the R_1 and R_2 groups are in close proximity, in preparation for the final step in the catalytic cycle. Reductive elimination is the fastest step in the catalytic cycle and

results in formation of the final cross-coupled product and regeneration of the active Pd catalyst, allowing the catalytic cycle to repeat.

1.8.3 Photophysics and optical properties of the BODIPY dye

BODIPY monomers are generally highly fluorescent, with fluorescent quantum yields often approaching unity and high molar absorption coefficients ($\sim 10^4 \text{ M}^{-1} \text{ cm}^{-1}$).¹¹⁴ They absorb in the visible region of the spectrum and display sharp emission bands, mirroring the symmetry of the corresponding absorption band maxima. In addition, they are soluble in a wide range of solvents and show good stability. Short lifetimes (τ) in the ns are observed owing to population of the singlet-excited state and for many, negligible triplet-state population.^{116,120}

Synthetic modification of the BODIPY core however facilitates tuning of the BODIPY properties. Halogenation of the dye at the 2 and 6 position results in a bathochromic shift and a quenching in fluorescence intensity ascribed to the ability to undergo ISC to the triplet-excited state (enhance in spin-orbit coupling). Interestingly, modification of the *meso* group has little or no effect on the photophysics of the BODIPY compounds and solvent polarities show little change in absorption spectra. An abundance of BODIPY derivatives have been synthesised, with aims to develop dyes with intrinsic properties for aforementioned applications. Synthetic alterations that have attracted much attention include pre and post functionalisation strategies.¹²⁰

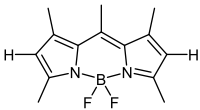
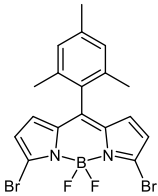
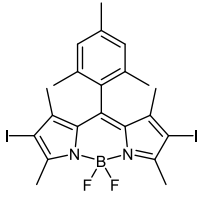
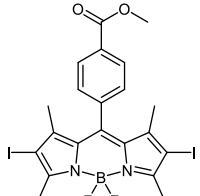
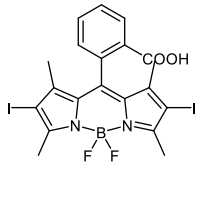
Herein, we introduce copolymers incorporating BODIPY dyes into the polymer backbone. It is postulated that incorporation of this dye into the polymer will also encompass its promising properties, such as increased visible light absorption and population of the triplet excited state, as well as the advantages of π -conjugation thus leading to an advanced PS for the water splitting reaction.

1.8.4 Homogeneous photocatalytic hydrogen evolution using BODIPY dyes

BODIPY monomers have been investigated for hydrogen generation under a range of experimental conditions including both in solution-based systems (homogeneous photocatalysis) and incorporating the BODIPY unit on a semiconductor or electrode surface (heterogeneous photo(electro)catalysis). Summarised in **Table 1.1** are some

of the homogenous BODIPY photocatalytic hydrogen experiments carried out to date, the conditions under which these experiments were performed, and the hydrogen evolved from the systems. From analysis of **Table 1.1**, it is evident that no set of experimental parameters are exactly the same and it is also clear that optimisation of each component is a vital consideration to improve the efficiency of the hydrogen evolving system.

Table 1.1. A brief summary of BODIPYs for hydrogen evolution obtained in homogenous photocatalysis. PS – photosensitiser, CAT – catalyst, sol – solvent mixture, SA – sacrificial agent, TON – turnover number, ref – reference, THF – tetrahydrofuran, TEA – triethylamine, TEOA – triethanolamine.

PS	CAT	solvent	SA	light source	TON	ref
	[Pd(PPh ₃)Cl ₂]	THF/water	TEA	300 W Xe Arc, λ > 420 nm	113	121
	[Pd(PPh ₃)Cl ₂]	THF/water	TEA	300 W Xe Arc, λ > 420 nm	43	121
	[Pd(PPh ₃)Cl ₂]	THF/water	TEA	300 W Xe Arc, λ > 420 nm	305	121
	Pt/TiO ₂	CH ₃ CN /water	TEOA	150 W Xe Arc, λ > 450 nm	100	122
	[Co(dmGH) ₂ pyCl]	CH ₃ CN/ Water	TEOA	300 W Xe Arc, λ > 420 nm	197	115

Recently, high TON have been reported with BODIPY iodinated monomers and a cobaloxime catalyst using ascorbic acid as the sacrificial agent. A BODIPY monomer, containing an iodine atom at the 2 and 6 position of the BODIPY core and phenylamine in the *meso* position (**Figure 1.40**) achieved hydrogen evolution TON ~ 93 (930 μmol) over 6 hr.¹²³

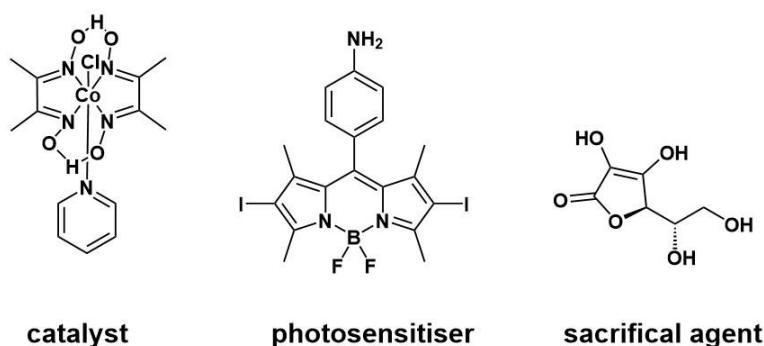


Figure 1.40. Multicomponent hydrogen evolution system comprising cobaloxime (2.5×10^{-3} M), a BODIPY PS (1.0×10^{-4} M), and ascorbic acid (0.1 M) as the SA in acidic homogenous solution pH 5 $\text{CH}_3\text{CN}/\text{H}_2\text{O}$, 1:1 (v/v).¹²³

Photocatalytic hydrogen experiments using the halogenated BODIPY monomers reported in this study and different sacrificial agents such as TEA and TEOA displayed negligible hydrogen evolution. It was also determined that the hydrogen evolution is pH dependant, with pH 5 yielding the most hydrogen. An explanation for the pH dependency on hydrogen evolution has been ascribed to the protonation/deprotonation of the phenylamine moiety in the *meso* position of the BODIPY core (photosensitiser, **Figure 1.40**). The amine group is unprotonated (neutral charge) under basic conditions and following excitation, electron transfer is thought to occur from the *meso* substituent to the BODIPY core, i.e., intramolecularly. This back-electron transfer results in decay of the excited state (PS^*) to the ground state, thus hindering hydrogen production. Under acidic conditions, the amine group at the *meso* position is protonated, which is thought to promote intermolecular electron transfer from the PS^* to the CAT. These results give insight into the structure-activity relationship of the PS and highlight the importance of choosing an appropriate SA/CAT for a multicomponent system.

Weare et al. published intramolecular BODIPY systems for hydrogen evolution which consisted of four photocatalytically active BODIPY-cobaloxime complexes (**B2 – B5**,

Figure 1.41).⁴¹ Photocatalytic experiments were conducted using CH₃CN: H₂O (6: 4, v/v) with TEOA (5% vol), pH adjusted to 7.7 and irradiated with 525 ± 10 nm (150 mW) green light for 17 hr at 18 °C. Halogenation of the 2 and 6 position of the BODIPY core was determined to be essential for population of the triplet state and hence efficient hydrogen evolution. This is confirmed by testing the non-halogenated reference BODIPY-cobaloxime complex, which displays no activity for hydrogen evolution under otherwise identical experimental conditions. An additional study was carried out on the effect of adding a methyl substituent on the pyridine group at the meso position of the BODIPY core (**B4** and **B5**, **Figure 1.41**). A maximum TON was obtained for **B5** (TON = 30.9) which contained the additional methyl group, which is superior for hydrogen evolution in comparison to **B3** (without the methyl group). This methyl group was thought to add stabilising effects during photocatalysis (electron donating methyl group improves the basicity of the pyridine moiety).

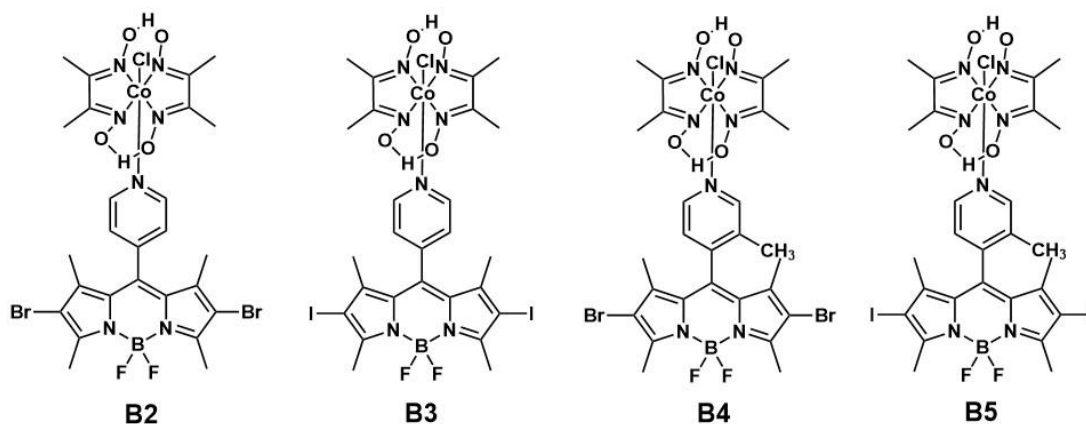


Figure 1.41. Intramolecular PS-CAT assemblies for hydrogen generation based on BODIPY-cobaloxime assemblies.⁴¹

The emission of the BODIPY-cobaloxime complexes was quenched in comparison to the BODIPY monomeric precursors, possibly due to electron transfer from the excited state BODIPY to the cobalt catalytic centre. Intermolecular studies were also carried out in this work, containing the BODIPY monomer and free cobaloxime catalyst. Insignificant hydrogen evolution (*ca.* 0.6 TONs) was observed for these systems; highlighting the importance of the covalent linkage for the electron transfer from the BODIPY moiety to the catalyst during photocatalysis. The methylated complexes

showed a higher TON overall attributed to greater stability of the complex, allowing a longer lifetime of the catalyst.

1.8.5 Heterogeneous hydrogen evolution using BODIPY dyes

In contrast to the findings from Weare et al. described above, intramolecular BODIPY-cobaloxime complexes (**Figure 1.42**) were previously reported in our research group and it was determined that these complexes did not produce hydrogen photocatalytically but did under electrocatalytic conditions.¹²⁴

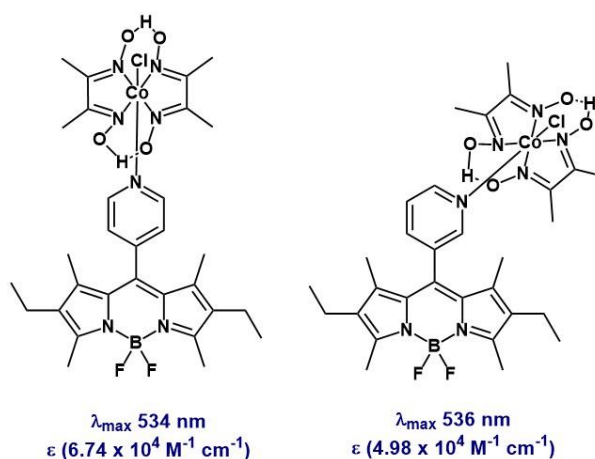


Figure 1.42. BODIPY-cobaloxime intramolecular assemblies for electrocatalytic hydrogen evolution.¹²⁴

Electrocatalytic hydrogen experiments for the BODIPY-cobaloxime complexes were carried out by drop casting the PS onto a glassy carbon electrode. These experiments were conducted at -1.2V vs. Ag/AgCl reference electrode. H₂ TON of 16.5 (x 10³) and 10.8 (x10³) were obtained for 4-pyr BODIPY cobaloxime and 3-pyr BODIPY cobaloxime, respectively. For intermolecular compounds H₂ TON of 5.2 (x 10³) and 5.5 (x10³) were obtained for 4-pyr BODIPY PS and 3-pyr BODIPY PS, respectively. This study demonstrates the instability of the BODIPY-cobaloxime complex under photocatalytic conditions but shows high TON values under photoelectrochemical conditions. Interestingly, the results obtained for both the 3-pyr and 4-pyr compounds were comparable, and one does not show greater stability in comparison to the other. Furthermore, the difference in TON obtained for the inter and intramolecular PEC studies, highlights the importance of tethered PS-CAT systems.

Incorporation of dyes onto the surface of electrodes, such as the study reported above by our research group, is a heterogeneous approach and this is a vast area of photocatalytic water splitting research. In comparison to homogenous catalysis, heterogeneous catalysis can offer more advantages for the overall hydrogen evolution ability of the system. For example, sometimes addition of the PS/CAT onto an electrode surface can have a stabilising effect and hence avoid biomolecular photodecomposition that is observed in solution photocatalysis. This section highlights several publications that incorporate BODIPY moieties into heterogeneous assemblies and summarises the conditions and principles behind these experiments.

Initial publications of BODIPY dyes for hydrogen evolution on surfaces commence with the work by McCamant and Eisenberg. They synthesised a series of BODIPY monomers and halogenated monomers containing ester groups in the *meso* position of the chromophore (**Figure 1.43**).¹²² These ester groups were postulated to undergo reduction to the corresponding carboxylic acid group, which would allow them to bind the TiO₂ surface during experiments.

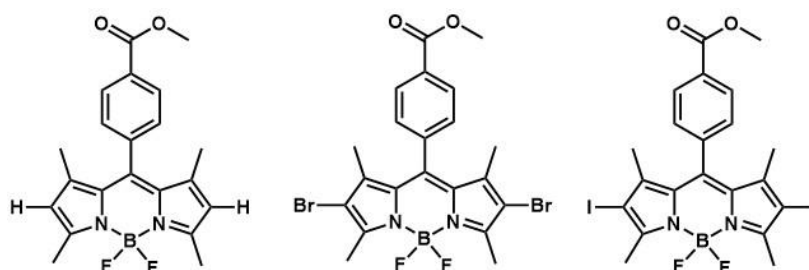


Figure 1.43. A series of BODIPY monomers and halogenated monomers for use as photosensitisers in hydrogen evolution.¹²²

Catalytic conditions of the above heterogeneous system involved use of 4 mg of 0.5 wt.% Pt/TiO₂ catalyst in a 1:1 H₂O: CH₃CN solvent with 10% (v/v) TEOA as the sacrificial agent with a 150 W Xe arc lamp. The hydrogen evolution was highly dependent of chromophore concentration with 0.01 mM, 0.05 mM and 0.2 mM concentrations employed. At lower concentrations (0.01 mM), photobleaching of PS was observed after 1 hr irradiation. Higher concentrations resulted in a higher TON (approx. 50 for brominated monomer, and approx., 100 for iodinated monomer); with stability of the iodinated monomer for 24-28 hr. Note that under all three concentrations of PS, the halogen-free monomer, no hydrogen was observed. This can

be explained by TA experiments carried out. The formation of an excited state absorption (ESA) peak at approximately 345 nm was observed for all three PS. This peak corresponds to the singlet excited state of the BODIPY monomer. Both of the halogenated monomers display short lifetimes for this excited state (1.1 ns for brominated monomer and 131 ps for iodinated monomer). The non-halogenated monomer had an ESA at 345 nm of 5 ns; showing excited singlet state is predominately formed. It was concluded that the highest activity was observed in the iodinated monomer and this is conclusive with the TA experiments wherein the formation of ESA peak attributed to the triplet state was formed within 0.5 ns. This is due to the larger-spin orbit coupling of the iodine atoms, which contributed towards enhanced ISC (heavy atom effect).

Gibson and co-workers published a series of push-pull BODIPY containing photosensitiser containing an anchoring carboxylic acid group for binding to a NiO surface (**Figure 1.44**).¹²⁵ A series of dyes synthesised with the best dye generating a photocurrent density of 5.87 mA cm⁻² and an IPCE of 53%.

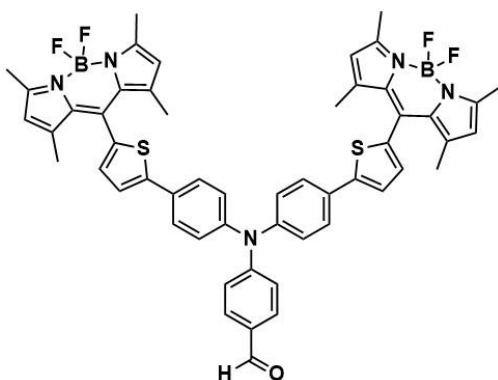


Figure 1.44. Dye for heterogeneous catalysis on NiO containing donor (triphenylamine) and acceptor (BODIPY) moieties with carboxylic acid anchoring group.¹²⁵

Recently, Kubo et al. reported heterogeneous hydrogen evolution using a BODIPY-phenothiazine conjugate deposited on a TiO₂ surface. Hydrogen evolution was reported TON of 11,100 after 10 h irradiation using a 300 W Xe lamp with $\lambda > 400$ nm. A conjugate dye was synthesised with an anchoring group for binding to the surface of a Pt/HPT TiO₂ electrode. This dye was a multi-component system, consisting of a donor- π -acceptor assembly; a dibenzo-BODIPY, a phenothiazine and an anchoring group (**Figure 1.45**).¹²⁶

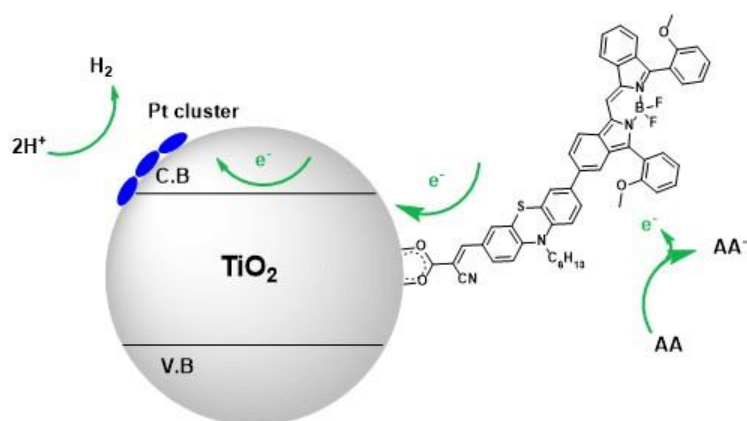


Figure 1.45. Heterogeneous catalysis showing a BODIPY dye and phenothiazine assembly on a TiO_2 surface, where AA is ascorbic acid used as the sacrificial agent.¹²⁶

The first example of a BODIPY-based metal organic framework (MOF) was synthesised using a BODIPY monomeric unit containing terminal pyridyl units in the 2,6 position of the BODIPY core (**Figure 1.46** (a)). This organic chromophore was incorporated into a Zn containing MOF denoted $[\text{Zn}_2(\text{BODIPY})(\text{BPDC})_2] \cdot \text{H}_2\text{O}$, resulting in a complex with enhanced light absorption from 200 – 800 nm in the absorption spectrum. Hydrogen evolution experiments displayed efficient activity with a rate of $4680 \mu\text{mol g}^{-1} \text{h}^{-1}$ obtained after 3 hr light irradiation (300 W Xe Arc lamp, $\lambda > 420 \text{ nm}$).¹²⁷ A Pt co-catalyst (0.13 wt.%) was embedded onto the surface of the BODIPY-based MOF to act as a co-catalyst and hydrogen evolution was not observed in the absence of Pt. All hydrogen evolution experiments were conducted using 50 mg of the Pt/BODIPY-MOF in 50 mL aqueous solution containing 0.1 M ascorbic acid solution and were stirred throughout irradiation (3 hr).

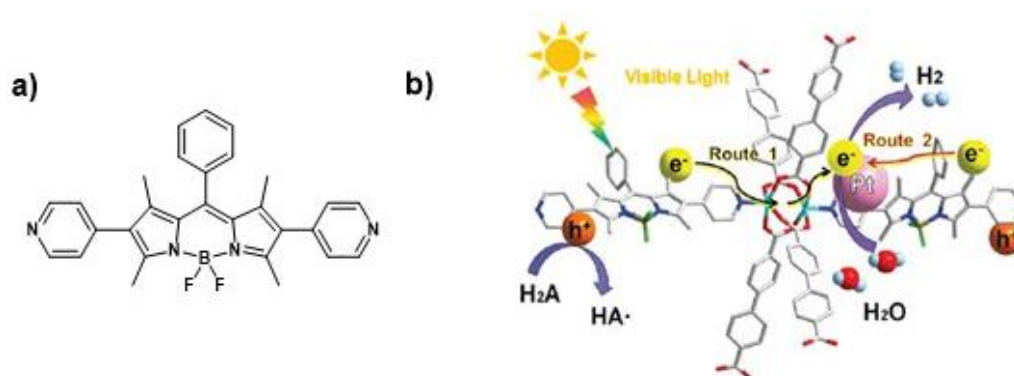


Figure 1.46. a) Molecular structure of BODIPY monomeric unit used as the organic linker in MOF, b) Proposed mechanism of BODIPY-based MOF for photocatalytic hydrogen evolution. Figure adapted from literature.¹²⁷

1.9 BODIPY copolymers

There has been a variety of reports of polymers containing the BODIPY chromophore throughout the literature. The structure of these polymers ranges from 2D linear polymers to 3D porous polymers or can also vary depending on position of polymerisation (i.e., the 2,6 position, the α , β position, the *meso* position or the fluorine position). Differences in the polymer architectures also occur depending on if the BODIPY is incorporated into the main polymer chain or as a pendant side chain. The majority of BODIPY polymers synthesised to date involve use of a more-substituted BODIPY core as opposed to less substituted chromophore (due to synthetic difficulties and poor stability of the unsubstituted pyrrole moiety). Applications of BODIPY polymers include optoelectronics, organic field transistors, batteries, photovoltaics, heterogenous photocatalysts and incorporation into nanoparticles for cellular imaging.^{128,129} To the best of our knowledge, BODIPY copolymers have not been reported to date, for photocatalytic water reduction. For the purpose of this literature survey, BODIPY polymers reported will be categorised into BODIPY polymers containing an ethynyl linkage along the polymeric backbone (section 1.9.1), non-ethynyl linked BODIPY polymers (section 1.9.2) and other BODIPY containing polymers (section 1.9.3). The polymers in section 1.9.3 review polymers in which polymerisation of the chromophore does not involve polymerisation through the 2 and 6 position in a linear fashion as with the previous polymer compounds reviewed.

1.9.1 Ethynyl linked BODIPY copolymers

Li et al. were among the first to report the incorporation of the BODIPY unit into a polymer backbone, reporting the synthesis of four novel BODIPY polymers in 2008 (**polymer 1 – polymer 4, Figure 1.47**).¹³⁰ These polymers were synthesised by Sonogashira polycondensation for potential application in third-order non-linear optical materials. Absorption and emission bands of these polymers were all bathochromically shifted with respect to their monomers (e.g. λ_{\max} 535 nm red shifted to 640 nm for **polymer 1** in the absorption spectra). Broadening of the absorption bands upon polymerisation can be attributed to extended π -conjugation upon polymerisation. It was concluded that in addition to these polymers being successful

in the use for nonlinear optics (in that incorporation of the chromophore enhanced the non-linear properties), the incorporation of the BODIPY chromophore into the polymer backbone, also incorporated the functional group properties of the chromophore. Indeed, this opened up an avenue for further research into polymers incorporating BODIPY moieties into their polymeric structure and paved the way for further development of these novel polymers for other potential applications.

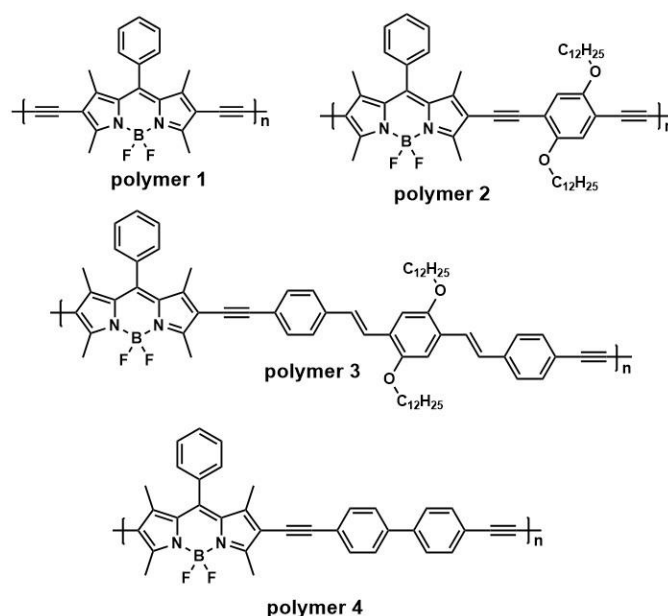


Figure 1.47. BODIPY polymers reported with tunable optical properties.¹³⁰

In 2009, a novel series of polymeric and copolymeric BODIPY dyes were reported (**polymers A-E, Figure 1.48**).¹³¹ As can be seen from the figure below, **polymer A** and **polymer B** are homopolymers containing only the BODIPY chromophore as the repeating unit. **Polymers C, D** and **E** are copolymers incorporating different monomeric repeating units; fluorene, benzene and thiophene, respectively. The monomeric units chosen for the copolymers each have a different band gap in order to study the effect this has on polymer properties. Interestingly, the singlet lifetime of **polymer E** is lower than the other polymers synthesised ($\tau = 0.23$ ns). This shorter lifetime is thought to be due to the presence of the sulfur atom in the thiophene unit causing an increase in intersystem crossing (ISC) to the triplet state due to the heavy-atom effect of the sulfur atom. This effect is also observed in the fluorescent quantum yield of **polymer E**, which is also lower than the other polymeric compounds (e.g. Φ_{fl}

= 0.06 vs. $\Phi_{fl} = 0.25$ for **polymer C**). This publication highlights how photophysical properties can be altered depending on what monomeric units are chosen for polymerisation. Fréchet et al. later used **polymers B** and **E** as donor units in bulk heterojunction solar cells (**Figure 1.48**).¹³²

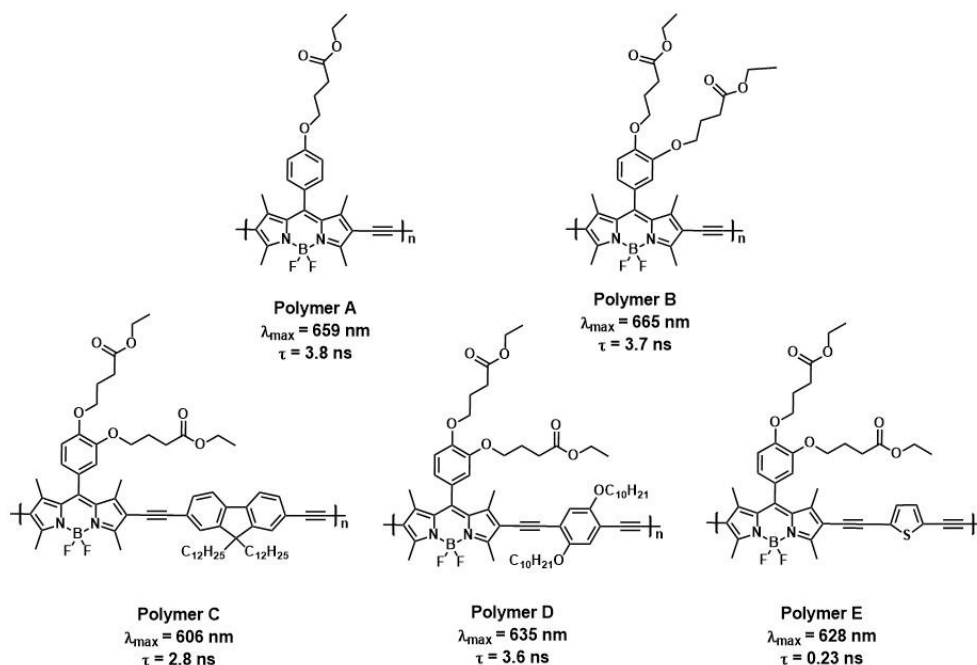


Figure 1.48. Homopolymers (**polymer A** and **polymer B**) and copolymers (**polymers C, D, E**) synthesised via Sonogashira polymerisation. All absorption spectra were recorded in CH_2Cl_2 at room temperature.¹³¹

After these influential publications in this area, other publications emerged reporting the same broad bathochromically-shifted absorbance for the conjugated BODIPY copolymers. Akkaya et al. reported a series of BODIPY oligomers synthesised via Sonogashira polycondensation (**Figure 1.49**). These oligomers displayed an overall red shift of 120 nm in the absorbance spectra.

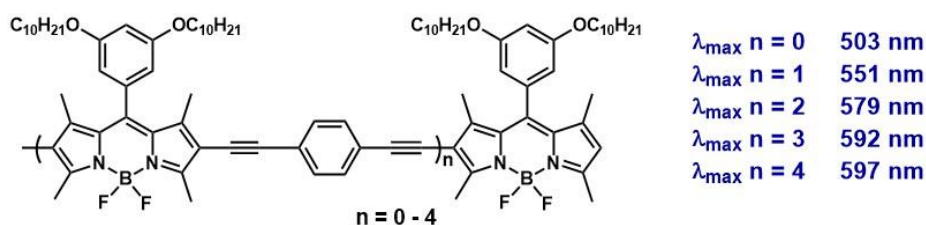


Figure 1.49. BODIPY oligomers with repeating unit varied from $n = 0 - 4$.¹³³

In the same year, Donuru et al. reported a series of **polymers A - C** (**Figure 1.50**) with a red shift up to 179 nm upon polymerisation (absorption maxima displayed below

molecular structures).¹³⁴ Characterisation was carried out using ^1H NMR and gel permeation chromatography (GPC). ^1H NMR showed a broadening of peaks in the polymer compounds with respect to their monomer equivalents. As can be seen in the figure below, the absorption maxima were further red-shifted upon deposition of the polymers on a thin film and this is thought to be due to the increase in intermolecular interaction, such as π - π stacking (increasing the conjugation) and/or increase in coplanarity in the solid state. The polymers also displayed high thermal stability when tested using thermogravimetric analysis (TGA) with decomposition occurring between 270-360 °C. Furthermore, solubility was seen to increase for these polymers with more substituents on the *meso* position of the BODIPY core (**polymer C**).

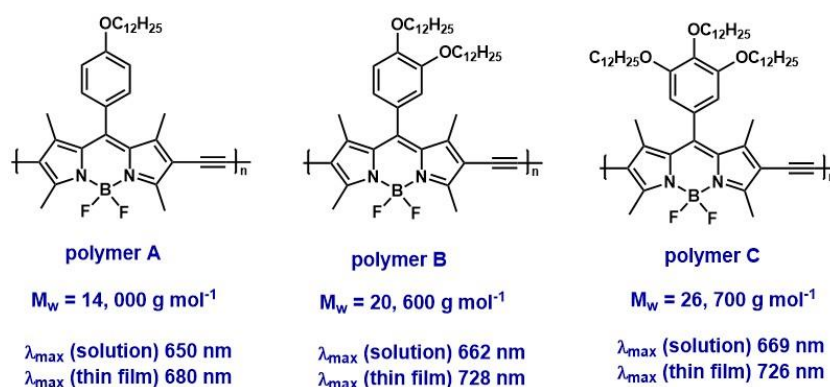


Figure 1.50. Deep red emissive polymers differing in the number of dodecyl substituents on the phenyl ring in the *meso* position of the BODIPY core.¹³⁵

In 2011, Thayumanavan and co-workers published a series of alternating acceptor-donor BODIPY copolymers. In this study, BODIPY was used as the donor unit and a combination of *o*-quinoid and rylene units were used as the acceptor units. From the *o*-quinoid family - Qx – quinoxaline and BzT - 2,1,3-benzothiadiazole were chosen. From the rylene family, NDI - N,N'-di(2'ethyl)hexyl-3,4,7,8-naphthalenetetracarboxylic diimide and PDI - N,N'-di(2'ethyl)hexyl-3,4,9,10-perylene tetracarboxylic diimide were chosen as the acceptor units (**Figure 1.51**).¹³⁶

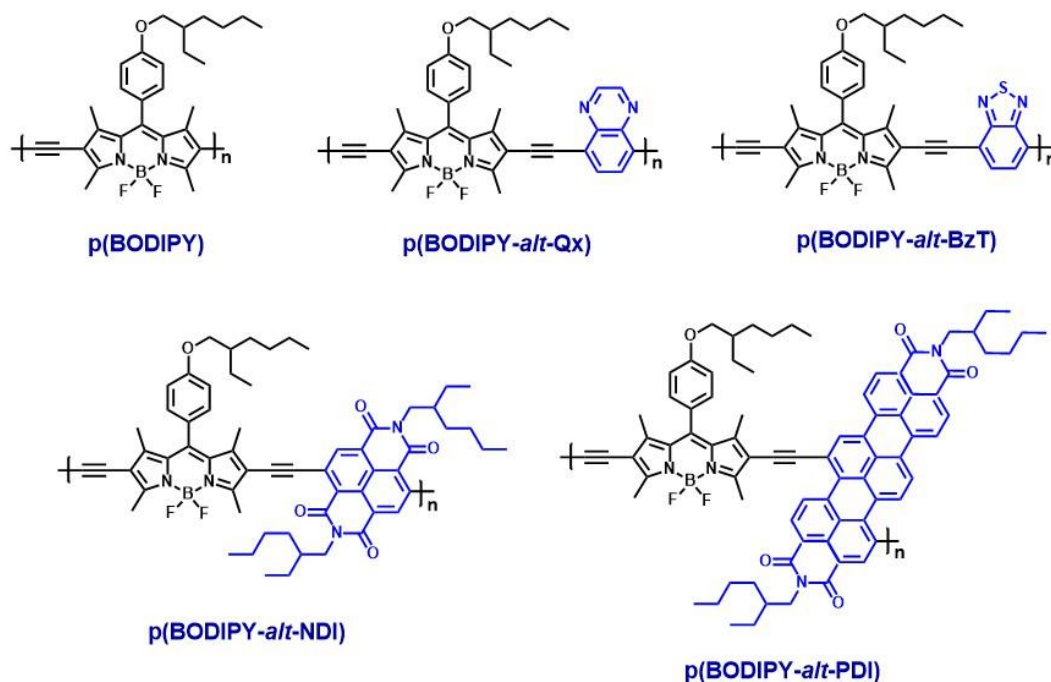


Figure 1.51. BODIPY alternating donor-acceptor copolymers. Qx - quinoxaline, BzT - 2,1,3-benzothiadiazole, NDI - N,N'-di(2-ethyl)hexyl-3,4,7,8-naphthalenetetracarboxylic diimide, PDI - N,N'-di(2-ethyl)hexyl-3,4,9,10-perylene tetracarboxylic diimide. Showing donor unit (BODIPY) in black, and acceptor units in blue.¹³⁶

The motivation behind this work was obtained from reports in the literature where copolymers that were synthesised containing donor-acceptor moieties, resulted in a decrease in the optical band gap and hence enhanced absorption in the visible region of the spectrum. All BODIPY copolymers displayed a broad absorption band of high intensity between 500 – 750 nm in dilute chloroform solution. This main absorption band is broader and more red-shifted when the absorption spectra of the polymers as thin films were measured e.g., **p(BODIPY-alt-NDI)**: $\lambda_{\text{abs}} = 634$ nm (CHCl_3 solution), $\lambda_{\text{abs}} = 660$ nm (thin film). The changes in the absorption spectra observed when thin film spectra were measured are attributed to planarisation of the polymeric backbone and interchain interactions of the polymer in the solid state. These polymers were tested for semiconductor behaviour properties, with Qx and BzT containing polymers displaying p-type properties and NDI and PDI polymers displaying n-type semiconductor properties.

Incorporation of other acceptor units into BODIPY conjugated copolymers was later carried out by Valiyaveettii et al.¹³⁷ Herein, the BODIPY unit acts as the donor, and a series of copolymers were synthesised containing varying acceptor units, 3,6-

dithienyldiketopyrrolopyrrole (**P2**), phthalimide (**P3**), benzotriazole (**P4**), 4,7-dithienyl [1,2,3]triazolo[4,5g]quinoxaline (**P5**) and dithienylthieno[3,4-b]pyrazine (**P6**) (Figure 1.52).

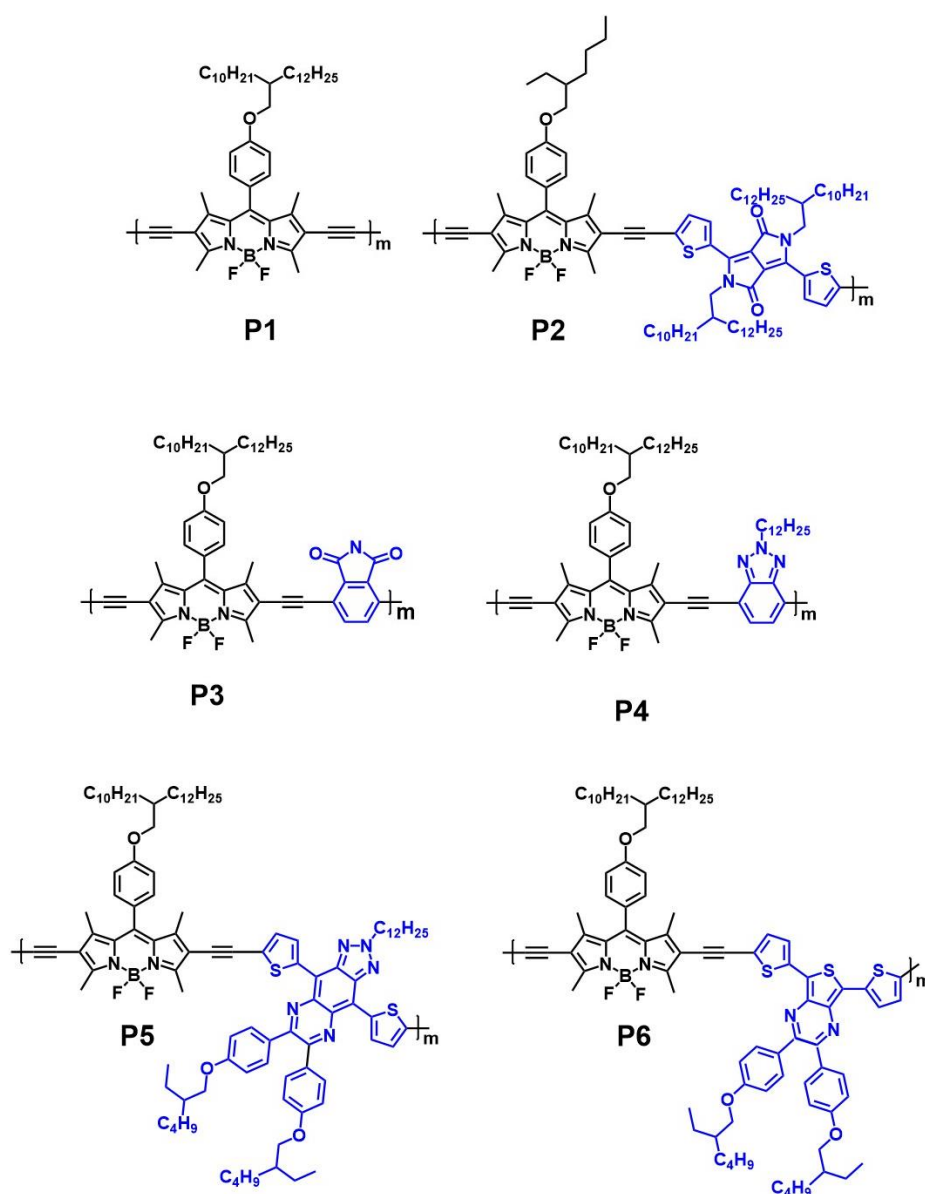


Figure 1.52. Alternating donor-acceptor copolymers. BODIPY unit as donor (black), acceptor units (blue).¹³⁷

As with previously reported BODIPY donor-acceptor copolymers a bathochromic shift was observed upon polymerisation (λ_{\max} solution = 760 nm **P2**), with an additional shift observed on thin film (λ_{\max} solid = 780 nm **P2**). Bandgaps of polymers were determined with a consistent LUMO level throughout all polymer samples, indicating the LUMO energy level is largely dependant on the BODIPY moiety.

Polymers were tested for detecting volatile organic compounds and the sensitivity for all polymers were in the order toluene > benzene > acetone > methanol > water. It is thought that the polymers are most sensitive to the aromatic solvents due to the strong π - π interaction between polymer and solvent molecules.

In 2017, Harvey et al. published a paper reporting the tunability of BODIPY polymers, specifically referring to the energy level modifications that can be achieved through post-functionalisation of the polymer.¹³⁸ As can be seen in **Figure 1.53**, **polymer 2** is the most red-shifted (approximately 189 nm with respect to the starting monomer) after addition of styrene moiety onto the **polymer 1** compound allowing further π -conjugation in the polymer backbone, leading to electronic displacement and hence lowering the band gap.

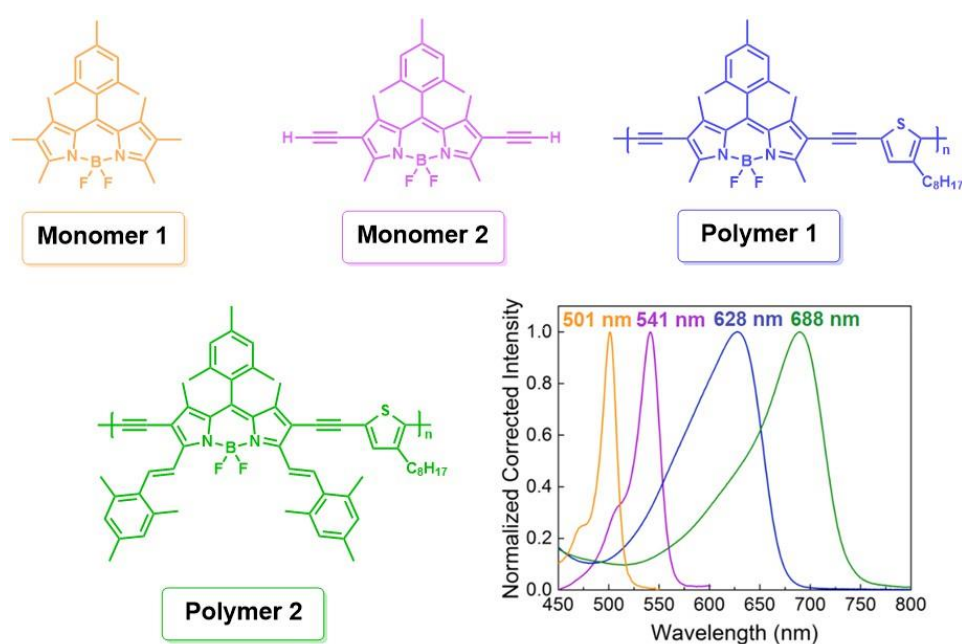


Figure 1.53. Absorption spectra of BODIPY monomers and polymers in 2-MeTHF. Monomer 1 (orange), Monomer 2 (purple), Polymer 1 (blue), Polymer 2 (green) - each colour corresponding compound to absorption spectra.¹³⁸

In addition to absorption spectra recorded of monomer and polymer compounds in solution, thin film absorption spectra of all compounds were also measured. As previously reported, upon comparison of solution vs. thin film absorption spectra, the absorption features are largely the same, however a slight broadening and red shift of polymers in thin film is observed. This can be attributed to the increased interchain π -

π interaction in the thin film assembly, allowing planarisation of polymer backbone, enhanced π -conjugation and hence a bathochromic displacement.

Referring to the earlier work carried out by Fréchet et al. using BODIPY polymers in bulk heterojunction (BHJ) solar cells, this area of research was expanded by Gros et al. in 2018. BHJ solar cells fall under the category of photovoltaic cells, using a voltage to split water. Specifically, BHJ cells consist of multilayers on a surface, typically an absorber layer (consisting of a donor and an acceptor), a photoactive layer between the anode and the cathode and other interfacial layers such as the hole transport layer and the electron transport layer.¹³⁹ Gros and co-workers developed BODIPY polymer materials explicitly for the active layer in order to overcome the 12-13% PCE achieved for fullerene based BHJ cells. BODIPY polymers offer advantages over the previously used fullerene devices, such as enhanced absorption in the visible region and appropriate energy levels to ensure charge transfer.¹⁴⁰ **Figure 1.54** displays the BODIPY copolymer used as a donor and the carbazole used as the acceptor. These two materials were used as the active layer in BHJ solar cells after optimisation of the morphology on the surface. The polymer solar cell demonstrated a PCE of 9.29% and a total energy loss of 0.48 eV (lower compared to PC₁₇BM counterpart of 0.83 eV).

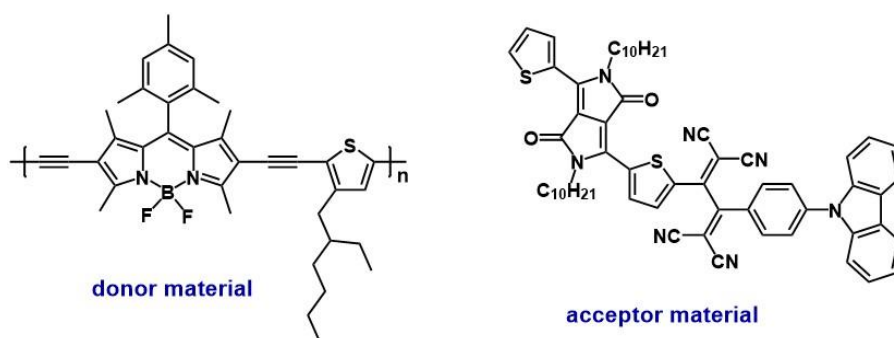


Figure 1.54. BODIPY copolymer (donor material) and carbazole-diketopyrrolopyrrole unit (acceptor material) used in BHJ solar cells.¹⁴⁰

Further expansion of this field has been seen in the synthesis of 3D architectures. Synthesis of these polymers usually requires building blocks that contain three (or more) reactive groups. Thus, the polymers formed contain permanent porosity with well-defined nanopores. The geometry of the linker can largely determine the size of these nanopores, as can the monomer used to determine the photophysical and

electronic properties. Advantages include extended π -conjugation, introduction of porosity, and high stability. These diverse properties pave the way for future applications using these polymers such as light-harvesting or energy storage, with interesting optoelectronic properties.^{75, 141}

Liras et al reported a 3D conjugated microporous polymer incorporating BODIPY moieties into porous molecular architecture (**Figure 1.55**).¹⁴² This conjugated microporous polymer (CMP) was used as a photocatalyst to oxidise thioanisole to its corresponding sulfoxide via singlet oxygen ($^1\text{O}_2$) production.

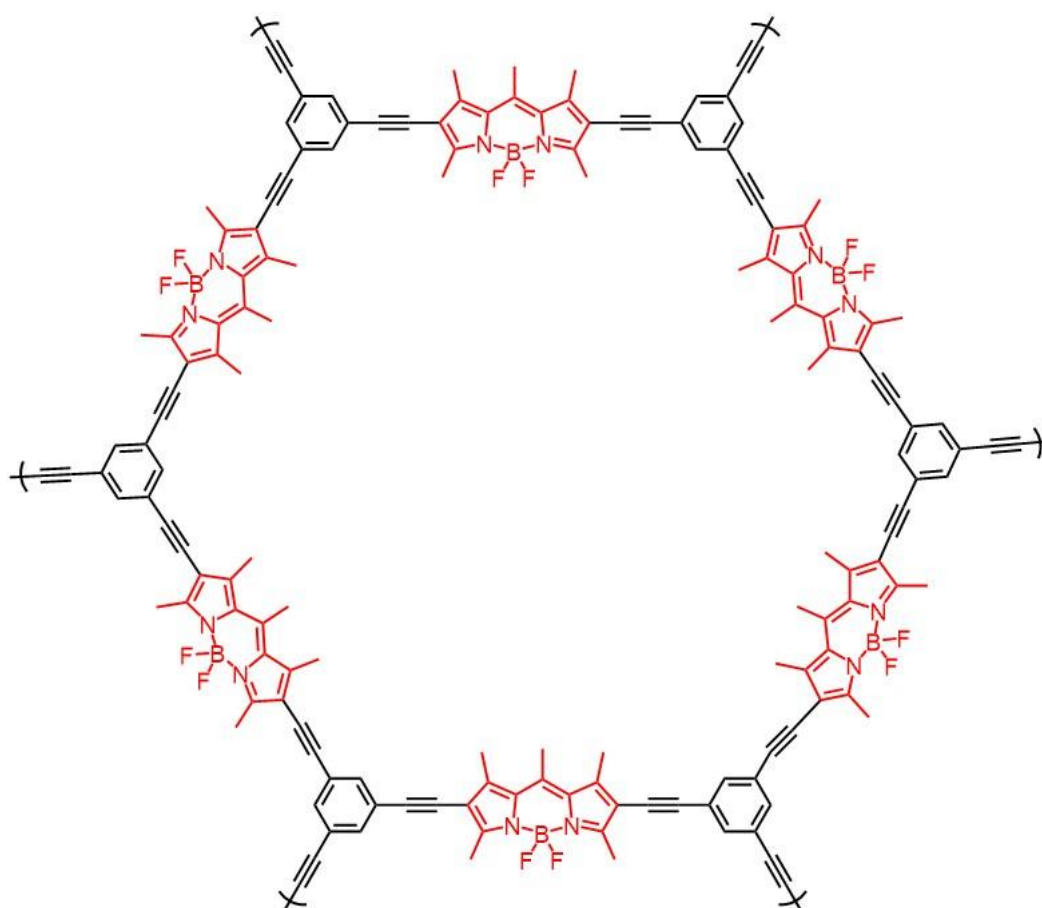


Figure 1.55. CMP synthesised incorporating the BODIPY chromophore for visible light photocatalysis. BODIPY chromophore (red), phenyl acetyl linker (black).¹⁴²

Conjugated porous polymers (CPP) containing the anthracene group at the *meso* position of the BODIPY were reported in 2018 (**Figure 1.56**).¹⁴³ The polymer was then subject to carbonisation, and used in lithium-ion storage applications as a potential energy storage, as these materials have high surface areas ($502 \text{ m}^2 \text{ g}^{-1}$).

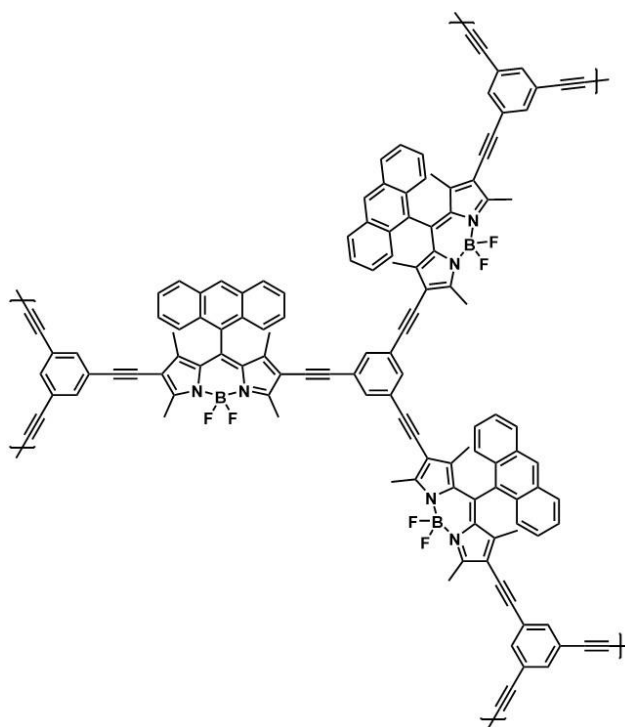


Figure 1.56. Anthracene containing BODIPY CPP synthesised for lithium-ion storage.¹⁴³

An insight into the complex photodynamics of a 3D BODIPY-based copolymer was more recently reported by Douhal et al. wherein excited state lifetimes were obtained using steady-state and femtosecond to nanosecond (fs-ns) time-resolved fluorescence spectroscopy. In this work, two model BODIPY monomers (**MD1** and **MD2**) and one conjugated microporous BODIPY copolymer (**CMPBDP**) were studied (**Figure 1.57**), reporting a relatively large red shift for the main absorption band of **CMPBDP** owed to the expansion of the π -conjugation framework (1158 cm^{-1} , in comparison to the BODIPY precursor).¹⁴⁴

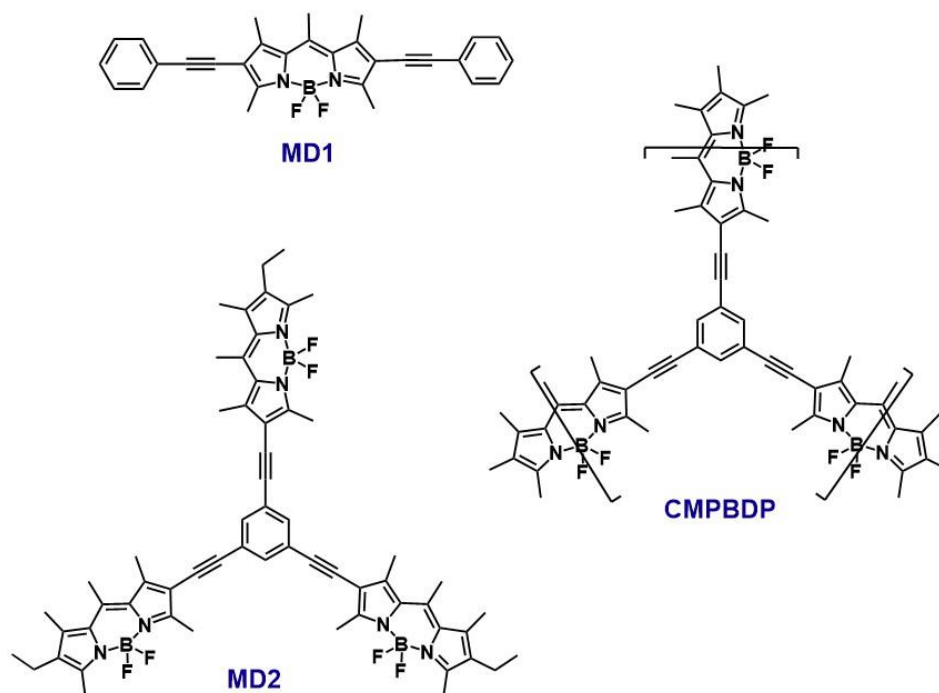


Figure 1.57. Molecular structure of BODIPY monomer **MD1**, **MD2** and BODIPY conjugated microporous polymer (**CMPBDP**) studied by Douhal and co-workers.¹⁴⁴

The theoretical calculations suggest that upon photoexcitation the electron density moves from the ethynylbenzene moiety to the BODIPY core in the case of **MD1**, whereas the electron density is shown to shift from the BODIPY core to the centre ethynylbenzene unit for **MD2** and **CMPBDP**. Fluorescence quantum yield were obtained for all compounds with values of; $\Phi_{fl} = 0.36$, $\Phi_{fl} = 0.17$ and $\Phi_{fl} = 0.02$ in DCM solution for **MD1**, **MD2** and **CMPBDP** respectively. Excitation spectra of **MD2** and **CMPBDP** are similar to the ground state absorption spectra ($\lambda_{obs} > 630$ nm) (**Figure 1.58** (a), red dashed line)). However, using a higher energy emission wavelength of detection (540 nm for **MD2**, 550 nm for **CMPBDP**) the maxima of the excitation spectra was blue shifted relative to the ground state absorption maxima (**Figure 1.58** (a), blue solid line). It was suggested that there are two ground state conformers present due to different torsional angles present between the BODIPY unit and the ethynylbenzene unit. Time-resolved fluorescence spectroscopy revealed three decay lifetimes for both **MD2** and **CMPBDP**, respectively. In the case of **MD2**, τ_1 and τ_2 appeared to be relatively unaffected by solvent polarity or excitation wavelength ($\lambda_{exc} = 371$ nm or $\lambda_{exc} = 490$ nm). However, in the case of the third lifetime component

(τ_3), there is a slight difference in lifetime with the excitation source used (e.g., in DCM solution at $\lambda_{\text{obs}} = 525 \text{ nm}$, $\tau_3 = 4.5 \text{ ns}$; at $\lambda_{\text{obs}} = 620 \text{ nm}$, $\tau_3 = 3.6 \text{ ns}$).

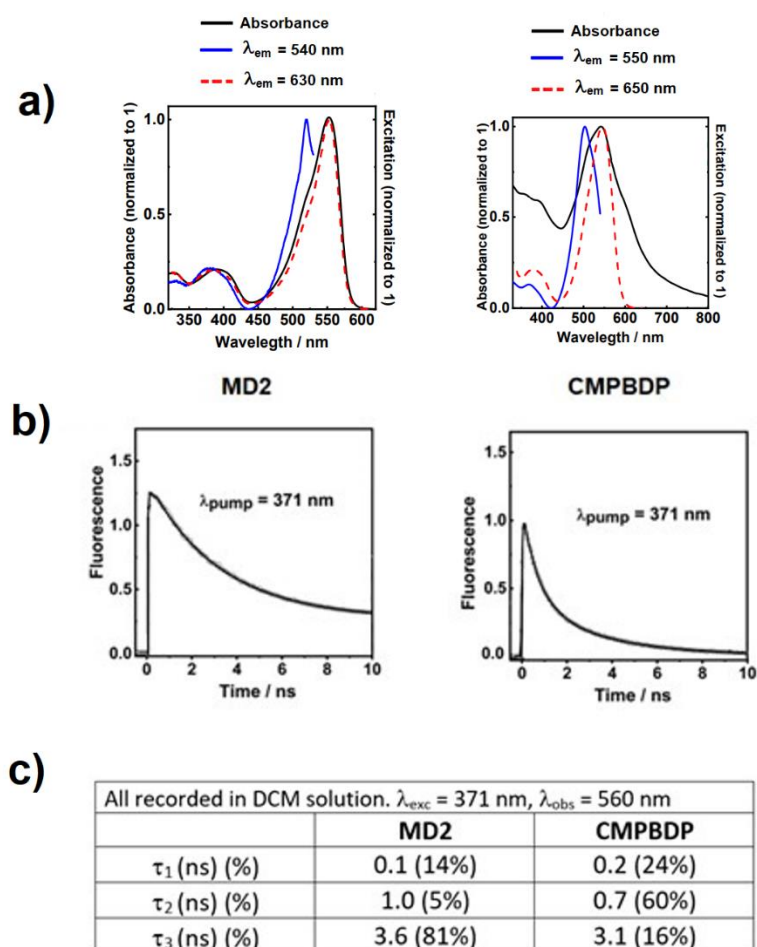


Figure 1.58. a) The absorption (black solid line) of **MD2** and **CMPBDP** in DCM solution and the excitation spectra of each compound (blue solid line, red dashed line) showing emission detection wavelength for each, b) The emission decay at 560 nm ($\lambda_{\text{exc}} = 371 \text{ nm}$) in DCM solution for **MD2** (left) and **CMPBDP** (right), c) the lifetime data obtained using exponential fitting to the decay curves in DCM solution shown in (b) including % decay of each lifetime component.¹⁴⁴

The photophysical properties of **MD2** and respective lifetimes are attributed to population of a singlet excited state, (S_1) by both structural conformers in the ground state, to populate two different excited states, S_1^I and S_1^{II} . From these excited states, **MD2** undergoes ultrafast ($\sim 0.3 \text{ ps}$) intramolecular charge transfer (ICT) to populate two separate ICT states (ICT^I and ICT^{II}) which decay with different time constants (0.1 – 1.0 ns, **Figure 1.58** (c)). As can be seen from **Figure 1.58** (c), these two lifetime components τ_1 and τ_2 are not the major contributors to the overall emission decay with

low percentage contributions of only 14% and 5% for τ_1 and τ_2 respectively. From the excited ICT states, it is reported that **MD2** twists to form a twisted intramolecular charge transfer state (TICT) which then decays with a higher percentage contribution and a lifetime range of $\sim 3.5 - 5.0$ ns. Similarly, **CMPBDP** displays three lifetime components, albeit slightly shorter lifetimes were obtained (**Figure 1.58** (c)). As a result of the multi-bands observed in the excitation spectra the case of the copolymer (**Figure 1.58** (a)), similar to that of **MD2**, it is also postulated that there are two ground state conformers of **CMPBDP**. Thus, the triexponential fit of the decay revealed three lifetime components and they are also believed to be a result of decay from two ICT states and two TICT states - however it is noted that the percentage contribution of the third lifetime component of the copolymer (percentage contribution of $\tau_3 = 16\%$) is significantly less than the model monomer, **MD2**. A reported advantage of expansion of the BODIPY copolymer in 2 dimensions (opposed to the one dimensional/linear BODIPY copolymers described above) in this work, is ascribed to the enhancement in planarity of the polymer, thus allowing a higher charge carrier mobility and improved interchain overlapping.

1.9.2 Non-ethynyl linked BODIPY copolymers

Focusing on polymers containing a single C-C σ bond as the linker for copolymeric units; Liu et al. studied the effect of the substituents on the phenyl ring in the *meso* position of BODIPY polymers. These polymers were synthesised via Suzuki copolymerisation containing fluorene linker unit (**Figure 1.59**).¹⁴⁸

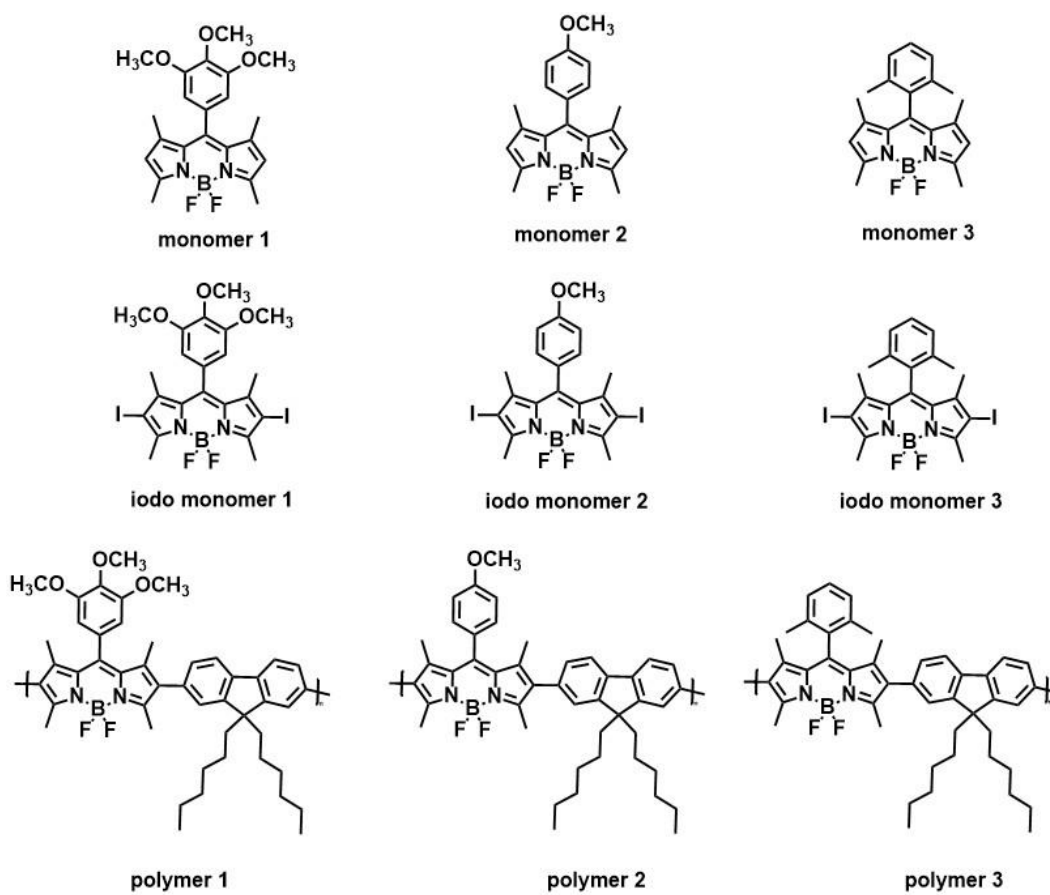


Figure 1.59. BODIPY based polyfluorene monomers, iodo monomers and copolymers.¹⁴⁸

For the polymers synthesised, a broadening and red shift in both the absorption spectra and the emission spectra were reported (**Table 1.2**). This expansion is attributed to increased π -conjugation in the main chain of the copolymer. Interestingly, the emission of the fluorene unit disappeared upon polymerisation with the BODIPY unit, indicating that photoinduced electron-transfer occurs, wherein the BODIPY unit acts as the acceptor unit and the fluorene acts as the donor unit. The BODIPY unit in the polymeric backbone hence served as an energy trap, with increased electron density on this moiety. The fluorescence quantum yields reflect this theory; as upon polymerisation fluorescent quantum yields increase in respect to the starting material iodo monomer (**BODIPY iodo monomer 1**, $\Phi_{fl} = 0.08$, vs. **BODIPY polymer 1**, $\Phi_{fl} = 0.64$, **Table 1.2**). The fluorescent quantum yields of iodo monomers are low due to the presence of the heavy atom, causing an increase in ISC, hence population of the triplet state. Fluorescent quantum yields of the polymers were significantly quenched in polar solvents ($\Phi_{fl} = 0.64$ in CH_2Cl_2 , $\Phi_{fl} = 0.16$ in DMF, **polymer 1**, **Figure 1.59**).

Table 1.2. Photophysical properties of BODIPY compounds as shown in **Figure 1.59**. All measurements recorded in dichloromethane solution.

Compound	λ_{\max} (nm)	λ_{em} (nm)	Φ_{fl}
BODIPY monomer 1	502	511	0.72
BODIPY iodo monomer 1	535	549	0.08
BODIPY polymer 1	557	587	0.64
BODIPY monomer 2	500	510	0.80
BODIPY iodo monomer 2	533	548	0.06
BODIPY polymer 2	547	585	0.56
BODIPY monomer 3	501	510	0.87
BODIPY iodo monomer 3	535	549	0.09
BODIPY polymer 3	549	588	0.85

Herrmann et al. studied the effect of different linker groups in the main chain of the polymer. Metal catalysed cross-coupling was used to synthesise **homopolymer** and **copolymer** (**Figure 1.60**).¹⁴⁹

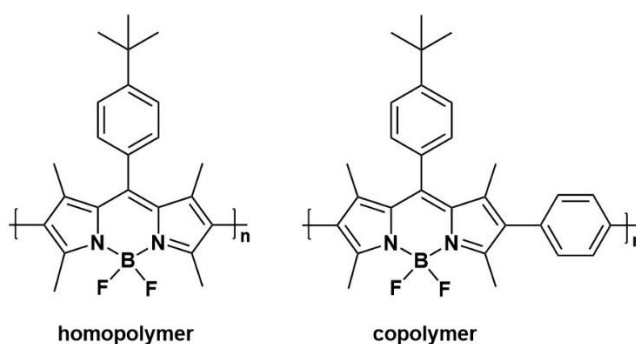


Figure 1.60. BODIPY polymers synthesised showing homopolymer (left) and copolymer with a benzene linker (right).¹⁴⁹

This paper reports extinction coefficients for polymers (ϵ) which is unusual, as polymers are based on a number average molecular weight and hence do not have a

defined mass, but rather a weight distribution (assumption that the value obtained is based on the weight of the repeating unit of the polymeric chain). Extinction coefficients calculation for the polymers shown in **Figure 1.60** are $475,000 \text{ M}^{-1} \text{ cm}^{-1}$ for **homopolymer** and $20,000 \text{ M}^{-1} \text{ cm}^{-1}$ for **copolymer**. From these values, it can be seen that the **homopolymer** has a much higher extinction coefficient, resembling the high molar extinction coefficient of the corresponding monomer. Interestingly, the **homopolymer** displays photophysical properties of the monomer (e.g., $\lambda_{\text{max}} = 503 \text{ nm}$), indicating that synthesis of copolymeric compounds incorporating a suitable unsaturated linker, provides the conjugation required to produce a bathochromic shift in the UV-visible absorption spectra.

Cihaner and Algi used electro-polymerisation to synthesise a novel conducting copolymer based on a 4-nitro phenyl BODIPY linked with a 3,4-ethylenedioxythiophene (EDOT) unit (**Figure 1.61**).¹⁵⁰ EDOT is an electron rich moiety – due to the presence of the alkoxy groups, and this has potential to make a conducting polymer with unique electroactive properties and also a low band gap conducting polymer.

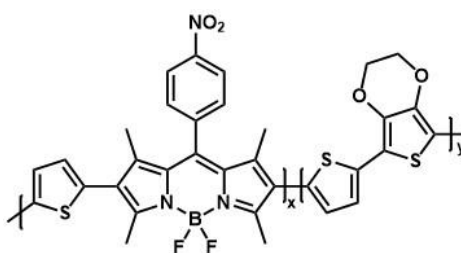


Figure 1.61. BODIPY-based conducting polymer bearing EDOT copolymeric unit.¹⁵⁰

Burgess et al. later reported the novel synthesis of a series of donor-acceptor BODIPY polymers incorporating various ratios of fluorene to BODIPY units.¹⁵¹ Herein, the donor unit (fluorene) absorbs light ($\lambda_{\text{abs}} = 358 \text{ nm}$) and through covalent bonds (allowing fast and efficient energy transfer) transfers energy to the accepting BODIPY unit, emitting light at a higher wavelength than the donor component of the polymer ($\lambda_{\text{em}} = 517 - 677 \text{ nm}$). This new design of donor-acceptor polymers eliminates the need to incorporate a sufficient overlap of donor emission spectra with acceptor absorption spectra for efficient energy transfer.

BODIPY polymers soluble in aqueous solution (at least 20 mg/mL) were later reported by Tiwari and co-workers (**polymer A** and **polymer B**, **Figure 1.62**).¹⁵² Incorporation of highly soluble oligo(ethylene glycol)methyl ether moieties enhanced the water solubility of the polymers and furthermore prevents π - π stacking interactions between the polymeric backbones.

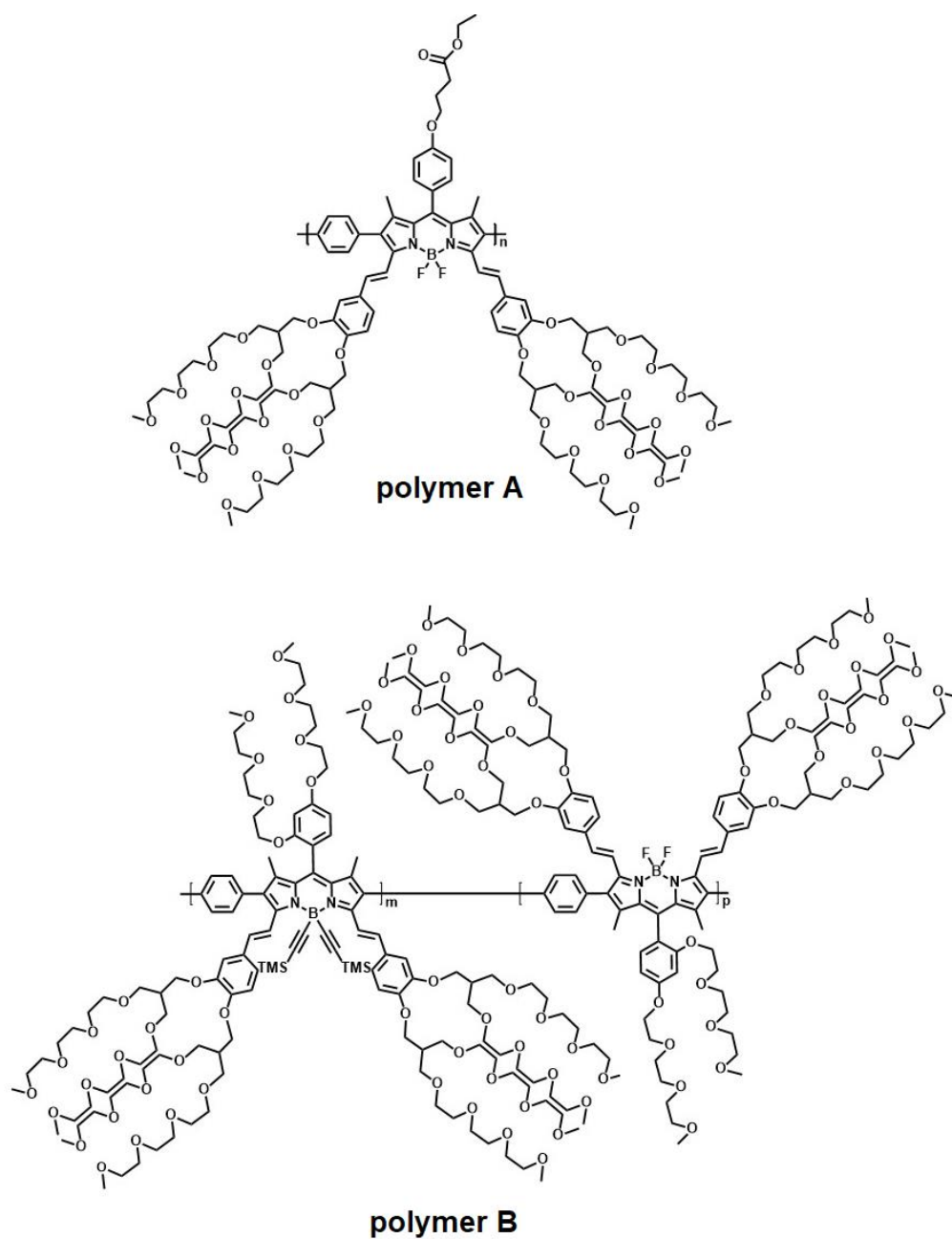


Figure 1.62. Water soluble NIR emissive BODIPYs polymers, **polymer A** and **polymer B**.¹⁵²

Polymer B involved partial replacement of the fluorine atom with ethynyl trimethylsilane (TMS) groups to achieve higher solubility of polymer in aqueous solution. **Table 1.3** displays the photophysical properties of **polymer A** and **polymer B** shown in **Figure 1.62**. Absorption and emission of the copolymers are bathochromically shifted, in comparison to polymers introduced thus far (virtue of distyryl groups in the 3,5 position of the BODIPY core). The fluorescence intensity of the polymers is quenched in aqueous media in comparison in dichloromethane solution (**Table 1.3**). One presumption of the observed quenching in water is due to the self-quenching of the polymers as a result of aggregation of polymer chains. However, there is little evidence for π - π stacking along the polymer backbone. Another possibility for the quenching of fluorescence in aqueous solution is thought to be due to the intramolecular charge transfer (ICT) that occurs between the push (distyryl) and pull (BODIPY) moiety of the polymeric compound in water. This is thought to be enhanced in water (polar solvent) and hence polymers undergo radiationless decay from the excited state. Understanding these charge-transfer dynamics principles, helps us to better design chromophoric polymers with niche applications.

Table 1.3. Photophysical properties of water soluble BODIPY compounds. Note absorption and emission spectra were recorded in CH_2Cl_2 .¹⁵² Structures shown in **Figure 1.62**.

Compound	λ_{abs} (nm)	λ_{em} (nm)	Φ_{fl} (CH_2Cl_2)	Φ_{fl} (H_2O)
Polymer A	683	696	0.091	0.018
Polymer B	673	685	0.089	0.009

In 2013, a publication on BODIPY polymers reported a series of five novel polymers (one homopolymer and four copolymers, **Figure 1.63**) synthesised using Pd(0) catalysed Stille polymerisation.¹⁵³ All polymers display a bathochromic shift of the main absorption band in comparison to the BODIPY monomeric precursor ($\lambda_{\text{max}} = 525$ nm in CHCl_3) as seen in inset **Figure 1.63**. The calculated optical gaps of the polymers were in good agreement with the electrochemically calculated band gaps e.g., **PBTBT**, $E_{\text{g}}^{\text{opt}} = 1.79$ eV versus $E_{\text{g}}^{\text{chem}} = 1.86$ eV.

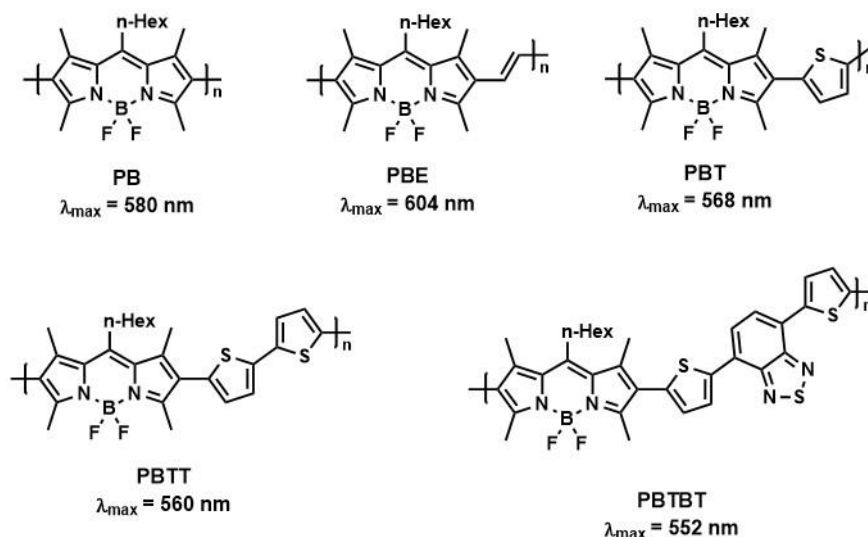


Figure 1.63. Conjugated polymers with different band gaps synthesised via Stille polymerisation. All polymerisation reactions were synthesised in the presence of $[\text{Pd}_2(\text{dba})_3]$ (2 mol%), $[(o\text{-Tol})_3\text{P}]$ (8 mol%) in toluene at *ca.* 110 °C for 24 hours. Inset shows absorption maxima for each polymer in chloroform solution.¹⁵³

A BODIPY copolymer (**P-BODIPY**, **Figure 1.64**) synthesised by Suzuki coupling has been reported as an efficient heterogeneous photocatalyst, displaying high thermal and photostability under irradiative conditions.¹⁵⁴ **P-BODIPY** was adsorbed onto silica powder prior to running photocatalytic reactions in order to improve the dispersibility of the copolymer in the reaction solution.

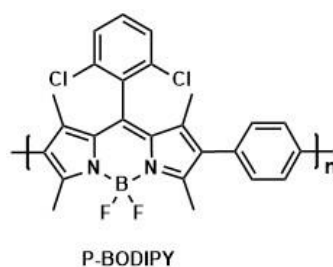


Figure 1.64. Molecular structure of the BODIPY copolymer (**P-BODIPY**) used as a heterogeneous photocatalyst in the oxidation reaction.¹⁵⁴

P-BODIPY was utilised for oxidative condensation of benzylamine (1 mmol) with 2-aminothiophenol (2 mmol) under visible light irradiation (35 W, Xe arc lamp, $\lambda > 385 \text{ nm}$) in aerated acetonitrile (**Scheme 1.13**). Light initiates the reaction and control reactions in the dark do not proceed. The suggested mechanism involves the use of **P-BODIPY** for the photosensitisation of ground state triplet oxygen ($^3\text{O}_2$) into singlet

More recently, Ramamurthy and co-workers studied the effect of structural isomerism on the photophysical properties of BODIPY-benzodithiophene linked copolymers through varying the α/β linkage position of the benzodithiophene donor unit (**Figure 1.66**).¹⁵⁶ It was found that the copolymer linked through the α -position of the BODIPY core resulted in a coiled geometry of the polymeric backbone, while the β -linked copolymer formed a linear geometry. The linear geometry of the β -linked copolymer resulted in a less soluble polymer than the α -linked counterpart due to enhancement of interchain interaction and thus a higher degree of π - π stacking in solution. The photoluminescence of the β -linked copolymer was significantly quenched in comparison to the α -linked copolymer, in addition to a smaller fluorescence quantum yield ($\Phi_{fl} = 0.002$ versus $\Phi_{fl} = 0.017$ for α -copolymer). Furthermore, the lifetime measurements revealed a shorter lifetime ($\tau = 0.31$ ns) for the β -copolymer in comparison to the α -copolymer ($\tau = 1.37$ ns) in CHCl_3 which is consistent with a faster and more efficient electron transfer in the case of the β -copolymer.

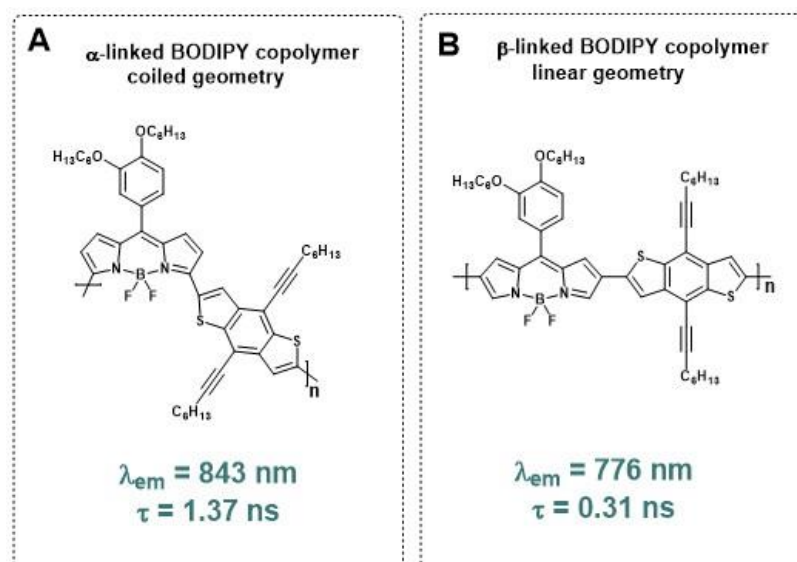


Figure 1.66. BODIPY-benzodithiophene copolymers a) α -linked (coiled geometry) and b) β -linked (linear geometry). Inset showing emission maxima ($\lambda_{exc} = 669$ nm) in chloroform solution and respective lifetime.¹⁵⁶

An insight into the effect of α/β linked BODIPY copolymers was obtained when BODIPY-fluorene based copolymers were reported including a comparative study of the effect of choosing different linkage sites for polymerisation (**Figure 1.67**).¹⁵⁷ The α -linked copolymer, **P1** displayed the largest bathochromic shift upon polymerisation

of the BODIPY monomeric unit with the fluorene moiety ($\Delta\lambda_{\text{max}} = 89$ nm from **M1** to **P1**, versus $\Delta\lambda_{\text{max}} = 42$ nm from **M2** to **P2**). The fluorescent quantum yields of the copolymers are low (**P2**, $\Phi_{\text{fl}} = 7.9\%$), however, this value is larger in comparison to the 2,6 diiodo BODIPY precursor (**M2**, $\Phi_{\text{fl}} = 1.6\%$) which displays significant quenching of the emission intensity due to the introduction of the iodine heavy atom at the 2 and 6 position of the BODIPY core.

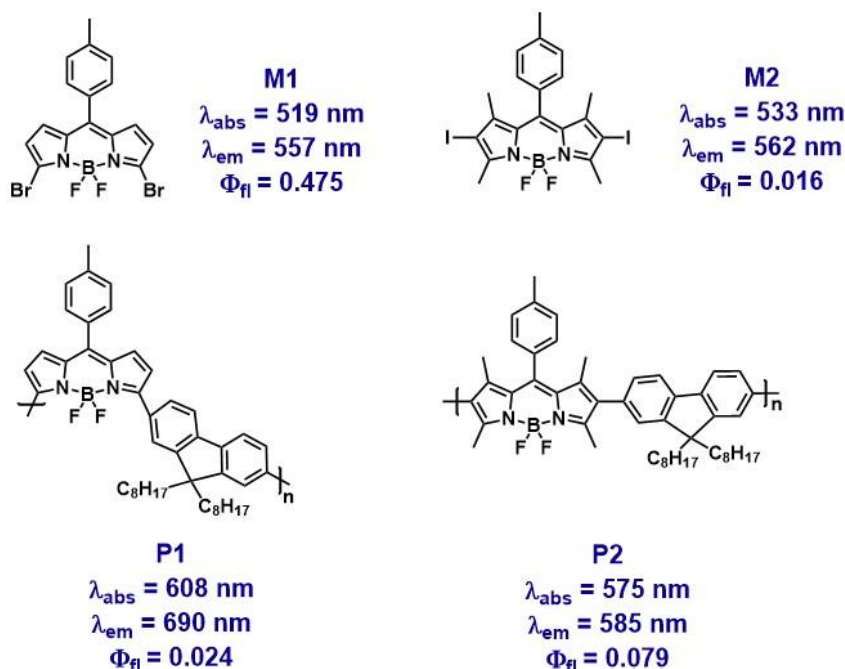


Figure 1.67. A series of BODIPY-fluorene copolymers **P1** (α -linked units) and **P2** (β -linked units). Corresponding monomeric precursors shown above (**M1** and **M2**). Photophysical properties of monomers and polymers shown in inset.¹⁵⁷

A series of donor-acceptor BODIPY copolymers (**P1** – **P3**, **Figure 1.68**) containing an electron deficient BODIPY monomer and three different electron rich donors (fluorene, benzo[1,2-b:4,5-b']dithiophene (BDT) and diketopyrrolopyrrole (DPP)) were synthesised and their optical and electrochemical properties were investigated.¹⁵⁸ Polymerisation of the monomeric units to form the resulting polymer with high planarity was carried out using Stille coupling (toluene as solvent, 50 °C) to yield the polymers with high molecular weight distributions (e.g. **P3** = 10.3 kDa) and good polydispersity (e.g. **P3**, PDI = 1.9). The absorption spectra of all polymers were significantly broader and red-shifted in comparison to the BODIPY monomeric precursor (BODIPY monomer full width at half-maximum (fwhm) = 23.4 nm ($\lambda_{\text{abs}} =$

635 nm), **P1** fwhm = 186 nm ($\lambda_{\text{abs}} = 760$ nm), **P2** fwhm = 385 nm ($\lambda_{\text{abs}} = 836$ nm) and **P3** fwhm = 746 nm ($\lambda_{\text{abs}} = 1005$ nm)). While **P1** displays NIR emission ($\lambda_{\text{em}} = 897$ nm with a shoulder 1043 nm), **P2** and **P3** are not emissive. The optical band gap ($E_{\text{g}}^{\text{opt}}$ **P1** = 1.24 eV) and the electrochemical band gap (E_{g}^{CV} **P1** = 1.40 eV) were in good agreement and all polymers were shown to have deep HOMO levels (< -5.2 eV), in addition to deep LUMO levels (< -4.0 eV). This results in an ultralow band gap of these novel BODIPY based copolymers. Furthermore, it is noted that while **P3** is non-emissive, the wide absorption of the copolymer across the solar spectrum (ranging from 500 nm – 1600 nm) makes this compound an ideal candidate for harvesting photons and coupled with a high electron mobility (**P3** = 5.4×10^{-4} cm² V⁻¹ s⁻¹), establishes this copolymer an attractive candidate for solar-driven applications.

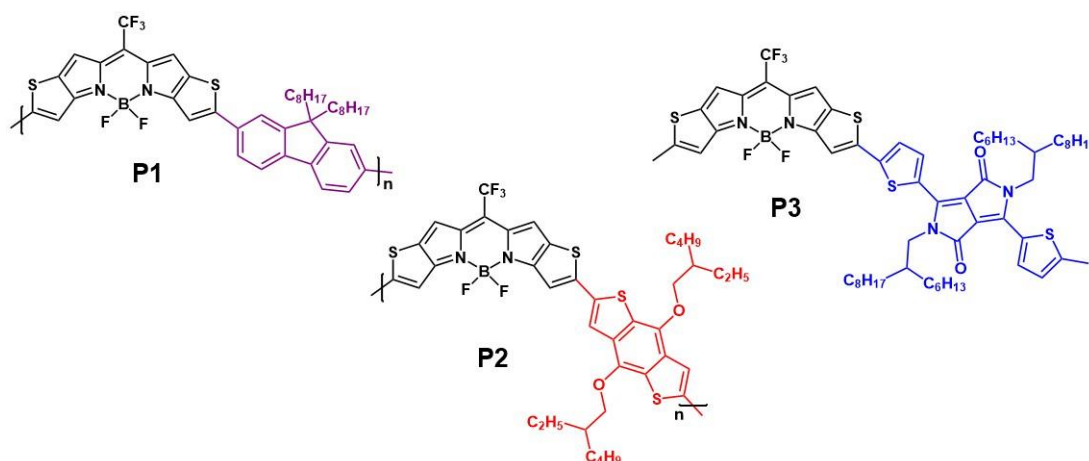


Figure 1.68. A series of donor-acceptor BODIPY copolymers (**P1** – **P3**) synthesised using Stille polycondensation reaction. BODIPY unit (black), fluorene (purple), BDT (red) and DPP (blue).¹⁵⁸

To summarise, the triplet state formation from unsubstituted BODIPY monomers is negligible ($>0.1\%$) and synthetic modification of the BODIPY core is required, to change the photophysical properties and thus promote ISC onto the triplet surface.^{116,129,145–147} Of the BODIPY copolymers reported to date (both ethynyl linked and non-ethynyl linked copolymers), none have been used in photocatalytic hydrogen evolution. The 1,3,5,7 tetramethyl substituted BODIPY core appears in the majority of published BODIPY polymer compounds due to synthetic difficulties and stability issues associated with the less substituted BODIPY core (i.e. without the methyl substituent in the α and β position of the BODIPY core).¹²⁸ While there are some

preliminary investigations involving BODIPY metal organic frameworks (such as those mentioned in section 1.8.5, **Figure 1.46**), these studies are in their infancy. This thesis introduces BODIPY copolymers as potential photosensitisers for photocatalytic hydrogen evolution (a novel investigation in this area) and furthermore, studies the time-resolved spectroscopies of BODIPY copolymers in a range of solvents, with the aim of investigation of the excited state dynamics of these novel copolymers.

1.9.3 Other BODIPY containing polymers

The polymers introduced thus far have all been polymerised through the 2 and 6 position of the BODIPY core. This synthetic approach does not account for all BODIPY polymers reported in the literature. Other BODIPY polymers include (but are not limited to); i) BODIPY moieties as pendant chains in polymer backbones (**1**, **Figure 1.69**),^{151,159} ii) fused BODIPY polymers (**2**, **Figure 1.69**),¹⁶² iii) aza BODIPY polymers (**3** and **4**, **Figure 1.69**),^{160,161} and iv) BODIPY units polymerised through the fluorine atom.¹⁶³

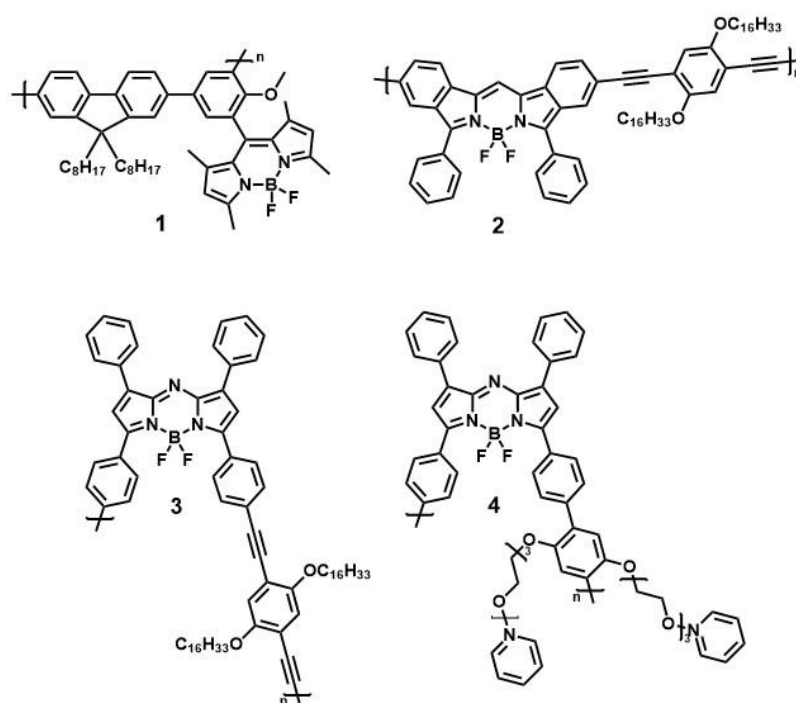


Figure 1.69. Examples of BODIPY polymers reported in the literature (examples show BODIPY polymers that are not linking the BODIPY chromophore by the 2 and 6 position).¹⁶²

There have been some interesting publications of the latter involving polymerisation of the BODIPY core through the fluorine atoms attached to the boron. Originally reported in 2008, the synthesis of these polymers via Sonogashira polymerisation reaction affords polymers exhibiting unique supramolecular assemblies (**Figure 1.70**).¹⁶³

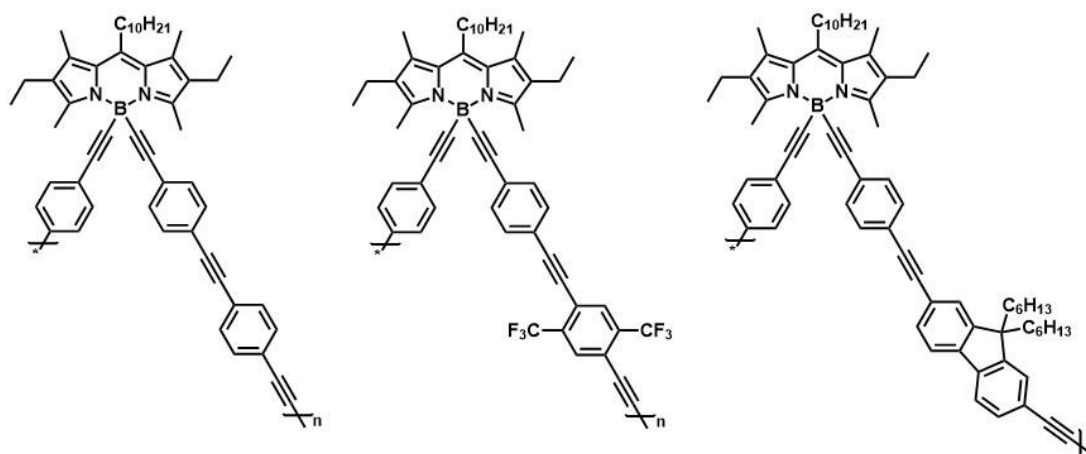


Figure 1.70. BODIPY copolymers containing different aromatic linking units.¹⁶³

Following on from this work, Chujo et al. reported a series of BODIPY copolymers using the fluorine atom to attached either electron withdrawing groups (EWG) or electron donating groups (EDG) (**Figure 1.71**).¹⁶⁴ The copolymers reported in this study consisted of a BODIPY unit (with different EWG/EDG attached to the boron atom) and fluorene as the co-monomer. Fluorene was chosen to increase the conjugation along the main chain of the polymeric backbone. The addition of side-chain substituents through the boron atom in the BODIPY unit further allowed for preservation of the conjugation of the polymeric backbone, while allowing for modification of the polymer properties. This series of polymers was synthesised via Suzuki-Miyaura coupling and includes a polymer containing i) no substituent, ii) OCH_3 as the EDG (both fluorine atoms substituted), iii) CF_3 as the EWG (both fluorine atoms substituted), iv) one of each CF_3 and OCH_3 and v) a phenyl substituent only to allow for comparison (**Figure 1.71**).¹⁶⁴ The EDG/EWG used in different polymeric chains have no effect of the degree of the bathochromic shift observed in the UV-vis absorption spectra upon polymerisation (fluorene copolymers λ_{max} of UV-visible absorption spectra = 541, 542, 540, 542 nm). This paper shows how main chain

conjugation can be preserved with addition of different groups off the boron atom on the BODIPY core.

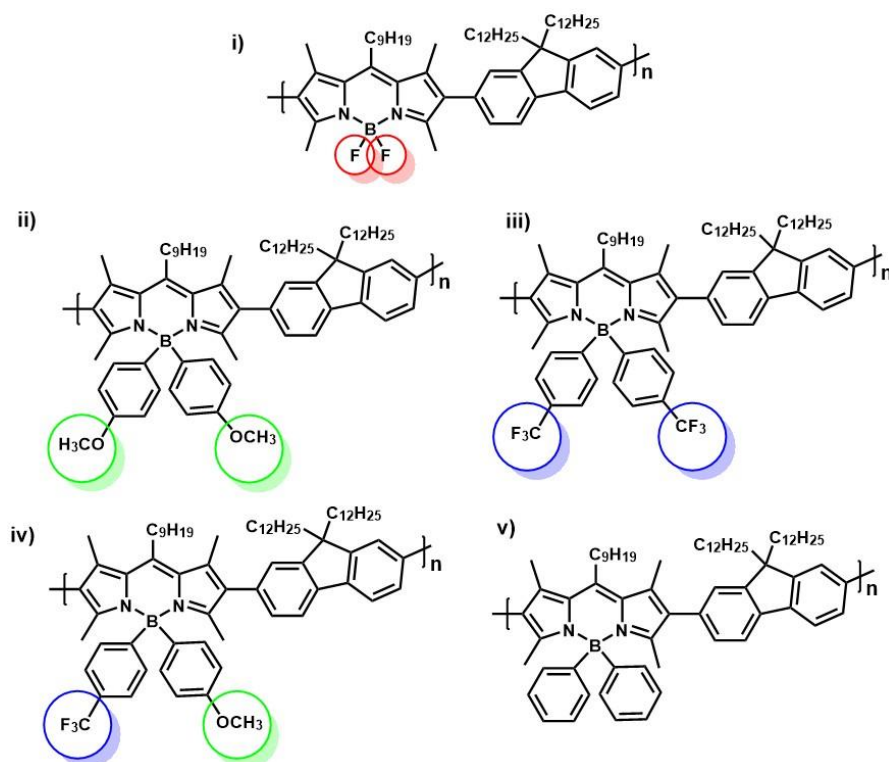


Figure 1.71. Novel BODIPY fluorene alternating copolymers, showing EWG (CF_3 , blue circle), EDG (OCH_3 , green circle) and fluorine atoms unsubstituted (red circle).¹⁶⁴

Radical copolymerisation using an initiator such as 2,2'-azobis(2-methylpropionitrile) (AIBN) has also been used as a synthetic approach for the synthesis of BODIPY polymers wherein a BODIPY unit is incorporated into the polymer as a pendant side-chain. This area has expanded recently by the work of Kobatake et al. reporting a random copolymer with varying BODIPY content from 0.042 to 100 mol% synthesised using AIBN as an indicator in toluene at 60 °C for 10 hours (**Figure 1.72**).¹⁶⁵ The emissive properties of the resulting series of BODIPY copolymers is alternated from green to red by changing the content of the BODIPY monomer from 0.042 to 100 mol%.

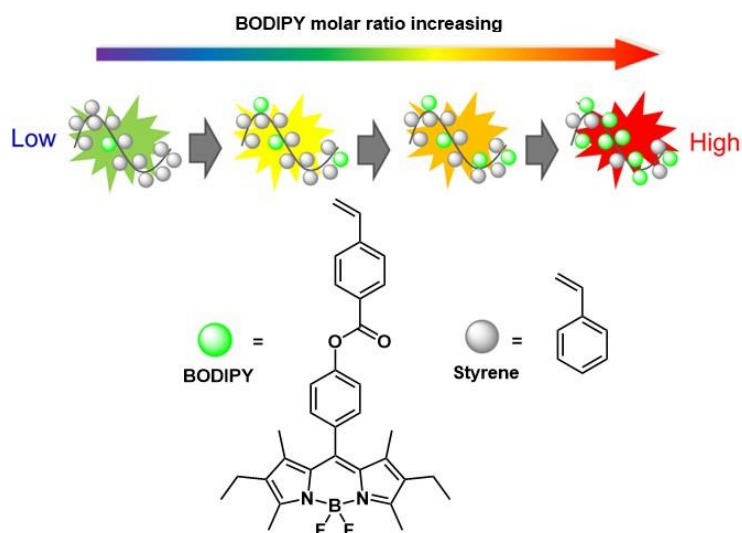


Figure 1.72. Random BODIPY copolymer showing BODIPY monomer (green circle) as pendant side chain and styrene (grey circle) used as spacer along polymeric backbone.¹⁶⁵

Radical copolymerisation was also used in efforts to develop room temperature phosphorescent materials using a diiodo BODIPY monomer (**p-2I-BDP**) with acrylamide in a radical copolymerisation reaction (**Figure 1.73 (a)**).¹⁶⁶ The solid state absorption properties of **p-2I-BDP** revealed three strong absorption peaks at 312, 420 and 540 nm (black solid line, **Figure 1.73 (b)**). A prompt emission band was observed at 565 nm ($\lambda_{\text{exc}} = 540$ nm) (red solid line, **Figure 1.73 (b)**), and a delayed photoluminescence measurement displayed an emission band in the NIR region of the spectrum at 770 nm (blue solid line, **Figure 1.73 (b)**), using 0.1 ms delay time. The band at 770 nm decayed with a lifetime of 710 μs and hence was attributed to phosphorescence from **p-2I-BDP**.

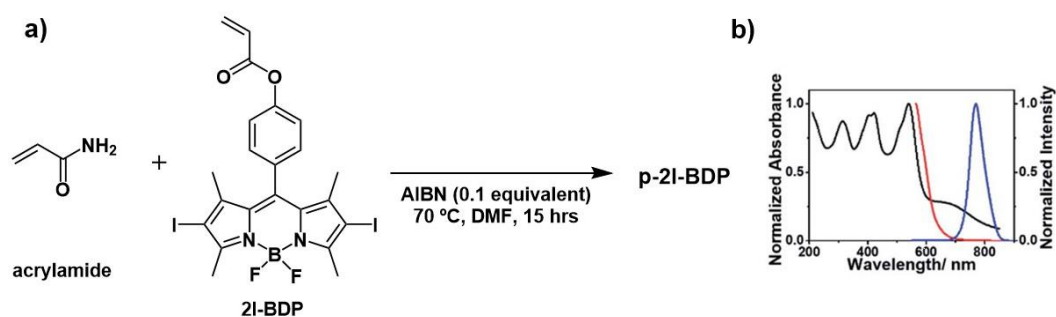


Figure 1.73. a) Synthesis of BODIPY copolymer (**p-2I-BDP**) using AIBN as an initiator in radical copolymerisation reaction and b) Solid UV-vis absorption spectrum of **p-2I-BDP** (solid black line), prompt photoluminescence spectrum (red solid line) and delayed photoluminescence spectrum (blue solid line).¹⁶⁶

BODIPY chromophores have also been incorporated into Merrifield resins (cross-linked polystyrene resin) in polymer supported ester linked BODIPY containing photosensitisers in continuous flow synthetic methods (**Figure 1.74**).¹⁶⁷

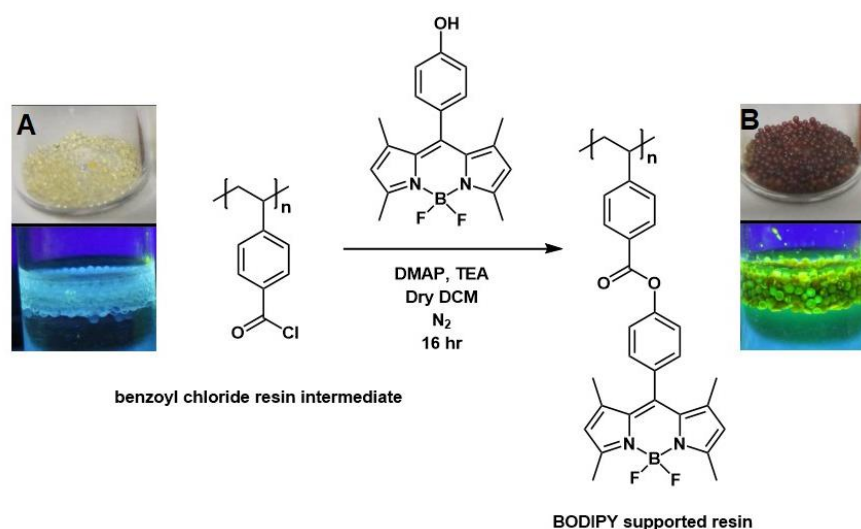


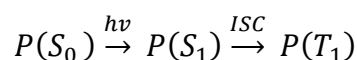
Figure 1.74. Synthesis of polystyrene polymer supported BODIPY resins using benzoyl chloride resin intermediate in a continuous flow procedure. DMAP – 4-dimethylaminopyridine.¹⁶⁷ Inset displays starting material resins (A) and BODIPY functionalised resins (B) both under ambient conditions (top image) and under UV light (bottom image).

Solid-state UV-visible spectroscopy confirmed attachment of the BODIPY monomer to the resin polystyrene material ($\lambda_{\text{abs}} = 505 \text{ nm}$), as did FTIR measurements displaying a characteristic C-O-C stretching vibration belonging to the ester linkage between the BODIPY unit and the polystyrene. The BODIPY functionalised resin was used to convert α -terpinene to ascaridole in a [4+2] cycloaddition using the BODIPY-resins as photosensitisers to generate singlet oxygen ($^1\text{O}_2$) *in situ* and thus oxidise the organic starting material. For the heterogeneous flow photoreaction, the vials were irradiated ($h\nu = 500 \text{ nm}$) and a conversion of 58% was observed after 2 hours.

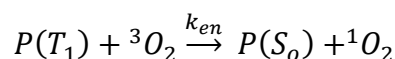
1.10 Photodynamic therapy (PDT)

1.10.1 Singlet oxygen (1O_2) generation

The application of BODIPYs for photodynamic therapy (PDT) or antimicrobial-PDT (aPDT) is plentiful, and this can be taken as an attest to how effective the chromophore is upon successful modification of the core scaffold. A large contributor to the success of BODIPYs in PDT is the ability of the chromophore to generate singlet oxygen (1O_2). Singlet oxygen is a form of reactive oxygen species (ROS) which cause cell death (apoptosis) through oxidative damage such as damage to DNA and oxidative deactivation of protein and/or enzymes. PDT consists of the utilisation of three components: a photosensitiser, light (wavelength appropriate of PS absorbance) and ground state oxygen (3O_2). The process of singlet oxygen generation occurs when the PS absorbs visible light and promotes an electron to the singlet excited state. ISC occurs and the triplet excited state is formed. This excited electron then undergoes energy transfer (Type II mechanism) and converts the surrounding ground state oxygen (3O_2) to singlet oxygen (1O_2) – see **Equation 1.15** and **Equation 1.16**.¹⁶⁸ Singlet oxygen a ROS and once formed, readily reacts, causing cytotoxic effects including apoptosis and destruction of cells used in the previously mentioned applications.



Equation 1.15. Formation of the triplet excited state of the PS.



Equation 1.16. Generation of singlet oxygen via an energy transfer mechanism.

Compounds containing the BODIPY chromophore have been investigated for the generation of singlet oxygen; specifically, the halogenated counterparts due to their enhanced rate of ISC. Halogenation of BODIPY dyes (in the 2/6 position) increase the yield of singlet oxygen due to the type II electron transfer process that occurs upon formation of the triplet excited state. However, there are concerns over the incorporation of said heavy-atoms such as iodine and bromine, as they are known to cause “dark-toxicity” and hence their biological application is dwindling.¹⁶⁹

Recently, there has been a publication involving alternative BODIPY systems that move away from the use of heavy atoms in the BODIPY structure. These systems involve electron-acceptor (BODIPY) and electron-donor (pyrene) dyads.¹⁷⁰ It is typical of these dyads to observed electron transfer from the donor to the acceptor upon excitation to form a highly dipolar, charge transfer (CT) state. Triplet state formation from this CT state was observed and the highest singlet oxygen quantum yield obtained was 0.75 in ethanol (**Figure 1.75**).

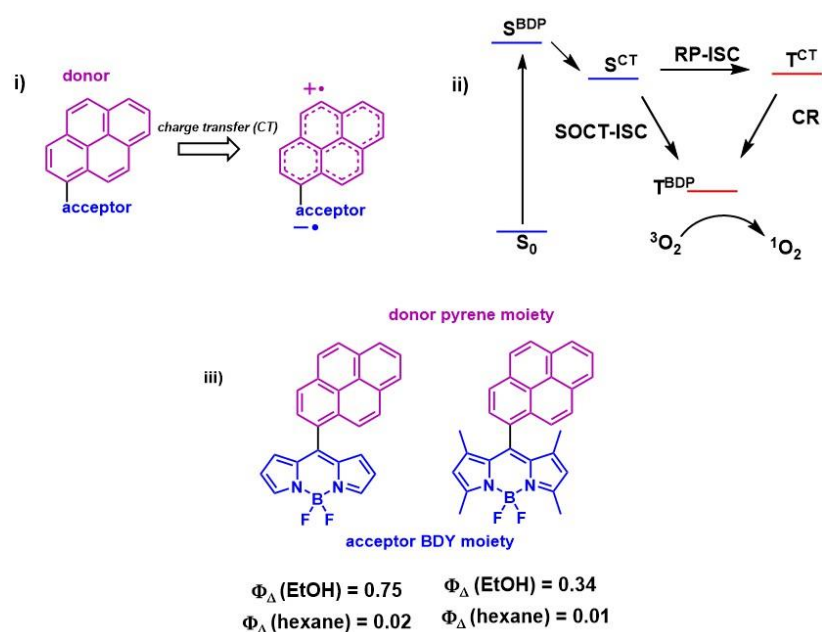


Figure 1.75. Pyrene-BODIPY BODIPY dyad for heavy-atom free PS for singlet oxygen generation. i) PeT to form a CT state from donor to acceptor, ii) photophysical processes that can occur to form triplet state iii) singlet oxygen yields in both polar and non-polar solvent for selected donor-acceptor dyads. SOCT-ISC: spin orbit charge transfer intersystem crossing, RP-ISC: radical pair intersystem crossing, CR: charge recombination, BODIPY = BDP.¹⁷⁰

Cationic-BODIPY dyes (**Figure 1.76**) have also been shown to be successful for singlet oxygen production and are successful antibacterial agents strains tested such as *E. coli*.¹⁷¹

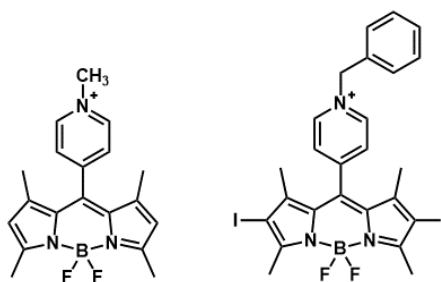


Figure 1.76. Cationic BODIPY compounds show singlet oxygen generation and antimicrobial activity.¹⁷¹

Other BODIPY compounds that have shown high singlet oxygen yields have also been reported (Figure 1.77).^{172,173}

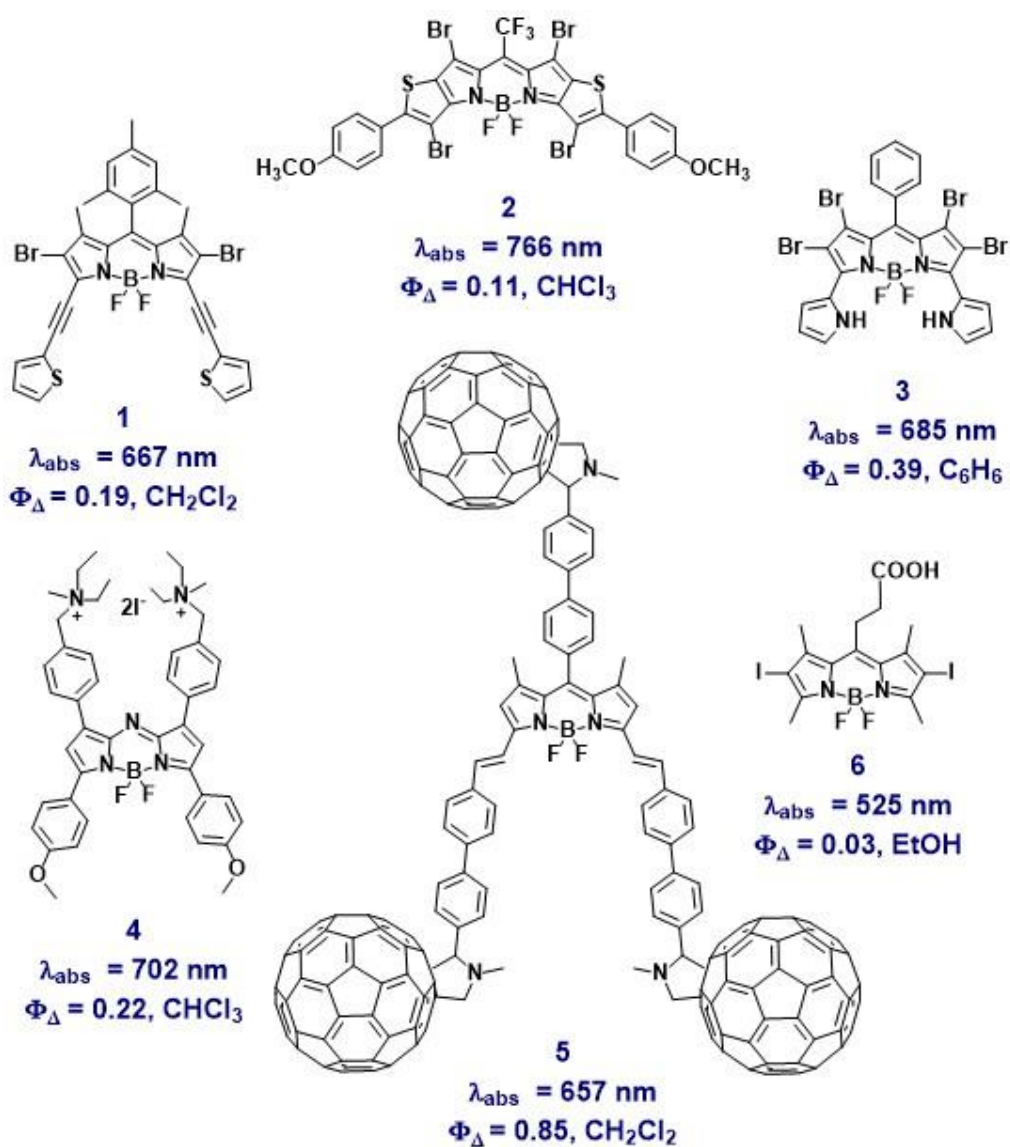


Figure 1.77. Range of BODIPY-based PS reported as singlet oxygen generating PS.^{172,173}

1.11 Conclusion

While there has been substantial progress in the use of conjugated polymers for the photocatalytic generation of hydrogen – there are still some crucial areas for improvement. For example, while there have been some insights into structure-activity relationships of polymeric systems (e.g. the superiority of donor-acceptor conjugated polymers), this only applies to a small group of polymers and more universal guidelines are required to expand these design rules.⁷³ The current understanding of the photoexcited state of conjugated polymers and how these states influence photocatalytic activity has not kept pace with the continuously growing body of publications on the topic. In addition, there is limited literature focusing time-resolved spectroscopy on conjugated polymers reported to date (including BODIPY copolymers) and an in-depth comprehension of the mechanism of hydrogen evolution is limited. This work investigates the excited state dynamics of BODIPY copolymers in efforts to explain the excited state population. Meanwhile, there are challenges associated with the long-term stability of the conjugated polymers and many authors note photodecomposition after extended periods of irradiation, which needs to be addressed in future work. Other challenges include the unstandardised reporting of the HER with some authors reporting the hydrogen evolved based on the mass of the polymer ($\mu\text{mol h}^{-1} \text{g}^{-1}$) while others do not ($\mu\text{mol h}^{-1}$). Finally, the outstanding challenge in the field of photocatalytic hydrogen evolution (not solely limited to conjugated polymers) is to eliminate the use of uneconomical SAs from the photocatalytic solution. One such approach is to immobilise the PS onto a photocathode in a p-type dye-sensitised photoelectrochemical cell (DSPEC). A common photocathode used for this approach is NiO and thus a PS | NiO photocathode in a DSPEC eradicates the need for a SA, resulting in a more economically viable scale-up design.¹⁷⁴ This will be the topic of future investigations of the novel BODIPY copolymers reported in this work.

This thesis focuses on BODIPY-based copolymers as fully metal-free, organic-based photosensitisers for hydrogen evolution. Polymerisation of the typical BODIPY monomeric unit with a conjugated ethynylbenzene linker extends the light absorbing capabilities of the BODIPY precursor and red shifts the main absorption band of the

compound into the visible region of the solar spectrum. This work is the first report wherein BODIPY copolymers were studied for both hydrogen evolution and antimicrobial applications. This thesis highlights the success of these copolymers for visible light-driven applications. To the best of our knowledge, this is the first report of detailed time-resolved transient absorption and time-resolved infrared spectroscopy that spans the early picosecond to the microsecond timescale for BODIPY based copolymers. A long-lived triplet species is observed for all BODIPY copolymers synthesised in this work. Chapter 4 confirms that singlet fission plays a dominant role in the excited state dynamics of these copolymers and explains the mechanism underpinning the conversion of the singlet excited state to the triplet species. Although singlet fission has been reported in copolymeric systems previously, the repertoire of copolymers known to successfully undergo SF is limited. BODIPY copolymers are highly absorbing in the visible region of the solar spectrum and strong experimental and theoretical evidence for the occurrence of singlet fission makes these systems an attractive candidate for organic-based light driven photocatalytic processes.

Chapter 5 reports the synthesis of two novel ruthenium complexes, one of which contains a carbazole unit through a single bond extension of the dipyridophenazine ligand, attached to a thiazole unit. Improving the visible light absorptivity of inorganic complexes is imperative towards advancing their efficiency for solar-driven hydrogen evolution. This chapter demonstrates how this can be achieved through attachment of electron donating moieties, in this case, a phenyl-carbazole. This work studies the excited state dynamics of two novel ruthenium complexes in great detail to gain an understanding of the $^1\text{MLCT}$, $^3\text{ILCT}$ and $^3\text{MLCT}$ states populated, which is an essential learning to optimise the photoactivity of these complexes. Chapter 6 studies the *light-switch effect* using both DFT and TD-DFT calculations to explain the role of water in the excited state dynamics of $[\text{Ru}(\text{phen})_2\text{dppz}]^{2+}$ and proposes an energy level schematic to explain how water directs the photophysics of the system to be more dppz-based, opposed to phen-based triplet excited states. The ground-state UV-visible absorption spectrum of $[\text{Ru}(\text{phen})_2\text{dppz}]^{2+}$ is measured in acetonitrile solution with different concentrations of water present to study the effect of hydrogen bonding of water with the phenazine unit on the dppz ligand.

1.12 Bibliography

- (1) Kim, J. H.; Hansora, D.; Sharma, P.; Jang, J. W.; Lee, J. S. *Chem. Soc. Rev.* **2019**, *48* (7), 1908–1971.
- (2) Wang, Y.; Suzuki, H.; Xie, J.; Tomita, O.; Martin, D. J.; Higashi, M.; Kong, D.; Abe, R.; Tang, J. *Chem. Rev.* **2018**, *118* (10), 5201–5241.
- (3) Energy in Ireland, report, can be found under <https://www.seai.ie/publications/Energy-i.-I.-2019-.pd>. **2019**, accessed December 2020.
- (4) Ireland’s Provisional Greenhouse Gas Emissions 1990-2018, report can be found under; https://www.epa.ie/pubs/reports/air/airemissions/ghgprovemissions2018/Report_GHG%201990-2018%20Provisional%20Inventory%20October%202019.pdf. **2019**, No. accessed December 2020.
- (5) NASA scientific visualisation studio, can be found under <https://svs.gsfc.nasa.gov>. 2018, p accessed December 2020.
- (6) IPCC Climate change 2014, synthesis report, can be found under https://www.ipcc.ch/site/assets/uploads/2018/02/AR5_SYR_FINAL_SPM.pdf. **2014**, accessed December 2020.
- (7) Zhang, F.; Zhao, P.; Niu, M.; Maddy, J. *Int. J. Hydrogen Energy* **2016**, *41* (33), 14535–14552.
- (8) Renewable energy in Ireland 2019, can be found under <https://www.seai.ie/resources/publications/Renewabl.-E.-I.-2019.pdf>. **2019**, accessed December 2020.
- (9) Directive 2009/28/EC of the European Parliament and of the Council on the promotion of the use of energy from renewable sources, can be found under <https://eur-lex.europa.eu/legal-content/EN/TXT/PDF/?uri=CELEX:32009L0028&from=E>. **2009**, *1* (accessed

- Decemeber 2020), 32–38.
- (10) Government of Ireland, Project Ireland 2040: National Development Plan 2018-2027, can be found under . <https://www.per.gov.ie/en/national-development-pla.-2018-2027>. **2018**, accessed December 2020.
 - (11) UNFCCC. Conference of the Parties (COP). *Adopt. Paris Agreement. Propos. by Pres.* **2015**, 21932 (December), 32.
 - (12) Dalle, K. E.; Warnan, J.; Leung, J. J.; Reuillard, B.; Karmel, I. S.; Reisner, E. *Chem. Rev.* **2019**, *119* (4), 2752–2875.
 - (13) Ahmad, H.; Kamarudin, S. K.; Minggu, L. J.; Kassim, M. *Renew. Sustain. Energy Rev.* **2015**, *43*, 599–610.
 - (14) Mazloomi, K.; Gomes, C. *Renew. Sustain. Energy Rev.* **2012**, *16* (5), 3024–3033.
 - (15) Crabtree, G. W. .; Dresselhaus, M. S. .; Buchanan, M. V. . *Phys. Today* **2004**, *57* (12), 39.
 - (16) Soloveichik, G. L. *Proc. IEEE* **2014**, *102* (6), 964–975.
 - (17) Niaz, S.; Manzoor, T.; Pandith, A. H. *Renew. Sustain. Energy Rev.* **2015**, *50*, 457–469.
 - (18) Nazir, H.; Muthuswamy, N.; Louis, C.; Jose, S.; Prakash, J.; Buan, M. E. M.; Flox, C.; Chavan, S.; Shi, X.; Kauranen, P.; Kallio, T.; Maia, G.; Tammeveski, K.; Lymperopoulos, N.; Carcadea, E.; Veziroglu, E.; Iranzo, A.; M. Kannan, A. *Int. J. Hydrogen Energy* **2020**, *45* (53), 28217–28239.
 - (19) Fajrina, N.; Tahir, M. *Int. J. Hydrogen Energy* **2019**, *44* (2), 540–577.
 - (20) Barber, J. *Chem. Soc. Rev.* **2009**, *38* (1), 185–196.
 - (21) Berardi, S.; Drouet, S.; Franca, L.; Gimbert-surin, C.; Guttentag, M.; Richmond, C.; Stoll, T.; Llobet, A. *Chem. Soc. Rev.* **2014**, *43*, 7501–7519.
 - (22) Qi, J.; Zhang, W.; Cao, R. *Adv. Energy Mater.* **2018**, *8* (5), 1–16.

- (23) Balzani, V.; Credi, A.; Venturi, M. *Photochemical conversion of solar energy*; 2008; Vol. 1.
- (24) Teets, T. S.; Nocera, D. G. *Chem. Commun.* **2011**, 47 (33), 9268.
- (25) Abe, R. *J. Photochem. Photobiol. C Photochem. Rev.* **2010**, 11 (4), 179–209.
- (26) Kudo, A.; Miseki, Y. *Chem. Soc. Rev.* **2009**, 38 (1), 253–278.
- (27) Kowacs, T.; Pan, Q.; Lang, P.; Reilly, L. O.; Rau, S.; Browne, W. R.; Pryce, M. T.; Vos, J. G. *Faraday Discuss.* **2015**, 185, 143–170.
- (28) Yuan, Y.-J.; Yu, Z.-T.; Chen, D.-Q.; Zou, Z.-G. *Chem. Soc. Rev.* **2017**, 46 (3), 603–631.
- (29) Wang, Y.; Vogel, A.; Sachs, M.; Sprick, R. S.; Wilbraham, L.; Moniz, S. J. A.; Godin, R.; Zwiijnenburg, M. A.; Durrant, J. R.; Cooper, A. I.; Tang, J. *Nat. Energy* **2019**, 4 (9), 746–760.
- (30) Cecconi, B.; Manfredi, N.; Montini, T.; Fornasiero, P.; Abbotto, A. *European J. Org. Chem.* **2016**, 2016 (31), 5194–5215.
- (31) Warnan, J.; Reisner, E. *Angew. Chemie - Int. Ed.* **2020**, 59, 2–13.
- (32) Rahman, M. Z.; Kibria, M. G.; Mullins, C. B. *Chem. Soc. Rev.* **2020**, 49 (6), 1887–1931.
- (33) O'Reilly, L.; Pan, Q.; Das, N.; Wenderich, K.; Kortarik, J. P.; Vos, J. G.; Pryce, M. T.; Huijser, A. *ChemPhysChem* **2018**, 19 (22), 3084–3091.
- (34) Yang, H.; Zhao, M.; Zhang, J.; Ma, J.; Wu, P.; Liu, W.; Wen, L. *J. Mater. Chem. A* **2019**, 7 (36), 20742–20749.
- (35) Feng, X.; Pi, Y.; Song, Y.; Brzezinski, C.; Xu, Z.; Li, Z.; Lin, W. *J. Am. Chem. Soc.* **2020**, 142 (2), 690–695.
- (36) Kalyanasundaram, K.; Kiwi, J.; Grätzel, M. *Helv. Chim. Acta* **1978**, 61 (7), 2727–2730.

- (37) Staehle, R.; Losse, S.; Filipovic, M. R.; Ivanović-Burmazović, I.; Vos, J. G.; Rau, S. *Chempluschem* **2014**, *79* (11), 1614–1621.
- (38) Wang, P.; Guo, S.; Wang, H. J.; Chen, K. K.; Zhang, N.; Zhang, Z. M.; Lu, T. *B. Nat. Commun.* **2019**, *10* (1), 1–12.
- (39) McCormick, T. M.; Calitree, B. D.; Orchard, A.; Kraut, N. D.; Bright, F. V.; Detty, M. R.; Eisenberg, R. *J. Am. Chem. Soc.* **2010**, *132* (44), 15480–15483.
- (40) Lazarides, T.; Delor, M.; Sazanovich, I. V.; McCormick, T. M.; Georgakaki, I.; Charalambidis, G.; Weinstein, J. A.; Coutsolelos, A. G. *Chem. Commun.* **2014**, *50* (5), 521–523.
- (41) Bartelmess, J.; Francis, A. J.; El Roz, K. A.; Castellano, F. N.; Weare, W. W.; Sommer, R. D. *Inorg. Chem.* **2014**, *53* (9), 4527–4534.
- (42) Kowacs, T.; O'Reilly, L.; Pan, Q.; Huijser, A.; Lang, P.; Rau, S.; Browne, W. R.; Pryce, M. T.; Vos, J. G. *Inorg. Chem.* **2016**, *55* (6), 2685–2690.
- (43) Shon, J. H.; Teets, T. S. *ACS Energy Lett.* **2019**, *4* (2), 558–566.
- (44) Fujishima, A., & Honda, K. *Nature* **1972**, *238*, 37–38.
- (45) Singh, R.; Dutta, S. *Fuel* **2018**, *220* (February), 607–620.
- (46) Reginato, G.; Zani, L.; Calamante, M.; Mordini, A.; Dessì, A. *Eur. J. Inorg. Chem.* **2020**, *2020* (11–12), 899–917.
- (47) Takata, T.; Domen, K. *ACS Energy Lett.* **2019**, *4* (2), 542–549.
- (48) Yang, J.; Wang, D.; Han, H.; Li, C. *Acc. Chem. Res.* **2013**, *46* (8), 1900–1909.
- (49) Warnan, J.; Willkomm, J.; Farré, Y.; Pellegrin, Y.; Boujtita, M.; Odobel, F.; Reisner, E. *Chem. Sci.* **2019**, *10* (9), 2758–2766.
- (50) Kärkäs, M. D.; Verho, O.; Johnston, E. V.; Åkermark, B. *Chem. Rev.* **2014**, *114* (24), 11863–12001.
- (51) Arias-Rotondo, D. M.; McCusker, J. K. *Chem. Soc. Rev.* **2016**, *45* (21), 5803–

5820.

- (52) Tayebjee, M. J. Y.; McCamey, D. R.; Schmidt, T. W. *J. Phys. Chem. Lett.* **2015**, *6* (12), 2367–2378.
- (53) Bhattacharyya, K.; Datta, A. *J. Phys. Chem. C* **2019**, acs.jpcc.8b11039.
- (54) Gish, M. K.; Pace, N. A.; Rumbles, G.; Johnson, J. C. *J. Phys. Chem. C* **2019**, *123* (7), 3923–3934.
- (55) Congreve, D.; Lee, J.; Thompson, N.; Hontz, E.; Yost, S.; Reusswig, P.; Bahlke, M.; Reineke, S.; Voorhis Van, T.; Baldo, M. A. *Science* (80-.). **2013**, *340* (1), 334–337.
- (56) Smith, M. B.; Michl, J. *Chem. Rev.* **2010**, *110* (11), 6891–6936.
- (57) Montero, R.; Martínez-Martínez, V.; Longarte, A.; Epelde-Elezcano, N.; Palao, E.; Lamas, I.; Manzano, H.; Agarrabeitia, A. R.; López Arbeloa, I.; Ortiz, M. J.; Garcia-Moreno, I. *J. Phys. Chem. Lett.* **2018**, *9* (3), 641–646.
- (58) Epelde-Elezcano, N.; Palao, E.; Manzano, H.; Prieto-Castañeda, A.; Agarrabeitia, A. R.; Tabero, A.; Villanueva, A.; de la Moya, S.; López-Arbeloa, Í.; Martínez-Martínez, V.; Ortiz, M. J. *Chem. – A Eur. J.* **2017**, *23* (20), 4837–4848.
- (59) Hu, J.; Xu, K.; Shen, L.; Wu, Q.; He, G.; Wang, J. Y.; Pei, J.; Xia, J.; Sfeir, M. Y. *Nat. Commun.* **2018**, *9* (2999), 1–9.
- (60) Fumanal, M.; Corminboeuf, C. *J. Phys. Chem. Lett.* **2020**, *11*, 9788–9797.
- (61) Musser, A. J.; Al-Hashimi, M.; Maiuri, M.; Brida, D.; Heeney, M.; Cerullo, G.; Friend, R. H.; Clark, J. *J. Am. Chem. Soc.* **2013**, *135* (34), 12747–12754.
- (62) Busby, E.; Xia, J.; Wu, Q.; Low, J. Z.; Song, R.; Miller, J. R.; Zhu, X. Y.; Campos, L. M.; Sfeir, M. Y. *Nat. Mater.* **2015**, *14* (4), 426–433.
- (63) Blaskovits, J. T.; Fumanal, M.; Vela, S.; Corminboeuf, C. *Chem. Mater.* **2020**, *32* (15), 6515–6524.

- (64) Phys, J. C.; He, G.; Busby, E.; Sfeir, M. Y.; Appavoo, K.; Wu, Q.; Campos, L. *M. J. Chem. Phys.* **2020**, *153* (December), 244902–244909.
- (65) Wahl, M. *PicoQuant* **2007**, *14* (11), 1–14.
- (66) Xu, J. Y.; Tong, X.; Yu, P.; Wenya, G. E.; McGrath, T.; Fong, M. J.; Wu, J.; Wang, Z. M. *Adv. Sci.* **2018**, *5* (12).
- (67) Berera, R.; van Grondelle, R.; Kennis, J. T. M. *Photosynth. Res.* **2009**, *101* (2–3), 105–118.
- (68) Greetham, G. M.; Burgos, P.; Qian, C.; Clark, I. P.; Codd, P. S.; Farrow, R. C.; George, M. W.; Kogimtzis, M.; Matousek, P.; Parker, A. W.; Pollard, M. R.; Robinson, D. A.; Zhi-Jun, X.; Towrie, M. *Appl. Spectrosc.* **2010**, *64* (12), 1311–1319.
- (69) Munson, K. T.; Kennehan, E. R.; Asbury, J. B. *J. Mater. Chem. C* **2019**, *7* (20), 5889–5909.
- (70) Ford, P. C.; Bridgewater, J. S.; Lee, B. *Photochem. Photobiol.* **1997**, *65* (1), 57–64.
- (71) Butler, J. M.; George, M. W.; Schoonover, J. R.; Dattelbaum, D. M.; Meyer, T. *J. Coord. Chem. Rev.* **2007**, *251* (3–4), 492–514.
- (72) Clark, I. P.; George, M. W.; Greetham, G. M.; Harvey, E. C.; Long, C.; Manton, J. C.; Pryce, M. T. *J. Phys. Chem. A* **2010**, *114* (43), 11425–11431.
- (73) Vyas, V. S.; Lau, V. W. H.; Lotsch, B. V. *Chem. Mater.* **2016**, *28* (15), 5191–5204.
- (74) Wang, L.; Zhang, Y.; Chen, L.; Xu, H.; Xiong, Y. *Adv. Mater.* **2018**, *30* (48), 1–12.
- (75) Xu, Y.; Jin, S.; Xu, H.; Nagai, A.; Jiang, D. *Chem. Soc. Rev.* **2013**, *42* (20), 8012–8031.
- (76) Sprick, R. S.; Jiang, J. X.; Bonillo, B.; Ren, S.; Ratvijitvech, T.; Guiglion, P.;

- Zwijnenburg, M. A.; Adams, D. J.; Cooper, A. I. *J. Am. Chem. Soc.* **2015**, *137* (9), 3265–3270.
- (77) Zhang, G.; Lan, Z.-A.; Wang, X. *Angew. Chemie Int. Ed.* **2016**, *55* (51), 15712–15727.
- (78) Lan, Z. A.; Zhang, G.; Chen, X.; Zhang, Y.; Zhang, K. A. I.; Wang, X. *Angew. Chemie - Int. Ed.* **2019**, *58* (30), 10236–10240.
- (79) Happ, B.; Kübel, J.; Pfeffer, M. G.; Winter, A.; Hager, M. D.; Dietzek, B.; Rau, S.; Schubert, U. S. *Macromol. Rapid Commun.* **2015**, *36* (7), 671–677.
- (80) Yong, W. W.; Lu, H.; Li, H.; Wang, S.; Zhang, M. T. *ACS Appl. Mater. Interfaces* **2018**, *10* (13), 10828–10834.
- (81) Wang, L.; Fernández-Terán, R.; Zhang, L.; Fernandes, D. L. A.; Tian, L.; Chen, H.; Tian, H. *Angew. Chemie - Int. Ed.* **2016**, *55* (40), 12306–12310.
- (82) Ong, W. J.; Tan, L. L.; Ng, Y. H.; Yong, S. T.; Chai, S. P. *Chem. Rev.* **2016**, *116* (12), 7159–7329.
- (83) Kumar, S.; Karthikeyan, S.; Lee, A. F. *Catalysts* **2018**, *8* (2).
- (84) Yi, J.; El-Alami, W.; Song, Y.; Li, H.; Ajayan, P. M.; Xu, H. *Chem. Eng. J.* **2020**, *382*, 122812.
- (85) Wang, X.; Maeda, K.; Thomas, A.; Takanabe, K.; Xin, G.; Carlsson, J. M.; Domen, K.; Antonietti, M. *Nat. Mater.* **2009**, *8* (1), 76–80.
- (86) Wang, Y.; Wang, X.; Antonietti, M. *Angew. Chemie - Int. Ed.* **2012**, *51* (1), 68–89.
- (87) Cao, S.; Yu, J. *J. Phys. Chem. Lett.* **2014**, *5* (12), 2101–2107.
- (88) Min, S.; Lu, G. *J. Phys. Chem. C* **2012**, *116* (37), 19644–19652.
- (89) Zhang, G.; Lan, Z. A.; Wang, X. *Chem. Sci.* **2017**, *8* (8), 5261–5274.
- (90) Yanagida, S.; Kabumoto, A.; Mizumoto, K.; Pac, C.; Yoshino, K. *J. Chem. Soc.*

Chem. Commun. **1985**, No. 8, 474–475.

- (91) Sprick, R. S.; Bonillo, B.; Clowes, R.; Guiglion, P.; Brownbill, N. J.; Slater, B. J.; Blanc, F.; Zwijnenburg, M. A.; Adams, D. J.; Cooper, A. I. *Angew. Chemie* **2016**, *128* (5), 1824–1828.
- (92) Schwarz, C.; Bässler, H.; Bauer, I.; Koenen, J. M.; Preis, E.; Scherf, U.; Köhler, A. *Adv. Mater.* **2012**, *24* (7), 922–925.
- (93) Ting, L. Y.; Jayakumar, J.; Chang, C. L.; Lin, W. C.; Elsayed, M. H.; Chou, H. *H. J. Mater. Chem. A* **2019**, *7* (40), 22924–22929.
- (94) Xu, C.; Zhang, W.; Tang, J.; Pan, C.; Yu, G. *Front. Chem.* **2018**, *6* (December), 1–12.
- (95) Yang, C.; Ma, B. C.; Zhang, L.; Lin, S.; Ghasimi, S.; Landfester, K.; Zhang, K. A. I.; Wang, X. *Angew. Chemie - Int. Ed.* **2016**, *55* (32), 9202–9206.
- (96) Xu, Y.; Mao, N.; Zhang, C.; Wang, X.; Zeng, J.; Chen, Y.; Wang, F.; Jiang, J. *X. Appl. Catal. B Environ.* **2018**, *228*, 1–9.
- (97) Li, L.; Lo, W. Y.; Cai, Z.; Zhang, N.; Yu, L. *Macromolecules* **2016**, *49* (18), 6903–6909.
- (98) Li, L.; Cai, Z.; Wu, Q.; Lo, W. Y.; Zhang, N.; Chen, L. X.; Yu, L. *J. Am. Chem. Soc.* **2016**, *138* (24), 7681–7686.
- (99) Liu, Y.; Liao, Z.; Ma, X.; Xiang, Z. *ACS Appl. Mater. Interfaces* **2018**, *10* (36), 30698–30705.
- (100) Zhang, X. H.; Wang, X. P.; Xiao, J.; Wang, S. Y.; Huang, D. K.; Ding, X.; Xiang, Y. G.; Chen, H. *J. Catal.* **2017**, *350*, 64–71.
- (101) Xiang, Y.; Wang, X.; Rao, L.; Wang, P.; Huang, D.; Ding, X.; Zhang, X.; Wang, S.; Chen, H.; Zhu, Y. *ACS Energy Lett.* **2018**, *3* (10), 2544–2549.
- (102) Ding, S. Y.; Wang, W. *Chem. Soc. Rev.* **2013**, *42* (2), 548–568.
- (103) Stegbauer, L.; Schwinghammer, K.; Lotsch, B. V. *Chem. Sci.* **2014**, *5* (7),

2789–2793.

- (104) Pachfule, P.; Acharjya, A.; Roeser, J.; Langenhahn, T.; Schwarze, M.; Schomäcker, R.; Thomas, A.; Schmidt, J. *J. Am. Chem. Soc.* **2018**, *140* (4), 1423–1427.
- (105) Banerjee, T.; Haase, F.; Savasci, G.; Gottschling, K.; Ochsenfeld, C.; Lotsch, B. V. *J. Am. Chem. Soc.* **2017**, *139* (45), 16228–16234.
- (106) Bi, J.; Fang, W.; Li, L.; Wang, J.; Liang, S.; He, Y.; Liu, M.; Wu, L. *Macromol. Rapid Commun.* **2015**, *36* (20), 1799–1805.
- (107) Meier, C. B.; Sprick, R. S.; Monti, A.; Guiglion, P.; Lee, J. S. M.; Zwijnenburg, M. A.; Cooper, A. I. *Polymer (Guildf)*. **2017**, *126*, 283–290.
- (108) Zhou, H.; Yang, L.; You, W. *Macromolecules* **2012**, *45* (2), 607–632.
- (109) Zhou, H.; Yang, L.; Stoneking, S.; You, W. *ACS Appl. Mater. Interfaces* **2010**, *2* (5), 1377–1383.
- (110) Zhao, Y.; Ma, W.; Xu, Y.; Zhang, C.; Wang, Q.; Yang, T.; Gao, X.; Wang, F.; Yan, C.; Jiang, J.-X. *Macromolecules* **2018**, *51*, 9502–9208.
- (111) Sprick, R. S.; Bai, Y.; Guilbert, A. A. Y.; Zbiri, M.; Aitchison, C. M.; Wilbraham, L.; Yan, Y.; Woods, D. J.; Zwijnenburg, M. A.; Cooper, A. I. *Chem. Mater.* **2019**, *31* (2), 305–313.
- (112) Sachs, M.; Sprick, R. S.; Pearce, D.; Hillman, S. A. J.; Monti, A.; Guilbert, A. A. Y.; Brownbill, N. J.; Dimitrov, S.; Shi, X.; Blanc, F.; Zwijnenburg, M. A.; Nelson, J.; Durrant, J. R.; Cooper, A. I. *Nat. Commun.* **2018**, 1–11.
- (113) Treibs, Alfred, Kreuzer, F.-H. *Justus Liebigs Ann Chem* **1968**, *718*, 208–223.
- (114) Banfi, S.; Nasini, G.; Zaza, S.; Caruso, E. *Tetrahedron* **2013**, *69* (24), 4845–4856.
- (115) Luo, G. G.; Lu, H.; Zhang, X. L.; Dai, J. C.; Wu, J. H.; Wu, J. J. *Phys. Chem. Chem. Phys.* **2015**, *17* (15), 9716–9729.

- (116) Loudet, A.; Burgess, K. *Chem. Rev.* **2007**, *107* (11), 4891–4932.
- (117) Wood, T. E.; Thompson, A. *Chem. Rev.* **2007**, *107* (5), 1831–1861.
- (118) Wang, X.; Song, Y.; Qu, J.; Luo, Y. *Organometallics* **2017**, *36* (5), 1042–1048.
- (119) Morisue, M.; Kawanishi, M.; Nakano, S. *J. Polym. Sci. Part A Polym. Chem.* **2019**, *57* (24), 2457–2465.
- (120) Noël Boens, Bram Verbelen, and W. D. *European J. Org. Chem.* **2015**, 6577–6595.
- (121) Dura, L.; Ahrens, J.; Pohl, M. M.; Höfler, S.; Bröring, M.; Beweries, T. *Chem. - A Eur. J.* **2015**, *21* (39), 13549–13552.
- (122) Sabatini, R. P.; McCormick, T. M.; Lazarides, T.; Wilson, K. C.; Eisenberg, R.; McCamant, D. W. *J. Phys. Chem. Lett.* **2011**, *2* (3), 223–227.
- (123) Xie, A.; Pan, Z. H.; Yu, M.; Luo, G. G.; Sun, D. *Chinese Chem. Lett.* **2019**, *30* (1), 225–228.
- (124) Manton, J. C.; Long, C.; Vos, J. G.; Pryce, M. T. *Phys. Chem. Chem. Phys.* **2014**, *16* (11), 5229–5236.
- (125) Summers, G. H.; Lefebvre, J. F.; Black, F. A.; Stephen Davies, E.; Gibson, E. A.; Pullerits, T.; Wood, C. J.; Zidek, K. *Phys. Chem. Chem. Phys.* **2016**, *18* (2), 1059–1070.
- (126) Suryani, O.; Higashino, Y.; Sato, H.; Kubo, Y. *ACS Appl. Energy Mater.* **2019**, *2* (1), 448–458.
- (127) Yang, H.; Wang, J.; Ma, J.; Yang, H.; Zhang, J.; Lv, K.; Wen, L.; Peng, T. *J. Mater. Chem. A* **2019**, *7* (17), 10439–10445.
- (128) Squeo, B. M.; Gregoriou, V. G.; Avgeropoulos, A.; Baysec, S.; Allard, S.; Scherf, U.; Chochos, C. L. *Prog. Polym. Sci.* **2017**, *71*, 26–52.
- (129) Lu, P.; Chung, K. Y.; Stafford, A.; Kiker, M.; Kafle, K.; Page, Z. A. *Polym. Chem.* **2021**, *12* (3), 327–348.

- (130) Zhu, Mei, Jiang, Li, Yuan, Mingjian, Liu, Xiaofeng, Ouyang, Cabin, Zheng, Haiuan, Yin, Ziaodong, Zuo, Zicheng, Liu, Huibiao, Li, Y. *J. Polym. Sci. Part A Polym. Chem.* **2008**, *46*, 7401–7410.
- (131) Donuru, V. R.; Vegesna, G. K.; Velayudham, S.; Green, S.; Liu, H. *Chem. Mater.* **2009**, *21* (10), 2130–2138.
- (132) Kim, B.; Ma, B.; Donuru, V. R.; Liu, H.; Fréchet, J. M. J. *Chem. Commun.* **2010**, *46* (23), 4148–4150.
- (133) Cakmak, Y.; Akkaya, E. U. *Org. Lett.* **2009**, *11* (1), 85–88.
- (134) Donuru, V. R.; Zhu, S.; Green, S.; Liu, H. *Polymer (Guildf)*. **2010**, *51* (23), 5359–5368.
- (135) Donuru, Venkat R. Vegesna, Giri. K, Velayudham, Ge Meng, Liu, H. *J. Polym. Sci. Part A Polym. Chem.* **2009**, *47*, 5354–5366.
- (136) Popere, B. C.; Pelle, A. M. Della; Thayumanavan, S. *Macromolecules* **2011**, *44* (12), 4767–4776.
- (137) Sen, C. P.; Shrestha, R. G.; Shrestha, L. K.; Ariga, K.; Valiyaveetil, S. *Chem. - A Eur. J.* **2015**, *21* (48), 17344–17354.
- (138) Bucher, L.; Aly, S. M.; Desbois, N.; Karsenti, P. L.; Gros, C. P.; Harvey, P. D. *J. Phys. Chem. C* **2017**, *121* (12), 6478–6490.
- (139) Rafique, S.; Abdullah, S. M.; Sulaiman, K.; Iwamoto, M. *Renew. Sustain. Energy Rev.* **2018**, *84* (December 2017), 43–53.
- (140) Bucher, L.; Desbois, N.; Harvey, P. D.; Gros, C. P.; Misra, R.; Sharma, G. D. *ACS Appl. Energy Mater.* **2018**, *1* (7), 3359–3368.
- (141) Bandyopadhyay, S.; Anil, A. G.; James, A.; Patra, A. *ACS Appl. Mater. Interfaces* **2016**, *8* (41), 27669–27678.
- (142) Liras, M.; Iglesias, M.; Sánchez, F. *Macromolecules* **2016**, *49* (5), 1666–1673.
- (143) Li, G.; Yin, J.-F.; Guo, H.; Wang, Z.; Zhang, Y.; Li, X.; Wang, J.; Yin, Z.;

- Kuang, G.-C. *ACS Omega* **2018**, *3* (7), 7727–7735.
- (144) Piatkowski, P.; Moreno, M.; Liras, M.; Sánchez, F.; Douhal, A. *J. Mater. Chem. C* **2019**, *7* (26), 7872–7884.
- (145) Filatov, M. A. *Org. Biomol. Chem.* **2020**, *18* (1), 10–27.
- (146) Zhao, J.; Xu, K.; Yang, W.; Wang, Z.; Zhong, F. *Chem. Soc. Rev.* **2015**, *44* (24), 8904–8939.
- (147) Chen, K.; Dong, Y.; Zhao, X.; Imran, M.; Tang, G.; Zhao, J.; Liu, Q. *Front. Chem.* **2019**, *7* (December), 1–14.
- (148) Meng, G.; Velayudham, S.; Smith, A.; Luck, R.; Liu, H. *Macromolecules* **2009**, *42* (6), 1995–2001.
- (149) Alemdaroglu, F. E.; Alexander, S. C.; Ji, D.; Prusty, D. K.; Borsch, M.; Herrmann, A. *Macromolecules* **2009**, *42* (17), 6529–6536.
- (150) Cihaner, A.; Algi, F. *React. Funct. Polym.* **2009**, *69* (1), 62–67.
- (151) Thivierge, C.; Loudet, A.; Burgess, K. *Macromolecules* **2011**, *44* (10), 4012–4015.
- (152) Zhu, S.; Dorh, N.; Zhang, J.; Vegesna, G.; Li, H.; Luo, F. T.; Tiwari, A.; Liu, H. *J. Mater. Chem.* **2012**, *22* (6), 2781–2790.
- (153) Economopoulos, S. P.; Chochos, C. L.; Ioannidou, H. A.; Neophytou, M.; Charilaou, C.; Zissimou, G. A.; Frost, J. M.; Sachetan, T.; Shahid, M.; Nelson, J.; Heeney, M.; Bradley, D. D. C.; Itskos, G.; Koutentis, P. A.; Choulis, S. A. *RSC Adv.* **2013**, *3* (26), 10221–10229.
- (154) Zhou, Y.; Zhou, Z.; Li, Y.; Yang, W. *Catal. Commun.* **2015**, *64*, 96–100.
- (155) Singh, S.; Chithiravel, S.; Krishnamoorthy, K. *J. Phys. Chem. C* **2016**, *120* (46), 26199–26205.
- (156) Tarafdar, G.; Pandey, U. K.; Sengupta, S.; Ramamurthy, P. C. *Sol. Energy* **2019**, *186* (March), 215–224.

- (157) Lin, X.; Tang, D.; He, T.; Xu, Z.; Qiu, H.; Zhang, Q.; Yin, S. *Spectrochim. Acta - Part A Mol. Biomol. Spectrosc.* **2019**, *217*, 164–169.
- (158) Zhang, Z.; Yuan, D.; Liu, X.; Kim, M. J.; Nashchadin, A.; Sharapov, V.; Yu, L. *Macromolecules* **2020**, *53* (6), 2014–2020.
- (159) Méallet-Renault, R.; Grazon, C.; Clavier, G.; Rieger, J.; Charleux, B. *Macromolecules* **2013**, *46* (13), 5167–5176.
- (160) Yoshii, R.; Nagai, A.; Chujo, Y. *J. Polym. Sci. Part A Polym. Chem.* **2010**, *48* (23), 5348–5356.
- (161) Yoshii, R.; Yamane, H.; Nagai, A.; Tanaka, K.; Taka, H.; Kita, H.; Chujo, Y. *Macromolecules* **2014**, *47* (7), 2316–2323.
- (162) Nagai, A.; Chujo, Y. *Macromolecules* **2010**, *43* (1), 193–200.
- (163) Nagai, A.; Miyake, J.; Kokado, K.; Nagata, Y.; Chujo, Y. *J. Am. Chem. Soc.* **2008**, *130* (46), 15276–15278.
- (164) Yamane, H.; Ito, S.; Tanaka, K.; Chujo, Y. *Polym. Chem.* **2016**, *7* (16), 2799–2807.
- (165) Shimizu, K.; Kitagawa, D.; Kobatake, S. *Dye. Pigment.* **2019**, *161* (September 2018), 341–346.
- (166) Zhang, T.; Ma, X.; Tian, H. *Chem. Sci.* **2020**, *11* (2), 482–487.
- (167) Thomson, C. G.; Jones, C. M. S.; Rosair, G.; Ellis, D.; Marques-Hueso, J.; Lee, A. L.; Vilela, F. *J. Flow Chem.* **2020**, 327–345.
- (168) DeRosa, M. C.; Crutchley, R. J. *Coord. Chem. Rev.* **2002**, *233–234*, 351–371.
- (169) Cakmak, Y.; Kolemen, S.; Duman, S.; Dede, Y.; Dolen, Y.; Kilic, B.; Kostereli, Z.; Yildirim, L. T.; Dogan, A. L.; Guc, D.; Akkaya, E. U. *Angew. Chemie - Int. Ed.* **2011**, *50* (50), 11937–11941.
- (170) Filatov, M. A.; Karuthedath, S.; Polestshuk, P. M.; Callaghan, S.; Flanagan, K. J.; Wiesner, T.; Laquai, F.; Senge, M. O. *ChemPhotoChem* **2018**, 606–615.

- (171) Caruso, E.; Banfi, S.; Barbieri, P.; Leva, B.; Orlandi, V. T. *J. Photochem. Photobiol. B Biol.* **2012**, *114*, 44–51.
- (172) Kamkaew, A.; Lim, S. H.; Lee, H. B.; Kiew, L. V.; Chung, L. Y.; Burgess, K. *Chem. Soc. Rev.* **2013**, *42* (1), 77–88.
- (173) Turksoy, A.; Yildiz, D.; Akkaya, E. U. *Coord. Chem. Rev.* **2019**, *379*, 47–64.
- (174) Pöldme, N.; O'Reilly, L.; Fletcher, I.; Portoles, J.; Sazanovich, I. V.; Towrie, M.; Long, C.; Vos, J. G.; Pryce, M. T.; Gibson, E. A. *Chem. Sci.* **2019**, *10* (1), 99–112.

Chapter 2

A time-resolved spectroscopic investigation of a novel BODIPY copolymer and its potential use as a photosensitiser for hydrogen evolution

This work was published in *Frontiers in Chemistry*, 2020, **8**, 1-14.

Aoibhín A. Cullen, Katharina Heintz, Laura O'Reilly, Conor Long, Andreas Heise, Robert Murphy, Joshua Karlsson, Elizabeth Gibson, Gregory M. Greetham, Michael Towrie and Mary T. Pryce*.

Within this work, I contributed towards the overall synthesis of the copolymer and the full characterisation. Dr. Katharina Heintz and Dr. Laura O'Reilly carried out the ns- μ s TA spectroscopy of the polymer. I specifically contributed towards the following sections: experimental design, steady-state photophysical measurements, photoluminescent studies, time-resolved spectroscopies, data interpretation and execution of photocatalytic experiments. I contributed towards writing the manuscript. Supporting information associated with this chapter can be found in Appendix A.

2.1 Abstract

A novel 4,4-difluoro-4-bora-3a,4a-diaza-s-indacene (BODIPY) copolymer with diethynylbenzene has been synthesised, and its ability to act as a photosensitiser for the photocatalytic generation of hydrogen was investigated by time-resolved spectroscopic techniques spanning the ps- to ns-timescales. Both transient absorption and time-resolved infrared spectroscopy were used to probe the excited state dynamics of this photosensitising unit in a variety of solvents. These studies indicated how environmental factors can influence the photophysics of the BODIPY polymer. A homogeneous photocatalytic hydrogen evolution system has been developed using the BODIPY copolymer and cobaloxime which provides hydrogen evolution rates of $319 \mu\text{mol h}^{-1} \text{g}^{-1}$ after 24 hours of visible irradiation.

2.2 Introduction

Increasing levels of CO₂ in the atmosphere has resulted in an increase in the rate of global warming, necessitating a move away from burning fossil fuels. Hydrogen has been proposed as a clean energy vector, which has led to the development of photocatalysts for hydrogen generation.^{1,2} Many inorganic photosensitisers, based on ruthenium, iridium, or rhenium, have been used for hydrogen generating systems in both inter- and intra-molecular assemblies. Knowledge of the photophysics of these systems is essential to “fine tune” the photocatalytic systems to increase their efficiencies.^{3–8} However, these systems have many drawbacks including high cost and inefficient use of the visible light spectrum. Organic photosensitisers for hydrogen evolution are less well developed, despite a number of welcome attributes, in particular, low cost.^{9–13}

Conjugated polymers offer many advantages over traditional inorganic-based systems for the production of hydrogen. They can facilitate energy transfer along the polymer backbone following photoexcitation, directing it to catalytically active sites for solar-driven hydrogen evolution.^{14–20} For instance, Zhang et al. reported the use of poly(fluorene-co-phenylene), as a photosensitiser (PS) for hydrogen generation. When used in conjunction with a Ni catalyst and EDTA as a sacrificial agent, efficiencies of up to 429 mmol g⁻¹ h⁻¹ were achieved.²¹ Graphitic carbon nitride (g-C₃N₄) based polymers have also been investigated because of their thermal stability and their high hydrogen evolution rates (HER).^{22,23} However, post-modification of g-C₃N₄, such as surface functionalisation or surface assembly, is necessary to maximise hydrogen evolution.^{24,25} However, harsh reaction conditions are required to synthesise pristine g-C₃N₄, which limits its application as a photocatalyst.²³

Many diverse conjugated polymers can be prepared under mild conditions using metal-catalysed cross-coupling reactions. To date, a range of conjugated polymers including linear polymers, conjugated microporous polymers (CMPs)^{26,27} covalent organic frameworks (COFs)^{28–30} and covalent triazine frameworks (CTFs) have been reported.^{31–33} While there are many limitations with polymeric photocatalysts, such as precise control of molecular weight distribution, there are also many advantages,

including the ability to establish structure-activity relationships by incorporating different molecular building blocks.³⁴ The first report of tunable organic polymers for hydrogen evolution was presented by Cooper et al. who using pyrene-based conjugated polymers with various monomeric compositions and optical gaps ranging from 1.94 – 2.95 eV.³⁵ The optical gap of the polymer is a key determinant of their efficiency as photocatalysts for hydrogen evolution. For instance, adding various comonomers in the preparation of poly(*p*-phenylene) enhanced hydrogen evolution. The highest activity was observed with incorporation of a dibenzo[*b,d*]thiophene sulfone moiety yielding an evolution rate of 92 $\mu\text{mol h}^{-1}$, compared to 2.0 $\mu\text{mol h}^{-1}$ for the homopolymer.²⁷ The superior performance of conjugated polymers and their successful use as photosensitisers has been explained by both their light-harvesting and electron transport capabilities.^{36,37} Certain barriers to improvement of photocatalytic activities or organic polymers remain however. A reduction in exciton binding energies for subsequent charge-carrier generation is required to improve the viability of polymer systems for hydrogen generation.

BODIPY dyes (**Figure 2.1** (a)) are one of the most extensively studied chromophores in recent years, due to ease of synthesis, thermal stability and solubility in a range of organic solvents.^{38–42} A variety of BODIPY architectures have been developed, involving substitution at the *meso* position, the pyrrole unit (β position), the boron atom, and post-functionalisation and polymerisation at the periphery of the chromophore (**Figure 2.1** (b)).^{43–47}

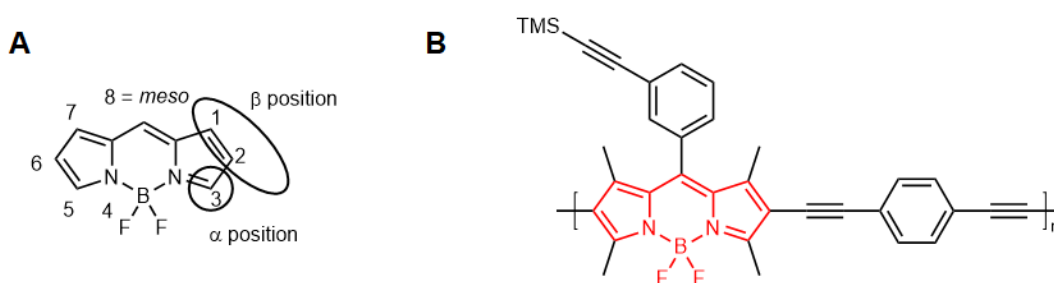


Figure 2.1. a) BODIPY core scaffold (4,4-difluoro-4-bora-3a,4a-diaza-s-indacene) showing IUPAC numbering system and b) 3-TMS polymer reported in this study (red bonds showing the BODIPY unit in the polymeric backbone).

Absorption and emission properties of BODIPYs may vary with substituents on the BODIPY core e.g. iodine or alkyl groups.⁴⁸ Synthetic modifications at the *meso* position have less effect on the photophysical properties of the BODIPY however.^{48,49} Copolymerisation of the BODIPY core at the 2 and 6 position can form linear copolymers.^{50–52} BODIPY polymers of this type have applications in areas such as optoelectronics, organic field transistors, batteries, photovoltaics and cellular imaging,⁵³ however their use in hydrogen evolution reactions (HER) is the focus of this manuscript. BODIPY monomers and iodinated BODIPY monomers have been used in homogeneous photocatalytic hydrogen evolution, including both intermolecular^{54–57} and intramolecular systems.^{58–61} Some heterogeneous systems incorporating BODIPY chromophore onto TiO₂ surfaces, have been shown to lead to H₂ evolution.^{62,63} BODIPY dyes have been immobilised onto photoanodes including NiO.^{13,64} Limitations in the systems described to date include the narrow absorption profiles of BODIPY chromophores, instability upon irradiation, fast rate of charge recombination and insufficient charge-separated state lifetimes.

Based on the features of the best performing chromophores, we have designed a novel conjugated copolymer containing the BODIPY core unit in the polymer backbone (**Figure 2.1** (b)), which absorb strongly in in the region of the solar irradiance spectrum. Irradiation of this polymer produces a long-lived triplet excited state, which in the presence a cobaloxime molecular catalyst acts as an effective hydrogen evolution catalyst. We also report the first time-resolved study of BODIPY based copolymers using transient absorption and time-resolved infrared spectroscopy to investigate the early-time photodynamics in a range of solvents for comparison with the parent BODIPY monomer.

2.3 Materials and Methods

All solvents were supplied by Aldrich Chemicals Co.[®] and anhydrous solvents containing sure/seal[®] were used under the flow of nitrogen. [3-(trimethylsilyl)ethynylbenzaldehyde] was purchased from Sigma-Aldrich and used as received. Reagents were obtained commercially from Aldrich Chemicals Co.[®], ABCR[®], Honeywell Fluka[®], Fluorochem Ltd.[®] and were used without any further purification.

Physical Measurements. ¹H and ¹³C NMR spectra were recorded on either a Bruker 400 MHz or 600 MHz spectrometer and were referenced to the deuterated solvent peak as an internal reference. Mass spectra were measured on a waters Q-TOF 6200 series. All UV spectra were recorded on the Agilent 8453 UV-vis spectrophotometer equipped with Agilent ChemStation software. FTIR measurements were carried out on Perkin-Elmer 2000 FTIR spectrophotometer in a liquid solution cell using spectrophotometric grade dichloromethane. All excitation spectra, emission spectra, emission maps and Time-correlated single photon counting (TCSPC) lifetimes were carried out using FLS1000 Photoluminescence Spectrometer (Edinburgh instruments), equipped with a Xe Arc lamp for steady-state measurements and a visible PMT-900 detector. All data analysis carried out using Fluoracle[®] software. All samples were measured at room temperature and were purged with N₂ prior analysis. For TCSPC, a 510 nm variable pulse length diode laser (VPL-510) was utilised to excite the ground state sample. The accuracy of the fit of the decays was judged by chi-squared (χ^2) and sum of residuals was always $\chi^2 < 1.1$. The fluorescence decay time (τ) was obtained from the slope of the decay curve. Accumulation of the steady-state spectra was obtained using 1 second dwell time and x 2 repeats per spectrum. All samples were measured in a 1 cm x 1 cm quartz cuvette and samples were < 0.2 at 510 nm to ensure an optically dilute solution to avoid inner-filter effects. Size exclusion chromatography (SEC) was used to determine the dispersities (D_M) and molecular weights of polymers. SEC was conducted in 1,1,1,3,3,3-Hexafluoro-2-propanol (HFIP) using an PSS SEcURITY SEC system equipped with a PFG 7 μ m 8 x 50 mm pre-column, a PSS 100 Å, 7 μ m 8 x 300 mm and a PSS 1000 Å, 7 μ m 8 x 300 mm column in series and a differential refractive index (RI) detector at a flow rate of 1.0

mL min⁻¹. The systems were calibrated against Agilent Easi-Vial linear poly(methyl methacrylate) (PMMA) standards and analysed by the software package PSS winGPC UniChrom.

Synthesis. 3-TMS BODIPY monomer and 3-TMS diiodo BODIPY monomer were synthesised as per previously reported methods and spectroscopic results are in accordance with previously reported^{65,66}. We report the first synthesis of 3-TMS BODIPY polymer using a previously reported method for Sonogashira polycondensation reaction⁵¹. The synthetic procedures used for the synthesis of all compounds are detailed in the Supporting Information.

Fluorescence quantum yield calculations. Steady-state fluorescence measurements were recorded using the LS50B luminescence spectrophotometer. Prior to obtaining the emission spectra, samples were diluted to ~ 0.2 abs units at λ_{exc} using the UV-vis spectrometer to inhibit inner-filter effect. The reference compound used was previously reported by Banfi et al. (3-pyridine H-BODIPY, $\Phi_{fl} = 0.62$ in CH₂Cl₂).⁴⁸ An excitation wavelength of 490 nm and a slit width of 2.5 nm was used for the samples and the standards. The compounds were measured in aerated solution at room temperature. Spectroscopic CH₂Cl₂ was the solvent used for all samples and standards. The emission quantum yield was the measured as per the following equation (1):

$$\Phi_{\text{sample}} = \Phi_{\text{std fl}} \times \left(\frac{I_{\text{sample}}}{I_{\text{std}}} \right) \times \left(\frac{Abs_{\text{std}}}{Abs_{\text{sample}}} \right) \quad (1)$$

Where I_{sample} and I_{standard} in the integrated area under the emission curve when the sample was excited at 490 nm. Abs denoted the optical density of the sample solution at the excitation wavelength.

Lifetime measurements: FLS1000 Photoluminescence Spectrometer (Edinburgh instruments). The lifetime was fit using Fluoracle[®] software and using the following formula (2):

$$\text{Fit} = \mathbf{A} + \mathbf{B}_1 e^{(-t/\tau_1)} + \mathbf{B}_2 e^{(-t/\tau_2)} \quad (2)$$

where the contribution (% relatively) of each of the different components is B_1 and B_2 respectively.

Singlet oxygen quantum yield calculations. The singlet oxygen ($^1\Delta_g$) quantum yield (Φ_Δ) was measured using zinc *meso*-tetraphenylporphyrin (ZnTPP) in CHCl_3 as the standard ($\Phi_\Delta = 0.72$).⁶⁷ The singlet oxygen near infrared emission (NIR) spectra were recorded using an Andor InGaAs detector coupled with a Shamrock 163 Spectrograph. The excitation sources were supplied by Thorlabs and the monochromatic line used was a 530 nm diode laser. All UV spectra were recorded both before and after singlet oxygen measurements and optical density of standards and samples were 0.3 absorption units at the excitation wavelength ($\lambda_{\text{exc}} = 530$ nm). Standard and sample measurements were run under identical experimental conditions employing the same solvent, excitation source, LED exposure time and accumulation cycles to allow for direct comparison of NIR emission spectra. The NIR emission spectra was then integrated using baseline correction software in the region of $\lambda_1 = 1230$ nm to $\lambda_2 = 1330$ nm and Φ_Δ calculated using the following equation (3):

$$\Phi_{\text{sample}} = \frac{\Phi_{\text{ref}}(\text{Area}_{\text{sample}} \times \text{Abs}_{\text{ref}})}{(\text{Area}_{\text{ref}} \times \text{Abs}_{\text{sample}})} \quad (3)$$

Where Φ_{ref} is the singlet oxygen quantum yield of the standard, $\text{Area}_{\text{sample}}$ and Area_{ref} are the integrated area between 1230 – 1330 nm of the phosphorescence of singlet oxygen respectively, Abs_{ref} and $\text{Abs}_{\text{sample}}$ are the absorption of both solutions at the wavelength of excitation.

ps-Transient absorption measurements and ps-Time Resolved Infrared measurements. ps-TA and ps-TRIR spectra were recorded using the ULTRA instrument at the Central Laser Facility in the Rutherford Appleton Laboratory in the U.K. and has been described elsewhere.⁶⁸

ns-Transient absorption measurements. ns transient absorption data were recorded on the LP980 transient absorption spectrometer (Edinburgh Instruments), $\lambda_{\text{exc}} = 355$ nm. All samples were degassed using three freeze-pump thaw cycles prior to sample measurement. The optical density of the sample was ~ 0.3 at 355 nm prior to transient absorption measurement on the LP980. Samples were checked for photodegradation by comparing UV-vis absorbance spectra before and after TA measurements and no changes were observed.

Photocatalytic homogeneous H₂ evolution experiments. For photocatalytic hydrogen evolution, each sample was prepared in a 23 mL glass Schlenk tube stoppered with an air-tight rubber septum. Prior to sample preparation, an aqueous solution of 0.2 M ascorbic acid was adjusted to the desired pH value by titrating the solution with an appropriate amount of 0.2 M NaOH solution. The polymer and the catalyst were dissolved in 4 mL of organic solvent (either CH₃CN or THF) followed by subsequent addition of 4 mL of the ascorbic acid solution to yield an 8 mL 1:1 (v/v) mixture of organic solvent and aqueous ascorbic acid solution (0.1 M final concentration of ascorbic acid). The components were dissolved in the photocatalytic solution and degassed using three freeze-pump thaw cycles prior to irradiation. The solution based photocatalytic experiments ($\lambda > 420$ nm) were all conducted for a period of 24 hours using a 300 W Xe arc lamp. All experiments for the detection of hydrogen evolution were carried out in triplicate. At each timepoint reported, 1 mL of the headspace from the Schlenk flask was injected onto the GC to quantify the amount of H₂ produced. For the heterogeneous photocatalysis on NiO, the reaction cell was degassed for at least 15 minutes with either nitrogen or argon. Aqueous electrolytes were freshly prepared and pH adjusted with concentrated HCl, and measured with a benchtop pH meter (Hanna Instruments). The cell was irradiated with simulated 1 sun intensity light (AM 1.5, 100 mW cm⁻²) using a 300 W Xe arc lamp (Oriol Instruments). Hydrogen was detected with a thermal conductivity detector (TCD) with the system operating at 80 °C. Gas sampling was done in flow, through an integrated cell block (**Figure S2.44**). Further details can be found in Supporting Information.

2.4 Results and Discussion

2.4.1 Synthesis

The synthesis of the BODIPY polymer was achieved in three steps (**Figure 2.2**), via initial synthesis of the BODIPY monomer⁴⁸ and subsequent iodination at the 2 and 6 position (3-TMS diiodo BODIPY). The polymer ($M_n = 7.5$ kDa, $\mathcal{D} = 1.4$, see Appendix A, **Figure S2.8**) was synthesised using Sonogashira polycondensation between the iodinated BODIPY core and a 1,4-diethynylbenzyl linker to yield the 3-TMS BODIPY polymer depicted in **Figure 2.2** (herein referred to as polymer). The resulting polymeric material exhibits a bimodal molecular weight distribution. SEC analysis confirmed the successful formation of polymeric structures well beyond the oligomer regime with a bimodal molecular weight distribution (**Figure S2.8**).

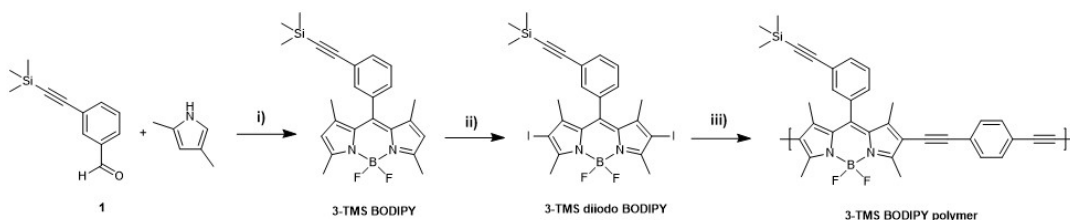


Figure 2.2. Synthesis of 3-TMS polymer. *Reagents and conditions* i) TFA, DDQ, BF₃OEt₂, TEA, dry CH₂Cl₂, N₂, RT, 3 days; ii) I₂, HIO₃, EtOH, r.t. overnight; iii) Pd(PPh₃)₂Cl₂, PPh₃, CuI, THF/Diisopropylamine, reflux, 3 days.

The photophysical properties of the polymer were investigated using a variety of techniques including UV/visible and luminescence spectroscopies, and the time-resolved techniques of luminescence lifetime, transient absorption, and time-resolved infrared spectroscopies. BODIPY compounds are well-established luminescent probes, characterised by high luminescence quantum yields.

2.4.2 UV-visible and emission spectroscopy

The UV-visible and emission spectra of the monomer and polymer are presented in **Figure 2.3** (recorded in CH₂Cl₂). The spectrum indicated with a solid red line corresponds to the absorption spectrum of the monomer. This spectrum displays the characteristic narrow absorption band of the BODIPY core ($\lambda_{\max} = 503$ nm; $\text{FWHM}_{\text{abs}} = 768$ cm⁻¹) which has been assigned to a S₀ to S₁ $\pi - \pi^*$ transition. A weak shoulder

is observed at 470 nm attributed to the $S_0 - S_2$ ($\pi - \pi^*$ transition). The associated emission spectrum (dashed red line) also displays the characteristic sharp band, λ_{\max} , at 516 nm representing a Stokes shift of 501 cm^{-1} , within the range typical for BODIPY materials. This indicates only a small change in dipole moment (or geometry) in transition from the ground to the excited state.⁵⁵

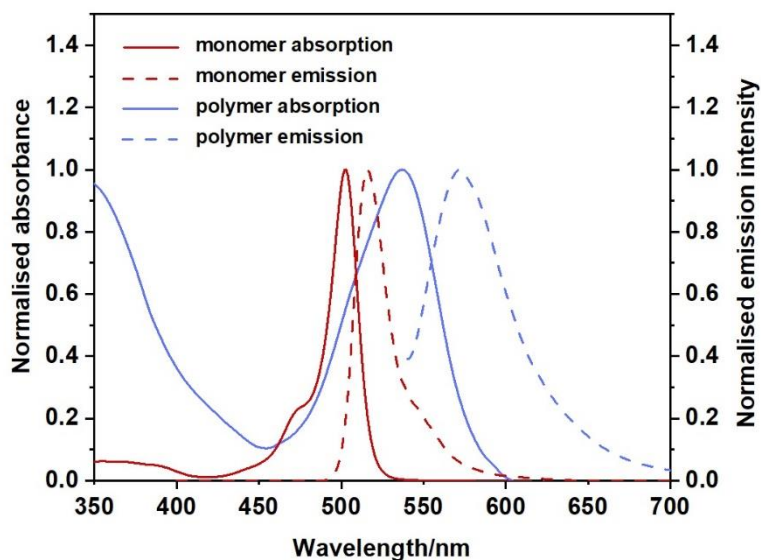


Figure 2.3. Normalised absorption spectra for monomer (solid red), polymer (solid blue) and normalised emission spectra for monomer (dashed red) and polymer (dashed blue). CH_2Cl_2 , 298 K.

The fluorescence quantum yield for the monomer is high ($\Phi_{\text{fl}} = 92\%$, **Table 2.1**), in agreement with the literature.^{45,46} The UV spectrum of the polymer is presented as the solid blue feature in **Figure 2.3** (with additional spectra in various solvents presented in **Figure S2.11**). The increased π -conjugation along the polymer backbone also results in a broadening of the BODIPY absorption.^{52,69,70} The lowest energy absorption feature of the polymer is broad ($\text{FWHM}_{\text{abs}} = 2209 \text{ cm}^{-1}$), with the λ_{\max} is red-shifted by 36 nm compared to the monomer. A new intense feature is present at about 350 nm, which is also displayed in the excitation spectrum of the polymer (**Figure S2.13**). In addition, the lowest energy absorption band is partially resolved into two features in some solvents, indicating the existence of different environments for the BODIPY moiety along the polymer backbone. In this regard, the BODIPY unit is acting as a probe to the various environments on the polymer, and these environments have a dramatic effect on the photophysical behaviour of the BODIPY chromophore. The

emission spectrum of the polymer is also broadened compared to the monomer with a larger Stokes shift of 1101 cm^{-1} (**Table 2.1**). The emission maximum of the polymer is shifted some 57 nm to the red compared to the monomer and the emission band extends to 700 nm. These observations are consistent with other studies on polymeric BODIPY systems and again implies the presence of a multiple of environments for the BODIPY chromophore.⁷¹ The fluorescence quantum yield of the polymer is greatly reduced compared to the monomer ($\Phi_{\text{fl}} = 0.09$, **Table 2.1**). It appears that incorporation of a conjugated linker unit is important in modulating the photophysical properties of BODIPY polymers and reducing the luminescence of the BODIPY core.⁵²

Table 2.1. Photophysical properties of the monomer and polymer. All spectra were recorded in CH_2Cl_2 at room temperature.

Compound	λ_{abs} (nm)	λ_{em} (nm) ^a	Stokes Shift $\Delta\nu$ (cm^{-1}) ^b	Optical gap (eV) ^c	Φ_{fl} ^d	Φ_{ISC} ^e	Φ_{Δ} ^f	τ_{s} (ns) ^g	τ_{T} (μs) ^h
monomer	503	516	501	2.41	0.92	0.08	0.05	4.3	-
polymer	539	572	1101	2.19	0.09	0.91	0.77	1.1, 3.9	61

^awavelength used to excite the compound correlated to the absorption maxima of each compound respectively.

^bStokes shift.

^ccalculated from the onset of absorption spectrum.⁷² See **Figure S2.30**.

^dfluorescence quantum yield calculated using 3-pyridine H-BODIPY as a reference standard, where $\Phi_{\text{fl}} = 62\%$ in CH_2Cl_2 .⁴⁸ Detailed in the experimental section.

^eIntersystem crossing efficiency, approximated by the Ermolev's rule: $\Phi_{\text{ISC}} = 1 - \Phi_{\text{fl}}$.⁷³

^fsinglet oxygen quantum yield.

^gobtained from TCSPC technique in CH_2Cl_2 .

^hobtained from transient absorption spectroscopy, λ_{exc} 355 nm, sample degassed using freeze-pump thaw method.

The emission spectra of the polymer were relatively insensitive to the nature of the solvent (**Figure 2.4** (a)) implying that BODIPY emission occurs from only selective environments. However, a slight hypsochromic shift (*ca.* - 9 nm) is observed in acetonitrile compared to other solvents (571 – 574 nm, **Table 2.1**). The emission map (**Figure 2.4** (b)) follows closely the absorption profile of the ground state, indicating coupling of the chromophores responsible for the two lowest energy features in the absorption spectrum to the emissive state.

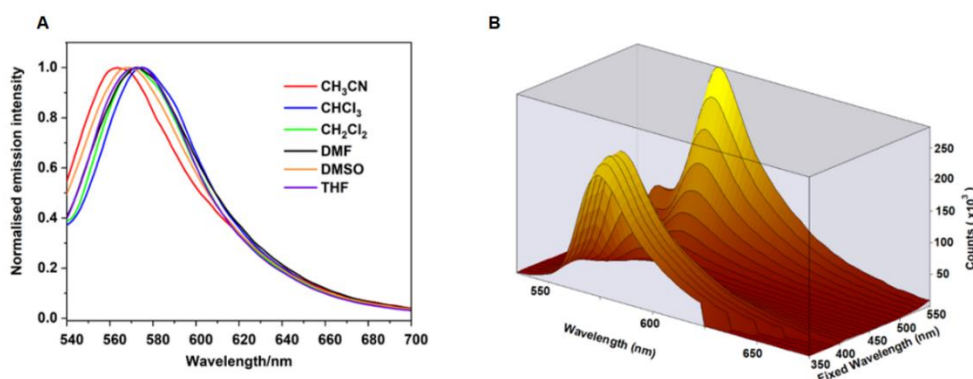


Figure 2.4. a) Emission spectra of the polymer in acetonitrile (red), chloroform (blue), dichloromethane (green), dimethylformamide (black), dimethyl sulfoxide (orange) and tetrahydrofuran (purple) following excitation at 530 nm, b) 3-D Emission map of polymer in dichloromethane, recorded at room temperature. Fixed wavelength axis indicates the various excitation wavelengths used. All spectra recorded in at room temperature.

Table 2.2. Fluorescence decay lifetimes of the monomer and polymer using 510 nm LED diode. %rel of each lifetime decay represents the relative contribution of each lifetime decay (%).[†]

Compound	Solvent	λ_{em}^a (nm)	τ_1^b (ns)	%rel τ_1	τ_2^b (ns)	%rel τ_2
Monomer	CH ₂ Cl ₂	513	-	-	4.3	100
Polymer	CH ₂ Cl ₂	572	1.1	8.7	3.9	91.3
	THF	573	0.8	9.4	3.8	90.6
	CHCl ₃	574	0.7	7.4	4.2	92.6
	CH ₃ CN	568	0.8	14.5	3.6	85.5
	DMSO	570	0.8	25.6	3.5	74.4
	DMF	572	0.4	27.8	3.8	72.2

2.4.3 Lifetime analysis using TCSPC

The fluorescence lifetime (τ_{fl}) of the monomer was measured in dichloromethane solution. The luminescence decay follows a single exponential profile yielding a τ_{fl} of 4.3 ns (**Figure S2.25**), typical of emission from the lowest energy singlet excited state.⁷⁴ As mentioned above the quantum yield for fluorescence is much lower for the

[†] The greater % contribution of τ_1 in more polar solvents may be due to induced changes in the ground state conformation of the polymer in more polar solvents.

polymer and, in addition, lifetime measurements showed biexponential decay profiles. A fast process with τ_{fl} on the order of 1 ns or less, and a slower process with a lifetime similar to that of the singlet emission from the monomer ($\tau_{fl} \approx 4$ ns). The lifetimes were measured in a variety of solvents and these data are presented in **Table 2.2**. It is clear that while the lifetimes of the two decay processes are largely insensitive to the solvent, however the relative proportions of the two decay processes vary. The fast process contributes more in DMF or DMSO than it does in CH_2Cl_2 or THF (**Figure 2.5**). These observations can be explained by proposing that the singlet emission only occurs from selective environments on the polymer, which do not facilitate intersystem crossing (ISC) to the triplet surface.⁷⁵ The proportion of the excited BODIPY centres, which undergo singlet emission, is strongly affected by the interaction between the polymer and the solvent. This explains the substantial decrease in Φ_{fl} for the polymer compared to the monomer. The majority of excited BODIPY centres can undergo charge transfer processes along the conjugated polymer which promotes ISC.⁷⁶ More details of the emission decay profiles are presented in the supporting information (**Figure S2.26 - Figure S2.29**).

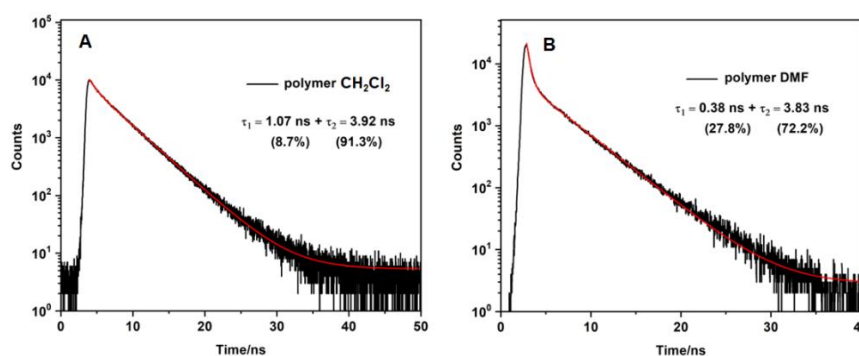


Figure 2.5. a) Emission decay of polymer in CH_2Cl_2 and b) DMF obtained using FLS1000 Photoluminescence spectrometer $\lambda_{exc} = 510$ nm. All solutions purged with N_2 for 20 minutes prior to sample measurement.

Biexponential decays have previously been reported for other BODIPY polymers and are consistent with the results in this study.⁷⁷ For instance Donuru et al., reported a lifetime of $\tau = 4.1$ ns for a BODIPY monomer, and a lifetime of $\tau = 1.1$ ns in the resulting polymer.⁵⁰ Other reports also follow similar trends of a decreased lifetimes for polymeric materials.⁷⁸ Douhal and co-workers reported three lifetime components for another conjugated BODIPY copolymer, $\tau_1 = 0.22$ ns, $\tau_2 = 0.7$ ns and $\tau_3 = 4.3$ ns in

CH_2Cl_2 , $\lambda_{\text{exc}} = 371 \text{ nm}$.⁷⁹ The latter two lifetimes are similar to those obtained in this work (**Table 2.1**) and it is possible that a third lifetime component exists for our polymer but on a timescale shorter than the instrument response time of 50 ps (see the transient absorption results outlined below).

2.4.4 Transient absorption spectroscopy

To investigate the early excited state dynamics, ps-ns transient absorption (TA) measurements were undertaken on the polymer in a range of solvents including CD_3CN , DMSO, CHCl_3 and CH_2Cl_2 . **Figure 2.6** (a) displays the colour 2-D TA plot for the polymer following excitation at 525 nm in CD_3CN and **Figure 2.6** (b) contains the corresponding time-resolved spectra. To aid in spectral interpretation the ground state absorption spectrum of the polymer (blue dashed line) and emission spectra (green dashed line) are plotted. The region of most interest is indicated with a downward arrow, while the region close to the upward arrow is subject to distortions because of emission.

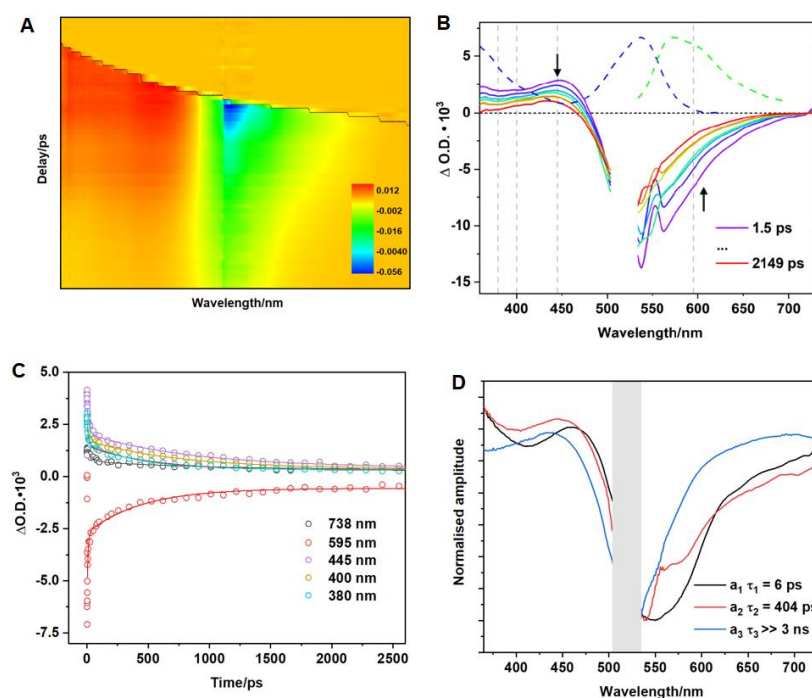


Figure 2.6. a) Transient absorption spectra of polymer in CD_3CN following excitation using 525 nm, b) Transient absorption spectra of polymer corresponding to indicated time delays, grey lines indicate kinetic traces analysed, c) Temporal evolution of the spectra at wavelengths indicated by grey broken lines in (b) together with the exponential best fit line (b) and d) Normalised Decay Associated Spectra (DAS) corresponding to the lifetimes extracted from modelling of the TA spectra in CD_3CN .

Excitation results in a ground state bleach (GSB) around 540 nm and the formation of an excited state absorption (ESA) at ~ 435 nm (**Figure 2.6** (b)). The ESA at 435 nm decays with three decay components (**Figure 2.6** (c)) with $\tau_1 = 6 \text{ ps} \pm 1 \text{ ps}$, and $\tau_2 = 404 \text{ ps} \pm 32 \text{ ps}$, and a third component with $\tau_3 > 3 \text{ ns}$ (**Table 2.3**). **Figure S2.32** shows the additional TA spectra obtained in DMSO, CHCl_3 and CH_2Cl_2 , all of which exhibit similar spectral features. The longer of these lifetimes are similar to those obtained in the emission studies described above (**Table 2.2**). The first component (τ_1), with lifetimes in the range 6 to 18 ps, is too short-lived to be detected in the luminescence studies. The time scale for this species is within the range of vibrational relaxation, however the spectroscopic behaviour of the bands is not typical of this process, and another possibility is structural relaxation of the BODIPY polymer.^{80,81} The second component, (τ_2) in the range 400 to 1400 ps corresponds to the fast component in the emission lifetime studies. The more rapid excited state decay in the more polar solvents suggests that the excited state is quenched by electron transfer to form a charge-separated triplet state, which is facilitated by polymer solvent interactions. The absorption of the triplet species persisted to greater than 3 ns after excitation as did the GSB. Triplet excited state formation is also observed in other heavy-atom-free BODIPY photosensitisers.⁷⁶ Halogenated BODIPY monomers also have an ESA feature in this region attributed to the formation of a triplet excited state.^{82,83}

Table 2.3. Summary of the lifetimes in the TAS experiments for the ESA feature at ~ 445 nm (using a biexponential function) following excitation at 525 nm.

Solvent	τ_1 (ps)	τ_2 (ps)
CD_3CN	6 ± 1	404 ± 32
DMSO	18 ± 3	522 ± 56
CHCl_3	15 ± 2	784 ± 56
CD_2Cl_2	9 ± 1	1359 ± 291

Figure 2.6 (d) displays the decay associated spectra (DAS) for the polymer in CD₃CN. The DAS spectra exhibit the amplitude (a_i) of each lifetime component (τ_i) along the absorption spectral window in the experimental set-up. The τ_1 DAS is dominated by a positive feature at 464 nm and, a negative feature corresponding to the GSB at \sim 546 nm. This initial species absorbs to the red of the parent and of the second species populated. The τ_2 DAS is structurally similar showing a slight blue shift of the ESA feature on the higher energy side of the spectra *ca.* - 18 nm. Finally, a positive feature is also present in the τ_3 DAS centered at 455 nm and persists on the ns-timescale. Consequently, we can assign the long-time life component to the absorption of a triplet state, which is further supported by ns-TA experiments.

For comparison, TAS was also carried out with the parent BODIPY monomer and the diiodo monomer in CD₃CN, following excitation at 525 nm (**Figure S2.34** and **Figure S2.35**). The lifetime obtained for the BODIPY monomer ($\tau \sim$ 4 ns), is consistent with the population of the S₁ state, followed by relaxation to the ground state. The GSB feature of the diiodo BODIPY monomer is long-lived and did not decay within the timeframe of the experiment. In the TA spectra for the diiodo BODIPY dye concurrent with decay of the band initially observed at 460 nm, a further band grows in at \sim 430 nm over *ca.* 50 ps (that is absent in the BODIPY monomer) that persists beyond the experimental times used (2 ns). This is attributed to ISC with formation of the triplet state which is characteristic of heavy-atom BODIPY analogues.⁶²

Time-resolved experiments on the polymer in CH₃CN, using ns laser pulses confirmed the formation of a long-lived excited state consistent with it being a triplet species with $\tau_T = 60 \mu\text{s}$. The ns-TA spectrum (**Figure 2.7**) exhibits a broad GSB in addition to two ESA features at approx. 435 nm and 585 nm, which resembles the final spectrum obtained in the ps-TA experiments described above. The triplet lifetime of 60 μs is similar to triplet state lifetimes measured for other conjugated polymers containing thiophene and fluorene moieties previously measured (20 – 120 μs).²¹ Lifetimes in the range 450 - 710 μs have been reported for polymers with pendant iodo-substituted BODIPY units.⁸⁴ Triplet excited state species have also been observed for a BODIPY polymer containing an ethynyl thiophene linker.⁷¹ The singlet oxygen quantum yield

for the polymer ($\Phi_{\Delta} = 0.77$, **Table 2.1**) represents more than a ten-fold increase over the singlet oxygen quantum yield of the monomer ($\Phi_{\Delta} = 0.05$, **Table 2.1**) (**Figure S2.24**).^{85,86}

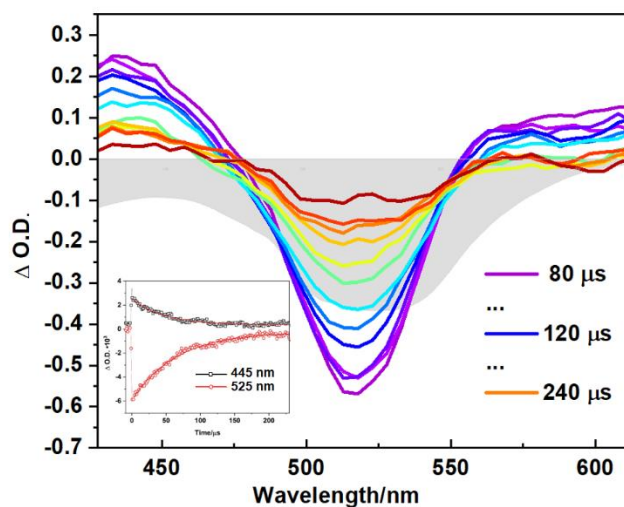


Figure 2.7. Transient absorption spectroscopy of polymer in CH_3CN , shown at different time delays, ($\lambda_{\text{exc}} = 355$ nm) and corresponding decay at ESA and GSB shown in inset at stated wavelength: 445 nm (black squares) and 525 nm (red circles) with red line showing monoexponential fitting to obtain triplet lifetime. Grey shaded curve represents the ground state absorption spectra of polymer in same solvent. All samples were prepared using freeze-pump thawed to degas.

2.4.5 Time resolved infrared spectroscopy

Time resolved infrared spectroscopy (TRIR) was also carried out on the polymer on the ps to ns timescales following excitation at 525 nm (in a range of solvents; DMSO, CD_3CN , CHCl_3 and CD_2Cl_2). A representative FTIR spectrum for the polymer is displayed in **Figure S2.9**, in conjunction with 1,4-diethynylbenzene which was used in the synthesis of the polymer.

Immediately following excitation, a depletion is evident at ~ 1547 cm^{-1} together with new bands at 1267, 1362 and 1452 (broad) cm^{-1} which are assigned to a singlet excited state of the BODIPY. Previously electron transfer dynamics for BODIPY chromophores in CH_2Cl_2 have been reported, with a GSB at 1543 cm^{-1} , and ESA features at 1339, 1297 and 1507 cm^{-1} respectively.⁸⁷ These spectroscopic features produced within the instrument response time in our studies, have identical lifetimes ($\tau = 25 (\pm 5)$ ps) and are assigned to a singlet excited state.⁶⁴ However, for the polymer in this study, additional positive features develop, principally that at 1316 cm^{-1} which

is fully formed within 1 ns and persists on the ns-timescale. We have assigned these features to a triplet excited state. Because of the substantial band overlap, accurate kinetic data could not be obtained for the growth of the triplet species, however it is clear that it forms at a rate similar to the fast decay component in the emission lifetime measurements (**Figure 2.8** (a)).

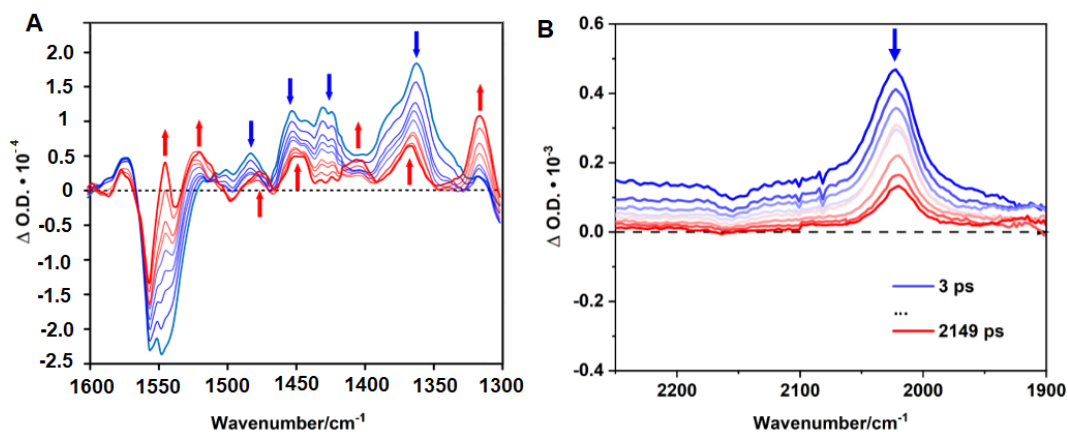


Figure 2.8. a) TRIR spectra following excitation at 525 nm of the polymer in CD₃CN in the fingerprint region and b) TRIR spectra following excitation at 525 nm of the polymer dissolved in chloroform the triple bond region. Blue spectra indicating initial time delays (ps), red spectra indicated final time delays (ps).

Figure 2.8 (b) displays the spectra obtained in the region where carbon-carbon triple bonds absorb. Following excitation of the polymer in CHCl₃ (FTIR, **Figure S2.9**) a positive feature was produced at 2023 cm⁻¹. The equivalent feature for the ground state polymer is observed at 2339 cm⁻¹. The substantial shift of this feature points to a substantial charge transfer from the triplet bond to the BODIPY unit in the excited state.⁸⁸⁻⁹⁰ Kinetic analysis of the signal at 2023 cm⁻¹ reveals two decay lifetimes, $\tau_1 = 13 \pm 2$ ps and $\tau_2 = 757 \pm 62$ ps corresponding to vibrational relaxation, and ISC to the triplet surface respectively. These lifetimes are consistent with those obtained in the TA experiments. Following ISC, a product feature persists to the ns timescale as expected for a triplet species.

TRIR studies were also performed using the diiodo BODIPY monomer. Following excitation, the diiodo monomer displayed a bleach at 1538 cm⁻¹ and positive bands at 1488 and 1442 (broad) cm⁻¹ (**Figure S2.38**). After *ca.* 30 ps, two additional bands form at 1525 and 1370 cm⁻¹ respectively and persist beyond the timeframe of the experiment. TRIR spectra of the BODIPY monomer under identical experimental

conditions reveal a monoexponential decay of the band at 1540 cm^{-1} , characteristic of BODIPY monomers. This indicates the decay of the singlet excited state, with no evidence for features which could be assigned to a triplet species. (**Figure S2.39**). TRIR spectra of the monomer and diiodo monomer in the carbon-carbon triple bond region were, as expected featureless (**Figure S2.40**).

2.4.6 Photocatalytic hydrogen generation studies

2.4.6.1 Solution studies

The polymer was assessed for hydrogen generation with cobaloxime as the catalyst, under both basic and acidic conditions. No hydrogen evolution was detected in CH_3CN under visible light irradiation ($\lambda > 420\text{ nm}$) when triethylamine was used as the sacrificial agent (SA). The polymer was unstable under these conditions as verified by UV/visible spectroscopy. However, using ascorbic acid as the SA, hydrogen evolution (*ca.* $108\text{ }\mu\text{mol h}^{-1}\text{ g}^{-1}$) was observed under visible light irradiation ($\lambda > 420\text{ nm}$).^{56,63}

The efficiency of hydrogen generation was investigated by varying the pH of the ascorbic acid solution added to the 8 mL 1:1 (v/v) photocatalytic solution. Preliminary photocatalysis experiments were carried out using 0.1 M ascorbic acid solution that was adjusted to a pH of ~ 2 prior to addition to the photocatalytic solution. It is assumed under these reaction conditions that ascorbic acid exists in its fully protonated form, H_2A (**Figure S2.42**, $\text{pK}_a = 4.17$).⁹¹ When we adjusted the pH of the ascorbic acid solution from 2 to 5 prior to sample preparation, an increase in hydrogen evolution ($0.2\text{ }\mu\text{mol h}^{-1}\text{ g}^{-1}$ to $108\text{ }\mu\text{mol h}^{-1}\text{ g}^{-1}$ respectively, **Table S2.3**) was observed. While we cannot accurately determine the pH value of the final photocatalytic solution, it is assumed that the decreased degree of acidity in the later photocatalytic solution results in monoprotic ascorbate anion (HA^-) as the dominating species. HA^- has previously been reported as a stronger reducing agent than the corresponding protonated form of the sacrificial agent, suggesting a plausible reason for the enhancement of hydrogen activity.^{92,93}

Changing the solvent system from a 1:1 CH₃CN/H₂O (v/v) 0.1 M ascorbic acid solution to a 1:1 THF/H₂O (v/v) 0.1 M ascorbic acid solution resulted in an increase in hydrogen generation from 108 $\mu\text{mol h}^{-1} \text{g}^{-1}$ after 24 hours of irradiation to 152 $\mu\text{mol h}^{-1} \text{g}^{-1}$ (Figure 2.9). Solvent effects are well known to affect hydrogen generation and THF has been previously reported to be the solvent of choice for photocatalytic systems utilising BODIPY chromophores.^{94,95}

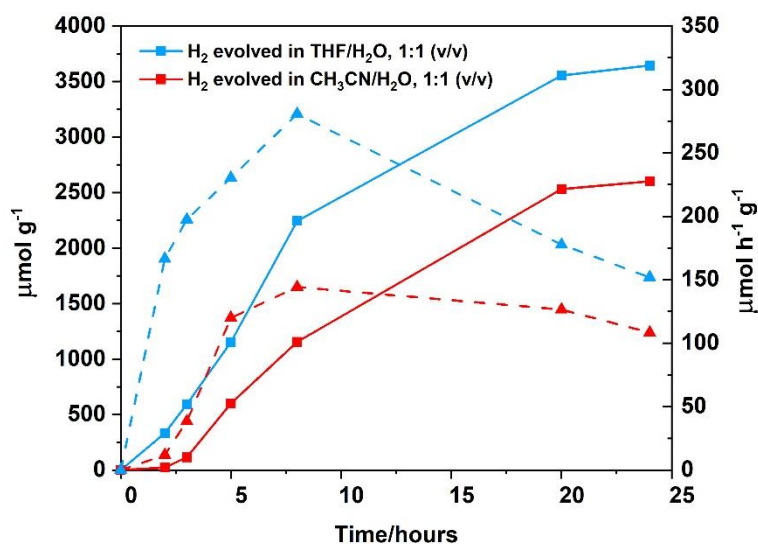


Figure 2.9. Photocatalytic results following irradiation at $\lambda > 420$ nm, cobaloxime as the catalyst (2.5 mM), ascorbic acid as the SA (0.1 M, which was adjusted to pH 5 prior to sample preparation using the appropriate amount of 2M NaOH), polymer as PS (0.06 mg/mL). Hydrogen evolution curve displayed for different solvent ratios: THF/H₂O, 1:1 (v/v) (blue squares, solid line) or CH₃CN/H₂O, 1:1 (v/v) (red squares, solid line). Hydrogen turnover frequency displayed for each solvent system in $\mu\text{mol h}^{-1} \text{g}^{-1}$: THF/H₂O, 1:1 (v/v) (blue triangles, dashed line) and CH₃CN/H₂O, 1:1 (v/v) (red triangles, dashed line). All samples were degassed using three freeze-pump thaw cycles prior to irradiation.

The amount of H₂ observed when 0.06 mg/mL concentration of the polymer was used was 3645 $\mu\text{mol g}^{-1}$, whereas when the concentration of polymer increased to 0.25 mg/mL only 7664 $\mu\text{mol g}^{-1}$ was observed (Figure 2.10). Furthermore, this increase in concentration of the polymer resulted in an increase in hydrogen turnover frequency of 152 $\mu\text{mol h}^{-1} \text{g}^{-1}$ (0.06 mg/mL) to 319 $\mu\text{mol h}^{-1} \text{g}^{-1}$ (0.25 mg/mL) after irradiation for 24 hours. At low concentration, the turnover frequency (TOF) increases until 8 hours of irradiation, after which the activity decreases. At 24 hours, the TOF is low and no further H₂ is evolved, indicating degradation of the catalyst (cobaloxime catalysts are known to have limited stability^{96,97} or the PS).

A summary of all photocatalytic conditions and hydrogen evolution data can be found in supporting information (**Figure S2.41** and **Table S2.3**), and a summary of hydrogen evolution rates of reported organic polymers can be found in **Table S2.4**. The majority of hydrogen evolution studies using polymeric materials, require a precious metal co-catalyst. For example a polybenzothiadazole conjugated network required the addition of 3 wt.% Pt to yield a hydrogen evolution rate of $116 \mu\text{mol h}^{-1}$.⁹⁸ The most notable difference between the polymer reported in this study and those reported in the literature to date, is the solubility of the polymer in a wide range of organic solvents. This offers the potential of further processing, for example post functionalisation or further fabrication onto a photocathode surface. Post-functionalisation options include displacement of the TMS group and addition of a carboxylic acid anchoring group to facilitate surface attachment.⁹⁹

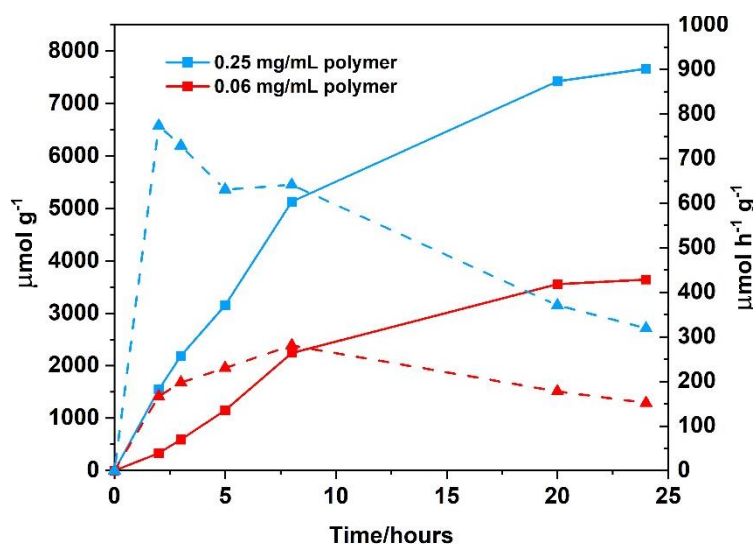


Figure 2.10. Photocatalytic results following irradiation at $\lambda > 420 \text{ nm}$, cobaloxime as the catalyst (2.5 mM), ascorbic acid as the SA (0.1 M, which was adjusted to pH 5 prior to sample preparation using the appropriate amount of 2M NaOH), solvent ratio THF/H₂O, 1:1 (v/v) and polymer as PS (0.25 mg/mL; blue squares, solid line) or (0.06 mg/mL; red squares, solid line). Hydrogen turnover frequency displayed for each polymer concentration analysed in $\mu\text{mol h}^{-1} \text{g}^{-1}$: 0.25 mg/mL (blue triangles, dashed line) and 0.06 mg/mL (red triangles, dashed line). All samples were degassed using three freeze-pump thaw cycles prior to irradiation.

2.4.6.2 Immobilisation Studies

While the mechanistic insights leading to the augmented activity of proton reduction using polymeric photosensitisers remains unclear, some limitations of polymeric species have been described, including the dispersion of the polymers in aqueous solution and hence separation of excitons, leading to enhanced charge carriers

generated. The limitations associated with dispersion may be overcome if the polymer is cast as a thin film, or furthermore, immobilised onto a surface such as NiO.^{13,100} This strategy may increase the stability of the polymer and also improve photon absorption, as an increase in conjugation on the surface (owed to more π - π stacking on the surface) will likely decrease the optical band gap. The importance of processability and incorporation of polymeric units onto thin films has previously been acknowledged in other work with polymers for hydrogen evolution.¹⁰⁰

Some preliminary studies were performed where the polymer was co-adsorbed in the first instance with 4,4'-dicarboxy-2,2'-bipyridine platinum dichloride as a catalyst for H₂ evolution. Photoelectrocatalysis experiments were carried at pH 5 in aqueous phthalate buffer due to problems with desorption at higher or lower pH. Optimum photocurrent was detected under these conditions. The absorption spectrum of the BODIPY polymer on NiO is largely consistent with that in solution, showing a broad absorption (**Figure S2.45**). The Pt-catalyst was difficult to co-adsorb on the NiO films due to limited solubility, but it was possible to confirm the presence of this additional layer with absorption spectroscopy and Energy-dispersive X-ray spectroscopy (EDX) analysis in conjunction with scanning electron microscopy (SEM) of the films. Representative examples of chronoamperometry measurements for the sensitised NiO films are shown in the supporting information (**Figures S2.48** and **S2.49**). Linear sweep voltammetry allowed us to determine a safe bias potential to apply to the system without permanent reduction of species at the electrode surface. This was optimised to a value of -0.3 V vs Ag/AgCl. It is also important to account for charging on the electrode surface at the beginning of each experiment. Control experiments confirmed that bare NiO did not produce any current due to irradiation with light, ruling out light absorbing impurities in the NiO. For the films with the BODIPY polymer and catalyst, over the timescale of the experiments (~ 40 mins) the photocurrent of the system decreased gradually once the period of continuous illumination commenced. The chronoamperometry measurements were concurrent with gas sampling for H₂ using the in-flow setup. While the in-flow gas sampling setup is more rigorous than headspace sampling, only trace amounts of H₂ were detected in the experiments (possibly due to the detection limit of the system), yet bubbles were generated on the

NiO surface during the experiment. Extended irradiation experiments up to 2 hrs 15 mins did not see an increase in the amount of hydrogen detected. Chronoamperometry measurements of the polymer with the Pt-catalyst show an initial current density of approximately $18 \mu\text{A cm}^{-2}$, but this decreased to $\sim 2.5 \mu\text{A cm}^{-2}$ after an initial decay (**Figures S2.48**). There are many possible losses in the system due to dye/catalyst desorption and reaction. Surface wetting is also a consideration as bubbles of gas can become stuck on the electrode surface. Future research will necessitate identifying a more suitable co-catalyst with better loading on the NiO surface. Few easily synthesised examples of such catalysts with suitable anchoring groups exist, even fewer derived from earth abundant metals. Alternative strategies such as surface treatments to improve wettability or doping the NiO with graphene to improve charge transport and dye loading are also attractive alternatives¹⁰¹ but beyond the scope of the present study.

2.5 Conclusion

In summary, the synthesis, characterisation and photophysical properties of a TMS-BODIPY monomer and a novel TMS-BODIPY copolymer is reported. Modification of the BODIPY monomer facilitating close proximity of multiple chromophores in a polymeric backbone led to significant changes in the photophysical properties. Time-resolved techniques such as TA and TRIR identified both singlet and triplet excited states and the related kinetics of these species. Solvent studies demonstrated the role of solvent on the photophysics of this polymer facilitating the formation of a triplet excited state via a charge transfer state. Photocatalytic hydrogen studies in solution demonstrated that hydrogen evolution occurs using visible light in solution. This work confirms that BODIPY copolymers can act as effective photosensitisers for hydrogen evolution and how they can be used in artificial photosynthetic applications.

2.6 Supporting information

The supplementary data associated with this chapter can be found in Appendix A.

2.7 Bibliography

- (1) Fajrina, N.; Tahir, M. *Int. J. Hydrogen Energy* **2019**, *44* (2), 540–577.
- (2) Dalle, K. E.; Warnan, J.; Leung, J. J.; Reuillard, B.; Karmel, I. S.; Reisner, E. *Chem. Rev.* **2019**, *119* (4), 2752–2875.
- (3) O'Reilly, L.; Pan, Q.; Das, N.; Wenderich, K.; Korterik, J. P.; Vos, J. G.; Pryce, M. T.; Huijser, A. *ChemPhysChem SUPP* **2018**, *19* (22), 3084–3091.
- (4) Kowacs, T.; O'Reilly, L.; Pan, Q.; Huijser, A.; Lang, P.; Rau, S.; Browne, W. R.; Pryce, M. T.; Vos, J. G. *Inorg. Chem.* **2016**, *55* (6), 2685–2690.
- (5) Singh Bindra, G.; Schulz, M.; Paul, A.; Groarke, R.; Soman, S.; Inglis, J. L.; Browne, W. R.; Pfeffer, M. G.; Rau, S.; MacLean, B. J.; Pryce, M. T.; Vos, J. G. *Dalt. Trans.* **2012**, *41* (42), 13050.
- (6) Das, N.; Bindra, G. S.; Paul, A.; Vos, J. G.; Schulz, M.; Pryce, M. T. *Chem. - A Eur. J.* **2017**, *23* (22), 5330–5337.
- (7) Rommel, S. A.; Sorsche, D.; Schönweiz, S.; Kübel, J.; Rockstroh, N.; Dietzek, B.; Streb, C.; Rau, S. *J. Organomet. Chem.* **2016**, *821*, 163–170.
- (8) Tong, L.; Zong, R.; Thummel, R. P. *J. Am. Chem. Soc.* **2014**, *136* (13), 4881–4884.
- (9) Mishra, A.; Fischer, M. K. R.; Büuerle, P. *Angew. Chemie - Int. Ed.* **2009**, *48* (14), 2474–2499.
- (10) Manton, J. C.; Long, C.; Vos, J. G.; Pryce, M. T. *Phys. Chem. Chem. Phys.* **2014**, *16* (11), 5229–5236.
- (11) Lai, H.; Liu, X.; Zeng, F.; Peng, G.; Li, J.; Yi, Z. *ACS Omega* **2020**, *5* (4), 2027–2033.
- (12) Luo, G. G.; Pan, Z. H.; Lin, J. Q.; Sun, D. *Dalt. Trans.* **2018**, *47* (44), 15633–15645.

- (13) Summers, G. H.; Lefebvre, J. F.; Black, F. A.; Stephen Davies, E.; Gibson, E. A.; Pullerits, T.; Wood, C. J.; Zidek, K. *Phys. Chem. Chem. Phys.* **2015**, *18* (2), 1059–1070.
- (14) Zhang, G.; Lan, Z.-A.; Wang, X. *Angew. Chemie Int. Ed.* **2016**, *55* (51), 15712–15727.
- (15) Guiglion, P.; Butchosa, C.; Zwijnenburg, M. A. *Macromol. Chem. Phys.* **2016**, *217* (3), 344–353.
- (16) Xu, C.; Zhang, W.; Tang, J.; Pan, C.; Yu, G. *Front. Chem.* **2018**, *6* (December), 1–12.
- (17) Wang, Y.; Vogel, A.; Sachs, M.; Sprick, R. S.; Wilbraham, L.; Moniz, S. J. A.; Godin, R.; Zwijnenburg, M. A.; Durrant, J. R.; Cooper, A. I.; Tang, J. *Nat. Energy* **2019**, *4* (9), 746–760.
- (18) Wang, L.; Zhang, Y.; Chen, L.; Xu, H.; Xiong, Y. *Adv. Mater.* **2018**, *30* (48), 1–12.
- (19) Jayakumar, J.; Chou, H. H. *ChemCatChem* **2020**, *12* (3), 689–704.
- (20) Dai, C.; Liu, B. *Energy Environ. Sci.* **2020**, *13* (1), 24–52.
- (21) Yong, W. W.; Lu, H.; Li, H.; Wang, S.; Zhang, M. T. *ACS Appl. Mater. Interfaces* **2018**, *10* (13), 10828–10834.
- (22) Wang, Q.; Hisatomi, T.; Katayama, M.; Takata, T.; Minegishi, T.; Kudo, A.; Yamada, T.; Domen, K. *Faraday Discuss.* **2017**, *197*, 491–504.
- (23) Ong, W. J.; Tan, L. L.; Ng, Y. H.; Yong, S. T.; Chai, S. P. *Chem. Rev.* **2016**, *116* (12), 7159–7329.
- (24) Wang, S.; Zhao, H.; Zhao, X.; Zhang, J.; Ao, Z.; Dong, P.; He, F.; Wu, H.; Xu, X.; Shi, L.; Zhao, C.; Wang, S.; Sun, H. *Chem. Eng. J.* **2020**, *381*, 122593.
- (25) Yi, J.; El-Alami, W.; Song, Y.; Li, H.; Ajayan, P. M.; Xu, H. *Chem. Eng. J.* **2020**, *382*, 122812.

- (26) Liu, Y.; Liao, Z.; Ma, X.; Xiang, Z. *ACS Appl. Mater. Interfaces* **2018**, *10* (36), 30698–30705.
- (27) Sprick, R. S.; Bonillo, B.; Clowes, R.; Guiglion, P.; Brownbill, N. J.; Slater, B. J.; Blanc, F.; Zwijnenburg, M. A.; Adams, D. J.; Cooper, A. I. *Angew. Chemie* **2016**, *128* (5), 1824–1828.
- (28) Stegbauer, L.; Schwinghammer, K.; Lotsch, B. V. *Chem. Sci.* **2014**, *5* (7), 2789–2793.
- (29) Banerjee, T.; Haase, F.; Savasci, G.; Gottschling, K.; Ochsenfeld, C.; Lotsch, B. V. *J. Am. Chem. Soc.* **2017**, *139* (45), 16228–16234.
- (30) Pachfule, P.; Acharjya, A.; Roeser, J.; Langenhahn, T.; Schwarze, M.; Schomäcker, R.; Thomas, A.; Schmidt, J. *J. Am. Chem. Soc.* **2018**, *140* (4), 1423–1427.
- (31) Li, L.; Fang, W.; Zhang, P.; Bi, J.; He, Y.; Wang, J.; Su, W. *J. Mater. Chem. A* **2016**, *4* (32), 12402–12406.
- (32) Meier, C. B.; Sprick, R. S.; Monti, A.; Guiglion, P.; Lee, J. S. M.; Zwijnenburg, M. A.; Cooper, A. I. *Polymer (Guildf)*. **2017**, *126*, 283–290.
- (33) Bi, J.; Fang, W.; Li, L.; Wang, J.; Liang, S.; He, Y.; Liu, M.; Wu, L. *Macromol. Rapid Commun.* **2015**, *36* (20), 1799–1805.
- (34) Woods, D. J.; Hillman, S.; Pearce, D.; Wilbraham, L.; Flagg, L.; Duffy, W.; McCulloch, I.; Durrant, J.; Guilbert, A.; Zwijnenburg, M.; Sprick, R. S.; Nelson, J.; Cooper, A. *Energy Environ. Sci.* **2020**, *13*, 1843–1855.
- (35) Sprick, R. S.; Jiang, J. X.; Bonillo, B.; Ren, S.; Ratvijitvech, T.; Guiglion, P.; Zwijnenburg, M. A.; Adams, D. J.; Cooper, A. I. *J. Am. Chem. Soc.* **2015**, *137* (9), 3265–3270.
- (36) Chen, L.; Honsho, Y.; Seki, S.; Jiang, D. *J. Am. Chem. Soc.* **2010**, *132* (19), 6742–6748.
- (37) Jiang, Y.; McNeill, J. *Chem. Rev.* **2017**, *117* (2), 838–859.

- (38) Loudet, A.; Burgess, K. *Chem. Rev.* **2007**, *107* (11), 4891–4932.
- (39) Azov, V. A.; Schlegel, A.; Diederich, F. *Angew. Chemie - Int. Ed.* **2005**, *44* (29), 4635–4638.
- (40) Wan, C. W.; Burghart, A.; Chen, J.; Bergström, F.; Johansson, L. B. .; Wolford, M. F.; Kim, T. G.; Topp, M. R.; Hochstrasser, R. M.; Burgess, K. *Chem. - A Eur. J.* **2003**, *9* (18), 4430–4441.
- (41) Kim, T. G.; Castro, J. C.; Loudet, A.; Jiao, J. G. S.; Hochstrasser, R. M.; Burgess, K.; Topp, M. R. *J. Phys. Chem. A* **2006**, *110* (1), 20–27.
- (42) Ziesel, R.; Goze, C.; Ulrich, G.; Césarío, M.; Retailleau, P.; Harriman, A.; Rostron, J. P. *Chem. - A Eur. J.* **2005**, *11* (24), 7366–7378.
- (43) Noël Boens , Bram Verbelen, and W. D. *European J. Org. Chem.* **2015**, 6577–6595.
- (44) Boens, N.; Verbelen, B.; Ortiz, M. J.; Jiao, L.; Dehaen, W. *Coord. Chem. Rev.* **2019**, 399.
- (45) Ulrich, G.; Ziesel, R.; Harriman, A. *Angew. Chemie - Int. Ed.* **2008**, *47* (7), 1184–1201.
- (46) Zhang, X. F.; Zhu, J. J. *Lumin.* **2019**, *205* (April 2018), 148–157.
- (47) Zhao, J.; Xu, K.; Yang, W.; Wang, Z.; Zhong, F. *Chem. Soc. Rev.* **2015**, *44* (24), 8904–8939.
- (48) Banfi, S.; Nasini, G.; Zaza, S.; Caruso, E. *Tetrahedron* **2013**, *69* (24), 4845–4856.
- (49) Guzow, K.; Kornowska, K.; Wiczak, W. *Tetrahedron Lett.* **2009**, *50* (24), 2908–2910.
- (50) Donuru, Venkat R. Vegesna, Giri. K, Velayudham, Ge Meng, Liu, H. *J. Polym. Sci. Part A Polym. Chem.* **2009**, *47*, 5354–5366.
- (51) Donuru, V. R.; Vegesna, G. K.; Velayudham, S.; Green, S.; Liu, H. *Chem.*

- Mater.* **2009**, *21* (10), 2130–2138.
- (52) Alemdaroglu, F. E.; Alexander, S. C.; Ji, D.; Prusty, D. K.; Borsch, M.; Herrmann, A. *Macromolecules* **2009**, *42* (17), 6529–6536.
- (53) Squeo, B. M.; Gregoriou, V. G.; Avgeropoulos, A.; Baysec, S.; Allard, S.; Scherf, U.; Chochos, C. L. *Prog. Polym. Sci.* **2017**, *71*, 26–52.
- (54) Sabatini, R. P.; Lindley, B.; McCormick, T. M.; Lazarides, T.; Brennessel, W. W.; McCamant, D. W.; Eisenberg, R. *J. Phys. Chem. B* **2016**, *120* (3), 527–534.
- (55) Luo, G. G.; Lu, H.; Zhang, X. L.; Dai, J. C.; Wu, J. H.; Wu, J. J. *Phys. Chem. Chem. Phys.* **2015**, *17* (15), 9716–9729.
- (56) Xie, A.; Pan, Z. H.; Yu, M.; Luo, G. G.; Sun, D. *Chinese Chem. Lett.* **2019**, *30* (1), 225–228.
- (57) Dura, L.; Wächtler, M.; Kupfer, S.; Kübel, J.; Ahrens, J.; Höfler, S.; Bröring, M.; Dietzek, B.; Beweries, T. *Inorganics* **2017**, *5* (2), 21.
- (58) Lazarides, T.; McCormick, T. M.; Wilson, K. C.; Lee, S.; Mccamant, D. W.; Eisenberg, R. *J. Am. Chem. Soc.* **2011**, *133* (ii), 350–364.
- (59) Luo, G. G.; Fang, K.; Wu, J. H.; Mo, J. *Chem. Commun.* **2015**, *51* (62), 12361–12364.
- (60) Zheng, B.; Sabatini, R. P.; Fu, W.-F.; Eum, M.-S.; Brennessel, W. W.; Wang, L.; McCamant, D. W.; Eisenberg, R. *Proc. Natl. Acad. Sci.* **2015**, *112* (30), E3987–E3996.
- (61) Bartelmess, J.; Francis, A. J.; El Roz, K. A.; Castellano, F. N.; Weare, W. W.; Sommer, R. D. *Inorg. Chem.* **2014**, *53* (9), 4527–4534.
- (62) Sabatini, R. P.; McCormick, T. M.; Lazarides, T.; Wilson, K. C.; Eisenberg, R.; McCamant, D. W. *J. Phys. Chem. Lett.* **2011**, *2* (3), 223–227.
- (63) Suryani, O.; Higashino, Y.; Sato, H.; Kubo, Y. *ACS Appl. Energy Mater.* **2019**, *2* (1), 448–458.

- (64) Black, F. A.; Clark, C. A.; Summers, G. H.; Clark, I. P.; Towrie, M.; Penfold, T.; George, M. W.; Gibson, E. A. *Phys. Chem. Chem. Phys.* **2017**, *19* (11), 7877–7885.
- (65) Li, Y.; Yang, L.; Du, M.; Chang, G. *Analyst* **2019**, *144* (4), 1260–1264.
- (66) Godoy, J.; Vives, G.; Tour, J. M. *Org. Lett.* **2010**, *12* (7), 1464–1467.
- (67) Redmond, R. W.; Gamlin, J. N. *Photochem. Photobiol.* **1999**, *70* (4), 391–475.
- (68) Greetham, G. M.; Burgos, P.; Qian, C.; Clark, I. P.; Codd, P. S.; Farrow, R. C.; George, M. W.; Kogimtzis, M.; Matousek, P.; Parker, A. W.; Pollard, M. R.; Robinson, D. A.; Zhi-Jun, X.; Towrie, M. *Appl. Spectrosc.* **2010**, *64* (12), 1311–1319.
- (69) Meng, G.; Velayudham, S.; Smith, A.; Luck, R.; Liu, H. *Macromolecules* **2009**, *42* (6), 1995–2001.
- (70) Khetubol, A.; Van Snick, S.; Clark, M. L.; Fron, E.; Coutiño-González, E.; Cloet, A.; Kennes, K.; Firdaus, Y.; Vlasselaer, M.; Leen, V.; Dehaen, W.; Van Der Auweraer, M. *Photochem. Photobiol.* **2015**, *91* (3), 637–653.
- (71) Bucher, L.; Aly, S. M.; Desbois, N.; Karsenti, P. L.; Gros, C. P.; Harvey, P. D. *J. Phys. Chem. C* **2017**, *121* (12), 6478–6490.
- (72) Wanwong, S.; Surawatanawong, P.; Khumsubdee, S.; Kanchanakungwankul, S.; Wootthikanokkhan, J. *Heteroat. Chem.* **2016**, *27* (5), 306–315.
- (73) Wu, W.; Guo, H.; Wu, W.; Ji, S.; Zhao, J. *J. Org. Chem.* **2011**, *76* (17), 7056–7064.
- (74) Krumova, K.; Cosa, G. *J. Am. Chem. Soc.* **2010**, *132* (49), 17560–17569.
- (75) Chen, K.; Dong, Y.; Zhao, X.; Imran, M.; Tang, G.; Zhao, J.; Liu, Q. *Front. Chem.* **2019**, *7* (December), 1–14.
- (76) Filatov, M. A. *Org. Biomol. Chem.* **2020**, *18* (1), 10–27.
- (77) Economopoulos, S. P.; Chochos, C. L.; Ioannidou, H. A.; Neophytou, M.;

- Charilaou, C.; Zissimou, G. A.; Frost, J. M.; Sachetan, T.; Shahid, M.; Nelson, J.; Heeney, M.; Bradley, D. D. C.; Itskos, G.; Koutentis, P. A.; Choulis, S. A. *RSC Adv.* **2013**, *3* (26), 10221–10229.
- (78) Donuru, V. R.; Zhu, S.; Green, S.; Liu, H. *Polymer (Guildf)*. **2010**, *51* (23), 5359–5368.
- (79) Piatkowski, P.; Moreno, M.; Liras, M.; Sánchez, F.; Douhal, A. *J. Mater. Chem. C* **2019**, *7* (26), 7872–7884.
- (80) Kee, H. L.; Kirmaier, C.; Yu, L.; Thamyongkit, P.; Youngblood, W. J.; Calder, M. E.; Ramos, L.; Noll, B. C.; Bocian, D. F.; Scheldt, W. R.; Birge, R. R.; Lindsey, J. S.; Holten, D. *J. Phys. Chem. B* **2005**, *109* (43), 20433–20443.
- (81) Suhina, T.; Amirjalayer, S.; Woutersen, S.; Bonn, D.; Brouwer, A. M. *Phys. Chem. Chem. Phys.* **2017**, *19* (30), 19998–20007.
- (82) Lee, Y.; Malamakal, R. M.; Chenoweth, D. M.; Anna, J. M. *J. Phys. Chem. Lett.* **2020**, *11* (3), 877–884.
- (83) Sabatini, R. P.; McCormick, T. M.; Lazarides, T.; Wilson, K. C.; Eisenberg, R.; McCamant, D. W. *J. Phys. Chem. Lett.* **2011**, *2* (3), 223–227.
- (84) Zhang, T.; Ma, X.; Tian, H. *Chem. Sci.* **2020**, *11* (2), 482–487.
- (85) DeRosa, M. C.; Crutchley, R. J. *Coord. Chem. Rev.* **2002**, *233–234*, 351–371.
- (86) McDonnell, S. O.; Hall, M. J.; Allen, L. T.; Byrne, A.; Gallagher, W. M.; O’Shea, D. F. *J. Am. Chem. Soc.* **2005**, *127* (47), 16360–16361.
- (87) Schoder, S.; Kord Daoroun Kalai, S.; Reissig, H. U. *Chem. - A Eur. J.* **2017**, *23* (51), 12527–12533.
- (88) Bandyopadhyay, S.; Anil, A. G.; James, A.; Patra, A. *ACS Appl. Mater. Interfaces* **2016**, *8* (41), 27669–27678.
- (89) Zhu, Y.; Ji, Y. J.; Wang, D. G.; Zhang, Y.; Tang, H.; Jia, X. R.; Song, M.; Yu, G.; Kuang, G. C. *J. Mater. Chem. A* **2017**, *5* (14), 6622–6629.

- (90) Zhu, Mei, Jiang, Li, Yuan, Mingjian, Liu, Xiaofeng, Ouyang, Cabin, Zheng, Haiuan, Yin, Ziaodong, Zuo, Zicheng, Liu, Huibiao, Li, Y. *J. Polym. Sci. Part A Polym. Chem.* **2008**, *46*, 7401–7410.
- (91) Pellegrin, Y.; Odobel, F. *Comptes Rendus Chim.* **2017**, *20* (3), 283–295.
- (92) Creutz, C. *Inorg. Chem.* **1981**, *20* (12), 4449–4452.
- (93) Reynal, A.; Pastor, E.; Gross, M. A.; Selim, S.; Reisner, E.; Durrant, J. R. *Chem. Sci.* **2015**, *6* (8), 4855–4859.
- (94) Artero, V.; Chavarot-Kerlidou, M.; Fontecave, M. *Angew. Chemie - Int. Ed.* **2011**, *50* (32), 7238–7266.
- (95) Suryani, O.; Higashino, Y.; Sato, H.; Kubo, Y. *ACS Appl. Energy Mater.* **2019**, *2* (1), 448–458.
- (96) Lazarides, T.; McCormick, T.; Du, P.; Luo, G.; Lindley, B.; Eisenberg, R. *J. Am. Chem. Soc.* **2009**, *131* (26), 9192–9194.
- (97) Willkomm, J.; Reisner, E. *Bull. Japan Soc. Coord. Chem.* **2018**, *71* (0), 18–29.
- (98) Yang, C.; Ma, B. C.; Zhang, L.; Lin, S.; Ghasimi, S.; Landfester, K.; Zhang, K. A. I.; Wang, X. *Angew. Chemie - Int. Ed.* **2016**, *55* (32), 9202–9206.
- (99) Ho, P. Y.; Mark, M. F.; Wang, Y.; Yiu, S. C.; Yu, W. H.; Ho, C. L.; McCamant, D. W.; Eisenberg, R.; Huang, S. *ChemSusChem* **2018**, *11* (15), 2517–2528.
- (100) Woods, D. J.; Sprick, R. S.; Smith, C. L.; Cowan, A. J.; Cooper, A. I. *Adv. Energy Mater.* **2017**, *7* (22), 1–6.
- (101) Zannotti, M.; Benazzi, E.; Stevens, L. A.; Minicucci, M.; Bruce, L.; Snape, C. E.; Gibson, E. A.; Giovannetti, R. *ACS Appl. Energy Mater.* **2019**, *2* (10), 7345–7353.

Chapter 3

Exploiting a neutral BODIPY copolymer as an effective agent for photodynamic antimicrobial inactivation

This work was published in *J. Phys. Chem. B.* 2021, **125**, 1550-1557.

Aoibhín A. Cullen, Ashwene Rajagopal, Katharina Heintz, Conor Long, Andreas Heise, Robert Murphy, Igor V. Sazanovich, Gregory M. Greetham, Michael Towrie, Deirdre Fitzgerald-Hughes* and Mary T. Pryce*.

Within this work, I contributed towards the overall synthesis of the copolymer and the full characterisation. Dr. Ashwene Rajagopal carried out both the solution and surface based antimicrobial studies in the Royal College of Surgeons, Ireland. I specifically contributed towards the following sections: experimental design, steady-state photophysical measurements, photoluminescent studies, time-resolved spectroscopies, and data interpretation. I contributed towards writing the manuscript. Supporting information associated with this chapter can be found in Appendix B.

3.1 Abstract

We report the synthesis and photophysical properties of a neutral BODIPY photosensitizing copolymer (poly-8-(4-hydroxymethylphenyl)-4,4-difluoro-2,6-diethynyl-4-bora-3a,4a-diaza-s-indacene) containing ethynylbenzene links between the BODIPY units. The copolymer absorbs further towards the red compared to the BODIPY precursor. Photolysis of the polymer produces a singlet excited state which crosses to the triplet surface in less than 300 ps. This triplet state was used to form singlet oxygen with a quantum yield of 0.34. The steps leading to population of the triplet state were studied using time resolved spectroscopic techniques spanning the pico- to nano-second timescales. The ability of the BODIPY polymer to generate a biocidal species, for bactericidal activity in both solution and coating based studies was assessed. When the BODIPY copolymer was dropcast onto a surface, 4 log and 6 log reductions in colony forming units/ml representative of Gram-positive and Gram-negative bacteria respectively under illumination at 525 nm were observed. The potent broad-spectrum antimicrobial activity of a neutral metal free copolymer when exposed to visible light conditions may have potential clinical applications in infection management.

3.2 Introduction

The increasing resistance of bacterial pathogens to antibiotics is a growing problem particularly in healthcare settings.^{1,2} Conventional antibiotics target the cell wall, DNA, and protein syntheses all of which are critical to bacterial survival. Unfortunately, infections such as those caused by methicillin-resistant *Staphylococcus aureus* or β -lactamase producing Enterobacterials are increasing, and the effectiveness of many antibiotics in clinical use are declining.³ Alternative multimodal approaches are now required to manage these life-changing or life-threatening infections.⁴

Photodynamic therapies have been used in various cancer treatments⁵⁻⁹ In contrast antimicrobial photodynamic therapies (aPDT) are less well developed although interest in this approach is increasing. These therapies rely on a mechanism that involves the production of reactive oxygen species (ROS), mainly singlet oxygen, which disrupts the bacterial cell membrane and other critical cellular processes.¹⁰ In the aPDT approach, photosensitizers are required to absorb photon energies in an appropriate spectral region. Photosensitizers (PS) with extensive π -conjugation such as porphyrins, (tetrapyrrole macrocycles resembling biological organic components),^{11,12} chlorins and phthalocyanines,¹³⁻¹⁵ have been used in aPDT and several of these have been approved for clinical use or are currently in clinical trials.¹⁶ The excellent photophysical properties such as high molar extinction coefficient in the visible region, long emission wavelength, high fluorescence quantum yield, photostability and low dark toxicity have ensured an increased interest in the use of boron-dipyrromethenes (BODIPYs) as photosensitizers. In addition, the chemical versatility of BODIPYs, enables a fine tuning of the photophysical processes by changing the nature and location of substituents on the BODIPY core. BODIPY derivatives have found applications in therapeutics, theragnostics, drug delivery agents, fluorescent switches, and other industrial applications.¹⁷⁻²¹

Singlet oxygen is generated by energy transfer from a triplet state photosensitizer (^3PS).^{22,23} However, excitation of BODIPY compounds produces singlet excited states which emit with high fluorescence quantum yields (Φ_{fl}).^{17,24} Nonetheless, the synthetic versatility of the BODIPY core provides several approaches to enhance

triplet state formation. One of these is to introduce a heavy element, such as iodine, which promotes greater spin-orbit coupling and crossing to the triplet manifold following excitation. While this synthetic modification enhances antimicrobial activity, it also results in high levels of dark toxicity, which is undesirable in therapeutic applications.^{25–31}

There are a few reports of heavy-atom-free BODIPY systems which can generate triplet excited states.^{19,32–38} The structural modifications to the BODIPY core required to promote triplet formation have been reviewed recently.^{21,39–42} Orlandi et al. reported that introducing cationic pyridinium groups to the *meso* position in the BODIPY core can enhance their performance in aPDTs.⁴³

An alternative approach is to add an acceptor or donor site to the BODIPY core. Excited states involving charge transfer to/from the BODIPY core are then accessible.⁴⁴ The addition of extended conjugation allows the charge separation in these excited states to be increased, and this promotes crossing to the triplet surface.⁴⁵ Extended conjugation of this type also results in a red shift of the absorption bands towards the “therapeutic window”.^{46,47} Li et al. showed that cationic polymers based on copolymerization of BODIPY with 2-(dimethylamino)ethylmethacrylate and galactose produce extensive PDT activity and increased cytocompatibility in dark conditions.^{48–50} Cationic BODIPY compounds have exhibited improved aPDT performance when polyamidoamines are used as adjuvants. Increased penetration of the lipid-rich layers of the outer membrane/cytoplasmic membrane was observed under these conditions. Copolymers of the BODIPY core with π -conjugated comonomers have lower band gaps and better optical properties including broader absorption profiles.^{47,51}

Building on these studies, we have synthesized a π -conjugated BODIPY copolymer with 1,4-diethynylbenzene. The BODIPY core contains a phenyl alcohol at the *meso*-position. The photophysical properties of the copolymer were investigated using both pico-second (ps) and nano-second (ns) transient absorption and time-resolved infrared spectroscopy. The polymer was assessed for antibacterial activity under visible light irradiation, with a resulting log 4–6 reduction against Gram-positive, and Gram-

negative bacteria, including multi-drug resistant strains. To our knowledge, this is the first example of a copolymer that does not contain a metal or heavy atom that demonstrates potent antimicrobial properties in combination with visible light.

3.3 Results and Discussion

3.3.1 Synthesis

The copolymer was synthesized using Sonogashira coupling between the diiodo BODIPY (**Figure 3.1** (a)) and a diethynylbenzene comonomers (Appendix B, **Section S3.2**). Size exclusion chromatography (SEC) revealed a monomodal weight distribution with some high molecular weight tailing (**Figure S3.4**). While exact molar masses cannot be determined due to the structural discrepancy between the calibration standard PMMA and the copolymer structure, SEC analysis confirms the successful formation of the copolymeric material. However, the presence of some low molecular weight oligomeric structures is also likely. **Figure 3.1** (b) represents the model BODIPY-2H which was used as a model for the photosensitizer and **Figure 3.1** (c) represents the repeat unit of the copolymer. (Appendix B, **Section S3.2** and **Section S3.3**).

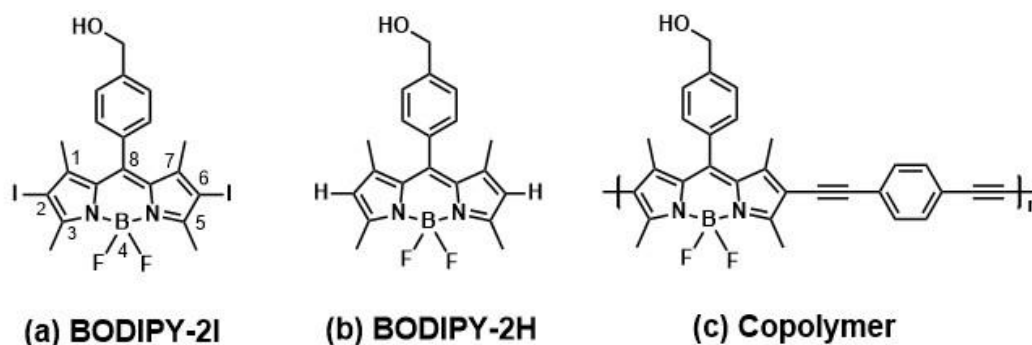


Figure 3.1. a) Chemical structure of 2,6-diiodo-8-(4-hydroxymethylphenyl)-4,4'-difluoro-1,3,5,7-tetramethyl-4-bora-3a,4a-diaza-s-indacene (BODIPY-2I), (b) 8-(4-hydroxymethylphenyl)-4,4'-difluoro-1,3,5,7-tetramethyl-4-bora-3a,4a-diaza-s-indacene (BODIPY-2H), and (c) the repeat unit of the copolymer.

3.3.2 Photophysical properties

The UV-Visible spectrum for the BODIPY-2H ($\lambda_{\text{max}} = 503 \text{ nm}$) is typical for BODIPY compounds. The lowest energy absorption populates the lowest energy singlet excited state. In comparison, the copolymer exhibits a λ_{max} at 574 nm and the absorption band is broader (**Figure 3.2**). This can be explained by enhanced conjugation along the backbone of the copolymer^{52,53}

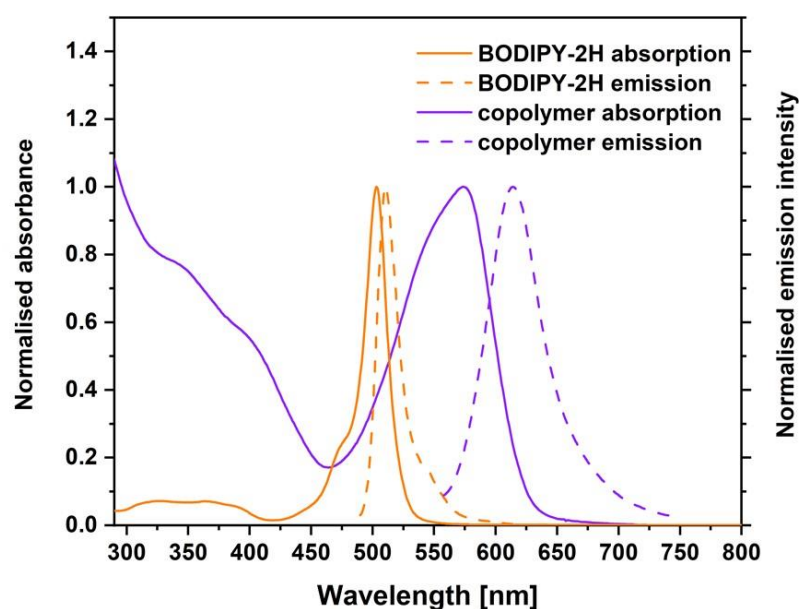


Figure 3.2. Normalised UV-visible absorption spectra of BODIPY-2H (orange solid line), copolymer (purple solid line) and normalized emission spectra of BODIPY-2H (orange dashed line) and copolymer (purple dashed line). Excitation wavelength corresponding to the maxima of the lowest energy absorption band for both systems. All spectra recorded in CH_2Cl_2 at room temperature.

The photophysical properties of BODIPY-2H were measured in a variety of solvents, (Section S3.4, S3.5, S3.6), and are typical of BODIPY compounds. The fluorescence quantum yield (Φ_{fl}) of 0.75 is typical of BODIPY compounds, where fluorescence efficiency close to unity is widely reported with emission lifetimes of 5 ns or less.^{54–56} The emission lifetime of BODIPY-2H was measured at 5.80 ns (± 0.09 ns) and this is consistent with previous reports. In the case of the copolymer, a red shift in the emission maxima was also observed when compared to BODIPY-2H, together with a large Stokes shift of the emission (1128 cm^{-1} compared to 273 cm^{-1} for BODIPY-2H) (Figure 3.2). In addition, the luminescence quantum yield for the copolymer was considerably lower at 0.17 than for BODIPY-2H. This difference suggests the presence of a radiationless pathway to deactivate the lowest energy singlet excited state in the copolymer which is not available to BODIPY-2H. This involves a transition to the triplet surface possibly by way of a singlet fission process.^{57–62} Emission lifetime measurements for the co-polymer suggest that the emission follows a biexponential decay profile yielding two lifetimes ($\tau_{\text{fl}} = 0.90\text{ ns}$ (± 0.03 ns) and 2.89 ns (± 0.05 ns)). One explanation for these emissions is that they originate from spin correlated triplet pairs produced in the singlet fission process. Such triplet pairs are

known to emit weakly.^{63–66} The observation of two emissive species suggests the presence of two emissive conformations on the co-polymer backbone, with one more localized near the BODIPY units and the other delocalized along the co-polymer backbone.

Following excitation of the copolymer at 525 nm, the characteristic emission band of singlet oxygen (~ 1270 nm) was observed, with a quantum yield (Φ_{Δ}) of 0.34 (see **Table 3.1, Section S3.6, Figure S3.8**), using rose bengal as the standard.^{22,67,68} This observation, further confirms that a triplet state must be populated, in this copolymer. In contrast, similar excitation of BODIPY-2H produced no detectable singlet oxygen, which is in agreement with the literature.

Table 3.1. Photophysical properties of BODIPY 2-H and copolymer carried out in CH_2Cl_2 .

Compound	λ_{abs} (nm)	λ_{em} (nm)	$\Phi_{\text{fl}}^{\text{c}}$	τ^{d}	Φ_{Δ}^{e}
BODIPY-2H	503	510 ^a	0.75	5.80 \pm 0.09	-
Copolymer	574	614 ^b	0.17	0.90 \pm 0.03, 2.89 \pm 0.05	0.34

^a $\lambda_{\text{exc}} = 490$ nm, ^b $\lambda_{\text{exc}} = 560$ nm, ^c3-pyridine H-BODIPY used as standard: $\Phi_{\text{fl}} = 0.62$ in CH_2Cl_2 ,⁶⁹ ^d $\lambda_{\text{exc}} = 510$ nm, ^eRose Bengal used as standard: $\Phi_{\Delta} = 0.53$ in CH_3CN .⁷⁰ For full experimental details see Appendix B.

3.3.3 Picosecond transient absorption (ps-TA)

Excitation of the copolymer at 525 nm resulted in a ground state bleach (GSB) for all solvent systems investigated, with concomitant formation of an excited state absorption (ESA) at approximately 450 nm. On this timescale, the GSB overlaps with the stimulated emission (SE), which occurs in the region 500 – 750 nm for the copolymer (**Figure 3.3** (a)). Notably, changing the solvent polarity does not significantly affect the transient absorption spectra. Global analysis of the transient-data matrix produces revealed three components (**Figure S3.10** and **Table 3.2**). The first component which decays over 4 – 20 ps (depending on the solvent) is assigned to a very rapid structural change to the copolymer.^{71–73} The second component, (τ_2), has lifetimes in the range 200 – 280 ps depending on the solvent, is the optically populated

singlet excited state. This decays to produce the triplet state. If a singlet fission mechanism pertains, the persistent triplet absorption may initially involve spin correlated triplet pairs. Alternatively as described in recent studies, twisted intramolecular charge-transfer states may be involved as precursors to the triplet state.^{74,75}

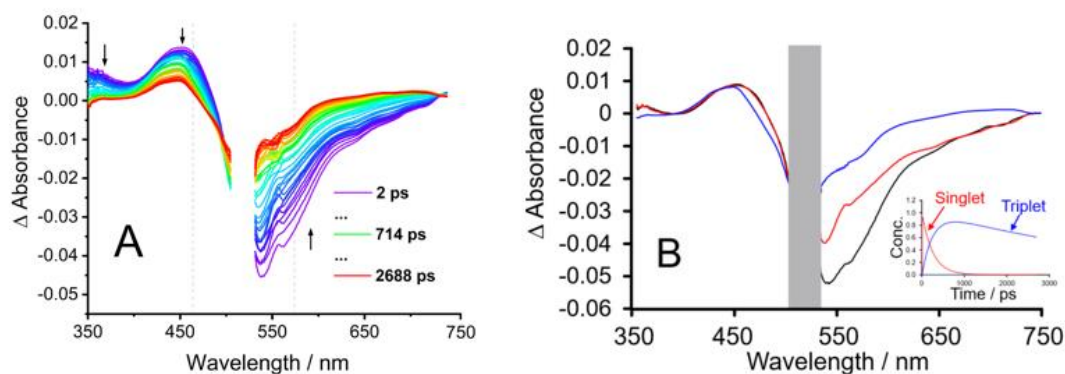


Figure 3.3. a) Transient absorption (TA) spectra of the copolymer in acetonitrile, and b) EAS in acetonitrile. $\lambda_{exc} = 525$ nm (0.4 μ J/pulse) (the gap in the TA plots corresponds to the excitation wavelength which is masked by a narrow band pass filter).

BODIPY-2I reveal significant differences in the excited state spectra of both the copolymer and BODIPY-2H. Initially, an ESA feature is apparent at 472 nm corresponding to the singlet excited state (S_1), which undergoes intersystem crossing (ISC) to the triplet state (τ of S_1 *ca.* 146 ps) (**Figure S3.9**). TA studies of other halogenated BODIPY compounds report similar spectroscopic features which have been assigned to a triplet excited states.^{20,76} While, the TA studies indicate that both the copolymer and BODIPY-2I form a triplet excited state, the time resolved experiments indicate that in the case of the copolymer the photophysics is much complex. While the precise mechanism for the formation of triplet excited states within the copolymer remains uncertain, a number of possible mechanisms exist including the formation of charge-transfer excited states which is known for many BODIPY compounds, but another possibility includes singlet fission.

The photophysics of BODIPY-2H is less complex than those of either BODIPY-2I or the copolymer. Following excitation of BODIPY-2H, a GSB occurs, together with an ESA feature that is produced at 430 nm (**Figure S3.11**) corresponding to the lowest energy singlet excited state (S_1). This absorption decays on a timescale similar to the

emission lifetime (5.8 ns, **Table 3.1**) although it is not possible to monitor the full decay because the emission lifetime lies outside the time response window of the TA apparatus (3 ns).

Table 3.2. Summary of lifetimes obtained using global analysis from psTAS experiments in different solvents following excitation at 525 nm. The Reichardt parameter $E_T(30)$ is shown to indicate solvent polarity.⁷⁷

Solvent	$E_T(30)$	λ_{\max} (of ESA)	τ_1 (ps)	τ_2 (ps)
CD ₃ CN	45.6	464 nm	4 ± 0.1	251 ± 6
d ₆ -DMSO	45.1	461 nm	14 ± 0.3	219 ± 5
CD ₂ Cl ₂	40.7	459 nm	26 ± 0.6	287 ± 5

3.3.4 Nanosecond transient absorption (ns-TA)

Nanosecond transient absorption spectra were measured in acetonitrile following freeze pump thawing of the samples and excitation at 355 nm using a LP980 transient absorption spectrometer (Edinburgh instruments as described in Appendix B). These studies confirmed the formation of a long-lived excited state. The spectral features obtained in these experiments are similar to the persistent species observed in the psTA experiments ($\lambda_{\text{exc}} = 525$ nm). An excited state absorption is evident in the range 420 – 470 nm, together with a bleach in the range of 500 – 550 nm, similar to that in the psTA studies. The recovery of the parent bleach occurs with the same rate as the band at 440 nm decays (inset in **Figure 3.4**). These spectra are consistent with the decay of a triplet species with $\tau_T = 32$ μ s (**Figure 3.4**).

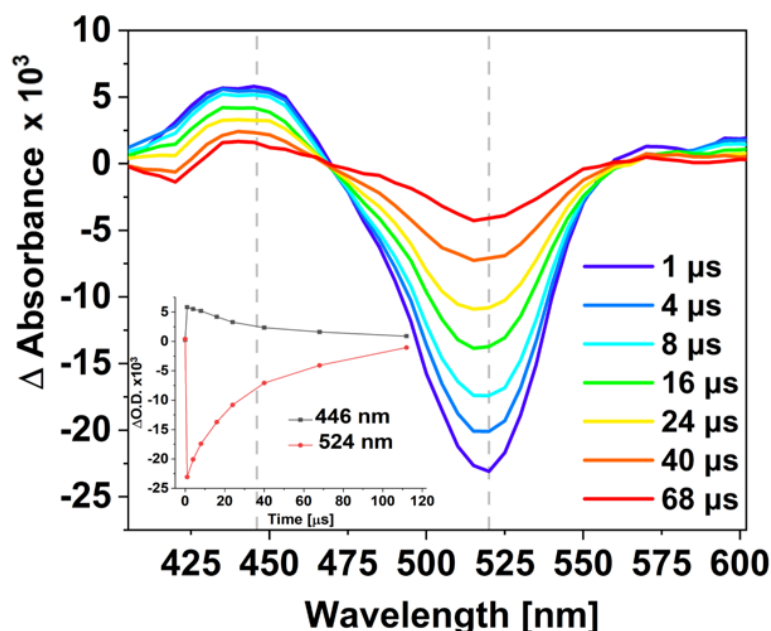


Figure 3.4. TA spectra of the copolymer in CH_3CN at different time delays ($< 1 \mu\text{s}$ - $68 \mu\text{s}$). Sample was degassed using three freeze-pump-thaw cycles. Grey dashed line on TA spectra indicates the wavelengths chosen for the kinetic traces shown in the inset which were used to determine the decay lifetimes.

3.3.5 Time resolved infrared spectroscopy

Displayed in **Figure 3.5** (a) are the time-resolved infrared spectra (TRIR) of the copolymer following excitation at 525 nm in CD_3CN . Following excitation, bleaching of the parent (attributed to the BODIPY core mixed with the phenyl modes) is evident at 1552, 1469 and 1308 cm^{-1} together with new features at 1574, 1498, 1452, 1366, and 1261 cm^{-1} . Further features appear at 1552, 1469 and 1308 cm^{-1} .⁷⁸ Global analysis of the data matrix revealed using a sequential model two components, the first is assigned to the S_1 species which decays with a lifetime of $114 \pm 5 \text{ ps}$ forming a second persistent component assigned to the triplet excited state (**Figure 3.5** (b)). The spectra for these two species are displayed in **Figure 3.5**. These results are similar to those obtained in the psTA experiments described above. The TRIR experiments were also carried out in CD_2Cl_2 and DMSO and confirmed that the spectral features were not sensitive to the solvent medium (**Section S3.9**, **Figure S3.13** and **Figure S3.14** respectively).

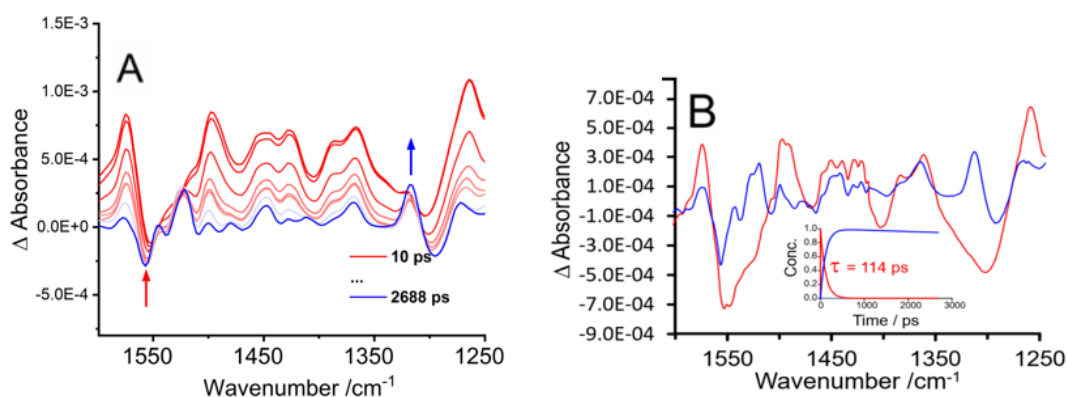


Figure 3.5. a) TRIR spectra of the copolymer in CD_3CN in the spectral window of $1610 - 1250 \text{ cm}^{-1}$ at various time delays following excitation at 525 nm and b) and the corresponding EAS.

The TRIR spectra were also obtained for the corresponding BODIPY-2H and BODIPY-2I compounds. In the case of BODIPY-2I, following excitation, depletion of the parent is evident at 1537 cm^{-1} and a band at 1490 cm^{-1} assigned to the singlet species is formed. This latter band decays over 80 ps , giving rise to a further band at 1523 cm^{-1} assigned to the triplet excited-state (that persists on the nanosecond timescale).⁷⁶ In the case of BODIPY-2H, photolysis results in depletion of the parent bands occurs, and new bands at $1551, 1512, 1451, 1416$ and 1276 cm^{-1} are formed. Analysis of the data indicates two components, a short-lived species that decays within 20 ps . As there is no significant shift in the infrared stretching vibrations, these initial IR bands are assigned to structural relaxation from the Franck-Condon state. A further species, assigned to the singlet state (S_1), persists onto the nanosecond time scale (**Figure S3.15** and **Figure S3.16**)

TRIR spectra in the carbon-carbon triple bond region were also obtained. Following excitation (525 nm), the weak parent band at 2203 cm^{-1} was depleted and a more intense feature at 2073 cm^{-1} was produced (**Figure 3.6**). This shift to lower energy indicates decreased electron density on the π linker along the copolymer backbone,⁷⁸ (confirmed from FTIR, **Figure S3.12**). The intensity of the feature at 2073 cm^{-1} relative to the ground-state bleach is large, and can be explained by a considerable change in dipole moment in these excited states.⁷⁹ This is strong evidence to support a charge-transfer character of both singlet and triplet excited state species. This feature decays with concomitant recovery of the parent bleach as indicated by the blue arrows

in **Figure 3.6**. Kinetic analysis of this signal yielded a lifetime of $\tau_1 = 4.9 \pm 5$ ps and $\tau_2 = 131 \pm 20$ ps in CHCl_3 (**Figure S3.17**). A further component that persists well into the ns-timescale ($\gg 3$ ns), is consistent with the formation of a long-lived triplet species. The short-lived component (τ_1) is assigned to a structural change along the polymer back bone, with τ_2 , corresponding to the decay of singlet to form the triplet excited state.

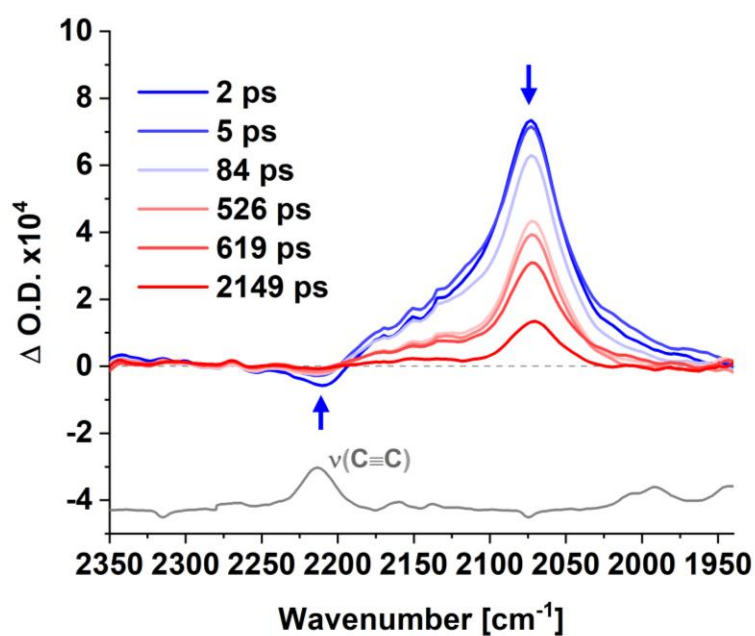


Figure 3.6. TRIR spectra of the copolymer in CHCl_3 following pulsed photolysis ($\lambda_{\text{exc}} = 525$ nm) in the triple bond region recorded at various time delays, with arrows indicating the time dependent behaviour of the spectral features. FTIR of copolymer displayed in the same IR region (grey solid line) for reference.

3.3.6 Antimicrobial photodynamic inactivation

Singlet oxygen generation ($^1\text{O}_2$) has been reported to contribute marked photoactive bactericidal properties to different chromophores.^{80,81} In the present study, for antimicrobial evaluation, a solution based bactericidal assay was performed on laboratory strains of *Staphylococcus aureus* (ATCC 25923), methicillin-resistant *S. aureus* [(MRSA), (ATCC 43300)], *Escherichia coli* (ATCC 25922) and an extended spectrum β -lactamase (ESBL) producing *E. coli* clinical isolate (CL11). Experimental details of assay preparation are provided in the ESI. Solvatochromic studies using UV-visible spectroscopy confirmed stability of the copolymer in DMSO/PBS (PBS = phosphate buffered saline) mixture relevant to the assay conditions (Appendix B,

Figure S3.18). The assays were irradiated under light of wavelength, $\lambda = 525$ nm. Control assays containing no copolymer (growth control) and non-irradiated samples (dark control) were included.

Antibacterial susceptibility testing indicated greater activity of the copolymer compared to the monomer at 1 $\mu\text{g/mL}$ and 5 $\mu\text{g/mL}$ for gram-positive and gram-negative bacteria respectively (**Section S3.10, Figure S3.19**). In darkness, the complexes had a negligible effect on bacterial growth. With light irradiation at 525 nm for ~ 15 min and concentrations of 1 $\mu\text{g/mL}$ and 5 $\mu\text{g/mL}$ of the copolymer resulted in a photoactivated bactericidal effect (**Figure 3.7**). At 1 $\mu\text{g/mL}$, the copolymer led to a $> 80\%$ killing of MRSA and Methicillin-susceptible *S. aureus* (MSSA). Killing of Gram-negatives (*E. coli* and ESBL *E. coli*) was not as effective, even at a higher concentration of 5 $\mu\text{g/mL}$. In contrast, the monomer exhibited negligible antibacterial activity in the same conditions.

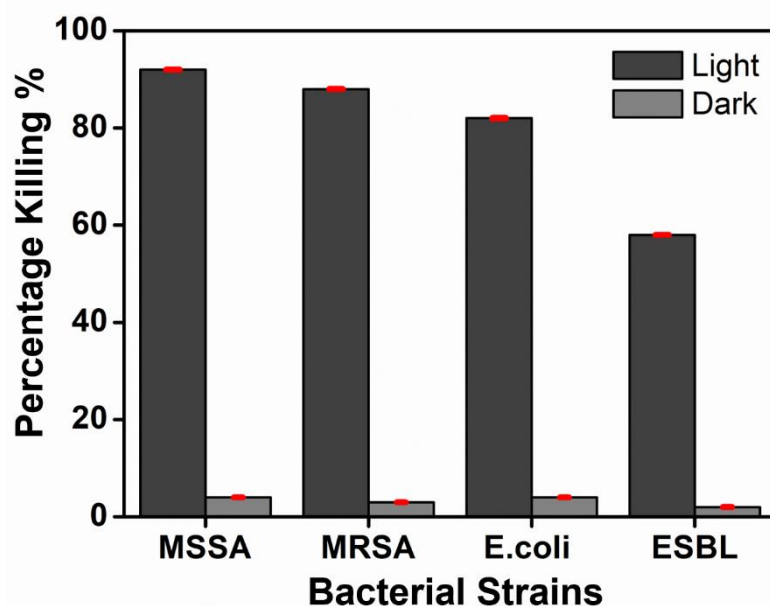


Figure 3.7. Antimicrobial activity of the copolymer under irradiation and non-irradiation conditions, with *S. aureus* (ATCC 25923 and ATCC 43300 (MRSA)) and *E. coli* (ATCC 25922 and CL11 (ESBL)), [copolymer] for *S. aureus*: 1 $\mu\text{g/mL}$, [copolymer] for *E. coli*: 5 $\mu\text{g/mL}$, time of irradiation: 15 minutes, wavelength of light for irradiation $\lambda \sim 525$ nm. Data represent percentage killing (CFU/mL relative to controls) and are the mean \pm SEM of three assays carried out in triplicate.

Concentration dependence of bacterial activity was observed for the copolymer in the range 1-5 $\mu\text{g/mL}$. However, the formation of interconnected aggregates at concentrations of copolymer > 10 $\mu\text{g/mL}$ precluded accurate determination of

antimicrobial activity in solution beyond this concentration. Therefore, the copolymer was drop coated onto surfaces for increased stability and to facilitate investigation of antimicrobial activity at higher concentrations.

Experimentally, the wells of a 96 well plate were drop coated with the copolymer (40 $\mu\text{g}/\text{mL}$) which was air-dried in a laminar flow cabinet before addition of bacterial suspension. Using this method, a homogeneous surface of the copolymer coating was observed with SEM measurement performed before irradiation (**Section S3.3.4, Figure S3.5**). No steric hindrance-associated aggregate formation was observed for the copolymer.⁸² This indicates a more stable improved ordering of the BODIPY core and planarity of copolymer backbone. The surface was irradiated using visible light ($\lambda = 525 \text{ nm}$). Greater bactericidal activity of the copolymer was observed for all bacteria when tested under coating conditions and for longer light exposure times, compared to aqueous conditions. Killing efficacy reached 5-6 log reduction for *E. coli* and 3-4 log reduction for *S. aureus*. Similar killing efficacy observed for the multidrug resistant strains compared to the antibiotic susceptible strains of each genera (**Figure 3.8**). The greater relative killing of *E.coli* compared to *S. aureus* when drop-coated was unexpected as studies of other BODIPYs, albeit in solution have shown lower activity towards Gram-negatives, based on their additional outer membrane.⁸³

Measurement of the copolymer cytotoxicity to cultured human keratinocytes (HaCaT cells) using the MTT assay revealed a IC_{50} value of 45.2 $\mu\text{g}/\text{mL}$ (**Section S3.11, Figure S3.20**). This is the concentration resulting in the loss of viability of up to 50 % of HaCaT cells. This indicates some cytotoxicity to keratinocytes at concentrations close to those that resulted in > 5 log reduction in Gram-negative and > 3 log reduction to Gram-positive bacteria.

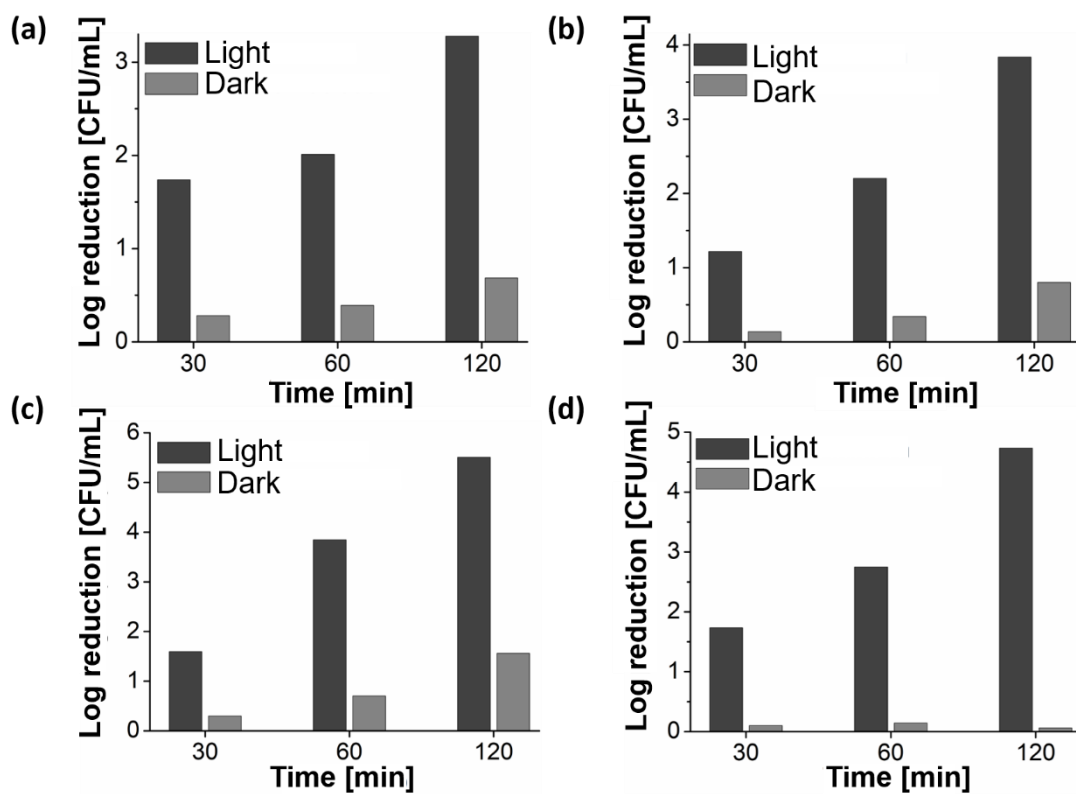


Figure 3.8. Comparison of the antimicrobial activity of drop coated copolymer on 96-well plate under irradiation and non-irradiation conditions for (a) *S. aureus* (ATCC 25923), (b) MRSA (ATCC 43300), (c) *E. coli* (ATCC 25922), (d) ESBL (CL11), [copolymer]: 40 µg/mL, varied irradiation time, wavelength of light for irradiation $\lambda \sim 525$ nm.

3.4 Conclusion

In this work we report a straightforward synthesis of a metal and heavy atom free neutral BODIPY-containing copolymer which has potent biocidal properties when irradiated with visible light ($\lambda > 500$ nm). A detailed investigation into the photophysical properties were performed using ps-ns transient absorption and time resolved infrared spectroscopic techniques, on both the copolymer and the corresponding BODIPY photosensitizers. These studies provided an insight into the photophysical properties of both the copolymer and BODIPY-based photosensitizers. In the case of the copolymer, we have tentatively assigned the pathway to singlet oxygen generation to occur via a singlet fission mechanism. Our research is currently focused on obtaining more definite evidence for this. Under irradiation with visible light, the copolymer produces singlet oxygen which explains the antimicrobial activity of this neutral polymer towards gram-negative bacteria. This work provides us with a basis where singlet fission can be exploited for the development of more potent polymeric-based materials with low cytotoxicity as surface coatings for antimicrobial therapeutics.

3.5 Supporting information

The supplementary data associated with this chapter can be found in Appendix B.

3.6 Bibliography

- (1) Richardson, L. A. *PLoS Biol.* **2017**, *15* (8), 1–5.
- (2) Theuretzbacher, U. *Integr. Med. Res.* **2013**, *1* (2), 63–69.
- (3) Blair, J. M. A.; Webber, M. A.; Baylay, A. J.; Ogbolu, D. O.; Piddock, L. J. V. *Nat. Rev. Microbiol.* **2015**, *13* (1), 42–51.
- (4) C. Lee Ventola, M. *Pharm. Ther.* **2015**, *40* (4), 277–283.
- (5) Sobotta, L.; Skupin-Mrugalska, P.; Piskorz, J.; Mielcarek, J. *Eur. J. Med. Chem.* **2019**, *175*, 72–106.
- (6) Degitz, K. *JDDG - J. Ger. Soc. Dermatology* **2009**, *7* (12), 1048–1054.
- (7) Fu, X.; Bai, H.; Lyu, F.; Liu, L.; Wang, S. *Chem. Res. Chinese Univ.* **2020**, *36* (2), 237–242.
- (8) Dichiarà, M.; Prezzavento, O.; Marrazzo, A.; Pittalà, V.; Salerno, L.; Rescifina, A.; Amata, E. *Eur. J. Med. Chem.* **2017**, *142*, 459–485.
- (9) Symonds, D. A.; Merchenthaler, I.; Flaws, J. A. *Toxicol. Sci.* **2008**, *105* (1), 182–187.
- (10) Dryden, M. *Int. J. Antimicrob. Agents* **2018**, *51* (3), 299–303.
- (11) Mora, S. J.; Cormick, M. P.; Milanesio, M. E.; Durantini, E. N. *Dye. Pigment.* **2010**, *87* (3), 234–240.
- (12) Alves, E.; Faustino, M. A. F.; Neves, M. G. P. M. S.; Cunha, Â.; Nadais, H.; Almeida, A. *J. Photochem. Photobiol. C Photochem. Rev.* **2015**, *22*, 34–57.
- (13) Ochoa, A. L.; Tempesti, T. C.; Spesia, M. B.; Milanesio, M. E.; Durantini, E. N. *Eur. J. Med. Chem.* **2012**, *50*, 280–287.
- (14) Ferreyra, D. D.; Spesia, M. B.; Milanesio, M. E.; Durantini, E. N. *J. Photochem. Photobiol. A Chem.* **2014**, *282*, 16–24.

- (15) Huang, L.; Krayner, M.; Roubil, J. G. S.; Huang, Y. Y.; Holten, D.; Lindsey, J. S.; Hamblin, M. R. *J. Photochem. Photobiol. B Biol.* **2014**, *141*, 119–127.
- (16) Baskaran, R.; Lee, J.; Yang, S.-G. *Biomater. Res.* **2018**, *22* (1), 25.
- (17) Loudet, A.; Burgess, K. *Chem. Rev.* **2007**, *107* (11), 4891–4932.
- (18) Ulrich, G.; Ziesel, R.; Harriman, A. *Angew. Chemie - Int. Ed.* **2008**, *47* (7), 1184–1201.
- (19) Zhao, J.; Xu, K.; Yang, W.; Wang, Z.; Zhong, F. *Chem. Soc. Rev.* **2015**, *44* (24), 8904–8939.
- (20) Chen, K.; Dong, Y.; Zhao, X.; Imran, M.; Tang, G.; Zhao, J.; Liu, Q. *Front. Chem.* **2019**, *7* (December), 1–14.
- (21) Kamkaew, A.; Lim, S. H.; Lee, H. B.; Kiew, L. V.; Chung, L. Y.; Burgess, K. *Chem. Soc. Rev.* **2013**, *42* (1), 77–88.
- (22) DeRosa, M. C.; Crutchley, R. J. *Coord. Chem. Rev.* **2002**, *233–234*, 351–371.
- (23) Fan, W.; Huang, P.; Chen, X. *Chem. Soc. Rev.* **2016**, *45* (23), 6488–6519.
- (24) Zhang, X. F.; Feng, N. *Chem. - An Asian J.* **2017**, *12* (18), 2447–2456.
- (25) Prasannan, D.; Raghav, D.; Sujatha, S.; Hareendrakrishna Kumar, H.; Rathinasamy, K.; Arunkumar, C. *RSC Adv.* **2016**, *6* (84), 80808–80824.
- (26) Ortiz, M. J.; Agarrabeitia, A. R.; Duran-Sampedro, G.; Bañuelos Prieto, J.; Lopez, T. A.; Massad, W. A.; Montejano, H. A.; García, N. A.; Lopez Arbeloa, I. *Tetrahedron* **2012**, *68* (4), 1153–1162.
- (27) Ye, J. H.; Hu, Z.; Wang, Y.; Zhang, W.; Zhang, Y. *Tetrahedron Lett.* **2012**, *53* (50), 6858–6860.
- (28) Zou, J.; Yin, Z.; Ding, K.; Tang, Q.; Li, J.; Si, W.; Shao, J.; Zhang, Q.; Huang, W.; Dong, X. *ACS Appl. Mater. Interfaces* **2017**, *9* (38), 32475–32481.
- (29) Carpenter, B. L.; Situ, X.; Scholle, F.; Bartelmess, J.; Weare, W. W.; Ghiladi,

- R. A. *Molecules* **2015**, *20* (6), 10604–10621.
- (30) Cakmak, Y.; Kolemen, S.; Duman, S.; Dede, Y.; Dolen, Y.; Kilic, B.; Kostereli, Z.; Yildirim, L. T.; Dogan, A. L.; Guc, D.; Akkaya, E. U. *Angew. Chemie Int. Ed.* **2011**, *50* (50), 11937–11941.
- (31) Wang, L.; Wang, J.-W.; Cui, A.; Cai, X.-X.; Wan, Y.; Chen, Q.; He, M.-Y.; Zhang, W. *RSC Adv.* **2013**, *3* (24), 9219–9222.
- (32) Filatov, M. A.; Karuthedath, S.; Polestshuk, P. M.; Savoie, H.; Flanagan, K. J.; Sy, C.; Sitte, E.; Telitchko, M.; Laquai, F.; Boyle, R. W.; Senge, M. O. *J. Am. Chem. Soc.* **2017**, *139* (18), 6282–6285.
- (33) Filatov, M. A. *Org. Biomol. Chem.* **2020**, *18* (1), 10–27.
- (34) Hu, W.; Lin, Y.; Zhang, X. F.; Feng, M.; Zhao, S.; Zhang, J. *Dye. Pigment.* **2019**, *164* (January), 139–147.
- (35) Zhang, X. F. *Dye. Pigment.* **2017**, *146*, 491–501.
- (36) Noël Boens, Bram Verbelen, and W. D. *European J. Org. Chem.* **2015**, 6577–6595.
- (37) Boens, N.; Verbelen, B.; Ortiz, M. J.; Jiao, L.; Dehaen, W. *Coord. Chem. Rev.* **2019**, 399.
- (38) Hu, W.; Zhang, X. F.; Lu, X.; Lan, S.; Tian, D.; Li, T.; Wang, L.; Zhao, S.; Feng, M.; Zhang, J. *Dye. Pigment.* **2018**, *149* (July 2017), 306–314.
- (39) Miao, X.; Hu, W.; He, T.; Tao, H.; Wang, Q.; Chen, R.; Jin, L.; Zhao, H.; Lu, X.; Fan, Q.; Huang, W. *Chem. Sci.* **2019**, *10* (10), 3096–3102.
- (40) Qi, S.; Kwon, N.; Yim, Y.; Nguyen, V. N.; Yoon, J. *Chem. Sci.* **2020**, *11* (25), 6479–6484.
- (41) Awuah, S. G.; You, Y. *RSC Adv.* **2012**, *2* (30), 11169–11183.
- (42) Durantini, A. M.; Heredia, D. A.; Durantini, J. E.; Durantini, E. N. *Eur. J. Med. Chem.* **2018**, *144*, 651–661.

- (43) Caruso, E.; Banfi, S.; Barbieri, P.; Leva, B.; Orlandi, V. T. *J. Photochem. Photobiol. B Biol.* **2012**, *114*, 44–51.
- (44) Gibbons, D. J.; Farawar, A.; Mazzella, P.; Leroy-Lhez, S.; Williams, R. M. *Photochem. Photobiol. Sci.* **2020**, *19* (2), 136–158.
- (45) Duman, S.; Cakmak, Y.; Kolemen, S.; Akkaya, E. U.; Dede, Y. *J. Org. Chem.* **2012**, *77* (10), 4516–4527.
- (46) Bill, N. L.; Lim, J. M.; Davis, C. M.; Bähring, S.; Jeppesen, J. O.; Kim, D.; Sessler, J. L. *Chem. Commun.* **2014**, *50* (51), 6758–6761.
- (47) Popere, B. C.; Della Pelle, A. M.; Thayumanavan, S. *Macromolecules* **2011**, *44* (12), 4767–4776.
- (48) Caruso, E.; Ferrara, S.; Ferruti, P.; Manfredi, A.; Ranucci, E.; Orlandi, V. T. *Lasers Med. Sci.* **2018**, *33* (6), 1401–1407.
- (49) Lu, Z.; Zhang, X.; Wu, Z.; Zhai, T.; Xue, Y.; Mei, L.; Li, C. *RSC Adv.* **2014**, *4* (37), 19495–19501.
- (50) Lu, Z.; Zhang, X.; Zhao, Y.; Xue, Y.; Zhai, T.; Wu, Z.; Li, C. *Polym. Chem.* **2015**, *6* (2), 302–310.
- (51) Alemdaroglu, F. E.; Alexander, S. C.; Ji, D.; Prusty, D. K.; Borsch, M.; Herrmann, A. *Macromolecules* **2009**, *42* (17), 6529–6536.
- (52) Donuru, V. R.; Vegesna, G. K.; Velayudham, S.; Green, S.; Liu, H. *Chem. Mater.* **2009**, *21* (10), 2130–2138.
- (53) Zhu, Mei, Jiang, Li, Yuan, Mingjian, Liu, Xiaofeng, Ouyang, Cabin, Zheng, Haiuan, Yin, Ziaodong, Zuo, Zicheng, Liu, Huibiao, Li, Y. *J. Polym. Sci. Part A Polym. Chem.* **2008**, *46*, 7401–7410.
- (54) Epelde-Elezcano, N.; Palao, E.; Manzano, H.; Prieto-Castañeda, A.; Agarrabeitia, A. R.; Tabero, A.; Villanueva, A.; de la Moya, S.; López-Arbeloa, Í.; Martínez-Martínez, V.; Ortiz, M. J. *Chem. – A Eur. J.* **2017**, *23* (20), 4837–4848.

- (55) Watley, R. L.; Awuah, S. G.; Bio, M.; Cantu, R.; Gobeze, H. B.; Nesterov, V. N.; Das, S. K.; D'Souza, F.; You, Y. *Chem. – An Asian J.* **2015**, *10* (6), 1335–1343.
- (56) Tram, K.; Yan, H.; Jenkins, H. A.; Vassiliev, S.; Bruce, D. *Dye. Pigment.* **2009**, *82* (3), 392–395.
- (57) Smith, M. B.; Michl, J. *Chem. Rev.* **2010**, *110* (11), 6891–6936.
- (58) Smith, M. B.; Michl, J. *Annu. Rev. Phys. Chem.* **2013**, *64*, 361–386.
- (59) Busby, E.; Xia, J.; Wu, Q.; Low, J. Z.; Song, R.; Miller, J. R.; Zhu, X. Y.; Campos, L. M.; Sfeir, M. Y. *Nat. Mater.* **2015**, *14* (4), 426–433.
- (60) Gish, M. K.; Pace, N. A.; Rumbles, G.; Johnson, J. C. *J. Phys. Chem. C* **2019**, *123* (7), 3923–3934.
- (61) Korovina, N. V.; Pompetti, N. F.; Johnson, J. C. *J. Chem. Phys.* **2020**, *152* (4), 1–21.
- (62) Hu, J.; Xu, K.; Shen, L.; Wu, Q.; He, G.; Wang, J. Y.; Pei, J.; Xia, J.; Sfeir, M. Y. *Nat. Commun.* **2018**, *9* (2999), 1–9.
- (63) Lukman, S.; Richter, J. M.; Yang, L.; Hu, P.; Wu, J.; Greenham, N. C.; Musser, A. J. *J. Am. Chem. Soc.* **2017**, *139* (50), 18376–18385.
- (64) Phys, J. C.; He, G.; Busby, E.; Sfeir, M. Y.; Appavoo, K.; Wu, Q.; Campos, L. M. *J. Chem. Phys.* **2020**, *153* (December), 244902–244909.
- (65) Stern, H. L.; Cheminal, A.; Yost, S. R.; Broch, K.; Bayliss, S. L.; Chen, K.; Tabachnyk, M.; Thorley, K.; Greenham, N.; Hodgkiss, J. M.; Anthony, J.; Head-Gordon, M.; Musser, A. J.; Rao, A.; Friend, R. H. *Nat. Chem.* **2017**, *9* (12), 1205–1212.
- (66) Yong, C. K.; Musser, A. J.; Bayliss, S. L.; Lukman, S.; Tamura, H.; Bubnova, O.; Hallani, R. K.; Meneau, A.; Resel, R.; Maruyama, M.; Hotta, S.; Herz, L. M.; Beljonne, D.; Anthony, J. E.; Clark, J.; Sirringhaus, H. *Nat. Commun.* **2017**, *8* (May), 15953.

- (67) Wilkinson, F.; Helman, W. P.; Ross, A. B. *J. Phys. Chem. Ref. Data* **1993**, *22* (1), 113–262.
- (68) Nonell, S.; Flors, C. *Singlet Oxygen: Applications in Biosciences and Nanosciences, Volume 1*; Comprehensive Series in Photochemical & Photobiological Sciences; The Royal Society of Chemistry, 2016; Vol. 1.
- (69) Banfi, S.; Nasini, G.; Zaza, S.; Caruso, E. *Tetrahedron* **2013**, *69* (24), 4845–4856.
- (70) Epelde-Elezcano, N.; Martínez-Martínez, V.; Peña-Cabrera, E.; Gómez-Durán, C. F. A.; Arbeloa, I. L.; Lacombe, S. *RSC Adv.* **2016**, *6* (48), 41991–41998.
- (71) Kee, H. L.; Kirmaier, C.; Yu, L.; Thamyongkit, P.; Youngblood, W. J.; Calder, M. E.; Ramos, L.; Noll, B. C.; Bocian, D. F.; Scheldt, W. R.; Birge, R. R.; Lindsey, J. S.; Holten, D. *J. Phys. Chem. B* **2005**, *109* (43), 20433–20443.
- (72) Suhina, T.; Amirjalayer, S.; Woutersen, S.; Bonn, D.; Brouwer, A. M. *Phys. Chem. Chem. Phys.* **2017**, *19* (30), 19998–20007.
- (73) Pryce, Mary T, Cullen, Aoibhin A.; O'Reilly, Laura, Heintz, Katharina; Long, C.; Heise, A.; Murphy, R.; Gibson, E. A.; Karlsson, Joshua; Towrie, Michael; Greetham, G. M. *Front. Chem.* **2020**, *8* (October), 1–14.
- (74) Dong, Y.; Dick, B.; Zhao, J. *Org. Lett.* **2020**, *22* (14), 5535–5539.
- (75) Hu, W.; Liu, M.; Zhang, X.; Shi, M.; Jia, M.; Hu, X.; Liu, L.; Wang, T. *J. Phys. Chem. C* **2020**.
- (76) Sabatini, R. P.; McCormick, T. M.; Lazarides, T.; Wilson, K. C.; Eisenberg, R.; McCamant, D. W. *J. Phys. Chem. Lett.* **2011**, *2* (3), 223–227.
- (77) Reichardt, C. *Chem. Rev.* **1994**, *94* (8), 2319–2358.
- (78) Black, F. A.; Clark, C. A.; Summers, G. H.; Clark, I. P.; Towrie, M.; Penfold, T.; George, M. W.; Gibson, E. A. *Phys. Chem. Chem. Phys.* **2017**, *19* (11), 7877–7885.

- (79) Dereka, B.; Rosspeintner, A.; Li, Z.; Liska, R.; Vauthey, E. *J. Am. Chem. Soc.* **2016**, *138* (13), 4643–4649.
- (80) Ghorbani, J.; Rahban, D.; Aghamiri, S.; Teymouri, A.; Bahador, A. *Laser Ther.* **2018**, *27* (4), 293–302.
- (81) Le Gall, T.; Lemercier, G.; Chevreux, S.; Tücking, K. S.; Ravel, J.; Thétiot, F.; Jonas, U.; Schönherr, H.; Montier, T. *ChemMedChem* **2018**, *13* (20), 2229–2239.
- (82) Nagai, A.; Miyake, J.; Kokado, K.; Nagata, Y.; Chujo, Y. *J. Am. Chem. Soc.* **2008**, *130* (46), 15276–15278.
- (83) Agazzi, M. L.; Ballatore, M. B.; Reynoso, E.; Quiroga, E. D.; Durantini, E. N. *Eur. J. Med. Chem.* **2017**, *126*, 110–121.

Chapter 4

Singlet fission in a diethynylbenzene-BODIPY copolymer; a time resolved spectroscopic, TD-DFT, electrochemical and hydrogen evolution study

This work is submitted to *Chemical Science*.

Aoibhín A. Cullen, Michael P. Brandon, Ashwene Rajagopal, Ruairí Brannigan, Joshua Karlsson, Michael Towrie, Gregory M. Greetham, Igor V. Sazanovich, Andreas Heise, Elizabeth A. Gibson, Conor Long* and Mary T. Pryce*.

Within this work, I contributed towards the overall synthesis of the copolymer and the full characterisation. Dr. Michael Brandon conducted the electrochemical experiments. Dr. Ashwene Rajagopal gave insight into the photocatalytic hydrogen experiments and deposited the Pt onto the TiO₂ surface. Prof. Conor Long carried out DFT calculations to support singlet fission. I specifically contributed towards the photoluminescent lifetime studies at various excitation wavelengths, time-resolved spectroscopies, hydrogen evolution experiments and writing of the manuscript. Supporting information associated with this chapter can be found in Appendix C.

4.1 Abstract

The synthesis and photophysical properties of a π -conjugated diethynylbenzene-BODIPY copolymer with an anthracenyl unit at the meso position is reported. Extending the π -conjugation at the 2,6 position in the BODIPY copolymer core induces significant changes in the photophysical properties compared to model BODIPY compounds. These include a bathochromic shift (*ca.* + 44 nm) in the UV-vis absorption and a large Stokes shift ($> 2100 \text{ cm}^{-1}$) with weak emission, a reduction in both the optical and electrochemical band gap and the formation of a long-lived triplet state ($\tau_T = 94 \text{ }\mu\text{s}$), and a singlet oxygen quantum yield of 1.1. DFT calculations and time-resolved studies support a mechanism for triplet formation involving intramolecular singlet fission (iSF). The polymer was used as a photosensitiser for hydrogen evolution which in the presence of $\text{TiO}_2 \mid \text{Pt}$ nanoparticles produced $13.9 \text{ mmol H}_2 \text{ g}^{-1}$ after 20 hours irradiation.

4.2 Introduction

Efforts to develop clean, sustainable, and renewable energy sources are urgent challenges for our time. Using solar energy to convert water to molecular hydrogen and oxygen is a viable approach to producing a clean energy store with minimal impact on the environment.¹⁻⁴ Some solar energy converters use triplet photosensitisers (PS) to absorb visible light.^{5,6} Of course these photosensitisers must be robust and generate long-lived excited states with appropriate redox potentials to catalyse the proton reduction half reaction.⁷ Many light absorbing assemblies have been designed for this purpose. Usually these are based on transition-metal complexes or incorporate heavy-atoms in order to enhance triplet formation.⁸⁻¹¹ Interest in organic based chromophores is increasing and one system which shows great promise is based on the 4,4-difluoro-4-bora-3a,4a-diaza-*s*-indacene (BODIPY) (**Figure 4.1** (a)) core. These systems are capable of hydrogen generation under photocatalytic conditions.¹²⁻¹⁴ They have the great advantage of being easy to synthesise and exhibit high molar extinction coefficients ($\sim 10^5 \text{ M}^{-1} \text{ cm}^{-1}$) in the visible region. They can also be modified to increase the efficiency of crossing to the triplet surface, and this has increased their use in photodynamic therapy,^{15,16} or triplet-triplet annihilation up-conversion processes.^{17,18} Inclusion of a heavy atom or complexation with transition metals can increase the triplet yield upon photolysis by increased spin-orbit coupling. Incorporation of other spin converters can also increase the triplet-formation efficiency.^{19,20} BODIPY based donor-acceptor dyads (**Figure 4.1** (b)) also have increased intersystem crossing (ISC) efficiencies via spin orbit charge-transfer intermediates.^{18,21-23} The triplet species thus produced have lifetimes which extend into the microsecond range.^{24,25} This makes them particularly suited to catalyse chemical reactions which require diffusion of reactants to the catalytic centre.

Polymeric materials incorporating BODIPY units were first reported in 2008. These materials were originally synthesised for use in organic solar cell technologies.²⁶⁻³⁰ More recently, linear BODIPY copolymers have been used to generate molecular hydrogen.³¹ These polymers have high extinctions in the visible region of the spectrum. Materials combining bis(difluoroboron)-1,2-bis((1H-pyrrol-2-yl)-methlyene)hydrazine (BOPHY) with TiO₂ nanoparticles can generate molecular

hydrogen under UV-visible irradiation. This process requires the presence of methanol as a sacrificial agent.³² Linear polymers,^{33,34} planarized polymers,^{35,36} conjugated microporous polymers³⁷⁻⁴⁰, covalent organic frameworks,^{41,42} covalent triazine frameworks,⁴³⁻⁴⁶ and polymer dots^{47,48} have all also been used for hydrogen generation.⁴⁹ Clearly polymeric materials incorporating BODIPY units offer many advantages over inorganic systems. These include low cost, ease of synthesis and modification, low toxicity, and broad visible light response.^{6,50-56}

Recently, it has been shown that some Donor-Acceptor (D-A) polymers can undergo intramolecular singlet fission (iSF).⁵⁷⁻⁶⁰ Singlet fission (SF) is a spin-allowed process where one excited singlet (S) exciton produces a spin correlated triplet pair $^1(\text{TT})$ which ultimately produces two spatially discrete triplet excitons $2\times(\text{T})$.^{61,62} This process is possible when the energy of the singlet exciton is at least twice the energy of the spatially discrete triplet excitons and where suitable “symmetry breaking” processes are available to facilitate spin dephasing of the initially produced $^1(\text{TT})$ species. Singlet fission has the potential to double the triplet formation, overcoming the maximum theoretical efficiency of a solar cell; the eponymous Shockley-Queisser limit (34%).⁶³ In 2018, an *iso*-indigo-based donor-acceptor (D-A) polymer produced triplet quantum yields in the range 160 – 200% via an iSF process.⁶⁰ A number of physical parameters can influence the efficiency of the iSF process, for example, interchain packing or solvent-polymer interactions. Intrachain SF is more attractive as it is less susceptible efficiency-reducing interchain processes^{57,60} and the strategic design of polymeric systems to promote intrachain SF may eliminate many of the inefficiencies associated with other systems.⁶⁴ For instance (D-A) copolymers offer modular tunability and have good charge transport mobilities. They also offer the possibility of expanding the chromophore to “A-D-A” units which “seeds” the formation of spatially discrete triplet excitons on the acceptor units which can then propagate along the polymer backbone.⁵⁹ While there has been significant progress in the area of SF recently, the range of materials known to undergo SF is relatively small.^{62,64-66}

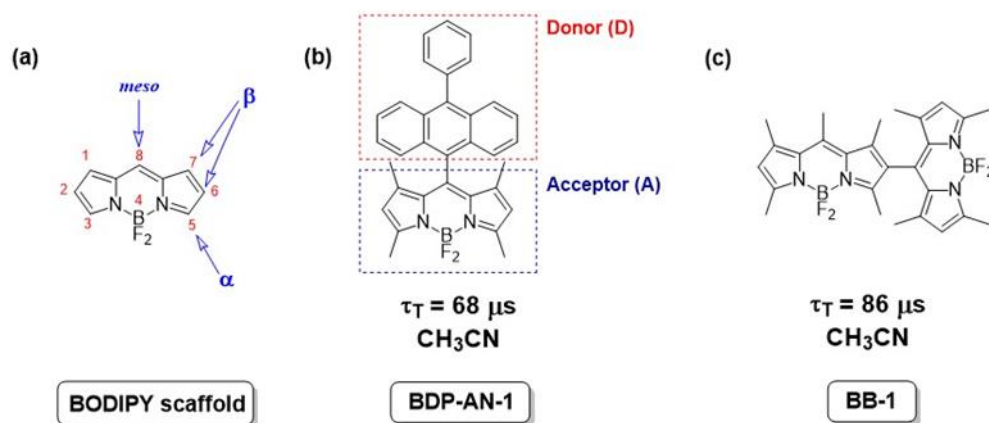


Figure 4.1. a) Molecular structure of BODIPY core, b) Donor-acceptor (D-A) dyad BODIPY derivative,²⁵ c) BODIPY dimer derivative.²⁴ Triplet lifetimes (τ_T) of each BODIPY derivative previously reported displayed below molecular structure (μs).

In this work we describe a novel BODIPY containing copolymer (**P1**, **Figure 4.2**) with diethynylbenzene linker moieties along the polymeric backbone. We examine the photophysical properties of this polymer in comparison to two model compounds (**M1** and **M2**, **Figure 4.2**). Steady-state and time-resolved spectroscopic techniques provide evidence for an iSF mechanism for triplet formation in **P1**. The optically produced singlet has considerable charge-transfer character as indicated by Time-Dependent Density Functional Theory. An intermediate spin-correlated triplet pair $^1(\text{TT})$ is produced from the singlet excited state, which separate along the polymer to produce spatially discrete triplet excitons. We also report the hydrogen evolution activity of **P1** when used in conjunction with Pt | TiO_2 and the results indicate that photocatalytic activity occurs via a “through particle” mechanism via electron injection into the conduction band (CB) of the semiconductor, followed by proton reduction at the surface of the nanoparticle (using electrochemical band gap of the polymer to deduce this mechanism).

4.3 Results and Discussion

4.3.1 Synthesis and characterisation

The synthesis of BODIPY model compounds **1** (**M1**)⁶⁷ and **2** (**M2**)⁶⁸ have been previously reported and their molecular structures and that of **P1** are presented in **Figure 4.2**.

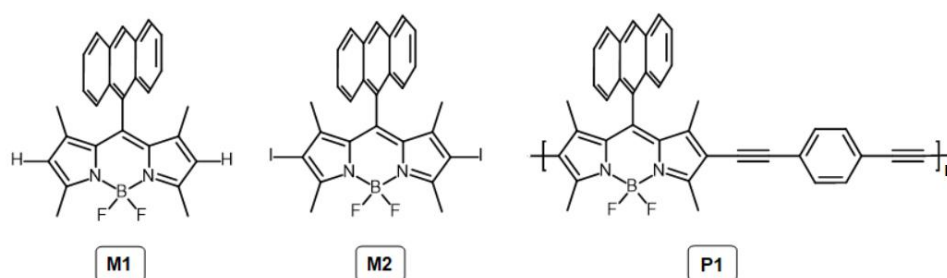


Figure 4.2. Molecular structures of **M1**, **M2** and **P1**.

The overall steps in the syntheses of **P1** (**Figure 4.2**) are displayed in **Scheme S4.1** (Appendix C). In brief, polymer **P1** (**Figure 4.2**) was obtained by palladium-catalysed Sonogashira cross coupling between **M2** and 1,4-diethynylbenzene (1:1 molar ratio) in the presence of tetrakis(triphenylphosphine)-palladium(0) and copper(I)iodide in diisopropylamine/THF at 80 °C for 3 days reflux (see Appendix C for details). ¹H NMR spectroscopy displayed broad peaks in the aromatic region indicative of both the aryl protons on the phenyl linker group and aryl protons from the anthracene moiety. The disappearance of the terminal ethynyl proton at 3.17 ppm from the precursor linker 1,4-diethynylbenzene demonstrated successful coupling between the two monomeric precursors. Size exclusion chromatography (SEC) was carried out on two different polymer batches to study the differences in molecular weight distribution under identical experimental procedures (**Figure S4.5** and **Table S4.1**). The copolymers obtained from each experiment revealed little differences in the molecular weight (M_n) and dispersity (\mathcal{D}_M) - **P1** batch 1, $M_n = 6.2$ kDa, $\mathcal{D}_M = 1.2$ and **P1** batch 2 $M_n = 7.2$ kDa, $\mathcal{D}_M = 1.3$. These values are similar to those of other BODIPY containing copolymers previously reported in the literature.^{31,69,70} FTIR spectroscopy further confirmed the formation of **P1**, as the appearance of the C≡C vibrational band

at 2203 cm^{-1} is evident in **P1**, corresponding to the triple bond along the main chain of the polymeric backbone (**Figure S4.6**, Appendix C). Vibrational bands corresponding to 1,4-diethynylbenzene are no longer apparent in the IR spectra of **P1**, for example, the $\text{C}\equiv\text{C}$ vibrational band at 2109 cm^{-1} or the terminal $\equiv\text{C-H}$ stretching vibration at 3297 cm^{-1} have disappeared in the FTIR spectrum of the polymer. Furthermore, in the case of the polymer, vibrational bands are observed at 1543 cm^{-1} (BODIPY ring) and $2854, 2925\text{ cm}^{-1}$ ($-\text{CH}_3$), concurrent with those observed for the BODIPY moiety in **M1** and **M2** and confirm the incorporation of the BODIPY core into the main chain of the polymer.^{68,71,72}

4.3.2 Photophysical properties

The photophysical properties of **P1** are compared to those of **M1** and **M2** using a range of time resolved spectroscopic techniques and quantum chemical calculations. These studies highlight the significant differences between the behaviour of **P1** and the model compounds. Specifically, the UV-visible spectrum of **P1** is broad and exhibits bimodal character as represented in **Figure 4.3** (a) (the figure also contains a spectrum of **M1** for comparison (dashed)). This bimodal character suggests the presence of discrete chromophores or domains along the polymer backbone rather than multiple transitions within each chromophore. While the relative contribution of each domain changes, the absorption maxima appear to be insensitive to solvent environment. As can be seen in **Figure 4.3**, the λ_{max} is relatively insensitive to changing the solvent from THF to DMSO, but the contribution of the shoulder on the low-energy side of the absorbance band is affected by this change. This suggests that the preponderance of absorption domains on the polymer backbone changes with solvent-polymer interactions.

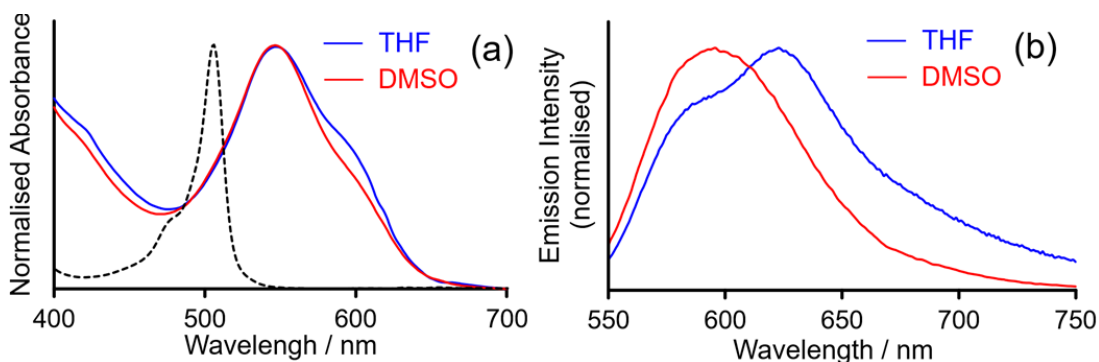


Figure 4.3. a) The normalised UV-visible absorption spectrum of **P1** in THF and DMSO with the spectrum of **M1** in THF (dashed) and b) the normalised emission spectra of **P1** in THF and DMSO following excitation at 550 nm.

In contrast to **M1**, which exhibits a moderate fluorescence quantum yield of 0.19 (**Table 4.1**), the emission from **P1** is very weak. The emission spectra also exhibit bimodal character (**Figure 4.3** (b) $\lambda_{\text{exc}} = 550$ nm). Again, this is suggestive of the presence of different emissive domains on the polymer backbone. In addition, the emission kinetics follow a biexponential decay profile ($\tau_1 = 1.48$ and $\tau_2 = 3.29$ ns in CH_2Cl_2) further supporting the presence of two emissive domains. The absorption and emissive parameters of **M1**, **M2**, and **P1** are presented in **Table 4.1**.

Table 4.1. The photophysical properties of **M1**, **M2** and polymer, **P1** recorded in CH_2Cl_2 at 298 K. ^aFluorescence quantum yields were calculated using 3-pyridine BODIPY as a std ($\Phi_{\text{std}} = 0.62$, $\lambda_{\text{exc}} = 490$ nm in CH_2Cl_2).⁷³ ^bFluorescence lifetimes were calculated using TCSPC ($\lambda_{\text{exc}} = 510$ nm in degassed CH_2Cl_2 solution). ^cSinglet oxygen quantum yield (Φ_{Δ}), diiodobodipy used as a standard ($\Phi_{\Delta} = 0.87$ in CH_2Cl_2).⁷⁴ ^d505 nm excitation. ^e530 nm excitation. For full experimental details see Appendix C.

Compound	$\lambda_{\text{max}} (\epsilon)^{\text{a}}/\text{nm}$ ($10^3 \text{ M}^{-1} \text{ cm}^{-1}$)	$\lambda_{\text{em}}/\text{nm}$	Stokes shift/ cm^{-1}	$\Phi_{\text{fl}}^{\text{a}}$	$\tau_{\text{fl}} (\text{ns})^{\text{b}}$	Φ_{Δ}^{c}
M1	506 (83)	515	345	0.19	5.69	0.40 ^d
M2	540 (43)	550	337	-	-	0.99 ^e
P1	550 (14)	589, 622	2105	0.04	1.48, 3.29	1.07 ^e

Table 4.2. Summary of emission decay lifetimes of the polymer, **P1** obtained using both 375 nm and 510 nm excitation sources. Luminescence decay recorded at 622 nm for toluene, THF, CHCl₃, CH₂Cl₂ and 590 nm for DMSO, DMF and CH₃CN. The percentage contribution of each radiative lifetime component (amplitude) is shown as a percentage of each lifetime (%). The Reichardt parameter, E_T is shown to indicate the variance in solvent polarity.⁷⁵

Solvent (E _T)	λ _{em} (nm)	375 nm excitation		510 nm excitation	
		τ ₁ (ns) (%)	τ ₂ (ns) (%)	τ ₁ (ns) (%)	τ ₂ (ns) (%)
Toluene (33.9)	627	1.67 (49)	3.05 (51)	1.81 (58)	3.43 (42)
THF (37.4)	623	1.22 (35)	2.70 (65)	1.36 (43)	2.98 (57)
CHCl₃ (39.1)	622	1.83 (52)	3.31 (48)	1.95 (56)	3.74 (44)
CH₂Cl₂ (40.7)	622	1.41 (46)	2.96 (54)	1.48 (50)	3.29 (50)
DMSO (45.1)	594	0.58 (27)	2.57 (73)	0.58 (29)	2.66 (71)
DMF (43.2)	591	0.73 (28)	2.67 (72)	0.64 (27)	2.79 (73)
CH₃CN (45.6)	589	0.60 (26)	2.52 (74)	0.59 (22)	2.85 (78)

The photophysical properties of **P1**, **M1**, and **M2**, were investigated using transient absorption (TA) and time-resolved infrared (TRIR) spectroscopies using 525 nm excitation. Additional ns TA experiments were conducted using 355 nm excitation. These studies were supported by quantum chemical calculations, including those of oligomeric models for **P1** consisting of two, four and six BODIPY units.

4.3.3 The photophysical properties of **M1**

Quantum chemical calculations indicates that the lowest energy singlet excited state (S₁) of **M1** is centred on the BODIPY core (**Figure 4.4** (d)). The small Stokes shift (345 cm⁻¹) of the emission suggests that this state is also the emissive state with a lifetime of 5.69 ns in CH₂Cl₂. The anthracenyl substituent contributes little to this excited state however the quantum yield of fluorescence is low (Φ_{fl} = 0.19) compared to unsubstituted BODIPY compounds⁷⁶ indicating the presence of a competing non-radiative decay path for the S₁ excited state. Time-Dependent Density Functional Theory (TD-DFT) calculations identified two triplet excited states at energies below

the S_1 state, one centred on the anthracenyl substituent (**Figure 4.4** (c)) and the other BODIPY-based (**Figure 4.4** (b)). The presence of the orthogonal anthracenyl substituent facilitates intersystem crossing to the triplet hypersurface via a spin orbital charge transfer mechanism.^{77,78}

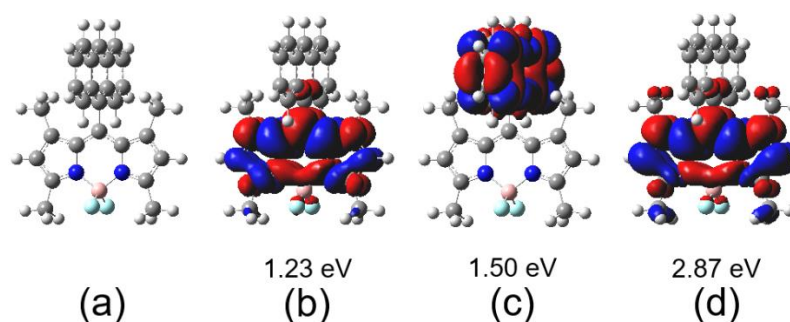


Figure 4.4. a) The optimised molecular structure of **M1** showing the anthracenyl substituent towards the top, light grey hydrogen, dark grey carbon, blue nitrogen, pink boron, and green fluorine atoms; (b) the electron density difference map (EDDM) for the T_1 excited state of **M1** (i.e. the lowest energy triplet excited state) (c) the EDDM for T_2 showing the anthracenyl-centred nature of this excited state and (d) the EDDM for the S_1 state (red volumes indicate regions where the electron density is greater in the excited state compared to the ground-state, and blue volumes are the regions where the electron density is less in the excited state compared to the ground-state, iso value 0.004).

The TA spectra obtained following 525 nm excitation of **M1** are presented in **Figure 4.5** (a) and (b). The spectra obtained up to 7 ps after the excitation pulse exhibit a growth of features marked with upward arrows which are assigned to the S_1 state of **M1**. It is important to note that these features are not formed within the excitation pulse, and this suggests the intermediate formation of a precursor (Franck-Condon) state, perhaps involving solvent reorientation or vibrational relaxation which ultimately forms the equilibrated S_1 state. This state exhibits four broad features (424, 568, 640, and 690 nm). These features subsequently decay with a rate identical to the measured emission lifetime of **M1** (**Figure 4.5** (b)), however, the absorption near 450 nm persists on the time base of this experiment (upward arrow marked with an asterisk). The three long-wavelength features in these spectra (568, 640, and 690 nm) are important characteristic bands of the S_1 state of BODIPY compounds while the persistent feature at 450 nm is diagnostic of a triplet species.

The TRIR data obtained under similar conditions (**Figure 4.5** (c)) again showed the formation of a precursor to the S_1 state in the initial 10 ps following photolysis (down arrows in **Figure 4.5** (c)). The S_1 state, with infrared stretching vibrations at 1394,

1358 and 1330 cm^{-1} , decays on the timescale of the fluorescence, with the concomitant formation of new bands at 1548, 1534, 1512, 1464 and 1306 cm^{-1} (**Figure 4.5** (d)) which persist on the timescale of the experiment (2.5 ns). The persistent bands are assigned to the lowest energy triplet state (T_1) (**Figure 4.4** (b)). Global analysis of the TRIR data revealed three components, a short-lived component which rapidly forms the S_1 excited state (red dashed spectrum in **Figure 4.5** (c)), and a persistent species formed as the S_1 state decays.^{79–81} The spectrum of the persistent triplet state is represented in **Figure 4.5** (d) as the blue dashed spectrum. Clearly the presence of the anthracenyl substituent on the BODIPY core facilitates crossing to the triplet hypersurface and this process competes with the radiative decay of the S_1 state reducing the fluorescence quantum yield (**Table 4.1**).^{77,82}

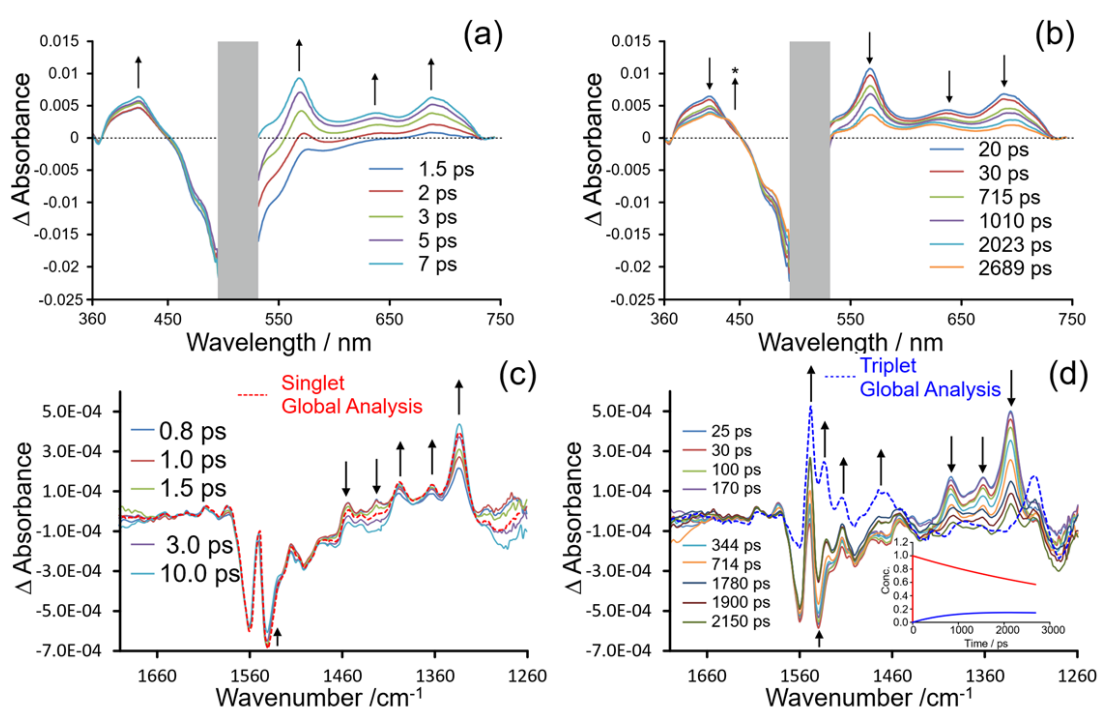


Figure 4.5. The difference spectra obtained following 525 nm photolysis of **M1** in CD₃CN, a) the early times showing the growth of S_1 , b) the TA spectra at later times showing the decay of features of S_1 and formation of weak features of the triplet species (up arrow with asterisk), c) early time TRIR spectra including the singlet spectrum from global analysis (red dashed) and d) late time TRIR spectra showing decay of the singlet features and the formation of the triplet with the triplet spectrum obtained from global analysis (blue dashed), the inset shows the time-dependent concentrations of singlet (red) and triplet (blue) components.

4.3.4 The photophysical properties of M2

The photophysics of **M2** is markedly different to that of **M1**. For this compound, the quantum chemical calculations suggest that the lowest energy singlet state of **M2** has considerable anthracenyl-to-BODIPY charge-transfer character (**Figure S4.22**). However, this state cannot be optically populated because the transition from the ground state is symmetry forbidden. Consequently, irradiation of **M2** results in the population of the S_2 state which is a BODIPY-centred π -to- π^* state (**Table S4.3**). This state is almost degenerate with its triplet equivalent and given the substantial involvement of the iodine orbitals provides an efficient crossing to the triplet hypersurface through spin-orbit coupling. The spectroscopic properties of the excited state of **M2** were investigated by TA (**Figure 4.6** (a) and (b)).

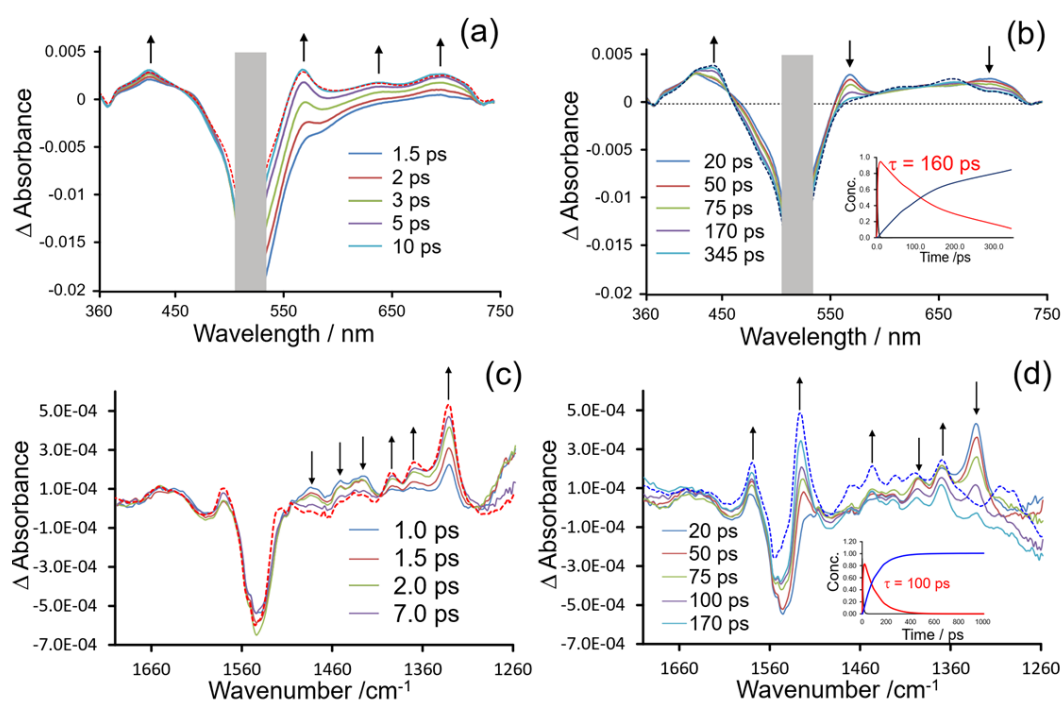


Figure 4.6. a) The TA difference spectra obtained following photolysis of **M2** in CD_3CN showing the formation of a singlet excited state and its evolution associated spectrum obtained from a global analysis (red dashed); b) the longer time spectroscopic changes showing the decay of the singlet state and formation of a triplet state with its evolution associated spectrum from global analysis (blue dashed) and the kinetic data obtained using a sequential model in the inset; c) the TRIR spectra showing the formation of a singlet excited state (the red dashed spectrum is the evolution associated spectrum from global analysis); and d) the longer time scale changes showing the formation of a persistent triplet state with the evolution associated spectrum (blue dashed) and the inset displays the time dependent concentration plot indicating a quantum yield of 1.0 for the formation of the triplet species.

These data suggest the initial formation of a singlet excited state as indicated by the four features at (425, 568, 640 and 695 nm) which are not produced in the excitation

pulse, but which rapidly appear in the first 10 ps (**Figure 4.6** (a)). The lower energy features are identical to the characteristic features for the S_1 state in **M1** (above). On this basis the species formed after 10 ps, it is assigned to the BODIPY-centred S_2 state of **M2**. These features decay with concomitant formation of a second species with a broad featureless absorption across the visible region and a more distinct absorption at 440 nm which persist outside the time-window of the experiment (> 2.5 ns). These absorptions are assigned to a triplet species with a characteristic broad absorption feature at 440 nm. Global analysis of the TA data confirms that the crossing to the triplet surface occurs with a time constant of 160 ps (blue dashed spectrum and inset in **Figure 4.6** (b)). The efficient crossing of the singlet to the triplet surface quenches the singlet emission.

The results of TRIR experiments for **M2** are presented in **Figure 4.6**. These show the immediate formation of a Franck-Condon state with absorbances at 1439, 1456, and 1487 cm^{-1} (down arrows) and the subsequent formation of the singlet excited state (S_2) at 1334, 1372, and 1339 cm^{-1} (up arrows). Spectra obtained at longer times show the decay of S_2 and the formation of the triplet state with bands at 1528 and 1580 cm^{-1} (up arrows in **Figure 4.6** (d)). The triplet state persists (> 2.5 ns) in these experiments.

4.3.5 The photophysical properties of **P1**

In order to better understand the photophysical properties of **P1**, a number of oligomeric models were studied using quantum chemical methods. These models were based around a central diethynylbenzene link and maintained a centre of symmetry on the central unit. The oligomers contained two, four and six BODIPY units (**Figure 4.7** (a) – (c)). Anthracenyl substituents were replaced by phenyl groups to reduce the electron count in the calculations. This was considered a reasonable simplification as this work was an attempt to model the behaviour of the conjugated polymer without the added complication of the spin orbital charge transfer route to triplet formation. The structures of the oligomers were optimised without symmetry constraints. The energies and electronic structures of optically accessible excited states were then modelled using TD-DFT methods. In the case of the smallest oligomer, consisting of a central diethynylbenzene and two BODIPY units each terminated with a

diethynylbenzene substituent (**Figure 4.7** (a)), the lowest energy optically accessible singlet state has mainly BODIPY π -to- π^* character but with substantial diethynylbenzene-to-BODIPY charge-transfer character (see the EDDM in **Figure 4.7** (a)). The oligomer behaves like an Acceptor-Donor-Acceptor (A-D-A) triad. The ethynylbenzene acts as the donor and the two BODIPY units are the acceptors. Likewise, the larger oligomers also exhibited diethynylbenzene-to-BODIPY charge-transfer character in the lowest energy singlet excited state. The conjugated backbone mimics a one-dimensional potential well, and the electron density differences tend to be at a maximum close to the centre of the oligomer with reduced effects at the extremes.⁸³ As a result, the chromophores extend over multiple monomer units in an ideal arrangement to promote singlet fission.

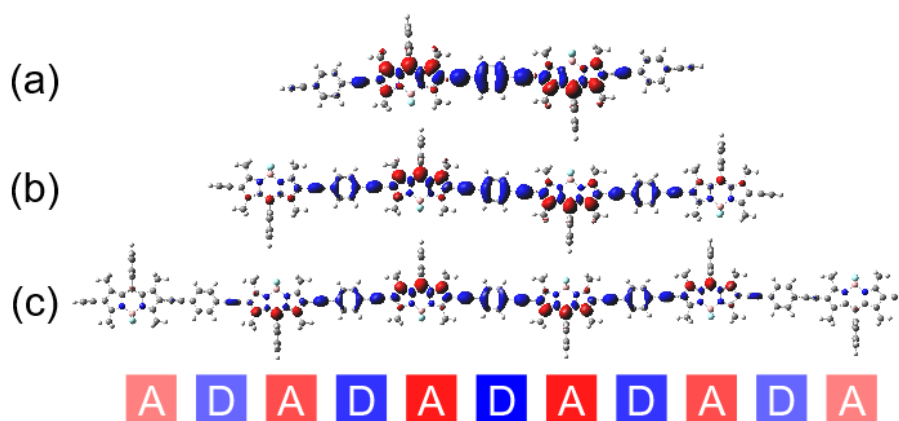


Figure 4.7. The EDDMs of the lowest energy singlet excited states of the three BODIPY oligomers a) the two-BODIPY, b) the four BODIPY, and c) the six BODIPY oligomers, blue volumes represent regions where the electron density is reduced compared to the ground state (donor) and red volumes represent regions where the electron density in the excited state is greater than the ground state (acceptor).

TA and TRIR techniques were used to investigate the photophysical properties of **P1**. The results are summarised in **Figure 4.8**. The spectral changes in the UV-visible region shows a ground state bleach within the excitation pulse (**Figure 4.8** (a)). The bleach only partially recovers over the timescale of the experiment (2.5 ns) indicating the formation of a persistent photoproduct. The appearance of a broad band at 450 nm (upward arrow) in **Figure 4.8** (a) is evidence for the formation of a triplet excited state. The time-wavelength matrix derived from the TA experiment was subjected to global analysis. Initially a sequential three component model was applied to these data, with the components corresponding to the Franck Condon, the singlet and finally the triplet species. The time profile of the triplet species obtained from this analysis displayed a

decay of 15% over the time-scale of the experiment, which is greatly in excess of the measured quantum yield of luminescence (0.04) for this system. Consequently, the observed triplet decay is the result of a further process forming a second triplet species. Global analysis was expanded to include a fourth species in the reaction sequence, namely the Franck Condon, the singlet, the spin-correlated triplet ($^1(TT)$) and the spatially discrete triplet pair $2(T)$. The UV-visible spectra of these four components are presented in **Figure 4.8** (b). A short-lived component decays within 5 ps to form a singlet excited-state (red spectrum). This spectrum displays weak features in the visible region (marked with *). These are the diagnostic features of a singlet excited-state observed following photolysis of **M1** (**Figure 4.5** (a)). This singlet state decays with a lifetime of 135 ps to form the spin-correlated triplet species (blue spectrum; inset blue trace), which in turn decays with a lifetime of 1.25 ns to produce the spatially discrete triplet pair with a quantum yield of approximately 0.6 (green spectrum and plot). The overall triplet yield would be twice this figure at approximately 1.2 (full timescale of kinetic plots are available in Appendix C, **Figure S4.24**).

The equivalent TRIR data following photolysis of **P1** in CH_3CN are presented in **Figure 4.8** (c). The parent bleach is evident at 1557 cm^{-1} and features are produced at 1488 and 1437 cm^{-1} (down arrows in **Figure 4.8** (c)). As these features decay a further species is produced (up arrows in **Figure 4.8** (c)) at 1526 , 1365 , 1308 cm^{-1} , along with a further feature at 1546 cm^{-1} which is obscured by the parent bleach which persist on the TRIR experimental time-scale. Global analysis, using a sequential model was used to analyse the TA data, revealed four components. The initial species (black spectrum) is short-lived with a lifetime of 4 ps (similar to the short-lived species observed in the TA experiments). This forms the singlet excited state (red spectrum). The red and black spectra are similar, apart from slight changes in relative intensities the broad features around 1460 cm^{-1} . In turn, the singlet species decays with a lifetime of 135 ps forming the spin-correlated triplet pair (blue spectrum). This in turn forms a further triplet species, which exhibits an IR spectrum similar but not identical to the blue spectrum of the spatially discrete triplet (green spectrum). We have assigned this species to the spatially discrete triplet pair. To highlight the spectroscopic differences between the spin-correlated triplet and the spatially discrete triplet pair, these spectra

were subtracted and the resulting spectrum (of these difference spectra) is presented as the black dashed spectrum at the top of **Figure 4.8** (d). This confirmed that the two triplet species are both temporally and are spectroscopically distinguishable. Similar difference spectra were obtained in CDCl_3 or DCM and are presented in Appendix C (**Figure S4.25** (b)). The time-dependence of the four components in this analysis is presented in the inset in **Figure 4.8** (d) (full timescale of kinetic plots are available in Appendix C, **Figure S4.25**). These plots indicate a quantum yield of approximately 0.7 for the spatially discrete triplet pair resulting in a triplet quantum yield of about 1.4. The spin-correlated triplet lifetime is 1.1 ns which lies within the range of the emission lifetimes presented in **Table 4.2**.

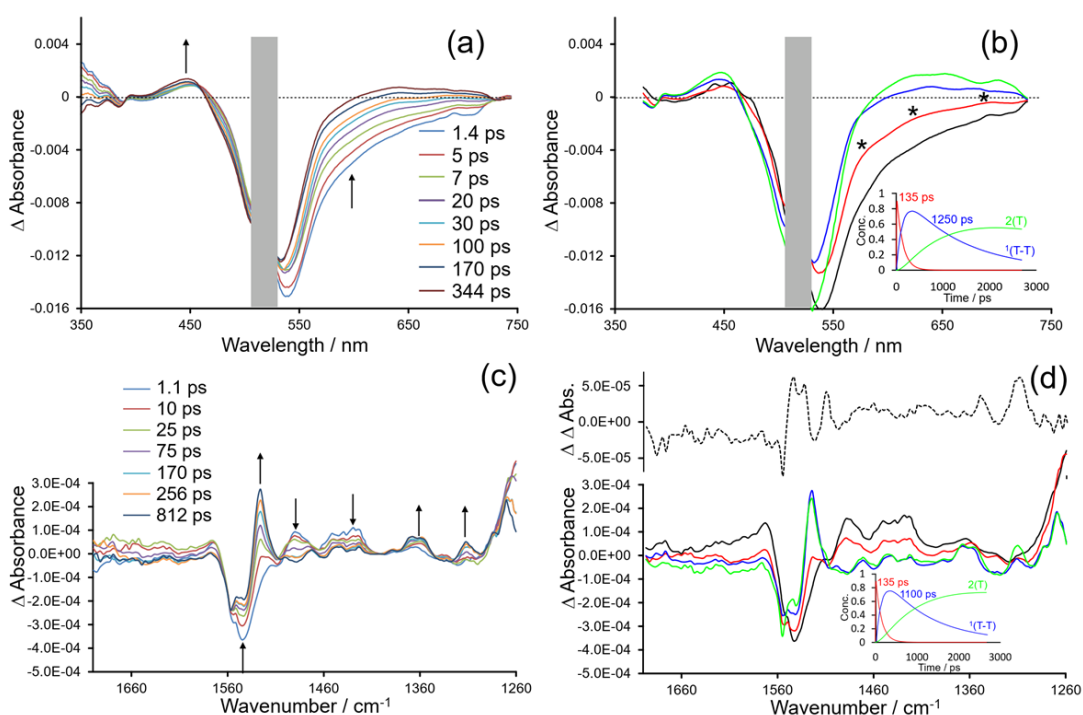


Figure 4.8. The time-resolved changes observed following photolysis of **P1** at 525 nm in CD_3CN ; a) the TA spectra showing the depletion of the parent and formation of a singlet and triplet excited states; b) the evolution adjusted difference spectra for an initially formed species (black) which reacts in 4ps to form the singlet (red) which in turn forms a triplet (blue) excited states, (the inset shows the kinetics of the reaction sequence indicating a lifetime for the singlet species of 165 ps); c) the TRIR spectra showing the decay (down arrows) of the initially produced singlet excited state and formation of the triplet excited state (up arrows), and d) the evolution adjusted difference spectra for the Franck-Condon species (black), singlet (red), and spin coherent triplet (blue) and spatially discrete triplet pair (green), the inset shows the kinetic behaviour of these components.

Quantum chemical calculations on the model oligomers confirm that the lowest energy singlet states have significant charge transfer character (**Figure 4.7** (a) – (c)) and that the A-D-A configuration on the polymer is suited to facilitate singlet fission. Singlet

fission is a spin-allowed process, where a singlet exciton (S_1) produces a spin-correlated triplet pair denoted $^1(TT)$ with overall singlet multiplicity. The $^1(TT)$ exciton can undergo a range of processes, it can dissociate into a pair of non-interacting triplets,⁸⁴ it can emit,⁸⁵ or simply relax to the ground-state by non-radiative processes.^{84,86} Obviously for the purpose of triplet formation, maximising the efficiency of triplet-pair dissociation into non-interacting or spatially discrete triplets is essential. Because of the large size of the oligomers in this study TD-DFT methods are the only viable option to aid in identifying their excited states. This presents a fundamental question, namely how will double exciton species like the spin-correlated triplet pairs be represented using single determinant DFT method? In these systems they appear as degenerate triplet pairs, where the spin densities span multiple BODIPY centres (**Figure 4.9** (a)) (because the centrosymmetry is not explicitly enforced in the optimisation of these oligomers the energies of “degenerate” states may be marginally different by a few meV.) It should be noted that in these systems, the spin-correlated triplet pairs retain significant diethynyl-to-BODIPY charge-transfer character, as evidenced by a significantly reduced electron density (blue volumes) on the central diethynylbenzene unit.

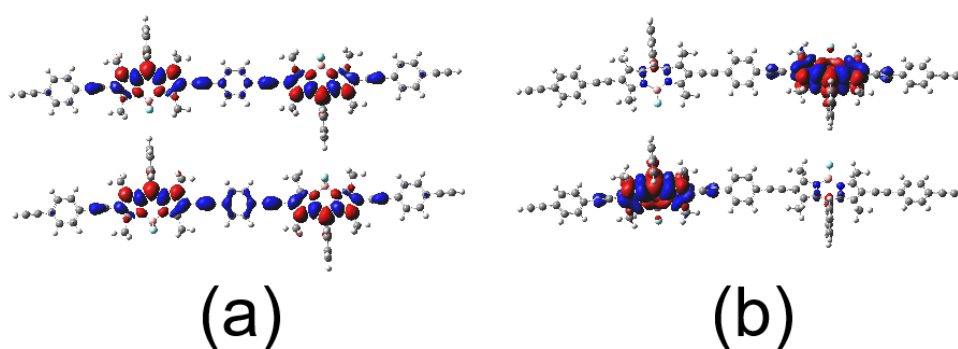


Figure 4.9. a) The EDDM for the two lowest energy (and almost degenerate) triplet states (T_1 and T_2 ; 1.37 and 1.38 eV respectively) in the optimised 2-BODIPY oligomer where the BODIPY units are coplanar, this represents a spin-correlated triplet pair $^1(TT)$ (iso value 0.004), b) the EDDM for the degenerate T_1 and T_2 states (1.27 eV) for the 2-BODIPY oligomer where the BODIPY units are set to be orthogonal showing two degenerate spatially discrete triplets with spin density located separately on each BODIPY unit.

For the 6-BODIPY oligomer, the calculations indicate the presence of eleven triplet states at energies lower than the optically accessible singlet state (S_1). These triplet states can be grouped to form two bands of energetically close states, one band (five states containing two sets of spin-correlated triplets) lies just below the energy of the

singlet state. The second band (six states) lies at an energy close to half the energy of the S_1 state (**Figure 4.10**). The triplet states in upper band retain significant charge-transfer character involving the diethynylbenzene links (see upper expansion in **Figure 4.10**) and are spin-correlated triplet states. The lower band consists of spatially discrete triplet states and have a greatly reduced charge-transfer character (lower expansion in **Figure 4.10**). The different charge-transfer characteristics of these two bands have important spectroscopic consequences particularly in the fingerprint region of the infrared spectrum which permits these two triplet species to be distinguished spectroscopically (**Figure 4.8** (d)).

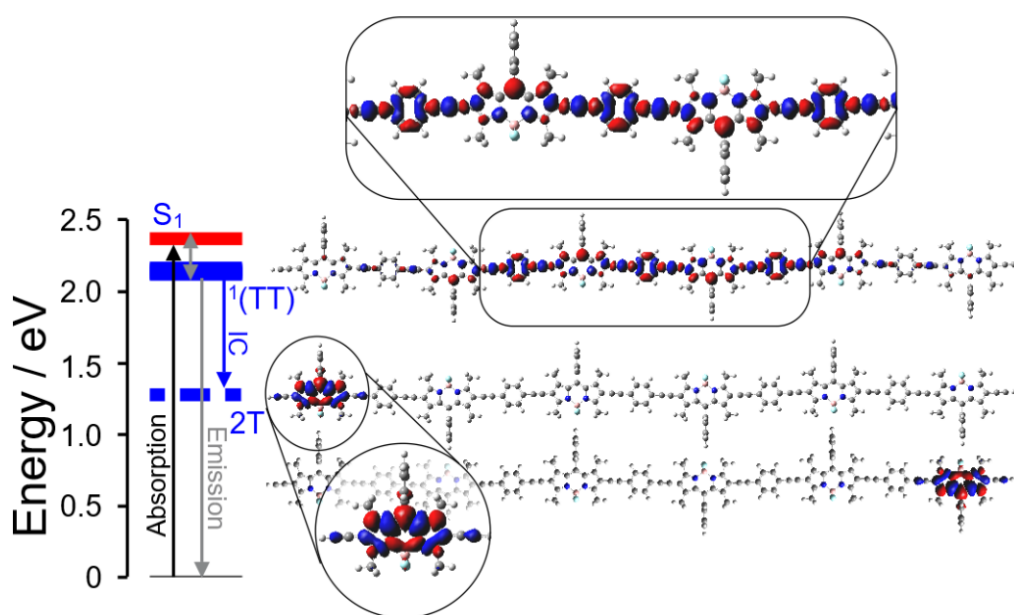


Figure 4.10. The energy levels for the optically accessible singlet state (S_1 ; red) of the 6-BODIPY oligomer and the lower energy triplet states (blue) which form two bands of energetically close states, the upper band consist of spin-correlated triplet states $^1(TT)$ and the lower band comprise spatially discrete triplets (T) (blue dashed) with lower two EDDMs representing two spatially discrete triplets at the extremes of the oligomer and the upper EDDM showing a typical spin-correlated triplet, expanded regions highlight the involvement or otherwise of the diethynylbenzene links which confirm a reduced charge-transfer character for the spatially discrete triplets compared to the spin correlated triplets.

TRIR experiments with monitoring in the 1900 to 2300 cm^{-1} range can provide supporting evidence for the nature of the triplet states outlined in **Figure 4.10**. By examining the 1900 to 2300 cm^{-1} region where absorptions associated with the $\text{-C}\equiv\text{C-}$ bonds are observed, two important features are apparent (CHCl_3 was used as solvent for these experiments because the strong absorbances of CH_3CN in this region preclude its use). Firstly, the depletion of the ground-state absorbance is small

compared to the transient absorbance of the photoproduct (**Figure 4.11**). In fact, it is approximately $1/6^{\text{th}}$ that of the photoproduct absorption. This points to the photoproduct exhibiting some degree of signal enhancement compared to the ground state. Secondly the photoproduct $\text{-C}\equiv\text{C-}$ stretching absorption is observed at a lower wavenumber (2070 cm^{-1}) compared to the ground-state (2215 cm^{-1}). This is strong evidence that the electron densities on the alkynyl links in the excited states are less than that in the ground-state and confirms the charge-transfer character of the excited states. The diethynylbenzene links act as electron donors to the BODIPY acceptors. This confirms the acceptor-donor-acceptor character of the chromophores as described in **Figure 4.7**. The enhanced absorption can be explained by the considerable change in the dipole moment associated with the $\text{-C}\equiv\text{C-}$ units in the excited state. This is analogous to the enhancement observed in resonance Raman experiments.⁸⁷

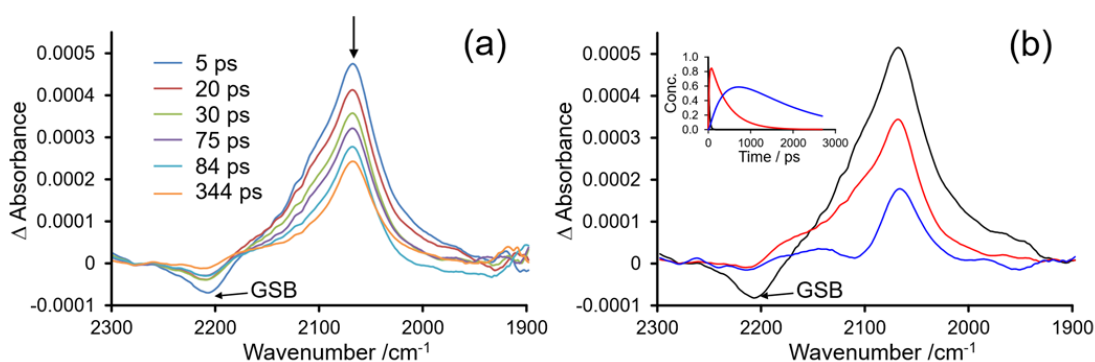


Figure 4.11. a) The TRIR spectra obtained in the $\text{-C}\equiv\text{C-}$ region in CHCl_3 showing the ground-state bleach (GSB) at 2215 cm^{-1} and the greatly enhanced excited state feature(s) at 2070 cm^{-1} ; and b) global analysis of the time dependent behaviour of spectra inset showing the decay of the singlet (red) and formation of triplet (blue) species.

Initial attempts to analyse the time-dependent behaviour of the features in the $\text{-C}\equiv\text{C-}$ region using the four-component model as used in the fingerprint region (**Figure 4.8** (d)) failed for two reasons. Firstly, the absorbance values in the $\text{-C}\equiv\text{C-}$ region are not directly proportional to the concentration of the components present i.e., the Beer-Lambert law breaks down. The $\text{-C}\equiv\text{C-}$ absorption of the spin-correlated triplet, with its greater alkyne-to-BODIPY charge-transfer character, will be enhanced to a greater extent than will the spatially discrete triplets where the alkyne-to-BODIPY charge-transfer character is less significant (**Figure 4.10**). Secondly, it is not possible to distinguish between different triplet species based on the single broad product feature in this region. As a consequence, the global analysis of the transient spectra in the -

$\text{C}\equiv\text{C}$ - region (**Figure 4.11** (b)) was limited to a three component sequential model. The first component is short-lived (black spectrum, $\tau \approx 20$ ps) and we have assigned this to the Franck-Condon state. This state rapidly forms the singlet state species (red). This species, in turn, decays to the persistent triplet-state species (blue) which encompasses both the spin-correlated and spatially discrete triplet species. The rate of intersystem crossing from singlet to triplet is slower ($\tau = 410 \pm 20$ ps) in CHCl_3 compared to that observed in CH_3CN solution (**Figure 4.8** (b) and (d) 135 ps). Rates of intersystem crossings are known to be sensitive to solvent.^{85,88,89} A further important feature in the lifetime measurements is the significant reduction (70%) in the intensity of the combined triplet signals within 2.5 ns (**Figure 4.11** (b) insert). A reduction in the signal enhancement is responsible for this rather than a significant reduction in the concentration of the triplet species. Thus, the rate of reduction of the $\text{-C}\equiv\text{C-}$ feature is a direct measure of the dissociation of the spin-correlated triplet to spatially discrete triplets, a key process in singlet fission. It is important to note also, that the decay of the spin-correlated triplet pairs (1.3 ± 0.1 ns) is similar to the emission lifetimes for the **P1** in CH_2Cl_2 (1.48 and 3.29 ns) (**Table 4.1**); an explanation for the dual lifetimes for this weak emission is presented in the following section. It is known that $^1(\text{TT})$ can be weakly emissive by borrowing oscillator strength from the singlet excited state.⁸⁵ For the 6-BODIPY oligomer, the calculated energies of the five triplet states below the S_1 state are in the range 2.13 ± 0.02 eV which corresponds to a photon wavelength of 580 ± 7 nm. The weak emission from **P1** is broad with maxima at 589 and 622 nm in CH_2Cl_2 which is consistent with emission from the band of spin-correlated triplet pairs (see Appendix C for electron density difference maps and energies of the low-lying triplet excited states, **Table S4.4**).

It is clear that the correlated triplet pairs in the polymer have lifetimes which stretch into the ns range,⁹⁰ and it has also been demonstrated that conformational changes or indeed small structural changes induced by solvents, can affect the dissociation of spin-correlated triplet pairs.⁹¹ In order to investigate this the relative conformation of the 2-BODIPY oligomer was changed from its optimised conformation where the BODIPY units are coplanar to one where the BODIPY units are orthogonal (**Figure 4.9** (b)). When the BODIPY units are orthogonal, the lowest two triplet states are

degenerate but spatially discrete. Consequently, relative rotation of the BODIPY units will promote dissociation of the spin-correlated triplet pairs.

4.3.6 Explanation of the bimodal character of the UV-visible absorption and emission of P1

As described earlier, the UV-visible absorption spectra of **P1** exhibit bimodal character which is sensitive to solvent. The weak emission signal also displays bimodal character with two emission lifetimes in the range 0.5 to 3.7 ns depending on solvent. To explain these observations, we propose the existence of different absorption and emission “domains” on the polymer backbone. These domains reflect different rotational conformations along the polymer backbone. In order to develop this argument a relaxed potential energy scan in which the dihedral angle between the BODIPY units was changed in the 2-BODIPY oligomer from the *anti*- to the *syn*-conformation in 10° steps (**Figure 4.12**) was developed.

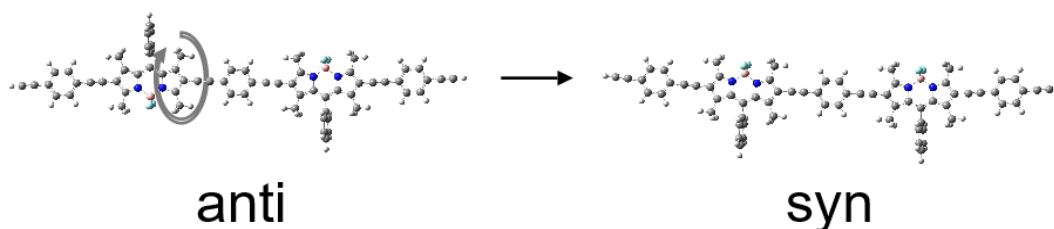


Figure 4.12. Different rotational conformations along the polymeric backbone showing *anti* and *syn* possible confirmations.

At each point along the reaction coordinate TD-DFT calculations yielded the energies of the ground state and six lowest energy excited-states, i.e., the excited states up to and including the lowest energy singlet excited-state. These are presented in **Figure S4.23**. Three features are of interest here, firstly the energy of the ground state does not change significantly along this reaction coordinate. This suggests a relatively free rotation of the BODIPY units along the oligomer backbone. Secondly triplet states T_3 , T_4 and T_5 become almost degenerate at twist angles close to 90°. Thirdly, the vertical excitation energy to S_1 increases slightly at a twist angle of 90° (**Table S4.5**). This means the absorption maximum is sensitive to the dihedral angle between BODIPY units in a freely rotating oligomer. These calculations also indicate that the electronic

structures of the excited states are insensitive to whether the system adopts a *syn* or an *anti*-conformation. The vertical excitation energy required to populate the S_1 state was then estimated which showed that the energy increased from -5.62° (the optimised angle at the cam-B3LYP/6-32G(d,p) level) to 94° which would result in a shift of the absorption from 512 to 501 nm (**Table S4.5**). Because of the considerable computational cost involved in performing a similar set of calculations on the larger oligomers, static model structures of the 6-BODIPY oligomer were constructed with twist angles of 0, 22.5, 45, 67.5 and 90° between sequential BODIPY units. The excited state energies for these “twisted” oligomers were then assessed by TD-DFT methods. The energies of the ground-state and all excited states below the lowest energy singlet excited state are presented in **Figure 4.13**. These calculations confirm that as the twist angle increases, the energies of both the ground-state and the lowest energy optically accessible state (S_1) increases. However, energy increase for S_1 is greater than that of the ground-state resulting in an increase in the transition energy and consequential blue shift of the UV-vis absorption (insert in **Figure 4.13**). The emission from the spin correlated triplet pairs is also affected by the twist angle, the larger the twist angle the shorter the emission wavelength (**Table S4.6**). These calculations offer a qualitative explanation for the red shift and broadness of the absorption profiles of **P1** compared to **M1**. They also explain the large Stokes shift of the weak emission from **P1**. As the twist angles in **P1** are likely to be affected by the nature of the solvent they also offer an explanation for the striking solvent dependence of both the absorption and emission profiles of **P1**.

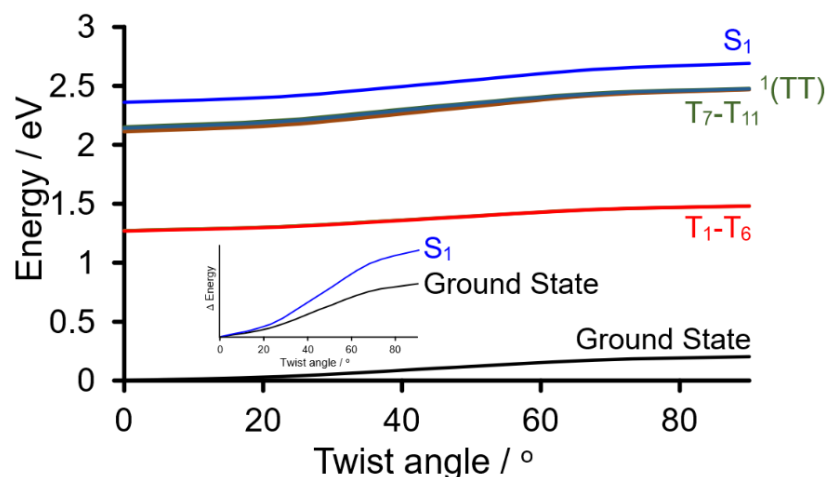


Figure 4.13. The variation in the energies of the ground state and excited states up to the lowest energy singlet excited state against the sequential twist angle in the 6-BODIPY oligomer, the inset shows the relative change in the ground-state and S_1 energies.

The energy gradient experienced by the oligomer in the S_1 state compared to the ground-state would impart a greater flexing impulse to the oligomer in the S_1 state (see insert in **Figure 4.13**) which in turn would produce a flexing relaxation from the Franck-Condon region. This provides an explanation for the rapid spectroscopic changes observed soon after (< 10 ps) the excitation event.

4.3.7 Nanosecond transient absorption studies and singlet oxygen quantum yields

Further evidence for population of a triplet state in **P1** was confirmed using ns- μ s TA spectroscopy. The observation of phosphorescence in BODIPY systems is rare and hence ns to μ s TA spectroscopy allows for the measurement of these states.⁷⁶ Following 355 nm excitation of **P1**, a broad GSB is evident at ~ 550 nm, together with ESA features at ~ 450 nm and in the range 625–700 nm (**Figure S4.26**). The transient absorption spectra have a similar profile to that discussed earlier in the pico-second studies (see **Figure 4.8**). The ESA features decay concomitantly to recovery of the GSB, with a lifetime 94 μ s, assigned to 3 BODIPY.⁹² The GSB and ESA spectral features displayed in **Figure S4.26** assigned to a triplet-state BODIPY are in agreement with the TA spectra reported for BODIPY compounds.^{17,93}

Under similar experimental parameters, triplet state lifetimes of 32 μ s and 16 μ s were obtained for **M2** and **M1**, respectively, following 355 nm excitation (**Figure S4.27**

and **Figure S4.28**, Appendix C). Other groups have indicated that $^3\text{Anthracene}$ and ^3CT states may also contribute to the triplet lifetime for **M1**, but the $^3\text{BODIPY}$ state remains dominant due to the lower energy level of the triplet surface.⁸² In the case of **M2** the heavy-atom effect of the iodine groups at the 2,6 position of the BODIPY core further enhances ISC to the triplet surface, with $\tau_T = 32 \mu\text{s}$. Similar triplet lifetimes (τ_T) have previously been reported for 2,6-iodinated BODIPY compounds.^{13,17} A summary of the triplet lifetimes is given in **Table 4.3**, for **M1**, **M2** and **P1**.⁹⁴

The phosphorescence spectra for singlet oxygen are shown in **Figure S4.14** following irradiation of the three samples in CH_2Cl_2 . The singlet oxygen quantum yield for **M2** ($\Phi_\Delta = 0.99$), is significantly higher than that of **M1**, which is expected due to ISC (**Table 4.1**), and in agreement with previous reports for diiodo BODIPY compounds.⁷⁴ In the case of the polymer, the singlet oxygen quantum yield is greater than 1 ($\Phi_\Delta = 1.07$), which further supports singlet fission in these type of BODIPY copolymers.

Table 4.3. A summary of TA spectral features for **M1**, **M2** and polymer **P1** following 355 nm excitation (in freeze pumped thawed THF solutions). Triplet lifetime (τ_T) values were obtained using mono-exponential decay fittings.

	λ_{GSB} (nm)	λ_{ESA} (nm)	τ_T (μs)
M1	500	421	16 (± 1.8)
M2	536	445, 672 (br)	32 (± 1.9)
P1	550	451, 625 – 700	94 (± 7.4)

4.3.8 Electrochemistry

Cyclic voltammetry (CV) has become routinely used to determine the frontier orbital energy levels of conjugated polymer films.^{95,96} For polymeric species deposited on an appropriate electrode substrate, the onset potential of significant oxidation current is interpreted as being due to the removal of electrons from the HOMO level (ionisation potential), while a reduction current onset arises from the injection of electrons into the LUMO level (electron affinity). CVs of glassy carbon (GC) electrodes modified with drop-cast thin films of **M1** and **P1** are presented in **Figure S4.29**. Oxidation (E'_{ox}) and reduction (E'_{red}) onset potentials have been determined by the common graphical

approach^{96,97} of taking the potential value at the intersection of tangents fitted to the featureless capacitive current region and the rising current edge. As outlined in Appendix C, (Experimental **Section S4.1.2**), these potentials can be correlated to the absolute energies E of the HOMO and LUMO levels. Furthermore, the difference in the HOMO and LUMO energies measured in this way, can be interpreted as the apparent electrochemical band-gap E_g^{elec} . The values for these parameters derived from **Figure S4.29** are summarised in **Table 4.4**.

Table 4.4. Summary of electrochemical results obtained for glassy carbon electrodes coated with thin films of **M1** and **P1** – see Appendix C, **Figure S4.29**.

Film	E'_{ox}/V	E'_{red}/V	Band gap $E_g^{elec}/$ eV	$E_{HOMO}/$ eV	$E_{LUMO}/$ eV
M1	0.72	-1.40	2.12	-5.52	-3.40
P1	0.65	-1.17	1.82	-5.45	-3.63

There is good agreement between the values of E_g^{elec} from **Table 4.4** and the measured optical gap values of 2.25 eV for **M1** and 1.94 eV for **P1** (**Figure S4.30** and **Figure S4.31**). The electrochemical results indicate that the bulk of the decrease in band gap for **P1** relative to **M1** arises at the LUMO edge, which stabilises by 0.23 eV in the case of the polymer. These HOMO/LUMO levels corresponds well to previously reported values for a similar BODIPY based conjugation polymer (HOMO -5.39 eV, LUMO -3.62 eV) containing a mesityl group in the *meso* position of the dye and a thiophene conjugated linker.⁹⁸

4.3.9 Photocatalytic hydrogen studies

Initially, homogeneous photocatalytic experiments were carried out using **P1**, together with a cobalt oxime catalyst which yielded 7.64 mmol H₂ g⁻¹ after 6 hours of irradiation (300 W Xe Arc lamp, ($\lambda > 420$ nm)). The generation of hydrogen prompted us to investigate the activity of **P1** together with TiO₂|Pt nanoparticles. In this approach it is possible that the TiO₂ may facilitate “through particle” electron transfer on the surface nanoparticle³¹ when used with a Pt co-catalyst for proton reduction.^{31,99,100} BODIPY dyes have previously been used in combination with TiO₂

for solar driven hydrogen evolution using both covalent attachment and chemisorption of the dye on the semiconductor surface^{12,101–103} and we envisaged that a conjugated BODIPY-containing polymer such as **P1**, with the possibility of electron transfer along the polymeric backbone could facilitate electron injection into the CB of the TiO₂.

Photocatalytic experiments using TiO₂|Pt nanoparticles were carried out in a 1:1 (v/v), THF: water solution using ascorbic acid as a sacrificial agent (see experimental methods, **Section S4.1.8**, Appendix C for details). The morphology of the prepared TiO₂|Pt nanoparticles were subjected to EDX-SEM analysis (**Figure S4.35** and **Figure S4.36**) to determine a Pt-loaded nanoparticle with a Pt loading amount of 1 wt.% (Pt/TiO₂). For a typical photocatalytic experiment, the TiO₂|Pt nanoparticles were dispersed in the sacrificial agent solution (0.1 M ascorbic acid) and the appropriate amount of polymer, **P1** was added. The solution was degassed using three freeze-pump thaw cycles, sonicated for 15 min, and irradiated using a 300 W Xe Arc lamp, $\lambda > 420$ nm. Photocatalytic hydrogen evolution was monitored at regular time intervals by gas chromatography, and control experiments in the dark indicated no hydrogen production. In the absence of any of the components, no hydrogen was generated, confirming the contribution of all components in the photocatalytic cycle. The concentration of the polymer was systematically altered to examine the effect of polymer concentration on the overall activity of the system (**Table S4.7**, **Figure 4.14**, note: the weight of the monomeric repeating unit in the polymer was used to approximate the different concentrations of the polymer at 0.1, 0.2, 0.4, 0.8 and 1.2 mM respectively). A concentration of 0.4 mM **P1** in the photocatalytic solution yielded the highest activity for hydrogen generation with 13.9 mmol H₂ g⁻¹ after 20 hours irradiation (**Figure S4.32**). A higher concentration of dye in solution has also been reported to lead to agglomeration on the surface of TiO₂ inhibiting a photocatalytic reaction.¹⁰² The lowest photocatalytic performance was observed using the lowest concentration of the polymer **P1** at 0.1 mM (0.6 mmol H₂ g⁻¹). Li et al. also observed an enhancement in hydrogen evolution when a zinc containing bipyridine conjugated polymer was used in combination with TiO₂ and Pt as a co-catalyst (162 μ mol g⁻¹ h⁻¹ without TiO₂ versus 1333 μ mol g⁻¹ h⁻¹ in a TiO₂ containing system) and

this was attributed to faster electron transfer from the photoexcited electrons of the polymer into the conduction band of the TiO_2 .¹⁰⁴

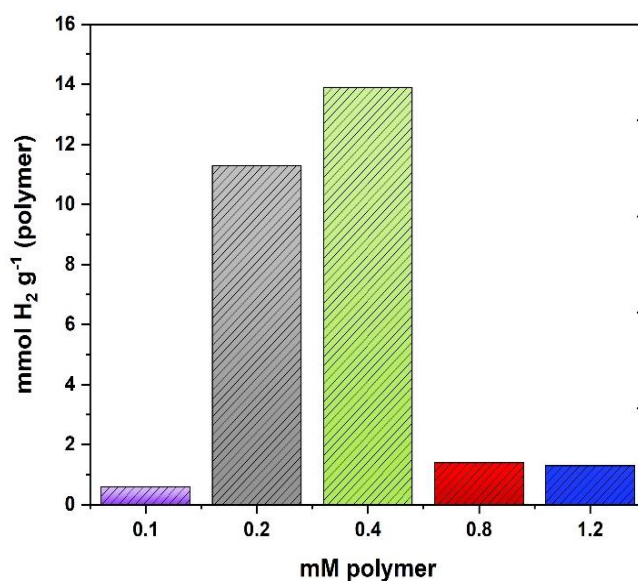


Figure 4.14. Photocatalytic activity of polymer, **P1** when irradiated using a Xe Arc lamp, $\lambda > 420$ nm in combination with TiO_2 | Pt nanoparticles (6 mg), 0.1 M ascorbic acid as sacrificial agent in a 4 mL 1:1 (v/v) THF:H₂O solution. Activity shown above in $\text{mmol H}_2 \text{ g}^{-1}$ (based on mass of polymer in photocatalytic solution). Various experiments studied the effect of different polymer concentration where 0.1 mM (purple dash), 0.2 mM (grey dash), 0.4 mM (green dash), 0.8 mM (red dash) and 1.2 mM (blue dash). Concentration of polymer, **P1** (in mM) in solution calculated based on the monomeric repeating unit of the polymer.

The choice of sacrificial agent was also studied, as BODIPY systems for hydrogen evolution have previously been reported using a variety of different sacrificial agents, most often TEOA or ascorbic acid.^{10,12,14,101,102,105,106} Photocatalytic experiment **1c** (**Table S4.7**) was replicated using TEOA (10 vol%) as the SA in lieu of ascorbic acid. The results can be found in Appendix C (**Figure S4.33** (a)) which illustrate significantly lower activity using TEOA as a sacrificial agent ($0.45 \text{ mmol H}_2 \text{ g}^{-1}$ versus $13.9 \text{ mmol H}_2 \text{ g}^{-1}$). In these latter experiments a colour change is evident in the Schlenk tube from pink/purple to yellow solution after 6 hours irradiation. This is attributed to the instability of the polymer under basic conditions and possible photodecomposition to the precursor BODIPY compound, **M1**. Evidence for the degradation of the polymer under these conditions is apparent from both the visible colour change of the photocatalytic solution and the growth of the band at 506 nm (matching the λ_{max} of **M1**, **Figure 4.3** (a) dashed line) after irradiation (**Figure S4.33** (b)). Stability studies of **P1** in 0.1 M AA solution show significantly less photodecomposition after 6 hours irradiation, in comparison to **P1** in TEOA (10 vol%) solution wherein a 56% reduction

of the main absorption band is apparent after irradiation (blue dashed line, **Figure S4.33** (b)). In addition, electron injection into the conduction band of the TiO₂ nanoparticle has also been reported to be more hindered at higher pH, which is another plausible rationale behind the decrease in activity using TEOA.¹⁰⁷

To compare the copolymer to monomeric BODIPY compounds, hydrogen evolution experiments were carried out using the model monomeric compound, **M1** (0.03 mM) as the photosensitising unit under otherwise identical experimental conditions. A concentration of 0.03 mM **M1** in the photocatalytic solution was used to ensure an optically matched photocatalytic solution between the monomer and that of the best performing copolymer concentration (0.4 mM, **Figure 4.14**). It was found that **M1** exhibited lower activity for hydrogen evolution under identical conditions (4.1 mmol g⁻¹ H₂ liberated versus 13.9 mmol g⁻¹ H₂ for **P1**). The moderate activity observed for **M1** can be explained by considering the time-resolved photophysical investigation carried out which revealed population of a triplet excited state (*vide supra*). In any case, an enhancement in performance of the copolymer provides further evidence for the improvement in proton reduction using conjugated BODIPY copolymers, opposed to their untethered monomeric precursors.

Considering the energy values of the frontier orbitals of **P1** as extracted from the electrochemical data (**Table 4.4**), a proposed mechanism for the photocatalytic hydrogen production is shown in **Figure S4.34**. The LUMO energy derived from the voltammetry measurements (-3.63 eV) is expected to approximately correspond to the singlet (S₁) energy level, which, as discussed in relation to the DFT calculations, lies just above the spin-correlated triplet states ¹(TT) energy levels. Therefore it is thermodynamically feasible for electron transfer to occur from either the singlet, or correlated triplet states of the photoexcited photosensitiser, **P1*** into the conduction band (CB) of the TiO₂ nanoparticle (where the CB value of -4.21 eV is based on the previously calculated conduction band edge (E_{CB}) for TiO₂ versus vacuum).¹⁰⁸ By contrast, the maximum possible energy of a triplet state generated by singlet fission would correspond to the midpoint energy of the HOMO-LUMO gap – approximately -4.54 eV on the basis of the data of **Table 4.4**. This suggests that electron injection into TiO₂ from the spatially discrete triplet (T) states is thermodynamically unlikely

in this system, and thereby implies that the observed photocatalytic activity is based on electrons that transfer to the TiO₂ particles from either the S₁ or ¹(TT) states of the excited polymer. These electrons are in turn relayed to the Pt⁰ particles on the surface of the TiO₂, where they reduce solution phase protons to generate molecular hydrogen (H₂). Finally the catalytic cycle is closed by the regeneration of the ground state dye through electron transfer from the ascorbic acid (AA) sacrificial agent to the HOMO level of the polymer.¹⁰⁰

Given that the measured lifetimes of the S₁ and ¹(TT) states are on the hundreds of ps and ns timescales respectively, it is apparent that rapid electronic transfer from the photoexcited polymer to the TiO₂ is operative. This situation is reminiscent of a recent study on the photophysical properties of 1,3-diphenylisobenzofuran (DPIBF) derivatives immobilised on nanocrystalline TiO₂.¹⁰⁹ In contrast to **P1**, electron transfer to TiO₂ is thermodynamically possible from a singlet fission generated triplet state for this DPIBF species, however femto-second transient absorption measurements indicated that the SF process was outcompeted by sub-nanosecond electron injection from the singlet excited state into the TiO₂. This suggests that to capitalise on the SF process in **P1** for heterogeneous photocatalysis, it will be essential not only to select a semiconductor particulate substrate with a CB edge lower in energy than the spatially discrete triplet (T) states, but also to devise a means of delaying electron transfer from the S₁ and ¹(TT) energy levels to that semiconductor in order to allow the population of the T states. Work is ongoing in our laboratory to design and implement a photocatalytic assembly based on **P1** and a suitable choice of semiconductor that can satisfy these criteria.

4.4 Experimental

4.4.1 Materials and Equipment

All chemicals were obtained commercially and were used as received. Chloroplatinic acid (H_2PtCl_6) was used as the Pt source (8 wt.% H_2O) and was commercially obtained via Sigma Aldrich. All reactions were carried out under inert conditions in Schlenk tubes. Analytical thin layer chromatography (silica) was used to determine the reaction progress for all synthetic procedures described and carried out on Merck silica gel plates. Column chromatography for the purification of the monomers was carried out using neutral silica gel (Merck) pH 6.5 – 7.5. The mobile phases were dried over MgSO_4 prior to running the column chromatography purification procedure. ^1H and ^{13}C NMR spectra were recorded on either a Bruker 600 MHz spectrometer and were referenced to the deuterated solvent peak as an internal reference. All photophysical measurements were carried out using spectrophotometric grade solvents and were used as received. All photophysical measurements were carried out at room temperature. All UV-visible absorption spectra were recorded on the Agilent 8453 UV-vis spectrophotometer equipped with Agilent ChemStation software. FTIR measurements were carried out on Perkin-Elmer 2000 FTIR spectrophotometer in a liquid solution cell using spectrophotometric grade dichloromethane. Scanning electron microscopy (SEM) was conducted using a Jeol JSM-5600LV instrument. Energy-dispersive X-ray spectroscopy (EDX) was obtained with an INCA x-act detector by Oxford Instruments. Sample areas for EDX analysis were taken at five different locations of the sample chosen at random. The magnification used for this analysis was x2500. Beam intensity for EDX was set to 20kV and the working distance was of 20mm. We thank the Advanced Chemical and Materials Analysis Electron Microscopy Unit at Newcastle University (United Kingdom) for analysing the samples. All excitation spectra and photoluminescence spectra were recorded using FLS1000 Photoluminescence Spectrometer (Edinburgh Instruments), equipped with a 450 W Xe Arc lamp as the excitation source for steady-state measurements and a visible PMT-900 detector. Time-correlated single photon counting (TCSPC) lifetimes were carried out using FLS1000 Photoluminescence Spectrometer (Edinburgh Instruments) using either a 375 nm or a 510 nm variable pulse length diode

laser (EPL-375 or EPL-510) to excite the ground state sample. Ns- μ s transient absorption measurements were recorded on a LP980 laser flash photolysis spectrometer (Edinburgh Instruments). Samples were excited by a nanosecond pulsed laser (Nd:YAG laser/OPO, LOTIS TII 2134) at 355 nm (~ 6.1 mJ per pulse) operating at 1 Hz with a pulse width of 5 ns. Size exclusion chromatography (SEC) was used to determine the dispersities (D_M) and molecular weights of polymers. SEC was conducted in 1,1,1,3,3,3-Hexafluoro-2-propanol (HFIP) using an PSS SECurity SEC system equipped with a PFG 7 μ m 8 \times 50 mm pre-column, a PSS 100 \AA , 7 μ m 8 \times 300 mm and a PSS 1000 \AA , 7 μ m 8 \times 300 mm column in series and a differential refractive index (RI) detector at a flow rate of 1.0 mL min⁻¹. The systems were calibrated against Agilent Easi-Vial linear poly(methyl methacrylate) (PMMA) standards and analysed by the software package PSS winGPC UniChrom. Additional experimental methods are described explicitly in Appendix C.

4.4.2 DFT calculations

A number of oligomers were investigated as models for the BODIPY-diethynyl copolymers. These oligomers were constructed to be symmetric with respect a central diethynyl comonomer, with an inversion centre in the centre of the aromatic ring. An ethynylbenzene substituent was used to terminate all oligomers and no symmetry constraints were applied. The initial structure of each oligomer was obtained from molecular mechanics calculations and the structure was optimised using the hybrid density functional method (B3LYP)^{110,111} with the 6-31G^{112,113} basis set as implemented in Gaussian 16.¹¹⁴ Subsequent calculations to model the both singlet and triplet excited states used Time-Dependent Density Theory (TD-DFT) and a larger 6-31G(d,p)¹¹² basis and the Coulomb attenuated model cam-B3LYP. All the calculations for the molecular fragment contribution to molecular orbitals were obtained using AOMix package.^{115,116}

4.4.3 Synthesis

Synthesis of 1,3,5,7-tetramethyl-8-(anthracen-9-yl)-4,4-difluoro-4-bora-3a,4a-diaza-s-indacene (M1). The synthesis of **M1** was according to the literature⁶⁷ and full

synthetic procedure is detailed in Appendix C. ^1H NMR (600 MHz, CDCl_3): δ 8.58 (s, 1H), 8.03 (dd, $J = 8.4$ Hz, 2H), 7.91 (dd, $J = 8.7$ Hz, 2H), 7.49 (m, 2H), 7.43 (m, 2H), 5.89 (s, 2H), 2.63 (s, 6H), 0.65 (s, 6H). ^{13}C NMR (600 MHz, CDCl_3): δ 155.77, 142.90, 138.95, 132.36, 131.30, 129.68, 128.34, 128.26, 126.95, 125.74, 125.11, 121.16, 14.70, 13.33. NMR spectra can be found in Appendix C.

Synthesis of 2,6-diiodo-1,3,5,7-tetramethyl-8-(anthracen-9-yl)-4,4-difluoro-4-bora-3a,4a-diaza-s-indacene (M2). The synthesis of **M2** was according to the literature⁶⁸ and full synthetic procedure is detailed in Appendix C. ^1H NMR (600 MHz, CDCl_3): δ 8.63 (s, 1H), 8.05 (dd, $J = 8.5$ Hz, 2H), 7.81 (dd, $J = 8.8$ Hz, 2H), 7.51 (m, 2H), 7.45 (m, 2H), 2.72 (s, 6H), 0.67 (s, 6H). ^{13}C NMR (600 MHz, CDCl_3): δ 157.22, 145.26, 145.07, 131.44, 129.04, 128.68, 127.56, 127.33, 126.10, 126.00, 125.05, 124.85, 82.32, 15.95, 13.71. NMR spectra can be found in Appendix C.

Synthesis of P1. The synthesis of novel **P1** was carried out as per previously reported in the literature for a similar Sonogashira polycondensation reaction between a halogenated BODIPY monomer and 1,4-diethynylbenzene.³¹ ^1H NMR (600 MHz, CDCl_3): δ 7.70-7.64 (br, Ar-H), 7.57-7.53 (br, Ar-H), 7.49-7.44 (br, Ar-H), 2.63 (br, CH_3 at 3, 5 position of BODIPY), 0.65 (br, CH_3 at 1, 7 position of BODIPY). SEC results Batch 1: M_n : 6194 g/mol, M_w : 7631 g/mol, PDI: 1.23. SEC results Batch 2: M_n : 7197 g/mol, M_w : 9521 g/mol, PDI: 1.31. Full synthetic procedures are described in the Appendix C.

4.5 Conclusion

The main purpose of this study was to investigate the use of conjugated polymers as photosensitisers for hydrogen generation. In particular we have examined a copolymer of a BODIPY unit and a diethynylbenzene linker. In these copolymers the diethynylbenzene acts not only as a linker between BODIPY units, but also an electron donor in charge-transfer excited states. These copolymers act as donor-acceptor systems which are ideally constituted to promote intramolecular singlet fission. Based on TD-DFT calculations we have proposed that the initial exciton generated can be characterised as a diethynylbenzene-to-BODIPY charge transfer singlet excited state. This was confirmed by time-resolved spectroscopic techniques. Both TA and TRIR spectroscopies were then used to monitor the formation of a spin-correlated triplet pair, an intermediate in the formation of two spatially discrete triplets which can progress along the conjugated polymer backbone. The quantum yield of triplet formation is greater than unity. This is achieved without the presence of heavy atoms. These copolymers can be used as effective visible light harvesting systems and work is underway to interface the long-lived excitons generated in this copolymer with suitable semiconductors capable of generating hydrogen gas.

4.6 Supporting information

The supplementary data associated with this chapter can be found in Appendix C.

4.7 Bibliography

- (1) Ahmad, H.; Kamarudin, S. K.; Minggu, L. J.; Kassim, M. *Renew. Sustain. Energy Rev.* **2015**, *43*, 599–610.
- (2) Barber, J. *Chem. Soc. Rev.* **2009**, *38* (1), 185–196.
- (3) Kim, J. H.; Hansora, D.; Sharma, P.; Jang, J. W.; Lee, J. S. *Chem. Soc. Rev.* **2019**, *48* (7), 1908–1971.
- (4) Zeng, Y.; Chen, J.; Yu, T.; Yang, G.; Li, Y. *ACS Energy Lett.* **2017**, *2*, 357–363.
- (5) Kim, J. H.; Hansora, D.; Sharma, P.; Jang, J.-W.; Lee, J. S. *Chem. Soc. Rev.* **2019**, *48*, 1908–1971.
- (6) Rahman, M. Z.; Kibria, M. G.; Mullins, C. B. *Chem. Soc. Rev.* **2020**, *49* (6), 1887–1931.
- (7) Zhao, J.; Wu, W.; Sun, J.; Guo, S. *Chem. Soc. Rev.* **2013**, *42* (12), 5323–5351.
- (8) Goldsmith, J. I.; Hudson, W. R.; Lowry, M. S.; Anderson, T. H.; Bernhard, S. *J. Am. Chem. Soc.* **2005**, *127* (20), 7502–7510.
- (9) Kowacs, T.; O'Reilly, L.; Pan, Q.; Huijser, A.; Lang, P.; Rau, S.; Browne, W. R.; Pryce, M. T.; Vos, J. G. *Inorg. Chem.* **2016**, *55* (6), 2685–2690.
- (10) Wang, P.; Guo, S.; Wang, H. J.; Chen, K. K.; Zhang, N.; Zhang, Z. M.; Lu, T. *B. Nat. Commun.* **2019**, *10* (1), 1–12.
- (11) Dalle, K. E.; Warnan, J.; Leung, J. J.; Reuillard, B.; Karmel, I. S.; Reisner, E. *Chem. Rev.* **2019**, *119* (4), 2752–2875.
- (12) Luo, G. G.; Lu, H.; Zhang, X. L.; Dai, J. C.; Wu, J. H.; Wu, J. J. *Phys. Chem. Chem. Phys.* **2015**, *17* (15), 9716–9729.
- (13) Dura, L.; Wächtler, M.; Kupfer, S.; Kübel, J.; Ahrens, J.; Höfler, S.; Bröring, M.; Dietzek, B.; Beweries, T. *Inorganics* **2017**, *5* (2), 21.

- (14) Xie, A.; Pan, Z. H.; Yu, M.; Luo, G. G.; Sun, D. *Chinese Chem. Lett.* **2019**, *30* (1), 225–228.
- (15) Awuah, S. G.; You, Y. *RSC Adv.* **2012**, *2* (30), 11169–11183.
- (16) Kamkaew, A.; Lim, S. H.; Lee, H. B.; Kiew, L. V.; Chung, L. Y.; Burgess, K. *Chem. Soc. Rev.* **2013**, *42* (1), 77–88.
- (17) Wu, W.; Guo, H.; Wu, W.; Ji, S.; Zhao, J. *J. Org. Chem.* **2011**, *76* (17), 7056–7064.
- (18) Chen, K.; Yang, W.; Wang, Z.; Iagatti, A.; Bussotti, L.; Foggi, P.; Ji, W.; Zhao, J.; Di Donato, M. *J. Phys. Chem. A* **2017**, *121* (40), 7550–7564.
- (19) Zhao, J.; Xu, K.; Yang, W.; Wang, Z.; Zhong, F. *Chem. Soc. Rev.* **2015**, *44* (24), 8904–8939.
- (20) Chen, K.; Dong, Y.; Zhao, X.; Imran, M.; Tang, G.; Zhao, J.; Liu, Q. *Front. Chem.* **2019**, *7* (December), 1–14.
- (21) Dong, Y.; Sukhanov, A. A.; Zhao, J.; Elmali, A.; Li, X.; Dick, B.; Karatay, A.; Voronkova, V. K. *J. Phys. Chem. C* **2019**, *123*, 22793–22811.
- (22) Liang, H.; Sun, S.; Zafar, M.; Yuan, Z.; Dong, Y.; Ji, S.; Huo, Y.; Li, M. De; Zhao, J. *Dye. Pigment.* **2020**, *173* (October 2019), 108003.
- (23) Lei, Y.; Chen, K.; Tang, G.; Zhao, J.; Gurzadyan, G. G. *J. Photochem. Photobiol. A Chem.* **2020**, *398* (May), 112573.
- (24) Liu, Y.; Zhao, J.; Iagatti, A.; Bussotti, L.; Foggi, P.; Castellucci, E.; Di Donato, M.; Han, K. L. *J. Phys. Chem. C* **2018**, *122* (5), 2502–2511.
- (25) Wang, Z.; Zhao, J. *Org. Lett.* **2017**, *19* (17), 4492–4495.
- (26) Zhu, Mei, Jiang, Li, Yuan, Mingjian, Liu, Xiaofeng, Ouyang, Cabin, Zheng, Haiuan, Yin, Ziaodong, Zuo, Zicheng, Liu, Huibiao, Li, Y. *J. Polym. Sci. Part A Polym. Chem.* **2008**, *46*, 7401–7410.
- (27) Squeo, B. M.; Gregoriou, V. G.; Avgeropoulos, A.; Baysec, S.; Allard, S.;

- Scherf, U.; Chochos, C. L. *Prog. Polym. Sci.* **2017**, *71*, 26–52.
- (28) Kyeong, M.; Lee, J.; Lee, K.; Hong, S. *ACS Appl. Mater. Interfaces* **2018**, *10* (27), 23254–23262.
- (29) He, A.; Qin, Y.; Dai, W.; Luo, X. *Dye. Pigment.* **2019**, *162* (November 2018), 671–679.
- (30) Liu, B.; Ma, Z.; Xu, Y.; Guo, Y.; Yang, F.; Xia, D.; Li, C.; Tang, Z.; Li, W. *J. Mater. Chem. C* **2020**, *8* (7), 2232–2237.
- (31) Pryce, Mary T, Cullen, Aoibhin A.; O'Reilly, Laura, Heintz, Katharina; Long, C.; Heise, A.; Murphy, R.; Gibson, E. A.; Karlsson, Joshua; Towrie, Michael; Greetham, G. M. *Front. Chem.* **2020**, *8* (October), 1–14.
- (32) López-Calixto, C. G.; Barawi, M.; Gomez-Mendoza, M.; Oropeza, F. E.; Fresno, F.; Liras, M.; De La Penã O'Shea, V. A. *ACS Catal.* **2020**, *10* (17), 9804–9812.
- (33) Sprick, R. S.; Aitchison, C. M.; Berardo, E.; Turcani, L.; Wilbraham, L.; Alston, B. M.; Jelfs, K. E.; Zwijnenburg, M. A.; Cooper, A. I. *J. Mater. Chem. A* **2018**, *6* (25), 11994–12003.
- (34) Sprick, R. S.; Wilbraham, L.; Bai, Y.; Guignon, P.; Monti, A.; Clowes, R.; Cooper, A. I.; Zwijnenburg, M. A. *Chem. Mater.* **2018**, *30* (16), 5733–5742.
- (35) Bonillo, B.; Sprick, R. S.; Cooper, A. I. *Chem. Mater.* **2016**, *28* (10), 3469–3480.
- (36) Dai, C.; Xu, S.; Liu, W.; Gong, X.; Panahandeh-Fard, M.; Liu, Z.; Zhang, D.; Xue, C.; Loh, K. P.; Liu, B. *Small* **2018**, *14* (34), 1–6.
- (37) Zhao, Y.; Ma, W.; Xu, Y.; Zhang, C.; Wang, Q.; Yang, T.; Gao, X.; Wang, F.; Yan, C.; Jiang, J.-X. *Macromolecules* **2018**, *51*, 9502–9208.
- (38) Xiang, Y.; Wang, X.; Rao, L.; Wang, P.; Huang, D.; Ding, X.; Zhang, X.; Wang, S.; Chen, H.; Zhu, Y. *ACS Energy Lett.* **2018**, *3* (10), 2544–2549.

- (39) Yang, C.; Ma, B. C.; Zhang, L.; Lin, S.; Ghasimi, S.; Landfester, K.; Zhang, K. A. I.; Wang, X. *Angew. Chemie - Int. Ed.* **2016**, *55* (32), 9202–9206.
- (40) Xu, Y.; Mao, N.; Zhang, C.; Wang, X.; Zeng, J.; Chen, Y.; Wang, F.; Jiang, J. X. *Appl. Catal. B Environ.* **2018**, *228* (January), 1–9.
- (41) Stegbauer, L.; Schwinghammer, K.; Lotsch, B. V. *Chem. Sci.* **2014**, *5* (7), 2789–2793.
- (42) Pachfule, P.; Acharjya, A.; Roeser, J.; Langenhahn, T.; Schwarze, M.; Schomäcker, R.; Thomas, A.; Schmidt, J. *J. Am. Chem. Soc.* **2018**, *140* (4), 1423–1427.
- (43) Li, L.; Fang, W.; Zhang, P.; Bi, J.; He, Y.; Wang, J.; Su, W. *J. Mater. Chem. A* **2016**, *4* (32), 12402–12406.
- (44) Meier, C. B.; Sprick, R. S.; Monti, A.; Guiglion, P.; Lee, J. S. M.; Zwijnenburg, M. A.; Cooper, A. I. *Polymer (Guildf)*. **2017**, *126*, 283–290.
- (45) Wang, Y.; Wang, X.; Antonietti, M. *Angew. Chemie - Int. Ed.* **2012**, *51* (1), 68–89.
- (46) Yi, J.; El-Alami, W.; Song, Y.; Li, H.; Ajayan, P. M.; Xu, H. *Chem. Eng. J.* **2020**, *382* (July 2019), 122812.
- (47) Wang, L.; Fernández-Terán, R.; Zhang, L.; Fernandes, D. L. A.; Tian, L.; Chen, H.; Tian, H. *Angew. Chemie - Int. Ed.* **2016**, *55* (40), 12306–12310.
- (48) Zhao, P.; Wang, L.; Wu, Y.; Yang, T.; Ding, Y.; Yang, H. G.; Hu, A. *Macromolecules* **2019**, *52*, 4376–4384.
- (49) Sprick, R. S.; Jiang, J. X.; Bonillo, B.; Ren, S.; Ratvijitvech, T.; Guiglion, P.; Zwijnenburg, M. A.; Adams, D. J.; Cooper, A. I. *J. Am. Chem. Soc.* **2015**, *137* (9), 3265–3270.
- (50) Warnan, J.; Reisner, E. *Angew. Chemie - Int. Ed.* **2020**, *59*, 2–13.
- (51) Dai, C.; Liu, B. *Energy Environ. Sci.* **2020**, *13* (1), 24–52.

- (52) Zhao, C.; Chen, Z.; Shi, R.; Yang, X.; Zhang, T. *Adv. Mater.* **2020**, *32* (28), 1–52.
- (53) Jayakumar, J.; Chou, H. H. *ChemCatChem* **2020**, *12* (3), 689–704.
- (54) Wang, T. X.; Liang, H. P.; Anito, D. A.; Ding, X.; Han, B. H. *J. Mater. Chem. A* **2020**, *8* (15), 7003–7034.
- (55) Wang, L.; Zhang, Y.; Chen, L.; Xu, H.; Xiong, Y. *Adv. Mater.* **2018**, *30* (48), 1–12.
- (56) Zhang, G.; Lan, Z.-A.; Wang, X. *Angew. Chemie Int. Ed.* **2016**, *55* (51), 15712–15727.
- (57) Busby, E.; Xia, J.; Wu, Q.; Low, J. Z.; Song, R.; Miller, J. R.; Zhu, X. Y.; Campos, L. M.; Sfeir, M. Y. *Nat. Mater.* **2015**, *14* (4), 426–433.
- (58) Blaskovits, J. T.; Fumanal, M.; Vela, S.; Corminboeuf, C. *Chem. Mater.* **2020**, *32* (15), 6515–6524.
- (59) Fumanal, M.; Corminboeuf, C. *J. Phys. Chem. Lett.* **2020**, *11*, 9788–9797.
- (60) Hu, J.; Xu, K.; Shen, L.; Wu, Q.; He, G.; Wang, J. Y.; Pei, J.; Xia, J.; Sfeir, M. Y. *Nat. Commun.* **2018**, *9* (2999), 1–9.
- (61) Smith, M. B.; Michl, J. *Chem. Rev.* **2010**, *110* (11), 6891–6936.
- (62) Gish, M. K.; Pace, N. A.; Rumbles, G.; Johnson, J. C. *J. Phys. Chem. C* **2019**, *123* (7), 3923–3934.
- (63) Congreve, D.; Lee, J.; Thompson, N.; Hontz, E.; Yost, S.; Reuswig, P.; Bahlke, M.; Reineke, S.; Voorhis Van, T.; Baldo, M. A. *Science (80-.)*. **2013**, *340* (1), 334–337.
- (64) Smith, M. B.; Michl, J. *Annu. Rev. Phys. Chem.* **2013**, *64*, 361–386.
- (65) Lukman, S.; Chen, K.; Hodgkiss, J. M.; Turban, D. H. P.; Hine, N. D. M.; Dong, S.; Wu, J.; Greenham, N. C.; Musser, A. J. *Nat. Commun.* **2016**, *7*, 1–13.

- (66) Korovina, N. V.; Pompetti, N. F.; Johnson, J. C. *J. Chem. Phys.* **2020**, *152* (4), 1–21.
- (67) Sunahara, H.; Urano, Y.; Kojima, H.; Nagano, T. *J. Am. Chem. Soc.* **2007**, *129* (17), 5597–5604.
- (68) Li, G.; Yin, J. F.; Guo, H.; Wang, Z.; Zhang, Y.; Li, X.; Wang, J.; Yin, Z.; Kuang, G. C. *ACS Omega* **2018**, *3* (7), 7727–7735.
- (69) He, T.; Tang, D.; Lin, C.; Shen, X.; Lu, C.; Xu, L.; Gu, Z.; Xu, Z.; Qiu, H.; Zhang, Q.; Yin, S. *Polymers (Basel)*. **2017**, *9* (10), 13–18.
- (70) Morisue, M.; Kawanishi, M.; Nakano, S. *J. Polym. Sci. Part A Polym. Chem.* **2019**, *57* (24), 2457–2465.
- (71) Zhang, X.-F.; Feng, N. *Chem. – An Asian J.* **2017**, *12* (18), 2447–2456.
- (72) Black, F. A.; Clark, C. A.; Summers, G. H.; Clark, I. P.; Towrie, M.; Penfold, T.; George, M. W.; Gibson, E. A. *Phys. Chem. Chem. Phys.* **2017**, *19* (11), 7877–7885.
- (73) Banfi, S.; Nasini, G.; Zaza, S.; Caruso, E. *Tetrahedron* **2013**, *69* (24), 4845–4856.
- (74) Zhang, C.; Zhao, J.; Wu, S.; Wang, Z.; Wu, W.; Ma, J.; Guo, S.; Huang, L. *J. Am. Chem. Soc.* **2013**, *135* (28), 10566–10578.
- (75) Reichardt, C. *Chem. Rev.* **1994**, *94* (8), 2319–2358.
- (76) Ulrich, G.; Ziesel, R.; Harriman, A. *Angew. Chemie - Int. Ed.* **2008**, *47* (7), 1184–1201.
- (77) Wang, Z.; Zhao, J. *Org. Lett.* **2017**, *19* (17), 4492–4495.
- (78) Buck, J. T.; Boudreau, A. M.; DeCarmine, A.; Wilson, R. W.; Hampsey, J.; Mani, T. *Chem* **2019**, *5* (1), 138–155.
- (79) Snellenburg, J. J.; Laptinok, S.; Seger, R.; Mullen, K. M.; van Stokkum, I. H. M. *J. Stat. Softw.* **2012**, *49* (3), 1–22.

- (80) Mullen, K. M.; Vengris, M.; Van Stokkum, I. H. M. *J. Glob. Optim.* **2007**, *38* (2), 201–213.
- (81) Van Stokkum, I. H. M.; Larsen, D. S.; Van Grondelle, R. *Biochim. Biophys. Acta - Bioenerg.* **2004**, *1657* (2–3), 82–104.
- (82) Wang, Z.; Sukhanov, A. A.; Toffoletti, A.; Sadiq, F.; Zhao, J.; Barbon, A.; Voronkova, V. K.; Dick, B. *J. Phys. Chem. C* **2019**, *123* (1), 265–274.
- (83) Williams, J. R.; Tancogne-Dejean, N.; Ullrich, C. A. *J. Chem. Theory Comput.* **2021**, In Press.
- (84) Folie, B. D.; Haber, J. B.; Refaely-Abramson, S.; Neaton, J. B.; Ginsberg, N. S. *J. Am. Chem. Soc.* **2018**, *140* (6), 2326–2335.
- (85) Phys, J. C.; He, G.; Busby, E.; Sfeir, M. Y.; Appavoo, K.; Wu, Q.; Campos, L. *M. J. Chem. Phys.* **2020**, *153* (December), 244902–244909.
- (86) Miyata, K.; Conrad-Burton, F. S.; Geyer, F. L.; Zhu, X. Y. *Chem. Rev.* **2019**, *119* (6), 4261–4292.
- (87) Dereka, B.; Rosspeintner, A.; Li, Z.; Liska, R.; Vauthey, E. *J. Am. Chem. Soc.* **2016**, *138* (13), 4643–4649.
- (88) Sun, Z. B.; Li, S. Y.; Liu, Z. Q.; Zhao, C. H. *Chinese Chem. Lett.* **2016**, *27* (8), 1131–1138.
- (89) Ley, C.; Morlet-Savary, F.; Jacques, P.; Fouassier, J. P. *Chem. Phys.* **2000**, *255* (2–3), 335–346.
- (90) Karlsson, J. K. G.; Atahan, A.; Harriman, A.; Tkachenko, N. V.; Ward, A. D.; Schaberle, F. A.; Serpa, C.; Arnaut, L. G. *J. Phys. Chem. A* **2021**, *125*, 1184–1197.
- (91) Aster, A.; Zinna, F.; Rumble, C.; Lacour, J.; Vauthey, E. *J. Am. Chem. Soc.* **2021**, *143*, 2361–2371.
- (92) Galletta, M.; Campagna, S.; Quesada, M.; Ulrich, G.; Ziessel, R. *Chem.*

- Commun.* **2005**, No. 33, 4222–4224.
- (93) Pryce, Mary T, Cullen, Aoibhin A.; O'Reilly, Laura, Heintz, Katharina; Long, C.; Heise, A.; Murphy, R.; Gibson, E. A.; Karlsson, Joshua; Towrie, Michael; Greetham, G. M. *Front. Chem.* **2020**.
- (94) Zhao, J.; Xu, K.; Yang, W.; Wang, Z.; Zhong, F. *Chem. Soc. Rev.* **2015**, *44* (24), 8904–8939.
- (95) Cardona, C. M.; Li, W.; Kaifer, A. E.; Stockdale, D.; Bazan, G. C. *Adv. Mater.* **2011**, *23* (20), 2367–2371.
- (96) Holze, R. *Organometallics* **2014**, *33* (18), 5033–5042.
- (97) Squeo, B. M.; Gasparini, N.; Ameri, T.; Palma-Cando, A.; Allard, S.; Gregoriou, V. G.; Brabec, C. J.; Scherf, U.; Chochos, C. L. *J. Mater. Chem. A* **2015**, *3* (31), 16279–16286.
- (98) Bucher, L.; Aly, S. M.; Desbois, N.; Karsenti, P. L.; Gros, C. P.; Harvey, P. D. *J. Phys. Chem. C* **2017**, *121* (12), 6478–6490.
- (99) Gross, M. A.; Reynal, A.; Durrant, J. R.; Reisner, E. *J. Am. Chem. Soc.* **2014**, *136* (1), 356–366.
- (100) Cecconi, B.; Manfredi, N.; Montini, T.; Fornasiero, P.; Abbotto, A. *European J. Org. Chem.* **2016**, *2016* (31), 5194–5215.
- (101) Sabatini, R. P.; McCormick, T. M.; Lazarides, T.; Wilson, K. C.; Eisenberg, R.; McCamant, D. W. *J. Phys. Chem. Lett.* **2011**, *2* (3), 223–227.
- (102) Suryani, O.; Higashino, Y.; Sato, H.; Kubo, Y. *ACS Appl. Energy Mater.* **2019**, *2* (1), 448–458.
- (103) Shen, X.; Watanabe, M.; Takagaki, A.; Song, J. T.; Ishihara, T. *Catalysts* **2020**, *10* (5), 535.
- (104) Chen, J.; Tao, X.; Tao, L.; Li, H.; Li, C.; Wang, X.; Li, C.; Li, R.; Yang, Q. *Appl. Catal. B Environ.* **2019**, *241* (June 2018), 461–470.

- (105) Sabatini, R. P.; Lindley, B.; McCormick, T. M.; Lazarides, T.; Brennessel, W. W.; McCamant, D. W.; Eisenberg, R. *J. Phys. Chem. B* **2016**, *120* (3), 527–534.
- (106) Xiao, W. C.; Tao, Y. W.; Zhao, Y.; Luo, J. X.; Lai, W. Z. *Inorg. Chem. Commun.* **2020**, *113* (November 2019), 107800.
- (107) Warnan, J.; Willkomm, J.; Farré, Y.; Pellegrin, Y.; Boujtita, M.; Odobel, F.; Reisner, E. *Chem. Sci.* **2019**, *10* (9), 2758–2766.
- (108) Yong, X.; Schoonen, M. A. A. *Am. Mineral.* **2000**, *85* (3–4), 543–556.
- (109) Sundin, E.; Ringström, R.; Johansson, F.; Küçüköz, B.; Ekebergh, A.; Gray, V.; Albinsson, B.; Mårtensson, J.; Abrahamsson, M. *J. Phys. Chem. C* **2020**, *124* (38), 20794–20805.
- (110) Becke, A. D. *J. Chem. Phys.* **1993**, *98* (7), 5648–5652.
- (111) Lee, C. T.; Yang, W.; Parr, R. G. *Phys. Rev. B* **1988**, *37* (2), 785–789.
- (112) Pettersson, G. A.; Al-Laham, M. A. *J. Phys. Chem.* **1991**, *94*, 6081–6090.
- (113) Petersson, G. A.; Bennett, A.; Tensfeldt, T. G.; Al-Laham, M. A.; Shirley, W. A.; Mantzaris, J. *J. Phys. Chem.* **1988**, *89* (4), 2193–2218.
- (114) Frisch, M. J.; Trucks, G. W.; Schlegel, H. B.; Scuseria, G. E.; Robb, M. A.; Cheeseman, J. R.; Scalmani, G.; Barone, V.; Mennucci, B.; Petersson, G. A.; Nakatsuji, H.; Caricato, M.; Li, X.; Hratchian, H. P.; Izmaylov, A. F.; Bloino, J.; Zheng, G.; Sonnenberg, J. L.; Hada, M.; Ehara, M.; Toyota, K.; Fukuda, R.; Hasegawa, J.; Ishida, M.; Nakajima, T.; Honda, Y.; Kitao, O.; Nakai, H.; Vreven, T.; Montgomery, J. A.; Peralta, J. E.; Ogliaro, F.; Bearpark, M.; Heyd, J. J.; Brothers, E.; Kudin, K. N.; Staroverov, V. N.; Kobayashi, R.; Normand, J.; Raghavachari, K.; Rendell, A.; Burant, J. C.; Iyengar, S. S.; Tomasi, J.; Cossi, M.; Rega, N.; Millam, J. M.; Klene, M.; Knox, J. E.; Cross, J. B.; Bakken, V.; Adamo, C.; Jaramillo, J.; Gomperts, R.; Stratmann, R. E.; Yazyev, O.; Austin, A. J.; Cammi, R.; Pomelli, C.; Ochterski, J. W.; Martin, R. L.; Morokuma, K.; Zakrzewski, V. G.; Voth, G. A.; Salvador, P.; Dannenberg, J.

J.; Dapprich, S.; Daniels, A. D.; Farkas; Foresman, J. B.; Ortiz, J. V; Cioslowski, J.; Fox, D. J. *Gaussian 16, Revis. B.01, Gaussian, Inc.* **2016**, 1–20.

(115) Gorelsky, S. I. AOMix | Program for molecular orbital analysis <http://www.sg-chem.net/>.

(116) Gorelsky, S. I.; Lever, A. B. P. *J. Organomet. Chem.* **2001**, 635 (1–2), 187–196.

Chapter 5

Photophysics of Ruthenium(II) Complexes with thiazole π -extended dipyridophenazine ligands

This work was published in *Inorg. Chem.* 2021, **60**, 760-773.

Martin Kaufmann, Carolin Müller, Aoibhín A. Cullen, Michael Brandon, Benjamin Dietzek*, Mary T. Pryce*.

Within this work, I contributed towards the steady state emission studies and time correlated single photon counting (TCSPC) using the FLS1000 photoluminescence spectrometer. Dr. Martin Kaufmann carried out all the synthesis and characterisation. Dr. Martin Kaufmann and Carolin Müller carried out the fs-transient absorption studies in Fredrich Schiller University, Jena, Germany. Carolin Müller performed the DFT calculations. Dr. Michael Brandon completed the electrochemical studies. Supporting information associated with this chapter can be found in Appendix D.

5.1 Preface

The following chapter diverges from the investigation into BODIPY copolymers as visible-light absorbing chromophores for hydrogen evolution and focuses on ruthenium(II) polypyridyl complexes. The two novel ruthenium complexes (**Ru1** and **Ru2**) introduced in this chapter contain a 4-hydroxythiazole π -extended ligand which is known for its strong light absorbing properties such as a high molar extinction coefficient (up to $50,000 \text{ M}^{-1} \text{ cm}^{-1}$). The effect of structural modifications of these ruthenium complexes is investigated using time-resolved techniques using different excitation wavelengths and solvents. In particular, **Ru2** contains a carbazole unit on the 5 position of the thiazole moiety and this strong electron donating moiety also has strong visible light absorbing characteristics. Ultimately, to develop a hydrogen generating photocatalytic system with high efficiency in the solar region for future scale-up commercialisation projects, we must have an in-depth understanding of photodynamics of inorganic complexes and use this knowledge to better design organic-based photosensitisers, such as those studied in chapter 2 – 4.

5.2 Abstract

Transition-metal based donor-acceptor systems can produce long-lived excited charge-transfer states by visible light irradiation. The novel Ru(II) polypyridyl-type complexes **Ru1** and **Ru2** based on the dipyrrophenazine ligand (**L0**) directly linked to 4-hydroxythiazoles of different donor strengths were synthesized and photophysically characterized. The excited-state dynamics were investigated by fs- to ns-transient absorption and ns-emission spectroscopy complemented by time-dependent density-functional theory calculations. These results indicate that photoexcitation in the visible region leads to population of both, metal-to-ligand charge-transfer (¹MLCT) and thiazole induced intra-ligand charge-transfer (¹ILCT) states. Thus, the excited-state dynamics is described by two excited-state branches, namely, population of (i) a comparably short-lived phenazine centered ³MLCT state ($\tau \approx 150 - 400$ ps) and (ii) a long-lived ³ILCT state ($\tau \approx 40 - 300$ ns) with excess charge density localized on the phenazine and thiazole moieties. Notably, the Ru(II) complexes feature long-lived dual emission with lifetimes in the range $\tau_{\text{Em},1} \approx 40 - 300$ ns and $\tau_{\text{Em},2} \approx 100 - 200$ ns, which are attributed to emission from the ³ILCT and ³MLCT manifolds, respectively.

5.3 Introduction

The Ruthenium tris-diimine complexes have been studied over three decades due to their diverse and tunable photophysical and photochemical properties, with a multitude of applications, including dye-sensitized solar cells,¹⁻³ photocatalytic assemblies,⁴⁻⁸ light-induced sensing,^{9,10} and photodynamic therapy.^{10,11} An essential step to optimize any of these applications is understanding the dynamics of the excited states, such as metal-to-ligand charge-transfer (MLCT), ligand-to-metal charge-transfer (LMCT), intra-ligand charge-transfer (ILCT), metal-centered (MC) and ligand-centered (LC) states.¹²

The Ru(II) polypyridyl-type complex $[\text{Ru}(\text{bpy})_2\text{L0}]^{2+}$ (**Ru0**) based on the dipyrido[3,2-a:2',3'-c]phenazine (dppz) ligand **L0**, has been extensively studied, with one major feature of **Ru0** being the *light-switch* effect, which is primarily governed by the sensitivity of the photophysical properties towards the solvent environment *e.g.* ionic-strength, metal-ions or biological macromolecules like DNA.¹³ This interesting property is based on the surrounding dependent excited-state equilibrium between a non-luminescent phenazine-centered and a bright, phenanthroline-centered ³MLCT state. Transient absorption as well as time-resolved emission studies suggests that the *dark* ³MLCT_{phz} state, is formed from the *bright* ³MLCT_{phen} state within 5 ps and has a lifetime of 150 ps in aqueous solution,¹⁴ whereas the *bright* ³MLCT_{phen} state shows no relaxation on the ps-timescale in acetonitrile solution or upon intercalation to DNA.¹⁵⁻¹⁸

There is an ongoing interest in structural modifications of the **L0** ligand to further optimize the excited-state properties in these ruthenium complexes.^{19,20} One approach is via π -extension of the phenazine (phz) substructure, with annulated, ring-fused units.²¹⁻³⁰ Examples of such $[\text{Ru}(\text{bpy})_2(\text{L})]^{2+}$ complexes, with **L0** derived ligands, include; dppn (benzo[i]dipyrido[3,2-a:2',3'-c]phenazine),²⁸⁻³⁰ imdppz (dipyrido[3,2-a:2,3-c]phenazine-10,11-imidazole),²¹ TTF-dppz (4',5'-bis(propylthio)tetrathiafulvenyl[i]dipyrido-[3,2-a:2',3'-c]phenazine),²⁷ tpphz (tetrapyrido[3,2-a:2',3'c:3'',2'',-h:2''',3'''-j]phenazine),²³ Br-dppq (12-bromo-14-ethoxy-dipyrido[3,2-a:2',3'-c]quinolino[3,2-h]phenazine),²² oxo-dppqp

(dipyrido[3.2-a:2'.3'-c]pyrido[2'',3''-4.5.6]quinolino[2,3-h]phenazine-15-one)²⁴ and qdppz (naphtho[2,3-a]dipyrido[3,2-h:2,3-f]phenazine-5,18-dione)²⁶ as **L**. For all these examples, other than the oxo-dppqp and qdppz ligands, π -extension of **L0** leads to stabilization of the phenazine (phz) centered lowest-unoccupied molecular-orbital (LUMO) in the corresponding Ru(II) complexes. Thus, the ${}^3\text{MLCT}_{\text{phz}}$ state in those complexes is additionally stabilized with respect the energetically higher ${}^3\text{MLCT}_{\text{phen}}$ state, resulting a long-lived ${}^3\text{MLCT}_{\text{phen}}$ state, which deactivates *via* emission (between 617 and 638 nm), with lifetimes up to 1 μs . Noteworthy, only Ru(II) complexes bearing linear expanded dppz-ligands, namely dppn, imdppz and TTF-dppz, show dual emission from both, the ${}^3\text{MLCT}_{\text{phen}}$ and the ${}^3\text{ILCT}$ manifold. For the angular complexes $[\text{Ru}(\text{bpy})_2(\text{qdppz})]^{2+}$ and $[\text{Ru}(\text{bpy})_2(\text{oxo-dppqp})]^{2+}$ the LUMO is centered on the acridine or quinone unit of the ligand. Thus, photoexcitation directly populates the ${}^3\text{MLCT}$ and ${}^3\pi\pi^*$ states on the extended **L0** ligand, which rapidly decays back to the ground-state.

The second strategy for π -extension of the **L0** ligand is by using single bond-expansion (SB). Photophysical studies on $[\text{Ru}(\text{bpy})_2(\text{LSB})]^{2+}$ complexes, with 11,12-dimethyl-, -bromine and -cyanide substituted **L0** ligands as **LSB**,^{31–33} reveal no significant change of the **Ru0**-like electronic character. However, Ru(II) complexes bearing **L0** with aromatic substituents as **LSB** exhibit low-lying ILCT states accompanied with increasing molar absorptivity in the visible range with respect to **Ru0**. Extensively studied complexes include directly linked hetero-aromatic systems like the dppz-dimer of **L0**,³⁴ coumarin,³⁴ oxadiazol³¹ or *via* phenyl-, thiophene- and triazole-group linked triarylamin^{35–37} in the 11-position of **L0**. Due to the electron-donating character of those substituents the corresponding Ru(II) complexes $[\text{Ru}(\text{bpy})_2(\text{LSB})]^{2+}$ display low-lying ${}^3\text{ILCT}$ or ${}^3\pi\pi^*$ states. Those low-lying states effect the emissive ${}^3\text{MLCT}_{\text{phen}}$ states, yielding an excited-state lifetimes of up to 2 μs .^{34,36} Systematic alteration of the donor-acceptor distance in a series of Ru(II) complexes with triarylamine expanded **L0** ligands revealed, that the linker between the donor and acceptor units had a strong impact on the ground-state absorption properties, while the excited-state dynamics is primarily governed by the energy gap law and not influenced by the nature of the linker itself.^{35–37}

Recently a novel bridging unit, the 4-hydroxythiazole, was introduced into various donor-acceptor luminophores.³⁸⁻⁴⁰ The fluorescent properties of this class of compounds was extensively studied by the *Beckert* group over the last decade.⁴¹ Features of these materials include, high molar extinction coefficients of up to 50,000 $\text{M}^{-1}\text{cm}^{-1}$ ^{42,43} and fluorescence quantum yields of 90% and higher for many dyes⁴⁴⁻⁴⁶, which leads to numerous applications including, ion sensing,⁴⁷ photosensitizers in organic solar cells,⁴⁸⁻⁵⁰ or as building blocks for luminescent polymers for OLEDs and energy upconversion.⁵¹⁻⁵³ More recently, a series of donor-acceptor chromophores incorporating thiazole donors were synthesized, displaying very low-lying LUMO levels and small optical gaps down to 1.13 eV.⁵⁴ All these results suggest strong communication between the donor and acceptor groups of the respective molecules, a key parameter for light-driven applications like photocatalysis. Thus, an extension of the well-known dppz ligand, with a thiazole group could lead to promising new complexes. However, to the best of our knowledge, no time-resolved studies of single-bonded extended ruthenium dppz complexes with thiazoles have been reported to date, which enables a mechanistic insight into the photophysics of these ruthenium complexes.

In this contribution, we present the synthesis and photophysical properties of two Ru(II) complexes, **Ru1** and **Ru2**, (see **Figure 5.1**) incorporating novel 4-hydroxythiazoles (tz), thus viewed as π -extended ligands of **L0**, labelled **L1** and **L2**. By introducing either a methyl- (**Ru1**) or a phenyl-carbazole-moiety (**Ru2**) in the 5-position of the thiazole moiety, the donor strength and donor-acceptor distance of this ligand increases, with **Ru2** showing a greater spectral change with respect to **Ru1**. Carbazole-substituents are well known as strong electron donating units and are used in manifold photophysical or photochemical applications.^{50,55-58} Herein, we demonstrate the use of time resolved studies and quantum chemical techniques are central in helping to elucidate the excited-state relaxation pathways following excitation, and the differences which are dependent on the electronic properties of the tz group. Firstly, localization of the photoexcited-states within the Franck-Condon region were studied by means of steady-state absorption spectroscopy and the energetics of the relaxed excited states by cyclic voltammetry. Secondly,

photoinduced relaxation kinetics were probed using time-resolved studies, such as ultrafast transient absorption spectroscopy at delay-times up to 10 ns and transient absorption and emission measurements on the sub- μ s timescale. All measurements and calculations support the population of two long-lived emissive excited-states with lifetimes on the sub- μ s timescale.

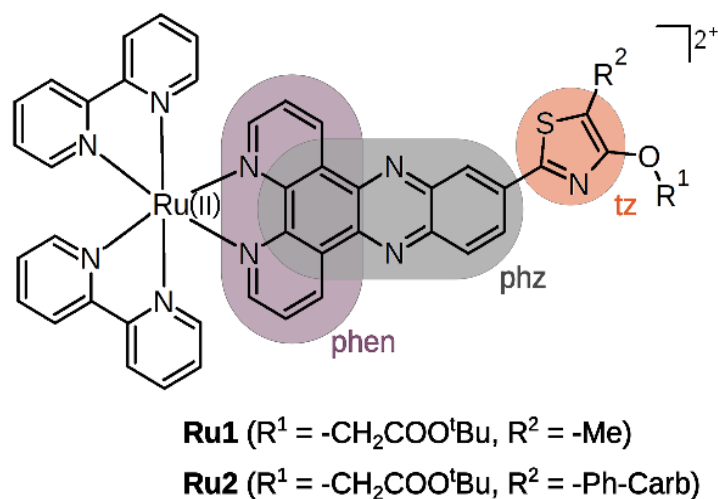


Figure 5.1. General structural formula of **Ru1** and **Ru2**. The photophysically important moieties, namely the phenanthroline- (phen), phenazine- (phz) and thiazole-unit (tz), are highlighted.

5.4 Experimental Section

All starting materials and solvents were commercially available (Sigma Aldrich, Fluorochem, TCI) and used as purchased. Ru(II)(bpy)₂Cl₂ was synthesized as reported elsewhere. Detailed synthetic procedures can be found in the supporting in the electronic supplementary information (Appendix D).

All ¹H and ¹³C NMR spectra were recorded at either 400 and 100 MHz or 600 and 150 MHz respectively using Bruker spectrometers in deuterated solvent. The spectra were processed using Mestrelab Mnova software and were calibrated against solvent peaks according to published values.

The steady state UV-Vis absorption spectra were recorded on a Shimadzu 3100 UV-Vis/NIR spectrophotometer using 1 cm path length quartz cell with a detection range of 190–800 nm. The steady state emission spectra were recorded on a Perkin-Elmer LS50B luminescence spectrophotometer. The solvent used were of spectroscopic grade.

All electrochemical experiments were conducted using a CH Instruments CHI600a potentiostat. All solvents and materials were of spectrophotometric grade and were used as purchased without previous purification. All experiments were carried out in a V-shaped cell with a typical set up consisting of a ~1 mM compound solution in 0.1M TBAPF₆ as solvent ACN, a glassy carbon working electrode, a platinum wire counter electrode, and a Ag/Ag⁺ reference electrode in ACN. Prior to all measurement runs the setup has purged with a nitrogen stream for 15 minutes. All potentials were referenced with respect to the Fe²⁺/Fe³⁺ couple of ferrocene.

The photoinduced processes in-the Ru(II) complexes **Ru1** and **Ru2** were monitored by fs-transient absorption (TA) spectroscopy at delay-times up to 10 ns and on an extended timescale (30 ns to 2 μs) by means of nanosecond time-resolved transient absorption (ns-TA) and emission (ns-Em) measurements. The samples (c = 20 – 100 μM) were dissolved in either acetonitrile or dichloromethane. The samples yielded an OD of 0.15 – 0.40 at the used excitation wavelengths. Note that the ultrafast measurements were performed in 0.1 cm cuvettes, while the transient

absorption and emission spectra of the sub- μ s timescale were recorded in cuvettes with 1 cm path length. During all measurements sample integrity was ensured by recording absorption spectra prior to and after each measurement.

The excitation light source for the measurements on the sub- μ s timescale is based on a Nd:YAG Laser (Continuum Surelite) yielding 5 ns pulses at 1064 nm with a repetition rate of 10 Hz. The fundamental pump-pulses were frequency-tripled (yielding 355 nm) which was used as input for generating pump-pulses centered at 410 and 470 nm using an optic parametric oscillator (Continuum Surelite). The kinetics were studied using probe-light provided by a 75 W xenon arc lamp, which was focused on the sample by a concave mirror. After passing through the sample the probe-pulses were spectrally dispersed (Acton Princeton Instrument 2300), detected on a photomultiplier (Hamamatsu R928) and processed (Pascher Instruments AB). TA kinetics were detected as single-wavelength kinetic between 350 and 800 nm in steps of 10 nm. Emission kinetics were recorded using the ns-TA system without probe-light between 520 and 850 nm in 10 nm steps. To correct for the contribution of emission to the TA-signals, the TA and emission data were subsequently detected, while the emission signals were subtracted from the TA-signals.

The setup for collecting the fs-TA spectra (delay times up to 10 ns) is based on an Ti:Sapphire amplifier (Legend-Elite, Coherent inc.), which yields 35 fs pulses centered at 795 nm with a repetition rate of 1 kHz. The pump-pulses were generated from the amplifier output by either second harmonic generation (403 nm) or by means of a NOPA (470 nm). The excited-state dynamics were probed with white light, which was generated by focusing the fundamental beam into a CaF₂ plate. A mechanical chopper was used to halve the repetition rate of the pump-pulses (to 500 Hz). The probe-pulses were delayed with respect to the arrival of the pump-pulses at the sample position using optical delay stages yielding either a time-resolution of 2 or 10 ns. The probe-pulses were split into a probe and reference beam. The probe-pulses were focused onto the sample using a concave mirror in such a manner, that the probe- and pump-pulses are spatially and temporally overlapped at the sample position. The polarization of the pump- with respect to the probe-pulses were set to magic-angle configuration (54.7°) using a Berek compensator and a polarizer. After passing

through the sample the probe-pulses as well as the reference-pulses were spectrally dispersed and detected on a diode array (Pascher Instruments AB).

Time-correlated single photon counting (TCSPC) lifetimes were carried out using a FLS1000 photoluminescence spectrometer (Edinburgh instruments), equipped with a Xe Arc lamp for steady-state measurements and a visible PMT-900 detector. All data analysis carried out using Fluoracle[®] software. All samples were measured at room temperature and were purged with N₂ prior analysis. For TCSPC, a 360 nm variable pulse length diode laser (VPL-360) was utilized to excite the ground state sample. The accuracy of the fit of the decays was judged by chi-squared (χ^2) and sum of residuals was always $\chi^2 < 1.1$. The fluorescence decay time (τ) was obtained from the slope of the decay curve. Accumulation of the steady-state spectra was obtained using 1 s dwell time and $\times 2$ repeats per spectrum. All samples were measured in a 1 \times 1 cm quartz cuvette and samples were < 0.2 at 360 nm.

The decay rates of the transient absorption and emission data were globally fitted using python 3 (libraries: numpy, pandas, scipy, scipy.optimize, fit: scipy.optimize minimize function) employing a sum of exponential function: $\Delta A(\lambda, t) = \sum_{i,j} A_i(\lambda) \cdot \exp(-k_j \cdot t)$. Prior to global analysis of the j the decay rates (k_j) the fs- and ns-data were dispersion corrected. To avoid prominent contributions from coherent artifact signals the pulse overlap region (± 200 fs) around time-zero was excluded in the fitting procedure of the ultrafast transient absorption data. The wavelength-dependent pre-exponential factors $A_i(\lambda)$ correspond to the decay associated spectra (DAS).

Quantum chemical computations on **Ru1** and **Ru2** and their corresponding ligands **L1** and **L2** were performed using Gaussian 16.⁵⁹ The fully relaxed equilibrium singlet ground-state geometries, were obtained at the density functional level of theory (DFT) using the B3LYP hybrid functional.⁶⁰ To describe the electronic structure of the ruthenium atom the relativistic LANL2DZ⁶¹ pseudo potential and its basis set were applied, while all other atoms were described by the Def2-TZVP triple- ξ basis set.^{62,63} To verify that the optimized geometry is a local minimum on the potential energy

hypersurface a subsequent vibrational analysis on the optimized geometry was performed.

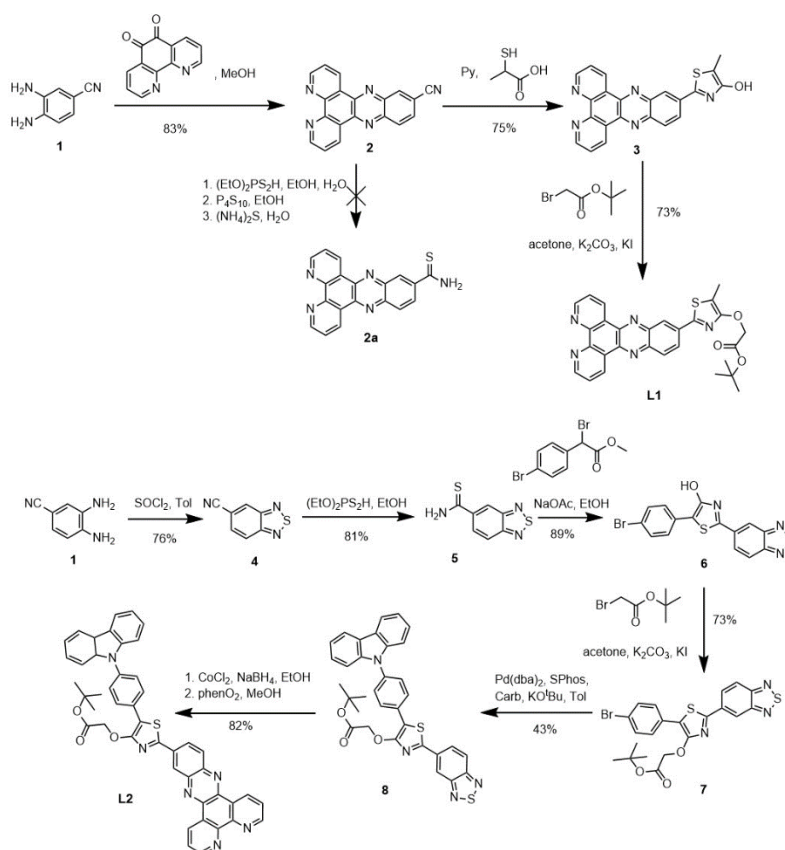
The geometries of the lowest triplet state were obtained by time-dependent DFT (TD-DFT) simulations on the preliminary optimized singly reduced geometries on the same computational level as used for the singlet ground-states. Vertical excitation energies and oscillator strengths were calculated by TD-DFT simulations on the optimized ground-state and lowest triplet-state geometries on the same computational level. The 80 lowest singlet-singlet or triplet-triplet excitations were calculated within the Franck-Condon region. Solvent effects for acetonitrile ($\epsilon = 35.69$, $n = 1.344$) were considered for equilibrium structures, vibrational frequencies and the vertical excitation energies using the SMD variation⁶⁴ of the integral equation formalism variant (IEFPCM).⁶⁵ All simulations were performed including the Grimme-D3 dispersion correction with Becker-Johnson damping.⁶⁶

5.5 Results and Discussion

5.5.1 Synthesis

The first step in the synthesis of the **L1** ligand begins with a condensation reaction of the phenylenediamine **1** with 1,10-phenanthroline-5,6-dione to yield the dppz moiety following the procedure of *Loeb et al.*⁶⁷ The cyano-group is subsequently cyclized with 2-mercaptolactic acid to the 4-Hydroxy-thiazole **3**, which is followed by an alkylation of the hydroxy-group to the final ligand **L2** in 45% yield over 3 steps (see **Scheme 5.1**). To synthesize the ligand **L2** the synthetic procedure was changed from the previous approach. For the planned *Hantzsche Thiazole synthesis*⁶⁸⁻⁷⁰ the CN-dppz **2** requires conversion into a thioamide **2a**, for cyclization to the corresponding thiazole. However various methods and conditions were attempted but the thioamide **2a** could not be isolated in satisfactory yields. In an alternative synthetic route, the phenylenediamine **1** was cyclized to the thiadiazole **4** as a protected precursor for the dppz unit. The conversion of **4** to the thioamide **5** was successfully carried out following a procedure reported by *Gampe et al.*⁷¹ which was used for a similar thiadiazole. The reaction sequence from **5-7** followed the typical route for 4-Hydroxy thiazoles described in the literature.^{38,50,72} Subsequently the thioamide **5** is cyclized with an α -bromo-phenylacetate to the Hydroxythiazoles **6**, which is then etherified to the alkoxythiazole **7**. Finally, a Hartwig-Buchwald cross-coupling was used to install the carbazole unit as a potential photosensitizing moiety to the dye. Last the sulfur of the thiadiazol unit is cleaved out by a reductive ring-opening reaction to form the intermediate with 1,10-phenanthroline dione (phenO₂) to the final ligand **L2**. The dppz-based ligand **L1** and **L2** were then reacted with Ru(bpy)₂Cl₂ in ethanol (under light exclusion) to obtain the tris-diimine type complexes **Ru1** and **Ru2**. The resulting chloride salts were transformed into the PF₆⁻ analogues via an anion exchange reaction with yields of 53% and 42%, respectively.

The ligands and complexes were characterized via NMR spectroscopy, mass spectrometry and elemental analysis.



Scheme 5.1. Synthetic route of the ligands **L1** and **L2**.

5.5.2 Electrochemical properties

In order to assist interpretation of the photophysical properties, electrochemical studies were performed. In this context the molecular orbitals, which are involved in the first oxidation and reduction can be considered as the orbitals, which are involved in the lowest charge-transfer states. Therefore, cyclic voltammograms (CVs) of the Ru(II) complexes in acetonitrile were recorded and the resulting redox potentials are summarized in **Table 5.1**. The cyclic voltammograms of both complexes show one oxidation wave and several, partly reversible reduction processes (*cf.* **Figure S5.2**). The reduction for this type of complexes are typically centered at: 1. dppz-moiety (esp. phz), 2. bpy-ligands and 3. possible further reductions at the dppz (esp. phen).^{21,36,73} In case of **Ru1**, the first dppz-based reduction appears at -1.13 V. Even though a thiazole group is considered an electron donating group and thus a decreased potential compared to **Ru0** is expected, an anodic shift is observed. This can be attributed to the π -extension of dppz unit, namely the tz-moiety, which increases the conjugation of the

phz⁻ radical anion and stabilizes the lowest unoccupied molecular orbital (LUMO). This behavior was observed in donor substituted dppz-derived copper complexes by Fraser et al.,⁷⁴ where extension by a thiocarbonate group and alkylthioether led to a stabilization of the phz MO. Similar observations were reported by Larsen et al. for aryl-amino substituted rhenium complexes.⁷⁵ Furthermore, this is supported by TD-DFT simulations, which show the influence of the thiazole extension on the LUMO (*cf.* **Figure S5.1**). The reductions on the bpy-ligands at -1.78 V and -1.98 V are not influenced by this effect and are not shifted, with respect to **Ru0**. For **Ru2** no reversible reductions at the dppz-moiety were observed and the first reduction is cathodically shifted to -1.64 V. This is attributed to the strong electron donating character of the carbazole which increases the electron density on the phz-sphere and induces a shift to more negative potentials. The bpy ligand-based reductions are again not significantly affected. The oxidation of **Ru1** occurs at 0.94 V vs. Fc/Fc⁺ and demonstrates the typical reversibility, and shape of the redox couple Ru²⁺/Ru³⁺, with a cathodic shift with respect to oxidation of the parent complex, **Ru0**. In agreement with the shift in the reduction potential in **Ru1**, stabilization of the LUMO increases the π -accepting character of the ligand and subsequently reduces the electron density at the metal center. A similar anodic shift was observed in donor-substituted dppz complexes³⁶ and is further supported by TD-DFT simulations, which indicate that the first oxidation is centered at the ruthenium core (*cf.* **Figure S5.1**). On the other hand, the first oxidation in **Ru2** appears as an intense, irreversible multi-electron process. This contrast suggests, that this redox feature is unlikely, due to oxidation of the Ru²⁺ center and is instead assigned to a ligand-centred (LC) oxidation on the carbazole moiety, which was observed in similar triarylamine-extended Ru(II) and Re(I) dppz complexes^{35,36,75} and is supported by TD-DFT simulations (*cf.* **Figure S5.1**). As discussed elsewhere,⁷⁶ the pathways of oxidation in carbazole derivatives is often of complicated nature and highly depended on the substitution of the nitrogen. Overall, the single bond π -extension exerts a strong influence on the Ru- and ligand-based redox behavior with respect to the unsubstituted Ru0. While the redox potentials of Ru1 are mainly influenced by the stabilization of the LUMO due to the conjugation-extension of the thiazole, the redox behavior of Ru2 is primarily altered by the strong electron donating character of the carbazole.

Table 5.1. Summary of the photophysical and electrochemical properties of **Ru1** and **Ru2**. As a reference to compare the literature known compound **Ru0** ($[[\text{Ru}(\text{bpy})_2\text{dppz}]^{2+}]$) was added to the table. values taken from: (a) Ref. ⁶¹, (b) Ref. ⁶³, (c) depicted potentials are peak potentials, corrected against $E_{1/2} \text{Fc}/\text{Fc}^+$.

	$\lambda_{\text{abs}}^{\text{max}} / \text{nm}$ ($\epsilon_{\text{abs}}^{\text{max}} / \text{M}^{-1}\text{cm}^{-1}$)	$\lambda_{\text{em}}^{\text{max}} / \text{nm}$	Stokes- Shift / eV	$\tau_{\text{Em}} / \text{ns}$ $\tau_{\text{Em},1}$ $\tau_{\text{Em},2}$	$E_{1/2}^{\text{ox}} / \text{V}$	$E_{1/2}^{\text{red1}}$	$E_{1/2}^{\text{red2}}$	$E_{1/2}^{\text{red3}}$
Ru0	446 (16,400)	622	0.79	– 180 ^(a)	+0.84 ^(b)	-1.36 ^(b)	-1.79 ^(b)	-2.01 ^(b)
Ru1	441 (25,700)	630/708	0.84/1.06	45 180	+0.94	-1.13	-1.78	-1.98
Ru2	444 (22,000)	630/708	0.82/1.04	75 180	+0.95 ^(c)	-1.64 ^(c)	-1.78 ^(c)	-1.96 ^(c)

5.5.3 Ground-state absorption properties

Understanding the nature of the electronic transitions and the initially populated excited-states is essential when interpreting the under-lying photophysical and photochemical processes. In **Figure 5.2** the ground-state absorption spectra of the Ru(II) complexes **Ru1** and **Ru2** in acetonitrile solution are shown.

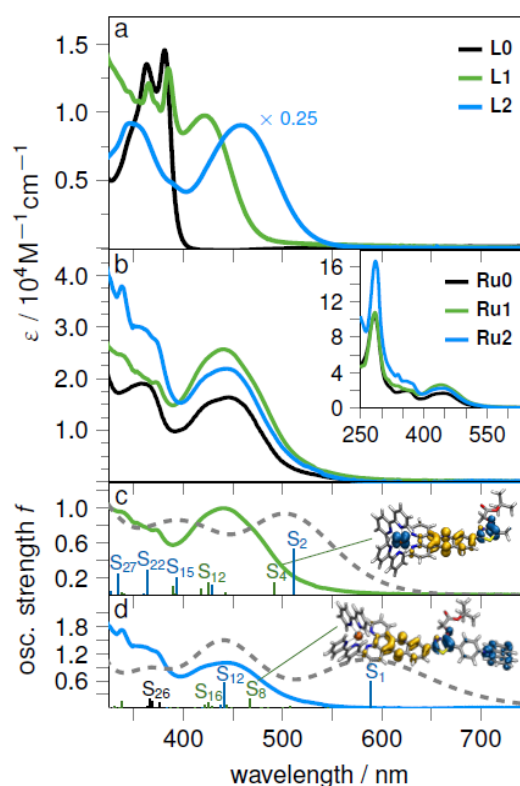


Figure 5.2. UV-vis spectra of the Ruthenium complexes **Ru1** and **Ru2** (b) and the corresponding dppz-ligands **L1** and **L2** (a) in acetonitrile. TD-DFT simulated absorption spectra (dashed grey lines) of **Ru1** and **Ru2** (solid lines in (c) and (d)) and charge density differences of MLCT_{phz} and $\text{ILCT}_{\text{tz/phz}}$ states. The character of the predicted states is highlighted in blue (ILCT), green (MLCT) and black ($\pi\pi^*$), respectively.

To understand the impact of the tz-substituents on the electronic properties of the Ru(II) complexes, the absorption spectra were compared to the well-known absorption spectra of **Ru0** and **L0** and the absorption spectra of the herein studied ligands **L1** and **L2** complemented by quantum chemical time-dependent density functional theory (TD-DFT) simulations (*cf.* **Figure S5.3** (b), (c), (e) and (f), Appendix D, **Section S5.1.3**).

The absorption spectra of **Ru1** and **Ru2** are comparable to other ruthenium tris-diimine complexes, such as **Ru0**. The complexes exhibit the (a) characteristic intense ligand-centered (LC) transitions on the phen/bpy sphere at 283 nm,⁷⁷ (b) several LC and metal-to-ligand charge-transfer (MLCT) features between 320 and 400 nm together with (c) broad MLCT and ILCT bands between 400 and 550 nm.^{78–80} The higher molar extinction coefficients of **Ru1** and **Ru2** with respect to the parent complex, **Ru0**, can be rationalized by contributions of the tz-moiety due to the π -extension of the dppz ligand with that unit. This is manifested in the visible absorption features of the corresponding ligands **L1** and **L2**, which exhibit a broad absorption band ranging from 400 to 500 nm. As these features are not observed in **L0**, they are associated to charge-transfer (CT) transitions with contributions from the tz-moiety. This is supported by TD-DFT simulations (*cf.* **Figure 5.2 c** and **d**), which predict low-lying ILCT states (**Ru1**: S₂, **Ru2**: S₁), where electron density is shifted from the tz- to the phz-moiety of the ligand (*cf.* **Table S5.1**). Such ILCT states usually lead to a red-shift in the absorption spectra.^{21,22,24} Moreover, LC states on the carbazole-unit of **L2** lead to a hyperchromic effect of the absorption features for **Ru2** in the region between 320 and 400 nm (*cf.* **Figure 5.2, e.g.** S₂₆) with respect to **Ru1**.^{35–37}

Additionally, **Ru1** and **Ru2** show typical **L0**-based features, namely higher-energy transitions assigned to LC states and lower energy bands attributed to $\pi\pi^*$ and $n\pi^*$ states between 330 and 380 nm.^{81,82} The absorption maxima of **Ru1** and **Ru2** (373 nm) appear red-shifted with respect to **Ru0** (358 nm). This is consistent with stabilization of phenazine centered LUMOs localized on **L1** and **L2** by the presence of the electron-donating tz-substituent in the 11-position of **L0**.^{31,34} This indicates that the **L0**-moiety of **L1** and **L2** acts as a relatively strong acceptor, as the position of the absorption maximum is dependent on the electron withdrawing strength of the acceptor

unit.^{35,36,38} Altogether, the absorption features of the Ru(II) complexes can be categorized into MLCT, ILCT and LC states, which are similar to those of **Ru0**. However, the visible absorption band of the π -extended complexes shows mixed character involving MLCT and ILCT transitions due to the tz-moiety (*cf.* blue lines in **Figure 5.2** (c) and (d) and CDDs **Table S5.1**).

5.5.4 Photoinduced dynamics

The excited-state dynamics of the Ru(II) complexes **Ru1** and **Ru2** were monitored by fs-transient absorption (TA) spectroscopy at delay-times up to 10 ns and on longer timescales (30 ns to 2 μ s) by means of ns-TA and ns-emission (ns-Em) spectroscopy. Initially we will discuss the excited-state properties of **Ru1** and **Ru2** upon blue excitation, i.e., at 410 and 403 nm for the ns-experiments and the fs-TA. In addition, the impact of excitation wavelength and solvent polarity (acetonitrile ($\epsilon = 37.5$), dichloromethane ($\epsilon = 8.9$)) on the ultrafast processes was probed, in an attempt to resolve the contributions of excited MLCT and ILCT states.⁸³

Long-lived excited-states of Ru1 upon excitation in acetonitrile.

The ns- and fs-experiments for Ru1 were performed upon excitation in the blue i.e., at 410 and 403 nm excitation, which both lead to population of MLCT_{phz} and $\text{ILCT}_{\text{tz/phz}}$ states. Initially the long-lived excited-states of **Ru1** will be discussed followed by the ultrafast processes on the ps-timescales. On a sub- μ s timescale ns-Em and ns-TA spectra were recorded (*cf.* **Figure 5.3** (a) and (d)). The transient-emission spectra decay bi-exponentially with maxima at 630 and 720 nm. The transient emission spectra do not resemble the steady-state emission spectrum, which exhibits only one maximum at ~ 630 nm (*cf.* **Figure 5.3** (b)). However, the steady-state emission spectrum is a superposition of the emission spectra of two different states. Global analysis yields lifetimes of $\tau_{\text{Em},1} = 45$ ns and $\tau_{\text{Em},2} = 184$ ns (*cf.* **Figure 5.3** (c)). Noteworthy, the latter emission lifetime is similar to that previously reported for **Ru0** in acetonitrile. The parent complex exhibits a phen centered emissive state ($^3\text{MLCT}_{\text{phen}}$), which decays monoexponentially with a lifetime of 180 ns.¹⁵⁻¹⁷ Additionally, the spectrum of **Ru1** attributed to $\tau_{\text{Em},2}$ resembles the steady-state emission spectrum of **Ru0** (*cf.* solid grey line in **Figure 5.3** (b)). Hence, $\tau_{\text{Em},2}$ can be

assigned to a bright $^3\text{MLCT}_{\text{phen}}$ state. Consequently, the shorter-lived emission signal is most a result of the π -extension of the dppz ligand.^{21,28–30,34}

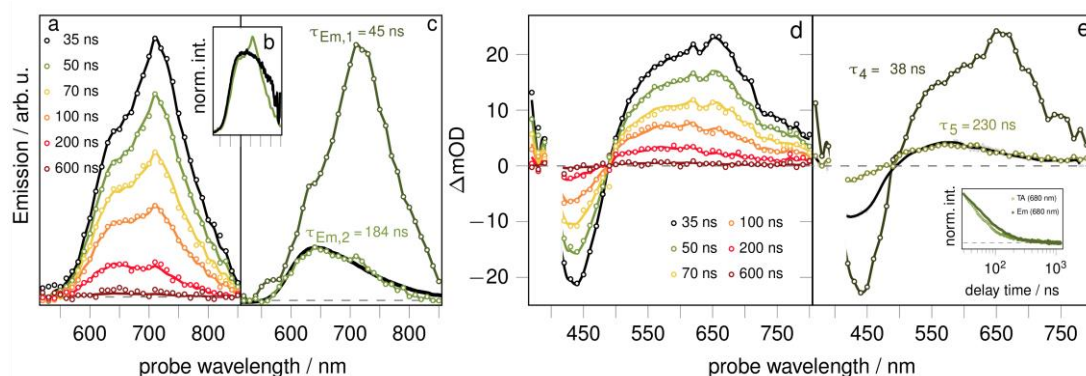


Figure 5.3. Nanosecond time-resolved emission (a) and transient absorption spectra (d) and their corresponding decay associated spectra (ns-Em: (c), ns-TA: (e)) of **Ru1** (22 μM) following excitation at 410 nm (3.0 mW, OD at $\lambda_{\text{exc}} = 0.44$), in acetonitrile. The steady-state emission (solid, grey line) together with the lifetime weighted transient emission spectrum (solid, green line) recorded following excitation at 410 nm are compared in (b). The inset in figure (e) displays the emission decay signal at 680 nm (dark green) compared to the transient absorption kinetic trace at 680 nm (green). The solid grey lines in figure (c) and (e) represent the steady-state emission spectrum and TA of the long-lived $^3\text{MLCT}_{\text{phen}}$ state of **Ru0**, respectively.

In the ns-TA spectra of **Ru1**, a ground-state bleach (GSB) ranging from 400 to 500 nm is evident together with an excited-state absorption (ESA) between 360 and 400 nm and above 500 nm (*cf.* **Figure 5.3** (d)) following excitation. Global analysis of the transient data reveals two excited-state lifetimes of $\tau_4 = 38$ ns and $\tau_5 = 230$ ns. These lifetimes obtained from ns-TA resemble those of the TCSPC experiments. Consequently, τ_4 and $\tau_{\text{Em},1}$ are attributed to the decay of the same species as are τ_5 and $\tau_{\text{Em},2}$. The spectral changes associated with τ_5 , $\text{DAS}(\tau_5)$, describe the decay of the ESA between 500 and 700 nm, with a maximum at 590 nm and a comparably weak ground-state bleach recovery. However, the ESA above 500 nm in the $\text{DAS}(\tau_5)$ is in agreement with the spectrum of the long-lived $^3\text{MLCT}_{\text{phen}}$ state of **Ru0** (*cf.* solid grey line in **Figure 5.3** (e)).^{17,84,85} This supports the assignment of τ_5 to the decay of a $^3\text{MLCT}$ state as in **Ru0**. $\text{DAS}(\tau_4)$ shows the decay of ESA centered at 660 nm (related to a $^3\text{ILCT}$ state), which leads to a sharpening of the ESA band at 590 nm in the first 100 ns. Thus, we assign τ_4 to deactivation of a phz/tz-centered ILCT state ($^3\text{ILCT}_{\text{phz/tz}}$). The emission maximum associated to $\tau_{\text{Em},1}$ at 708 nm is red shifted with respect to the $^3\text{MLCT}$ emission maximum (620 nm). This points towards emission from a lower-lying triplet state, associated with the extended dppz-structure: TD-DFT simulations predict a

$^3\text{ILCT}$ state as the lowest triplet state for **Ru1**. This state is localized on the tz- and phz-moiety of the π -extended ligand (*cf.* spin density distribution in **Figure 5.4** (d)). The simulated absorption spectrum of this $^3\text{ILCT}$ state resembles the features of the transient spectra at 590 and 700 nm (*cf.* **Figure 5.4** (d)). Therefore, both the experimental and computational studies support population of both MLCT and ILCT states, following excitation of **Ru1**, with these states yielding long-lived $^3\text{MLCT}$ and $^3\text{ILCT}$ states.

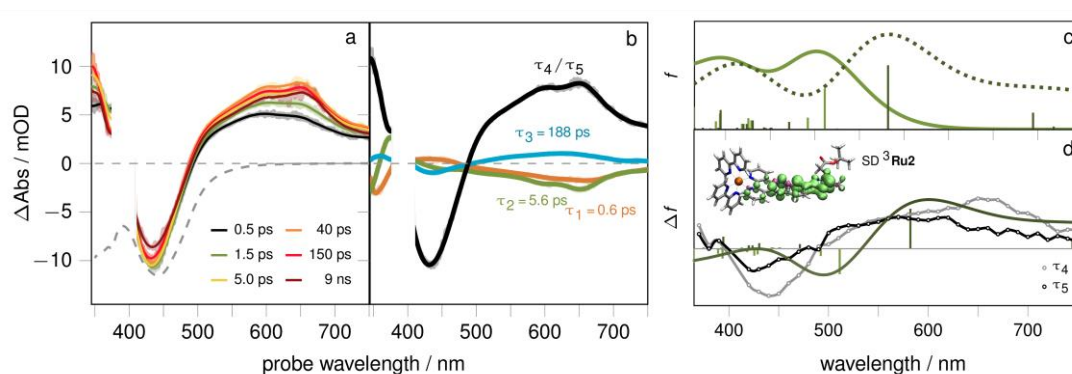


Figure 5.4. Transient absorption (a) and decay associated spectra (b) **Ru1** (90 μM) following excitation at 403 nm (0.5 mW, OD at $\lambda_{\text{exc}} = 0.16$) in acetonitrile. TD-DFT simulated absorption spectra of the optimized S_0 ($^1\text{Ru1}$, singlet-singlet excitations, solid, green line) and T_1 ($^3\text{Ru1}$, triplet-triplet-excitation, dotted, dark green line) geometries of **Ru1**. The vertical transition energies and their corresponding oscillator strength are shown by bars (c, d), which were broadened using Gaussian functions (c, full-width half-maximum of 0.30 eV). Comparison of the decay associated spectra (normalized at 550 nm) of τ_4 (grey marks) and τ_5 (black marks) to the simulated difference spectrum (solid, green line) for an $^1\text{Ru1}$ to $^3\text{Ru1}$ excitation and spin density distribution of **Ru1** in the lowest triplet state (d).

Characterisation of the sub-ns processes in Ru1 upon 403 nm excitation in acetonitrile.

The sub-ns processes of **Ru1** reflecting the formation of the long-lived excited $^3\text{MLCT}$ and $^3\text{ILCT}$ states were characterized by fs-TA spectroscopy. Those spectra display an instantaneous GSB, which reflects the shape of the ground-state absorption bands (*cf.* dashed, grey line in **Figure 5.4** (a)). The GSB contributions are accompanied by ESA features between 350 to 380 nm and a second differential absorption band above 500 nm. The spectrum recorded at 0.5 ps for **Ru1** display a broad ESA above 500 nm with a maximum at 590 nm. Within the first 5 ps this ESA band increases and sharpens at around 660 nm, yielding a long-lived band with distinct features at 590 and 660 nm. Employing a global fit, the sub-ns transient absorption kinetics of **Ru1** is best

described by three exponentials: 0.6 ps (τ_1), 5.6 ps (τ_2) and 188 ps (τ_3) (*cf.* **Figure 5.4** (b)).

The spectral changes associated with the first two time-constant, namely $\tau_1 = 0.6$ ps and $\tau_2 = 5.6$ ps, contain contributions of inter-system crossing⁸⁶ (ISC), inter-ligand hopping and vibrational cooling. This is manifested in an overall build-up of an ESA, regardless of the region of the ground-state absorption between 410 and 470 nm. As the DAS τ_1 is zero in this region, τ_1 can be assigned to relaxation of the photoexcited ¹MLCT and ¹ILCT states to an energetically lower triplet state *via* inter-system crossing (ISC),^{87–90} (population of states with ESA maxima at around 590 and 685 nm can be assigned to triplet states). The ESA maxima at 590 and 340 nm are associated with a shift of electron density to the phz sphere based on the spectral signatures of the structurally related phz radical anion of **Ru0**^{17,84,31–33} and other related π -extended systems^{23,24,28–31,34}. The ESA between 360 and 370 nm stems from IL absorption of the reduced bpy sphere, suggesting population of ³MLCT_{bpy} states. Hence, the shift of the ESA from 370 to 340 nm associated with the characteristic time τ_2 is ascribed to interligand hopping of electron density from the bpy to the extended dppz ligand. Vibrational cooling occurs in conjunction with interligand hopping is revealed with a blue-shift and a sharpening of the ESA yielding a maximum at ~ 660 nm. Finally, the 188 ps component reflects partial ground-state recovery with a decay of the phz associated absorption at 340 nm. Hence, this indicates the decay of a subset of the ensemble of complexes with a reduced phz moiety. Based on the literature for **Ru0** complexes^{15,24,32,71} we ascribe these spectral changes to the decay of the ³MLCT_{phz} state. In contrast to the fast deactivation of the ³MLCT_{phz} state, complexes populating the ³MLCT_{phen} and the ³ILCT state are long-lived and contribute to the ns-data (as discussed above).^{31,34,79}

Photoinduced dynamics of Ru2 upon 410 nm excitation in acetonitrile.

The long-lived excited-states of **Ru2** (ns-TA and ns-Em studies) reveal almost identical spectral features and decay associated spectra to **Ru1** upon 410 nm excitation (*cf.* **Figure S5.7** and **S5.8**). Thus, we conclude that both complexes exhibit two long-lived emissive states in the ³MLCT and ³ILCT manifold. However, the decreased

lifetime of the $^3\text{ILCT}$ excited-state of **Ru1** ($\tau_{\text{Em},1} \approx \tau_4 \approx 40$ ns) compared to **Ru2** ($\tau_{\text{Em},1} = 75$ ns and $\tau_4 = 55$ ns) is attributed to the increased donor-strength in **Ru2** due to the carbazole-unit. In contrast to **Ru1**, the spectra assigned to the decay of the two long-lived $^3\text{MLCT}$ and $^3\text{ILCT}$ states, show similar GSB contributions. This highlights the impact of the donor-strength of the tz-group on the excited-state properties.

Although, the additional electron donor in **Ru2** affects the lifetimes of the long-lived states, it has no impact on the ultrafast dynamics. The transient absorption spectra for the formation of the long-lived excited-states of **Ru2** are characterized by three time-constants ($\tau_1 = 0.8$ ps, $\tau_2 = 6.6$ ps and $\tau_3 = 150$ ps, *cf.* **Figure 5.5** (b) and (c)), whose spectral shapes and lifetimes are similar to the data obtained for **Ru1**.

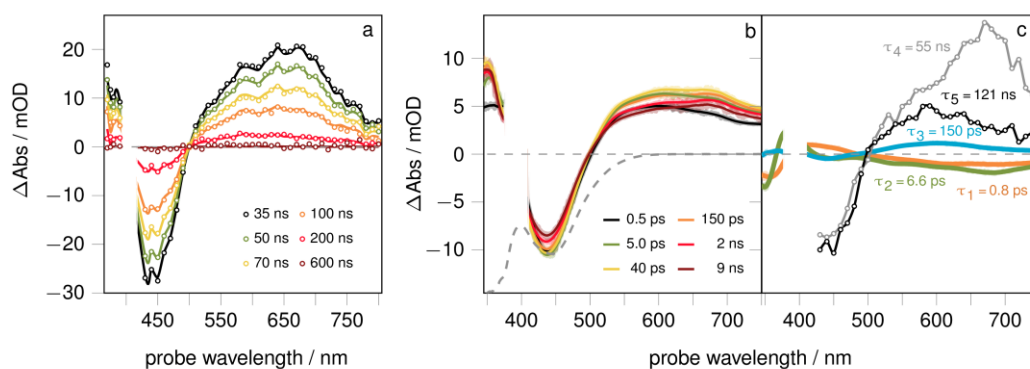


Figure 5.5. Nanosecond (a) and picosecond time-resolved transient absorption spectra (b) with their respective decay associated spectra (c) of **Ru2** upon excitation at 410 nm (ns-TA, 3.0 mW, OD at $\lambda_{\text{exc}} = 0.4$) or 403 nm (fs-TA, 0.5 mW, OD at $\lambda_{\text{exc}} = 0.2$) in acetonitrile.

Thus, the photoinduced relaxation processes in **Ru2** can be discussed in the proposed model in **Figure 5.6**. However, the additional donor moiety in **Ru2**, leads to a red shift in the ESA maxima in the $^3\text{ILCT}$ manifold, which is manifested in broader and featureless ESA bands with respect to **Ru1**.

In summary, photoexcitation at 410 nm initially populates an ensemble of $^1\text{MLCT}$ ($^1\text{MLCT}_{\text{bpy}}$, $^1\text{MLCT}_{\text{phen}}$, $^1\text{MLCT}_{\text{phz}}$) and $^1\text{ILCT}$ states. The subsequent photophysics is proposed to populate two long-lived excited-states in the $^3\text{MLCT}$ and $^3\text{ILCT}$ manifold. One subset in the $^1\text{MLCT}$ manifold relaxes into the long-lived $^3\text{MLCT}$ state (< 1 ps),¹⁵⁻¹⁷ while the other subset ($^3\text{MLCT}_{\text{phz}}$ states) non-radiatively decays back to the ground state (≈ 150 ps). In the ILCT branch, initial population of the $^1\text{ILCT}$ state relaxes into a long-lived phz/tz centered $^3\text{ILCT}$ state (≈ 6 ps). The long-lived excited

$^3\text{MLCT}$ and $^3\text{ILCT}$ states radiatively decay within $\sim 200 \text{ ns}^{15-17}$ and $\sim 40 \text{ ns}$, respectively (*cf.* **Figure 5.6**).

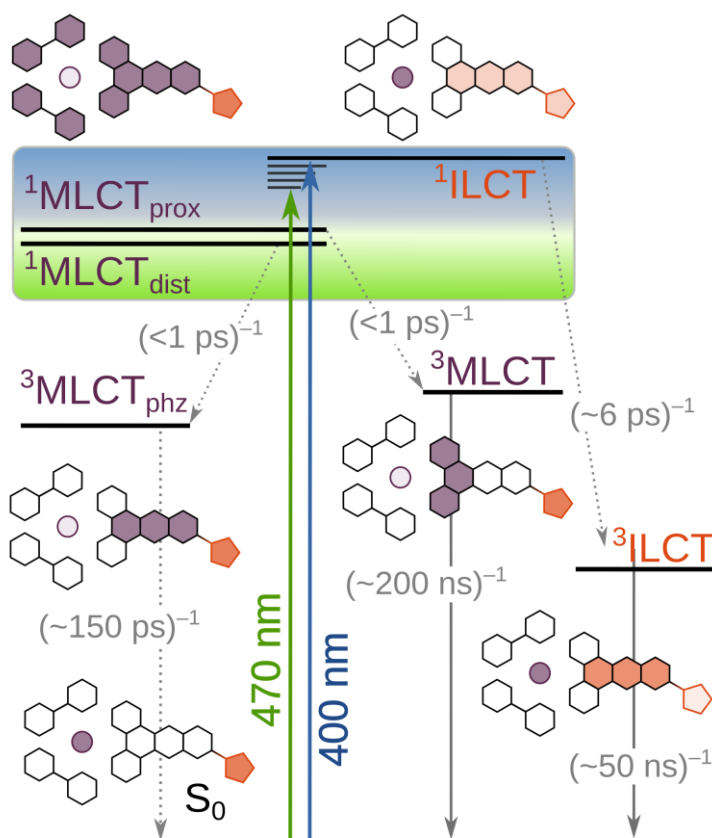


Figure 5.6. Jablonski diagram for the formation of the long-lived $^3\text{MLCT}$ and $^3\text{ILCT}$ states (right side) and the short-lived phz-centered $^3\text{MLCT}$ state ($^3\text{MLCT}_{\text{phz}}$, left side) upon photoexcitation of **Ru1** and **Ru2** at 400 and 470 nm. The relative population density in the $^3\text{MLCT}$ manifold is depicted by the green-blue-coloured box, indicating a higher population density of $^3\text{MLCT}_{\text{phz}}$ states upon excitation in the red-flank of the absorption band (470 nm, green shading) or the proximal $^3\text{MLCT}$ states upon 400 nm excitation (blue, shading). The colours in the schematically shown ground-state structure (S_0) depict the origin of the excess electron density, which is either from the tz-unit (ILCT character: orange) or the Ru(II) center (MLCT character: violet). In the sketches of the excited-state geometries the colours highlight the localization of the excess electron density either in the $^3\text{MLCT}$ (violet) or $^3\text{ILCT}$ sphere (orange). The numbers associated with the dotted arrows are the first order rate constants associated with the respective processes in acetonitrile.

Impact of excitation wavelength

To verify the proposed model, additional fs-transient absorption (using delay times up to 2 ns) at 470nm and ns-emission (ns-Em) experiments were performed. For both complexes the transient emission signals decay bi-exponentially (*cf.* **Figure 5.7** (g) and (h)), while global analysis of the fs-TA kinetics yields four components (*cf.* **Figure 5.7** (c) and (d)). The spectral shapes of the obtained decay signals and their kinetic components agree with the experiments carried out upon blue excitation.

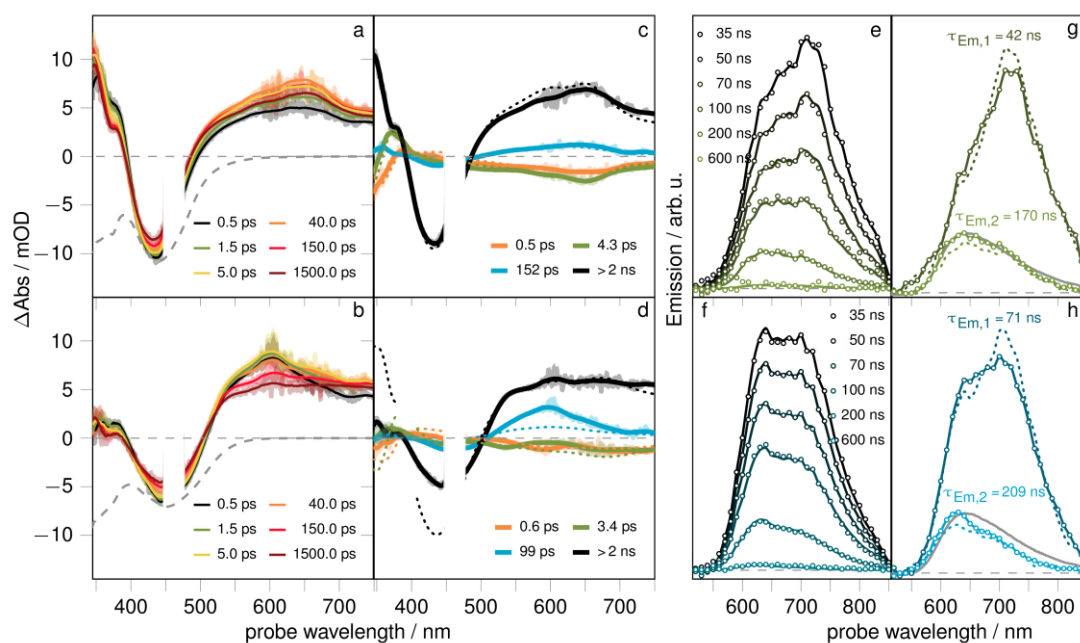


Figure 5.7. Time-resolved spectra of **Ru1** (top row, green) and **Ru2** (bottom row, blue) upon 470 nm excitation in acetonitrile: Ultrafast transient absorption spectra (a – b, 0.2 mW, OD at $\lambda_{\text{exc}} = 0.3 - 0.5$) and the corresponding decay associated spectra (c – d) and transient emission spectra (e – f, 3.5 mW, OD at $\lambda_{\text{exc}} = 0.1 - 0.3$) and corresponding decay associated spectra (g – h). The solid grey lines in figures g – h show the steady-state emission spectrum of **Ru0**. For reasons of comparability the decay associated spectra obtained upon 403 nm (410 nm) excitation are represented in figures c – d and g – h (dashed lines).

However, the spectral profiles of the ns-Em spectra of **Ru1** and **Ru2** and the fs-TA spectra of **Ru2** differ when comparing excitation at either 470 or 403 nm within the signal-to-noise ratio of the measurements. For both complexes the spectral weights associated to the decay of the long-lived $^3\text{MLCT}$ state increase with the increasing excitation wavelength. This can be seen in the higher amplitudes of DAS($\tau_{\text{Em},2}$) at the expense of DAS($\tau_{\text{Em},1}$) when moving from 410 to 470 nm excitation (*cf.* solid (470 nm) *vs.* dashed lines (410 nm) in **Figure 5.7** (c) and (d)). This might be related to a higher degree of population of the emissive $^3\text{MLCT}$ state (direct $^1\text{MLCT}$ excitation). In the fs-TA spectra of **Ru2**, the spectral weights of DAS(τ_3), increase upon increasing excitation wavelength. As this process is associated to relaxation of a $^3\text{MLCT}_{\text{phz}}$ subset of the excited-state ensemble, the increasing amplitude is indicative of a higher degree of population of the $^1\text{MLCT}_{\text{phz}}$ state with respect to $^1\text{MLCT}_{\text{bpy}}$ and $^1\text{MLCT}_{\text{phen}}$ states at 470 nm excitation, when compared to 403 nm excitation. Due to this, the transient spectra of **Ru2** obtained at 2 ns indicate weaker ground-state bleaching upon 470 nm with respect to the 403 nm excitation. However, the spectral weights of the TA-DAS of **Ru1** are almost independent of the excitation wavelength.

Thus, the changes in **Ru2** may be related to an altered Franck-Condon geometry due to the electron donating carbazole moiety. In summary, the changes in the ns-Em spectra indicate an increasing population density of long-lived $^3\text{MLCT}$ states at the expense of $^3\text{ILCT}$ states, which can be captured within the proposed model (*cf.* **Figure 5.6**).

Impact of solvent polarity

To gain an insight into the solvent dependence of the electron-transfer processes, the photoinduced dynamics of **Ru1** and **Ru2** following excitation at 470 nm were investigated in both DCM and ACN. The ground-state absorption spectra in DCM are very similar to those in ACN (*cf.* **Figure S5.4**). This indicates that the population of excited-states at the Franck-Condon point is only marginally influenced by the solvent polarity. The visible absorption maxima at around 470 nm are bathochromically shifted by *ca.* 20 meV, when the solvent is changed from ACN to DCM. This indicates stabilization of the proximal $^1\text{MLCT}$ states ($^1\text{MLCT}_{\text{bpy}}$ and $^1\text{MLCT}_{\text{phen}}$) with respect to the weakly absorbing $^1\text{MLCT}_{\text{phz}}$ state.

The fs-TA data (recorded at delay times up to 2 ns) of **Ru1** and **Ru2** obtained in DCM upon 470 nm excitation is best described by three exponentials (*cf.* **Figure 5.8** and **Figure S5.12**). However, the spectral shapes of the corresponding DAS do not match those obtained in ACN. The transient spectra in DCM display one pronounced feature at approximately 610 nm, whereas there are two strong features at 590 and 680 nm in ACN (at delay times > 5 ps). While population of the excited $^3\text{ILCT}$ and $^3\text{MLCT}$ states takes place with almost the same kinetic components as found in ACN ($\tau_{1,\text{ACN}} \approx \tau_{1,\text{DCM}} \approx 0.7$ ps and $\tau_{2,\text{ACN}} \approx \tau_{2,\text{DCM}} \approx 6$ ps), the solvent however affects τ_3 , which we previously assigned to the lifetime of the $^3\text{MLCT}_{\text{phz}}$ subset. In particular, in the case of **Ru2** the amplitudes of $\text{DAS}(\tau_1)$ and $\text{DAS}(\tau_3)$ between 500 and 700 nm (population and deactivation of $^3\text{MLCT}_{\text{phz}}$ states) are higher than those observed in ACN (transient spectra are area-normalized at a delay time of 0.5 ps). Additionally, the deactivation rates for **Ru1** and **Ru2** are lower in DCM ($\tau_{3,\text{Ru1}} \approx 250$ ps and $\tau_{3,\text{Ru2}} \approx 360$ ps) compared to ACN ($\tau_{3,\text{Ru1}} \approx 150$ ps and $\tau_{3,\text{Ru2}} \approx 100$ ps)^{31,34,85,91} and the maxima/minima of $\text{DAS}(\tau_1)$ and $\text{DAS}(\tau_3)$ appear red-shifted (610 nm) with respect

to those in ACN (590 nm). On the other excited-state branch, the lifetime of the $^3\text{ILCT}$ state is significantly decreased upon decreasing of the solvent polarity (*cf.* **Figure 5.7**, **Figure 5.8** and **Figure S5.11**). This is manifested in the transient emission spectra, which bi-exponentially decay but resemble the spectral shape of the $^3\text{MLCT}$ emission.

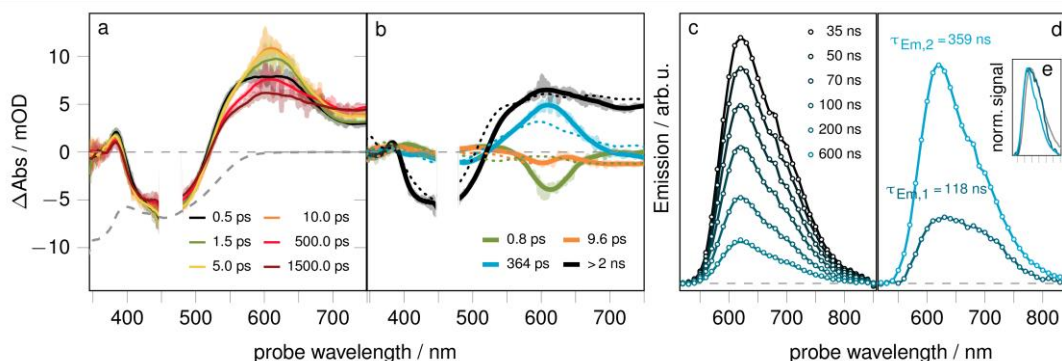


Figure 5.8. Time-resolved spectra of **Ru2** upon 470 nm excitation in dichloromethane: Ultrafast transient absorption spectra (a), 0.2 mW, OD at $\lambda_{\text{exc}} = 0.3$) and the corresponding decay associated spectra (b) and transient emission spectra (c), 3.5 mW, OD at $\lambda_{\text{exc}} = 0.3$) and corresponding decay associated spectra (d). For comparison the decay associated spectra obtained upon 470 nm excitation in acetonitrile are represented in figure (b) (dashed lines). The solid grey line in figure (e) shows the steady-state emission spectrum of **Ru0** compared to the normalized decay-associated spectra shown in panel (d).

In the less polar solvent both, the $^3\text{MLCT}_{\text{phz}}$ and $^3\text{ILCT}$ states (distal states) are destabilized with respect to the proximal MLCT states ($^3\text{MLCT}_{\text{phen}}$ and $^3\text{MLCT}_{\text{bpy}}$).^{22,32,92,93,94} Hence, the lifetimes of the $^3\text{ILCT}$ ($\tau_{\text{Em},1} \approx 120$ ns) and $^3\text{MLCT}_{\text{phz}}$ ($\tau_3 \approx 300$ ps) states are increased in DCM compared to ACN ($\tau_{\text{Em},1} \approx 50$ ns and $\tau_3 \approx 120$ ps). It can be presumed that the $^3\text{ILCT}$ state is more destabilized than the $^3\text{MLCT}_{\text{phz}}$ state due to the larger donor-acceptor distance. Hence, the complexes show dual emission in DCM and ACN solution. The less structured ESA bands (fs-TA) and the similar ns-Em spectra from the $^3\text{MLCT}$ and $^3\text{ILCT}$ manifold in DCM are moreover indicative of similar excited-state geometries of the two long-lived states in DCM solution, whereas the two excited-state branches in ACN are characterized by different excited-geometries. Thus, the emission associated decay spectra assigned to the deactivation of the triplet-states in the two excited-state branches exhibit a similar spectral shape and cannot be spectroscopically distinguished by transient emission spectra but yielding two DAS of similar shape but different lifetimes (*cf.* **Figure 5.7** (g) and (h) vs. **Figure 5.8** (d) and **Figure S5.11** (d)).

Therefore, the weaker stabilization of CT states in DCM with respect to ACN yields *i)* similar excited-state geometries in the two excited-state branches and *ii)* increased lifetimes of the equilibrated $^3\text{ILCT}$ and $^3\text{MLCT}$ states in DCM (**Ru1**: $\tau_{\text{Em},1} \approx 120$ ns and $\tau_{\text{Em},2} \approx 170$ ns; **Ru2**: $\tau_{\text{Em},1} \approx 120$ ns and $\tau_{\text{Em},2} \approx 360$ ns) with respect to ACN solution (**Ru1**: $\tau_{\text{Em},1} \approx 40$ ns and $\tau_{\text{Em},2} \approx 170$ ns; **Ru2**: $\tau_{\text{Em},1} \approx 70$ ns and $\tau_{\text{Em},2} \approx 200$ ns).

5.6 Conclusion

The syntheses of two novel Ru(II) complexes, **Ru1** and **Ru2**, which combined the well-known Ru(bpy)₂dppz motif with a 4-hydroxythiazole donor group is presented. Thiazoles are versatile and tunable chromophore, and in our studies were utilized for π -extension from the dppz-ligand. The photophysics of **Ru1** and **Ru2**, were investigated using both time-resolved transient absorption and emission experiments in combination with time-dependent density-functional theory. Photoexcitation in the visible region populates two excited-state branches onto the ³MLCT and ³ILCT manifolds. Within the MLCT sphere a phenazine centered subset of the excited-state ensemble non-radiatively decays back to the ground-state within \sim 150 ps and a long-lived (phenanthroline centered) ³MLCT state is formed, which radiatively decays back to the ground-state within *ca.* 180 ns. The second excited-state branch populates a long-lived ³ILCT state with excess charge density delocalized on the thiazole and phenazine units of the π -extended ligand, that subsequently deactivates *via* emission, with lifetimes of 40 – 60 ns.

The excitation wavelength depend experiments allow us to determine the population ratio of the ³MLCT and ³ILCT states. Excitation in the red region of the absorption band (470 nm) leads to enhanced population in the ³MLCT manifold when compared to excitation at \sim 403 nm, which is attributed to a greater population of the ¹MLCT states in the Franck-Condon region. However, ILCT states are also populated upon excitation at 470 nm, most likely due to rapid interconversion between the MLCT and ILCT manifold prior to thermal equilibration. The polarity of the solvent influences the relative energy of the charge-transfer states in such a manner, that the ³ILCT states are higher destabilized than *e.g.*, a ³MLCT_{phz} state due a higher-donor acceptor distance. Thus, the solvent polarity determines the excited-state geometries in the ³MLCT and ³ILCT manifold in such a way, that in a less polar medium both excited-state branches are characterized by similar geometries. Thus, we observed an increased lifetime of the long-lived ³ILCT ($\tau_{Em,1}$) and ³MLCT ($\tau_{Em,2}$) states in dichloromethane ($\tau_{Em,1} \approx 310 - 360$ ns, $\tau_{Em,2} \approx 120$ ns) with respect to acetonitrile ($\tau_{Em,1} \approx 40 - 70$ ns, $\tau_{Em,2} \approx 180$ ns).

We have demonstrated in this study, that dual emission together with tunable lifetimes occurs, following the attachment of a thiazole donating unit to the dppz ligand. This observation depends not only on the substituent on the thiazole moiety (methyl vs. carbazole), but also the excitation wavelengths and the solvent medium. This demonstrates the potential of incorporating single-bond π -extended chromophores, as opposed to the more popular ring-fused approaches. On-going studies in this area focuses on related structural derivatives, in addition to pH-dependent studies on the excited state properties, which can be used to guide the suitability of these systems as potential photosensitizers in catalytic applications such as photocatalytic hydrogen generation.

5.7 Supporting information

The supplementary data associated with this chapter can be found in Appendix D.

5.8 Bibliography

- (1) Grätzel, M. Dye-Sensitized Solar Cells. *J. Photochem. Photobiol. C Photochem. Rev.* **2003**, *4* (2), 145–153. [https://doi.org/10.1016/S1389-5567\(03\)00026-1](https://doi.org/10.1016/S1389-5567(03)00026-1).
- (2) Vos, J. G.; Kelly, J. M. Ruthenium Polypyridyl Chemistry; from Basic Research to Applications and Back Again. *Dalton Trans.* **2006**, No. 41, 4869. <https://doi.org/10.1039/b606490f>.
- (3) Ludin, N. A.; Al-Alwani Mahmoud, A. M.; Bakar Mohamad, A.; Kadhum, Abd. A. H.; Sopian, K.; Abdul Karim, N. S. Review on the Development of Natural Dye Photosensitizer for Dye-Sensitized Solar Cells. *Renew. Sustain. Energy Rev.* **2014**, *31*, 386–396. <https://doi.org/10.1016/j.rser.2013.12.001>.
- (4) O'Reilly, L.; Pan, Q.; Das, N.; Wenderich, K.; Korterik, J. P.; Vos, J. G.; Pryce, M. T.; Huijser, A. Hydrogen-Generating Ru/Pt Bimetallic Photocatalysts Based on Phenyl-Phenanthroline Peripheral Ligands. *ChemPhysChem* **2018**, *19* (22), 3084–3091. <https://doi.org/10.1002/cphc.201800658>.
- (5) Das, N.; Bindra, G. S.; Paul, A.; Vos, J. G.; Schulz, M.; Pryce, M. T. Enhancing Photocatalytic Hydrogen Generation: The Impact of the Peripheral Ligands in Ru/Pd and Ru/Pt Complexes. *Chem. - Eur. J.* **2017**, *23* (22), 5330–5337. <https://doi.org/10.1002/chem.201605980>.
- (6) Huber, F. L.; Nauroozi, D.; Mengele, A. K.; Rau, S. Synthesis and Characterization of a Ruthenium(II) Complex for the Development of Supramolecular Photocatalysts Containing Multidentate Coordination Spheres. *Eur. J. Inorg. Chem.* **2017**, *2017* (34), 4020–4027. <https://doi.org/10.1002/ejic.201700565>.
- (7) Staniszewska, M.; Kupfer, S.; Guthmuller, J. Effect of the Catalytic Center on the Electron Transfer Dynamics in Hydrogen-Evolving Ruthenium-Based Photocatalysts Investigated by Theoretical Calculations. *J. Phys. Chem. C* **2019**, *123* (26), 16003–16013. <https://doi.org/10.1021/acs.jpcc.9b03621>.

- (8) Teegardin, K.; Day, J. I.; Chan, J.; Weaver, J. Advances in Photocatalysis: A Microreview of Visible Light Mediated Ruthenium and Iridium Catalyzed Organic Transformations. *Org. Process Res. Dev.* **2016**, *20* (7), 1156–1163. <https://doi.org/10.1021/acs.oprd.6b00101>.
- (9) Keefe, M. Luminescent Sensor Molecules Based on Coordinated Metals: A Review of Recent Developments. *Coord. Chem. Rev.* **2000**, *205* (1), 201–228. [https://doi.org/10.1016/S0010-8545\(00\)00240-X](https://doi.org/10.1016/S0010-8545(00)00240-X).
- (10) Shi, G.; Monro, S.; Hennigar, R.; Colpitts, J.; Fong, J.; Kasimova, K.; Yin, H.; DeCoste, R.; Spencer, C.; Chamberlain, L.; Mandel, A.; Lilge, L.; McFarland, S. A. Ru(II) Dyads Derived from α -Oligothiophenes: A New Class of Potent and Versatile Photosensitizers for PDT. *Coord. Chem. Rev.* **2015**, *282–283*, 127–138. <https://doi.org/10.1016/j.ccr.2014.04.012>.
- (11) White, J. K.; Schmehl, R. H.; Turro, C. An Overview of Photosubstitution Reactions of Ru(II) Imine Complexes and Their Application in Photobiology and Photodynamic Therapy. *Inorganica Chim. Acta* **2017**, *454*, 7–20. <https://doi.org/10.1016/j.ica.2016.06.007>.
- (12) Farrer, N. J.; Salassa, L.; Sadler, P. J. Photoactivated Chemotherapy (PACT): The Potential of Excited-State d-Block Metals in Medicine. *Dalton Trans.* **2009**, No. 48, 10690. <https://doi.org/10.1039/b917753a>.
- (13) Friedman, A. E.; Chambron, J. C.; Sauvage, J. P.; Turro, N. J.; Barton, J. K. A Molecular Light Switch for DNA: Ru(Bpy)₂(Dppz)₂⁺. *J. Am. Chem. Soc.* **1990**, *112* (12), 4960–4962. <https://doi.org/10.1021/ja00168a052>.
- (14) De la Cadena, A.; Davydova, D. D.; Tolstik, T.; Reichardt, C.; Shukla, S.; Akimov, D.; Heintzmann, R.; Popp, J.; Dietzek, B. Ultrafast in Cellulo Photoinduced Dynamics Processes of the Paradigm Molecular Light Switch [Ru(Bpy)₂dppz]₂⁺. *Sci. Rep.* **2016**, *6* (1), 33547. <https://doi.org/10.1038/srep33547>.
- (15) Olson, E. J. C.; Hu, D.; Hörmann, A.; Jonkman, A. M.; Arkin, M. R.; Stemp, E. D. A.; Barton, J. K.; Barbara, P. F. First Observation of the Key Intermediate in the

“Light-Switch” Mechanism of [Ru(Phen) 2 Dppz] 2+. *J. Am. Chem. Soc.* **1997**, *119* (47), 11458–11467. <https://doi.org/10.1021/ja971151d>.

(16) Brennaman, M. K.; Alstrum-Acevedo, J. H.; Fleming, C. N.; Jang, P.; Meyer, T. J.; Papanikolas, J. M. Turning the [Ru(Bpy) 2 Dppz] 2+ Light-Switch On and Off with Temperature. *J. Am. Chem. Soc.* **2002**, *124* (50), 15094–15098. <https://doi.org/10.1021/ja0279139>.

(17) Brennaman, M. K.; Meyer, T. J.; Papanikolas, J. M. [Ru(Bpy)2dppz]2+ Light-Switch Mechanism in Protic Solvents as Studied through Temperature-Dependent Lifetime Measurements. *J. Phys. Chem. A* **2004**, *108* (45), 9938–9944. <https://doi.org/10.1021/jp0479670>.

(18) Schoonover, J. R.; Bates, W. D.; Meyer, T. J. Application of Resonance Raman Spectroscopy to Electronic Structure in Metal Complex Excited States. Excited-State Ordering and Electron Delocalization in Dipyrido[3,2-a:2',3'-c]Phenazine (Dppz): Complexes of Re(I) and Ru(II). *Inorg. Chem.* **1995**, *34* (26), 6421–6422. <https://doi.org/10.1021/ic00130a004>.

(19) Barnsley, J. E.; Shillito, G. E.; Larsen, C. B.; van der Salm, H.; Horvath, R.; Sun, X. Z.; Wu, X.; George, M. W.; Lucas, N. T.; Gordon, K. C. Generation of Microsecond Charge-Separated Excited States in Rhenium(I) Diimine Complexes: Driving Force Is the Dominant Factor in Controlling Lifetime. *Inorg. Chem.* **2019**, *58* (15), 9785–9795. <https://doi.org/10.1021/acs.inorgchem.9b00792>.

(20) Reichardt, C.; Monro, S.; Sobotta, F. H.; Colón, K. L.; Sainuddin, T.; Stephenson, M.; Sampson, E.; Roque, J.; Yin, H.; Brendel, J. C.; Cameron, C. G.; McFarland, S.; Dietzek, B. Predictive Strength of Photophysical Measurements for in Vitro Photobiological Activity in a Series of Ru(II) Polypyridyl Complexes Derived from π -Extended Ligands. *Inorg. Chem.* **2019**, *58* (5), 3156–3166. <https://doi.org/10.1021/acs.inorgchem.8b03223>.

(21) Isakov, D.; Giereth, R.; Nauroozi, D.; Tschierlei, S.; Rau, S. Two Emissive Long-Lived Excited States of an Imidazole-Functionalized Ruthenium

Dipyridophenazine Complex. *Inorg. Chem.* **2019**, *58* (19), 12646–12653. <https://doi.org/10.1021/acs.inorgchem.9b01372>.

(22) Schindler, J.; Traber, P.; Zedler, L.; Zhang, Y.; Lefebvre, J.-F.; Kupfer, S.; Gräfe, S.; Demeunynck, M.; Chavarot-Kerlidou, M.; Dietzek, B. Photophysics of a Ruthenium Complex with a π -Extended Dipyridophenazine Ligand for DNA Quadruplex Labeling. *J. Phys. Chem. A* **2018**, *122* (32), 6558–6569. <https://doi.org/10.1021/acs.jpca.8b05274>.

(23) Tschierlei, S.; Presselt, M.; Kuhnt, C.; Yartsev, A.; Pascher, T.; Sundström, V.; Karnahl, M.; Schwalbe, M.; Schäfer, B.; Rau, S.; Schmitt, M.; Dietzek, B.; Popp, J. Photophysics of an Intramolecular Hydrogen-Evolving Ru-Pd Photocatalyst. *Chem. - Eur. J.* **2009**, *15* (31), 7678–7688. <https://doi.org/10.1002/chem.200900457>.

(24) Schindler, J.; Zhang, Y.; Traber, P.; Lefebvre, J.-F. J.-F.; Kupfer, S.; Demeunynck, M.; Graefe, S.; Chavarot-Kerlidou, M.; Dietzek, Benjamin.; Gräfe, S.; Chavarot-Kerlidou, M.; Dietzek, Benjamin. A $\Pi\pi^*$ State Enables Photoaccumulation of Charges on a π -Extended Dipyridophenazine Ligand in a Ru(II) Polypyridine Complex. *J. Phys. Chem. C* **2018**, *122* (1), 83–95. <https://doi.org/10.1021/acs.jpcc.7b08989>.

(25) Randell, N. M.; Rendon, J.; Demeunynck, M.; Bayle, P.; Gambarelli, S.; Artero, V.; Mouesca, J.; Chavarot-Kerlidou, M. Tuning the Electron Storage Potential of a Charge-Photoaccumulating Ru II Complex by a DFT-Guided Approach. *Chem. – Eur. J.* **2019**, *25* (61), 13911–13920. <https://doi.org/10.1002/chem.201902312>.

(26) Whittemore, T. J.; White, T. A.; Turro, Claudia. New Ligand Design Provides Delocalization and Promotes Strong Absorption throughout the Visible Region in a Ru(II) Complex. *J. Am. Chem. Soc.* **2018**, *140* (1), 229–234. <https://doi.org/10.1021/jacs.7b09389>.

(27) Goze, C.; Leiggenger, C.; Liu, S.-X. X.; Sanguinet, L.; Levillain, E.; Hauser, A.; Decurtins, S. Fused Donor–Acceptor Ligands in RuII Chemistry: Synthesis, Electrochemistry and Spectroscopy of $[\text{Ru}(\text{Bpy})_3\text{-n}(\text{TTF-Dppz})_n](\text{PF}_6)_2$. *ChemPhysChem* **2007**, *8* (10), 1504–1512. <https://doi.org/10.1002/cphc.200700066>.

- (28) Foxon, S. P.; Alamiry, M. A. H.; Walker, M. G.; Meijer, A. J. H. M.; Sazanovich, I. V.; Weinstein, J. A.; Thomas, J. A. Photophysical Properties and Singlet Oxygen Production by Ruthenium(II) Complexes of Benzo[i]Dipyrido[3,2-a:2',3'-c]Phenazine: Spectroscopic and TD-DFT Study. *J. Phys. Chem. A* **2009**, *113* (46), 12754–12762. <https://doi.org/10.1021/jp906716g>.
- (29) Sun, Y.; Joyce, L. E.; Dickson, N. M.; Turro, Claudia. DNA Photocleavage by an Osmium(II) Complex in the PDT Window. *Chem. Commun.* **2010**, *46* (36), 2426. <https://doi.org/10.1039/b925574e>.
- (30) Albani, B. A.; Peña, B.; Leed, N. A.; De Paula, N. A. B. G.; Pavani, C.; Baptista, M. S.; Dunbar, K. R.; Turro, C. Marked Improvement in Photoinduced Cell Death by a New Tris-Heteroleptic Complex with Dual Action: Singlet Oxygen Sensitization and Ligand Dissociation. *J. Am. Chem. Soc.* **2014**, *136* (49), 17095–17101. <https://doi.org/10.1021/ja508272h>.
- (31) Lundin, N. J.; Walsh, P. J.; Howell, S. L.; Blackman, A. G.; Gordon, K. C. A Synthetic, Structural, Spectroscopic and DFT Study of ReI, CuI, RuII and IrIII Complexes Containing Functionalized Dipyrido[3,2-a:2',3'-c]Phenazine (Dppz). *Chem. - Eur. J.* **2008**, *14* (36), 11573–11583. <https://doi.org/10.1002/chem.200801369>.
- (32) Kuhnt, C.; Karnahl, M.; Tschierlei, S.; Griebenow, K.; Schmitt, M.; Schäfer, B.; Kriek, S.; Görls, H.; Rau, S.; Dietzek, B.; Popp, J. Juergen. J.; Schaefer, B.; Kriek, S.; Goerls, H.; Rau, S.; Dietzek, B.; Popp, J. Juergen. J. Substitution-Controlled Ultrafast Excited-State Processes in Ru-Dppz-Derivatives. *Phys. Chem. Chem. Phys.* **2010**, *12* (6), 1357–1368. <https://doi.org/10.1039/B915770K>.
- (33) Sun, Y.; Lutterman, D. A.; Turro, Claudia. Role of Electronic Structure on DNA Light-Switch Behavior of Ru(II) Intercalators. *Inorg. Chem.* **2008**, *47* (14), 6427–6434. <https://doi.org/10.1021/ic800560x>.
- (34) Ji, S.; Guo, H.; Wu, W. W. W. W.; Wu, W. W. W. W.; Zhao, Jianzhang. Ruthenium(II) Polyimine-Coumarin Dyad with Non-Emissive 3IL Excited State as Sensitizer for Triplet-Triplet Annihilation Based Upconversion. *Angew. Chem. Int.*

Ed. **2011**, *50* (36), 8283–8286, S8283/1-S8283/26.
<https://doi.org/10.1002/anie.201008134>.

(35) Adams, B. S.; Shillito, G. E.; van der Salm, H.; Horvath, R.; Larsen, C. B.; Sun, X.-Z.; Lucas, N. T.; George, M. W.; Gordon, K. C. Alteration of Intraligand Donor–Acceptor Interactions Through Torsional Connectivity in Substituted Re-Dppz Complexes. *Inorg. Chem.* **2017**, *56* (21), 12967–12977.
<https://doi.org/10.1021/acs.inorgchem.7b01710>.

(36) Shillito, G. E.; Larsen, C. B.; McLay, J. R. W.; Lucas, N. T.; Gordon, K. C. Effect of Bridge Alteration on Ground- and Excited-State Properties of Ruthenium(II) Complexes with Electron-Donor-Substituted Dipyrido[3,2- a :2',3'- c]Phenazine Ligands. *Inorg. Chem.* **2016**, *55* (21), 11170–11184.
<https://doi.org/10.1021/acs.inorgchem.6b01810>.

(37) van der Salm, H.; Larsen, C. B.; McLay, J. R. W.; Huff, G. S.; Gordon, K. C. Effects of Protonation on the Optical and Photophysical Properties of ReCl(CO)₃(Dppz–TAA) and [Ru(Bpy)₂(Dppz–TAA)]²⁺. *Inorganica Chim. Acta* **2015**, *428*, 1–7. <https://doi.org/10.1016/j.ica.2015.01.006>.

(38) Gampe, D. M.; Hänsch, V. G.; Schramm, S.; Menzel, R.; Weiß, D.; Beckert, R. Mixing Chromophores: Donor-Acceptor Dyes with Low-Lying LUMOs and Narrow Band Gaps by Connecting 4-Alkoxythiazoles and Azaacenes. *Eur. J. Org. Chem.* **2017**, *2017* (10), 1369–1379. <https://doi.org/10.1002/ejoc.201601521>.

(39) Menzel, R.; Kupfer, S.; Mede, R.; Görls, H.; González, L.; Beckert, R. Synthesis, Properties and Quantum Chemical Evaluation of Solvatochromic Pyridinium-Phenyl-1,3-Thiazol-4-Olate Betaine Dyes. *Tetrahedron* **2013**, *69* (5), 1489–1498. <https://doi.org/10.1016/j.tet.2012.12.016>.

(40) Ortiz, L. K. C.; Würfel, H.; Täuscher, E.; Weiß, D.; Birckner, E.; Görls, H.; Beckert, R. From Liquid to Solid-State Fluorescence: Tricyclic Lactones Based on 4-Hydroxy-1,3-Thiazoles. *Synthesis* **2014**, *46* (01), 126–134. <https://doi.org/10.1055/s-0033-1340048>.

- (41) Schramm, S.; Weiß, D. Chapter Two - Fluorescent Heterocycles: Recent Trends and New Developments. In *Advances in Heterocyclic Chemistry*; Scriven, E. F. V., Ramsden, C. A., Eds.; Academic Press, 2019; Vol. 128, pp 103–179. <https://doi.org/10.1016/bs.aihch.2018.10.003>.
- (42) Hupfer, M. L.; Kaufmann, M.; Preiß, J.; Weiß, D.; Beckert, R.; Dietzek, B.; Presselt, M. Assembly of T-Shaped Amphiphilic Thiazoles on the Air–Water Interface: Impact of Polar Chromophore Moieties, as Well as Dipolarity and π -Extension of the Chromophore on the Supramolecular Structure. *Langmuir* **2019**, *35* (7), 2587–2600. <https://doi.org/10.1021/acs.langmuir.8b04063>.
- (43) Habenicht, S. H.; Rohland, P.; Reichel, J.; Biver, T.; Minei, P.; Jakobi, D.; Pucci, A.; Weiß, D.; Beckert, R.; Görls, H. Small Molecules as Long-Wavelength Fluorophores: Push-Pull Substituted 4-Alkoxy-1,3-Thiazoles. *Synthesis* **2017**. <https://doi.org/10.1055/s-0036-1588581>.
- (44) Grummt, U.-W.; Weiss, D.; Birckner, E.; Beckert, R. Pyridylthiazoles: Highly Luminescent Heterocyclic Compounds. *J. Phys. Chem. A* **2007**, *111* (6), 1104–1110. <https://doi.org/10.1021/jp0672003>.
- (45) Menzel, R.; Tauscher, E.; Weiß, D.; Beckert, R.; Görls, H. The Combination of 4-Hydroxythiazoles with Azaheterocycles: Efficient Bidentate Ligands for Novel Ruthenium Complexes. *Z. Für Anorg. Allg. Chem.* **2010**, *636* (7), 1380–1385. <https://doi.org/10.1002/zaac.200900523>.
- (46) Wolfram, S.; Würfel, H.; Habenicht, S. H.; Lembke, C.; Richter, P.; Birckner, E.; Beckert, R.; Pohnert, G. A Small Azide-Modified Thiazole-Based Reporter Molecule for Fluorescence and Mass Spectrometric Detection. *Beilstein J. Org. Chem.* **2014**, *10* (1), 2470–2479. <https://doi.org/10.3762/bjoc.10.258>.
- (47) Calderón-Ortiz, L. K.; Täuscher, E.; Leite Bastos, E.; Görls, H.; Weiß, D.; Beckert, R. Hydroxythiazole-Based Fluorescent Probes for Fluoride Ion Detection. *Eur. J. Org. Chem.* **2012**, *2012* (13), 2535–2541. <https://doi.org/10.1002/ejoc.201200140>.

- (48) Breul, A. M.; Moraes, I. R. de; Menzel, R.; Pfeffer, M.; Winter, A.; Hager, M. D.; Rau, S.; Dietzek, B.; Beckert, R.; Schubert, U. S. Light-Harvesting of Polymerizable 4-Hydroxy-1,3-Thiazole Monomers by Energy Transfer toward Photoactive Os(II) Metal Complexes in Linear Polymers. *Polym. Chem.* **2014**, *5* (8), 2715–2724. <https://doi.org/10.1039/C3PY00915G>.
- (49) Menzel, R.; Ogermann, D.; Kupfer, S.; Weiß, D.; Görls, H.; Kleinermanns, K.; González, L.; Beckert, R. 4-Methoxy-1,3-Thiazole Based Donor-Acceptor Dyes: Characterization, X-Ray Structure, DFT Calculations and Test as Sensitizers for DSSC. *Dyes Pigments* **2012**, *94* (3), 512–524. <https://doi.org/10.1016/j.dyepig.2012.02.014>.
- (50) Menzel, R.; Kupfer, S.; Mede, R.; Weiß, D.; Görls, H.; González, L.; Beckert, R. Arylamine-Modified Thiazoles as Donor-Acceptor Dyes: Quantum Chemical Evaluation of the Charge-Transfer Process and Testing as Ligands in Ruthenium(II) Complexes. *Eur. J. Org. Chem.* **2012**, *2012* (27), 5231–5247. <https://doi.org/10.1002/ejoc.201200688>.
- (51) Breul, A. M.; Pietsch, C.; Menzel, R.; Schäfer, J.; Teichler, A.; Hager, M. D.; Popp, J.; Dietzek, B.; Beckert, R.; Schubert, U. S. Blue Emitting Side-Chain Pendant 4-Hydroxy-1,3-Thiazoles in Polystyrenes Synthesized by RAFT Polymerization. *Eur. Polym. J.* **2012**, *48* (7), 1339–1347. <https://doi.org/10.1016/j.eurpolymj.2012.03.021>.
- (52) Pietsch, C.; Schäfer, J.; Menzel, R.; Beckert, R.; Popp, J.; Dietzek, B.; Schubert, U. S. Förster Resonance Energy Transfer in Poly(Methyl Methacrylates) Copolymers Bearing Donor–Acceptor 1,3-Thiazole Dyes. *J. Polym. Sci. Part Polym. Chem.* **2013**, *51* (22), 4765–4773. <https://doi.org/10.1002/pola.26898>.
- (53) Happ, B.; Schäfer, J.; Menzel, R.; Hager, M. D.; Winter, A.; Popp, J.; Beckert, R.; Dietzek, B.; Schubert, U. S. Synthesis and Resonance Energy Transfer Study on a Random Terpolymer Containing a 2-(Pyridine-2-Yl)Thiazole Donor-Type Ligand and a Luminescent [Ru(Bpy)₂(2-(Triazol-4-Yl)Pyridine)]²⁺ Chromophore. *Macromolecules* **2011**, *44* (16), 6277–6287. <https://doi.org/10.1021/ma201193e>.

- (54) Gampe, D. M.; Schramm, S.; Nöller, F.; Weiß, D.; Görls, H.; Naumov, P.; Beckert, R. Pushing to the Low Limits: Tetraazaanthracenes with Very Low-Lying LUMO Levels and near-Infrared Absorption. *Chem. Commun.* **2017**, 53 (73), 10220–10223. <https://doi.org/10.1039/C7CC05224C>.
- (55) Tu, Q.; Yin, Z.; Ma, Y.; Chen, S.-C.; Zheng, Q. Ladder-Type Heteroheptacene-Cored Semiconductors for Small-Molecule Solar Cells. *Dyes Pigments* **2018**, 149, 747–754. <https://doi.org/10.1016/j.dyepig.2017.11.052>.
- (56) Huang, L.; Ma, P.; Deng, G.; Zhang, K.; Ou, T.; Lin, Y.; Wong, M. S. Novel Electron-Deficient Quinoxalinedithienothiophene- and Phenazinedithienothiophene-Based Photosensitizers: The Effect of Conjugation Expansion on DSSC Performance. *Dyes Pigments* **2018**, 159, 107–114. <https://doi.org/10.1016/j.dyepig.2018.06.010>.
- (57) Al Mousawi, A.; Garra, P.; Dumur, F.; Bui, T.-T.; Goubard, F.; Toufaily, J.; Hamieh, T.; Graff, B.; Gimes, D.; Fouassier, J. P.; Lalevée, J. Novel Carbazole Skeleton-Based Photoinitiators for LED Polymerization and LED Projector 3D Printing. *Molecules* **2017**, 22 (12), 2143. <https://doi.org/10.3390/molecules22122143>.
- (58) Yu, Z.-J.; Lou, W.-Y.; Junge, H.; Pöpcke, A.; Chen, H.; Xia, L.-M.; Xu, B.; Wang, M.-M.; Wang, X.-J.; Wu, Q.-A.; Lou, B.-Y.; Lochbrunner, S.; Beller, M.; Luo, S.-P. Thermally Activated Delayed Fluorescence (TADF) Dyes as Efficient Organic Photosensitizers for Photocatalytic Water Reduction. *Catal. Commun.* **2019**, 119, 11–15. <https://doi.org/10.1016/j.catcom.2018.09.018>.
- (59) M. J. Frisch, G. W. Trucks, H. B. Schlegel, G. E. Scuseria, M. A. Robb, J. R. Cheeseman, G. Scalmani, V. Barone, G. A. Petersson, H. Nakatsuji, X. Li, M. Caricato, A. V. Marenich, J. Bloino, B. G. Janesko, R. Gomperts, B. Mennucci, H. P. Hratchian, J. V., and D. J. F. Gaussian 16, Revision B.01. Gaussian, Inc., Wallingford CT, 2016.
- (60) Becke, A. D. Density-functional Thermochemistry. III. The Role of Exact Exchange. *J. Chem. Phys.* **1993**, 98 (7), 5648–5652. <https://doi.org/10.1063/1.464913>.

- (61) Hay, P. J.; Wadt, W. R. Ab Initio Effective Core Potentials for Molecular Calculations. Potentials for K to Au Including the Outermost Core Orbitals. *J. Chem. Phys.* **1985**, *82* (1), 299–310. <https://doi.org/10.1063/1.448975>.
- (62) Weigend, F.; Ahlrichs, R. Balanced Basis Sets of Split Valence, Triple Zeta Valence and Quadruple Zeta Valence Quality for H to Rn: Design and Assessment of Accuracy. *Phys. Chem. Chem. Phys.* **2005**, *7* (18), 3297. <https://doi.org/10.1039/b508541a>.
- (63) Andrae, D.; Häußermann, U.; Dolg, M.; Stoll, H.; Preuß, H. Energy-Adjusted ab Initio Pseudopotentials for the Second and Third Row Transition Elements. *Theor. Chim. Acta* **1990**, *77* (2), 123–141. <https://doi.org/10.1007/BF01114537>.
- (64) Marenich, A. V.; Cramer, C. J.; Truhlar, D. G. Universal Solvation Model Based on Solute Electron Density and on a Continuum Model of the Solvent Defined by the Bulk Dielectric Constant and Atomic Surface Tensions. *J. Phys. Chem. B* **2009**, *113* (18), 6378–6396. <https://doi.org/10.1021/jp810292n>.
- (65) Mennucci, B.; Cappelli, C.; Guido, C. A.; Cammi, R.; Tomasi, J. Structures and Properties of Electronically Excited Chromophores in Solution from the Polarizable Continuum Model Coupled to the Time-Dependent Density Functional Theory. *J. Phys. Chem. A* **2009**, *113* (13), 3009–3020. <https://doi.org/10.1021/jp8094853>.
- (66) Grimme, S.; Ehrlich, S.; Goerigk, L. Effect of the Damping Function in Dispersion Corrected Density Functional Theory. *J. Comput. Chem.* **2011**, *32* (7), 1456–1465. <https://doi.org/10.1002/jcc.21759>.
- (67) Zúñiga, C.; Crivelli, I.; Loeb, B. Synthesis, Characterization, Spectroscopic and Electrochemical Studies of Donor–Acceptor Ruthenium(II) Polypyridine Ligand Derivatives with Potential NLO Applications. *Polyhedron* **2015**, *85*, 511–518. <https://doi.org/10.1016/j.poly.2014.09.004>.

- (68) Täuscher, E.; Weiß, D.; Beckert, R.; Görls, H. Synthesis and Characterization of New 4-Hydroxy-1,3-Thiazoles. *Synthesis* **2010**, *2010* (10), 1603–1608. <https://doi.org/10.1055/s-0029-1219759>.
- (69) Habenicht, S. H.; Siegmann, M.; Kupfer, S.; Kübel, J.; Weiß, D.; Cherek, D.; Möller, U.; Dietzek, B.; Gräfe, S.; Beckert, R. And yet They Glow: Thiazole Based Push–Pull Fluorophores Containing Nitro Groups and the Influence of Regioisomerism. *Methods Appl. Fluoresc.* **2015**, *3* (2), 025005. <https://doi.org/10.1088/2050-6120/3/2/025005>.
- (70) Kaufmann, M.; Hupfer, M. L.; Sachse, T.; Herrmann-Westendorf, F.; Weiß, D.; Dietzek, B.; Beckert, R.; Presselt, M. Introducing Double Polar Heads to Highly Fluorescent Thiazoles: Influence on Supramolecular Structures and Photonic Properties. *J. Colloid Interface Sci.* **2018**, *526*, 410–418. <https://doi.org/10.1016/j.jcis.2018.04.105>.
- (71) Gampe, D. M.; Nöller, F.; Hänsch, V. G.; Schramm, S.; Darsen, A.; Habenicht, S. H.; Ehrhardt, S.; Weiß, D.; Görls, H.; Beckert, R. Surprising Characteristics of D–A-Type Functional Dyes by Introducing 4-Alkoxythiazoles as the Donor-Unit. *Tetrahedron* **2016**, *72* (23), 3232–3239. <https://doi.org/10.1016/j.tet.2016.04.046>.
- (72) Habenicht, S. H.; Schramm, S.; Zhu, M.; Freund, R. R. A.; Langenstück, T.; Strathausen, R.; Weiß, D.; Biskup, C.; Beckert, R. π -Extension of a 4-Ethoxy-1,3-Thiazole via Aryl Alkyne Cross Coupling: Synthesis and Exploration of the Electronic Structure. *Photochem. Photobiol. Sci.* **2015**, *14* (11), 2097–2107. <https://doi.org/10.1039/C5PP00219B>.
- (73) Bolger, J.; Gourdon, A.; Ishow, E.; Launay, J.-P. Mononuclear and Binuclear Tetrapyrido[3,2-a:2',3'-c:3'',2''-h:2''',3''''-j]Phenazine (Tpphz) Ruthenium and Osmium Complexes. *Inorg. Chem.* **1996**, *35* (10), 2937–2944. <https://doi.org/10.1021/ic951436w>.
- (74) Fraser, M. G.; van der Salm, H.; Cameron, S. A.; Barnsley, J. E.; Gordon, K. C. Structural, Electronic and Computational Studies of Heteroleptic Cu(I) Complexes

of 6,6'-Dimesityl-2,2'-Bipyridine with Sulfur-Substituted Dipyridophenazine Ligands. *Polyhedron* **2013**, *52*, 623–633. <https://doi.org/10.1016/j.poly.2012.08.001>.

(75) Larsen, C. B.; van der Salm, H.; Clark, C. A.; Elliott, A. B. S.; Fraser, M. G.; Horvath, R.; Lucas, N. T.; Sun, X.-Z.; George, M. W.; Gordon, K. C. Intraligand Charge-Transfer Excited States in Re(I) Complexes with Donor-Substituted Dipyridophenazine Ligands. *Inorg. Chem.* **2014**, *53* (3), 1339–1354. <https://doi.org/10.1021/ic402082m>.

(76) Ambrose, J. F.; Nelson, R. F. Anodic Oxidation Pathways of Carbazoles: I. Carbazole and N-Substituted Derivatives. *J. Electrochem. Soc.* **1968**, *115* (11), 1159. <https://doi.org/10.1149/1.2410929>.

(77) Juris, A.; Balzani, V.; Barigelletti, F.; Campagna, S.; Belser, P.; von Zelewsky, A. Ru(II) Polypyridine Complexes: Photophysics, Photochemistry, Electrochemistry, and Chemiluminescence. *Coord. Chem. Rev.* **1988**, *84*, 85–277. [https://doi.org/10.1016/0010-8545\(88\)80032-8](https://doi.org/10.1016/0010-8545(88)80032-8).

(78) Fees, J.; Ketterle, M.; Klein, A.; Fiedler, J.; Kaim, W. Electrochemical, Spectroscopic and EPR Study of Transition Metal Complexes of Dipyrido[3,2-a:2',3'-c]Phenazine. *J. Chem. Soc. Dalton Trans.* **1999**, No. 15, 2595–2600. <https://doi.org/10.1039/a903417j>.

(79) Ambrosek, D.; Loos, P.-F.; Assfeld, X.; Daniel, C. A Theoretical Study of Ru(II) Polypyridyl DNA Intercalators: Structure and Electronic Absorption Spectroscopy of [Ru(Phen)2(Dppz)]²⁺ and [Ru(Tap)2(Dppz)]²⁺ Complexes Intercalated in Guanine–Cytosine Base Pairs. *J. Inorg. Biochem.* **2010**, *104* (9), 893–901. <https://doi.org/10.1016/j.jinorgbio.2010.04.002>.

(80) Véry, T.; Ambrosek, D.; Otsuka, M.; Gourlaouen, C.; Assfeld, X.; Monari, A.; Daniel, C. Photophysical Properties of Ruthenium(II) Polypyridyl DNA Intercalators: Effects of the Molecular Surroundings Investigated by Theory. *Chem. – Eur. J.* **2014**, *20* (40), 12901–12909. <https://doi.org/10.1002/chem.201402963>.

- (81) Fees, J.; Ketterle, M.; Klein, A.; Fiedler, J.; Kaim, W. Electrochemical, Spectroscopic and EPR Study of Transition Metal Complexes of Dipyrido[3,2-a:2',3'-c]Phenazine. *J. Chem. Soc. Dalton Trans.* **1999**, No. 15, 2595–2600. <https://doi.org/10.1039/a903417j>.
- (82) Waterland, M. R.; Gordon, K. C.; McGarvey, J. J.; Jayaweera, P. M. Spectroscopic and Electrochemical Studies of a Series of Copper(I) and Rhenium(I) Complexes with Substituted Dipyrido[3,2-a:2',3'-c]Phenazine Ligands †. *J. Chem. Soc. Dalton Trans.* **1998**, No. 4, 609–616. <https://doi.org/10.1039/a706110b>.
- (83) Abboud, J.-L. M.; Notari, R. Critical Compilation of Scales of Solvent Parameters. Part I. Pure, Non-Hydrogen Bond Donor Solvents. *Pure Appl. Chem.* **1999**, 71 (4), 645–718. <https://doi.org/10.1351/pac199971040645>.
- (84) De la Cadena, A.; Davydova, D. D.; Tolstik, T.; Reichardt, C.; Shukla, S.; Akimov, D.; Heintzmann, R.; Popp, J.; Dietzek, B. Ultrafast in Cellulo Photoinduced Dynamics Processes of the Paradigm Molecular Light Switch [Ru(Bpy)2dppz]2+. *Sci. Rep.* **2016**, 6 (1), 33547. <https://doi.org/10.1038/srep33547>.
- (85) Sun, Y.; Liu, Y.; Turro, C. Ultrafast Dynamics of the Low-Lying 3 MLCT States of [Ru(Bpy)2(Dppp2)]2+. *J. Am. Chem. Soc.* **2010**, 132 (16), 5594–5595. <https://doi.org/10.1021/ja101703w>.
- (86) McCusker, J. K. Femtosecond Absorption Spectroscopy of Transition Metal Charge-Transfer Complexes. *Acc. Chem. Res.* **2003**, 36 (12), 876–887. <https://doi.org/10.1021/ar030111d>.
- (87) Sun, Y.; Joyce, L. E.; Dickson, N. M.; Turro, C. Efficient DNA Photocleavage by [Ru(Bpy)2(Dppn)]2+ with Visible Light. *Chem. Commun.* **2010**, 46 (14), 2426. <https://doi.org/10.1039/b925574e>.
- (88) Shaw, J. R.; Webb, R. T.; Schmechl, R. H. Intersystem Crossing to Both Ligand-Localized and Charge-Transfer Excited States in Mononuclear and Dinuclear Ruthenium(II) Diimine Complexes. *J. Am. Chem. Soc.* **1990**, 112 (3), 1117–1123. <https://doi.org/10.1021/ja00159a035>.

- (89) Wang, X.; Del Guerso, A.; Schmehl, R. H. Photophysical Behavior of Transition Metal Complexes Having Interacting Ligand Localized and Metal-to-Ligand Charge Transfer States. *J. Photochem. Photobiol. C Photochem. Rev.* **2004**, *5* (1), 55–77. <https://doi.org/10.1016/j.jphotochemrev.2004.01.002>.
- (90) Tyson, D. S.; Luman, C. R.; Zhou, X.; Castellano, F. N. New Ru(II) Chromophores with Extended Excited-State Lifetimes. *Inorg. Chem.* **2001**, *40* (16), 4063–4071. <https://doi.org/10.1021/ic010287g>.
- (91) Sun, Y.; Turro, C. Highly Solvent Dependent Luminescence from [Ru(Bpy)_n(Dppp)_{2-_n}]²⁺ (n = 0–2). *Inorg. Chem.* **2010**, *49* (11), 5025–5032. <https://doi.org/10.1021/ic100106b>.
- (92) Pfeffer, M. G.; Zedler, L.; Kupfer, S.; Paul, M.; Schwalbe, M.; Peuntinger, K.; Guldi, D. M.; Guthmuller, J.; Popp, J.; Gräfe, S.; Dietzek, B.; Rau, S.; Kuhnt, C.; Tschierlei, S.; Karnahl, M.; Rau, S.; Dietzek, B.; Schmitt, M.; Popp, J.; Schwalbe, M.; Karnahl, M.; Tschierlei, S.; Uhlemann, U.; Schmitt, M.; Dietzek, B.; Popp, J.; Groake, R.; Vos, J. G.; Rau, S.; Pfeffer, M. G.; Zedler, L.; Kupfer, S.; Paul, M.; Schwalbe, M.; Peuntinger, K.; Guldi, D. M.; Guthmuller, J.; Popp, J.; Gräfe, S.; Dietzek, B.; Rau, S.; Braumüller, M.; Schulz, M.; Sorsche, D.; Pfeffer, M. G.; Schaub, M.; Popp, J.; Park, B. W.; Hagfeldt, A.; Dietzek, B.; Rau, S. Tuning of Photocatalytic Activity by Creating a Tridentate Coordination Sphere for Palladium. *Dalton Trans.* **2014**, *43* (30), 11676–11686. <https://doi.org/10.1039/c4dt01034e>.
- (93) Chen, P.; Meyer, T. J. Medium Effects on Charge Transfer in Metal Complexes. *Chem. Rev.* **1998**, *98* (4), 1439–1478. <https://doi.org/10.1021/cr941180w>.
- (94) Caspar, J. V.; Meyer, T. J. Photochemistry of Tris(2,2'-Bipyridine)Ruthenium(2+) Ion (Ru(Bpy)₃²⁺). Solvent Effects. *J. Am. Chem. Soc.* **1983**, *105* (17), 5583–5590. <https://doi.org/10.1021/ja00355a009>.

Chapter 6

Explaining the role of water in the “light-switch” probe for DNA intercalation; modelling water loss from $[\text{Ru}(\text{phen})_2(\text{dppz})]^{2+} \cdot 2\text{H}_2\text{O}$ using DFT and TD-DFT methods

This work was published in *J. Photochem. Photobiol. A.* 2021, **410**, 113169.

[Aoibhín A. Cullen](#), Mary T. Pryce* and Conor Long*.

Within this work, I contributed towards the experimental section by carrying out a photophysical investigation of $[\text{Ru}(\text{phen})_2\text{dppz}]^{2+}$ in the ground state in dry acetonitrile, followed by studying the effects of water addition to these spectra. I also carried out a detailed investigation of the excited state lifetime of this complex in various aqueous concentrations and while this is not included in this manuscript, these results are part of ongoing work in the group. Prof. Conor Long executed the DFT and TD-DFT calculations to determine the excited state energies of the complex when hydrogen bonded to water. Supporting information associated with this chapter can be found in Appendix E.

6.1 Abstract

The photophysics of $[\text{Ru}(1,10\text{-phenanthroline})_2(\text{dipyrido}[3,2\text{-}1:2',3'\text{-c}]\text{phenazine})]^{2+}$ and $[\text{Ru}(1,10\text{-phenanthroline})_2(\text{dipyrido}[3,2\text{-}1:2',3'\text{-c}]\text{phenazine})]^{2+}\cdot 2\text{H}_2\text{O}$ are investigated by Density Functional and Time-Dependent Density Functional methods. Evidence to support the formation of hydrogen bonds with water in the ground state is presented, and the effects of hydrogen-bonded water on the electronic structure of the complex are described. The excited-state energies were calculated along water-loss reaction coordinates in the ground state and these studies identified specific excited states, with n-to- π^* character on both the singlet and triplet hypersurfaces. These are repulsive with respect to the hydrogen-bonding interaction with the phenazine nitrogen atoms. These so-called “drain-pipe” states expel water and proceed to form a “dry” state which is quenched by reaction with bulk water which of course also quenches the luminescence.

6.2 Introduction

Polypyridyl complexes of ruthenium possess many useful properties, such as long-lived triplet excited states, chemical stability, and solubility in aqueous media. These features make them particularly useful as spectroscopic probes for DNA structures.¹⁻³ For instance, the luminescence intensity of $[\text{Ru}(\text{phen})_3]^{2+}$ (phen = 1,10-phenanthroline) increases upon addition of double-helical DNA to the solution. This effect was initially attributed to intercalation of the complex with DNA, but is now better described as semi-intercalation.²⁻⁵ This prompted the design of analogues of $[\text{Ru}(\text{phen})_3]^{2+}$ in which one phen ligand was replaced by a phenanthroline derivative containing extended heteroaromatic units, which are more appropriate for intercalation between DNA base-pairs. Of these ligands, dppz has been extensively studied (dppz = dipyrido[3,2-a:2',3'-c]phenazine), not only because $[\text{Ru}(\text{phen})_2(\text{dppz})]^{2+}$ is structurally better suited to interact with DNA, but also because this complex exhibited the so-called “light switch” effect (**Figure 6.1**).⁶ In aqueous solutions, the complex is only very weakly emissive, but the emission is “turned on” in the presence of DNA. The emission intensity increases by at least four orders of magnitude because of intercalation of the dppz, or perhaps more correctly, the phenazine portion of the dppz ligand into DNA. This remarkable observation increased the interest in such complexes and a wide variety of photophysical and spectroscopic techniques have been applied to understanding the workings of this “light-switch” effect.⁷⁻¹²

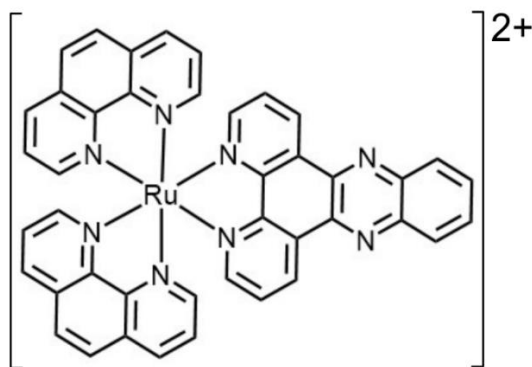


Figure 6.1. A representation of the molecular structure of $[\text{Ru}(\text{phen})_2\text{dppz}]^{2+}$.

Early investigations, which measured luminescent lifetimes and time-resolved UV/vis absorption spectra, identified a “dark” excited state in the photophysics of $[\text{Ru}(\text{phen})_2(\text{dppz})]^{2+}$. It was proposed that this “dark” state is energetically close to, and in equilibrium with, a “bright” luminescent state. The relative energies of these two states was used to explain the light switch phenomenon.⁷ Quenching studies, where water was added to acetonitrile solutions containing $[\text{Ru}(\text{phen})_2(\text{dppz})]^{2+}$, indicated that the “dark” state undergoes a fast radiationless decay ($\tau \approx 250$ ps) in the presence of water. The reaction with water, which involves substantial restructuring of the bulk water around the complex, quenches the luminescent excited state. It was suggested that while the ground state does not interact significantly with water the phenazine nitrogen atoms form hydrogen bonds with water in the “dark” excited state. Since then, a variety of techniques have been used to detect and characterise this “dark” state, including time-resolved resonance Raman⁸ and time-resolved infrared spectroscopy.¹³ However a satisfactory explanation for this differential hydrogen bonding regime has yet to be established.

In addition to experimental investigations, a number of computational studies have addressed the photophysics of the “light switch” effect.¹⁴⁻¹⁸ Quantum chemical calculations on $[\text{Ru}(\text{phen})_2(\text{dppz})]^{2+}$ and the related $[\text{Ru}(\text{bipy})_2(\text{dppz})]^{2+}$ (bipy = 2,2'-bipyridine) complex, indicate that the optically accessible excited states fall into two general classifications, those involving the ancillary ligands (phen or bipy) and those involving the dppz ligand.¹⁵ Current understanding, based on these calculations and the time-resolved resonance Raman investigations, suggest that the dark state involves mainly orbitals on the dppz ligand while the bright state appears to involve orbitals with some phenanthroline character centred either on the phenanthroline fragment of the dppz ligand¹⁰ or, in the case of $[\text{Ru}(\text{phen})_2(\text{dppz})]^{2+}$ derivatives, on the ancillary phen ligands. What is not clear from these studies, is how the presence of water can induce such a rapid and efficient dissipation of the “dark” state energy. However, differential hydrogen bonding interactions between ground and excited state points to a dynamic process, which is not readily described by static quantum chemical calculations. Furthermore, it is not clear from these investigations whether the phenazine nitrogen atoms engage in hydrogen bonding to water molecules in the

ground state, or why changes to the hydrogen bonding interaction occurs by progression to the excited state.

In this contribution we address these questions, firstly by investigating the hydrogen bonding status of the ground state. Then the excited state behaviour during changes to the hydrogen bonding interactions of water molecules was modelled. We present a more complete picture of how hydrogen bond formation in bulk water deactivates specific excited states on both the singlet and triplet hypersurfaces. The computational approach used here involves the modelling of a specific reaction coordinate in the ground state, namely the loss of hydrogen-bonded water molecules on the phenazine nitrogen atoms. These yield sets of atomic coordinates which are then used in TD-DFT calculations to estimate the energies of the excited states at each point along the reaction coordinate. This approach has been applied successfully to other large inorganic or organometallic systems,¹⁹⁻²⁶ and we believe represents a significant contribution to our understanding the “light switch” effect.

6.3 Experimental

All quantum chemical calculations were performed using Gaussian 16 (Revision B.01) as implemented at the Irish Centre for High-End Computing.²⁷ Molecular structure and density maps were visualised using GaussView 6,²⁸ while molecular fragment contributions to orbitals were extracted using AOMix.^{29,30} Unrestricted B3LYP hybrid Density Functional Theory (DFT) was used in all quantum chemical calculations,^{31,32} coupled to the double zeta quality LanL2DZ basis set.³³ The unrestricted B3LYP was used because TD-DFT calculations yield the energies of both singlet and triplet excited states for each calculation.³⁴⁻³⁶ The starting structure of $[\text{Ru}(\text{phen})_2(\text{dppz})]^{2+} \cdot 2\text{H}_2\text{O}$ was obtained from molecular mechanics calculations and was subsequently optimised to tight convergence criteria at the UB3LYP/LanL2DZ model chemistry. The Hessian matrix contained no negative eigenvalues, which confirms that the structure sits in a minimum on the potential energy hypersurface. Corrections for solvent dielectric were not applied in these calculations, instead two hydrogen bonded water molecules were treated explicitly, one on each of the phenazine nitrogen atoms.²⁴ This was because the light switch effect is observed when the solvent medium is changed from organic solvents to aqueous solvents which would introduce complexities into the calculations resulting from changes to the dielectric constant of the medium. In this work we adopted the philosophy that if the effect of one parameter is to be probed in the calculation (namely the effect of hydrogen-bonded water), every effort must be made to change just one parameter in the calculations. Fragment contributions to the overall electronic structure of ground and excited states were obtained using AOMix.²⁹ Absorption spectra were measured on an Agilent 8453 UV/Visible spectrophotometer in a 1 cm quartz cell using dry spectrophotometric grade solvents. $[\text{Ru}(\text{phen})_2(\text{dppz})]^{2+}$ was prepared and purified by a literature procedure and isolated as the PF_6^- salt (see supplementary information, Appendix E).³⁷

6.4 Results

6.4.1 UV/visible spectrum of $[\text{Ru}(\text{phen})_2(\text{dppz})]^{2+}$; Does the ground state engage in hydrogen bonding to water?

The UV-visible spectrum of $[\text{Ru}(\text{phen})_2(\text{dppz})]^{2+}$ in dry acetonitrile is presented in **Figure 6.2** along with spectra obtained following the addition of various aliquots of water. These spectra are normalised at 450 nm to compensate for concentration changes. It is clear from previous reports, and quantum chemical calculations, that the broad absorption from the visible region to 400 nm corresponds mainly to metal-to-ligand charge-transfer transitions (MLCT) either Ru-to-phen or Ru-to-dppz. The sharper features between 400 and 320 nm consist largely of dppz-based π -to- π^* transitions.^{16, 18} It is also clear from the spectra in **Figure 6.2** that the addition of water enhances the dppz-based π -to- π^* transitions relative to those of MLCT character. A full explanation for this relative enhancement awaits further investigation, however it may be the result of changes to the ion pairing with the PF_6^- counterions.³⁸ This hyperchromic behaviour is reversed upon addition of DNA to aqueous solutions, and indeed these features are almost extinguished upon complete intercalation into DNA.^{18, 37, 39} Thus, it would appear that the relative intensities of the MLCT and π -to- π^* absorptions are sensitive to the presence of water and its effect on the time-averaged positions of the counter-ions relative to the dppz ligand.^{38, 40-42}

These observations, coupled with computational results described below, strongly suggest some interaction between the complex in the ground state and water, and that this interaction is close to the dppz ligand. It is therefore reasonable to propose that the two phenazine nitrogen atoms undergo hydrogen bonding interactions with water in the ground state. Consequently, two water molecules were explicitly added to the dppz ligand, and this hydrate species, $[\text{Ru}(\text{phen})_2(\text{dppz})]^{2+} \cdot 2\text{H}_2\text{O}$, was the starting point in subsequent quantum chemical calculations. The effect of a systematic removal of these water molecules on the ground and excited state energies provide an overview of the dynamic role that water plays following excitation, and more specifically the role water plays in the deactivation of specific excited states.

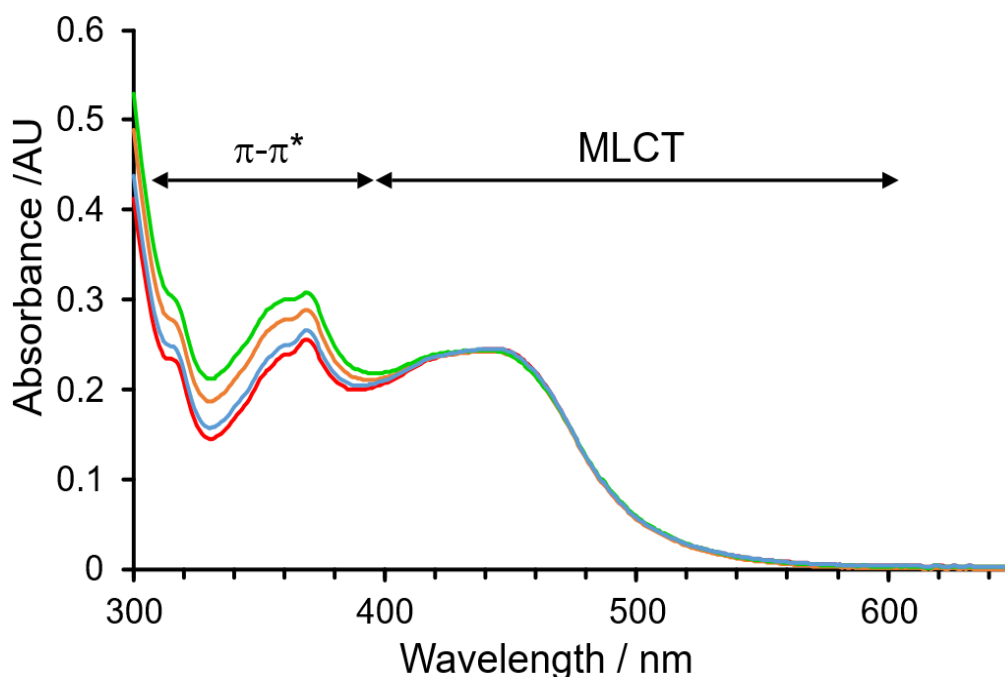


Figure 6.2. The UV-visible absorption spectrum of $[\text{Ru}(\text{phen})_2(\text{dppz})]^{2+} \cdot 2(\text{PF}_6^-)$ in dry acetonitrile (red $1.12 \times 10^{-5} \text{ M dm}^{-3}$, 2.5 mL solution volume) and acetonitrile containing water (blue + 160 μL ; orange +360 μL ; green + 1000 μL of H_2O respectively) normalised at 450 nm, showing the relative increase in the extinction of the features close to 360 nm with respect to the broad feature centred at 450 nm.

6.4.2 Modelling the UV/visible spectrum of $[\text{Ru}(\text{phen})_2(\text{dppz})]^{2+}$ and $[\text{Ru}(\text{phen})_2(\text{dppz})]^{2+} \cdot 2\text{H}_2\text{O}$

It is certainly the case that multiconfigurational methods can provide very accurate excited-state energies, but these wavefunctional approaches can be computationally very expensive. For large organometallic and inorganic systems such as those described in this work, DFT and TD-DFT methods provide a good compromise between accuracy and computational cost. This is particularly important for this work, which involves the estimation of a large number of excited state energies at many points along an evolving reaction coordinate. For these reasons TD-DFT methods were chosen to estimate vertical excitation energies for both $[\text{Ru}(\text{phen})_2(\text{dppz})]^{2+}$ and $[\text{Ru}(\text{phen})_2(\text{dppz})]^{2+} \cdot 2\text{H}_2\text{O}$ complexes. A similar analysis for $[\text{Ru}(\text{phen})_2(\text{dppz})]^{2+}$ has been published previously where a more detailed description of the electronic structure of the complex is presented.¹⁸ The contribution of various molecular fragments to the overall electronic structure of both $[\text{Ru}(\text{phen})_2(\text{dppz})]^{2+}$ and $[\text{Ru}(\text{phen})_2(\text{dppz})]^{2+} \cdot 2\text{H}_2\text{O}$ was calculated. For the $[\text{Ru}(\text{phen})_2(\text{dppz})]^{2+}$ complex the fragments chosen were the ruthenium atom, the dppz ligand and individually, the two

phen ligands. For $[\text{Ru}(\text{phen})_2(\text{dppz})]^{2+} \cdot 2\text{H}_2\text{O}$ the same fragment designations were used with the addition of a fragment comprising both water molecules. These data are presented graphically in **Figure 6.3** and energy data and fragment contributions are presented in **Table 6.1**, with a fuller description available in Appendix E along with electron density difference maps for the low-lying excited states, and representations of the valence molecular orbitals. In **Figure 6.3** the vertical energies indicated in red correspond to transitions to excited states which involve predominantly electron density changes on the dppz ligand. Those coloured blue indicate transitions which involve the phen ligands and those which involve both dppz and phen ligands are indicated by red/blue dashed lines. The length of the vertical lines corresponds to the calculated oscillator strength for the particular transition. Previous TD-DFT studies on this complex and similar complexes used similar classifications.¹⁵ A further reason for classifying excited states in this way is because water can only hydrogen bond to the dppz ligand and it is therefore important to understand how this interaction affects the excited states involving the dppz ligand. These calculations show that addition of water alters the electronic structure of the metal complex. What is clear from **Table 6.1**, is that the nature of the HOMO is unaffected by hydrogen bonded water, whereas the HOMO-1 and LUMO characters are changed. The HOMO-1 is predominantly dppz-based in $[\text{Ru}(\text{phen})_2(\text{dppz})]^{2+}$ while in $[\text{Ru}(\text{phen})_2(\text{dppz})]^{2+} \cdot 2\text{H}_2\text{O}$ it has substantial metal character. The LUMO is dppz-based in $[\text{Ru}(\text{phen})_2(\text{dppz})]^{2+} \cdot 2\text{H}_2\text{O}$, while it involves all ligands, phen and dppz, in $[\text{Ru}(\text{phen})_2(\text{dppz})]^{2+}$. LUMO+1 and LUMO+2 appear to have switched between the two systems. Likewise, HOMO-1 and HOMO-3 seem also to have switched. It is also clear from the spectroscopic changes observed upon addition of water described above (**Figure 6.2**), and confirmed by these TD-DFT calculations, that the nature of the Frank-Condon state of $[\text{Ru}(\text{phen})_2(\text{dppz})]^{2+}$ for any given excitation wavelength is not the same as that of $[\text{Ru}(\text{phen})_2(\text{dppz})]^{2+} \cdot 2\text{H}_2\text{O}$. For instance, excitation at wavelengths close to 400 nm which is the excitation wavelength commonly used in “light-switch” experiments, will tend to populate charge transfer excited states with greater Ru-to-dppz character for $[\text{Ru}(\text{phen})_2(\text{dppz})]^{2+} \cdot 2\text{H}_2\text{O}$ than for $[\text{Ru}(\text{phen})_2(\text{dppz})]^{2+}$. This affects the nature of the resulting triplet species, and directs the system towards dppz-based triplet excited states. It is important to note that other workers have modelled the UV/visible

spectrum of $[\text{Ru}(\text{phen})_2(\text{dppz})]^{2+}$ complexes using the same density functional/basis set combination as used in this work. None of these calculations accurately modelled the π to π^* region however (see **Figure 6.2**).^{18,37} We believe that this is because none of these studies (including ours) can account for the position or influence of the counterion on these transitions. The hypochromic effect on the π -to- π^* features when the $[\text{Ru}(\text{phen})_2(\text{dppz})]^{2+}$ complex intercalates with DNA is likely the result of a reduced contact between the counterion and the dppz ligand.

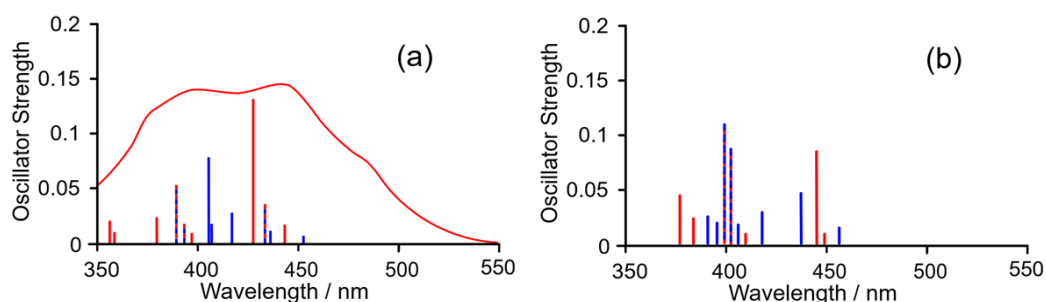


Figure 6.3. a) The calculated vertical transitions for $[\text{Ru}(\text{phen})_2(\text{dppz})]^{2+}$ and the experimental UV/visible spectrum (red) of $[\text{Ru}(\text{phen})_2(\text{dppz})]^{2+}$ intercalated with poly[d(AT)₂] which removes the effects of hydrogen bonded water and the counterion, this spectrum was obtained from reference [18] and b) the calculated vertical transitions of $[\text{Ru}(\text{phen})_2(\text{dppz})]^{2+}\cdot 2\text{H}_2\text{O}$ (the magnitude of the transitions are represented by the height of the lines); red lines represent dppz-centred excited states, blue lines represent phen-based excited states, and dashed lines represent excited states involving both phen and dppz ligands.

Table 6.1. The orbital energies for orbitals close to the valence level with the contributions of molecular fragments to those orbitals

$[\text{Ru}(\text{phen})_2(\text{dppz})]^{2+}$										
Label	HOMO-3	HOMO-2	HOMO-1	HOMO	LUMO	LUMO+1	LUMO+2	LUMO+3	LUMO+4	LUMO+5
MO	171	172	173	174	175	176	177	178	179	180
Energy (eV)	-10.89	-10.88	-10.81	-10.78	-7.35	-7.26	-7.25	-7.16	-7.11	-7.05
Fragment	% contribution of Fragment to orbital									
dppz	4.0	18.1	99.9	6.0	21.7	77.1	0.3	1.0	6.3	89.6
Ru	70.9	69.3	0.0	82.0	0.5	3.2	6.4	1.2	0.1	3.2
phen1	12.5	6.3	0.0	5.6	38.9	9.9	46.6	48.9	46.8	3.6
phen2	12.5	6.3	0.0	5.6	38.9	9.9	46.6	48.9	46.8	3.6

$[\text{Ru}(\text{phen})_2(\text{dppz})]^{2+}\cdot 2\text{H}_2\text{O}$										
Label	HOMO-3	HOMO-2	HOMO-1	HOMO	LUMO	LUMO+1	LUMO+2	LUMO+3	LUMO+4	LUMO+5
MO	181	182	183	184	185	186	187	188	189	190
Energy (eV)	-11.16	-10.77	-10.77	-10.66	-7.44	-7.25	-7.16	-7.07	-7.02	-6.96
Fragment	% contribution of Fragment to orbital									
dppz	99.8	3.9	15.6	6.4	98.8	4.8	0.3	1.3	0.7	90.6
Water	0.2	0.0	0.2	0.0	0.1	0.0	0.0	0.0	0.0	0.1
Ru	0.0	71.4	71.2	82.6	0.2	1.4	6.5	1.3	0.4	4.8
phen1	0.0	11.2	7.7	5.4	0.5	45.3	48.1	45.2	52.8	2.3
phen2	0.0	13.6	5.2	5.5	0.5	48.5	45.1	52.2	46.0	2.1

6.4.3 Water-loss reaction coordinates

The standard hydrated structure $[\text{Ru}(\text{phen})_2(\text{dppz})]^{2+} \cdot 2\text{H}_2\text{O}$, was optimised to tight convergence at the UB3LYP/LanL2DZ level. The resulting molecular structure is presented in **Figure 6.3**, showing the positions of the two water molecules. In the ground state, the water molecules lie slightly out of the plane of the dppz ligand by approximately 20° . This indicates a secondary interaction between the oxygen atoms of the water and the phenanthroline 4,7-hydrogens as indicated by dashed lines in **Figure 6.4**.

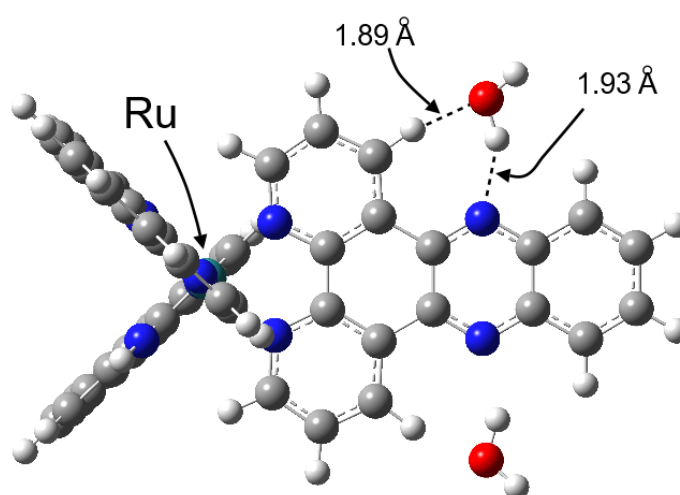


Figure 6.4. The molecular structure of $[\text{Ru}(\text{phen})_2(\text{dppz})]^{2+} \cdot 2\text{H}_2\text{O}$ showing the two hydrogen bonding water molecules and the location of the ruthenium atom which is obscured by the ancillary phen ligands in this orientation.

Two reaction coordinates were used to model the concerted loss to the water molecules from the $[\text{Ru}(\text{phen})_2(\text{dppz})]^{2+} \cdot 2\text{H}_2\text{O}$ complex. In both reaction coordinates (RCs), the nitrogen to hydrogen distance was lengthened in a concerted manner starting with the ground state equilibrium N-H distance. The reason for following two reaction coordinates in these calculations was because the fully relaxed potential energy scan became unstable at large N-H distances. Other water to ligand interactions, such as the water-oxygen to phenanthroline C-H units, became dominant at these N-H distances. The first reaction coordinate (RC1, **Figure 6.5** (a)) involved the loss of the two water molecules where only the structural parameters associated with the metal complex were optimised at each step along the potential energy scan. All bond lengths, angles and angles associated with the two water molecules were frozen. While allowing a

greater range of N-H distances to be modelled (N-H bond lengths ranged from approximately 1.94 to 5.90 Å with a step size of 0.01 Å), this RC suffered the disadvantage that calculations overestimated the ground state energy particularly at the extreme of the reaction coordinate. It is important to note that in these calculations, no account is taken of the counterion nor can they account for weaker forces such as van der Waals forces. This results in increasing potential energy between the ruthenium di-cation species and the distant water molecules. These calculations were able to model the behaviour of relevant excited states as these hydrogen bonding interactions become negligible at extreme N-H distances. The second reaction coordinate (RC2) also involved the concerted loss of both hydrogen bonded water molecules. In this case all other structural parameters were optimised along this reaction coordinate, this was a fully relaxed potential energy scan. However as indicated above the range of the N-H distance that could be modelled was restricted and at large N-H distances the oxygen atoms in the waters were subject to strong interactions with the hydrogen atoms of the phenanthroline fragment of the dppz ligand. Both N-H bonds were stretched from an initial distance of approximately 1.94 Å to 3.02 Å with a step size, initially of 0.01 Å, increasing to 0.04 Å after a bond length of 2.02 Å was reached (**Figure 6.5** (b)). The ground state energy change was estimated in these calculations and this indicated that the hydrogen bond dissociation energy for both bonds is approximately 10 kJ mol⁻¹.⁴³ Unfortunately, at the extreme of this reaction coordinate the optimisations became unstable because of the interactions between the water molecules and the aromatic protons on the phenanthroline fragment of the dppz ligand described above.

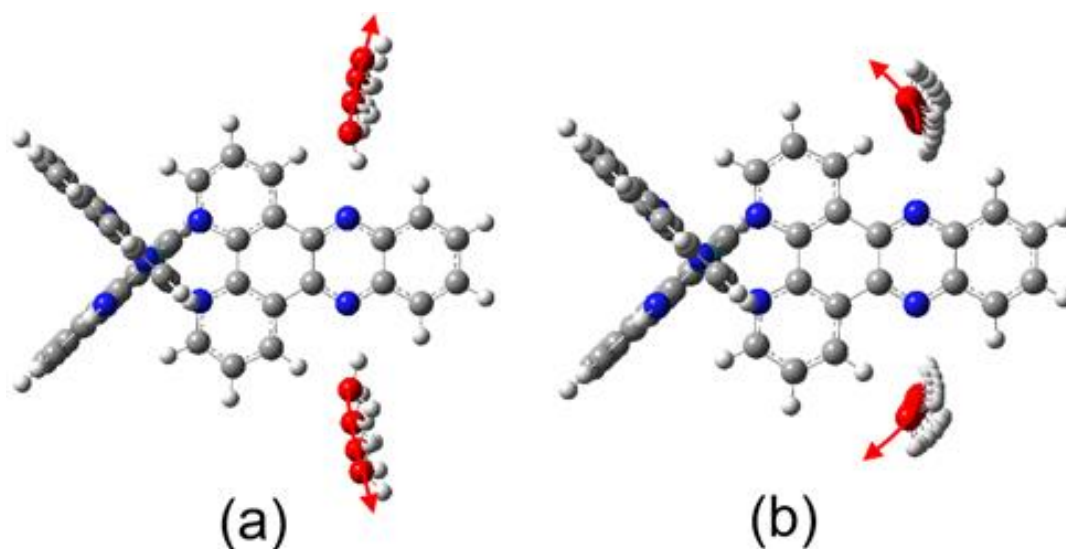


Figure 6.5. a) The structural change along the reaction coordinate 1 (RC1), modelling the loss of two hydrogen-bonded water molecules; (b) the structural changes along reaction coordinate 2 (RC2); the red arrows indicate the trajectory of the oxygen nuclei.

6.4.4 Excited state Dynamics; Identifying “Drain-Pipe” States

The behaviour of excited states along the two (RC1 and RC2) reaction coordinates was then investigated by Time-Dependent Density Functional Theory (TD-DFT). The energies of the lowest eighty excited states were calculated at each point using the unrestricted B3LYP functional and the LanL2DZ basis set. The unrestricted B3LYP functional was used because it yields the energies of both singlet and triplet excited states. While only some singlet states can be optically populated, a complete description of all excited states is required to model energy changes along the chosen reaction coordinate as these can involve multiple state crossings. Plotting the energies of the excited states against the N-H distance provides an adiabatic description of the excited state behaviour. The likely consequence to the hydrogen bonding interaction of specific excited states emerges from these plots.

As described above, early explanations of the light switch effect suggested that the ground state of $[\text{Ru}(\text{phen})_2(\text{dppz})]^{2+}$ does not engage in significant hydrogen bonding interactions with water, in contrast to the behaviour of the lowest energy triplet MLCT which was proposed to interact strongly with water.⁷ To test this proposal, the lowest energy triplet excited states of $[\text{Ru}(\text{phen})_2(\text{dppz})]^{2+} \cdot 2\text{H}_2\text{O}$ were modelled along RC2 (**Figure 6.6**, ES1 (red, dppz-based) and ES2 to ES4 (blue, phen-based)). This reaction coordinate was chosen because it provides a better estimate of the ground state energy

change. From our calculations, none of the low-lying triplet excited states exhibit a particularly attractive potential energy profile in favour of the hydrogen bond formation relative to the ground state. Indeed, the lowest energy triplet state (ES1) appears to mirror the energy change of the ground state as the N-H distance varies. Consequently, these data cannot support a preferential hydrogen bonding regime for the lowest energy triplet excited state over the ground state.

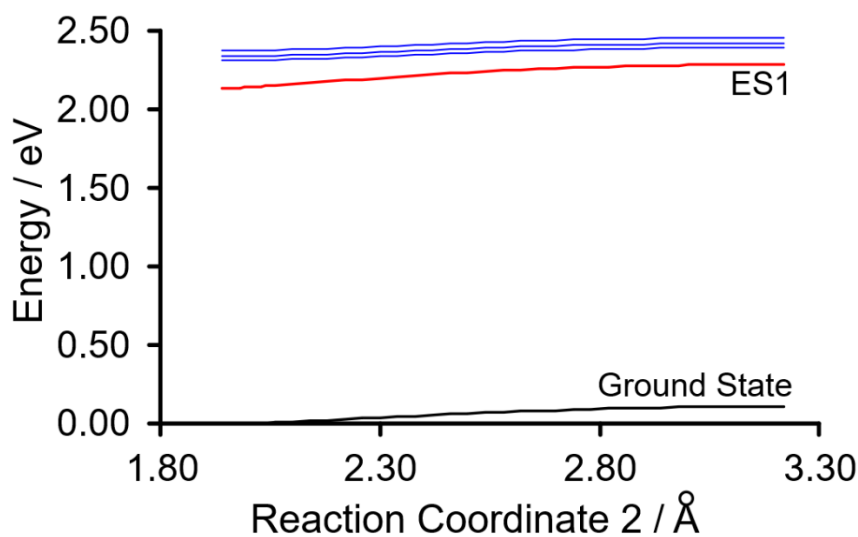


Figure 6.6. The energy change along RC2 for the lowest three triplet excited states (ES1 to ES4), showing that ES1 mirrors the ground state in being slightly attractive to hydrogen bond formation with water (red indicates a dppz-based state and blue the phen-based states).

Notwithstanding the lack of any significant variation in the energy profiles of the lowest energy excited state, the behaviour of higher excited states is more informative. A selected subset of the excited state energies is presented in **Figure 6.7** which indicate that while most excited states are bound states with respect to the hydrogen bonding interaction i.e., they exhibit an increase in potential energy as the N-H bond lengthened, a few offer repulsive energy profiles. In particular, the 14th excited state (ES14 triplet; 2.7 eV) and the 46th state (ES46 singlet; 3.2 eV) are the lowest states which are repulsive with respect to the hydrogen bonding interaction. Constructing electron density difference maps for these excited states reveal that they are both dppz-centred (electron density difference maps in **Figure 6.7**) with substantial n-to- π^* character. The triplet state also has additional metal-to-dppz charge-transfer character, and this is an important observation as such a state represents a link between purely metal-to-ligand charge transfer character and intra-ligand dppz-based states.

Population of these states would tend to expel water from the complex as indicated by the energy drop as the N-H distance increases. For this reason, we have dubbed these states “drain-pipe” states.

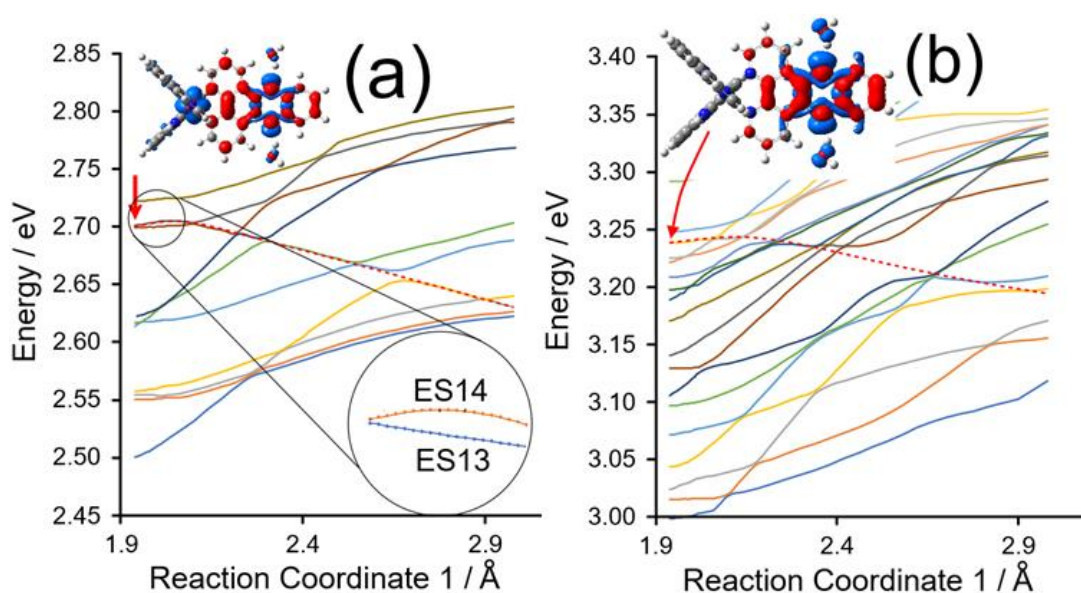


Figure 6.7. Selective energy profiles along RC2 (a) highlighting the behaviour of the lowest energy triplet “drain-pipe” state (ES14) with the early data showing a small energy barrier highlighted (excited states below 2.5 eV are removed for clarity) while (b) highlights the lowest energy singlet drain-pipe state at an energy not accessible to 400 nm excitation; the electron density difference maps indicate the regions of reduced electron density in blue, and the regions of increased electron density in red (iso value set at 0.001).

Electron density difference maps were then constructed along the RC of the triplet drain-pipe state. As the system moves along this energy profile, the character of the excited state changes and the metal-to-dppz charge-transfer character is lost, (an animation of these changes is presented with the Supporting Information, Appendix E). The state becomes more dppz-centred and indeed mainly located on the phenazine part of the dppz ligand (**Figure 6.8**, RC1 was used in this plot because of the greater N-H range). The development of the electron distribution in this excited state shows how excitation into, for instance, a metal-to-ligand charge-transfer excited state can transform into a mainly ligand-based excited state accompanied by the expulsion of the hydrogen bonded water molecules. Subsequent relaxation produces an excited state with mainly π -to- π^* character which has lost its n-to- π^* character. The electron density difference map for the final π -to- π^* state indicates an increased electron density (red volumes) on the phenazine nitrogen atoms compared to the ground state, making these better sites for hydrogen bonding interactions with water.

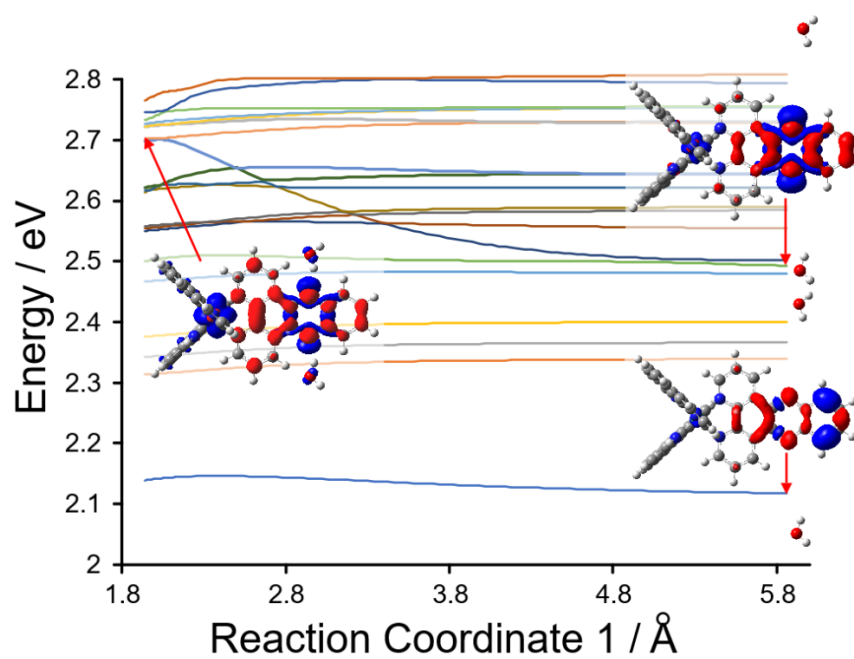


Figure 6.8. An expanded view of an adiabatic description of the excited state energies along RC1 highlighting the lowest energy drain-pipe state, the electron density difference maps for the extremes of the drain-pipe and the electron density difference map for the lowest energy triplet excited state resulting from internal conversion at the extreme of the reaction coordinate.

6.5 Discussion

This description of water expulsion and its role in altering the development of excited states can now be applied to a better understanding of the light switch effect. In previous studies time-resolved absorption and emission spectroscopies were used to study the photophysics of $[\text{Ru}(\text{phen})_2(\text{dppz})]^{2+}$ in aqueous and non-aqueous solution.⁷ These studies identified two distinct excited states implicated in the light-switch phenomenon, the so-called “bright” and “dark” states on the triplet hypersurface as represented in **Figure 6.9**. The light switch mechanism is attributed to the interconversion of the “bright” and “dark” states.^{12,44} The energy of this “dark” state is sensitive to the solvent medium. Protonation of the excited state,⁴⁵ or the energy gap law^{46,47} are among some previous proposals to explain the rapid decay of the “dark” state, but the most favoured explanation involves a reaction with bulk water which quenches luminescence in 250 ps.^{7,12,48}

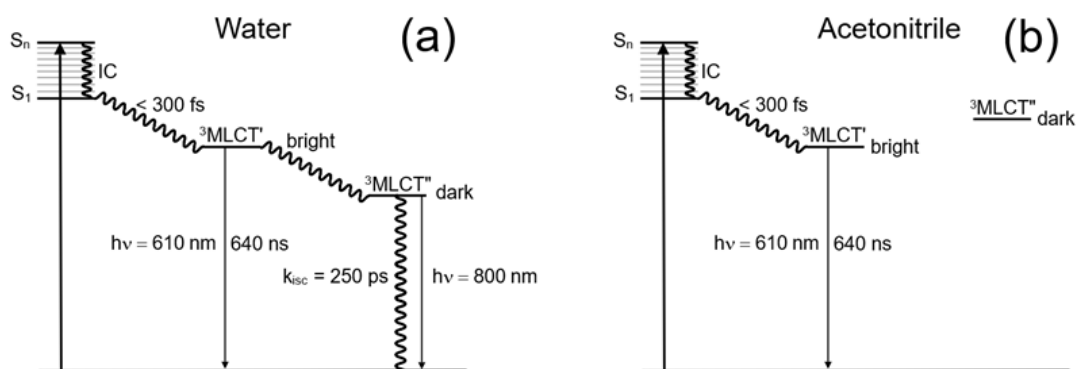


Figure 6.9. Historical energy level diagram describing the photophysics of $[\text{Ru}(\text{phen})_2(\text{dppz})]^{2+}$ in (a) water or (b) acetonitrile derived from E. J. C. Olson, D. Hu, A. Hormann, A. M. Jonkman, M. R. Arkin, E. D. A. Stemp, J. K. Barton and P. F. Barbara, *J. Am. Chem. Soc.*, 1997, 119, 11458-11467.

A range of time-resolved spectroscopic techniques have been applied to characterise both the bright and dark excited states. Resonance Raman and its time-resolved variant is particularly informative in this regard.⁴⁹ Picosecond time-resolved resonance Raman studies on $[\text{Ru}(\text{phen})_2(\text{dppz})]^{2+} \cdot 2\text{Cl}^-$ in water confirmed the formation of a triplet excited state with characteristics, principally in terms of its lifetime, which were consistent with the proposed “dark” state.⁸ This state exhibited resonance enhancement of dppz centred vibrations and these developed within 30 ps of

excitation. This species then decays to the ground state following an exponential time profile with a time constant of 250 ps identical to that obtained in luminescence lifetime and transient absorption measurements.⁷

Building on the experimental and computational results presented here, it is possible to propose a mechanism to explain the operation of the light-switch which also explains the time-resolved resonance Raman results outlined above. Firstly, the observation of spectroscopic changes to the ground-state UV/visible spectrum following addition of water to an acetonitrile solution of $[\text{Ru}(\text{phen})_2(\text{dppz})]^{2+}$ strongly suggests some form of interaction of the complex in the ground state with water. The DFT calculations have located water molecules within hydrogen bonding distances of the two phenazine nitrogen atoms and the calculated hydrogen bond-dissociation energy for two water molecules of about 10 kJ mol^{-1} is consistent with other hydrogen bonding interactions with amine nitrogens.⁵⁰ It is therefore not unreasonable to conclude that $[\text{Ru}(\text{phen})_2(\text{dppz})]^{2+}$ engages in hydrogen bonding interactions with water, and that $[\text{Ru}(\text{phen})_2(\text{dppz})]^{2+} \cdot 2\text{H}_2\text{O}$ represents a reasonable model for the ground state of the complex in the presence of water.

The TD-DFT calculations on both $[\text{Ru}(\text{phen})_2(\text{dppz})]^{2+}$ and $[\text{Ru}(\text{phen})_2(\text{dppz})]^{2+} \cdot 2\text{H}_2\text{O}$ demonstrate that the photophysics of these systems is affected by the interaction of the complex with water (see Appendix E for more details). Other researchers have proposed that $[\text{Ru}(\text{phen})_2(\text{dppz})]^{2+}$ and related complexes have two types of excited states available to them, one centred on the dppz ligand and the other on the ancillary, phen ligands.^{15,51} While the TD-DFT calculations presented here also supports this classification, it is clear that complexes exhibiting the light switch effect must preferentially populate dppz-based excited states. The efficiency at which either dppz-based or phen-based excited states are populated reflects the nature of the Franck-Condon state, i.e. the nature of the initially populated singlet state. It is unlikely that internal conversion to the lowest energy singlet state occurs before intersystem crossing to the triplet surface because the lowest energy singlet state is metal-to-phen charge-transfer in character. This would favour phen-based triplet states which, if populated, would result in emission.

Next to an explanation of the light switch effect. It is generally accepted that the initially populated singlet excited states of MLCT character, quickly (< 300 fs) crosses to the triplet surface.⁵²⁻⁵⁴ We can assume that Kasha's rule holds for this system,⁵⁵ and that the lowest energy triplet state will be emissive.^{56, 57} Accepting that two independent excited states can be produced following excitation, this will produce two independent emissive states, one phen-based and the other dppz-based.⁵⁸ Both of these states have similar energies and lifetimes and consequently are difficult to distinguish using emission spectroscopy.^{59,60} In non-aqueous solution both states could be populated, and both emit strongly (**Figure 6.10** (a)) which is derived from the Jablonski diagrams proposed by Rau and co-workers.⁶¹ This is the case when $[\text{Ru}(\text{phen})_2(\text{dppz})]^{2+}$ intercalates with DNA when both water and the counterions are removed from close contact with the dppz ligand. In the presence of water, however, the nature of the Franck-Condon state is altered by hydrogen bonding of water to the phenazine nitrogen atoms. This may also affect the location of the counterions which also increase the extinction of dppz-based transitions. All these factors contribute to the dppz-based triplet states being preferentially populated (**Figure 6.10** (b)).

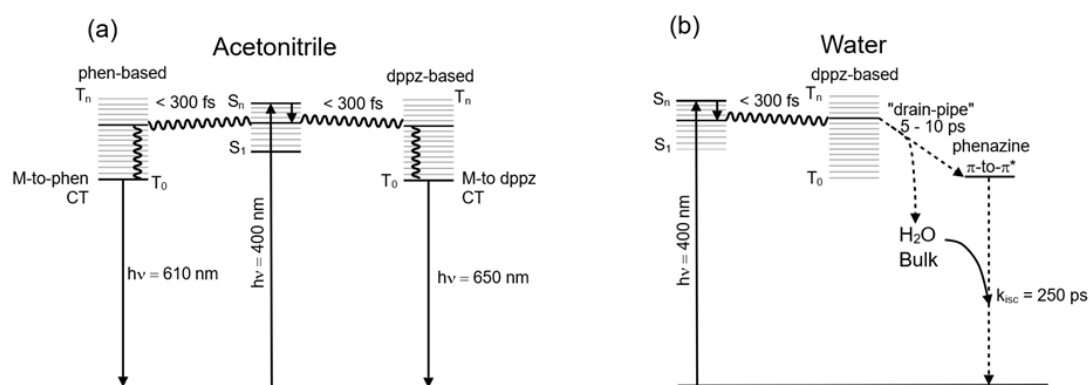


Figure 6.10. a) A schematic energy level diagram for the photophysics of $[\text{Ru}(\text{phen})_2(\text{dppz})]^{2+}$ in acetonitrile and b) A schematic energy level diagram describing the development of the excited states following excitation of $[\text{Ru}(\text{phen})_2(\text{dppz})]^{2+} \cdot 2\text{H}_2\text{O}$ showing the greater population of dppz-centred triplet states and the deactivation by expulsion of water producing a "dry" dark state and its subsequent reaction with bulk water.

The role of water in quenching the luminescence must now be addressed. It is unlikely that water can affect luminescence from phen-based triplet states as $[\text{Ru}(\text{phen})_3]^{2+}$ is strongly luminescent in aqueous solution.³ However, dynamic behaviour of the dppz-based triplets are somewhat more complicated. By internal conversion through the dppz-centred triplet states the system reaches a state with n-to- π^* character i.e., the

drain-pipe state at 2.7 eV above the ground state (equivalent to a photon energy of 450 nm). It should also be noted that this state also has some Ru-to-dppz charge-transfer character (**Figure 6.11** (b)) and links a state which has substantial metal-to-ligand charge transfer character to one which is localised on the dppz ligand. This state is repulsive with respect to the hydrogen bonding water molecules and rapidly expels them over a small energy barrier (0.2 kJ mol^{-1} ; **Figure 6.12**).

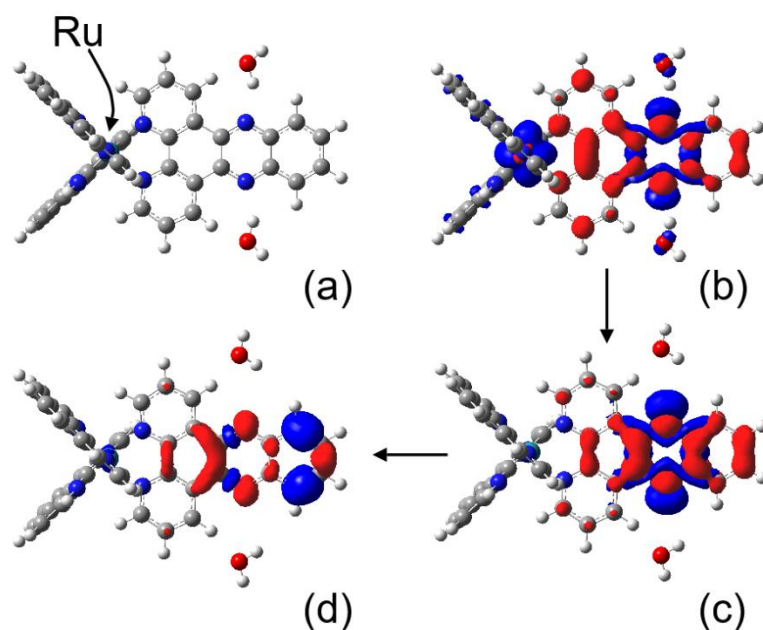


Figure 6.11. a) The molecular structure showing the orientation used for the e-density maps including the location of the ruthenium atom, b) the electron density difference map for the 14th excited state (triplet drain-pipe) showing both the metal-to-dppz and n-to- π^* character of this state (iso value 0.001), c) the electron density difference map for the 6th excited state (triplet, drain-pipe at its extreme) for a N-H distance of 3.1 Å showing the dppz-centred nature of this excited state, and d) the lowest energy triplet excited state for a N-H distance of 3.1 Å; blue regions have reduced electron density relative to the ground state, and red region have increased electron density relative to the ground state, carbon atoms are coloured grey, hydrogens light grey, and nitrogen atoms are blue and oxygen atoms red.

Calculating electron density difference maps along the “drain-pipe” shows that as this state develops along the water loss reaction coordinate it becomes progressively more dppz-centred (**Figure 6.11** (c)) ultimately producing a dppz-centred state which has lost its n-to- π^* character (**Figure 6.11** (d)). It is informative to note that time-resolved resonance Raman studies in an aqueous environment observed a progression from an excited state which initially was polarised more towards the phenanthroline segment of the dppz ligand to one in which the excess spin resides on the phenazine portion of the ligand.⁸ This process takes from 5 to 10 ps, which while slow for the interconversion between closely related excited states, it is on the timescale of water

reorientation times and is therefore consistent with water loss to the bulk solvent.⁶² At the extreme of the reaction coordinate the lowest triplet state is no longer repulsive to water as it is phenazine-based π -to- π^* in nature (**Figure 6.11** (d)) and corresponds to “dark” state although it would be better classified as “dry” at this stage. It then reacts with bulk water which involves a considerable reorganisation of the bulk water causing quenching of the excited state non-radiative relaxation to the ground state (**Figure 6.10** (b)).⁶³

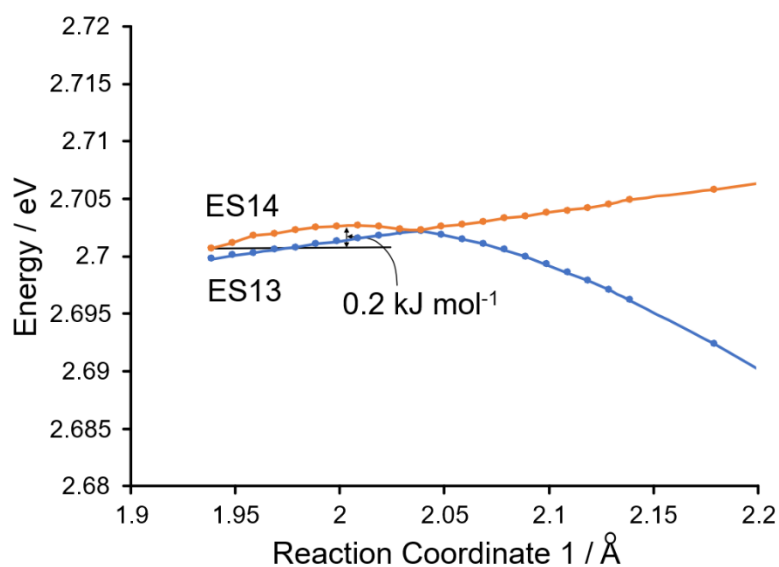


Figure 6.12. An expanded view of the energy changes (adiabatic) to ES13 and ES14 (“drain-pipe”) in the early stages of RC1 showing a very small (0.2 kJ mol^{-1}) barrier to progression of ES14 along this reaction coordinate.

We can now propose a scheme the underpins the light switch effect and is consistent with the concept of differential hydrogen bonding interactions and is also consistent with the time-resolved resonance Raman characterisation of the “dark” state (**Figure 6.10** (b)).

6.6 Conclusion

The results of our calculations strongly suggest that the direction the photophysical pathway in these systems is dictated by the characteristics of the singlet manifold close to the Franck-Condon region. Indeed time-resolved resonance Raman studies using different probe wavelengths produced different enhancement patterns.⁸ It would appear that intersystem crossing to the triplet manifold(s) occurs very rapidly for MLCT excited states and before internal conversion to the lowest energy singlet excited state. There is also strong evidence, from experimental and computational results, that two independent sets of triplet states are available to this system and we have classified these as phen-based and dppz-based. However, only dppz-based states will interact with water.^{15,58} Consequently, we expect that the solvent in these systems does not simply act as a diluent, but rather can influence the nature of the Franck-Condon state and thus the direction of the photophysics. The changes to the ground state UV/visible spectrum of $[\text{Ru}(\text{phen})_2(\text{dppz})]^{2+}$ when water is added to the acetonitrile solution is a direct manifestation of this. The photophysics of $[\text{Ru}(\text{phen})_2(\text{dppz})]^{2+}$ is not the same as the photophysics of $[\text{Ru}(\text{phen})_2(\text{dppz})]^{2+} \cdot 2\text{H}_2\text{O}$. Water directs the photophysics of the system to dppz-based rather than phen-based triplet excited states. The dppz-based excited states relax to a “drain-pipe” state which ejects hydrogen bonded water ultimately producing a phenazine-centred π -to- π^* excited state. This excited state then reacts with bulk water, and the substantial rearrangement of the bulk water quenches the excited state and associated emission. This clarifies the operation of the so-called differential hydrogen bonding interaction and its role in the $[\text{Ru}(\text{phen})_2(\text{dppz})]^{2+}$ light-switch.

6.7 Supporting information

The supplementary data associated with this chapter can be found in Appendix E.

6.8 Bibliography

- (1) A. Juris, V. Balzani, F. Barigelletti, S. Campagna, P. Belser, A. Vonzelewsky, Ru(II) Polypyridine Complexes - Photophysics, Photochemistry, Electrochemistry, and Chemi-luminescence, *Coord. Chem. Rev.*, 84 (1988), 85-277, [https://doi.org/10.1016/0010-8545\(88\)80032-8](https://doi.org/10.1016/0010-8545(88)80032-8).
- (2) J.K. Barton, J.M. Goldberg, C.V. Kumar, N.J. Turro, Binding Modes and Base Specificity of Tris(Phenanthroline)Ruthenium(II) Enantiomers with Nucleic-Acids - Tuning the Steroselectivity, *J. Am. Chem. Soc.*, 108 (1986), 2081-2088, <https://doi.org/10.1021/ja00268a057>.
- (3) C.V. Kumar, J.K. Barton, N.J. Turro, Photophysics of Ruthenium Complexes Bound to Double Helical DNA, *J. Am. Chem. Soc.*, 107 (1985), 5518-5523, <https://doi.org/10.1021/ja00305a032>.
- (4) J.M. Kelly, A.B. Tossi, D.J. McConnell, C. Ohuigin, A Study of the Interactions of some Polypyridylruthenium(II) Complexes with DNA using Fluorescence Spectroscopy Topoisometization and Thermal Denaturation, *Nucleic Acids Res.*, 13 (1985), 6017-6034, <https://doi.org/10.1093/nar/13.17.6017>.
- (5) S. Satyanarayana, J.C. Dabrowiak, J.B. Chaires, Neither Δ -Tris(Phenanthroline)Ruthenium(II) nor Λ -Tris(Phenanthroline)Ruthenium(II) Binds to DNA by Classical Intercalation, *Biochemistry*, 31 (1992), 9319-9324, <https://doi.org/10.1021/bi00154a001>.
- (6) A.E. Friedman, J.C. Chambron, J.P. Sauvage, N.J. Turro, J.K. Barton, Molecular "Light Switch" for DNA - Ru(Bpy)₂(DPPZ)²⁺, *J. Am. Chem. Soc.*, 112 (1990), 4960-4962, <https://doi.org/10.1021/ja00168a052>.
- (7) E.J.C. Olson, D. Hu, A. Hormann, A.M. Jonkman, M.R. Arkin, E.D.A. Stemp, J.K. Barton, P.F. Barbara, First observation of the key intermediate in the "light-switch" mechanism of [Ru(phen)₂dppz]²⁺, *J. Am. Chem. Soc.*, 119 (1997), 11458-11467, <https://doi.org/10.1021/ja971151d>.

- (8) C.G. Coates, J. Olofsson, M. Coletti, J.J. McGarvey, B. Onfelt, P. Lincoln, B. Norden, E. Tuite, P. Matousek, A.W. Parker, Picosecond Time-Resolved Resonance Raman Probing of the Light-Switch States of $[\text{Ru}(\text{Phen})_2\text{dppz}]^{2+}$, *J. Phys. Chem. B*, 105 (2001), 12653-12664, <https://doi.org/10.1021/jp0127115>.
- (9) C.G. Coates, P. Callaghan, J.J. McGarvey, J.M. Kelly, L. Jacquet, A. Kirsch-De Mesmaeker, Spectroscopic studies of structurally similar DNA-binding Ruthenium (II) complexes containing the dipyrrophenazine ligand, *J. Mol. Struct.*, 598 (2001), 15-25, [https://doi.org/10.1016/S0022-2860\(01\)00800-6](https://doi.org/10.1016/S0022-2860(01)00800-6).
- (10) C.G. Coates, P.L. Callaghan, J.J. McGarvey, J.M. Kelly, P.E. Kruger, M.E. Higgins, Transient resonance Raman investigation of excited states of $[\text{Ru}(\text{phen})_2\text{dppz}]^{2+}$ and deuterated analogues in aqueous and non-aqueous environments, *J. Raman Spec.*, 31 (2000), 283-288, [https://doi.org/10.1002/\(sici\)1097-4555\(200004\)31:4<283::aid-jrs540>3.0.co;2-a](https://doi.org/10.1002/(sici)1097-4555(200004)31:4<283::aid-jrs540>3.0.co;2-a).
- (11) C.G. Coates, L. Jacquet, J.J. McGarvey, S.E.J. Bell, A.H.R. AlObaidi, J.M. Kelly, Resonance Raman probing of the interaction between dipyrrophenazine complexes of Ru(II) and DNA, *J. Am. Chem. Soc.*, 119 (1997), 7130-7136, <https://doi.org/10.1021/ja970064i>.
- (12) J. Olofsson, B. Onfelt, P. Lincoln, Three-state light switch of $[\text{Ru}(\text{phen})_2\text{dppz}]^{2+}$: Distinct excited-state species with two, one, or no hydrogen bonds from solvent, *J. Phys. Chem. A*, 108 (2004), 4391-4398, <https://doi.org/10.1021/jp037967k>.
- (13) F.E. Poynton, J.P. Hall, P.M. Keane, C. Schwarz, I.V. Sazanovich, M. Towrie, T. Gunnlaugsson, C.J. Cardin, D.J. Cardin, S.J. Quinn, C. Long, J.M. Kelly, Direct observation by time-resolved infrared spectroscopy of the bright and the dark excited states of the $[\text{Ru}(\text{phen})_2(\text{dppz})]^{2+}$ light-switch compound in solution and when bound to DNA, *Chem. Sci.*, 7 (2016), 3075-3084, <https://doi.org/10.1039/c5sc04514b>.
- (14) G. Pourtois, D. Beljonne, C. Moucheron, S. Schumm, A. Kirsch-De Mesmaeker, R. Lazzaroni, J.L. Bredas, Photophysical properties of ruthenium(II) polyazaaromatic compounds: A theoretical insight, *J. Am. Chem. Soc.*, 126 (2004), 683-692, <https://doi.org/10.1021/ja034444h>.

(15) S. Fantacci, F. De Angelis, A. Sgamellotti, N. Re, A TDDFT study of the ruthenium(II) polyazaaromatic complex $[\text{Ru}(\text{dppz})(\text{phen})_2]^{2+}$ in solution, *Chem. Phys. Lett.*, 396 (2004), 43-48, <https://doi.org/10.1016/j.cplett.2004.07.101>.

(16) M. Atsumi, L. Gonzalez, C. Daniel, Spectroscopy of Ru(II) polypyridyl complexes used as intercalators in DNA: Towards a theoretical study of the light switch effect, *J. Photochem. Photobiol., A*, 190 (2007), 310-320, <https://doi.org/10.1016/j.jphotochem.2007.01.015>.

(17) X. Gao, S. Shi, J.-L. Yao, J. Zhao, T.-M. Yao, Impacts of terminal modification of $[\text{Ru}(\text{phen})_2\text{dppz}]^{2+}$ on the luminescence properties: a theoretical study, *J. Chem. Soc., Dalton Trans.*, 44 (2015), 19264-19274, <https://doi.org/10.1039/c5dt03373j>.

(18) J. Li, J.C. Chen, L.C. Xu, K.C. Zheng, L.N. Ji, A DFT/TDDFT study on the structures, trend in DNA-binding and spectral properties of molecular "light switch" complexes $[\text{Ru}(\text{phen})_2(\text{L})]^{2+}$ (L = dppz, taptp, phehat), *J. Organomet. Chem.*, 692 (2007), 831-838, <https://doi.org/10.1016/j.jorganchem.2006.10.029>.

(19) J.C. Manton, F.J.R. Cerpentier, E.C. Harvey, I.P. Clark, G.M. Greetham, C. Long, M.T. Pryce, Photochemical or electrochemical bond breaking - exploring the chemistry of $(\mu^2\text{-alkyne})\text{Co}_2(\text{CO})_6$ complexes using time-resolved infrared spectroscopy, spectro-electrochemical and density functional methods, *J. Chem. Soc., Dalton Trans.*, 48 (2019), 14642-14652, <https://doi.org/10.1039/c9dt03006a>.

(20) J.C. Manton, S. Amirjalayer, A.C. Coleman, S. McMahon, E.C. Harvey, G.M. Greetham, I.P. Clark, W.J. Buma, S. Woutersen, M.T. Pryce, C. Long, Excited state evolution towards ligand loss and ligand chelation at group 6 metal carbonyl centres, *J. Chem. Soc., Dalton Trans.*, 43 (2014), 17797-17805, <https://doi.org/10.1039/c4dt01544d>.

(21) C. Long, Potential Energy Mapping of the Excited-States of $(\eta^6\text{-Arene})\text{Cr}(\text{CO})_3$ Complexes: the Evolution Toward CO-Loss or Haptotropic Shift Processes, *J. Phys. Chem. A*, 116 (2012), 6845-6850, <https://doi.org/10.1021/jp301118v>.

(22) I.P. Clark, M.W. George, G.M. Greetham, E.C. Harvey, C. Long, J.C. Manton, H. McArdle, M.T. Pryce, Photochemistry of $(\eta^6\text{-Anisole})\text{Cr}(\text{CO})_3$ and $(\eta^6\text{-$

Thioanisole)Cr(CO)₃: Evidence for a Photoinduced Haptotropic Shift of the Thioanisole Ligand, a Picosecond Time-Resolved Infrared Spectroscopy and Density Functional Theory Investigation, *J. Phys. Chem. A*, 116 (2012), 962-969, <https://doi.org/10.1021/jp211726j>.

(23) I.P. Clark, M.W. George, G.M. Greetham, E.C. Harvey, C. Long, J.C. Manton, M.T. Pryce, Photochemistry of (η^6 -Arene)Cr(CO)₃ (Arene = Methylbenzoate, Naphthalene, or Phenanthrene) in n-Heptane Solution: Population of Two Excited States Following 400 nm Excitation As Detected by Picosecond Time-Resolved Infrared Spectroscopy, *J. Phys. Chem. A*, 115 (2011), 2985-2993, <https://doi.org/10.1021>.

(24) C. Daniel, Photochemistry and photophysics of transition metal complexes: Quantum chemistry, *Coord. Chem. Rev.*, 282 (2015), 19-32, <https://doi.org/10.1016/j.ccr.2014.05.023>.

(25) N. Ben Arnor, S. Villaume, D. Maynaud, C. Daniel, The electronic spectroscopy of transition metal carbonyls: The tough case of Cr(CO)₆, *Chem. Phys. Lett.*, 421 (2006), 378-382, <https://doi.org/10.1016/j.cplett.2006.02.002>.

(26) A. Dreuw, M. Head-Gordon, Single-reference ab initio methods for the calculation of excited states of large molecules, *Chem. Rev.*, 105 (2005), 4009-4037, <https://doi.org/10.1021/cr0505627>.

(27) M.J. Frisch, G.W. Trucks, H.B. Schlegel, G.E. Scuseria, M.A. Robb, J.R. Cheeseman, G. Scalmani, V. Barone, G.A. Petersson, H. Nakatsuji, X. Li, M. Caricato, A.V. Marenich, J. Bloino, B.G. Janesko, R. Gomperts, B. Mennucci, H.P. Hratchian, J.V. Ortiz, A.F. Izmaylov, J.L. Sonnenberg, D. Williams-Young, F. Ding, F. Lipparini, F. Egidi, J. Goings, B. Peng, A. Petrone, T. Henderson, D. Ranasinghe, V.G. Zakrzewski, J. Gao, N. Rega, G. Zheng, W. Liang, M. Hada, M. Ehara, K. Toyota, R. Fukuda, J. Hasegawa, M. Ishida, T. Nakajima, Y. Honda, O. Kitao, H. Nakai, T. Vreven, K. Throssell, J.A. Montgomery, J.E. Peralta, F. Ogliaro, M.J. Bearpark, J.J. Heyd, E.N. Brothers, K.N. Kudin, V.N. Staroverov, T.A. Keith, R. Kobayashi, J. Normand, K. Raghavachari, A.P. Rendell, J.C. Burant, S.S. Iyengar, J. Tomasi, M.

Cossi, J.M. Millam, M. Klene, C. Adamo, R. Cammi, J.W. Ochterski, R.L. Martin, K. Morokuma, O. Farkas, J.B. Foresman, D.J. Fox, Gaussian 16, Revision B.01, 2016.

(28) R.D. Dennington II, T.A. Keith, J.M. Millam, GaussView, 2016.

(29) S.I. Gorelsky, AOMix Program for Molecular Orbital Analysis <http://www.sg-chem.net/>, version 6.88, 2013.

(30) S.I. Gorelsky, A.B.P. Lever, Electronic structure and spectra of ruthenium diimine complexes by density functional theory and INDO/S. Comparison of the two methods, *J. Organomet. Chem.*, 635 (2001), 187-196, [https://doi.org/10.1016/S0022-328X\(01\)01079-8](https://doi.org/10.1016/S0022-328X(01)01079-8).

(31) A.D. Becke, Density-Functional Thermochemistry 3. The Role of Exact Exchange, *J. Chem. Phys.*, 98 (1993), 5648-5652, <https://doi.org/10.1063/1.464913>.

(32) C.T. Lee, W.T. Yang, R.G. Parr, Development of the Colle-Salvetti Correlation-Energy Formula into a Functional of the Electron-Density, *Phys. Rev. B*, 37 (1988), 785-789, <https://doi.org/10.1103/physrevb.37.785>.

(33) T.H. Dunning Jr, P.J. Hay, Modern Theoretical Chemistry, in: H.F. Schaefer III (Ed.) Modern Theoretical Chemistry, Plenum Press, New York, 1977.

(34) R.E. Stratmann, G.E. Scuseria, M.J. Frisch, An efficient implementation of time-dependent density-functional theory for the calculation of excitation energies of large molecules, *J. Chem. Phys.*, 109 (1998), 8218-8224, <https://doi.org/10.1063/1.477483>.

(35) R. Bauernschmitt, R. Ahlrichs, Treatment of electronic excitations within the adiabatic approximation of time dependent density functional theory, *Chem. Phys. Lett.*, 256 (1996), 454-464, [https://doi.org/10.1016/0009-2614\(96\)00440-X](https://doi.org/10.1016/0009-2614(96)00440-X).

(36) M.E. Casida, C. Jamorski, K.C. Casida, D.R. Salahub, Molecular excitation energies to high-lying bound states from time-dependent density-functional response theory: Characterization and correction of the time-dependent local density approximation ionization threshold, *J. Chem. Phys.*, 108 (1998), 4439-4449, <https://doi.org/10.1063/1.475855>.

- (37) C. Hiort, P. Lincoln, B. Norden, DNA-Binding of Δ - and Λ - [Ru(phen)₂DPPZ]²⁺, *J. Am. Chem. Soc.*, 115 (1993), 3448-3454, <https://doi.org/10.1021/ja00062a007>.
- (38) D. Magde, M.D. Magde, E.C. Glazer, So-called "dual emission" for (MLCT)-M-3 luminescence in ruthenium complex ions: What is really happening?, *Coord. Chem. Rev.*, 306 (2016), 447-467, <https://doi.org/10.1016/j.ccr.2015.01.003>.
- (39) J.G. Liu, Q.L. Zhang, X.F. Shi, L.N. Ji, Interaction of [Ru(dmp)₂(dppz)]²⁺ and [Ru(dmb)₂(dppz)]²⁺ with DNA: Effects of the ancillary ligands on the DNA-binding behaviors, *Inorg. Chem.*, 40 (2001), 5045-5050, <https://doi.org/10.1021/ic001124f>.
- (40) T. Very, S. Despax, P. Hebraud, A. Monari, X. Assfeld, Spectral properties of polypyridyl ruthenium complexes intercalated in DNA: theoretical insights into the surrounding effects of [Ru(dppz)(bpy)₂]²⁺, *PCCP*, 14 (2012), 12496-12504, <https://doi.org/10.1039/c2cp40935f>.
- (41) V. Rajendiran, M. Palaniandavar, V.S. Periasamy, M.A. Akbarsha, Ru(phen)₂(dppz) (2+) as an efficient optical probe for staining nuclear components, *J. Inorg. Biochem.*, 104 (2010), 217-220, <https://doi.org/10.1016/j.jinorgbio.2009.10.018>.
- (42) A. Chantzis, T. Very, C. Daniel, A. Monari, X. Assfeld, Theoretical evidence of photo-induced charge transfer from DNA to intercalated ruthenium (II) organometallic complexes, *Chem. Phys. Lett.*, 578 (2013), 133-137, <https://doi.org/10.1016/j.cplett.2013.05.068>.
- (43) P.R. Rablen, J.W. Lockman, W.L. Jorgensen, Ab initio study of hydrogen-bonded complexes of small organic molecules with water, *J. Phys. Chem. A*, 102 (1998), 3782-3797, <https://doi.org/10.1021/jp980708o>.
- (44) M.K. Brennaman, J.H. Alstrum-Acevedo, C.N. Fleming, P. Jang, T.J. Meyer, J.M. Papanikolas, Turning the [Ru(bpy)₂dppz]²⁺ light-switch on and off with temperature, *J. Am. Chem. Soc.*, 124 (2002), 15094-15098, <https://doi.org/10.1021/ja0279139>.

- (45) P.F. Barbara, P.K. Walsh, L.E. Brus, Picosecond Kinetic and Vibrationally Resolved Spectroscopic Studies of Intramolecular Excited-State Hydrogen-Atom Transfer, *J. Phys. Chem.*, 93 (1989), 29-34, <https://doi.org/10.1021/j100338a011>.
- (46) R. Englman, J. Jortner, The energy gap law for radiationless transitions in large molecules, *Mol. Phys.*, 18 (1970), 145-164, <https://doi.org/10.1080/00268977000100171>.
- (47) J.L. Yao, X. Gao, W.L. Sun, S. Shi, T.M. Yao, [Ru(bpy)₂dppz-idzo]²⁺: a colorimetric molecular "light switch" and powerful stabilizer for G-quadruplex DNA, *J. Chem. Soc., Dalton Trans.*, 42 (2013), 5661-5672, <https://doi.org/10.1039/c3dt32640c>.
- (48) A.W. McKinley, P. Lincoln, E.M. Tuite, Environmental effects on the photophysics of transition metal complexes with dipyrido 2,3-a:3',2'-c phenazine (dppz) and related ligands, *Coord. Chem. Rev.*, 255 (2011), 2676-2692, <https://doi.org/10.1016/j.ccr.2011.06.012>.
- (49) W.R. Browne, J.J. McGarvey, Raman scattering and photophysics in spin-state-labile d(6) metal complexes, *Coord. Chem. Rev.*, 250 (2006), 1696-1709, <https://doi.org/10.1016/j.ccr.2006.01.009>.
- (50) J.H. Chen, Y. Zheng, A. Melli, L. Spada, T. Lu, G. Feng, Q. Gou, V. Barone, C. Puzzarini, Theory meets experiment for elucidating the structure and stability of non-covalent complexes: water-amine interaction as a proof of concept, *PCCP*, 22 (2020), 5024-5032, <https://doi.org/10.1039/c9cp06768j>.
- (51) E. Amouyal, A. Homsí, J.C. Chambron, J.P. Sauvage, Synthesis and Study of a Mixed-Ligand Ruthenium(II) Complex in its Ground and Excited-States - Bis(2,2'-Bipyridine)dipyrido[3,2-a:2',3'-c]Phenazine-N⁴N⁵)Ruthenium(II), *J. Chem. Soc., Dalton Trans.*, (1990), 1841-1845, <https://doi.org/10.1039/dt9900001841>.
- (52) A.C. Bhasikuttan, M. Suzuki, S. Nakashima, T. Okada, Ultrafast fluorescence detection in tris(2,2'-bipyridine)ruthenium(II) complex in solution: Relaxation dynamics involving higher excited states, *J. Am. Chem. Soc.*, 124 (2002), 8398-8405, <https://doi.org/10.1021/ja026135h>.

- (53) J. Eng, C. Gourlaouen, E. Gindensperger, C. Daniel, Spin-Vibronic Quantum Dynamics for Ultrafast Excited-State Processes, *Acc. Chem. Res.*, 48 (2015), 809-817, <https://doi.org/10.1021/ar500369r>.
- (54) N.H. Damrauer, G. Giulio Cerullo, A. Yeh, T.R. Bousie, C.V. Shank, J.K. McCusker, Femtosecond Dynamics of Excited-State Evolution in $[\text{Ru}(\text{bpy})_3]^{2+}$, *Science*, 275 (1997), 54-57,
- (55) G.N. Lewis, M. Kasha, Phosphorescence in Fluid Media and the Reverse Process of Singlet-Triplet Absorption, *J. Am. Chem. Soc.*, 67 (1945), 994-1003, <https://doi.org/10.1021/ja01222a032>.
- (56) G.D. Hager, R.J. Watts, G.A. Crosby, Charge-Transfer Excited States of Ruthenium(II) Complexes. II. Relationship of Level Parameters to Molecular-Structure, *J. Am. Chem. Soc.*, 97 (1975), 7037-7042, <https://doi.org/10.1021/ja00857a014>.
- (57) G.D. Hager, G.A. Crosby, Charge-Transfer Excited-States of Ruthenium(II) Complexes. I. Quantum Yield and Decay Measurements, *J. Am. Chem. Soc.*, 97 (1975), 7031-7037, <https://doi.org/10.1021/ja00857a013>.
- (58) D. Isakov, R. Giereth, D. Nauroozi, S. Tschierlei, S. Rau, Two Emissive Long-Lived Excited States of an Imidazole-Functionalized Ruthenium Dipyridophenazine Complex, *Inorg. Chem.*, 58 (2019), 12646-12653, <https://doi.org/10.1021/acs.inorgchem.9b01372>.
- (59) E.C. Glazer, D. Magde, Y. Tor, Ruthenium complexes that break the rules: Structural features controlling dual emission, *J. Am. Chem. Soc.*, 129 (2007), 8544-8551, <https://doi.org/10.1021/ja071124f>.
- (60) E.C. Glazer, D. Magde, Y. Tor, Dual emission from a family of conjugated dinuclear Ru-II complexes, *J. Am. Chem. Soc.*, 127 (2005), 4190-4192, <https://doi.org/10.1021/ja0440304>.
- (61) M. Schwalbe, M. Karnahl, S. Tschierlei, U. Uhlemann, M. Schmitt, B. Dietzek, J. Popp, R. Groake, J.G. Vos, S. Rau, The switch that wouldn't switch - unexpected

luminescence from a ruthenium(II)-dppz-complex in water, *J. Chem. Soc., Dalton Trans.*, 39 (2010), 2768-2771, <https://doi.org/10.1039/b924944n>.

(62) B. Onfelt, P. Lincoln, B. Norden, J.S. Baskin, A.H. Zewail, Femtosecond linear dichroism of DNA-intercalating chromophores: Solvation and charge separation dynamics of $[\text{Ru}(\text{phen})_2\text{dppz}]^{2+}$ systems, *PNAS*, 97 (2000), 5708-5713, <https://doi.org/10.1073/pnas.100127397>.

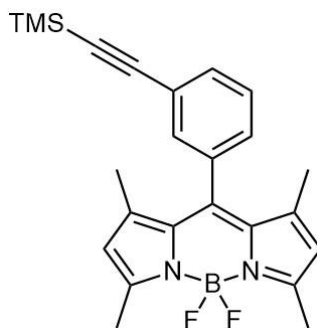
(63) J.A. Mondal, V. Samant, M. Varne, A.K. Singh, T.K. Ghanty, H.N. Ghosh, D.K. Palit, The Role of Hydrogen-Bonding Interactions in the Ultrafast Relaxation Dynamics of the Excited States of 3-and 4-Aminofluoren-9-ones, *Chemphyschem*, 10 (2009), 2995-3012, <https://doi.org/10.1002/cphc.200900325>.

Appendices A - E

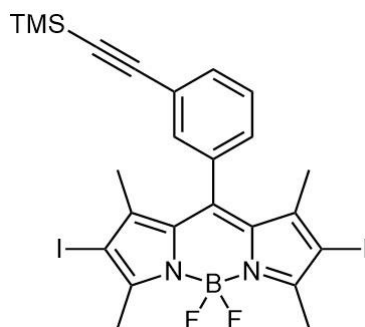
Appendix A

Supporting information associated with Chapter 2.

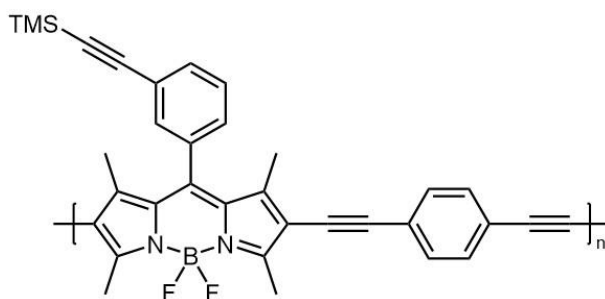
S2.1. Synthetic procedure



3-TMS BODIPY monomer. The synthesis of BODIPY monomers were carried out as previously reported with some minor modifications.¹ To an oven dried flask fitted with magnetic stir-bar, 25 mL CH₂Cl₂ was added and allowed to purge with N₂ for 15 min. To the degassed solvent, 3-[(trimethylsilyl)ethynyl] benzaldehyde (2.5 mmol) and 2,4-dimethylpyrrole (0.51 mL, 5.0 mmol) were added. A few drops of TFA was added and the solution was stirred overnight at room temperature, in the absence of light. DDQ (2.48 mmol) was added and the solution was allowed to stir for a further 4 h. After this time, boron trifluoride diethyl etherate (18.4 mmol) was added, following in quick succession by TEA (41 mmol). The reaction was allowed to stir overnight at room temperature under the flow of nitrogen. After this time, the reaction was stopped, and the organic layer was collected after washing three times with saturated sodium bicarbonate solution. The organic layer was collected and dried over magnesium sulphate to yield a dark purple crude product. Purification was carried out using column chromatography with on silica (hexane: ethyl acetate 70:30) to yield a red solid. ¹H NMR (600 MHz, CDCl₃): δ 7.56 (dt, J = 7.8 Hz, 1H), 7.45 – 7.42 (m, 2H), 7.24 (dt, J = 7.6 Hz, 1H), 5.98 (s, 2H), 2.55 (s, 6H), 1.41 (s, 6H), 0.24 (s, 9H). ¹³C NMR (600 MHz, CDCl₃): δ 155.9, 143.2, 140.5, 135.3, 132.6, 131.6, 131.5, 129.3, 128.2, 124.6, 121.5, 104.0, 96.0, 14.9, 14.8, 0.1. HRMS (ESI) calculated for C₂₄H₂₇BF₂N₂Si (M+H), 421.2077, obtained 421.2074.

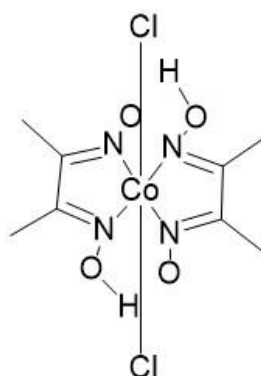


3-TMS diiodo BODIPY: This procedure was carried out as per previous reported with some minor modifications.¹ 3-TMS BODIPY monomer (0.26 mmol) and iodine (76 mg, 0.30 mmol) were added to an oven-dried round bottom flask equipped with stir-bar, dissolved in 30 mL of EtOH and purged for 30 min with nitrogen. Iodic acid (93 mg, 0.53 mmol) was dissolved in 1.5 mL deionised water and also allowed to purge with nitrogen for 30 min. After this time, both solutions were combined and allowed to reflux at 60 °C for 20 min. When the complete conversion of the monomer was observed by monitoring the reaction by TLC, the solvent was removed using distillation, followed by dissolving the crude product in CH₂Cl₂ and washing three times with saturated sodium thiosulphate solution. The organic layer was collected, and the product was dried using rotary evaporation to yield pure product. ¹H NMR (600 MHz, CDCl₃): δ 7.61 (d, J = 7.7 Hz, 1H), 7.47 (t, 1H), 7.38 (s, 1H), 7.20 (d, J = 7.6 Hz, 1H), 2.64 (s, 6H), 1.43 (s, 6H), 0.25 (s, 9H). ¹³C NMR (600 MHz, CDCl₃): δ 157.3, 145.5, 140.2, 135.1, 133.1, 131.4, 131.3, 129.6, 127.9, 125.0, 103.6, 96.6, 86.0, 17.5, 16.2, 0.1. HRMS (ESI) calculated for C₂₄H₂₅BF₂I₂N₂Si, 671.9937, obtained 671.9922.



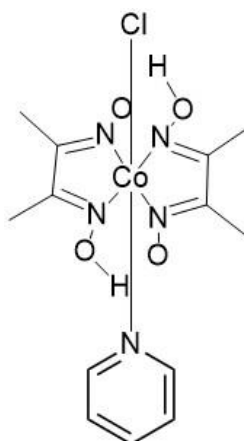
3-TMS BODIPY polymer: To an oven-dried Schlenk equipped with stir-bar, anhydrous tetrahydrofuran (THF) (15 mL) and anhydrous diisopropylamine (DiiPA) (15 mL) were added. All glass taps were greased and the Schlenk was degassed using

three freeze-pump-thaw cycles. Addition of the solids to the Schlenk was then carried out – BODIPY iodo monomer, B2, (0.15 mmol), 1,4-diethynylbenzene (19 mg, 0.15 mmol), bis(triphenylphosphine) palladium(II) dichloride (16 mol%), copper iodide (8 mol%), triphenylphosphine (8 mol%) were added, and the freeze-pump-thaw cycle was repeated to ensure the reaction would occur in the absence of air. The solution was allowed to reflux for 48 hr at 75-85 °C, until complete consumption of the IODO BODIPY was monitored by TLC. After this time, the solvents were removed by distillation. The crude polymer was dissolved in CH₂Cl₂ and washed three times with saturated sodium bicarbonate solution. The organic layer was dried over MgSO₄. Purification was carried out by washing in EtOH and collection of the precipitate to yield a pink/purple solid. This process was repeated to yield a pure polymer free of residual catalytic system. 3-TMS polymer was obtained as a dark purple solid (94 mg). ¹H NMR (600 MHz, CDCl₃): δ 7.73-7.27 (br, Ar-H), 2.64 (br, CH₃ at 3, 5 position of BODIPY), 1.43 (br, CH₃ at 1, 7 position of BODIPY), 0.26 (br, CH₃ x 3 in TMS group at *meso* position of BODIPY). SEC results: Peak 1: M_n = 12260, M_w = 13990, PDI = 1.141; Peak 2: M_n = 4801, M_w = 4952, PDI = 1.031.



Synthesis of dichlorobis(dimethylglyoximate) cobalt (IV) cobaloxime [Co(dm_g)₂Cl₂]: 1.1g (4.62 mmol) of cobalt (II) chloride hexahydrate was added to an oven-dried 50 mL round bottom flask followed by 15 mL acetone. 1.07 g (9.24 mmol) of dimethylglyoxime was dissolved in an additional 15 mL acetone and added to the reaction flask. Sonication was required to fully dissolve the dimethylglyoxime in acetone prior to addition to the flask. The reaction was allowed to stir for 60 min at room temperature under the flow of air to allow oxidation to occur. A dark green precipitate was observed in the reaction flask after this time. The flask was cooled over

ice and the green solid was collected via vacuum filtration, washing 10 mL x 2 with ice-cold acetone. A green solid was obtained, 1.03 g, 2.85 mmol, 71%. $^1\text{H NMR}$ (600 MHz, $\text{d}^6\text{-DMSO}$) δ 2.33 (s, 12 H).



Synthesis of chloro(pyridine)bis(dimethylglyoximate) cobalt (III) cobaloxime [Co(dm g) $_2$ pyCl]: Synthesis of [Co(dm g) $_2$ pyCl] was carried out as per previously reported with some minor modifications.² 0.3 g of [Co(dm g) $_2$ Cl $_2$] previously synthesised, was suspended in 15 mL MeOH (poor solubility) in a 100 mL round-bottomed flask. 0.07 mL (0.833 mmol) pyridine was added in quick succession and the reaction was allowed to stir at room temperature for 30 min. A brown precipitate was observed in the reaction flask after this time. 20 mL deionised water was added to the flask, before cooling on ice for 20 min. The precipitate was collected via vacuum filtration, washing with 3 x 15 mL solution of 2:1, H $_2$ O: MeOH, followed by 2 x 10 mL of diethyl ether. A light brown solid results, 0.214 g, 0.530 mmol, 64%. $^1\text{H NMR}$ (400 MHz, CDCl $_3$) δ 8.24 ppm (d, 2H), 7.68 (m, 1H), 7.15 (d, 2H), 2.40 (s, 12H).

S2.2. NMR spectra

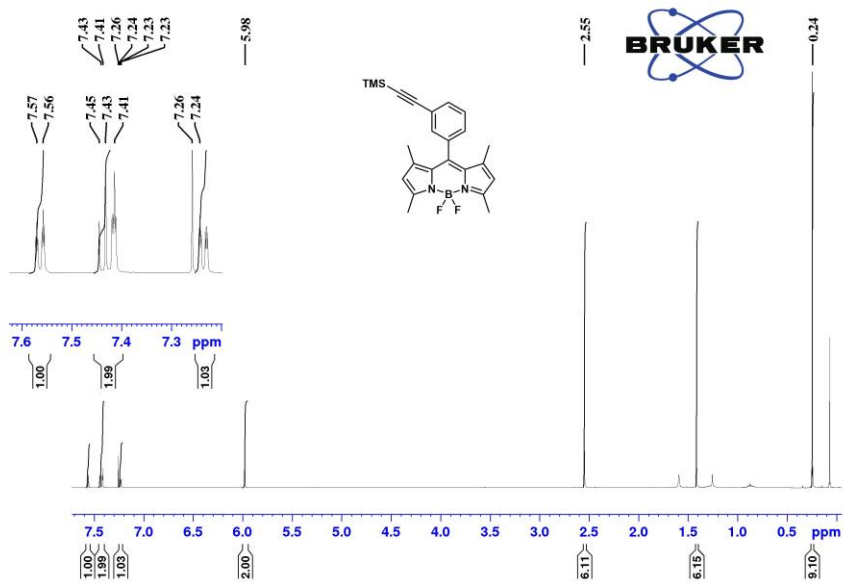


Figure S2.1. ¹H NMR spectra of monomer. CDCl₃ as calibration standard, $\delta = 7.26$ ppm.

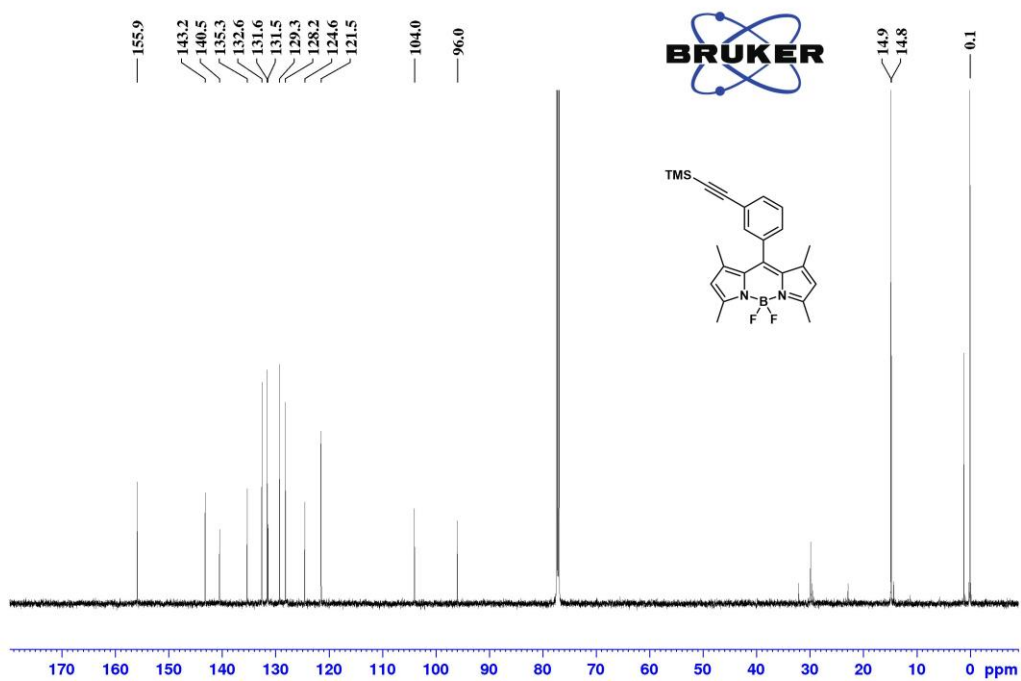


Figure S2.2. ¹³C NMR spectra of monomer. CDCl₃ as calibration standard, $\delta = 77.16$ ppm.

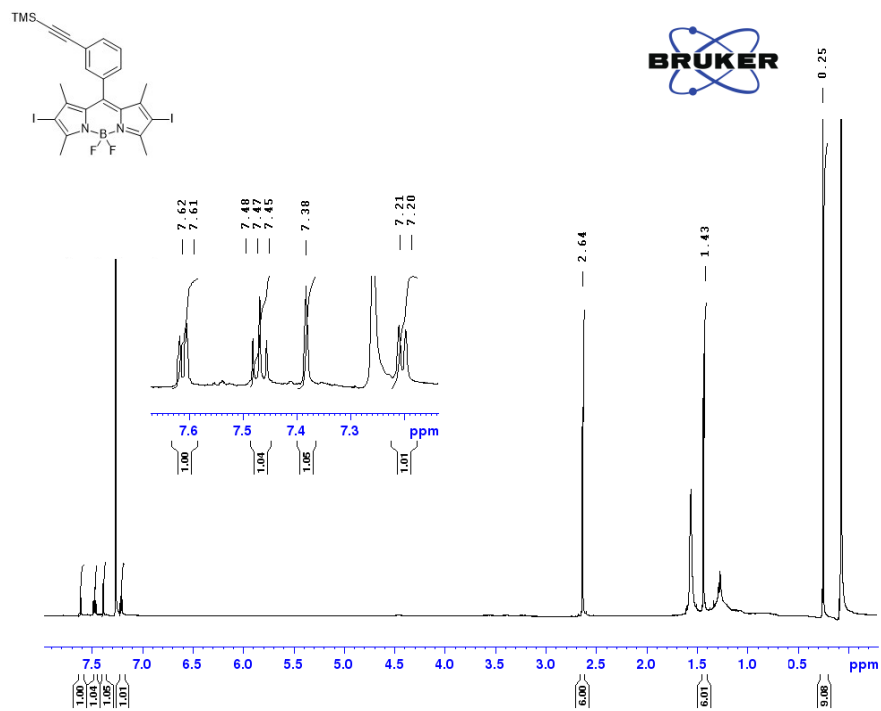


Figure S2.3. ¹H NMR spectra of diiodo monomer. CDCl₃ as calibration standard, $\delta = 7.26$ ppm.

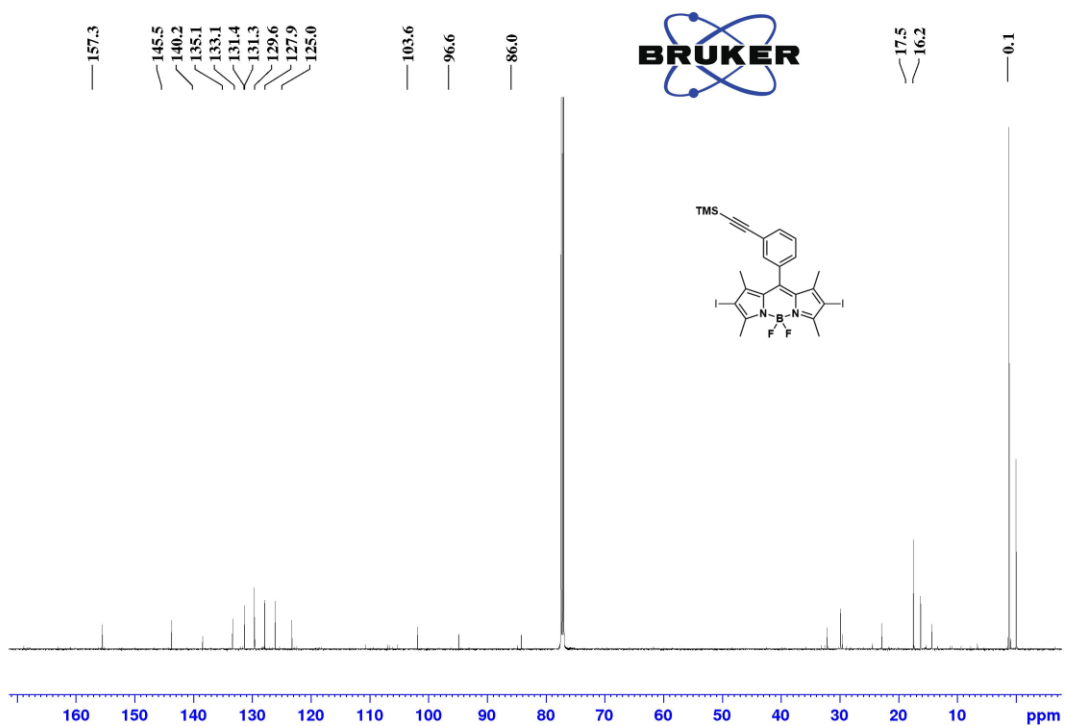


Figure S2.4. ¹³C NMR spectra of diiodo monomer. CDCl₃ as calibration standard, $\delta = 17.16$ ppm.

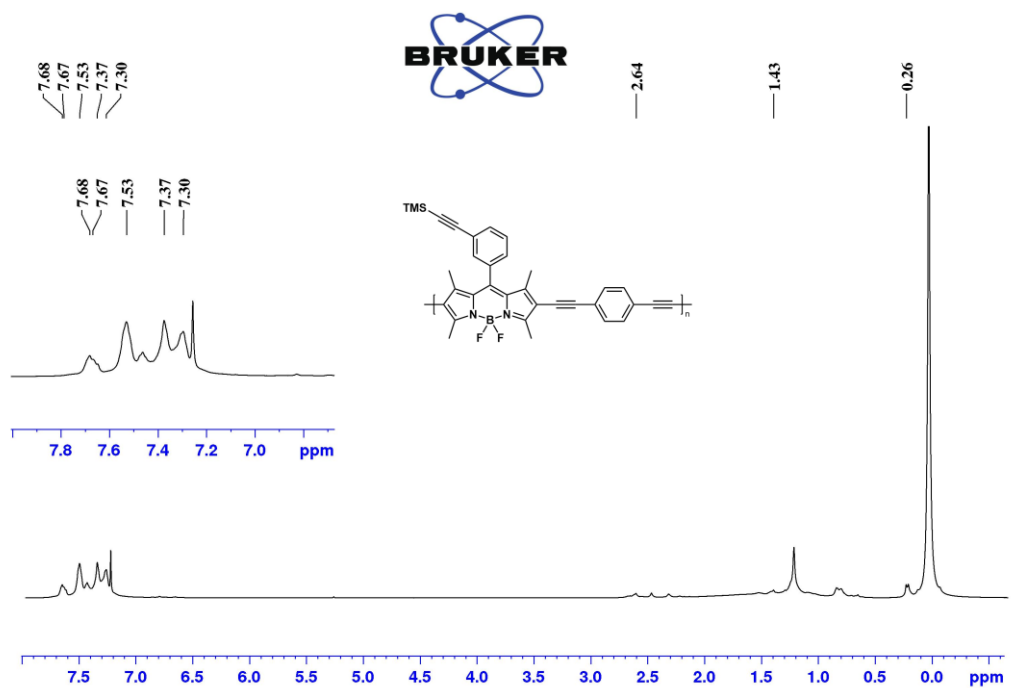


Figure S2.5. ^1H NMR spectra of polymer. CDCl_3 as calibration standard, $\delta = 7.26$ ppm.

S2.3. Mass Spectroscopy

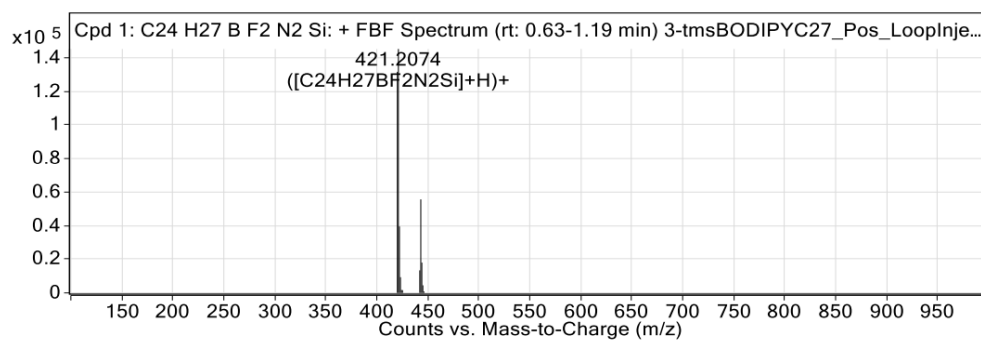


Figure S2.6. MS spectra $[M+H]$ for 3-TMS BODIPY monomer.

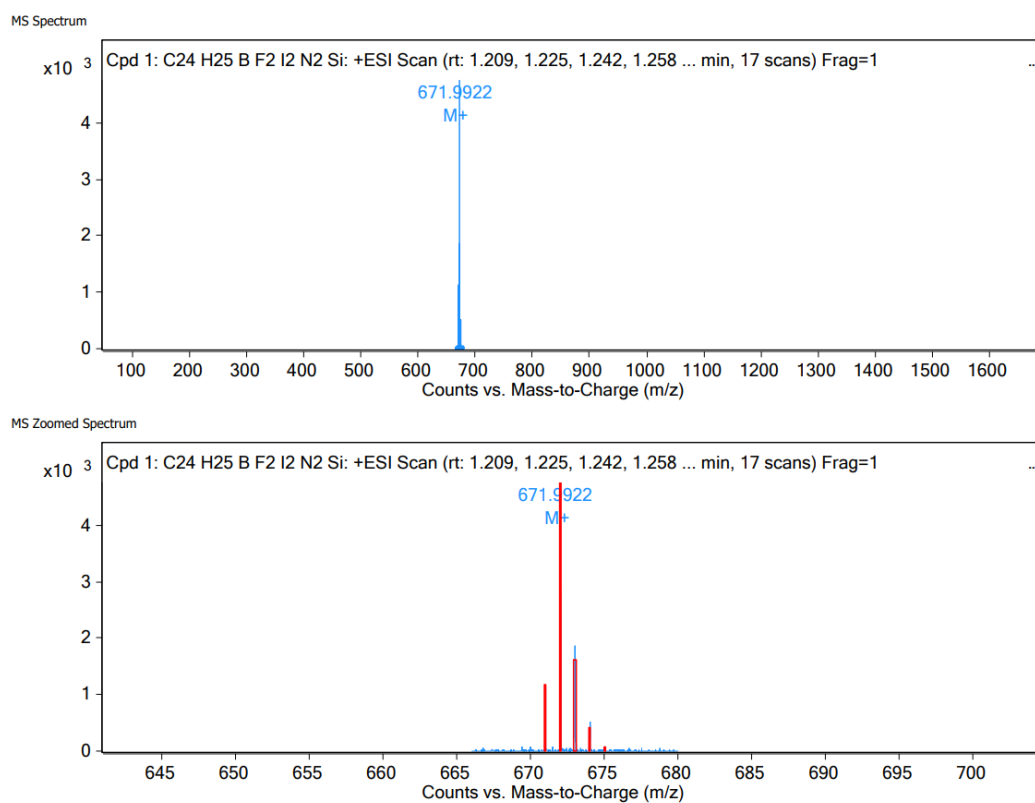
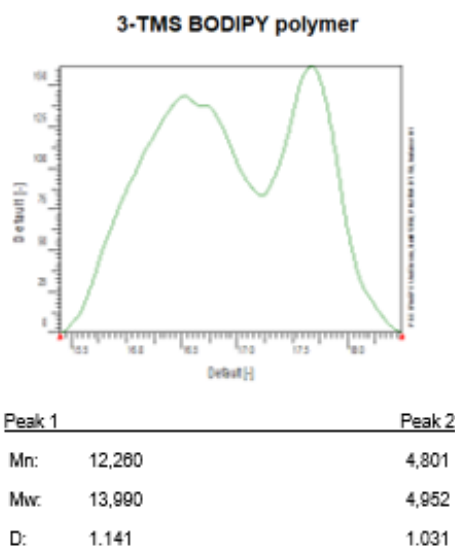


Figure S2.7. MS spectra for $[M^+]$ for 3-TMS diiodo BODIPY monomer.

S2.4. Size Exclusion Chromatography (SEC)



Whole peak (since it does not return to baseline it's considered a bimodal peak)

Mn: 7,590
Mw: 10,261
D: 1.351

Figure S2.8. SEC results obtained for polymer showing molecular weight distribution of the polymer.

S2.5. FTIR spectra

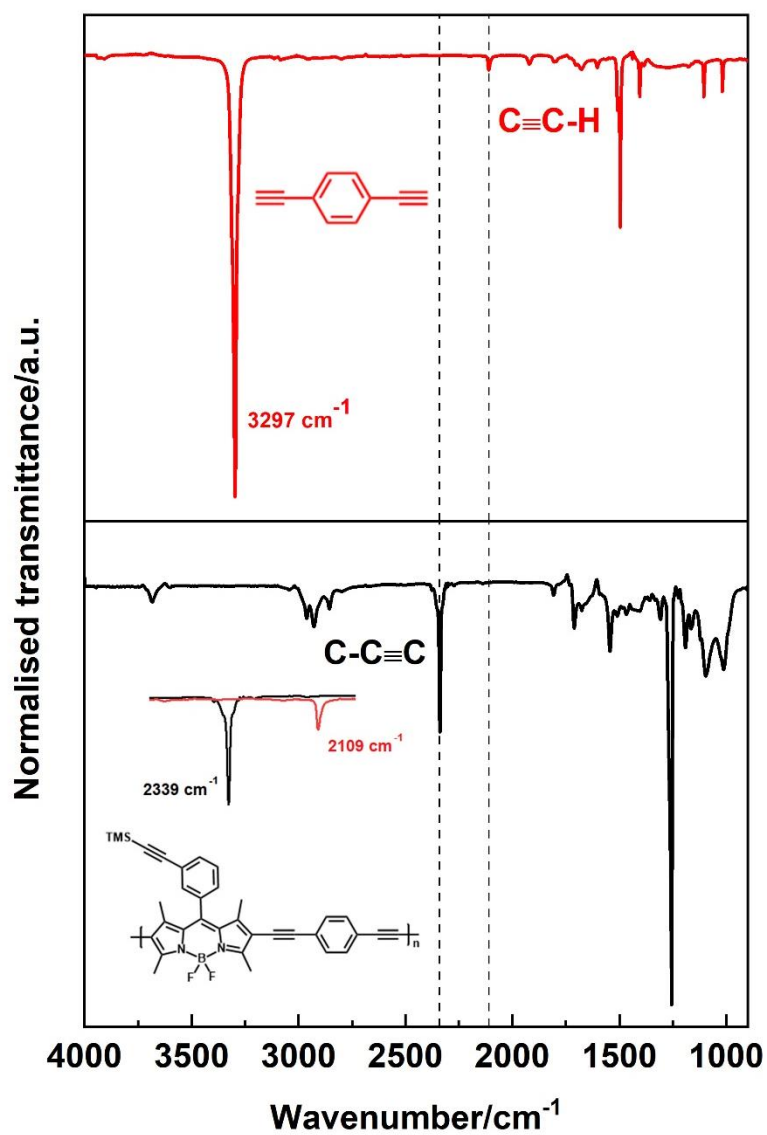


Figure S2.9. FTIR spectra of 1,4-diethynylbenzene (red spectra, top) and polymer (black spectra, bottom), recorded in a solution cell in spectrophotometric grade dichloromethane. Structures inserted below each IR spectra. Inset showing details between 2400 – 2000 cm⁻¹.

S2.6. Absorption Spectra

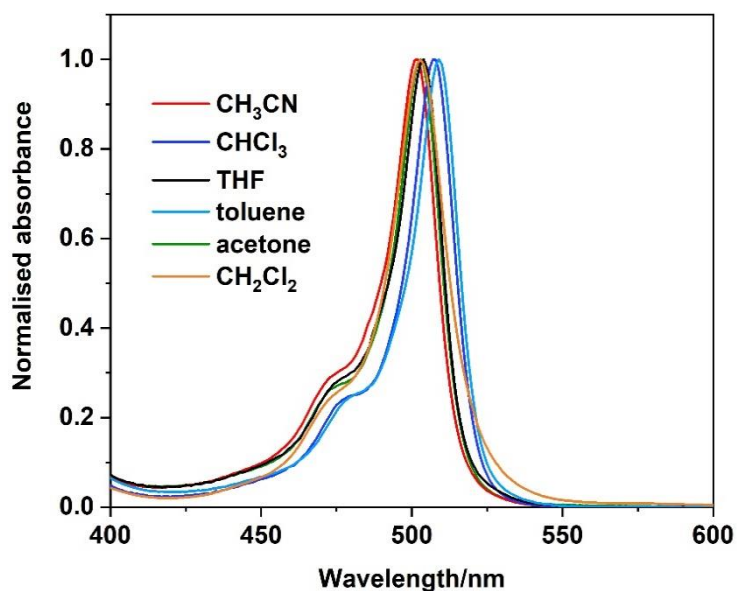


Figure S2.10. Normalised absorption spectra of monomer in acetonitrile (red), chloroform (dark blue), THF (black), toluene (light blue) and acetone (green), dichloromethane (orange). Recorded at room temperature.

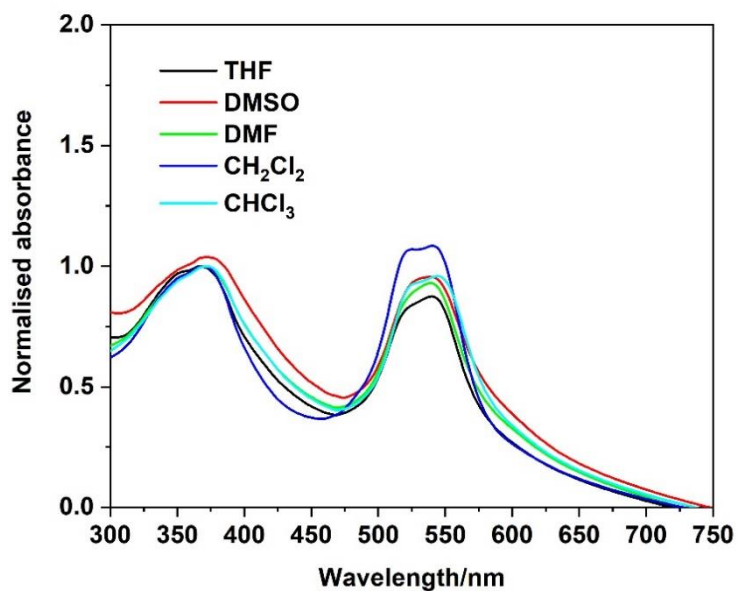


Figure S2.11. Normalised absorption spectra of polymer in THF (black), DMSO (red), DMF (green), dichloromethane (dark blue), chloroform (light blue). Recorded at room temperature.

S2.7. Excitation Spectra

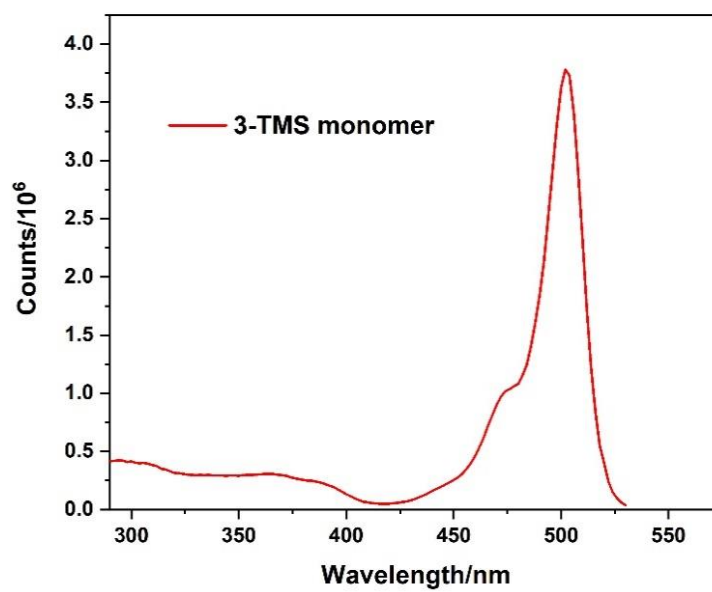


Figure S2.12. Excitation spectra of monomer in CH_2Cl_2 . Recorded at the emission maxima.

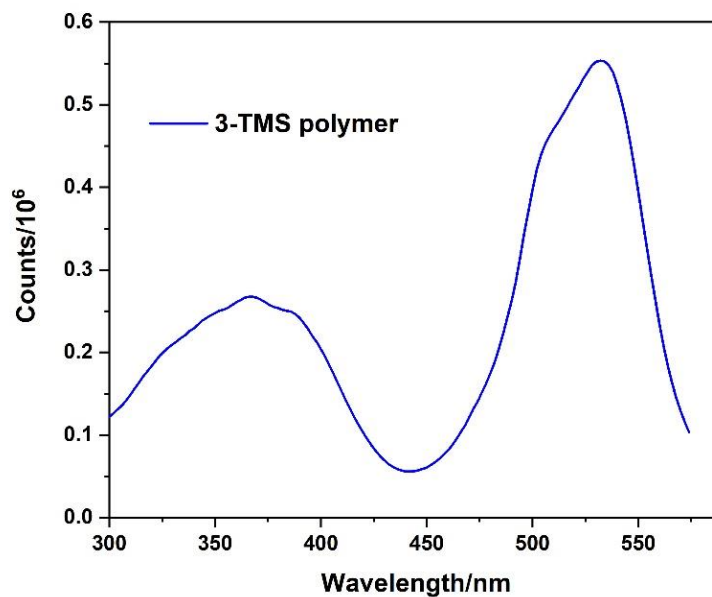


Figure S2.13. Excitation spectra of polymer in CH_2Cl_2 . Recorded at the emission maxima.

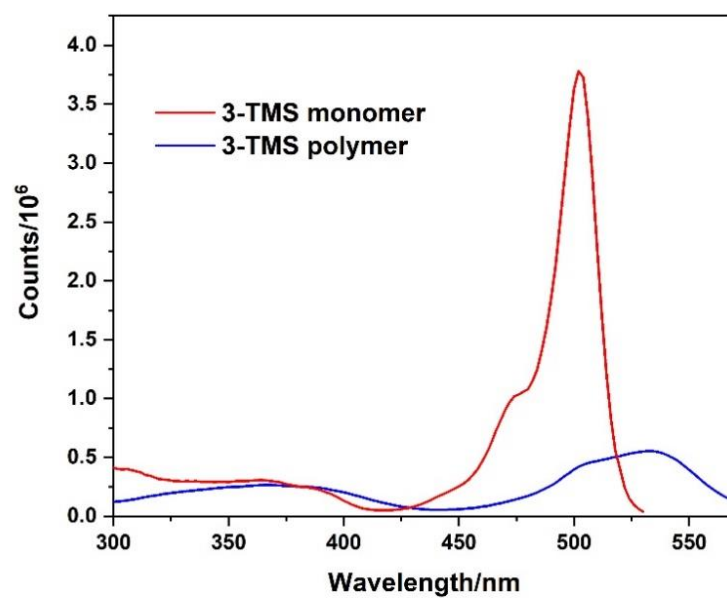


Figure S2.14. Excitation spectra of monomer (red) and polymer (blue) in CH₂Cl₂. Recorded at each emission maxima respectively.

S2.8. Emission Spectra

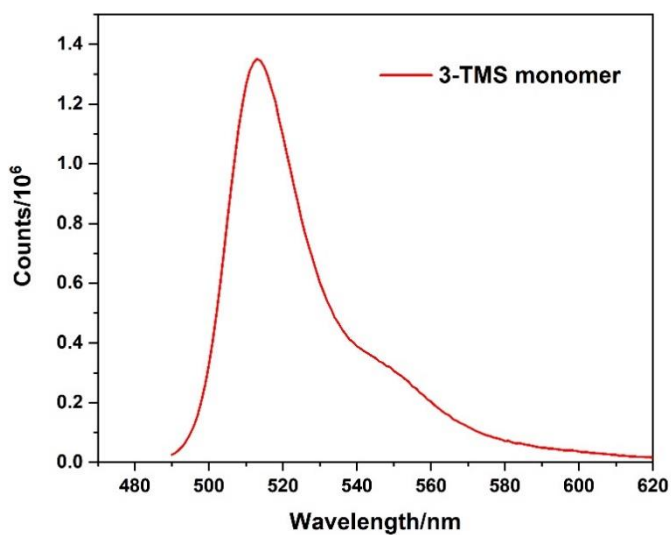


Figure S2.15. Emission spectra monomer in CH₂Cl₂. λ_{exc} corresponding to lowest energy absorption band.

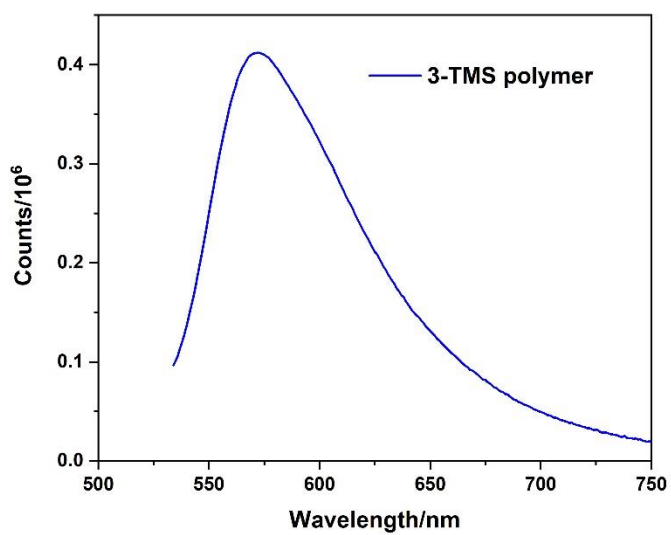


Figure S2.16. Emission spectra polymer in CH₂Cl₂. λ_{exc} corresponding to lowest energy absorption band.

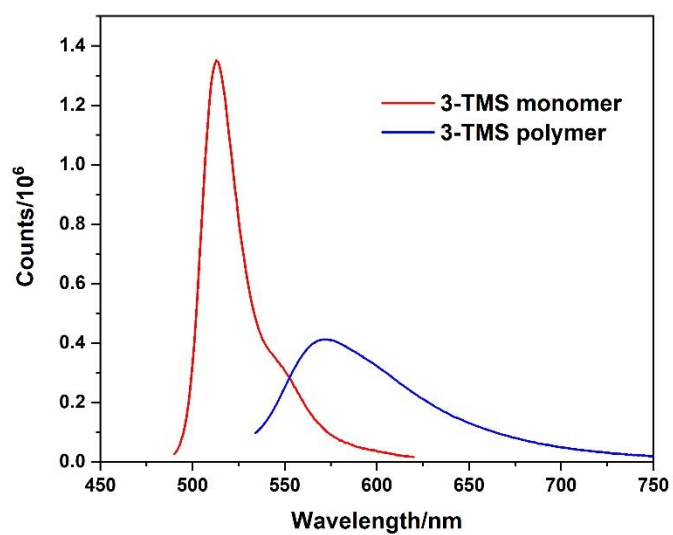


Figure S2.17. Emission spectra monomer (red) and 3-TMS polymer (blue) in CH_2Cl_2 . λ_{exc} corresponding to lowest energy absorption band.

S2.9. Emission map experiments

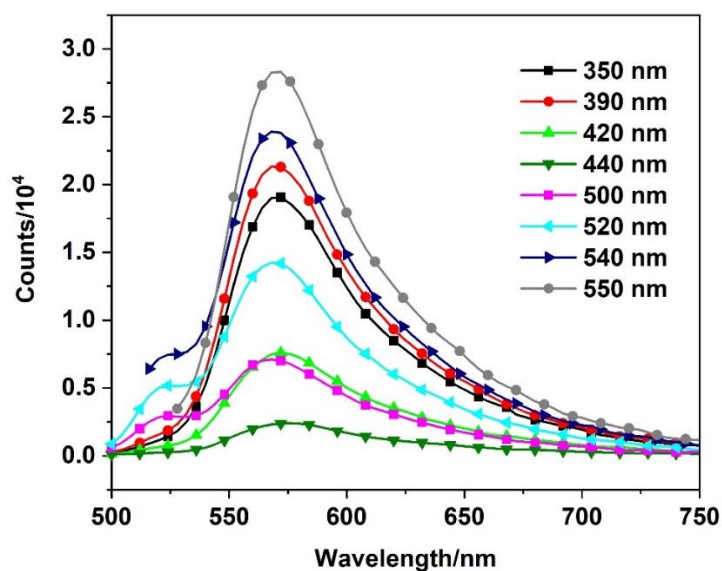


Figure S2.18. Emission map of polymer in dichloromethane, recorded at room temperature. Excitation wavelengths shown in inset: 350 nm (black squares), 390 nm (red circles), 420 nm (green triangles), 440 nm (olive triangles), 500 nm (magenta squares), 520 nm (cyan triangles), 540 nm (navy triangles), 550 nm (grey circles).

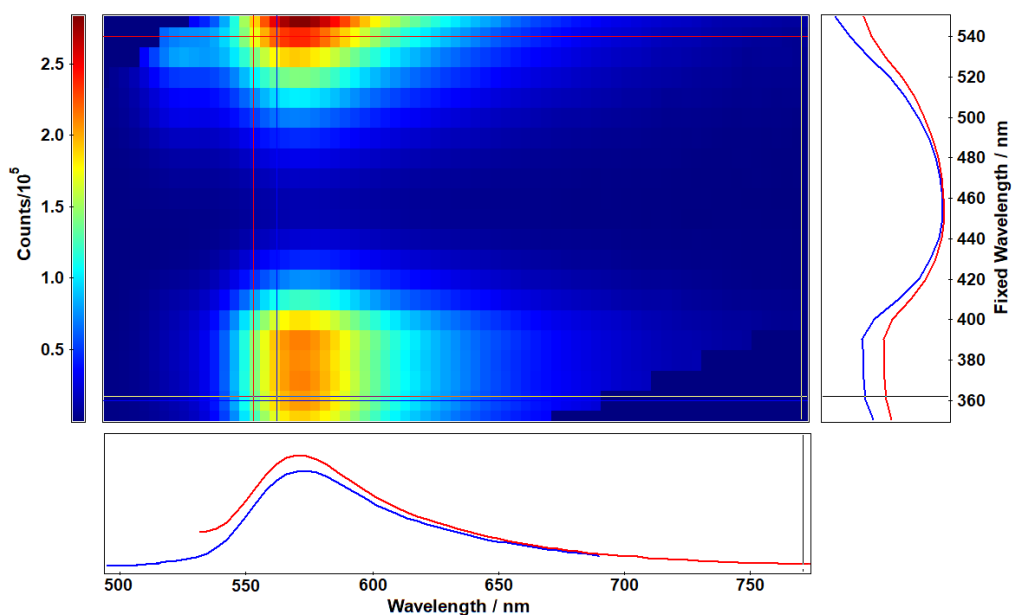


Figure S2.19. Excitation Emission contour map of polymer in dichloromethane, recorded at room temperature. Emission spectra shown at the bottom using $\lambda_{\text{exc}} = 360$ nm (blue) and $\lambda_{\text{exc}} = 540$ nm (red).

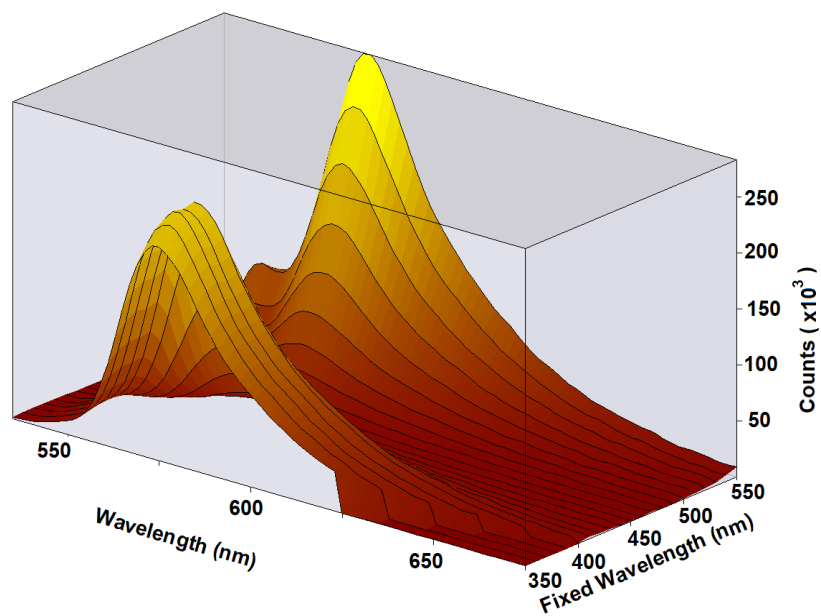


Figure S2.20. Emission map of polymer in dichloromethane, recorded at room temperature. Fixed wavelength axis shows varying excitation wavelengths used.

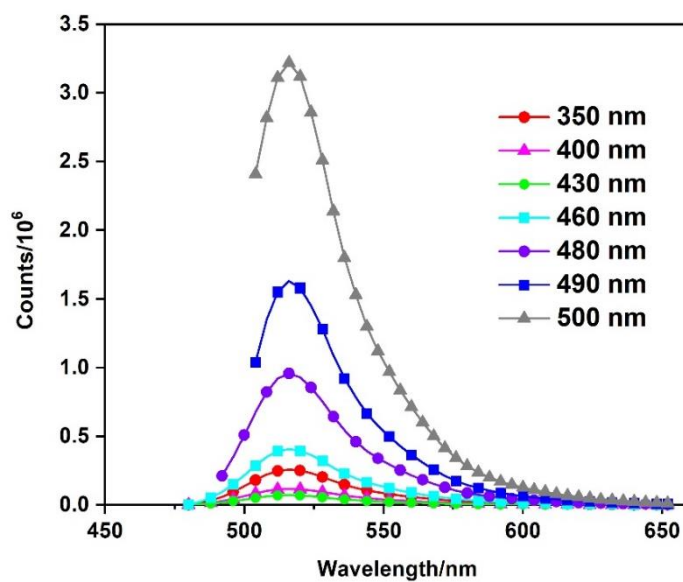


Figure S2.21. Emission map of monomer in dichloromethane, recorded at room temperature. Excitation wavelengths shown in inset: 350 nm (red circles), 400 nm (magenta triangles), 430 nm (green circles), 460 nm (cyan squares), 480 nm (violet circles), 490 nm (blue squares), 500 nm (grey triangles).

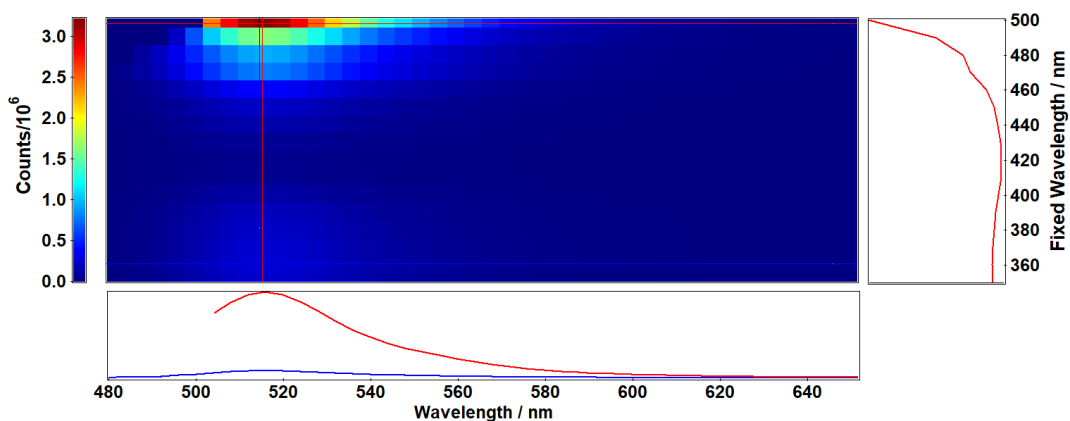


Figure S2.22. Excitation Emission contour map of monomer in dichloromethane, recorded at room temperature. Emission spectra shown at the bottom using $\lambda_{\text{exc}} = 360$ nm (blue) and $\lambda_{\text{exc}} = 500$ nm (red).

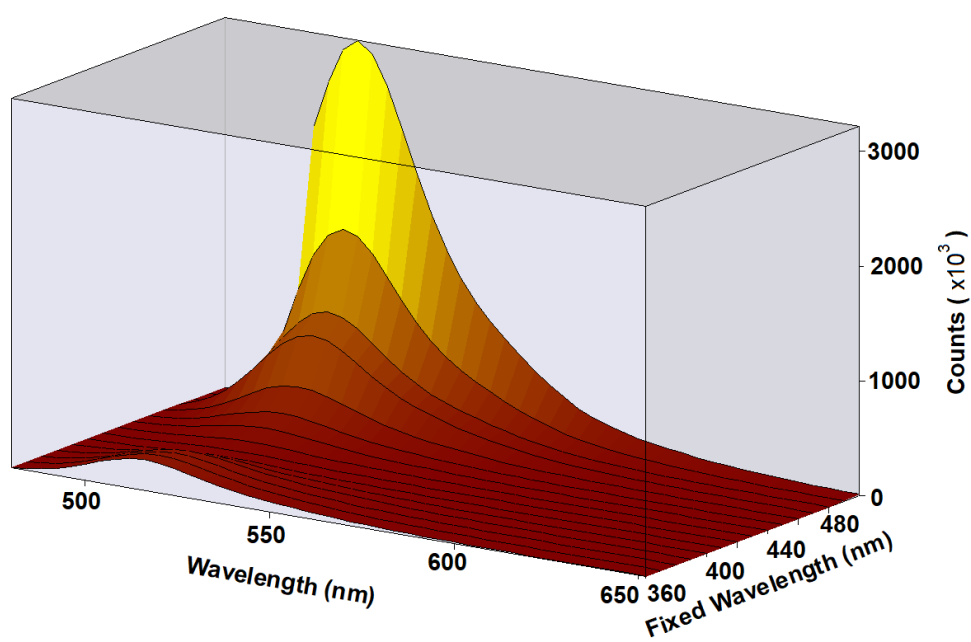


Figure S2.23. 3-D Emission map of monomer in dichloromethane, recorded at room temperature. Fixed wavelength axis shows varying excitation wavelengths used.

S2.10. Singlet oxygen measurements

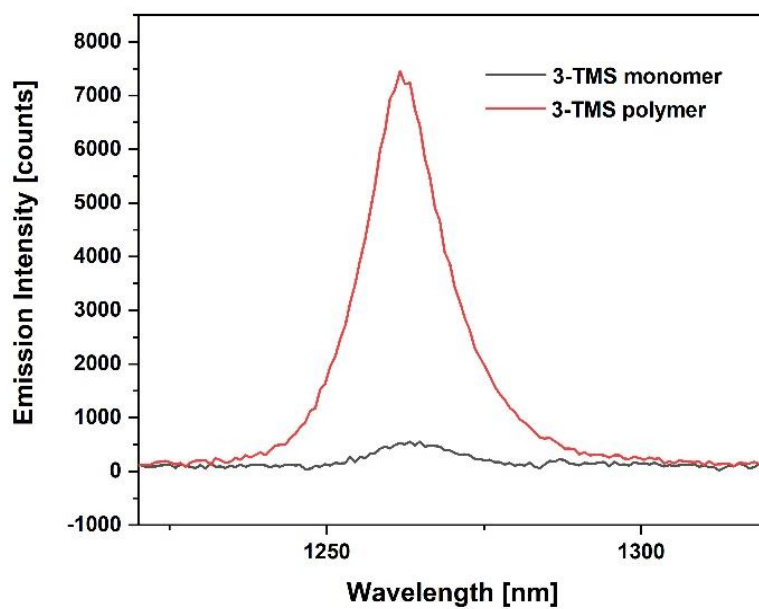


Figure S2.24. NIR Singlet oxygen emission spectra of monomer (grey spectra) and 3-TMS polymer (red spectra) in CHCl_3 using λ_{exc} 530 nm. Φ_{Δ} displayed in **Table S2.2**.

S2.11. Lifetime measurements

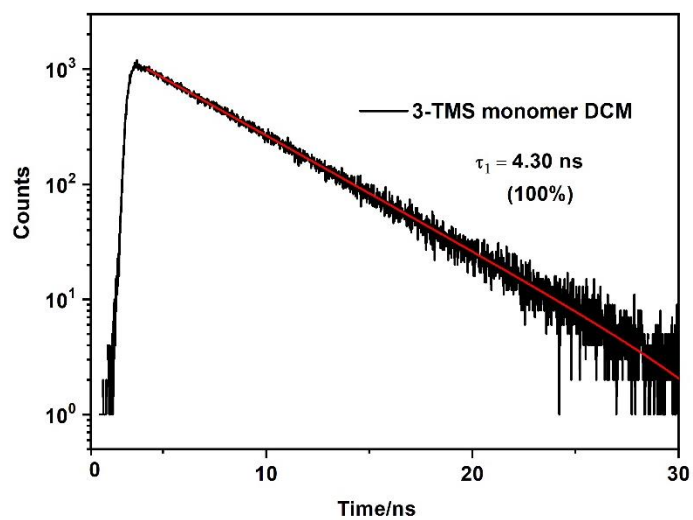


Figure S2.25. Emission decay of monomer in dichloromethane, $\lambda_{\text{exc}} = 510$ nm. Solution purged with N_2 for 20 minutes prior to sample measurement. Red line showing exponential fit.

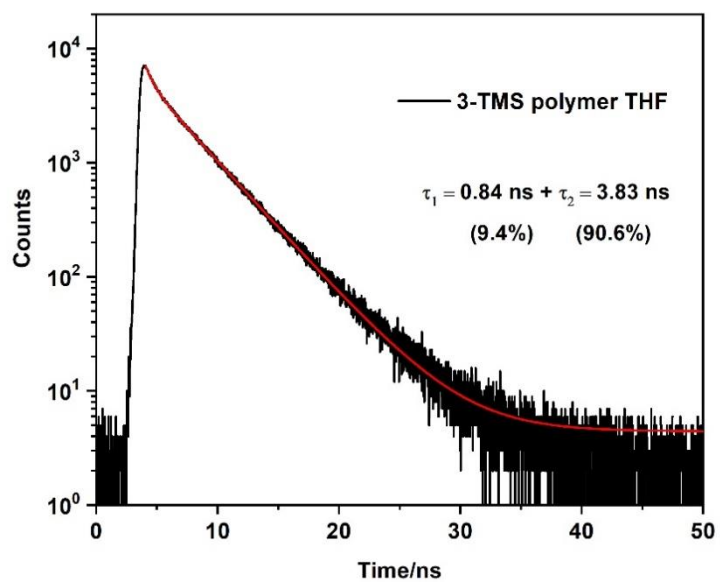


Figure S2.26. Emission decay of polymer in THF, $\lambda_{\text{exc}} = 510$ nm. Solution purged with N_2 for 20 minutes prior to sample measurement. Red line showing biexponential fit.

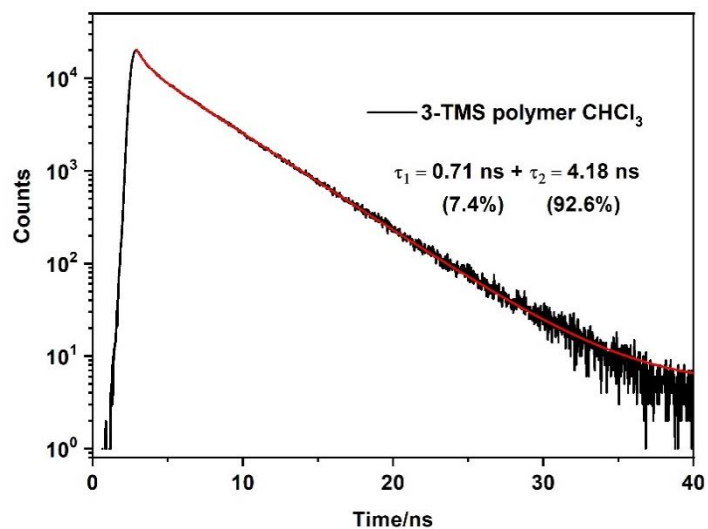


Figure S2.27. Emission decay of polymer in CHCl_3 , $\lambda_{\text{exc}} = 510 \text{ nm}$. Solution purged with N_2 for 20 minutes prior to sample measurement. Red line showing biexponential fit.

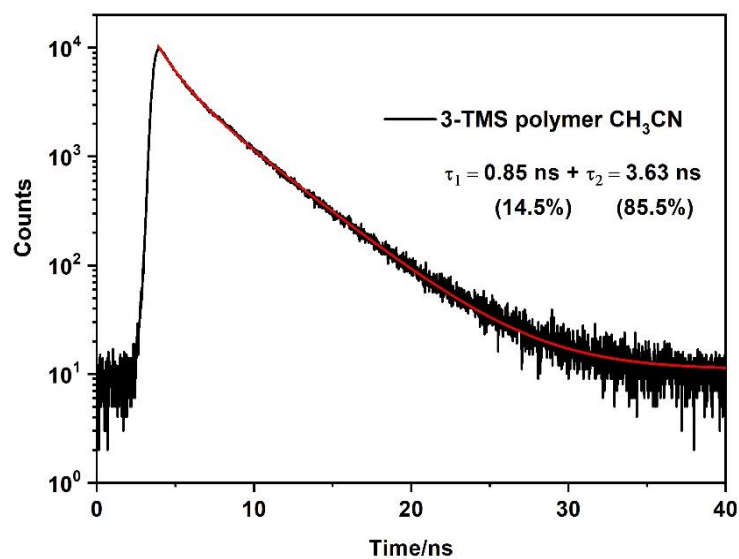


Figure S2.28. Emission decay of polymer in CH_3CN , $\lambda_{\text{exc}} = 510 \text{ nm}$. Solution purged with N_2 for 20 minutes prior to sample measurement. Red line showing biexponential fit.

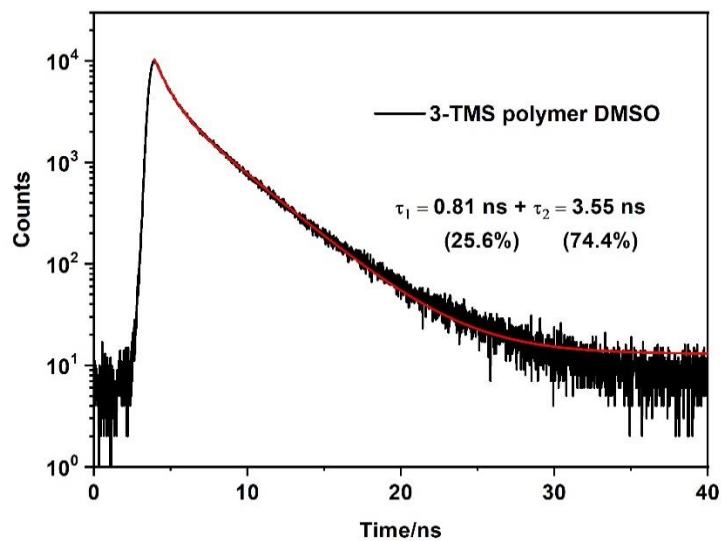


Figure S2.29. Emission decay of polymer in DMSO, $\lambda_{\text{exc}} = 510 \text{ nm}$. Solution purged with N_2 for 20 minutes prior to sample measurement. Red line showing biexponential fit.

S2.12. Optical gap determination

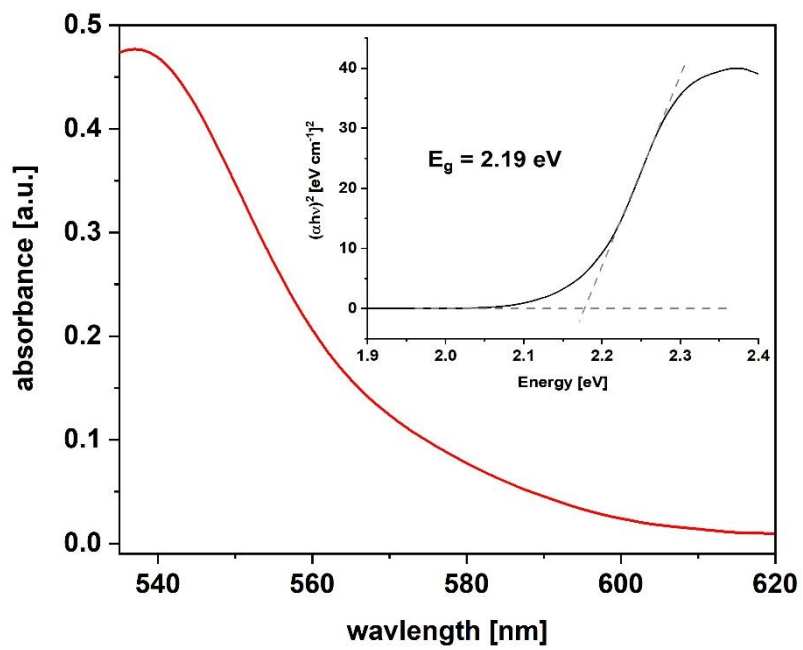


Figure S2.30. UV- visible absorption spectra of polymer in CH_2Cl_2 . Inset showing Tauc Plot used to calculate the optical gap from the onset of absorption.^{3,4}

S2.13. Steady state UV-visible absorption and emission spectra

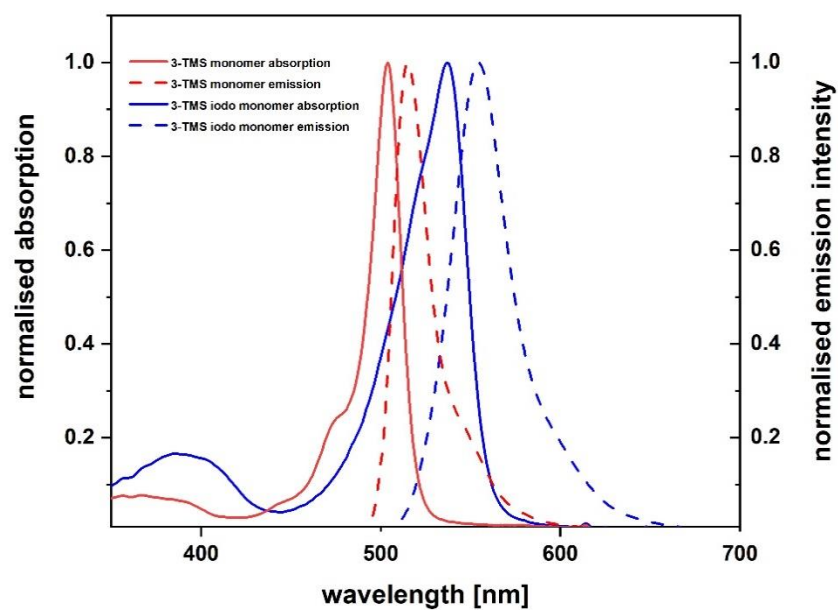


Figure S2.31. Normalised UV-visible absorption and emission spectra for monomer absorption (solid red), emission (dashed red), diiodo monomer absorption (solid blue) and emission (dashed blue). Recorded in CHCl_3 .

Table S2.1. Summary of photophysical properties monomer and diiodo monomer in CHCl_3 .

Compound	λ_{abs} (nm)	λ_{em} (nm)
monomer	503	516
diiodo monomer	539	573

S2.14. Transient absorption spectra (ps-timescale)

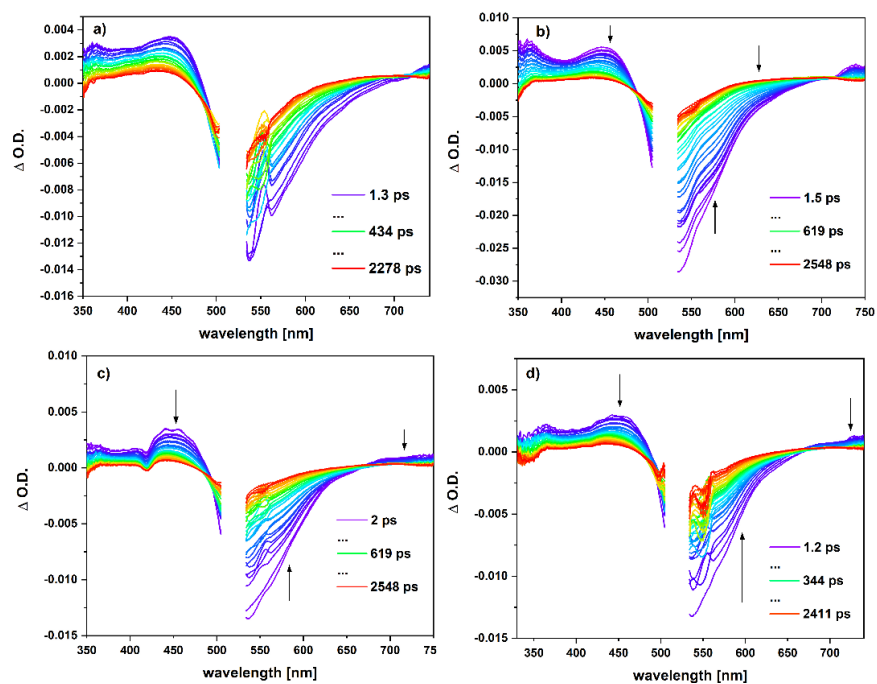


Figure S2.32. Transient absorption spectra of polymer in a) CD_3CN , b) DMSO, c) chloroform and d) dichloromethane. Time delays indicated in inset. $\lambda_{\text{exc}} = 525 \text{ nm}$.

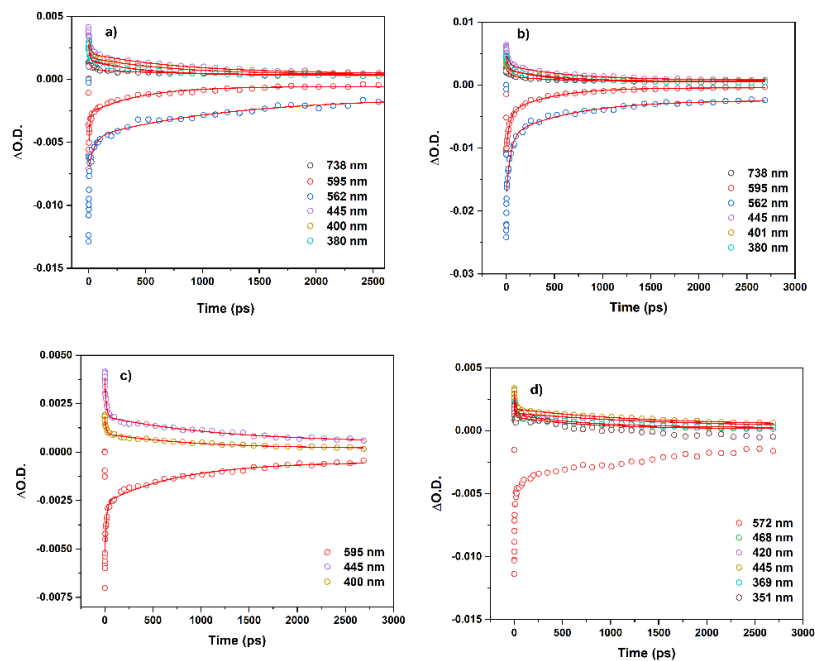


Figure S2.33. Exponential fitting (red curve) of polymer TA spectra at stated wavelengths in a) CD_3CN , b) DMSO, c) chloroform and d) dichloromethane. Red line indicates exponential decay.

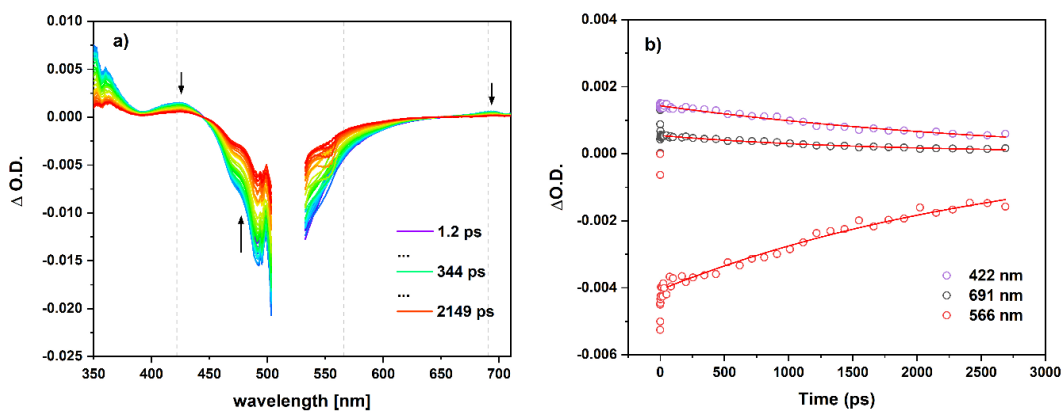


Figure S2.34. Transient absorption spectra of a) monomer in CD_3CN at random time delays. Notch in graph where excitation wavelength occurred, grey dashed lines indicate the kinetic traces analysis and b) kinetic traces at stated wavelength, red lines indicate the exponential fit used, $\lambda_{\text{exc}} = 525 \text{ nm}$.

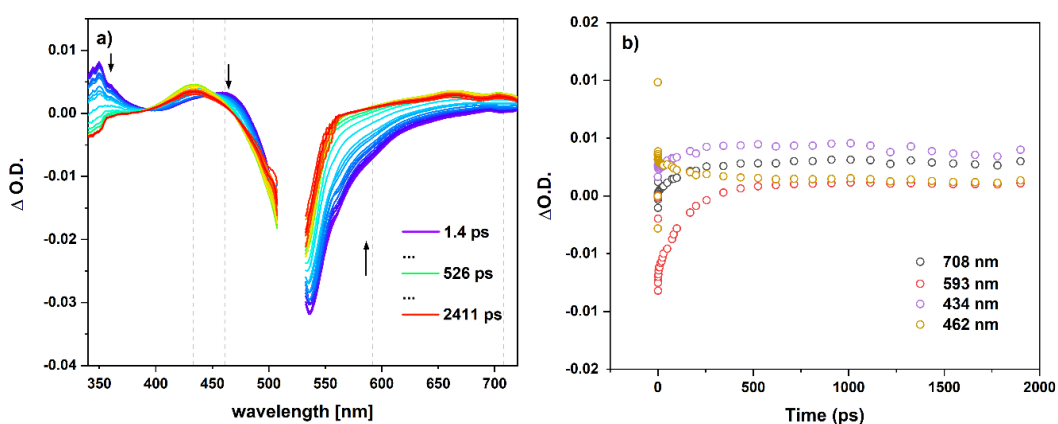


Figure S2.35. Transient absorption spectra of a) diiodo monomer in CD_3CN at random time delays. Notch in graph where excitation wavelength occurred, grey dashed lines indicate the kinetic traces analysis and b) kinetic traces at stated wavelength, $\lambda_{\text{exc}} = 525 \text{ nm}$.

S2.15. Transient absorption spectra (ns-timescale)

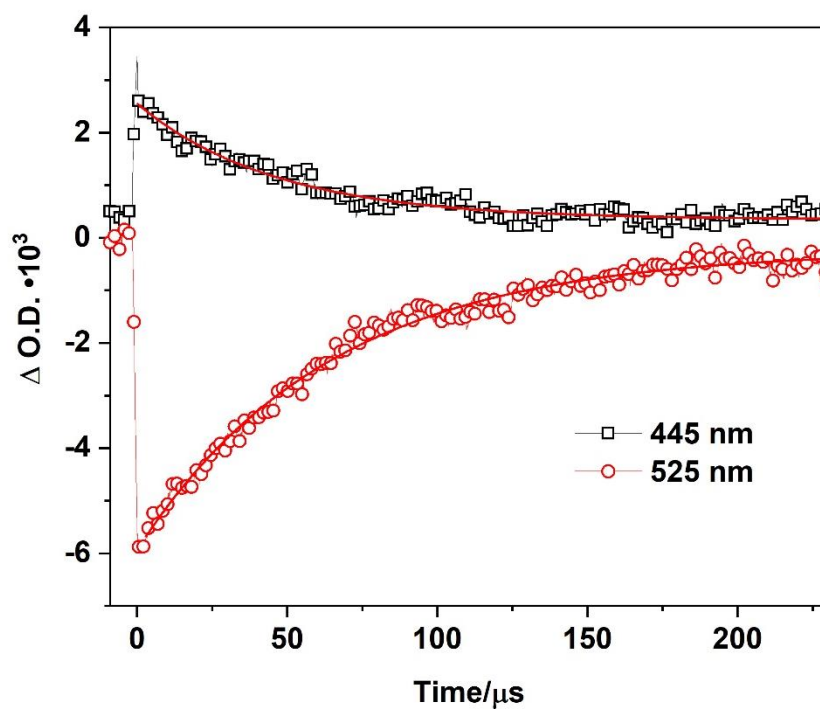


Figure S2.36. Transient absorption decays at stated wavelengths for 3-TMS polymer in CH_3CN at stated wavelengths: 445 nm (black squares) and 525 nm (red circles). $\lambda_{\text{exc}} = 355$ nm. Red lines indicate exponential fit.

For monoexponential fitting the formula used is shown in equation (1).

$$y = y_0 + A_1 e^{-x/\tau_1} \quad (1)$$

S2.16. Time resolved Infrared Spectroscopy (ps-timescale)

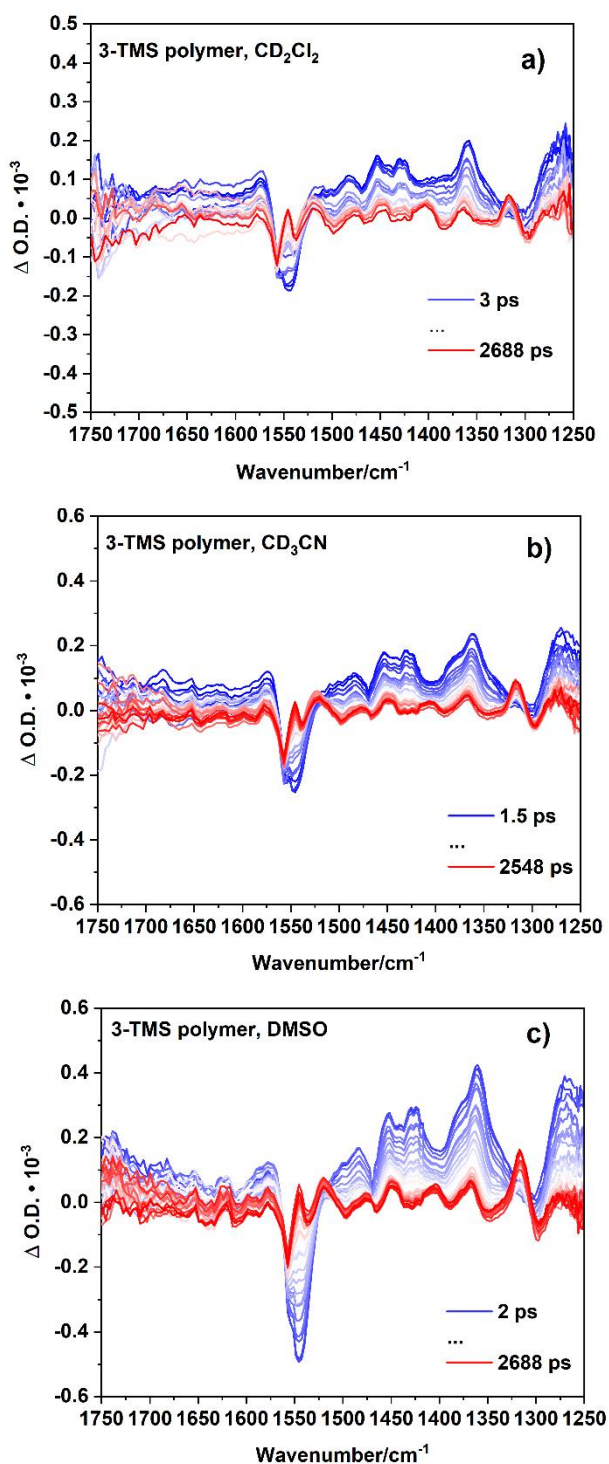


Figure S2.37. TRIR spectra of 3-TMS polymer in a) CD_2Cl_2 (top), b) CD_3CN (centre) and c) DMSO (bottom) in the IR spectral window of 1750 cm^{-1} - 1250 cm^{-1} . Blue spectra indicating initial time delays (ps), red spectra indicating final time delays (ps), $\lambda_{\text{exc}} = 525 \text{ nm}$.

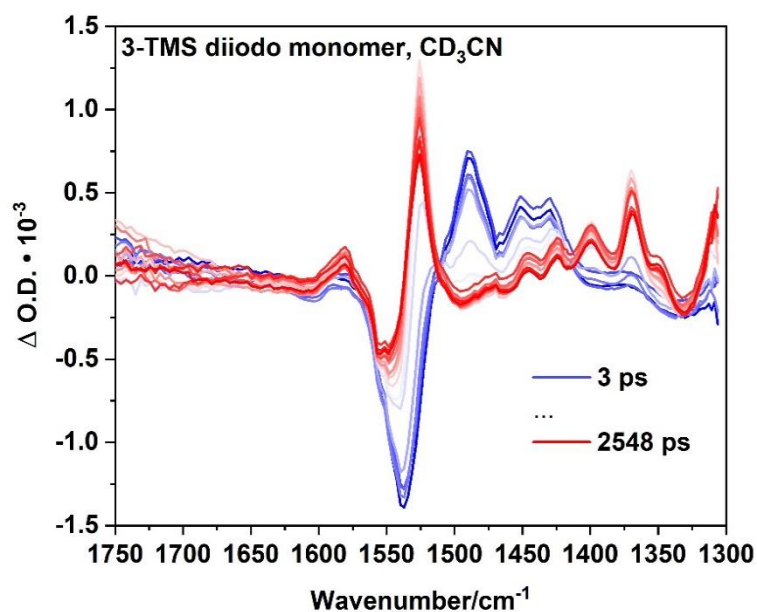


Figure S2.38. TRIR of 3-TMS diiodo monomer in CD_3CN showing the spectral window of 1750 cm^{-1} – 1300 cm^{-1} in the IR region. Blue spectra indicating initial time delays (ps), red spectra indicating final time delays (ps), $\lambda_{\text{exc}} = 525\text{ nm}$.

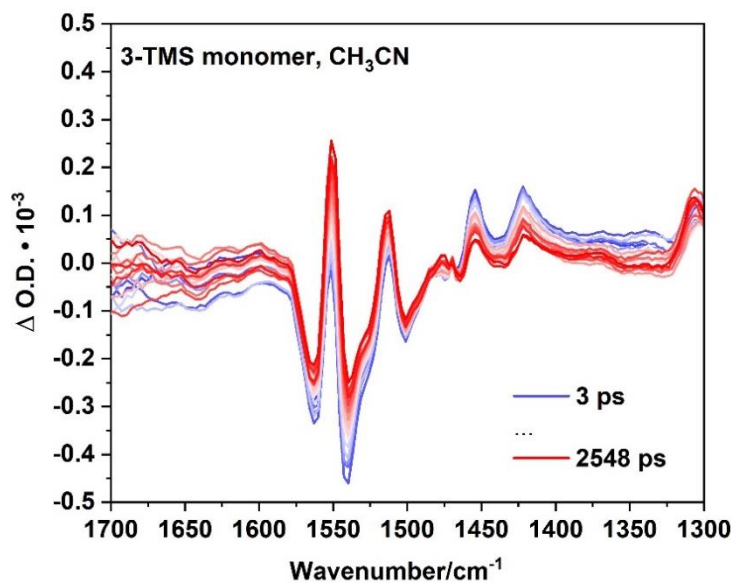


Figure S2.39. TRIR spectra of 3-TMS monomer in CH_3CN showing the spectral window of 1750 cm^{-1} – 1300 cm^{-1} approximately in the IR region. Blue spectra indicating initial time delays (ps), red spectra indicating final time delays (ps), $\lambda_{\text{exc}} = 525\text{ nm}$.

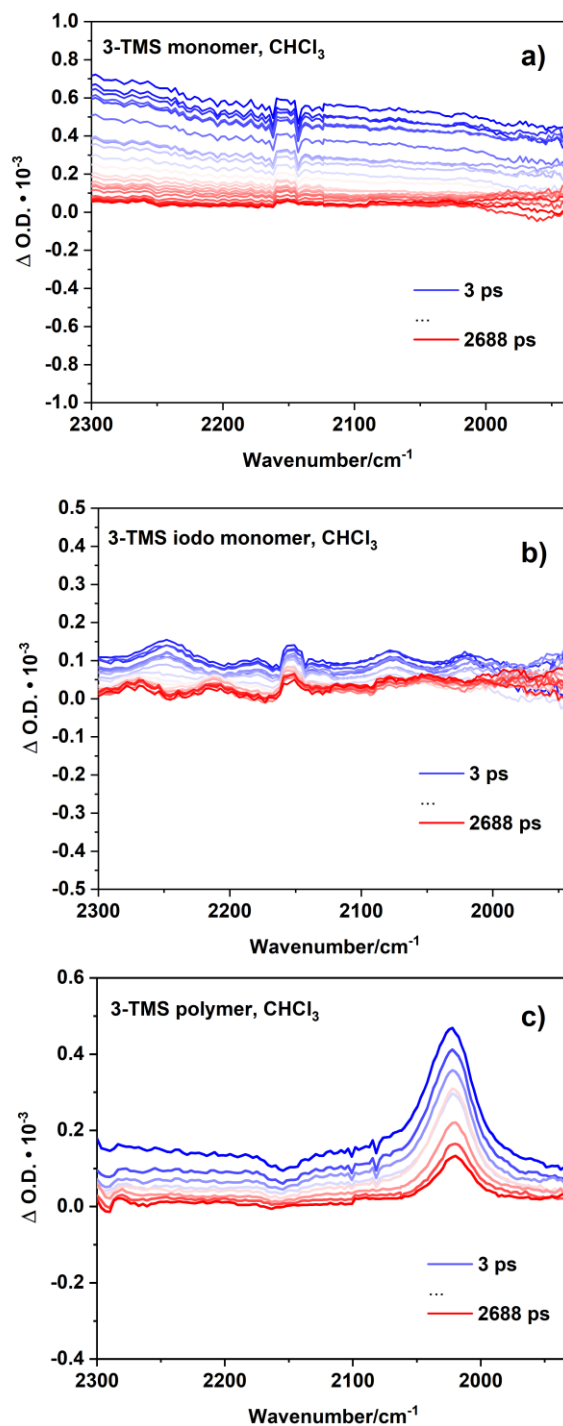


Figure S2.40. TRIR spectra of a) 3-TMS monomer, b) 3-TMS diiodo monomer and c) 3-TMS polymer in CHCl₃, showing the spectral window of 2300 cm⁻¹ – 1930 cm⁻¹ in the IR region. Blue spectra indicating initial time delays (ps), red spectra indicating final time delays (ps), $\lambda_{\text{exc}} = 525$ nm.

S2.17. Summary of photophysical properties

Table S2.2. Summary of photophysical properties of 3-TMS monomer and 3-TMS polymer.

Compound	λ_{abs} (nm) ^a (ϵ , $10^3 \text{ M}^{-1} \text{ cm}^{-1}$) ^b	λ_{em} (nm) ^a	$\Delta\nu$ (cm^{-1})	FWHM_{abs} ^c (cm^{-1})	FWHM_{em} ^c (cm^{-1})	Φ_{fl} ^d	τ_{s} (ns) ^e	χ^2 ^f	τ_{T} (μs) ^g	Φ_{Δ} ^h	Optical gap (eV) ⁱ
monomer	503 (63)	516	501	768	857	0.92	4.3	1.1	-	0.05	2.41
polymer	539 (17)	573	1101	2209	2363	0.09	1.1, 3.9	1.2	61	0.77	2.19

^ameasured in CH_2Cl_2 .

^b approx. molar absorptivity of the polymer calculated using the molecular weight of the monomeric repeating unit.

^cFull Width at Half Maximum of stated absorption or emission band.

^dfluorescence quantum yield calculated using 3-pyridine H-BODIPY as a reference standard, where $\Phi_{\text{fl}} = 62\%$ in CH_2Cl_2 .¹

^emeasured using TCSPC.

^fthe chi-squared value for determining the accuracy of the decay fit.

^gdetermined from the decay kinetics obtained from ns-transient absorption spectroscopy in a sample that was degassed using freeze-pump thaw method.

^hsinglet oxygen quantum yield calculated using ZnTPP as a reference standard, where $\Phi_{\Delta} = 0.72$ in CHCl_3 .⁵

ⁱthe optical gap determined from the absorption edge.

S2.18. Photocatalytic hydrogen evolution experiments in solution

Hydrogen experiments were carried out as per previously reported by the group.⁶⁻⁸ In brief, all photocatalytic experiments to assess the activity of the polymer for hydrogen evolution were carried out in 23 mL Schlenk tubes, with 8 mL volume of photocatalytic solution. All Schlenk tubes were equipped with an air-tight septum to allow samples of headspace to be measured at different timepoints throughout the experiment. Degassing of photocatalytic solution was carried out using three freeze-pump-thaw cycles to ensure oxygen was not present during photocatalysis. The Schlenk tube was blocked to external light prior to irradiation to ensure only the Xe arc lamp incident on the photocatalytic tube was the cause of the photocatalytic activity. For hydrogen experiments employing 0.1 M ascorbic acid, the appropriate amount of 0.2 M NaOH solution was titrated into the solution to obtain the desired pH prior to addition to the reaction Schlenk tube containing the polymer and the catalyst components of the desired concentration. The Schlenk tube was placed in a black box equipped with a fan to avoid thermal processes driving the catalytic cycle. All samples were irradiated with 300 W Xe arc lamp equipped with cut-off filter, $\lambda > 420$ nm. Control samples were left in the dark and measured at the same timepoints as described, no hydrogen was observed. Hydrogen production was monitored by gas chromatography (Shimadzu GC-2010) with a BID detector on a 5 Å molecular sieve column using He as a carrier gas, with oven temperature at 30 °C. Hydrogen obtained was measured against a calibration curve of standard injections, using commercially available standards of 0.01%, 0.1%, 1%, 2% and 5% respectively. **Figure S2.41** depicts the hydrogen evolution results obtained using the polymer as a photosensitiser in this study with specific conditions summarized in **Table S2.3**.

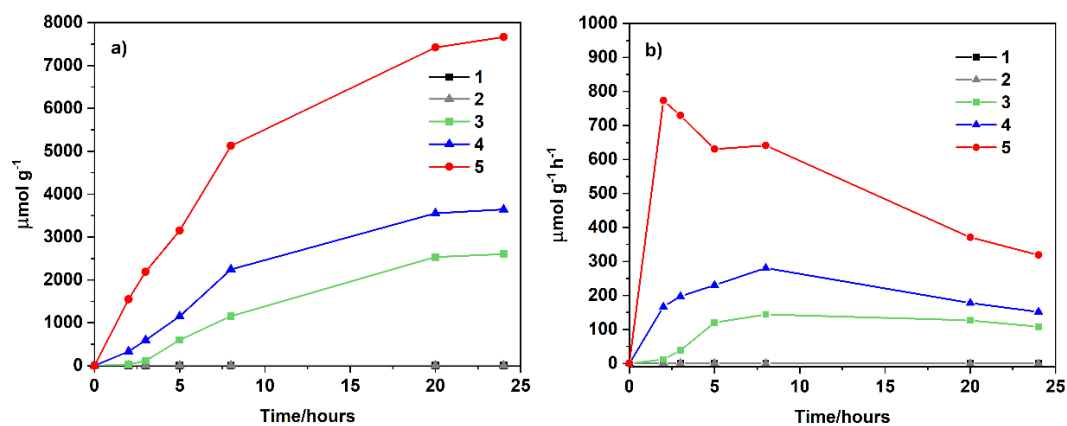


Figure S2.41. a) Hydrogen evolution of the polymer over 24 hours and b) corresponding turnover frequencies. Conditions summarised in **Table S2.3** for 1-5.

Table S2.3. Summary of experimental parameters using polymer as PS and cobalt cobaloxime as catalyst, irradiation Xe arc lamp, $\lambda > 420 \text{ nm}$. SA – sacrificial agent, TEA – triethylamine, AA – ascorbic acid. A parameter altered in every subsequent experiment is shown in red.

Entry	mass polymer (mg)	concentration catalyst (mM)	solvent system ^a	SA (concentration)	pH	$\mu\text{mol g}^{-1}$	$\mu\text{mol h}^{-1} \text{g}^{-1}$
1	0.5	1.8	ACN: H ₂ O, 9: 1 (v/v)	TEA (2.2 M)	8.5	2	0.1
2	0.5	2.5	ACN: H ₂ O	AA (0.1 M)	2 ^b	3	0.2
3	0.5	2.5	ACN: H ₂ O	AA (0.1 M)	5 ^b	2602	108
4	0.5	2.5	THF: H ₂ O	AA (0.1 M)	5 ^b	3645	152
5	2	2.5	THF: H ₂ O	AA (0.1 M)	5 ^b	7664	319

^aall solvent systems were prepared in a 1:1 (v/v) solvent ratio unless otherwise stated.

^brefers to the pH of the ascorbic acid solution prior to addition to the photocatalytic Schlenk tube containing the polymer and catalyst dissolved in the stated organic solvent.

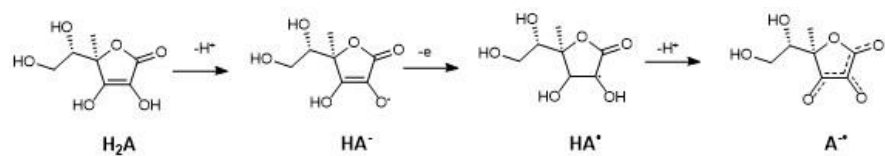


Figure S2.42. Ascorbic acid showing multiple deprotonation steps and monooxidation step in different pH environments.⁹

S2.19. Photoelectrochemical hydrogen evolution using NiO photocathodes

Preparation of NiO Films. Mesoporous NiO films were prepared according to a previously reported procedure.¹⁰ Precursor solution comprised anhydrous NiCl₂ and tri-block co-polymer F108 (poly (ethylene glycol)-block-poly (propylene glycol)-block-poly (ethylene glycol)). 1 g of each was dissolved in ethanol (6 mL) and ultrapure Milli-Q water (5 mL). The resulting solution was left to age in a vial for 1-2 weeks and centrifuged to remove any large, aggregated polymer before doctor blading onto cleaned conductive glass, fluorine doped tin oxide (FTO)-coated TECTM 15 (Pilkington), cut into 2x2 cm squares. The area of the NiO was 0.79 cm⁻¹, masked off by Scotch Magic Tape.

Three layers of NiO were deposited for each film, annealing each layer in a furnace at 450 °C for 30 mins in the presence of O₂. BODIPY 3-TMS polymer sensitizer was adsorbed onto the NiO surface by chemical bath deposition where dye was dissolved in dry acetonitrile (0.3 mM) and films submerged in a sealed container for at least 16 hours (overnight). Film thickness was 1.5 μm on average, determined by surface profilometry (Bruker Dektak³XT Surface Profile Measuring System). Pt counter electrodes were prepared by dissolving chloroplatinic acid on 2x2 TEC 8 (Pilkington) FTO glass films and annealing in the presence of oxygen at 150 °C for 15 mins.

Preparation of co-catalyst. (4',4'-dicarboxy-2',2'-bipyridine)dichloroplatinum (II) was prepared by modification of a previously reported procedure.¹¹ 4,4'-dicarboxy-2,2'-bipyridine with K₂PtCl₄ (Sigma) were refluxed in water for one hour at 80 °C to give the Pt-bipyridine complex (named Pt-bipy for convenience). The filtered product was washed and recrystallized in acetonitrile. The compound was sparingly soluble in alcohols. Characterization was by high-resolution mass spectrometry.

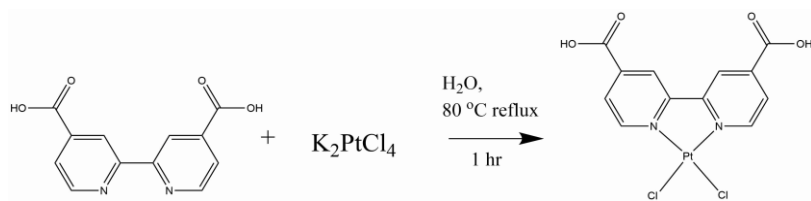


Figure S2.43. Reaction scheme for synthesis of (4',4'-dicarboxy-2',2'-bipyridine)dichloroplatinum(II).

Electrochemistry. Electrochemical measurements were conducted in a three-electrode cell where the NiO films with the adsorbed sensitizer and catalyst were the working electrode, a Pt-coated FTO glass film the counter electrode, and the reference electrode Ag/AgCl (3.0 M NaCl, E_o Ag/AgCl = 0.210 V vs. NHE). Potential was applied with an IviumStat EmStat 3 Blue potentiostat.

Before each photoelectrocatalysis experiment, the reaction cell was degassed for at least 15 minutes with either nitrogen or argon. Aqueous electrolytes were freshly prepared and pH adjusted with concentrated HCl, and measured with a benchtop pH meter (Hanna Instruments). The cell was irradiated with simulated 1 sun intensity light (AM 1.5, 100 mW cm^{-2}) using a 300 W Xe arc lamp (Oriol Instruments).

Analysis of Gases. Gas chromatography measurements were carried out using a Shimadzu GC-2014 instrument fitted with a ShinCarbon ST Micropacked column (Restek) using Ar as a carrier gas at 25 mL min^{-1} . Gases were detected with a thermal conductivity detector (TCD) with the system operating at $80 \text{ }^\circ\text{C}$. Gas sampling was done in flow, through a integrated cell block (**Figure S2.44**), where research grade argon was used as a carrier gas to a 2-position 6-port Rheodyne switch at 1 SCCM maintained by a Bronkhorst E-flow series mass flow controller. The flow setup was programmed to run automated analysis every 3 minutes. Calibration of hydrogen measurements were undertaken by dosing known amounts of pure H_2 (99.9995%) into the GC in flow dosing via a second 2-position, 6-port Rheodyne switch. All measurements were repeated several times.

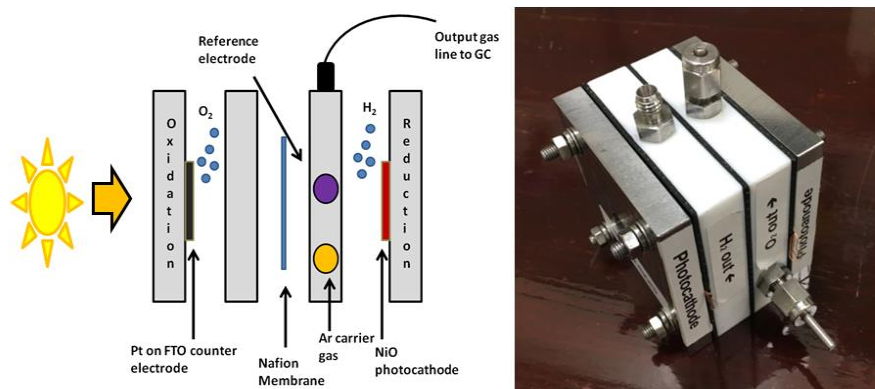


Figure S2.44. Photoelectrocatalysis cell block exploded view and photo of the device.

Optical Measurements. UV-visible absorption measurements for films were obtained using an Ocean Optics USB2000+ spectrophotometer where fibre optic cables enabled effective measurements through the film.

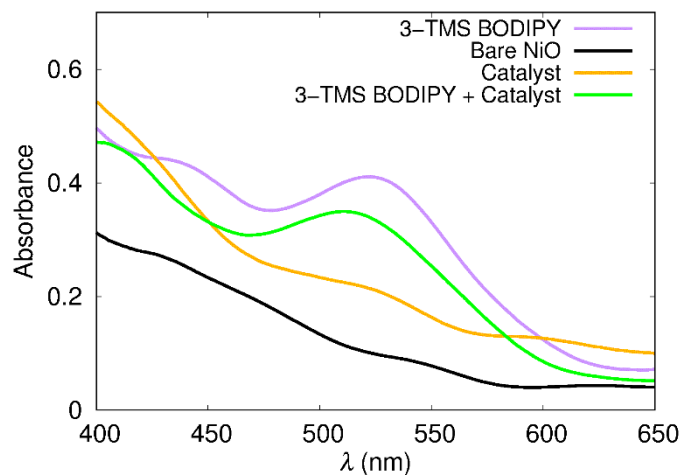


Figure S2.45. Steady-state absorption spectra of sensitised NiO films.

Microscopy. Scanning electron microscopy was undertaken at Northumbria University (UK) using a Tescan Mira 3 microscope with an Oxford Instruments X-ray detector. Typical imaging conditions employed an in-beam SE detector with the electron source set at 5kV.

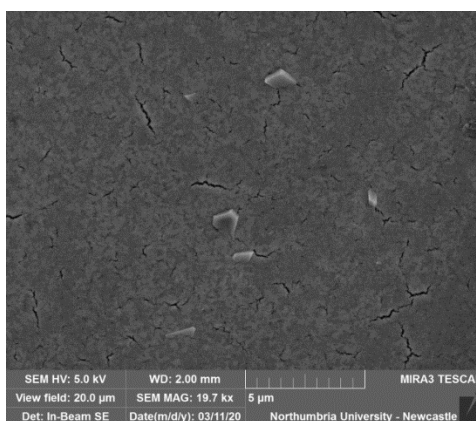


Figure S2.46. SEM image of the dye-sensitized NiO surface containing 3-TMS BODIPY polymer and Pt-bipy catalyst.

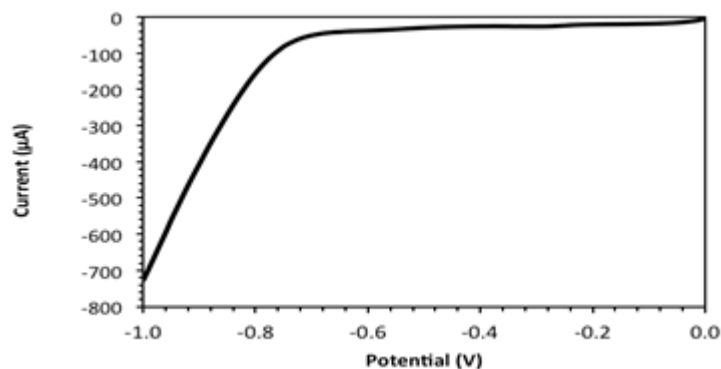


Figure S2.47. Linear sweep (in the dark) for a NiO film sensitized with 3-TMS BODIPY polymer and Pt-bipy catalyst in pH 5 phthalate buffer vs Ag/AgCl. Scan speed 0.05 V/s.

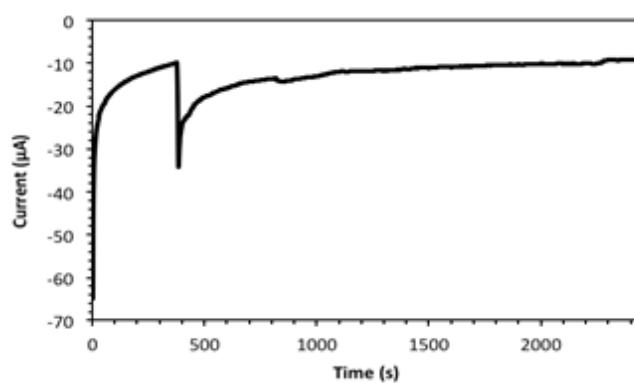


Figure S2.48. Chronoamperometry measurement of NiO sensitized with 3-TMS BODIPY polymer and Pt-bipy, in pH 5 phthalate buffer with an applied potential of -0.3 V vs Ag/AgCl. A period of equilibration in the dark takes place till AM 1.5 1 sun illumination is introduced at approximately 380 seconds.

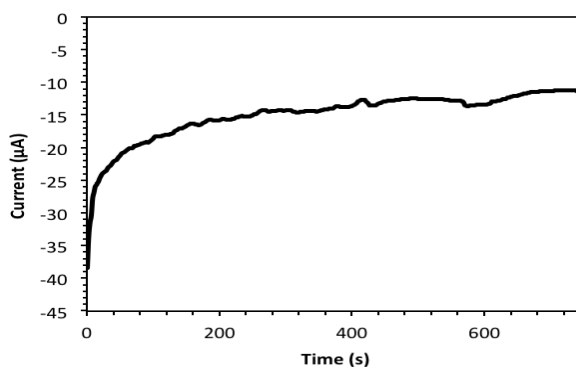


Figure S2.49. Control chronoamperometry experiment with bare NiO in pH 5 phthalate buffer with an applied potential of -0.3 V vs Ag/AgCl under 1 sun illumination. Chopping the light output had no impact on the current.

S2.20. Literature review of organic-based polymers for hydrogen evolution

Table S2.4. Comparison of photocatalytic experimental conditions and hydrogen evolution rate (HER) of organic polymeric photocatalysts reported in the literature. COF – covalent organic framework, CMP – conjugated microporous polymer.

Polymer type	Conditions	Light source	Catalysts	H ₂ (μmol) (irradiation time)	H ₂ (μmol h ⁻¹) (irradiation time)	H ₂ (μmol h ⁻¹ g ⁻¹)	ref
PPP	20 mg polymer, 2 mL H ₂ O, 2 mL diethylamine	300 (Hg)	-	8.3 (4 hours)	-	-	12
Nitrogen-PPP (P31)	25 mg polymer, water/methanol/triethylamine solution	300 W Xe Arc, λ > 295 nm	-	-	37.5 ± 1.1	-	13
Nitrogen-PPP (P31)	25 mg polymer, water/methanol/triethylamine solution	300 W Xe Arc, λ > 420 nm	-	-	15.2 ± 0.06	-	13
Poly(axomethine) networks	100 mg polymer, 100 mL aqueous solution with 10% vol TEOA	Xe Arc, λ > 300 nm	3 wt.% Pt	26.7	7	-	14
Hydrazone based COF	4 mg polymer, 9mL H ₂ O, 10% vol TEOA		2.2 wt.% Pt			1970	3
Hydrazone based COF	10 mg polymer, 100 mg sodium ascorbate, 10 mL H ₂ O	300 W Xe Arc, λ > 420 nm	2.2 wt.% Pt	97.6 (52 hours)		230	3
CP-CMP10	100 mg polymer, 100 mL diethylamine/water solution (20 vol%)	300 W Xe Arc, λ > 420 nm	-	100 (6 hours)	17.4 ± 0.9	-	15

Dibenzo-[b,d]-thiophene sulfone copolymer (P7)	25 mg polymer, water/methanol/triethylamine solution	300 W Xe Arc, $\lambda > 295$ nm	-	-	145 \pm 7 (5 hours)	-	16
Dibenzo-[b,d]-thiophene sulfone copolymer (P7)	25 mg polymer, water/methanol/triethylamine solution	300 W Xe Arc, $\lambda > 420$ nm	-	-	92 \pm 2 (5 hours)	-	16
Conjugated polybenzothiadiazole	50 mg polymer, 10% vol TEOA, 110 mL H ₂ O	300 W Xe Arc, $\lambda > 420$ nm	-	-	12	-	17
Conjugated polybenzothiadiazole	50 mg polymer, 10% vol TEOA, 110 mL H ₂ O	300 W Xe Arc, $\lambda > 420$ nm	3 wt.% Pt	-	116	-	17
P8-i	25 mg polymer, water/methanol/triethylamine solution	300 W Xe Arc, $\lambda > 295$ nm	-	-	21.5 \pm 0.1 (5 hours)	-	18
P8-i	25 mg polymer, water/methanol/triethylamine solution	300 W Xe Arc, $\lambda > 420$ nm	-	-	3.1 \pm 0.02 (5 hours)	-	18
P8-s	25 mg polymer, water/methanol/triethylamine solution	300 W Xe Arc, $\lambda > 295$ nm	-	-	2.0 \pm 0.05 (5 hours)	-	18
P8-s	25 mg polymer, water/methanol/triethylamine solution	300 W Xe Arc, $\lambda > 420$ nm	-	-	0.5 \pm 0.05 (5 hours)	-	18
Perylene CMP	100 mg polymer, 100 mL 20% vol TEOA aqueous solution	300 W Xe Arc, $\lambda > 300$ nm	3 wt.% Pt	-	12.1	-	19

S2.21. Compounds in solution



Figure S2.50. Quartz cuvettes showing monomer (left), diiodo monomer (centre) and polymer (right) in CH_2Cl_2 , aerated solution.

S2.22. Bibliography

- (1) Banfi, S.; Nasini, G.; Zaza, S.; Caruso, E. *Tetrahedron* **2013**, *69* (24), 4845–4856.
- (2) Du, P.; Schneider, J.; Luo, G.; Brennessel, W. W.; Eisenberg, R. *Inorg. Chem.* **2009**, *48* (11), 4952–4962.
- (3) Stegbauer, L.; Schwinghammer, K.; Lotsch, B. V. *Chem. Sci.* **2014**, *5* (7), 2789–2793.
- (4) Yu, J.; Sun, X.; Xu, X.; Zhang, C.; He, X. *Appl. Catal. B Environ.* **2019**, 257 (March), 117935.
- (5) Redmond, R. W.; Gamlin, J. N. *Photochem. Photobiol.* **1999**, *70* (4), 391–475.
- (6) O'Reilly, L.; Pan, Q.; Das, N.; Wenderich, K.; Kortterik, J. P.; Vos, J. G.; Pryce, M. T.; Huijser, A. *ChemPhysChem* **2018**, *19* (22), 3084–3091.
- (7) Das, N.; Bindra, G. S.; Paul, A.; Vos, J. G.; Schulz, M.; Pryce, M. T. *Chem. - A Eur. J.* **2017**, *23* (22), 5330–5337.
- (8) Manton, J. C.; Long, C.; Vos, J. G.; Pryce, M. T. *Phys. Chem. Chem. Phys.* **2014**, *16* (11), 5229–5236.
- (9) Pellegrin, Y.; Odobel, F. *Comptes Rendus Chim.* **2017**, *20* (3), 283–295.
- (10) Sumikura, S.; Mori, S.; Shimizu, S.; Usami, H.; Suzuki, E. *J. Photochem. Photobiol. A Chem.* **2008**, *199* (1), 1–7.
- (11) Morgan, T. G.; Burstall, H. F. *J. Chem. Soc.* **1934**, 323, 1498–1500.
- (12) Yanagida, S.; Kabumoto, A.; Mizumoto, K.; Pac, C.; Yoshino, K. *J. Chem. Soc. Chem. Commun.* **1985**, No. 8, 474–475.
- (13) Sprick, R. S.; Wilbraham, L.; Bai, Y.; Guiglion, P.; Monti, A.; Clowes, R.; Cooper, A. I.; Zwiijnenburg, M. A. *Chem. Mater.* **2018**, *30* (16), 5733–5742.
- (14) Schwab, M. G.; Hamburger, M.; Feng, X.; Shu, J.; Spiess, H. W.; Wang, X.; Antonietti, M.; Müllen, K. *Chem. Commun.* **2010**, 46 (47), 8932–8934.

- (15) Sprick, R. S.; Jiang, J. X.; Bonillo, B.; Ren, S.; Ratvijitvech, T.; Guiglion, P.; Zwijnenburg, M. A.; Adams, D. J.; Cooper, A. I. *J. Am. Chem. Soc.* **2015**, *137* (9), 3265–3270.
- (16) Sprick, R. S.; Bonillo, B.; Clowes, R.; Guiglion, P.; Brownbill, N. J.; Slater, B. J.; Blanc, F.; Zwijnenburg, M. A.; Adams, D. J.; Cooper, A. I. *Angew. Chemie* **2016**, *128* (5), 1824–1828.
- (17) Yang, C.; Ma, B. C.; Zhang, L.; Lin, S.; Ghasimi, S.; Landfester, K.; Zhang, K. A. I.; Wang, X. *Angew. Chemie - Int. Ed.* **2016**, *55* (32), 9202–9206.
- (18) Woods, D. J.; Sprick, R. S.; Smith, C. L.; Cowan, A. J.; Cooper, A. I. *Adv. Energy Mater.* **2017**, *7* (22), 1–6.
- (19) Xu, Y.; Mao, N.; Feng, S.; Zhang, C.; Wang, F.; Chen, Y.; Zeng, J.; Jiang, J. X. *Macromol. Chem. Phys.* **2017**, *218* (14), 1–9.

Appendix B

Supporting information associated with Chapter 3.

S3.1. Experimental section

S3.1.1. Instrumentation

Steady-state spectroscopy: UV-vis spectra was measured using an Agilent 8453 UV-vis spectrophotometer in a 1 cm quartz cell using spectroscopic grade solvents. Emission spectra were recorded using the FLS1000 Edinburgh Instruments equipped with a Xe Arc lamp and a visible PMT detector and 1 sec scan rate to accumulate the spectra.

Time-correlated single photon counting (TCSPC): TCSPC lifetimes were carried out using FLS1000 Photoluminescence Spectrometer (Edinburgh instruments), equipped with a 510 nm variable pulse length diode laser (VPL-510) as the excitation source and a visible PMT-900 detector. All data analysis carried out using Fluoracle[®] software. The accuracy of the fit of the decays was judged by chi-squared (χ^2) and sum of residuals was always $\chi^2 < 1.1$. The fluorescence decay time (τ) was obtained from the slope of the decay curve. All samples were measured in a 1 cm x 1 cm quartz cuvette and samples were < 0.2 at 510 nm to ensure an optically dilute solution to avoid inner-filter effects.

NMR spectroscopy: ¹H-NMR was recorded on either a Bruker AC 400 MHz or 600 MHz spectrophotometer in CDCl₃ and were calibrated according to the deuterated solvent peak.

IR spectroscopy: FTIR measurements were carried out on Perkin-Elmer 2000 FTIR spectrophotometer in a liquid solution cell using spectrophotometric grade dichloromethane.

Transient absorption spectroscopy: TA spectra recorded on the ps-ns timescale were measured in the ULTRA facility located in Rutherford Appleton Laboratories,

UK. Experimental set-up is reported elsewhere.¹ ns-TA was recorded using the LP980 Edinburgh Instruments ($\lambda_{\text{exc}} = 355$ nm).

Time resolved Infrared spectroscopy: TRIR spectra were measured in the ULTRA facility located in Rutherford Appleton Laboratories, UK, and all experimental parameters as per previously described with the TA measurements.

Scanning electron microscopy (SEM): SEM was performed on a Hitachi S3400n electron microscope with a magnification x 300K, resolution 3.0 nm. The samples were mounted on carbon tabs and sputtered with gold coating before the measurement. SEM studies were performed at an acceleration voltage of 20 kV.

Size exclusion chromatography (SEC): SEC was conducted in 1,1,1,3,3,3-Hexafluoro-2-propanol (HFIP) using a PSS SECurity GPC system equipped with a PFG 7 μm 8 \times 50 mm pre-column, a PSS 100 \AA , 7 μm 8 \times 300 mm and a PSS 1000 \AA , 7 μm 8 \times 300 mm column in series and a differential refractive index (RI) detector at a flow rate of 1.0 mL min⁻¹. The systems were calibrated against Agilent Easi-Vial linear poly(methyl methacrylate) (PMMA) standards and analysed by the software package PSS winGPC UniChrom.

S3.1.2. Experimental Methods

Commercial reagents were used as received without further purifications. All reactions were carried out using standard Schlenk techniques. Anhydrous solvents were purchased from Sigma Aldrich[®]. 4-hydroxymethylbenzaldehyde was purchased from Sigma Aldrich[®].

Fluorescence quantum yield measurement: Steady-state fluorescence measurements were recorded using the FLS1000 photoluminescence spectrometer. Prior to obtaining the emission spectra, samples were diluted to ~ 0.2 abs units at λ_{exc} using the UV-vis spectrometer to inhibit inner-filter effect. The reference compound used was previously reported by Banfi et al. (3-pyridine H-BODIPY, $\Phi_{\text{fl}} = 0.62$ in CH_2Cl_2).² An excitation wavelength of 490 nm was used for the samples and the standards. A slit width of 2.5 nm was used for all measurements. The compounds were

measured in aerated solution at room temperature. The following formula was used to calculate the Φ_{fl} :

$$\Phi_{fl} = \Phi_{fl}^{std} \cdot \left(\frac{I_{fl}^{sample}}{I_{fl}^{std}} \right) \cdot \left(\frac{A^{std}}{A^{sample}} \right) \quad (1)$$

where $I_{fl}^{sample \text{ or } std}$ is the area under the curve of the emission spectra and $A^{sample \text{ or } std}$ denotes the absorbance of the sample at 490 nm prior to sample measurement.

Singlet oxygen quantum yield measurement: All singlet oxygen generation experiments were carried out by recording a near infrared emission (NIR) spectra and were recorded using an Andor InGaAs detector coupled with a Shamrock 163 Spectrograph. The excitation sources were supplied by Thorlabs and the monochromatic line used was a 530 nm diode laser. All UV spectra were recorded both before and after singlet oxygen measurements and it was ensured the optical density (OD) of the sample was below 0.3 absorbance units at the wavelength of excitation, prior to the sample and standard measurement. Standard and sample measurements were run under the same experimental conditions using the same solvent, excitation sources and identical experimental parameters were utilised. All samples were run in aerated solvent at room temperature. Background measurements were carried out before running the samples. The singlet oxygen quantum yields were calculated using the following formula:

$$\Phi_{sample} = \frac{\Phi_{ref}(Area_{sample} \cdot Abs_{ref})}{(Area_{ref} \cdot Abs_{sample})} \quad (2)$$

Where Φ_{ref} is the singlet oxygen quantum yield of the standard (in the same solvent), $Area_{sample}$ and $Area_{ref}$ are the integrated area between 1200 – 1360 nm of the phosphorescence of singlet oxygen respectively, Abs_{ref} and Abs_{sample} are the absorption of both solutions at 530 nm. Rose Bengal was used as a reference, $\Phi_{\Delta} = 0.53$ in ACN.³

Lifetime analysis: The numerical procedure towards determining the lifetime of each decay (τ_i) and the corresponding % relativity of each lifetime component (B_i) is the Marquardt-Levenberg algorithm, ultimately to produce a “goodness of fit”, χ^2 value:

$$\chi^2 = \sum_k w_k^2 (F_k - S_k)^2 \quad (3)$$

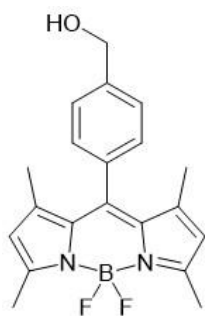
where χ^2 for each lifetime fit was ~ 1.2 .

Time resolved kinetic analysis: For TA and TRIR, either decay or growth of bands were fit using either mono (4) or biexponential fitting (4) using OriginLab[®] software and R^2 value > 0.99 was obtained for every lifetime reported, using the followed formula for exponential fitting:

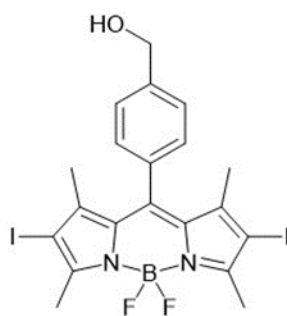
$$y = y_0 + Ae^{-x/\tau_1} \quad (4)$$

$$y = y_0 + A_1e^{-x/\tau_1} + A_2e^{-x/\tau_2} \quad (5)$$

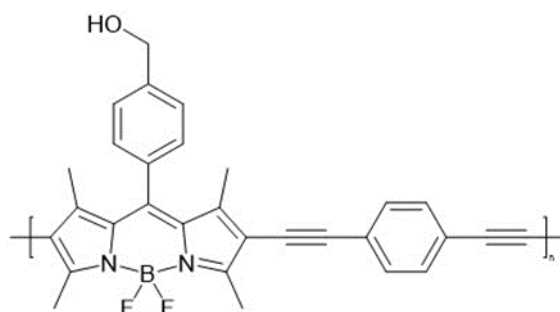
S3.2. Synthesis



8-(4-Hydroxymethylphenyl)-4,4-difluoro-1,3,5,7-tetramethyl-4-bora-3a,4a-diazas-indacene (BODIPY-2H, monomer): The synthesis of BODIPY monomers were carried out as previously reported with some minor modifications.⁴ To an oven dried flask fitted with magnetic stir-bar, 25 mL CH₂Cl₂ was added and allowed to purge with N₂ for 15 min. To the degassed solvent, aldehyde (2.5 mmol) and 2,4-dimethylpyrrole (0.51 mL, 5.0 mmol) were added. A few drops of TFA was added and the solution was stirred overnight at room temperature, in the absence of light. DDQ (2.48 mmol) was added and the solution was continuously stirred for further 4 h. After this time, boron trifluoride diethyl etherate (18.4 mmol) was added, following in quick succession by TEA (41 mmol). The reaction was stirred overnight at room temperature under a continuous flow of nitrogen. Then the reaction was stopped, and the organic layer was collected after washing three times with saturated sodium bicarbonate solution. The organic layer was collected and dried over magnesium sulphate to yield a dark purple crude product. Purification was carried out using column chromatography with on silica (hexane: ethyl acetate 70:30) to yield a red solid. ¹H NMR (600 MHz, CDCl₃): δ 1.37 (s, 6H), 1.80 (broad s, 1H), 2.55 (s, 6H), 4.81 (s, 2H), 5.97 (s, 2H), 7.27 (d, 2H, J = 8.2 Hz), 7.49 (d, 2H, J = 8.2 Hz). ¹³C NMR (600 MHz, CDCl₃): δ 14.5, 14.6, 64.8, 121.2, 127.4, 128.2, 131.5, 134.2, 141.5, 141.9, 143.1, 155.5. NMR data is as per previously reported.^{5,6}



2,6-diiodo-8-(4-Hydroxymethylphenyl)-4,4-difluoro-1,3,5,7-tetramethyl-4-bora-3a,4a-diaza-s-indacene (BODIPY-2I, diiodo monomer): This procedure was carried out as per previous reported with some minor modifications.² BODIPY monomer (0.26 mmol) and Iodine (76 mg, 0.30 mmol) were added to an oven-dried round bottom flask equipped with stir-bar, dissolved in 30 mL of EtOH and purged for 30 min with nitrogen. Iodic acid (93 mg, 0.53 mmol) was dissolved in 1.5 mL deionised water and allowed to purge with nitrogen for 30 min. After that, both solutions were combined and allowed to reflux at 60 °C for 20 min. The solvent was removed using distillation, followed by dissolving the crude product in CH₂Cl₂ and washing three times with saturated sodium thiosulphate solution. The organic layer was collected, and the product was dried using rotary evaporation to yield pure product. ¹H NMR (600 MHz, CDCl₃): δ 1.32 (s, 6H), 1.52 (broad s, 1H), 2.58 (s, 6H), 4.77 (s, 2H), 7.18 (d, 2H, J = 8.4 Hz), 7.46 (d, 2H, J = 8.1 Hz). ¹³C NMR (600 MHz, CDCl₃): δ 15.0, 16.1, 63.6, 84.6, 126.6, 126.9, 132.8, 140.2, 141.5, 144.3, 144.3, 155.8. MS MALDI-TOF [M]: (*m/z*) mass observed 605.9640, mass theoretical 605.9762 for C₂₀H₂₀BF₂I₂N₂.



Copolymer: To an oven-dried Schlenk equipped with stir-bar, anhydrous tetrahydrofuran (THF) (15 mL) and anhydrous diisopropylamine (DiiPA) (15 mL) were added. All glass taps were greased and the Schlenk was degassed using three

freeze-pump-thaw cycles. Addition of the solids to the Schlenk was then carried out - IODO-BODIPY (0.15 mmol), 1,4-diethynylbenzene (19 mg, 0.15 mmol), bis(triphenylphosphine) palladium(II) dichloride (16 mol%), copper iodide (8 mol%), triphenylphosphine (8 mol%) were added, and the freeze-pump-thaw cycle was repeated to ensure the reaction would occur in the absence of air. The solution was refluxed for 48 hr at 75-85 °C, until complete consumption of the IODO BODIPY was monitored by TLC. After this time, the solvents were removed by distillation. The crude polymer was dissolved in CH₂Cl₂ and washed three times with saturated sodium bicarbonate solution. The organic layer was dried over MgSO₄. Purification was carried out by washing in EtOH and collection of the precipitate to yield a pink/purple solid. This process was repeated to yield a pure copolymer free of residual catalytic system. ¹H NMR (600 MHz, CDCl₃): δ 7.69 – 7.37 (br, Ar-H), 4.83 (br, CH₂O-), 2.58 (br, CH₃ at 3, 5 position of BODIPY), 1.58 (br, OH as *meso* position of BODIPY), 1.33 (br, CH₃ at 1, 7 position of BODIPY). SEC results: M_n = 11,100, PDI = 1.1.

S3.3. Characterisation

S3.3.1. NMR spectra

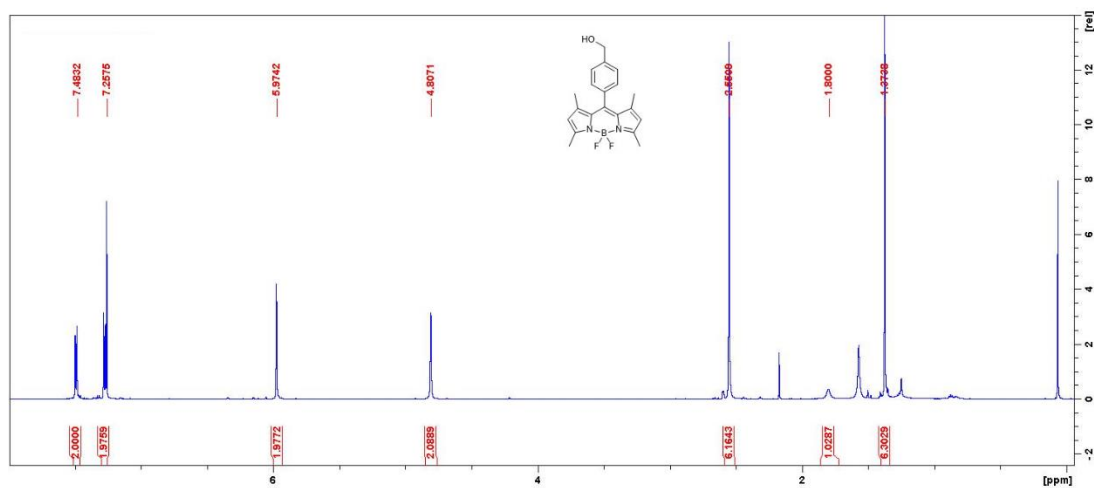


Figure S3.1. ¹H NMR (600 MHz) of BODIPY-2H in CDCl₃.

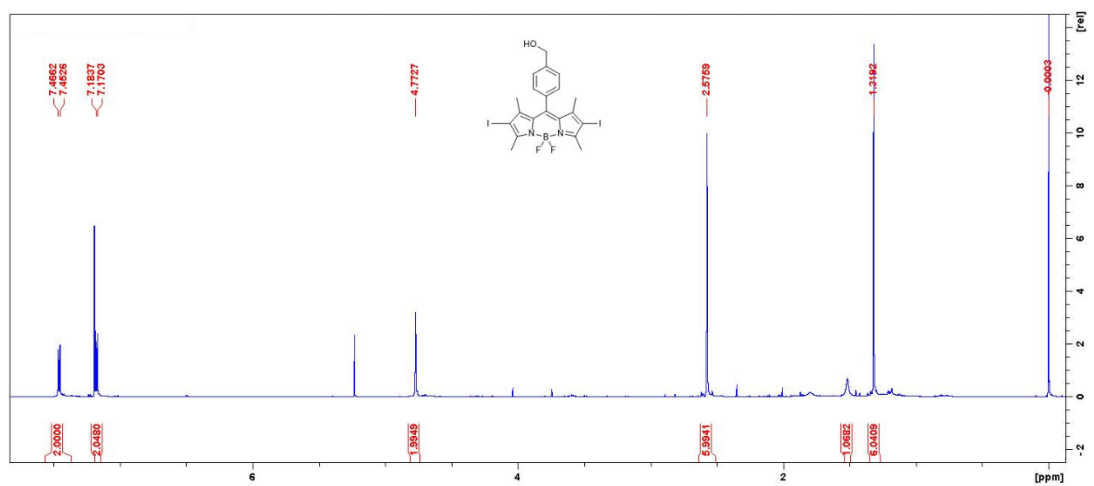


Figure S3.2. ¹H NMR (600 MHz) of BODIPY-2I in CDCl₃.

S3.3.2. Mass spectroscopy

Figure: Extracted ion chromatogram (EIC) of compound.

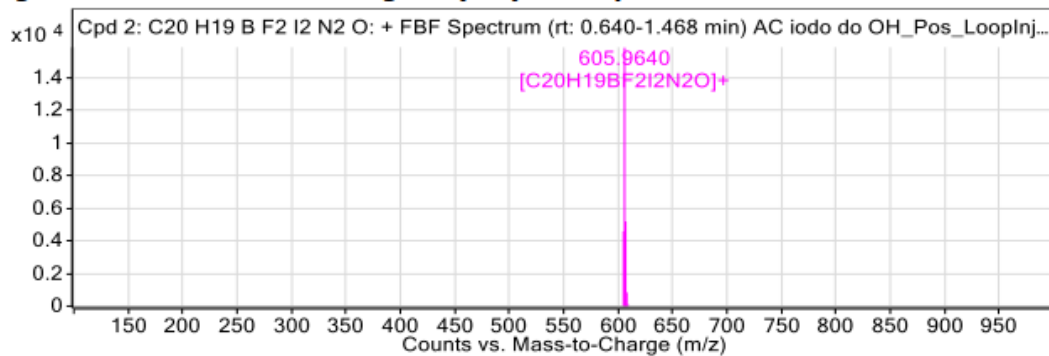


Figure: Full range view of Compound spectra and potential adducts.

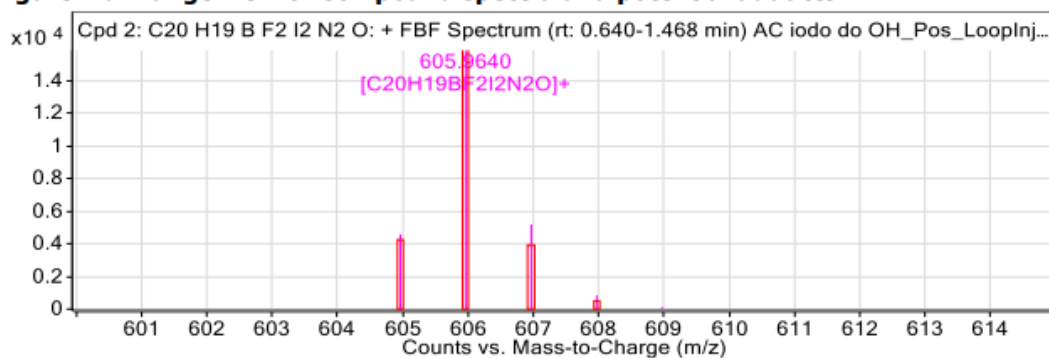


Figure S3.3. Mass spectra for $[M^+]$ for BODIPY-2I, diiodo monomer.

S3.3.3. Size exclusion chromatography

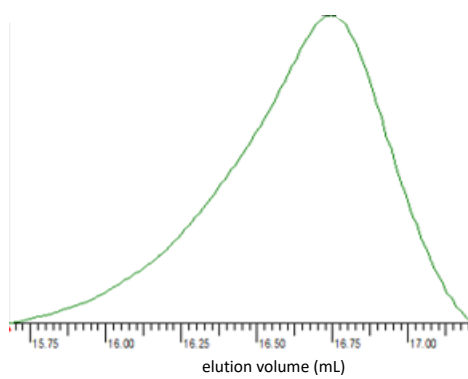


Figure S3.4. Size exclusion chromatography (SEC) trace of copolymer (dRI detection, PMMA standards).

S3.3.4. Stability of drop coated copolymer surface

The copolymer was drop coated on a cuvette surface and performed UV-visible spectroscopy. We could observe that the OH copolymer spectra is similar in both solution and on solid surface (as shown in **Figure S3.5** (a)) thereby allowing to use the drop coated surface for further antimicrobial studies. Using the scanning electron microscope, we could observe the morphological appearance of the OH copolymer when drop coated on a carbon surface which is sputter coated with gold. The SEM image (**Figure S3.5** (b)) below show the homogeneous surface of the OH copolymer where it is unable to see and aggregation or agglomeration formation.

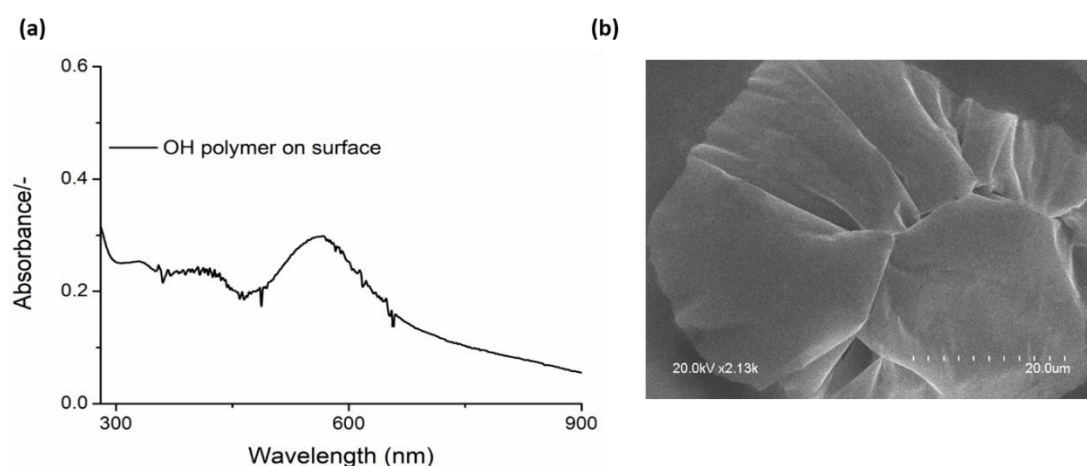


Figure S3.5. a) UV-visible spectra of OH copolymer drop coated onto a cuvette surface, b) SEM image representing the morphology of the OH copolymer when drop coated on a surface.

S3.4. Absorption and emission spectra

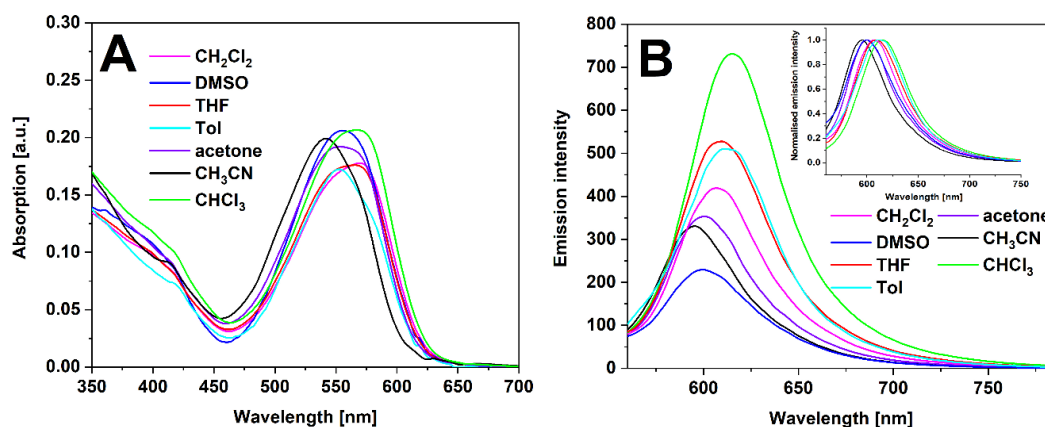


Figure S3.6. a) UV-visible absorption spectra of copolymer in a range of solvents; dichloromethane (solid magenta), DMSO (solid blue), THF (solid red), toluene (solid cyan), acetone (solid violet), acetonitrile (solid black), chloroform (solid green) and b) Emission spectra of copolymer in the same range of solvents, $\lambda_{\text{exc}} = 560$ nm, 15 nm slit width. Inset shows normalised emission spectra of copolymer. All spectra recorded at room temperature in aerated solution.

Table S3.1. Summary of photophysical properties of copolymer analysed in a range of solvents – dichloromethane, dimethyl sulfoxide, THF, toluene, acetone, acetonitrile and chloroform. The Reichardt parameter $E_T(30)$ (kcal mol⁻¹) is shown beside each solvent in brackets to indicate solvent polarity.⁷ All spectra recorded at room temperature in aerated solution. 560 nm excitation wavelength was used for emission spectra with 15.0 nm slit width. All samples were isoabsorptive at the excitation wavelength.

	Solvent						
	CH ₂ Cl ₂	DMSO	THF	toluene	acetone	CH ₃ CN	CHCl ₃
$E_T(30)$	(40.7)	(45.1)	(37.4)	(33.9)	(42.2)	(45.6)	(39.1)
λ_{abs} (nm)	570	555	565	553	553	542	569
λ_{em} (nm)	607	599	609	611	601	595	615
Stokes shift (cm ⁻¹) ^a	1069	1324	1279	1717	1444	1643	1315

^acalculated using the absorption maxima and emission maxima of copolymer.

S3.5. Lifetime measurements (TCSPC measurements)

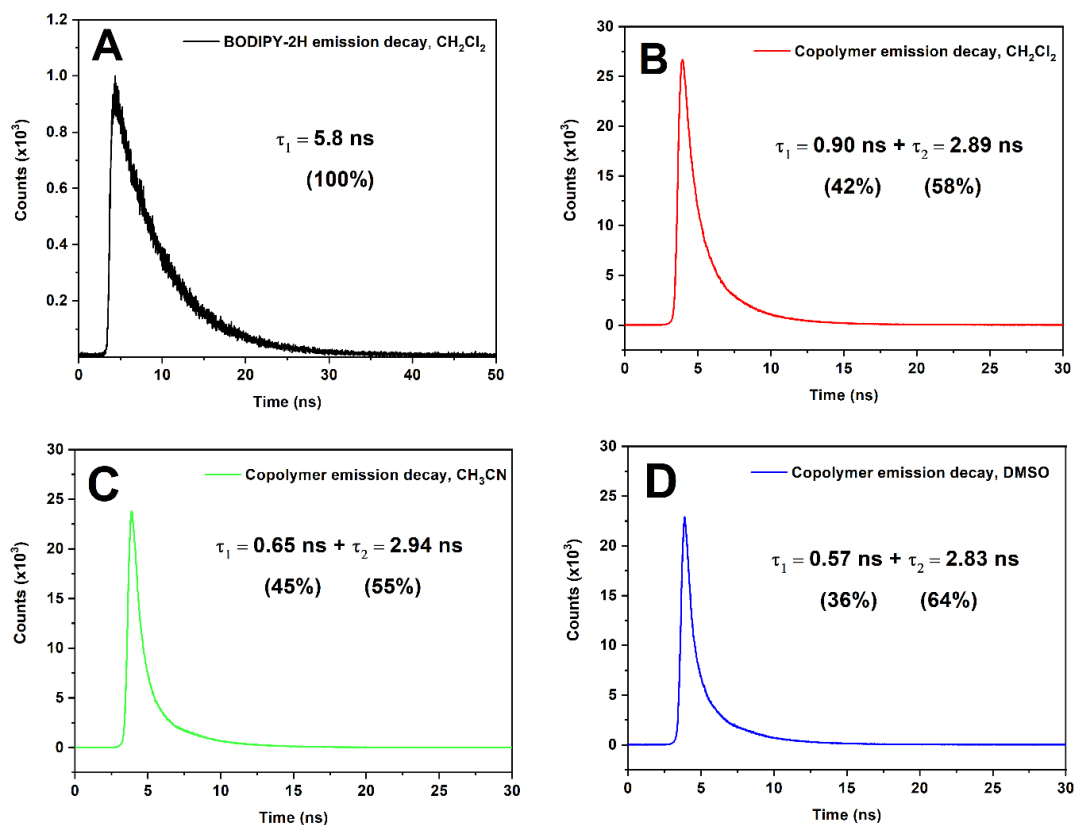


Figure S3.7. Emission decay profiles for a) BODIPY-2H in CH_2Cl_2 , b) copolymer in CH_2Cl_2 , c) copolymer in CH_3CN and d) copolymer in DMSO. The $\lambda_{\text{exc}} = 510$ nm for all samples, and a detection wavelength of 520 nm for BODIPY-2H and 610 for the copolymer. All emission decays recorded at room temperature in aerated solution.

Table S3.2. Fluorescence decay lifetimes (τ) including margin of error associated with each lifetime, % relativity of each component (B_i) for BODIPY-2H in CH_2Cl_2 and copolymer in CH_2Cl_2 , CH_3CN and DMSO. $\lambda_{\text{exc}} = 510$ nm using FLS1000 photoluminescence spectrometer.

Compound	Solvent	τ_1 (ns)	B_1 (%)	τ_2 (ns)	B_2 (%)
BODIPY-2H	CH_2Cl_2	5.80+/-0.09	100	-	-
Copolymer	CH_2Cl_2	0.90+/-0.03	42	2.89+/-0.05	58
Copolymer	CH_3CN	0.65+/-0.02	45	2.94+/-0.05	55
Copolymer	DMSO	0.57±0.02	36	2.83±0.04	64

S3.6. Singlet oxygen measurements

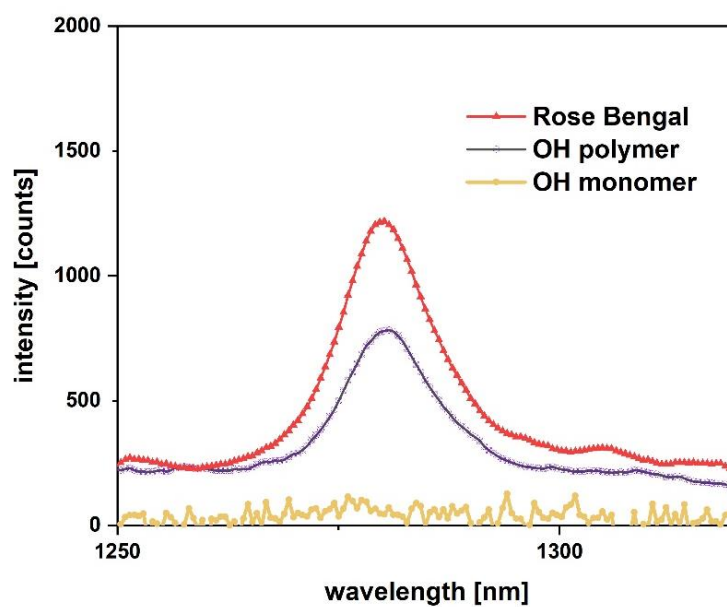


Figure S3.8. NIR singlet oxygen emission spectrum of Rose Bengal (red), copolymer (purple), BODIPY-2H (orange) in CH_3CN , following excitation at 525 nm.

S3.7. Transient absorption (TA) spectroscopy

S3.7.1. Picosecond transient absorption

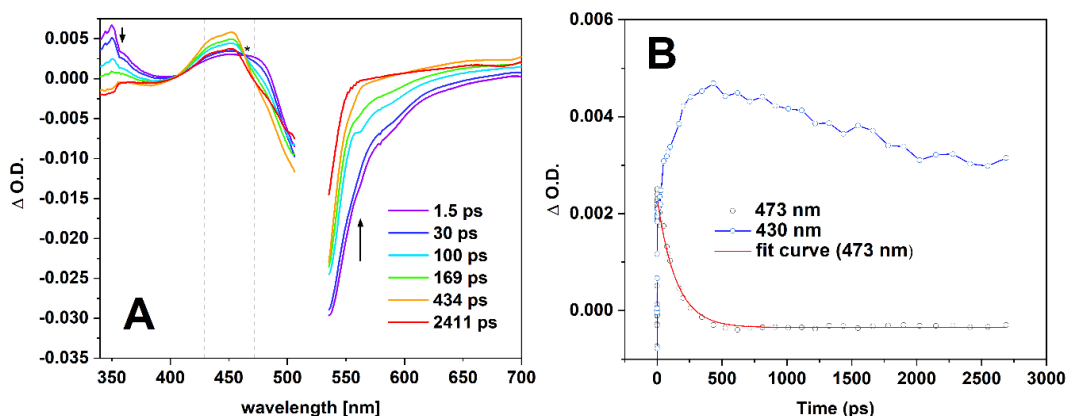


Figure S3.9. a) TA spectra of diiodo monomer (BODIPY-2I) in CD₃CN shown at indicated time decays in ps and b) corresponding kinetic traces at 430 nm (blue) and 473 nm (red). The red line corresponding to the kinetic trace at 473 nm shows the monoexponential fit used to obtain S₁ lifetime of halogenated species. As the signal at 473 nm decays ($\tau = 146$ ps), an additional species grows in at 430 nm ($\tau = 137$ ps). These are assigned to the decay of the BODIPY singlet state and formation of the triplet state which persists beyond the time frame of the experimental set-up. The grey dashed lines on the TA spectra correspond to kinetic traces on the right. The asterisk indicates the isosbestic point at 463 nm. $\lambda_{\text{exc}} = 525$ nm (0.4 $\mu\text{J}/\text{pulse}$).

Table S3.3. Lifetimes obtained (ps) for the species observed in the diiodo monomer at 472 and 430 nm, corresponding to decay of the singlet, and formation of the triplet state.

	τ_1 (ps)	R ²
430 nm	137 (± 5)	0.99
472 nm	146 (± 2)	0.99

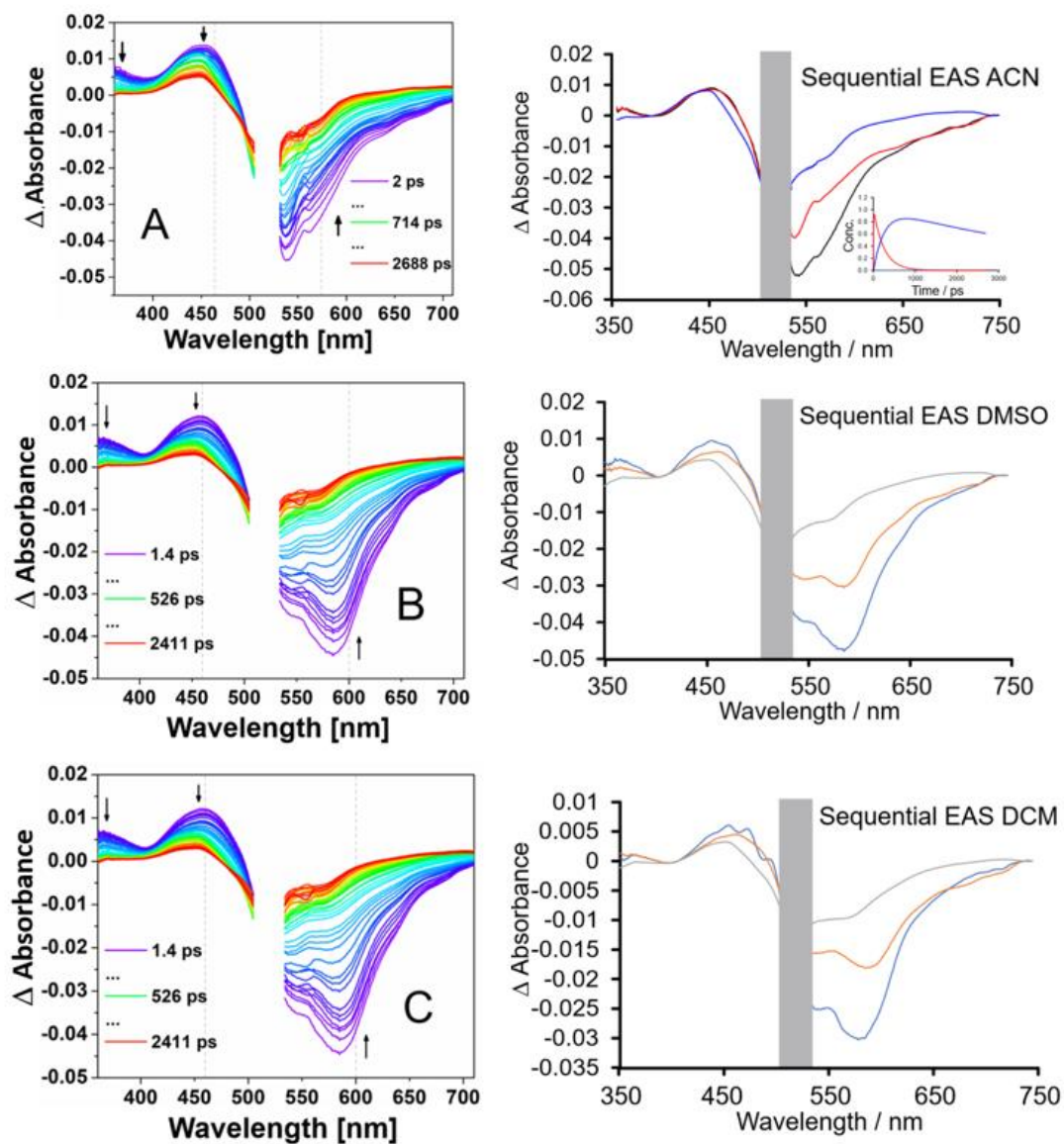


Figure S3.10. Transient absorption (TA) spectra of the copolymer and corresponding EAS spectra in (A) d_3 -acetonitrile, (B) d_6 -DMSO and (C) d_2 -dichloromethane, following excitation ($\lambda_{exc} = 525$ nm (0.4 μ J/pulse) (the gap in the TA plots corresponds to the excitation wavelength which is masked by a narrow band pass filter).

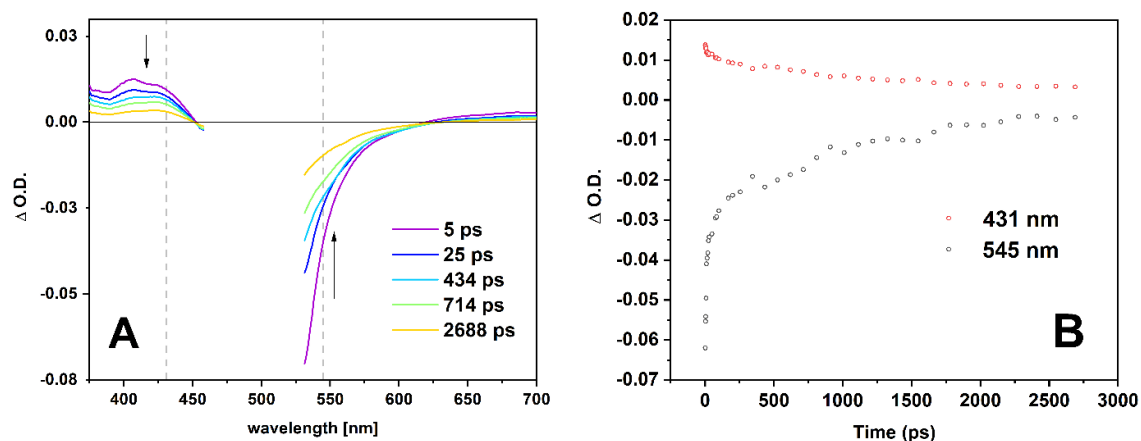


Figure S3.11. a) TA spectra of H-monomer (BODIPY-2H) in CH_3CN and b) corresponding kinetic traces at 431 nm (red) and 545 nm (grey). The grey dashed lines on the TA spectra correspond to kinetic traces on the right which do not decay to the baseline within the timeframe of the experiment. $\lambda_{\text{exc}} = 525 \text{ nm}$ ($0.4 \mu\text{J}/\text{pulse}$).

S3.7.2. Nanosecond transient absorption

Table S3.4. Summary of lifetimes obtained (μs) of the copolymer from a monoexponential fit of both the ESA feature (446 nm) and GSB feature (524 nm).

	τ_1 (μs)	R^2
Acetonitrile		
446 nm	32 ± 3	0.99
524 nm	29 ± 2	0.99

S3.8. FTIR spectra

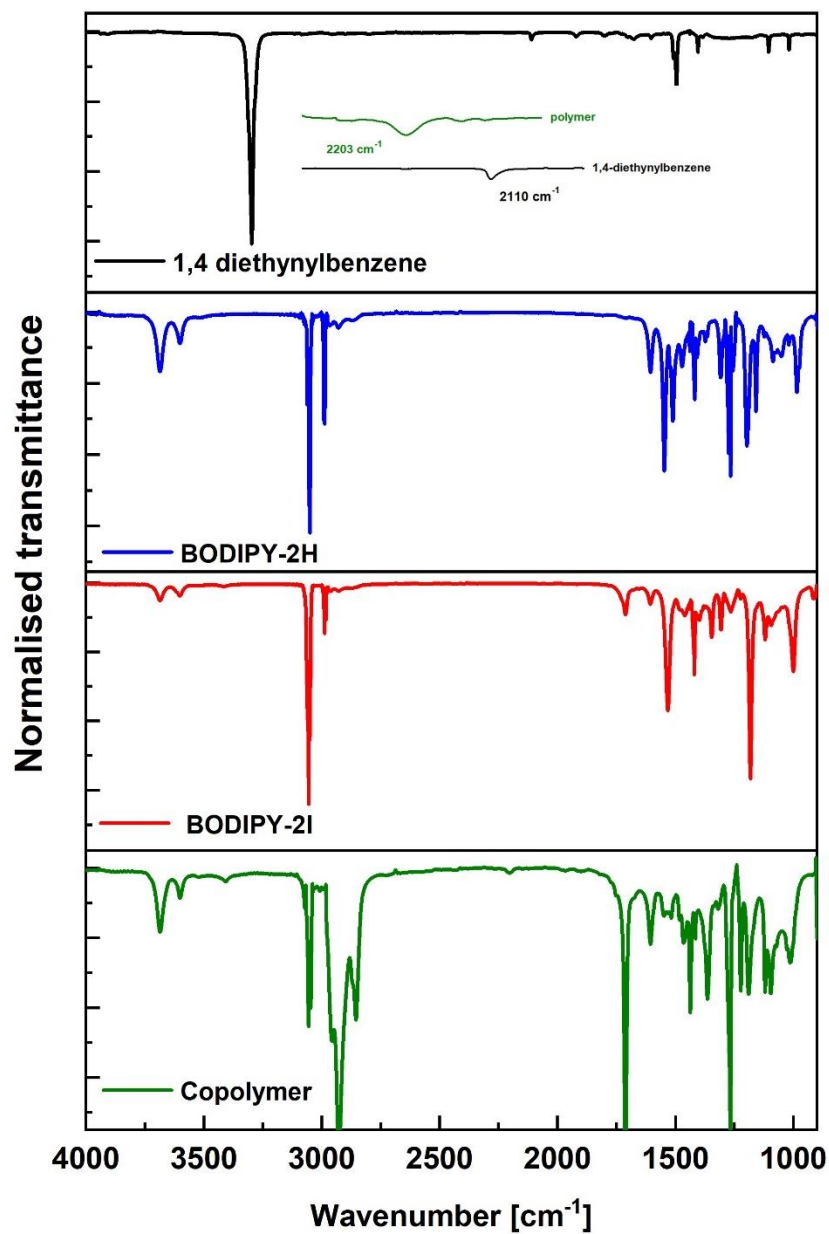


Figure S3.12. FTIR spectra of 1,4-diethynylbenzene (black), BODIPY-2H (blue), BODIPY-2I (red) and copolymer (green) recorded in dichloromethane solution. Inset displays triple bond region 2400 – 2000 cm⁻¹.

S3.9. Time resolved infrared spectroscopy (TRIR)

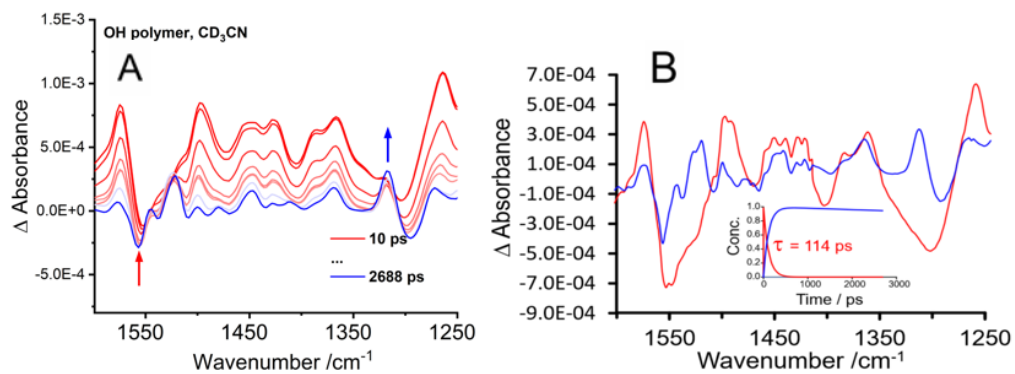


Figure S3.13. a) TRIR spectra of the copolymer in CD₃CN in the spectral window of 1610 – 1290 cm⁻¹ at various time delays following excitation at 525 nm, and b) the corresponding EAS.

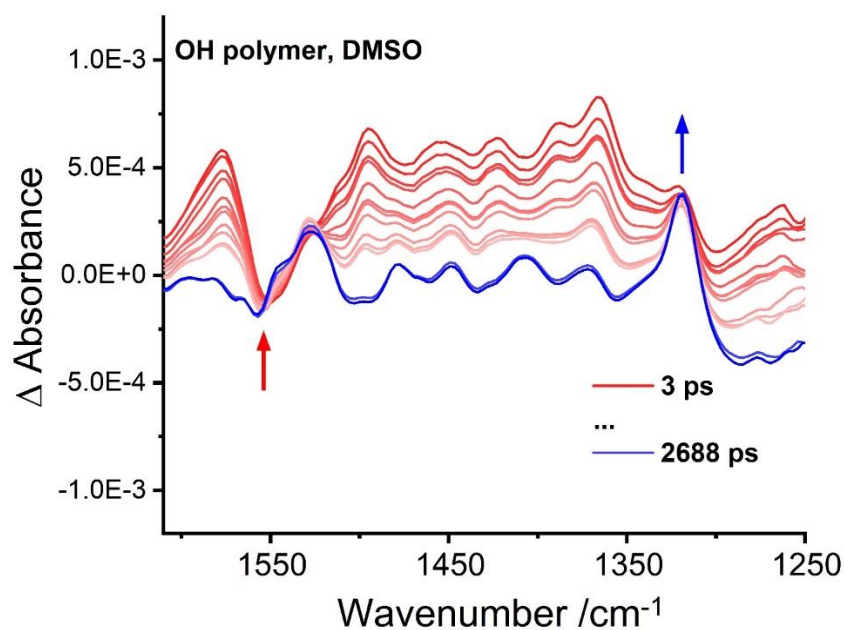


Figure S3.14. TRIR spectra of copolymer in DMSO in the spectral window of 1610 – 1290 cm⁻¹ at various time delays following excitation at 525 nm. Arrows display spectral changes observed throughout the course of the experiment.

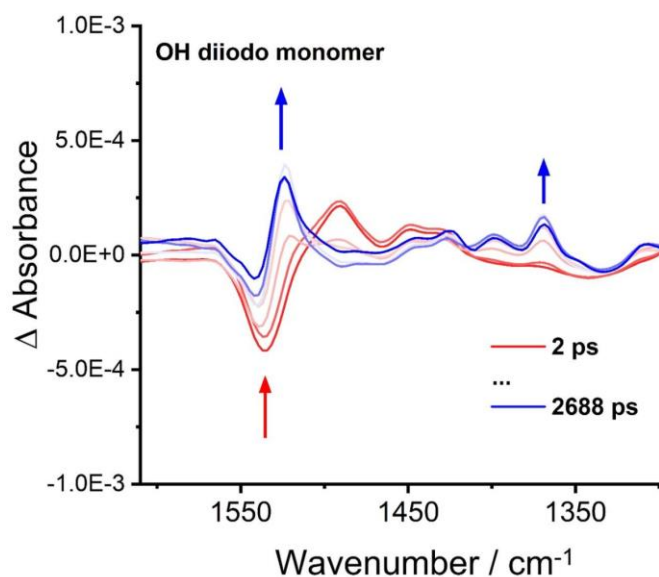


Figure S3.15. TRIR spectra of BODIPY-2I in CD_3CN in the spectral window of 1610 – 1290 cm^{-1} at various time delays following excitation at 525 nm. Arrows display spectral changes observed throughout the course of the experiment.

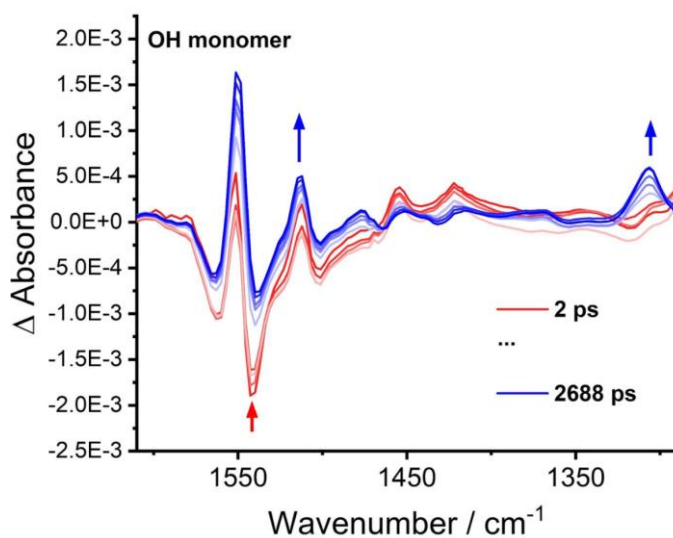


Figure S3.16. TRIR spectra of BODIPY-2H in CD_3CN in the spectral window of 1610 – 1290 cm^{-1} at various time delays following excitation at 525 nm. Arrows display spectral changes observed throughout the course of the experiment.

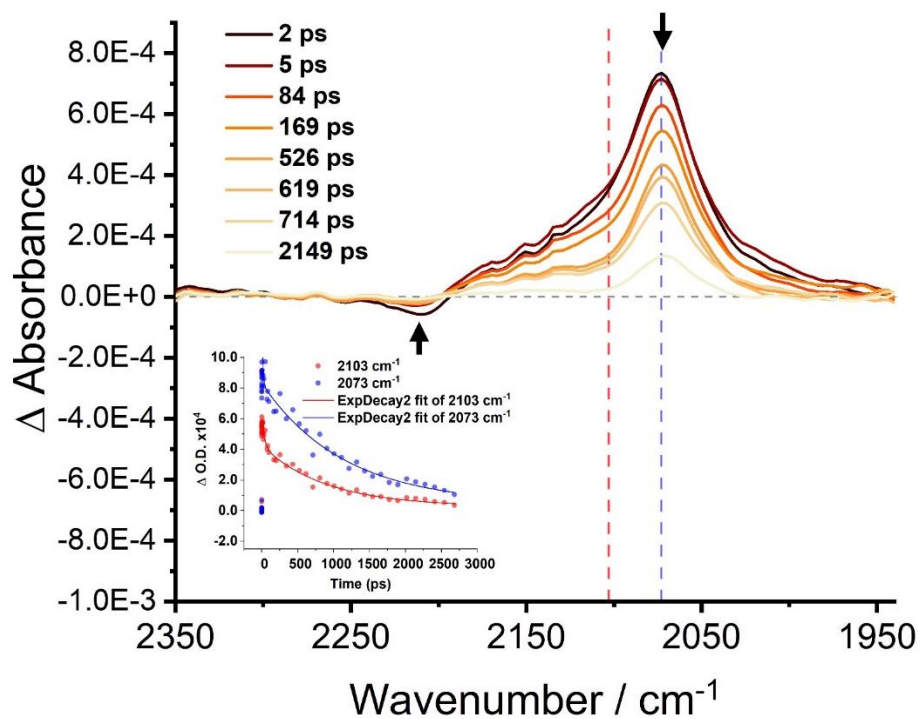


Figure S3.17. TRIR spectra of the copolymer in CHCl_3 following pulsed photolysis ($\lambda_{\text{exc}} = 525 \text{ nm}$) in the triple bond spectral region, recorded at various time delays, with arrows indicating the time dependent behaviour of the spectral features. Inset displays the kinetic traces at both 2103cm^{-1} and 2073cm^{-1} (corresponding to both red and blue dashed lines on spectra) and the biexponential fit (solid red and solid blue line) to obtain the decay lifetimes.

S3.10. Antimicrobial Evaluation

The antimicrobial activity of the copolymer was assessed using four different reference bacterial strain such as *Staphylococcus aureus* (*S.aureus*, ATCC 25923), methicillin-resistant *S.aureus* (MRSA, ATCC 43300), *Esherichia.coli* (*E.coli*, ATCC 25922) and an extended spectrum β -lactamase (ESBL) producing *E.coli* (CL11). All the bacterial strains were grown overnight at 37 °C on Mueller-Hinton (MH) agar and suspensions were prepared from isolated colonies to the density of a 0.5 McFarland standard (bioMèrieux, Ireland) and were further diluted 1/100 in phosphate buffered saline (PBS), pH 7.4 (approximately 1×10^6 CFU/mL, where CFU is colony forming units). Assays were prepared in micro centrifuge tubes and contained approximately 1×10^5 CFU/mL of Gram-positive and Gram-negative bacteria with 1 μ g/mL (1% DMSO) and 5 μ g/mL (5% DMSO) of OH polymer/monomer in phosphate buffered solution (PBS) respectively. The stability of the compound was confirmed in the solvent mixture using its absorption spectra, as shown in **Figure S3.18**. For irradiation, 100 μ L aliquots were transferred to the wells of a 96 well tissue culture plate which was irradiated for 15 minutes using a LED lamp with wavelength ($\lambda_{exc.} \sim 525$ nm). For non-irradiated controls, aliquots were transferred to another 96-well plate which was incubated in the dark for 15 minutes. The contents of the wells were then diluted, 1/100 with PBS and 100 μ L spread onto MH agar and incubated at 37 °C overnight before counting colony forming units (CFU). Control assays consisted of non-irradiated samples, addition of only DMSO and without addition of the copolymer.

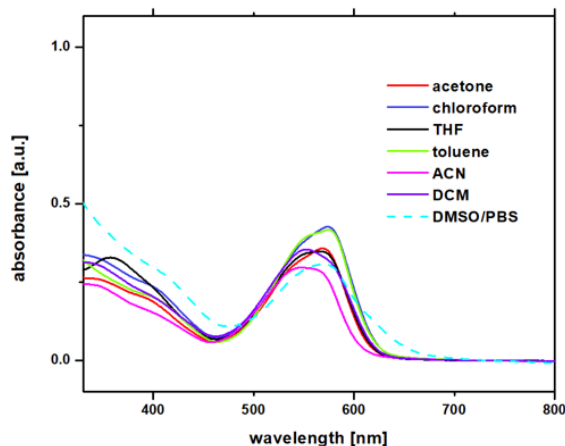


Figure S3.18. UV-visible absorption spectra of copolymer in a range of solvents; especially depicting the stability of the compound in a DMSO/PBS solvent mixture (cyan colour).

A comparative study on the activity of the copolymer over its monomer were performed. The similar assay as mentioned above were performed and the results are presented in **Figure S3.19** found below. Only on irradiation of the copolymer and monomer we can observe some bactericidal activity, where the copolymer shows an enhanced activity of > 80% killing of the gram-positive *S.aureus* and its resistant strain. The monomer shows < 5% killing for the Gram-positive bacteria whereas > 10% killing for Gram-negative strain only with the increased concentration of the complex. As we know, Gram-negative bacteria are more resistant to antibodies and antibiotics than Gram-positive bacteria, because they have a largely impermeable cell wall. We could observe a similar trend for our complexes as it shows around 60-80 % killing for the Gram-negative *E.coli* strain was observed under higher concentration of the copolymer. The huge leap in the activity of the complex from its monomeric form to copolymer opens up new approaches towards the BODIPY in their polymeric forms.

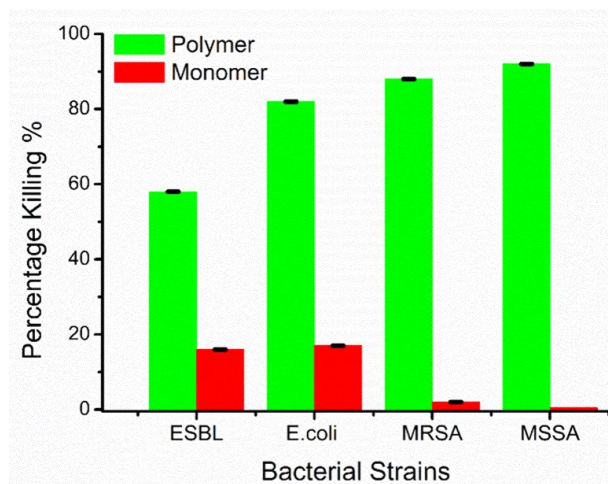


Figure S3.19. Comparison on the photoactivated bactericidal activity of copolymer and its BODIPY-2H, Conditions: Bacterial strains *Staphylococcus aureus* (MSSA, ATCC 25923), methicillin-resistant *S.aureus* (MRSA, ATCC 43300), *Esherichia.coli* (E.coli, ATCC 25922) and an extended spectrum β -lactamase (ESBL) producing *E.coli* (CL11), [copolymer/BODIPY-2H] for gram-positive bacteria: 1 $\mu\text{g}/\text{ml}$, [copolymer/monomer] for gram-negative bacteria: 5 $\mu\text{g}/\text{ml}$, time of irradiation: 15 minutes, wavelength of light for irradiation $\lambda \sim 525 \text{ nm}$.

S3.11. Cytotoxic study using MTT assay

Cell lines and Culture conditions

A human keratinocyte cell line (HaCaT) obtained from the American Type Culture Collection (ATCC) was used. Cells were routinely cultured in Dulbecco's modified Eagle's medium (DMEM) supplemented with 10% (v/v) fetal bovine serum (FBS) and maintained at 37 °C and 5% CO₂ atmosphere. Cells were passaged/harvested by detaching from tissue culture flasks using TrypLE™ Express (Gibco) for 5-10 min at 37 °C.

Cell Viability – MTT Assay

HaCaT cells were seeded in 96-well microtitre plates at a density of 1×10^5 cells/mL in 100 µL culture medium (DMEM with 10% (v/v) FBS) and incubated at 37 °C, 5% CO₂ for 48 h for cell attachment. Plates were washed with 100 µL Phosphate Buffered Saline (PBS) and treated with novel agents (5 µg to 250 µg) for 2h. Control wells were treated with triton X-100 (1%) instead of test agent. Following treatment, wells were washed with 100 µL PBS before adding 100 µL DMEM with 10% (v/v) FBS. Plates were incubated at 37 °C and 5% CO₂ for 24 hrs. Freshly prepared MTT (3-(4,5-dimethylthiazol-2-yl)-2,5-diphenyltetrazolium bromide) (100 µL of 5 mg/mL in culture medium without FBS or supplements) was added to each well, followed by incubation for 4h at 37 °C with 5% CO₂. The medium was discarded, and the cells were washed with PBS before adding 100 µL of MTT fixative solution (isopropanol) and incubating at room temperature with shaking for 4 min. Absorbance at 595 nm was measured in a Thermo Multiskan Ex plate reader.

Cytotoxicity of OH BODIPY to HaCaT cells

Measurement of OH BODIPY cytotoxicity to HaCaT cells using the MTT assay revealed a IC₅₀ value of 45.2 µg. This is the concentration resulting in the loss of viability of up to 50 % of HaCaT cells. This indicates some cytotoxicity to keratinocytes at concentrations close to those that resulted in > 5 log reduction in Gram-negative and > 3 log reduction to Gram-positive bacterial colony forming units.

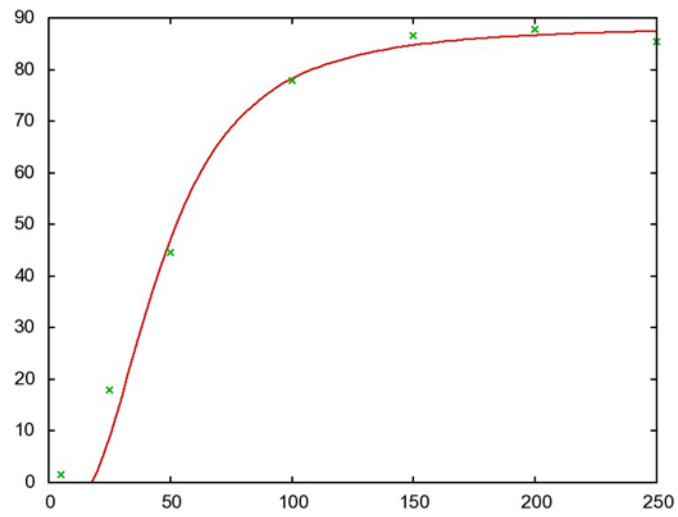


Figure S3.20. The half maximal inhibitory concentration (IC_{50}) curve of OH copolymer under varied concentration on the keratinocyte HaCaT cells.

S3.12.Bibliography

- (1) Greetham, G. M.; Burgos, P.; Qian, C.; Clark, I. P.; Codd, P. S.; Farrow, R. C.; George, M. W.; Kogimtzis, M.; Matousek, P.; Parker, A. W.; Pollard, M. R.; Robinson, D. A.; Zhi-Jun, X.; Towrie, M. *Appl. Spectrosc.* **2010**, *64* (12), 1311–1319.
- (2) Banfi, S.; Nasini, G.; Zaza, S.; Caruso, E. *Tetrahedron* **2013**, *69* (24), 4845–4856.
- (3) Epelde-Elezcano, N.; Martínez-Martínez, V.; Peña-Cabrera, E.; Gómez-Durán, C. F. A.; Arbeloa, I. L.; Lacombe, S. *RSC Adv.* **2016**, *6* (48), 41991–41998.
- (4) Yue, Y.; Guo, Y.; Xu, J.; Shao, S. *New J. Chem.* **2011**, *35* (1), 61–64.
- (5) Matsumoto, T.; Urano, Y.; Takahashi, Y.; Mori, Y.; Terai, T.; Nagano, T. *J. Org. Chem.* **2011**, *76* (10), 3616–3625.
- (6) Ozdemir, T.; Sozmen, F. *RSC Adv.* **2016**, *6* (13), 10601–10605.
- (7) Reichardt, C. *Chem. Rev.* **1994**, *94* (8), 2319–2358.

Appendix C

Supporting information associated with Chapter 4.

S4.1. Experimental Methods

S4.1.1. Fluorescence quantum yield calculation

Photoluminescence spectra of all samples were measured using the FLS1000 photoluminescence spectrometer (Edinburgh Instruments) using a 0.6 nm slit width for both the excitation and emission beam and 490 nm excitation wavelength. Accumulation of the steady-state spectra were obtained using 1 second dwell time and x 2 repeats per spectrum. All samples were isoabsorptive at the excitation wavelength ($\lambda_{\text{exc}} = 490 \text{ nm}$) i.e., all samples had the same optical density (~ 0.2) at the excitation wavelength. All emission spectra were recorded in CH_2Cl_2 at room temperature. The standard used was 3-pyridine H-BODIPY monomer where $\Phi_{\text{std}} = 0.62$ as per previously reported.¹ Fluorescence quantum yield was calculated using the following formula:

$$\Phi_{\text{sample}} = \Phi_{\text{std}} \cdot \left(\frac{I_{\text{sample}}}{I_{\text{std}}} \right) \cdot \left(\frac{\text{Abs}_{\text{std}}}{\text{Abs}_{\text{sample}}} \right)$$

where I_{sample} and I_{std} refers to the area under the emission curve of both the sample and the standard following 490 nm excitation. Abs_{std} and $\text{Abs}_{\text{sample}}$ denotes the absorbance of the sample and the standard at 490 nm in the UV-visible absorption spectrum prior to excitation. Corresponding emission spectra are displayed in **Figure S4.9**.

S4.1.2. Singlet oxygen quantum yield calculation

The singlet oxygen quantum yield (Φ_{Δ}) was measured using diiodo BODIPY monomer (IBDP) as the standard ($\Phi_{\text{std}} = 0.87$) in aerated dichloromethane solution using either 505 nm or 530 nm excitation.² The experimental set-up was identical to previously reported in the literature.³ The singlet oxygen quantum yield was calculation using the following formula:

$$\Phi_{\text{sample}} = \Phi_{\text{std}} \cdot \left(\frac{\text{Area}_{\text{sample}}}{\text{Area}_{\text{std}}} \right) \cdot \left(\frac{\text{Abs}_{\text{std}}}{\text{Abs}_{\text{sample}}} \right)$$

where $\text{Area}_{\text{sample}}/\text{Area}_{\text{std}}$ is the integrated area between 1230 – 1330 nm of the phosphorescence signal from singlet oxygen production and $\text{Abs}_{\text{std}}/\text{Abs}_{\text{sample}}$ is the absorption at 530 nm of both the standard and the sample, respectively.

S4.1.3. Electrochemical characterisation

Solutions of **M1** (17 mg.cm⁻³) and the polymer, **P1** (5.6 mg.cm⁻³) were prepared in anhydrous DMF. A glassy carbon electrode (3 mm diameter) was used as the working electrode. This electrode was polished successively with 1, 0.3 and 0.05 micron alumina powder with rinsing and ultrasonication after each polishing step, and was then allowed to dry in air. A micropipette was used to carefully drop cast 1.5 μL quantities of **M1** or **P1** solution onto the glassy carbon surface. The modified electrode was then stored in the dark overnight to allow the DMF solvent to evaporate. The nominal loading of the polymer films on the electrode was 0.36 mg.cm⁻² for **M1** and 0.12 mg.cm⁻² for **P1**. The experiments were conducted using a CH instruments 706c potentiostat in a standard three electrode cell with a background electrolyte of 0.1 M tetrabutylammonium hexafluorophosphate (TBAPF₆) in dry acetonitrile. A platinum wire served as the counter electrode. An Ag/Ag⁺ nonaqueous reference electrode (in 0.1 M TBAPF₆ and 0.01 M AgNO₃ in acetonitrile) was employed as the reference electrode. This electrode was calibrated against the ferrocene/ ferrocenium (Fc/Fc⁺) couple after each experiment, and all potentials are reported relative to Fc/Fc⁺. The electrolyte solution was degassed with nitrogen for at least 30 minutes before each measurement and an inert blanket of nitrogen was maintained above the solution during the recording of the voltammograms. The scan rate was 100 mV.s⁻¹ in all cyclic voltammetry experiments.

The absolute energies of the HOMO and LUMO levels were determined from the oxidation (E'_{ox}) and reduction onset potentials (E'_{ox} or E'_{red}) using the following equations:

$$E_{HOMO} = -(E'_{ox} \text{ (vs Fc/Fc}^+) + 4.8) \text{ eV}$$

$$E_{LUMO} = -(E'_{red} \text{ (vs Fc/Fc}^+) + 4.8) \text{ eV,}$$

where the difference between the Fc/Fc^+ level and the vacuum level is taken as 4.8 eV.⁴

S4.1.4. Time correlated single photon counting (TCSPC)

All samples were measured at room temperature and were purged with N_2 prior analysis. Samples were measured in a 1 cm x 1 cm quartz cuvette and the optical density was < 0.2 at 375 nm and 510 nm, ensuring an optically dilute solution to avoid inner-filter effects. For TCSPC, either a 375 nm or a 510 nm variable pulse length diode laser (EPL-375 or EPL-510) was utilised to excite the ground state sample. The accuracy of the fit of the decays was judged by chi-squared (χ^2) and sum of residuals was always $\chi^2 < 1.1$ for both monoexponential and biexponential fitting of decay curves. The fluorescence decay lifetime (τ) was obtained by the slope of the decay curve. All data analysis carried out using Edinburgh instrument Fluoracle[®] software.

S4.1.5. Time resolved spectroscopy

ps-ns TA and ps-ns TRIR experiments were carried out using the ULTRA instrument at the Central Laser Facility in the Rutherford Appleton Laboratory in the U.K. and the full experimental set-up is reported elsewhere.⁵ ns- μs transient absorption data were recorded using an Edinburgh Instruments LP980 Transient absorption spectrometer. Full details of the experimental set-up has previously been reported by us.⁶ All samples were degassed using three freeze-pump-thaw cycles in anhydrous THF solution in-house designed quartz cuvette (1 cm x 1 cm) prior to analysis. Samples were prepared to ensure an absorbance of 0.3 at the excitation wavelength of the laser (355 nm). UV-vis absorbance spectra for all compounds were obtained both before and after analysis to ensure no photodegradation had occurring during photoexcitation of the sample and no changes were observed. Triplet lifetimes of all samples in degassed THF solution was obtained from the slope of the recorded decay curves at the stated wavelengths using the LP900[®] software.

S4.1.6. Homogeneous photocatalytic hydrogen generation

Photocatalytic hydrogen experiments were carried out as per previously reported by the group.³ In brief, the multi-component photocatalytic solution consisting of the

polymer (2 mg), cobalt cobaloxime (2.5 mM) and ascorbic acid (0.1 M) in a 1:1 (v/v) THF: H₂O solvent system (8 mL total volume) was added to a 23 mL Schlenk tube equipped with an air-tight septum. Degassing of photocatalytic solution was carried out using three freeze-pump-thaw cycles to ensure oxygen was not present during photocatalysis. The Schlenk tube was blocked to external light prior to irradiation to ensure only the Xe arc lamp incident on the photocatalytic tube was the cause of the photocatalytic activity. The polymer (2 mg), cobalt cobaloxime (2.5 mM), ascorbic acid (0.1 M) was added to a 1:1 (v/v) THF: H₂O solvent system and degassed prior to irradiation. The aqueous solution containing the sacrificial agent was adjusted to pH = 5, using the appropriate amount of 0.2 M NaOH before addition to the photocatalytic solution. After degassing, the Schlenk tube was placed in a black box equipped with a fan to avoid thermal processes driving the catalytic cycle. All samples were irradiated with 300 W Xe arc lamp equipped with cut-off filter, $\lambda > 420$ nm. Control samples were left in the dark and measured at the same timepoints as described, no hydrogen was observed. Hydrogen formation was monitored over a period of 6 hours and quantified by taking a 1 mL sample of headspace from the Schlenk tube and then by injecting sample to a gas chromatogram (Shimadzu GC-2010) with a BID detector on a 5 Å molecular sieve column using He as a carrier gas, with oven temperature at 30 °C. Hydrogen obtained was measured against a calibration curve of standard injections, using commercially available standards of 0.01%, 0.1%, 1%, 2% and 5% respectively. All measurements were carried out in triplicate.

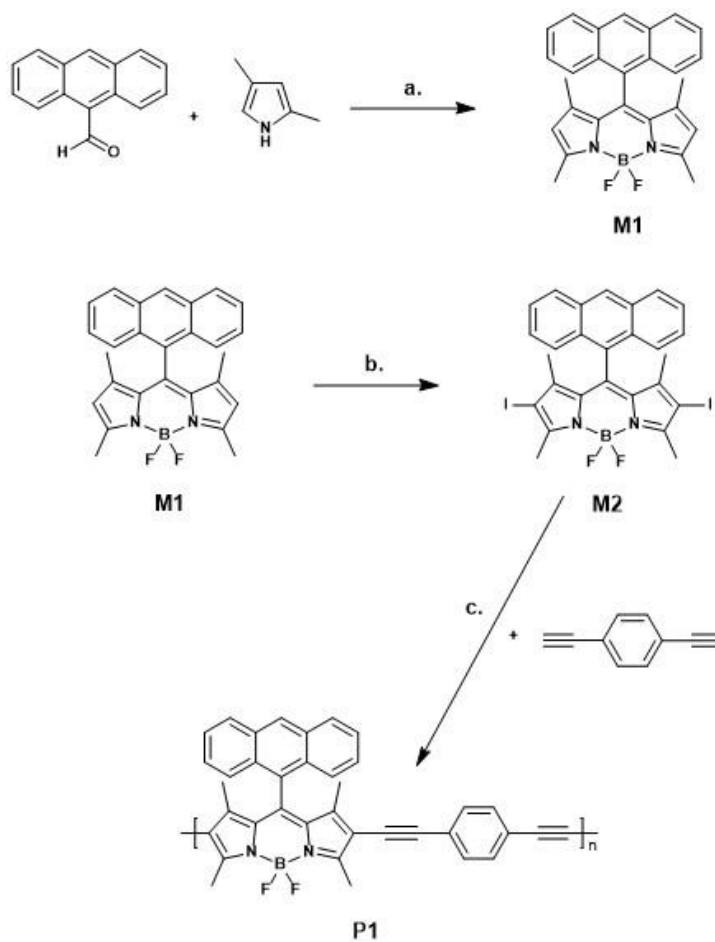
S4.1.7. Photodeposition of Pt on TiO₂

The photocatalyst Pt was deposited on TiO₂ nanoparticles through the photodeposition method.⁷ The solid powder of TiO₂ (50 mg) was added to an aqueous solution of H₂PtCl₆ (12.5 μL, 8 wt.% aqueous solution) and methanol (1.25 mL) in a Schlenk tube under nitrogen condition. The Schlenk tube was then subjected to irradiation by a 300 W Xenon arc lamp with continuous stirring for 40 minutes (no optical filter used). After irradiation, a grey solid was obtained which was collected by filtration and dried under vacuum at 70 °C. Therefore, approximately 30 mg of photodeposited Pt on TiO₂ was obtained which was further used for photocatalysis experiments.

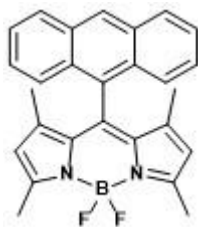
S4.1.8. Photocatalytic hydrogen evolution using Pt | TiO₂

For photocatalytic hydrogen evolution experiments containing Pt | TiO₂ nanoparticles (as prepared above), an appropriate amount of polymer, **P1** (0.1 – 1.2 mM), ascorbic acid (0.1 M) and Pt | TiO₂ nanoparticles (6 mg) were added to a 1:1 (v/v) THF: H₂O solvent system (4 mL total volume) in a 23 mL Schlenk tube. The resultant solution was then sealed with an air-tight septum and degassed (as above). The solution was sonicated for 15 minutes prior to irradiation to ensure a well dispersed solution. During the photocatalytic reaction, the reaction mixture was mixed using a magnetic stir bar at a rate of 300 rpm. All photocatalytic other irradiative conditions and hydrogen measurements were carried out as described above for the homogeneous photocatalytic set-up.

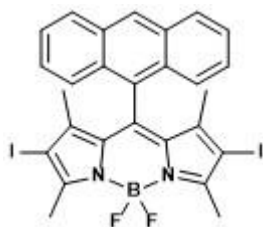
S4.2. Synthesis



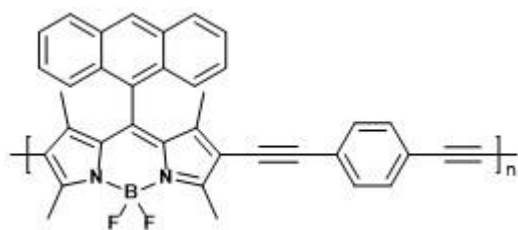
Scheme S4.1. Synthetic outline of **M1**, **M2** and **P1**. Reaction conditions a) i) TFA, ii) DDQ, iii) BF_3OEt_2 , TEA in dry CH_2Cl_2 under flow of N_2 , 2 days at room temperature, b) HIO_3 , I_2 in $\text{EtOH}/\text{H}_2\text{O}$ under flow of N_2 , 2 hours at 60°C , c) $[\text{Pd}(\text{PPh}_3)_4]$, CuI , dry THF/Diisopropylamine, 1:1 (v/v) under flow of N_2 , 3 days at 80°C .



Monomer 1, M1.⁸ To an oven-dried flask, 9-anthracene carboxaldehyde (413 mg, 2 mmol), 2,4-dimethylpyrrole (0.41 mL, 4 mmol) and 25 mL anhydrous CH₂Cl₂ were added under the flow of nitrogen. A drop of trifluoroacetic acid (TFA) was added to initiate the reaction (resulting in an immediate colour change from a clear pale yellow solution to a darker purple solution) and the solution was left to stir overnight at room temperature under inert conditions. After complete consumption of the aldehyde was confirmed using TLC (silica, CH₂Cl₂), 2,3-dichloro-5,6-dicyano-1,4-benzoquinone (DDQ) (454 mg, 2 mmol) was added and reaction was continually stirred for a further 4 hours. Then, boron trifluoride etherate (BF₃OEt₂) (2 mL) and triethylamine (TEA) (2 mL) were added dropwise over 15 minutes, the reaction solution was quickly stoppered and allowed to stir at overnight at room temperature under inert conditions. After this time, the reaction was stopped, and the resulting reaction solution was washed with saturated sodium bicarbonate solution and extracted with CH₂Cl₂. The organic phase was dried over MgSO₄ by stirring for 1 hour before filtration and removing the solvent under reduced pressure to give the crude product (dark purple solid). The crude product was purified by silica gel column chromatography (hexane: ethyl acetate, 8:1) to yield a red solid (178 mg, yield 21%). ¹H NMR (600 MHz, CDCl₃): δ 8.58 (s, 1H), 8.03 (dd, J = 8.4 Hz, 2H), 7.91 (dd, J = 8.7 Hz, 2H), 7.49 (m, 2H), 7.43 (m, 2H), 5.89 (s, 2H), 2.63 (s, 6H), 0.65 (s, 6H). ¹³C NMR (600 MHz, CDCl₃): δ 155.77, 142.90, 138.95, 132.36, 131.30, 129.68, 128.34, 128.26, 126.95, 125.74, 125.11, 121.16, 14.70, 13.33.



Monomer 2, M2.⁹ To an oven-dried flask, **M1** (110 mg, 0.26 mmol) and an excess amount of iodine (132 mg, 0.52 mmol) were added and dissolved in 30 mL ethanol (EtOH) under the flow of nitrogen. Iodic acid (114 mg, 0.65 mmol) was dissolved in 1.5 mL water and purged for 15 minutes. After this time, the aqueous iodic acid solution was added dropwise to the reaction solution over 10 minutes. The reaction was allowed to stir for 2 hours at 60 °C. After complete consumption of the **M1** was confirmed using TLC (silica, CH₂Cl₂), the solvent was removed using distillation. The crude product was then dissolved in CH₂Cl₂ and washed three times with saturated sodium thiosulphate solution. The organic phase was dried over MgSO₄ by stirring for 1 hour before filtration and removing the solvent under reduced pressure. Purification was carried out using silica gel column chromatography (CH₂Cl₂ 100%) to yield a dark red solid (162 mg, yield 92%). ¹H NMR (600 MHz, CDCl₃): δ 8.63 (s, 1H), 8.05 (dd, J = 8.5 Hz, 2H), 7.81 (dd, J = 8.8 Hz, 2H), 7.51 (m, 2H), 7.45 (m, 2H), 2.72 (s, 6H), 0.67 (s, 6H). ¹³C NMR (600 MHz, CDCl₃): δ 157.22, 145.26, 145.07, 131.44, 129.04, 128.68, 127.56, 127.33, 126.10, 126.00, 125.05, 124.85, 82.32, 15.95, 13.71.



Copolymer, P1. The synthetic procedure for the synthesis of the polymer was carried out as per previously reported with slight modifications.³ To an oven-dried flask, **M2** (162 mg, 0.24 mmol), 1,4-diethynylbenzene (30 mg, 0.24 mmol), copper (I) iodide (5 mg, 0.02 mmol, 10 mol%) and tetrakis(triphenylphosphine)-palladium(0) (28 mg, 0.02 mmol, 10 mol%) were added under the flow of nitrogen. The flask was evacuated three times using vacuum, before addition of anhydrous THF (10 mL) and diisopropylamine (10 mL) under the flow of nitrogen. The reaction flask was stirred at reflux ~ 80 °C for 72 hours, until complete consumption of **M2** was confirmed using TLC (silica, CH_2Cl_2). After this time, the solvent mixture was removed by distillation. The crude polymer was dissolved in CH_2Cl_2 and washed three times with saturated sodium bicarbonate solution. The organic layer was dried over MgSO_4 . Purification was carried out by addition of a concentrated solution of the polymer in CH_2Cl_2 to ice-cold EtOH (~ 80 mL). The precipitate was collected via vacuum filtration and allowed to dry overnight to yield a dark purple solid (82 mg). ^1H NMR (600 MHz, CDCl_3): δ 7.70-7.64 (br, Ar-H), 7.57-7.53 (br, Ar-H), 7.49-7.44 (br, Ar-H), 2.63 (br, CH_3 at 3, 5 position of BODIPY), 0.65 (br, CH_3 at 1, 7 position of BODIPY). SEC results Batch 1: M_n : 6194 g/mol, M_w : 7631 g/mol, PDI: 1.23. SEC results Batch 2: M_n : 7197 g/mol, M_w : 9521 g/mol, PDI: 1.31.

S4.3. NMR spectra

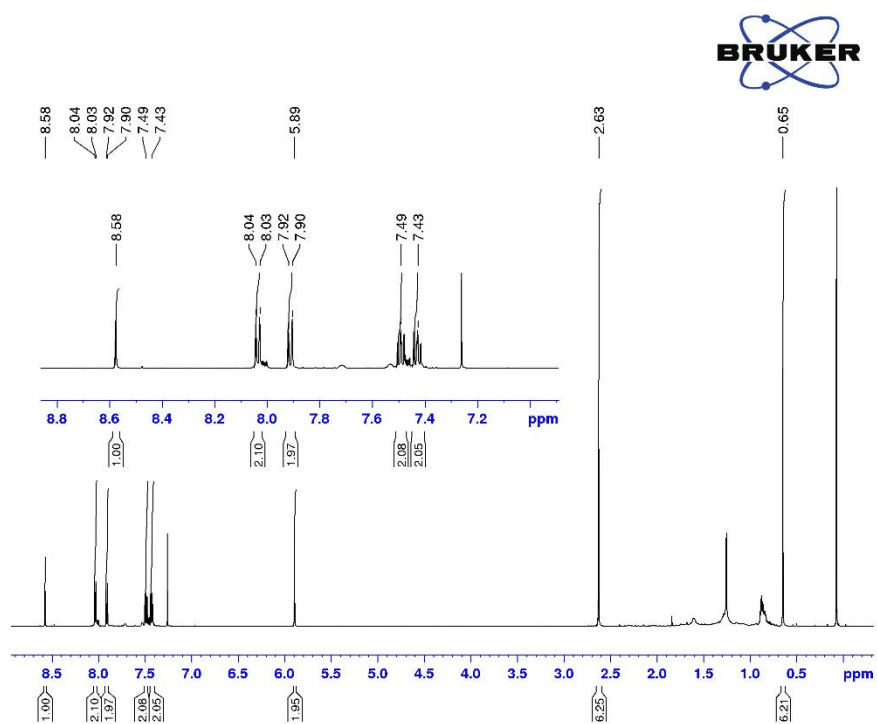


Figure S4.1. ^1H NMR spectra of **M1**. CDCl_3 as a calibration standard, $\delta = 7.26$ ppm.

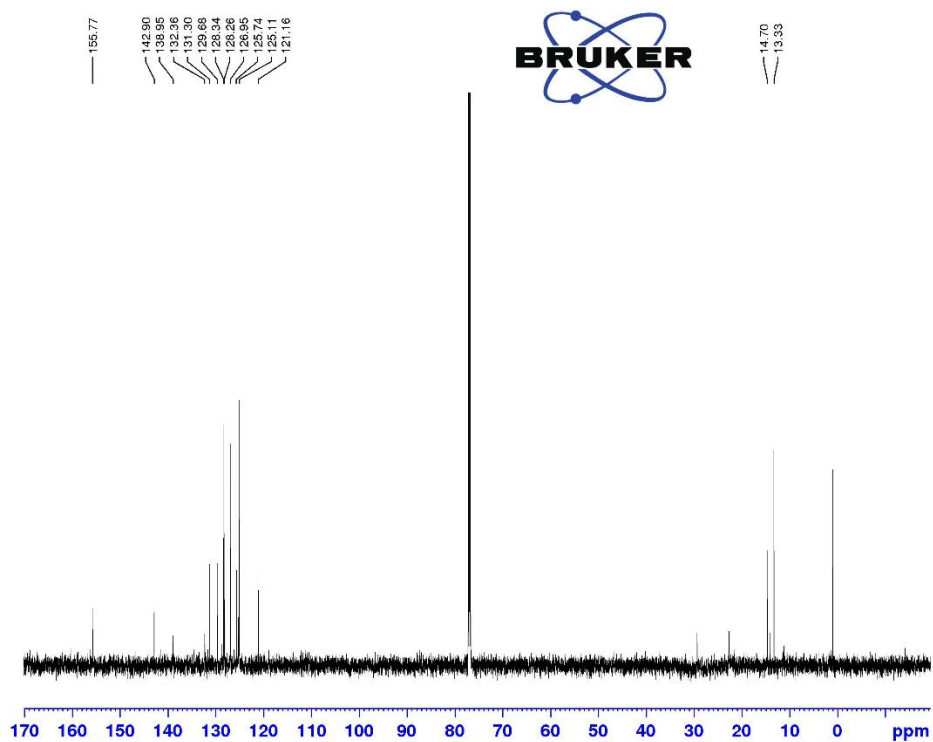


Figure S4.2. ^{13}C NMR spectra of **M1**. CDCl_3 as a calibration standard, $\delta = 77.16$ ppm.

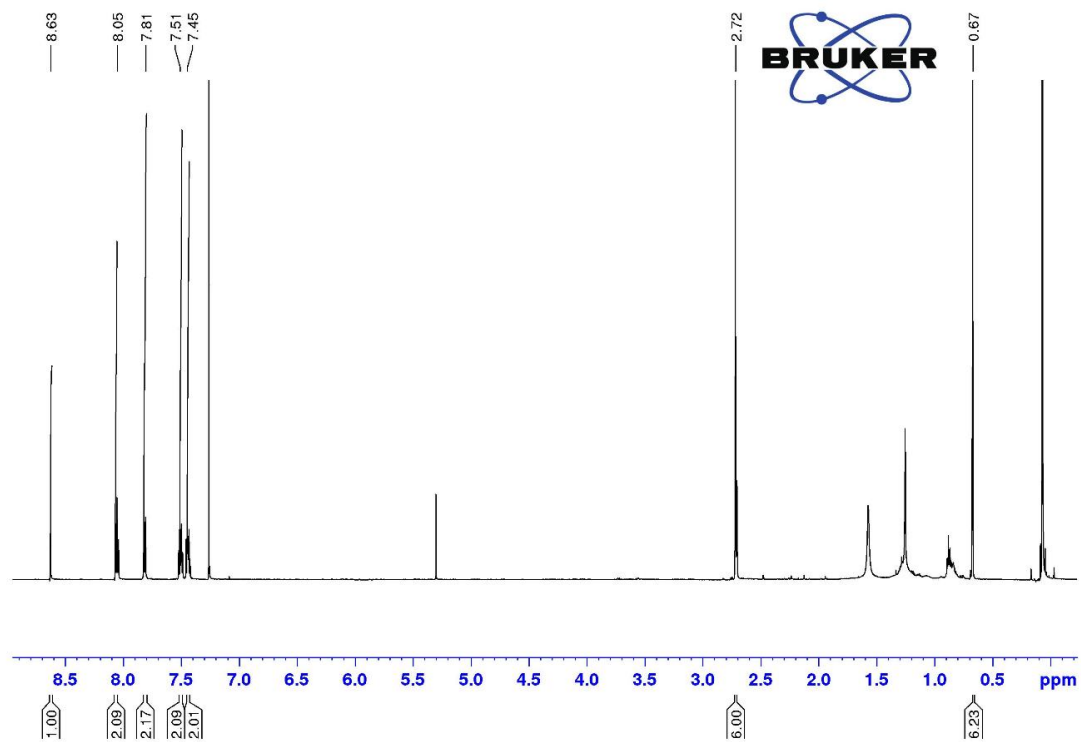


Figure S4.3. ^1H NMR spectra of **M2**. CDCl_3 as a calibration standard, $\delta = 7.26$ ppm.

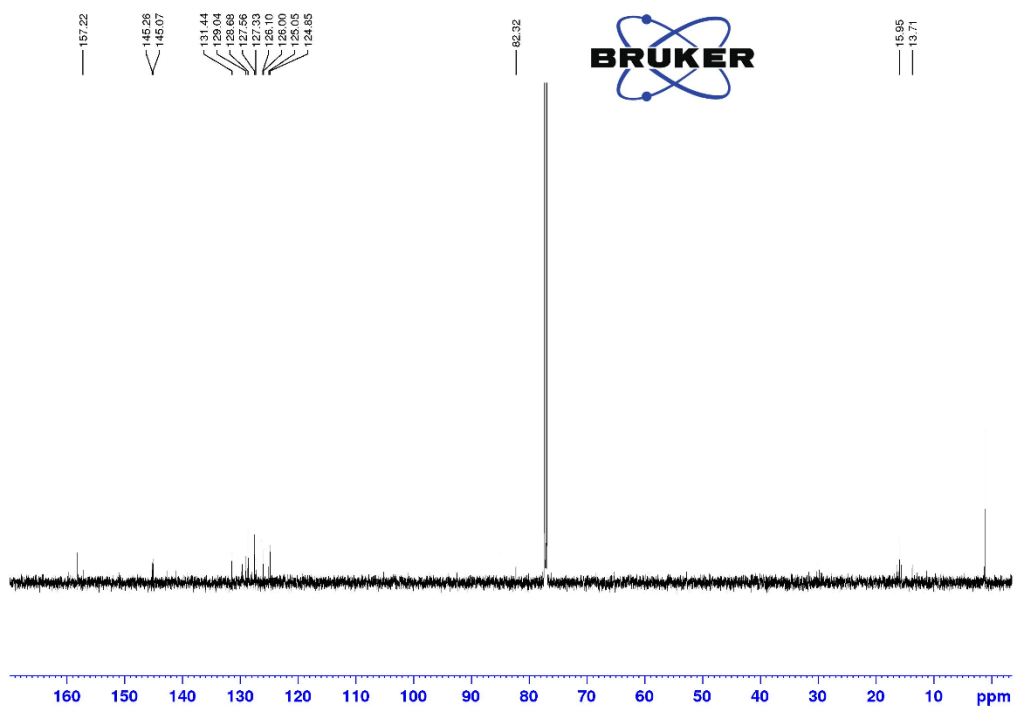


Figure S4.4. ^{13}C NMR spectra of **M2**. CDCl_3 as a calibration standard, $\delta = 77.16$ ppm.

S4.4. Size exclusion chromatography (SEC)

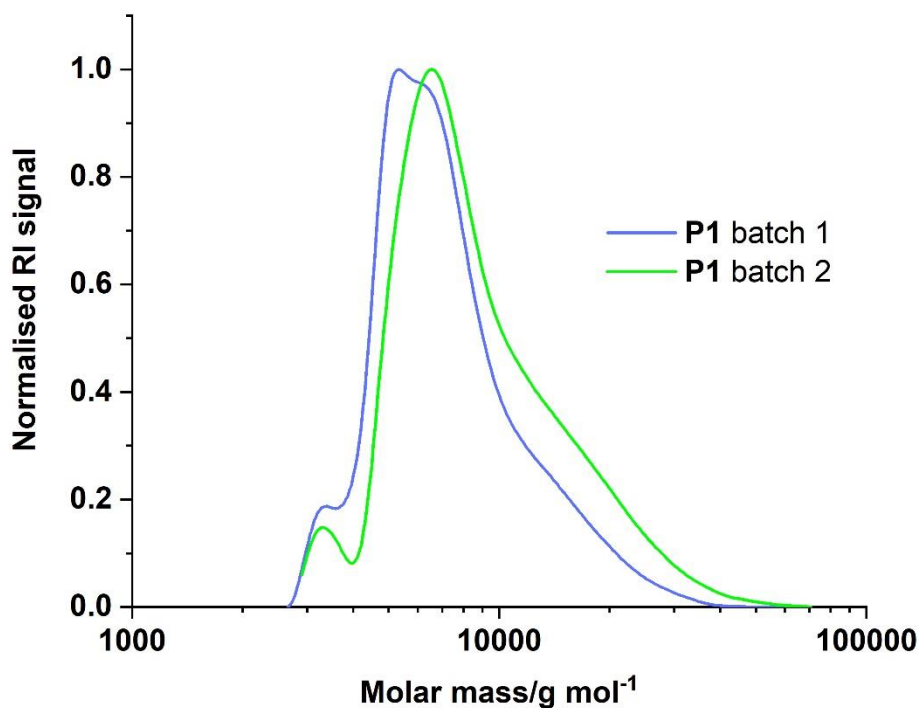


Figure S4.5. SEC results of **P1** showing the molecular weight distribution (g/mol) of the copolymeric chain for batch 1 (blue solid line) and batch 2 (green solid line). Both synthetic procedures for the synthesis of the polymer were carried out under identical experimental conditions, as per synthetic method described.

Table S4.1. SEC results of **P1** showing the number average molecular weight of the polymer (M_n), the weight average molecular weight (M_w) and the polydispersity of the polymer (\mathcal{D}_M), calculated by M_w/M_n . The different batches of polymer indicate separate synthetic reactions under identical experimental conditions.

	M_n (g/mol)	M_w (g/mol)	\mathcal{D}_M
P1 (batch 1)	6200	7631	1.2
P1 (batch 2)	7200	9521	1.3

S4.5. FTIR spectra

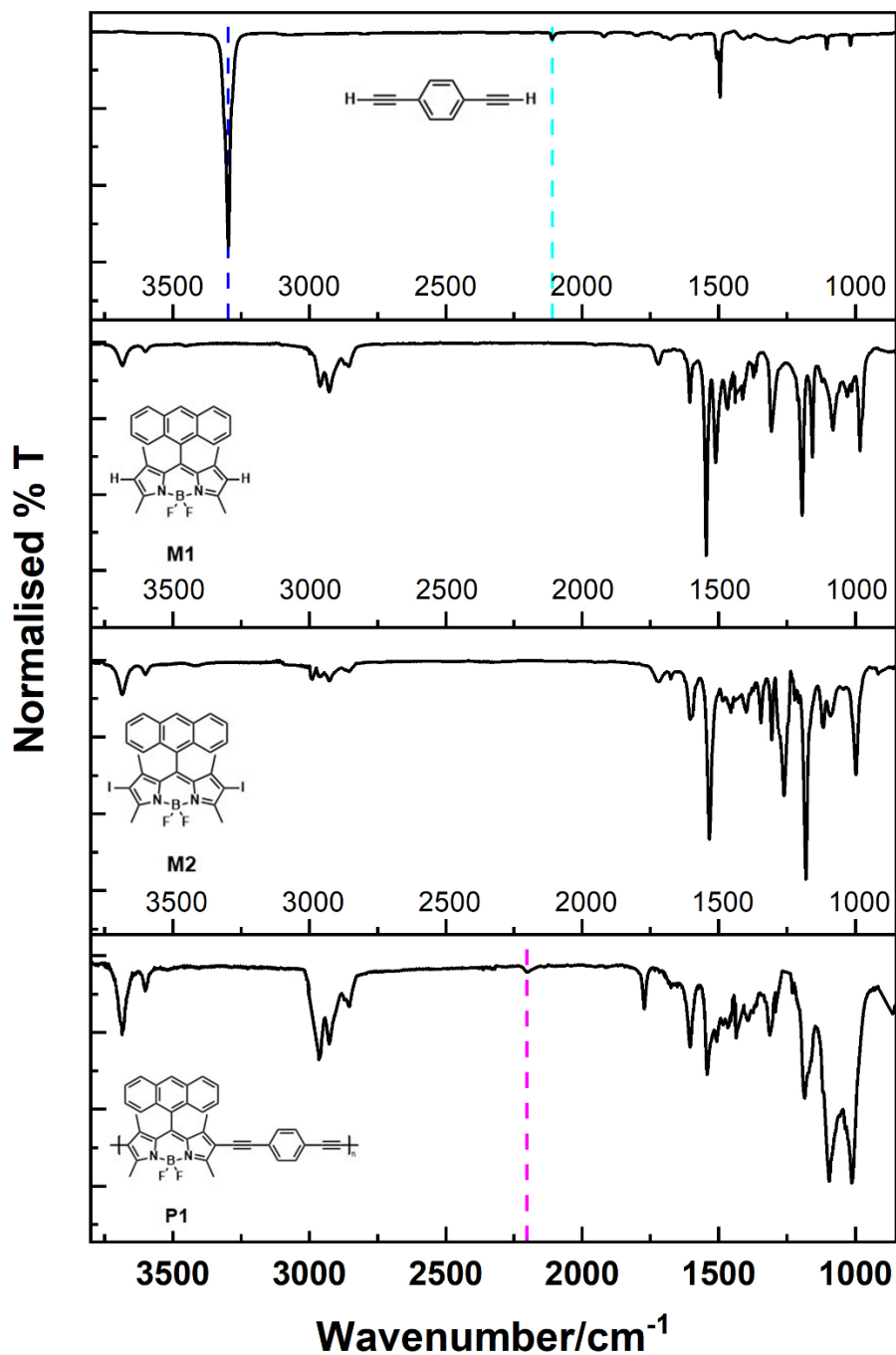


Figure S4.6. FTIR spectra of 1,4-diethynylbenzene, **M1**, **M2** and **P1** in CH₂Cl₂ showing the molecular structure of each compound in inset. The assignment of vibrational bands are shown for C≡C at 2109 cm⁻¹ (cyan dashed line) and for terminal C≡C-H at 3297cm⁻¹ (blue dashed line) for 1,4-diethynylbenzene and at 2203cm⁻¹ for C≡C of **P1** (magenta dashed line).

S4.6. UV-visible absorption and emission spectra

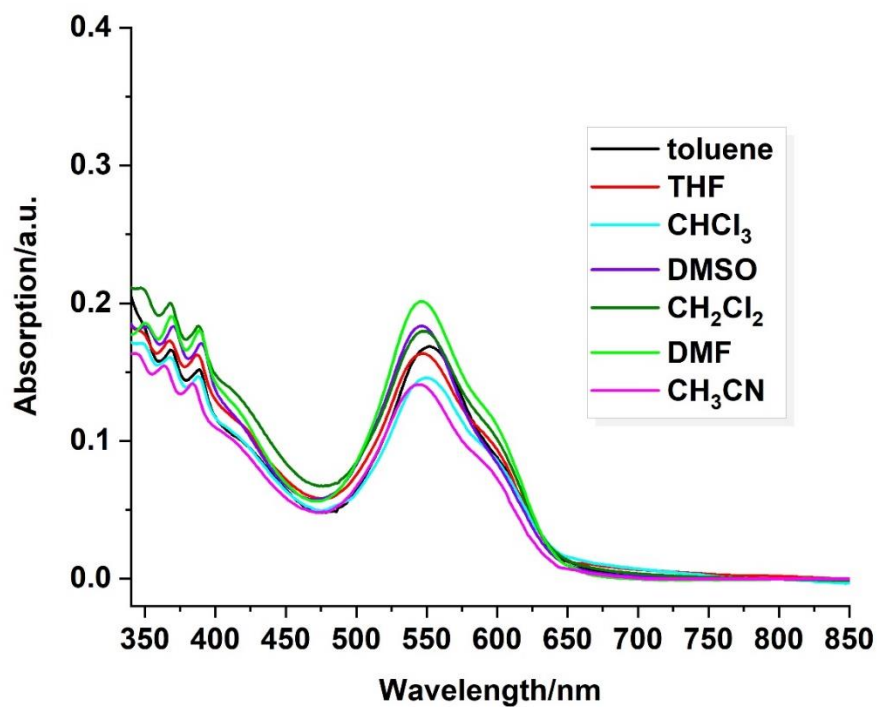


Figure S4.7. UV-visible absorption spectra of **P1** in toluene (black solid line), THF (red solid line), CHCl₃ (cyan solid line), DMSO (violet solid line), CH₂Cl₂ (olive solid line), DMF (green solid line) and CH₃CN (magenta solid line).

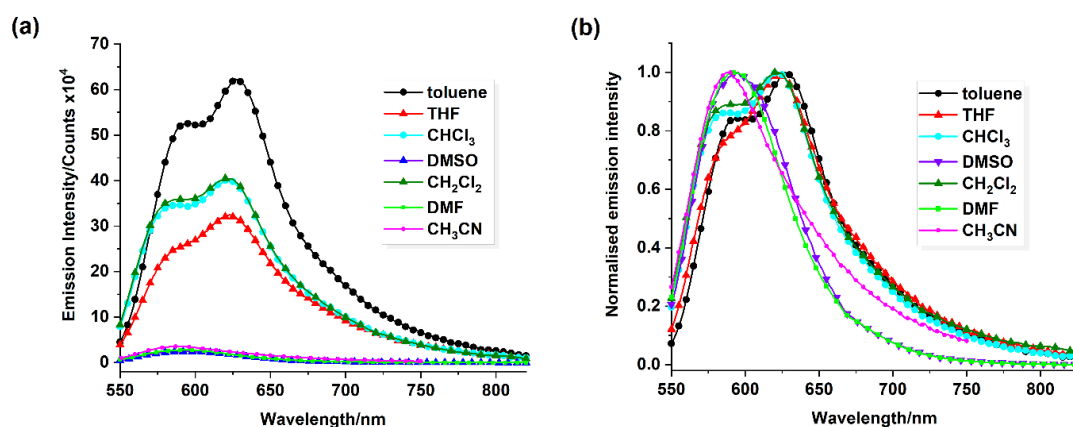


Figure S4.8. a) Photoluminescence spectra of **P1** in toluene (black circles), THF (red triangles), CHCl₃ (cyan circles), DMSO (violet triangles), CH₂Cl₂ (olive triangles), DMF (green circles) and CH₃CN (magenta circles), recorded using 1.0 nm slit width, $\lambda_{\text{exc}} = 540$ nm and (b) normalised spectra in the same solvents, $\lambda_{\text{exc}} = 540$ nm.

Table S4.2. Summary of absorption and emission maxima for **P1** in toluene, THF, CHCl₃, DMSO, CH₂Cl₂, DMF and CH₃CN. Reichardt parameter (E_T) is shown to indicate the solvent polarity.¹⁰ Emission spectra were collected following 540 nm excitation wavelength with 1.0 nm slit width for all samples. All samples recorded at room temperature.

Solvent (E_T)	λ_{abs} (nm)	λ_{em} (nm)
Toluene (33.9)	552	627
THF (37.4)	548	623
CHCl ₃ (39.1)	550	622
CH ₂ Cl ₂ (40.7)	550	622
DMSO (45.1)	546	594
DMF (43.2)	546	591
CH ₃ CN (45.1)	544	589

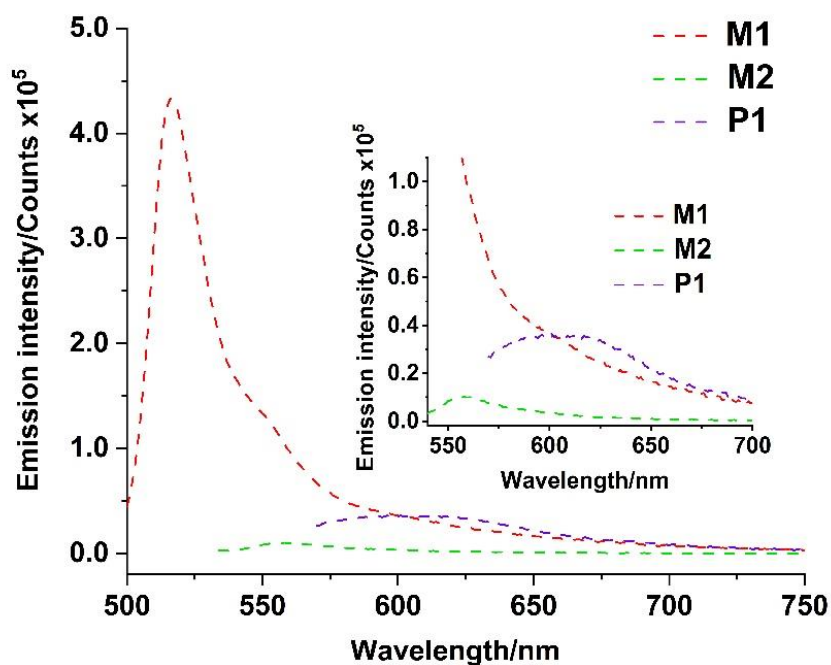


Figure S4.9. Photoluminescence spectra of **M1** (red dashed line), **M2** (green dashed line) and **P1** (purple dashed line) using 490 nm excitation and 0.6 nm slit width for both the excitation and emission beam. Samples were isoabsorptive at the excitation wavelength. All samples recorded at room temperature in CH₂Cl₂. Inset displays zoomed part of the spectra between 540 – 700 nm.

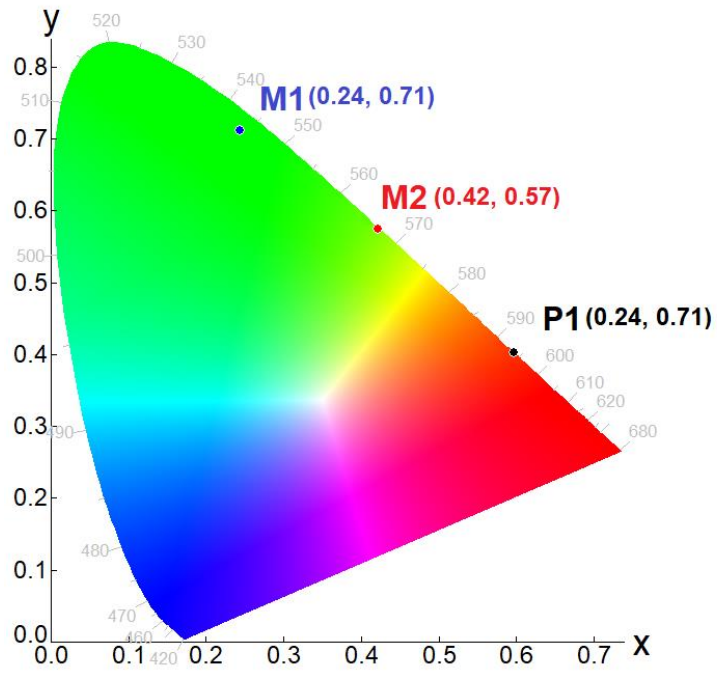


Figure S4.10. CIE diagram of the luminescence of **M1** (blue), **M2** (red) and **P1** (black) each showing x and y co-ordinates in brackets.

S4.7. Excitation spectra

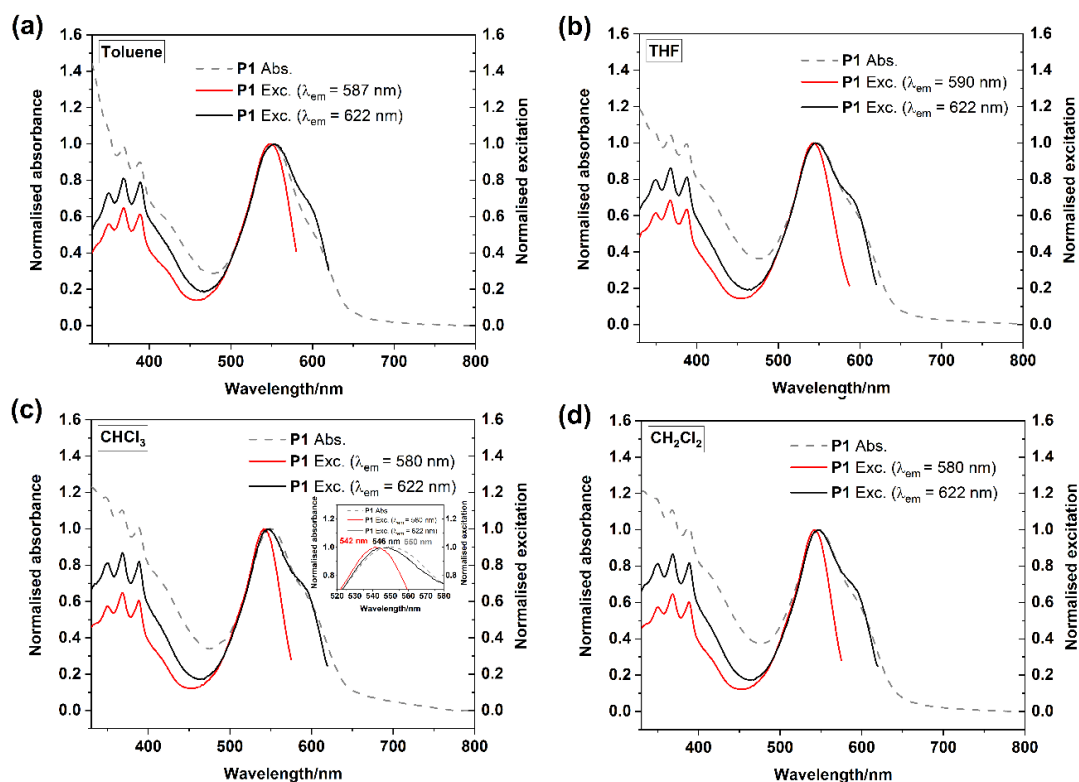


Figure S4.11. Normalised absorption (grey dashed spectra) and excitation spectra (solid red and solid black line) of **P1** in (a) toluene, (b) THF, (c) CHCl_3 (inset showing zoomed part of spectra from 520 – 580 nm) and (d) CH_2Cl_2 . Emission detection wavelengths used for each excitation spectra are shown in the legend.

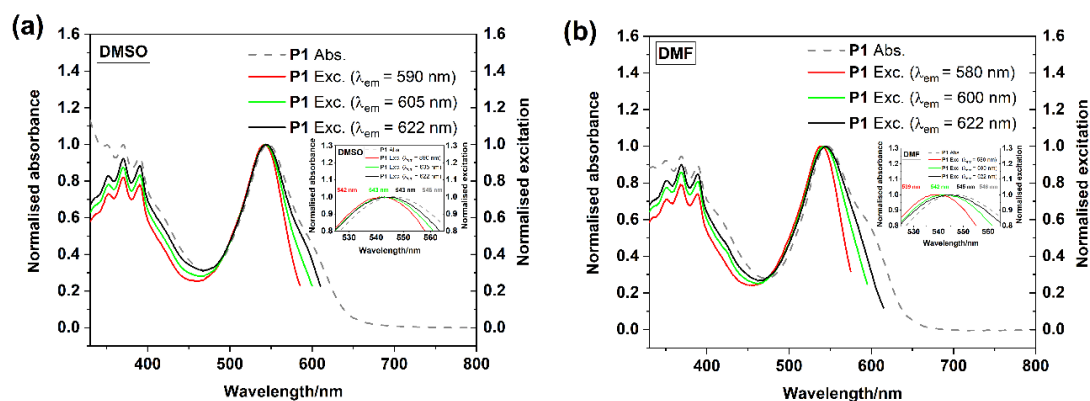


Figure S4.12. Normalised absorption (grey dashed spectra) and excitation spectra (solid red, solid green, and solid black line) of **P1** in (a) DMSO and (b) DMF. Insets showing zoomed part of spectra from 525 – 565 nm. Emission detection wavelengths used for each excitation spectra are shown in the legend.

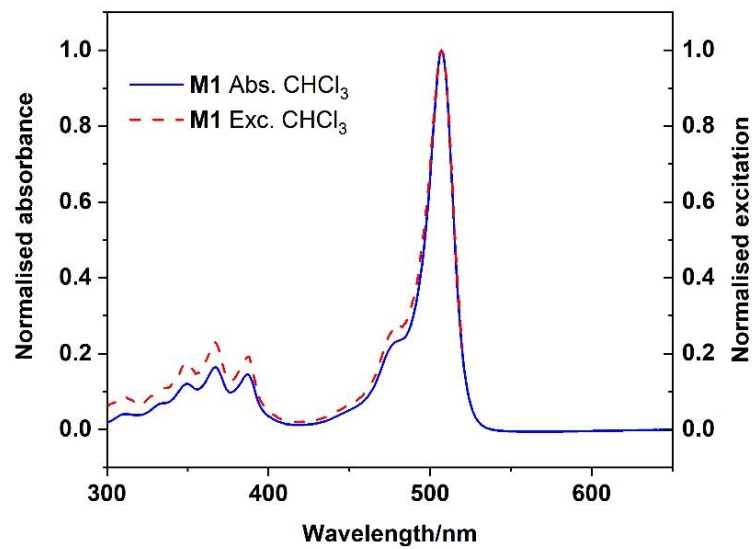


Figure S4.13. Normalised absorption spectra (blue solid line) and excitation spectra (red dashed line) of **M1** in CHCl₃. The excitation spectrum is observed at 530 nm.

S4.8. Singlet oxygen NIR emission spectra

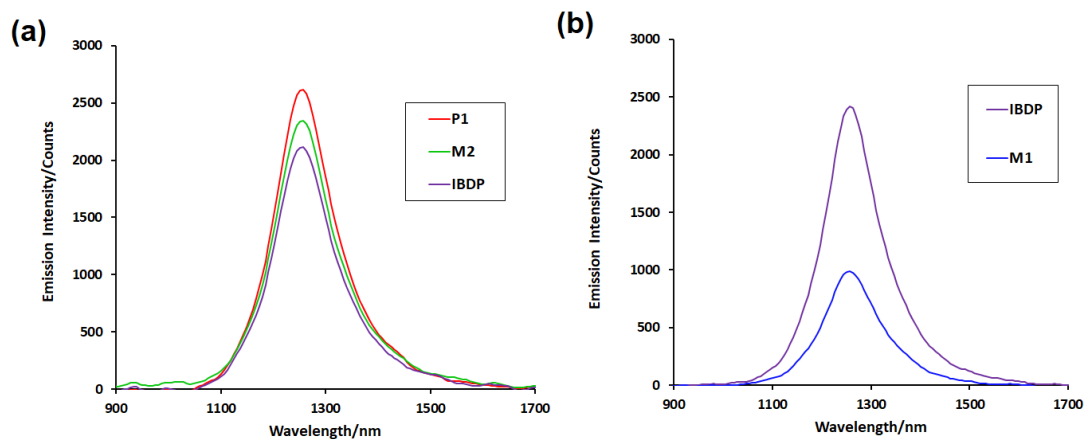


Figure S4.14. a) Singlet oxygen NIR emission of **P1** (red solid line) and **M2** (green solid line) following 530 nm excitation and b) singlet oxygen NIR emission of **M1** (blue solid line) following 505 nm excitation. The purple spectra in (a) and (b) represent the standard, diiodo BODIPY monomer ($\Phi_{\Delta} = 0.87$), **IBDP**.² All samples were recorded in aerated dichloromethane solution at room temperature.

S4.9. Time correlated single photon counting (TCSPC)

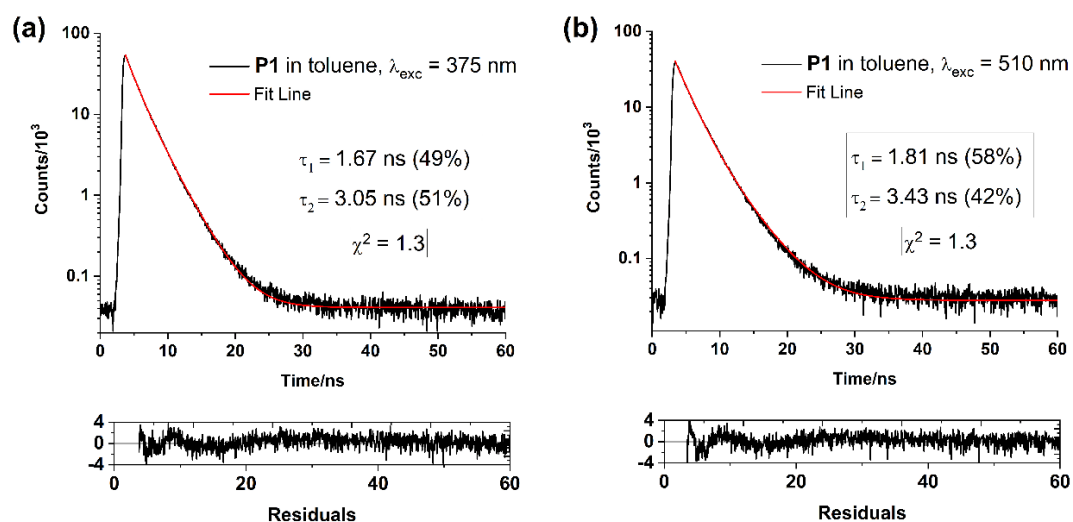


Figure S4.15. Emission decay of **P1** in toluene using a) 375 nm LED as excitation source and b) 510 nm LED as excitation source. $\lambda_{\text{det}} = 622$ nm. Inset shows biexponential lifetimes obtained (τ_1 and τ_2 (ns)), the percentage contribution of each lifetime component in brackets (%) and the goodness of fit (χ^2). The sum of residuals is shown below each emission decay curve.

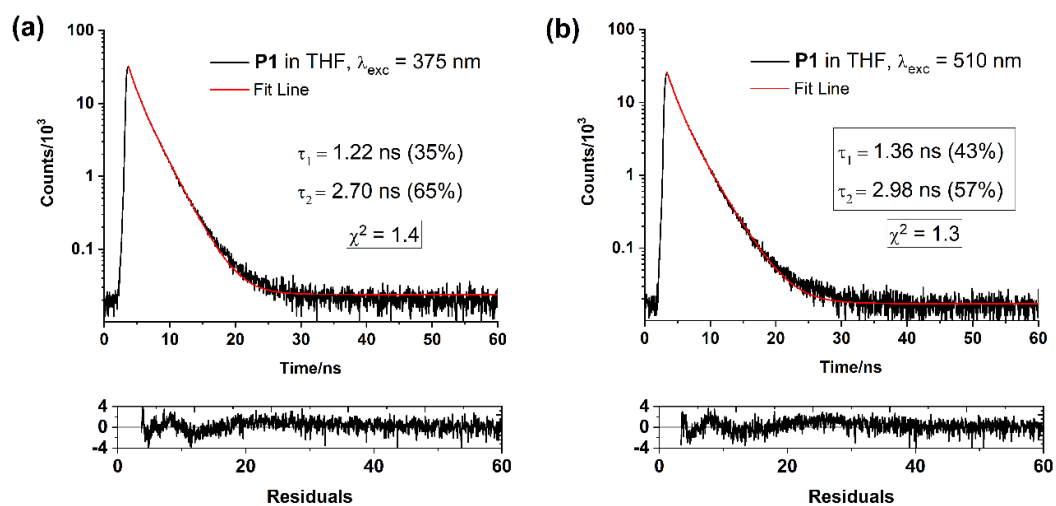


Figure S4.16. Emission decay of **P1** in THF using a) 375 nm LED as excitation source and b) 510 nm LED as excitation source. $\lambda_{\text{det}} = 622$ nm. Inset shows biexponential lifetimes obtained (τ_1 and τ_2 (ns)) and the percentage contribution of each lifetime component in brackets (%) and the goodness of fit (χ^2). The sum of residuals is shown below each emission decay curve.

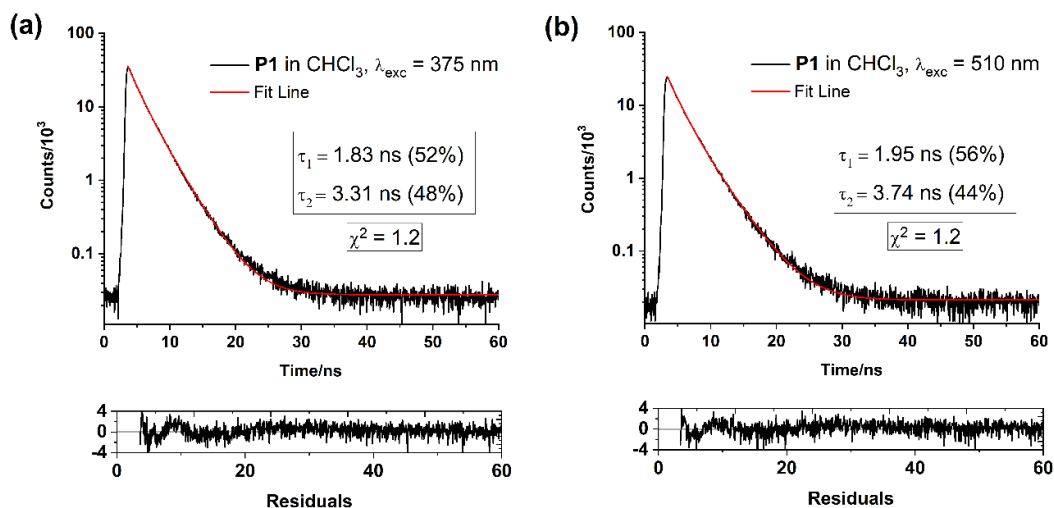


Figure S4.17. Emission decay of **P1** in CHCl₃ using a) 375 nm LED as excitation source and b) 510 nm LED as excitation source. $\lambda_{\text{det}} = 622$ nm. Inset shows biexponential lifetimes obtained (τ_1 and τ_2 (ns)) and the percentage contribution of each lifetime component in brackets (%) and the goodness of fit (χ^2). The sum of residuals is shown below each emission decay curve.

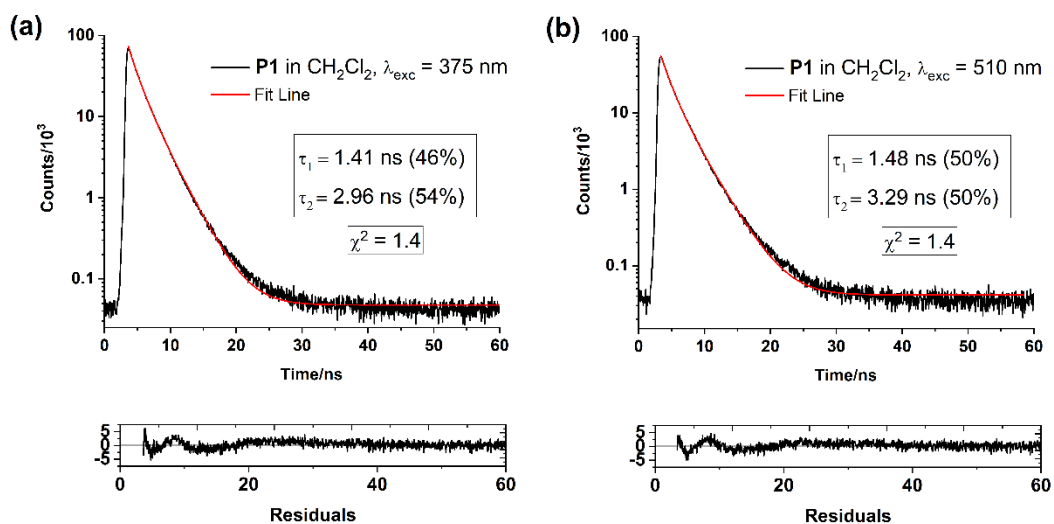


Figure S4.18. Emission decay of **P1** in CH₂Cl₂ using a) 375 nm LED as excitation source and b) 510 nm LED as excitation source. $\lambda_{\text{det}} = 622$ nm. Inset shows biexponential lifetimes obtained (τ_1 and τ_2 (ns)) and the percentage contribution of each lifetime component in brackets (%) and the goodness of fit (χ^2). The sum of residuals is shown below each emission decay curve.

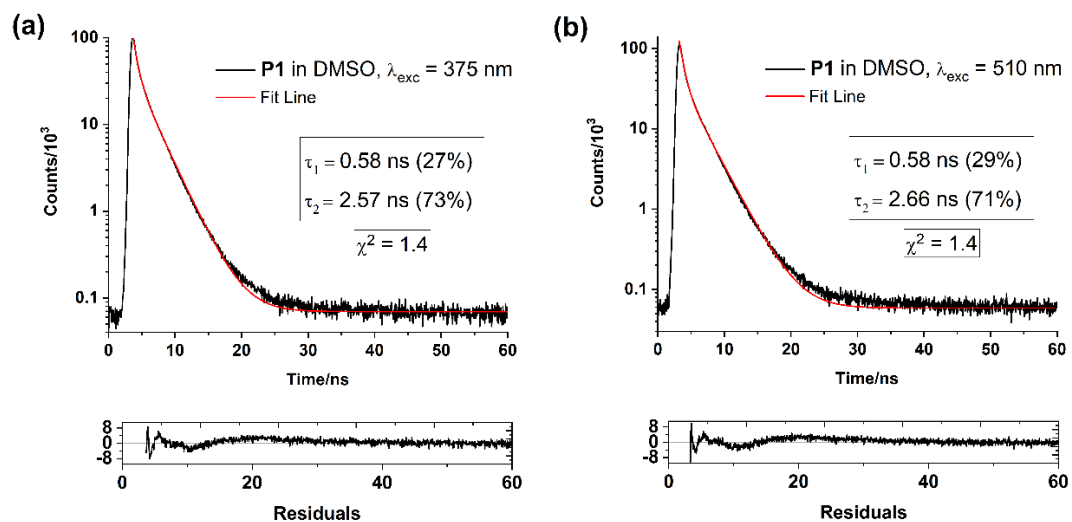


Figure S4.19. Emission decay of **P1** in DMSO using a) 375 nm LED as excitation source and b) 510 nm LED as excitation source. $\lambda_{\text{det}} = 590$ nm. Inset shows biexponential lifetimes obtained (τ_1 and τ_2 (ns)) and the percentage contribution of each lifetime component in brackets (%) and the goodness of fit (χ^2). The sum of residuals is shown below each emission decay curve.

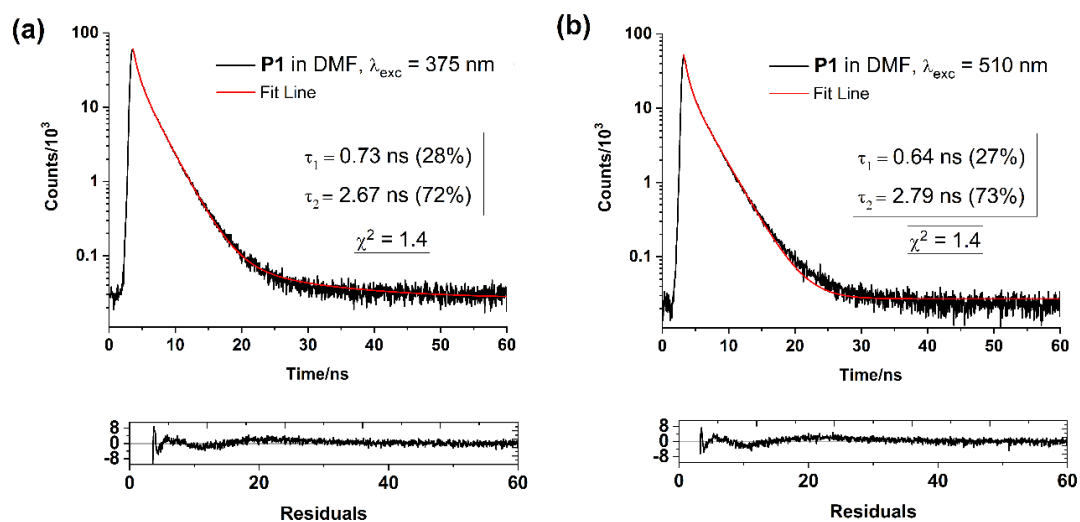


Figure S4.20. Emission decay of **P1** in DMF using a) 375 nm LED as excitation source and b) 510 nm LED as excitation source. $\lambda_{\text{det}} = 590$ nm. Inset shows biexponential lifetimes obtained (τ_1 and τ_2 (ns)) and the percentage contribution of each lifetime component in brackets (%) and the goodness of fit (χ^2). The sum of residuals is shown below each emission decay curve.

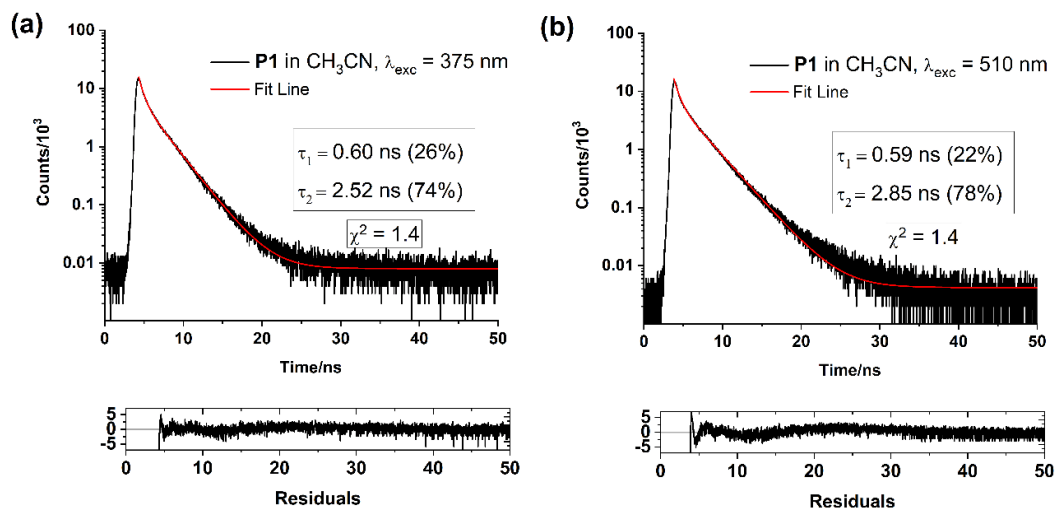


Figure S4.21. Emission decay of **P1** in CH₃CN using a) 375 nm LED as excitation source and b) 510 nm LED as excitation source. $\lambda_{\text{det}} = 590$ nm. Inset shows biexponential lifetimes obtained (τ_1 and τ_2 (ns)) and the percentage contribution of each lifetime component in brackets (%) and the goodness of fit (χ^2). The sum of residuals is shown below each emission decay curve.

S4.10. Quantum chemical calculations

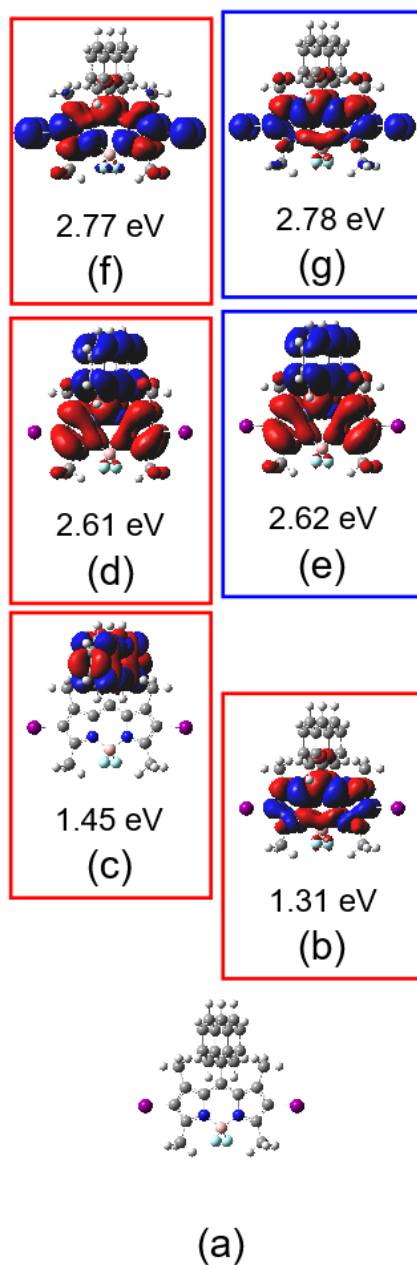


Figure S4.22. a) The optimised molecular structure of M2 with the two iodine atoms indicated in purple and the anthracenyl substituents towards the top of the molecule, b) the EDDM for the lowest energy triplet state T_1 , c) the T_2 state which is an anthracenyl-based state, d) and e) are nearly degenerate anthracenyl-to-BODIPY charge-transfer states (T_3 and S_1) while f) and g) are BODIPY-centred states where (g) can be optically populated (i.e., the S_2 state) (red boxes indicate triplet and blue represent singlet states).

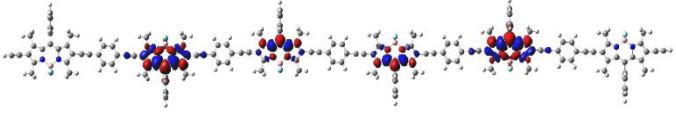
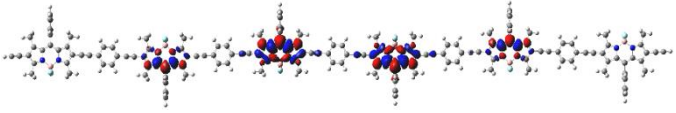
Table S4.3. The energy (eV), multiplicity, oscillator strength and electron density difference maps for **M2** (red volumes are regions where the electron density is greater in the excited state compared to the ground state and blue volumes are regions where the electron density in the excited state is less than that of the ground state).

Energy eV	Multiplicity	Oscillator Strength	Electron Density Map
2.7799	Singlet	0.8062	
2.7717	Triplet	0	
2.6191	Singlet	0	
2.6092	Triplet	0	

1.4520	Triplet	0	
1.3124	Triplet	0	
0	Singlet	Ground State	

Table S4.4. The multiplicity, energy (eV) and electron density difference maps (iso value 0.0002) for the twelve lowest energy excited states of the 6-BODIPY oligomer (cam-B3LYP/6-31G(d,p) (red volumes are regions where the electron density is greater in the excited state compared to the ground state and blue volumes are regions where the electron density in the excited state is less than that in the ground state).

Excited State	Multiplicity	Energy eV	Electron Density Difference Map (iso value =0.0002)
12	Singlet	2.3601	
11	Triplet	2.1531	
10	Triplet	2.1429	
9	Triplet	2.1304	
8	Triplet	2.1189	
7	Triplet	2.1111	
6	Triplet	1.2729	
5	Triplet	1.2729	
4	Triplet	1.2692	
3	Triplet	1.2689	

2	Triplet	1.2685	
1	Triplet	1.2682	

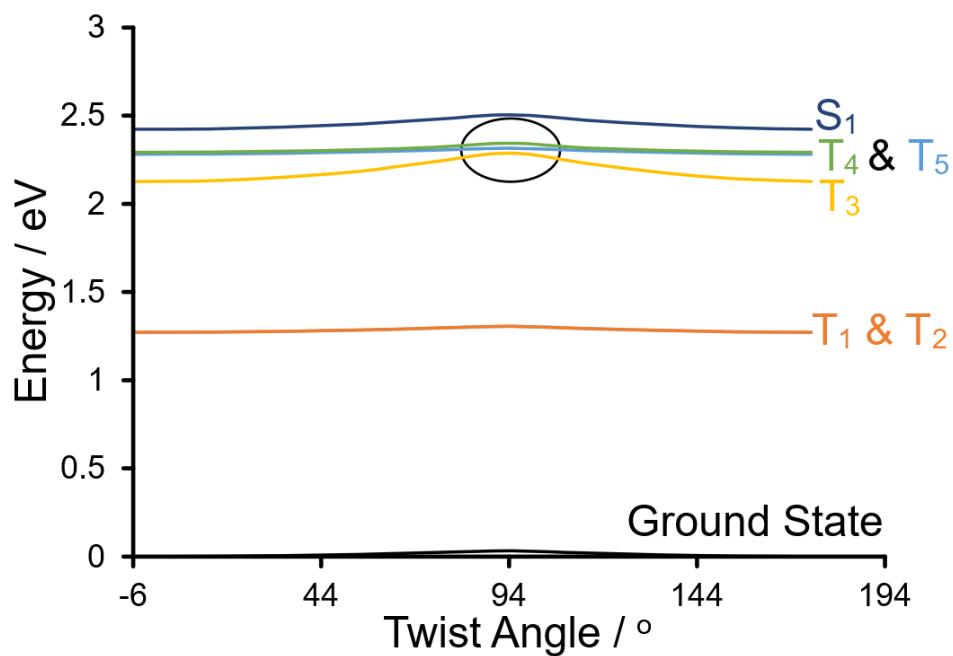


Figure S4.23. The energy variation of the ground-state and all excited states up to and including the lowest energy singlet excited state against dihedral angle between BODIPY units in the 2-BODIPY oligomer.

Table S4.5. The vertical excitation energies to the lowest energy singlet state, and equivalent wavelengths as the dihedral angle between the BODIPY units in the 2-BODIPY oligomer was varied.

Dihedral angle	eV	nm
174	2.423	512
154	2.427	511
134	2.438	508
114	2.455	505
94	2.474	501
74	2.457	505
54	2.440	508
34	2.430	510
14	2.423	512
-6	2.422	512

Table S4.6. The calculated absorption (based on the energy difference between the ground-state and S_1 state) and emission based on the energy difference between the $^1(TT)$ states and the ground-state) wavelengths for various sequential twist angles for the 6-BODIPY oligomer.

Twist angle	Emission nm	Absorption nm
0	575	525
22.5	570	522
45	557	513
67.5	547	503
90	545	498

S4.11. Transient absorption measurements (ps-ns)

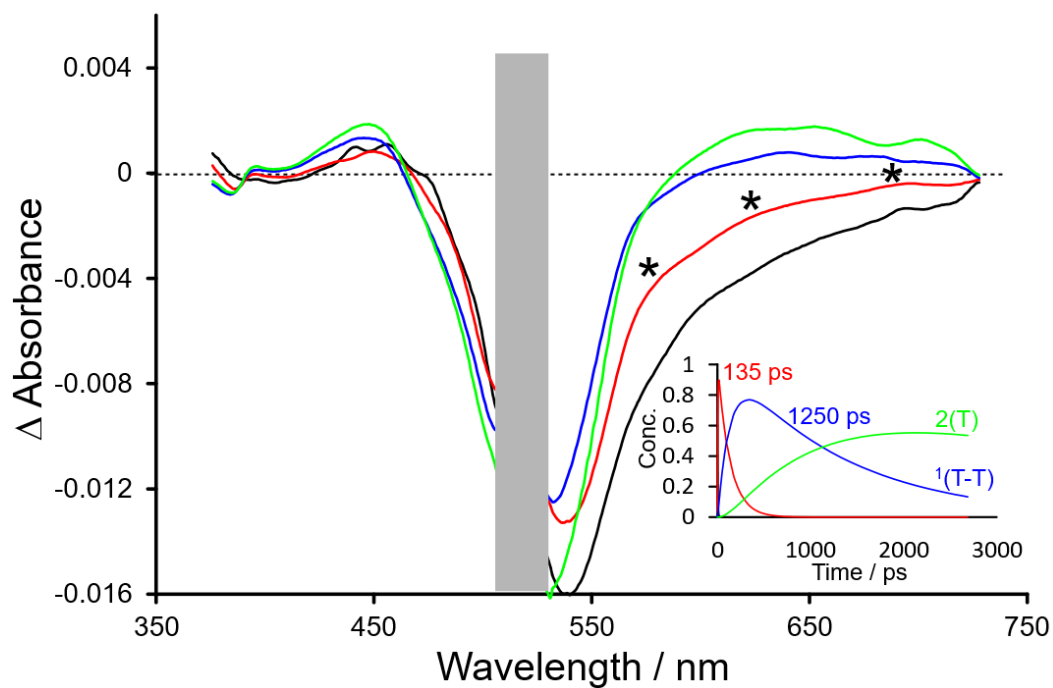


Figure S4.24. The evolution adjusted difference spectra of the TA spectra following photolysis of **P1** at 525 nm in CD₃CN displaying an initially formed species (black) which reacts in 4 ps to form the singlet (red) which forms a spin-coherent triplet (blue) excited state which in turn forms the spatially discrete triplet pair (green) (the inset shows the kinetics of the reaction sequence).

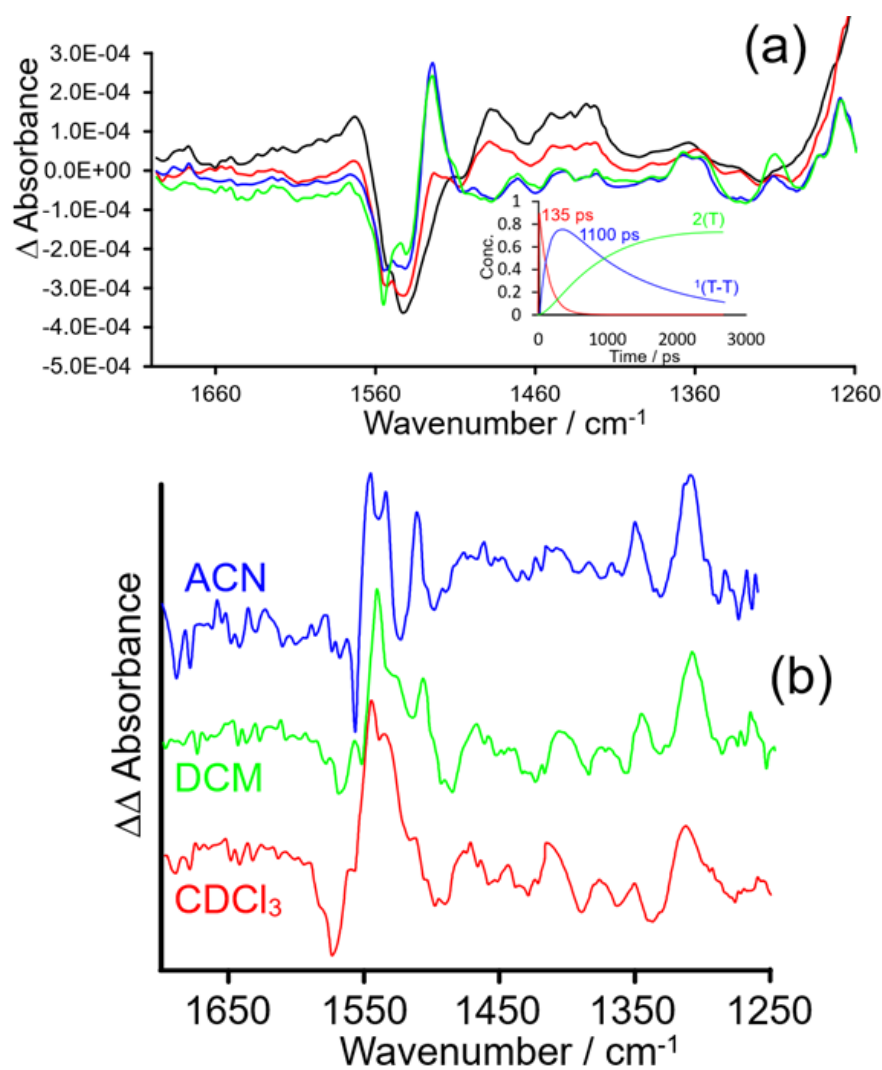


Figure S4.25. a) The evolution difference spectra of the TRIR spectra following photolysis of **P1** at 525 nm in CD_3CN displaying a Franck-Codon state (black), singlet (red) and spin coherent triplet (blue) and spatially discrete triplet (green) (the inset shows the kinetics of the reaction sequence showing singlet decay (red) and spin coherent triplet decay (blue) and production of the spatially discrete triplet (green) over the course of the experiment); b) the difference spectra generated by subtracting the evolution adjusted difference spectrum of the spin-coherent triplet from the equivalent spectrum of the spatially discrete triplet in CDCl_3 (red), DCM (green) and ACN (blue).

S4.12. Transient absorption measurements (ns- μ s)

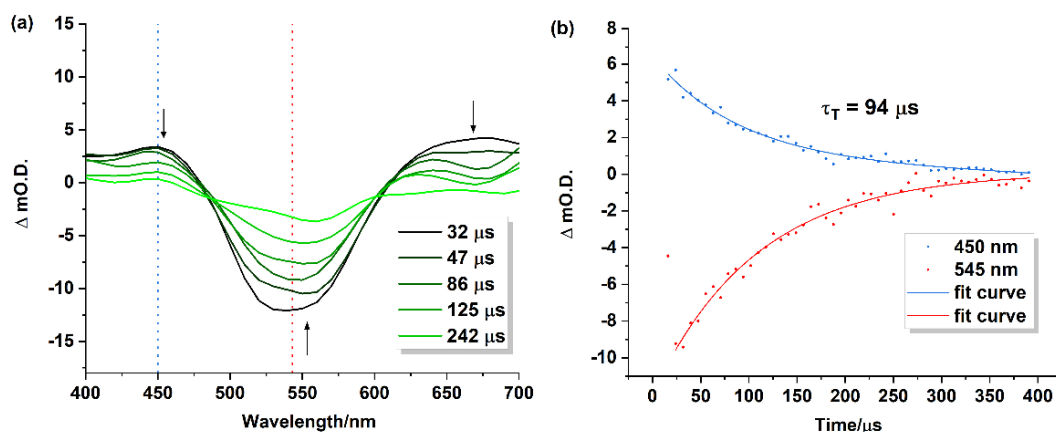


Figure S4.26. a) Transient absorption spectra of polymer **P1** in THF solution at 32 μ s, 47 μ s, 86 μ s, 125 μ s and 242 μ s following excitation with pump laser 355 nm. Sample degassed using three freeze-pump-thaw-cycles. Arrows indicate the depletion of features during measurement, b) Kinetic traces at 445 nm (dotted blue) and 545 nm (dotted red). Monoexponential fit lines at 445 nm (solid blue) and 545 nm (solid red). Inset displays triplet lifetime obtained in μ s.

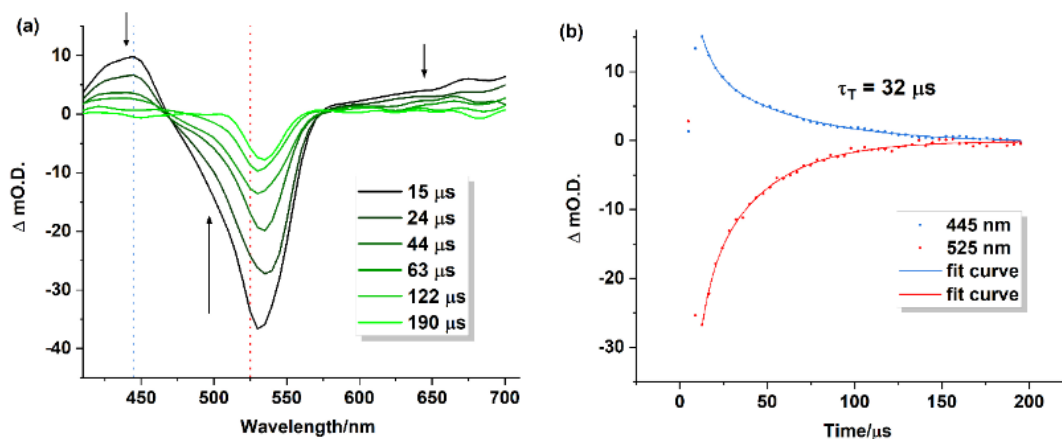


Figure S4.27. a) Transient absorption spectra of diiodo BODIPY monomer (**M2**) in deoxygenated THF solution measured at 15 μ s, 24 μ s, 44 μ s, 63 μ s, 122 μ s and 190 μ s after laser excitation ($\lambda_{exc} = 355$ nm). Sample degassed using three freeze-pump-thaw cycles, b) Kinetic decay traces at 445 nm (dotted blue) and 525 nm (dotted red). Monoexponential fit lines at 445 nm (solid blue) and 525 nm (solid red). Inset triplet lifetime obtained in microseconds (μ s).

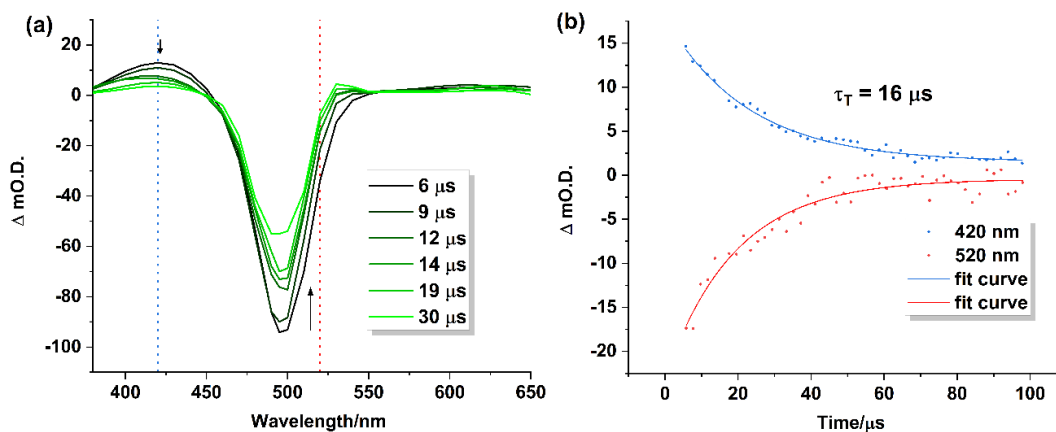


Figure S4.28. a) Transient absorption spectra of BODIPY monomer (M1) in deoxygenated THF solution measured at 6 μs , 9 μs , 12 μs , 14 μs , 15 μs , 19 μs and 30 μs after laser excitation ($\lambda_{\text{exc}} = 355$ nm). Sample degassed using three freeze-pump-thaw cycles and b) Kinetic decay traces at 420 nm (dotted blue) and 520 nm (dotted red). Monoexponential fit lines at 420 nm (solid blue) and 520 nm (solid red). Inset triplet lifetime obtained in microseconds (μs).

S4.13. Electrochemistry

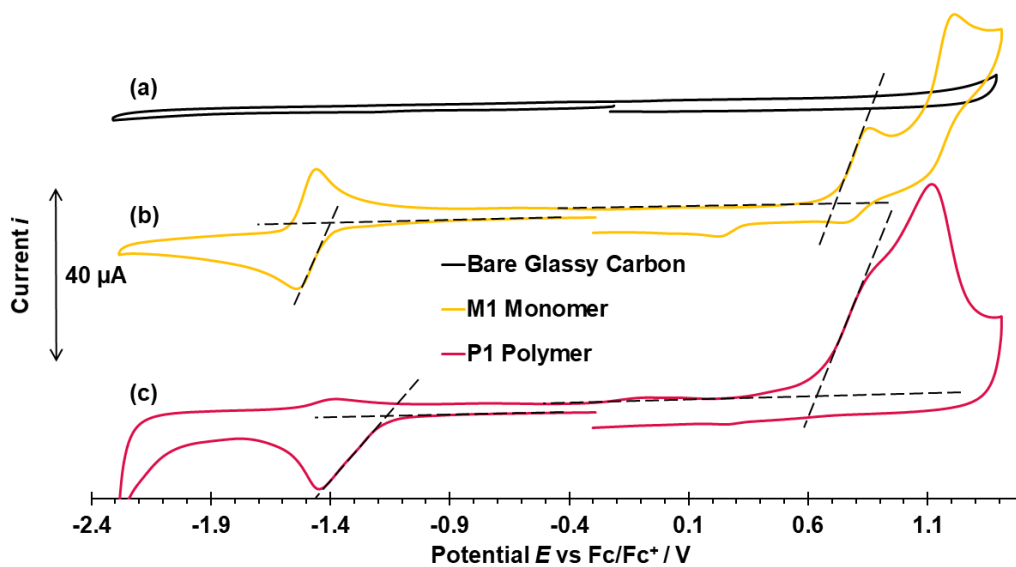


Figure S4.29. Cyclic voltammograms of a bare glassy carbon (GC) electrode (a), a GC electrode coated with a film of **M1** (b), and a GC electrode coated with a film of **P1** (c). All voltammograms were recorded initially negative sweep direction at a scan rate of $100 \text{ mV}\cdot\text{s}^{-1}$ at room temperature in a deoxygenated $0.1 \text{ M TBAPF}_6/\text{acetonitrile}$ electrolyte solution.

S4.14. Optical gap determination

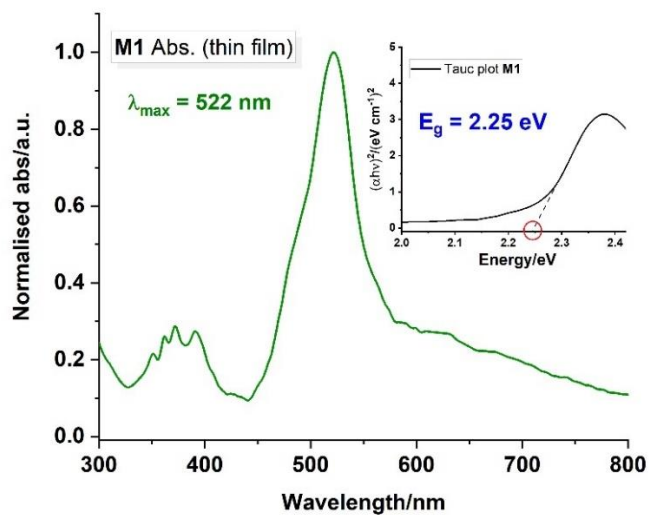


Figure S4.30. UV-visible absorption spectra of M1 on a thin film (green solid line). Inset showing Tauc Plot used to calculate the optical band gap energy by the onset of absorption. Band gap energy (E_g) shown in blue.

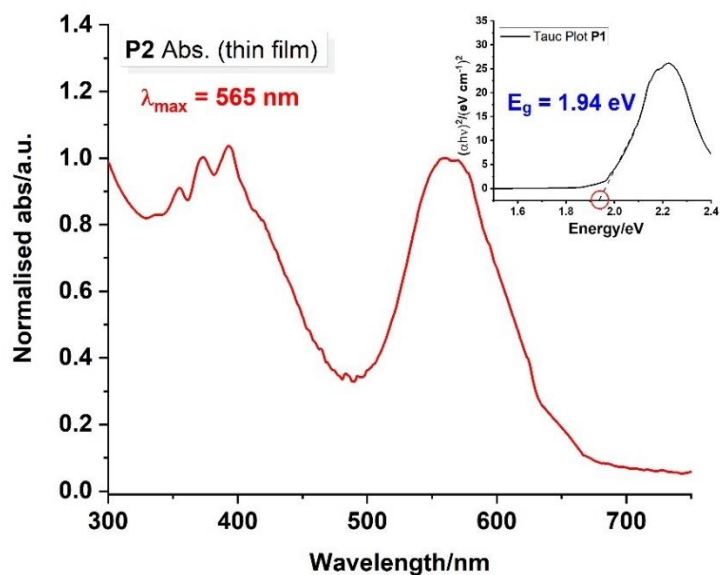


Figure S4.31. UV-visible absorption spectra of P1 on a thin film (red solid line). Inset showing Tauc Plot used to calculate the optical band gap energy by the onset of absorption. Band gap energy (E_g) shown in blue.

S4.15. Photocatalytic hydrogen evolution

Table S4.7. Table of experimental parameters and resulting hydrogen evolution of the polymer under various photocatalytic conditions. Conditions remaining constant – TiO₂ | Pt nanoparticles (6 mg), ascorbic acid (0.10 M) in 1:1 (v/v) THF: H₂O solution (4 mL total volume). Concentration of polymer, **P1** described in table. Irradiation with Xe arc lamp, $\lambda > 420$ nm.

Exp #	Polymer concentration/mM (mass mg/mL)	Sacrificial agent	TiO ₂ Pt nanoparticles	$n(\text{H}_2)/\text{mmol g}^{-1}$ (polymer)
1a	0.1 (0.2 mg/mL)	AA (0.10 M)	6 mg	0.6
1b	0.2 (0.5 mg/mL)	AA (0.10 M)	6 mg	11.3
1c	0.4 (1.0 mg/mL)	AA (0.10 M)	6 mg	13.9
1d	0.8 (2.0 mg/mL)	AA (0.10 M)	6 mg	1.4
1e	1.2 (3.0 mg/mL)	AA (0.10 M)	6 mg	1.3

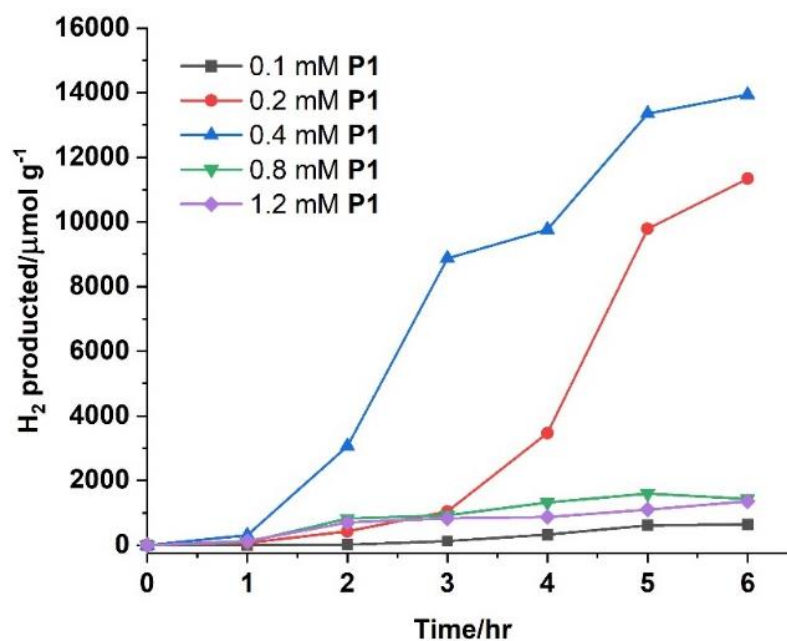


Figure S4.32. Photocatalytic activity of polymer, **P1** (0.1, 0.2, 0.4, 0.8 and 1.2 mM) using TiO₂ | Pt nanoparticles (6 mg) and 0.1 M ascorbic acid in a 4 mL 1:1 THF/H₂O (v/v) under 300 W Xe arc lamp irradiation, $\lambda > 420$ nm. Graph displaying hydrogen generation ($\mu\text{mol g}^{-1}$).

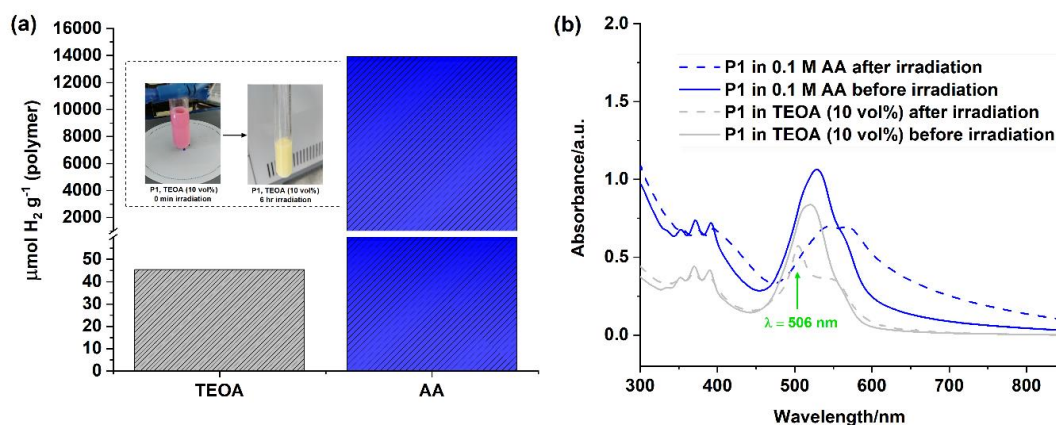


Figure S4.33. a) Photocatalytic activity of polymer, **P1** (0.4 mM) using $\text{TiO}_2 | \text{Pt}$ nanoparticles in a 1:1 THF/ H_2O (v/v) solution and either TEOA (10 vol%) – grey dashed column or ascorbic acid (0.1 M) – blue dashed column. Hydrogen evolution displayed in $\mu\text{mol H}_2 \text{g}^{-1}$ based on mass of **P1**. Inset shows colour change of photocatalytic solution after 6 hr irradiation (300 W Xe arc lamp, $\lambda > 420 \text{ nm}$) using TEOA (10 vol%) as SA. (b) UV-visible absorption spectra of **P1** in 0.1 M AA solution before irradiation (blue solid), after 6 hours irradiation (blue dash) and **P1** in TEOA solution (10 vol%) before irradiation (grey solid) and after 6 hours irradiation (grey dash). Green arrow shows growth of new band at 506 nm.

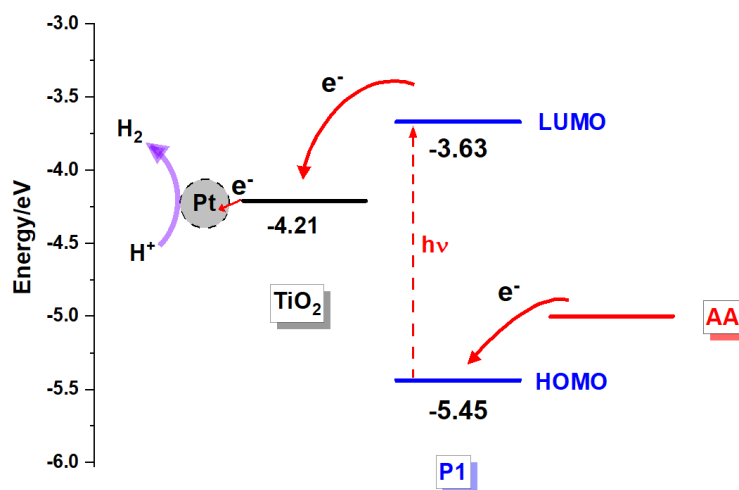


Figure S4.34. Energy level diagram (eV) showing the TiO_2 conduction band (CB) edge, the **P1** HOMO (-5.45 eV) and LUMO (-3.63 eV) band edge (calculated with the data extracted from the CV experiments). Red arrows indicate direction of electron transfer mechanisms during photocatalysis. Purple arrow shows the proton reduction reaction to liberate hydrogen gas at the Pt^0 particles catalytic site.

S4.16. SEM-EDX

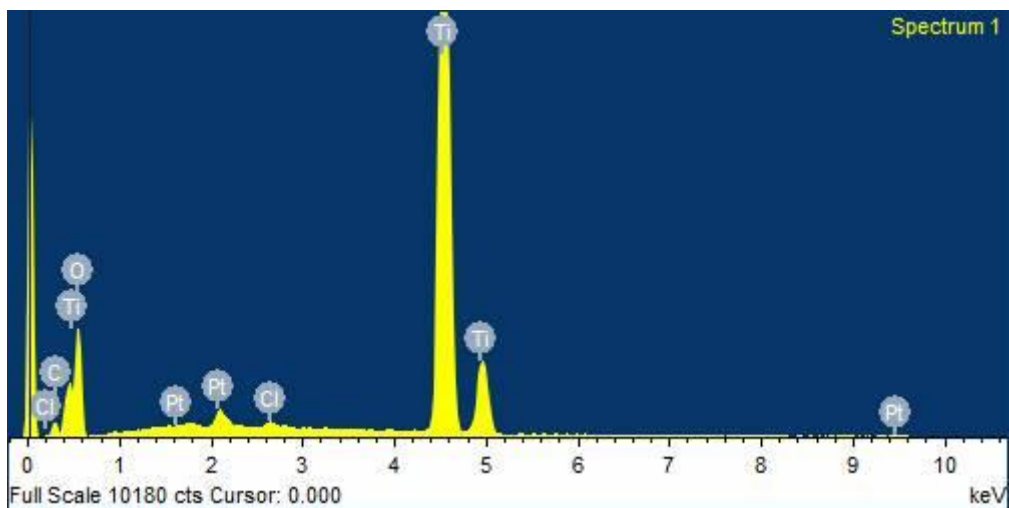


Figure S4.35. EDX spectrum of Pt | TiO₂ nanoparticles. Signals for Pt are detected.

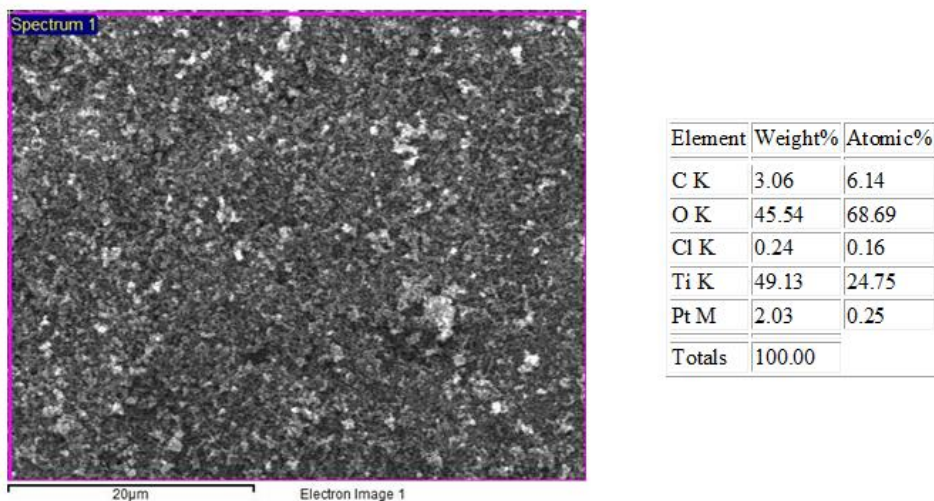


Figure S4.36. Scanning electron micrograph elemental mapping image of Pt | TiO₂ nanoparticles showing Pt detection (grey particles) on TiO₂ surface (dark background).

S4.17. Bibliography

- (1) Banfi, S.; Nasini, G.; Zaza, S.; Caruso, E. *Tetrahedron* **2013**, *69* (24), 4845–4856.
- (2) Zhang, C.; Zhao, J.; Wu, S.; Wang, Z.; Wu, W.; Ma, J.; Guo, S.; Huang, L. *J. Am. Chem. Soc.* **2013**, *135* (28), 10566–10578.
- (3) Pryce, Mary T, Cullen, Aoibhin A.; O'Reilly, Laura, Heintz, Katharina; Long, C.; Heise, A.; Murphy, R.; Gibson, E. A.; Karlsson, Joshua; Towrie, Michael; Greetham, G. M. *Front. Chem.* **2020**, *8* (October), 1–14.
- (4) Pommerehne, J.; Vestweber, H.; Guss, W.; Mahrt, R. F.; Bassler, H.; Porsch, M.; Daub, J. *Adv. Mater.* **1995**, *7*, 551–554.
- (5) Greetham, G. M.; Burgos, P.; Qian, C.; Clark, I. P.; Codd, P. S.; Farrow, R. C.; George, M. W.; Kogimtzis, M.; Matousek, P.; Parker, A. W.; Pollard, M. R.; Robinson, D. A.; Zhi-Jun, X.; Towrie, M. *Appl. Spectrosc.* **2010**, *64* (12), 1311–1319.
- (6) O'Reilly, L.; Pan, Q.; Das, N.; Wenderich, K.; Kortterik, J. P.; Vos, J. G.; Pryce, M. T.; Huijser, A. *ChemPhysChem* **2018**, *19* (22), 3084–3091.
- (7) Herrmann, J. M.; Disdier, J.; Pichat, P. *J. Phys. Chem.* **1986**, *90* (22), 6028–6034.
- (8) Sunahara, H.; Urano, Y.; Kojima, H.; Nagano, T. *J. Am. Chem. Soc.* **2007**, *129* (17), 5597–5604.
- (9) Li, G.; Yin, J. F.; Guo, H.; Wang, Z.; Zhang, Y.; Li, X.; Wang, J.; Yin, Z.; Kuang, G. C. *ACS Omega* **2018**, *3* (7), 7727–7735.
- (10) Reichardt, C. *Chem. Rev.* **1994**, *94* (8), 2319–2358.

Appendix D

Supporting information associated with Chapter 5.

S5.1. Synthetic procedure

All starting materials and solvents were commercially available (Sigma Aldrich, Fluorochem, TCI, VWR) and were used as purchased. Ru(II)(bpy)₂Cl₂ was synthesised as reported in elsewhere.

dipyrido[3,2-a:2',3'-c]phenazine-11-carbonitrile (CN-dppz) (2)

The product was synthesised by a modified method of Beltrán-Leiva et al.¹

0.32 g (2.4 mmol) of **1** and 0.5 g of 1,10-phenanthroline-5,6-dione were suspended in 30 mL methanol stirred for 15 min at room temperature. The resulting solution was heated to reflux for 6 hours. The stirrer bar was removed, and the solution was allowed to cool down to room temperature and left for crystallisation overnight. The resulting precipitate was filtered off, washed 3 times with old methanol and dried *in vacuo* to yield in a slightly cream-white solid.

Yield: 611 mg (83%) ¹H NMR (600 MHz, CDCl₃) δ 9.54 (ddd, *J* = 19.0, 8.1, 1.7 Hz, 2H), 9.34 – 9.26 (m, 2H), 8.70 (d, *J* = 1.4 Hz, 1H), 8.40 (d, *J* = 8.7 Hz, 1H), 8.02 (dd, *J* = 8.7, 1.8 Hz, 1H), 7.81 (ddd, *J* = 7.9, 4.3, 2.3 Hz, 2H). ¹³C NMR (151 MHz, CDCl₃) δ 150.94, 150.80, 146.25, 146.00, 140.76, 140.61, 140.17, 138.56, 133.19, 131.78, 131.58, 128.64, 128.17, 124.38, 121.99, 121.94, 115.43, 111.44, 74.71, 74.49, 74.28.

2-(dipyrido[3,2-a:2',3'-c]phenazin-11-yl)-5-methyl-1,3-thiazol-4-ol (3)

0.446 g (0.145 mmol) of **2** and 0.13 mL (0.145 mmol) of 2-mercaptopropionic acid were suspended in 2 mL pyridine and heated to reflux for 5 hours. The mixture was allowed to cool down to room temperature and 20 mL of ethanol were added. The resulting slurry was stirred at room temperature for an additional hour. The solid was filtered off and was successively washed 3 times each with water, a small amount of

ethanol and pentane. After drying *in vacuo* the desired product was obtained as an orange solid.

Yield: 430 mg (75%) ¹H NMR (600 MHz, d₆-DMSO) δ 9.60 – 9.43 (m, 2H), 9.23 – 9.12 (m, 2H), 8.47 (t, *J* = 6.0 Hz, 1H), 8.38 – 8.31 (m, 1H), 8.25 (dd, *J* = 8.4, 4.1 Hz, 1H), 8.02 – 7.83 (m, 2H), 2.14 (s, 3H).

tert-butyl 2-((2-(dipyrido[3,2-a:2',3'-c]phenazin-11-yl)-5-methyl-1,3-thiazol-4-yl)oxy)acetate (L1)

0.123 g (0.31 mmol) **3**, 0.13 g potassium carbonate (0.93 mmol) were suspended in 20 mL DMSO. The mixture was stirred for 30 min. at 50 °C until a dark green-blue slurry is formed from the deprotonated thiazole. Afterwards 0.067 g tert-butyl 2-bromoacetate dissolved in 1 mL DMSO and a catalytic amount of potassium iodide was added, and the mixture was heated to reflux overnight. The progress of the reaction was controlled via TLC. The reaction is finished when all deprotonated thiazole is consumed. After cooling down to room temperature the solution was poured into 50 mL water and extracted three times with DCM. The organic layer was successively washed with saturated sodium carbonate solution, water and brine. The solution was dried over magnesium sulfate and the solvent was distilled off. The crude product was purified by column chromatography (alumina/DCM:EtOAc, 4:1) to yield the title compound as orange solid.

Yield: 115 mg (73%) ¹H NMR (600 MHz, CDCl₃) δ 9.54 – 9.50 (m, 2H), 9.30 – 9.27 (m, 2H), 8.56 (d, *J* = 1.8 Hz, 1H), 8.33 (dd, *J* = 8.8, 1.9 Hz, 1H), 7.99 (d, *J* = 1.8 Hz, 1H), 7.82 – 7.77 (m, 2H), 5.04 (s, 2H), 2.44 (s, 3H), 1.51 (s, 9H).

benzo[c][1,2,5]thiadiazole-5-carbonitrile (4)

This product was synthesised by a modified method from Gieren et al.²:

0.5 g of **1** were dissolved in 20 mL anhydrous and freshly distilled toluene. The mixture was cool down to 0 °C with an ice water bath and slowly 1 mL thionylchloride was added dropwise. The mixture was stirred for additional 15 min at 0 °C, then the ice bath was removed, and the reaction was heated to reflux for 5 hours. The solvent was distilled of, 10 mL of water was added, and the suspension was stirred for 5 min.

The mixture was extracted 3 times with DCM and the organic layer was dried with magnesium sulfate. The solid was recrystallized from ethanol to yield in a white solid.

Yield: 460 mg (76%) ¹H NMR (600 MHz, CDCl₃) δ 8.47 (dd, *J* = 1.5, 0.9 Hz, 1H), 8.14 (dd, *J* = 9.0, 0.9 Hz, 1H), 7.74 (dd, *J* = 9.0, 1.6 Hz, 1H). ¹³C NMR (151 MHz, CDCl₃) δ 155.58, 153.45, 129.64, 128.21, 123.34, 117.95, 113.53, 77.37, 77.16, 77.16, 76.95.

benzo[c][1,2,5]thiadiazole-5-carbothioamide (5)

This product was synthesised by a modified method from Gampe et al.:³

A mixture of **4** (0.3 g, 1.7 mmol), O,O'-diethyldithiophosphate (0.31 mL, 1.94 mmol), 3 drops of water and 1 mL of ethanol was heated to reflux for 8 hours. The reaction was allowed to cool down to room temperature and was quenched by adding 40 mL of saturated NaHCO₃ solution and stirring for an additional hour. The resulting yellow precipitate was filtrated and washed with warm water and small amount of cold ethanol and pentane to obtain the product as a yellow powder.

Yield: 294 mg (81%) ¹H NMR (600 MHz, d₆-DMSO) δ 10.21 (s, 1H), 9.87 (s, 1H), 8.41 (d, *J* = 1.1 Hz, 1H), 8.25 (dd, *J* = 9.2, 1.8 Hz, 1H), 8.09 (dd, *J* = 9.2, 0.5 Hz, 1H). ¹³C NMR (151 MHz, d₆-DMSO) δ 204.09, 160.13, 158.90, 145.34, 135.49, 125.57, 123.01.

2-(benzo[c][1,2,5]thiadiazol-5-yl)-5-(4-bromophenyl)-1,3-thiazol-4-ol (6)

0.2 g of **5** (1.02mmol), 0.41 g of methyl 2-bromo-2-(4-bromophenyl)acetate (1.33 mmol) and 0.21 g sodium acetate (2.56 mmol) were placed in a round flask and were suspended in 40 mL ethanol. The mixture was heated to reflux for 24 hours. The progress of the reaction was monitored by TLC. After completion, the reaction mixture was cooled down to room temperature and poured into 60 mL of water, whereby the product starts to participate. After 30 minutes of stirring at room temperature the mixture was filtrated and the solid was washed successively with water, ethanol and pentane. The product was obtained as orange powder.

Yield: 461 mg (89%) ¹H NMR (400 MHz, d₆-DMSO) δ 12.09 (s, 1H), 8.53 (t, *J* = 1.1 Hz, 1H), 8.25 – 8.13 (m, 2H), 7.72 (d, *J* = 8.8 Hz, 2H), 7.61 (d, *J* = 8.8 Hz, 2H).

tert-butyl 2-((2-(benzo[c][1,2,5]thiadiazol-5-yl)-5-(4-bromophenyl)-1,3-thiazol-4-yl)oxy)acetate (7)

The reaction was carried out by using the same procedure of (**L1**) using 0.4 g of (**6**) (1.02 mmol), 425 mg (3.07 mmol) K₂CO₃ and 0.25 g tert-butyl 2-bromoacetate as starting materials. The product was obtained as an orange solid.

Yield: 461 mg (73%) ¹H NMR (600 MHz, CDCl₃) δ 8.48 (dd, *J* = 1.7, 0.7 Hz, 1H), 8.17 (dd, *J* = 9.2, 1.7 Hz, 1H), 8.03 (dd, *J* = 9.1, 0.7 Hz, 1H), 7.69 (dt, 2H), 7.52 (dt, 2H), 5.00 (s, 2H), 1.50 (s, 9H). ¹³C NMR (151 MHz, CDCl₃) δ 168.16, 166.41, 158.38, 158.36, 155.43, 155.07, 134.41, 132.05, 129.97, 128.71, 127.59, 122.07, 121.11, 117.49, 112.72, 83.03, 82.42, 77.16, 28.26, 27.96.

tert-butyl 2-((5-(4-(9H-carbazol-9-yl)phenyl)-2-(benzo[c][1,2,5]thiadiazol-5-yl)-1,3-thiazol-4-yl)oxy)acetate (8)

This product was synthesised by a modified method from Gampe et al.⁴:

In a Schlenk tube were 150 mg **7** (0.297mmol), 55 mg of carbazole (0.327 mmol) and 40 mg of KO^tBu (1.2 equiv.) mixed and degassed. 10 mL of toluene were added, and the resulting solution was degassed over 15 min with nitrogen. 8 mg of Pd(dba)₂ (0.05 equiv.) and 12 mg of SPhos (0.10 equiv.) were added and the solution was heated to reflux overnight. The progress of the reaction was monitored by TLC. The solvent was distilled of and the residue was dissolved with DCM (50 mL) and washed 3 times with water. The organic layer was dried with magnesium sulfate, filtered and the solvent was removed under vacuum. The crude product was purified by flash chromatography (silica, DCM) and afterwards recrystallised from toluene/methanol.

Yield: 77 mg (43%) ¹H NMR (600 MHz, CDCl₃) δ 8.48 – 8.45 (m, 1H), 8.16 (dd, *J* = 9.1, 1.7 Hz, 1H), 8.09 (d, *J* = 7.8 Hz, 2H), 7.99 (d, *J* = 8.7 Hz, 3H), 7.56 (d, *J* = 8.5 Hz, 3H), 7.41 (d, *J* = 8.2 Hz, 2H), 7.39 – 7.33 (m, 3H), 7.23 (t, *J* = 7.4 Hz, 2H), 5.00 (s, 2H), 1.46 (s, 9H). ¹³C NMR (151 MHz, CDCl₃) δ 168.11, 158.32, 158.28, 155.32, 154.97, 143.36, 140.73, 136.44, 134.34, 130.53, 129.99, 128.99, 128.50, 128.42, 127.52, 127.30, 126.02, 125.43, 123.48, 121.96, 120.36, 120.08, 117.37, 112.94, 109.85, 82.34, 77.24, 77.03, 76.82, 67.18, 28.16.

tert-butyl 2-((5-(4-(9H-carbazol-9-yl)phenyl)-2-(dipyrido[3,2-a:2',3'-c]phenazin-11-yl)-1,3-thiazol-4-yl)oxy)-acetate (L2)

In a round bottle flask 12.5 mg of **8** (21.2 μmol) and 15 mg of sodium borohydride (397 μmol) were dissolved in 10 mL of ethanol, degassed for 30 minutes with nitrogen and heated to 50 °C. A catalytic amount of $\text{CoCl}_2 \cdot (\text{H}_2\text{O})_5$ was added and the mixture was heated to reflux. The reaction is finished after no further gas evolution was observed (evolving H_2S). The diamine intermediate is recognisable through its strong green fluorescence. A short flash chromatography (silica, DCM) was used to separate the crude product from the inorganic materials. The solvent was removed and 5 mg of 1,10-phenanthroline-5,6-dione was added and the mixture was dissolved in 10 mL of methanol. The reaction mixture was heated to reflux for 3 hours. The solvent was removed, and the crude product was purified by column chromatography (silica, DCM/heptane 2/1) to yield in the desired product as a red solid.

Yield: 13 mg (83%) ^1H NMR (600 MHz, CDCl_3) δ 9.79 – 9.58 (m, 2H), 9.33 (s, 2H), 8.84 (d, $J = 1.8$ Hz, 1H), 8.52 (dd, $J = 8.8, 1.9$ Hz, 1H), 8.40 (d, $J = 8.8$ Hz, 1H), 8.13 (dd, $J = 30.7, 8.1$ Hz, 4H), 7.92 – 7.77 (m, 2H), 7.65 (d, $J = 8.4$ Hz, 2H), 7.50 (d, $J = 8.2$ Hz, 2H), 7.47 – 7.42 (m, 2H), 7.31 (t, $J = 7.4$ Hz, 2H), 5.13 (s, 2H), 1.57 (s, 9H). ^{13}C NMR (151 MHz, CDCl_3) δ 168.15, 158.53, 158.28, 152.67, 152.60, 143.25, 142.61, 141.94, 140.72, 136.52, 135.21, 134.20, 130.28, 130.00, 128.56, 128.53, 128.13, 127.62, 127.54, 127.32, 126.03, 125.38, 124.44, 123.49, 120.37, 120.11, 113.39, 109.85, 82.38, 77.23, 77.02, 76.81, 67.29, 28.20.

[Ru(bpy)₂(dppz-Tz-OCH₂COOtBu-Me)](PF₆)₂ (Ru1)

In a round bottle flask 18 mg of **L1** and 22 mg of $\text{Ru}(\text{bpy})_2\text{Cl}_2$ were dissolved in 10 mL of ethanol, the reaction vessel was covered with aluminium foil and heated to reflux for 18 hours under light exclusion. In a beaker 50 mg of ammonium hexafluorophosphate was dissolved in 10 mL of deionised water. After the reaction mixture was cooled to room temperature, it was poured into the hexafluorophosphate solution, which forms a red solid, immediately. The solid was collected via vacuum filtration and was washed with 3 times with water and diethyl ether. The crude product was purified via column chromatography (silica, ACN/water/ KNO_3 (aq. 30%))

90/10/1) and transformed again into the PF₆ salt to obtain the title compound as a deep red solid.

Yield: 26 mg (53%) ¹H NMR (600 MHz, CD₃CN) δ 9.72 – 9.54 (m, 2H), 8.95 (dd, *J* = 1.8, 0.6 Hz, 1H), 8.61 – 8.47 (m, 5H), 8.31 – 7.98 (m, 7H), 7.94 – 7.78 (m, 5H), 7.72 (ddt, *J* = 9.2, 8.5, 5.7 Hz, 2H), 7.50 – 7.41 (m, 2H), 7.31 – 7.24 (m, 2H), 5.16 (s, 2H), 2.15 (s, 3H). HRMS: [ESI pos.] calcd for C₄₄H₃₁N₉O₃RuS [M-C(CH₃)₃]⁺ m/z: 867.1214. Found: m/z 866.0970, UV-vis in ACN λ_{abs}(ε) 441 nm (25,000 M⁻¹cm⁻¹).

[Ru(bpy)₂(dppz-Tz-OCH₂COOtBu-Ph-Carb)](PF₆)₂ (Ru2)

The reaction was carried out by using the same procedure of **Ru1** using 9 mg of **L2** and 7 mg of Ru(bpy)₂Cl₂ as starting materials. The product was obtained as a red solid.

Yield: 8 mg (42%) ¹H NMR (600 MHz, d₆-acetone) δ 9.84 – 9.75 (m, 2H), 8.87 (dd, *J* = 19.4, 8.1 Hz, 4H), 8.64 – 8.56 (m, 3H), 8.28 (t, *J* = 7.9 Hz, 2H), 8.26 – 8.22 (m, 3H), 8.22 – 8.15 (m, 5H), 8.15 – 8.08 (m, 4H), 7.77 (d, *J* = 8.6 Hz, 1H), 7.68 – 7.64 (m, 3H), 7.57 (d, *J* = 8.3 Hz, 1H), 7.51 (d, *J* = 8.2 Hz, 3H), 7.48 – 7.37 (m, 7H), 7.34 – 7.30 (m, 2H), 7.27 (ddd, *J* = 7.9, 6.9, 1.1 Hz, 2H), 5.22 (s, 2H), 1.53 (s, 9H). HRMS: [ESI pos.] calcd for C₆₅H₄₈N₁₀O₃RuSPF₆ [M-(PF₆)]⁺ m/z: 1295.2328, Found: m/z 1295.2319, UV-vis in ACN λ_{abs}(ε) 444 nm (22,000 M⁻¹cm⁻¹).

S5.2. Steady-state experiments

S5.2.1. Electrochemical measurements

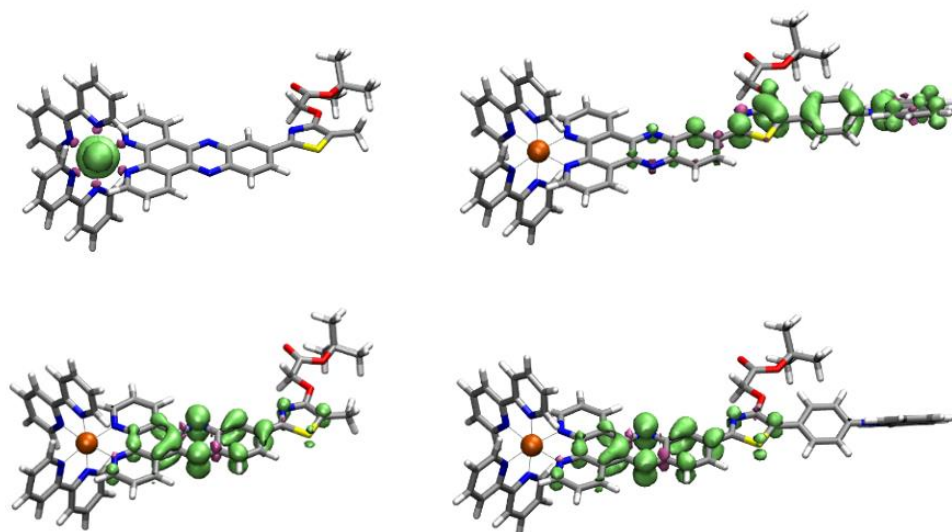


Figure S5.1. (TD)-DFT simulated iso-density surface ($\rho = \pm 0.002$) of the spin density distribution of singly oxidized (*top row*) and singly reduced **Ru1** (*right*) and **Ru2** (*left*).

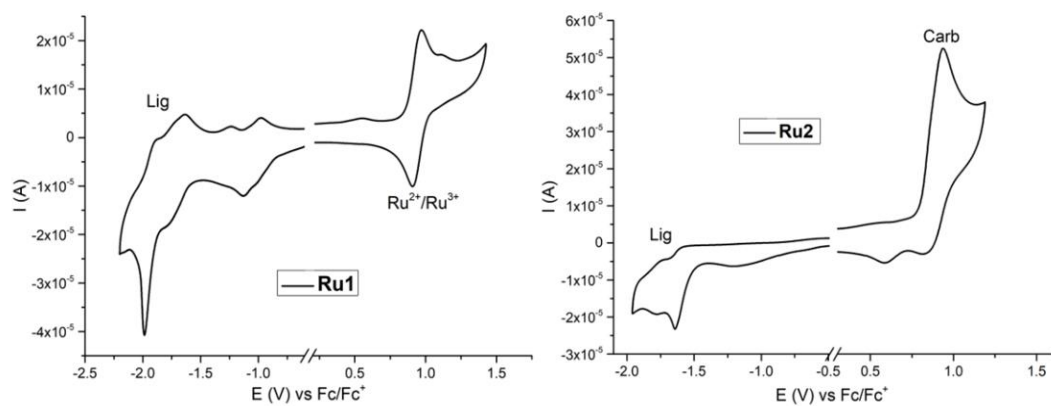


Figure S5.2. Cyclic voltammograms of solutions of **Ru1** and **Ru2** at room temperature in acetonitrile (scan rate: $0.2 \text{ V} \cdot \text{s}^{-1}$, supporting electrolyte: $0.1 \text{ M } n\text{-Bu}_4\text{PF}_6$). The peak potentials are referenced vs. the Fc^+/Fc redox couple.

S5.2.2. Ground-state absorption properties

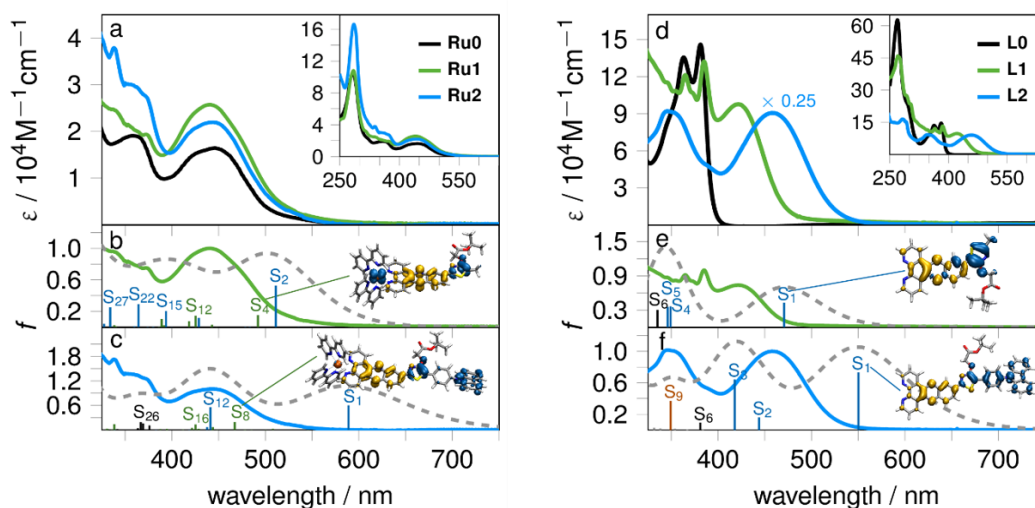


Figure S5.3. Mean molar extinction coefficients of the Ruthenium complexes **Ru1** and **Ru2** (a) and the corresponding dppz-ligands **L1** and **L2** (d) in acetonitrile. TD-DFT simulated absorption spectra (dashed grey lines) of **Ru1** (b), **Ru2** (c), **L1** (e) and **L2** (f) and charge density differences of MLCT_{phz} and ILCT_{tz/phz} states. The states of ILCT_{tz/phz}, MLCT, $\pi\pi^*$ _{dppz} and $\pi\pi^*$ _{carb} character are highlighted in blue, green, black and orange, respectively.

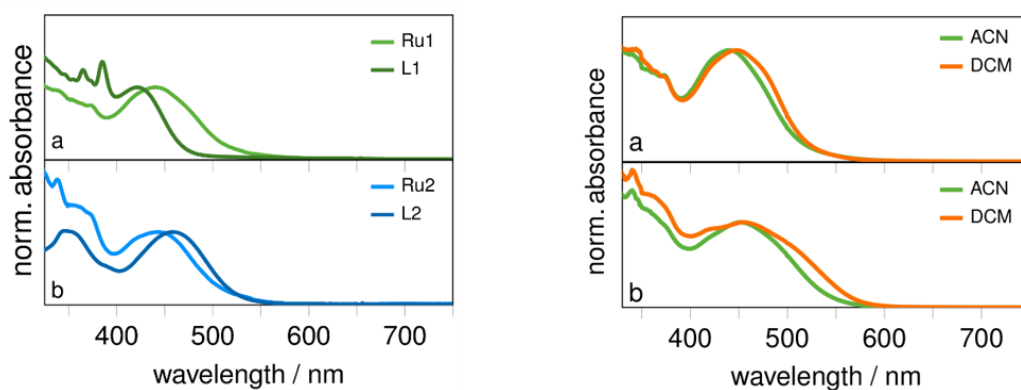
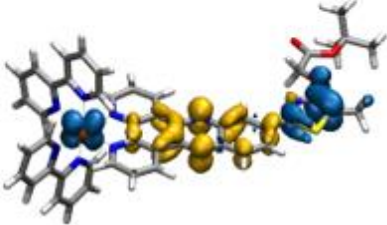
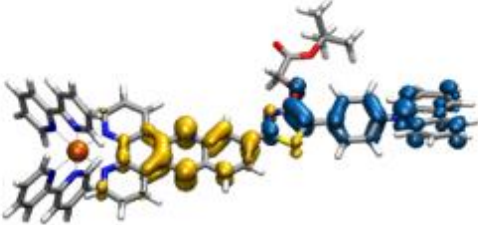
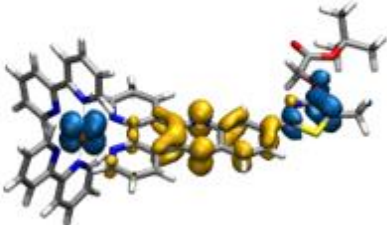
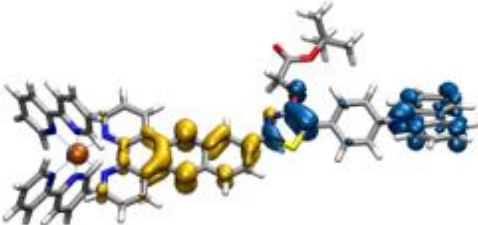
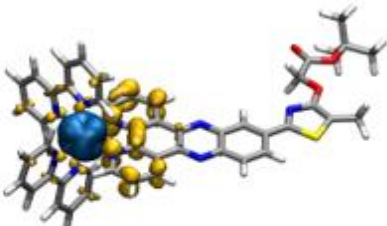
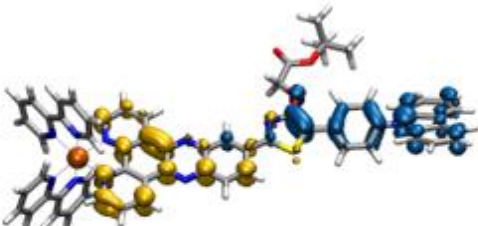


Figure S5.4. *Left:* Normalized UV-vis absorption spectra of the Ru(II) complexes – **Ru1** and **Ru2** – and their corresponding ligands – **L1** and **L2** – in acetonitrile. *Right:* Normalized absorption spectra of **Ru1** (a) and **Ru2** (b) in dichloromethane (DCM) and acetonitrile (ACN).

Table S5.1. Change density differences (CDD, TD-B3LYP/TZVP) of some singlet states involved in the photoexcitation of **Ru1** and **Ru2**. Excitation occurs from blue to yellow ($\rho = \pm 0.0015$).

Ru1	Ru2
E in eV (λ in nm)	E in eV (λ in nm)
<i>f</i>	<i>f</i>
S₂	S₁
	
2.43 (511)	2.11 (589)
0.492	0.741
S₄	S₈
	
2.52 (492)	2.65 (467)
0.141	0.191
S₁₁	S₁₂
	
2.89 (429)	2.81 (441)
0.109	0.553

S5.2.3. Steady-state emission properties

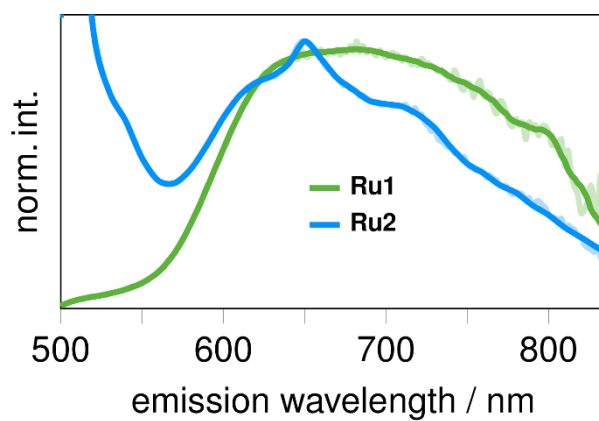


Figure S5.5. Steady-state emission spectra of **Ru1** and **Ru2** in acetonitrile upon excitation at 420 nm.

S5.3. Transient absorption and emission spectroscopy

S5.3.1. Photoexcitation at 403 nm (fs-TA) and 410 nm (ns-TA, ns-Em) in acetonitrile

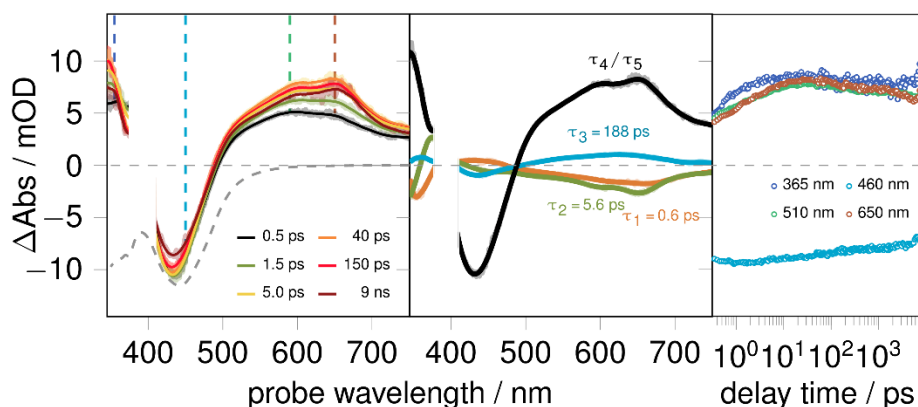


Figure S5.6. Ultrafast transient absorption spectra, decay associated spectra and kinetic traces at some selected probe wavelengths (as indicated by vertical lines in the transient spectra) of **Ru1** at 403 nm excitation (0.5 mW, OD at $\lambda_{\text{exc}} = 0.16$) in acetonitrile.

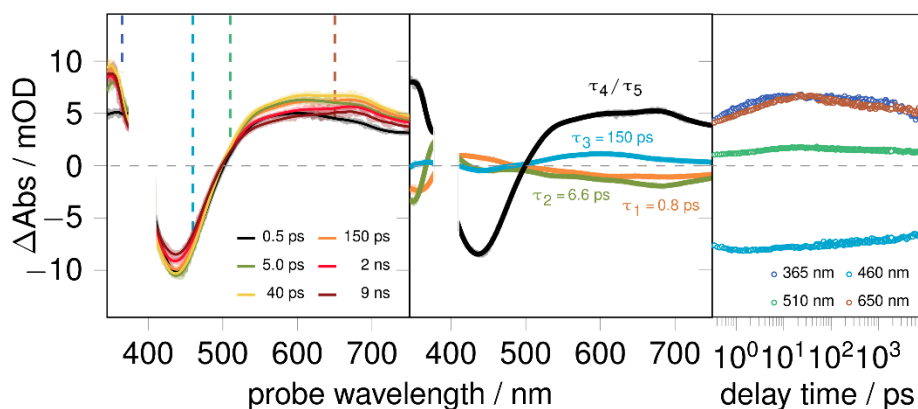


Figure S5.7. Ultrafast transient absorption spectra, decay associated spectra and kinetic traces at some selected probe wavelengths (as indicated by vertical lines in the transient spectra) of **Ru2** at 403 nm excitation (0.5 mW, OD at $\lambda_{\text{exc}} = 0.20$) in acetonitrile.

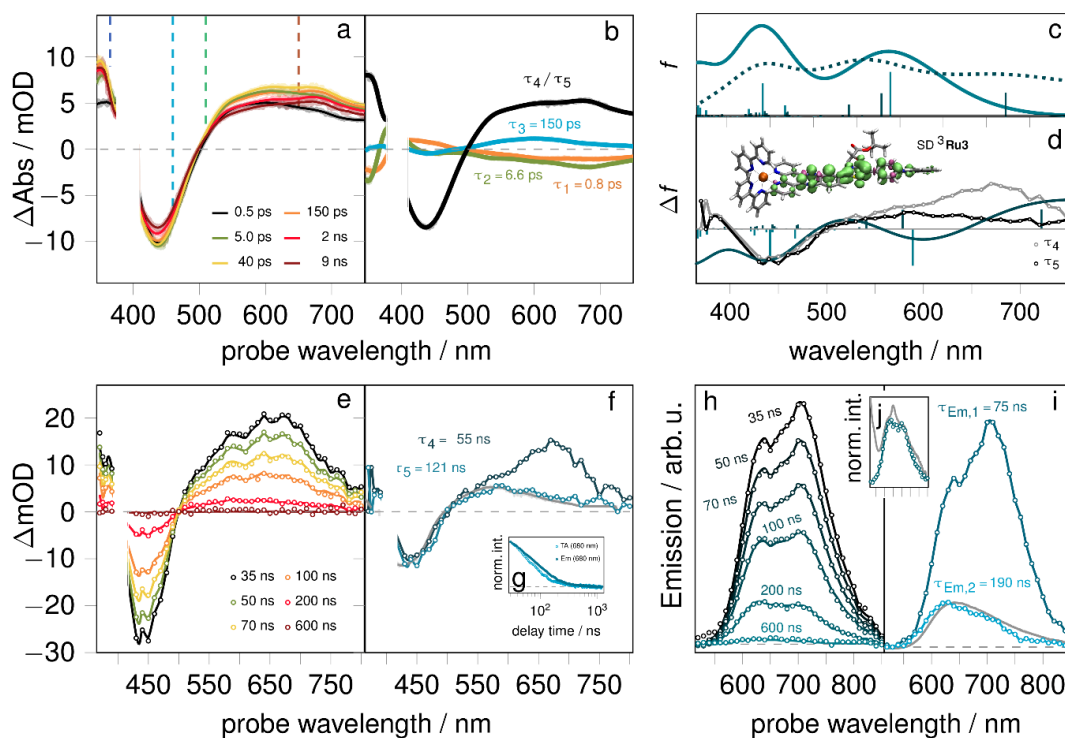


Figure S5.8. Time-resolved data of **Ru2** in acetonitrile at delay times up to 10 ns (a, b) and on a sub- μ s timescale (e-i): Ultrafast transient absorption spectra (a) and decay associated spectra (b) at 403 nm excitation (0.5 mW, OD at $\lambda_{\text{exc}} = 0.20$). Nanosecond transient absorption (e) and emission spectra (h) and their corresponding decay associated spectra (ns-TA: f, ns-Em: i) at 410 nm excitation (3.0 mW, OD at $\lambda_{\text{exc}} = 0.12$). TD-DFT simulated absorption spectra of $^1\text{Ru2}$ (solid, orange line) and $^3\text{Ru2}$ (dotted, dark orange line). The vertical transition energies and their corresponding oscillator strength are shown by bars (c, d), which were broadened using Gaussian functions (c, full-width half-maximum of 0.30 eV). Comparison of the decay associated spectra of τ_4 (grey marks) and τ_5 (black marks) to the simulated difference spectrum (solid, orange line) for an $^1\text{Ru2}$ to $^3\text{Ru2}$ excitation and spin density distribution of **Ru2** in the lowest triplet state (d). Comparison of the steady-state and transient emission spectrum (j) recorded upon excitation at 410 nm (ns-Em spectrum at a delay time of 100 ns). The inset figure g shows the emission decay kinetic at 680 nm (filled marks) compared to the transient absorption kinetic trace at 680 nm (empty marks). The kinetic traces are normalized at 30 ns. The solid grey lines in figure f and i represent the steady-state emission spectrum and TA of the long-lived $^3\text{MLCT}_{\text{phen}}$ state of **Ru0**, respectively.

S5.3.2. Photoexcitation at 470 nm (fs-TA, ns-TA, ns-Em) in acetonitrile

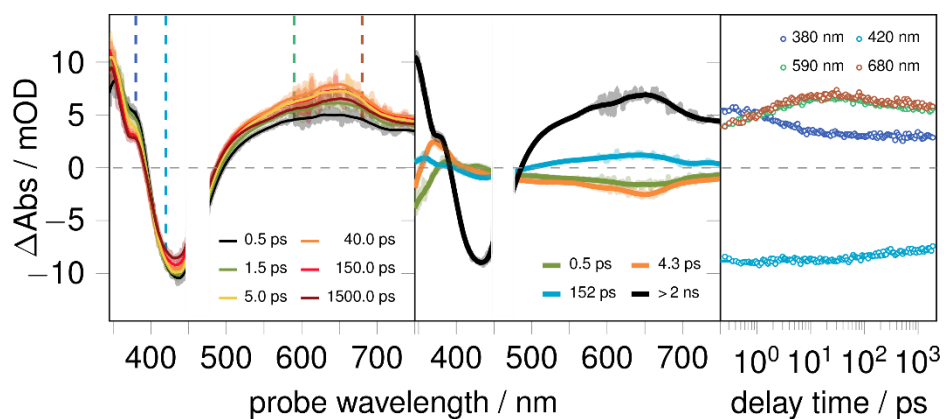


Figure S5.9. Ultrafast transient absorption spectra, decay associated spectra and kinetic traces at some selected probe wavelengths (as indicated by vertical lines in the transient spectra) of **Ru1** at 470 nm excitation (0.15 mW, OD at $\lambda_{\text{exc}} = 0.30$) in acetonitrile.

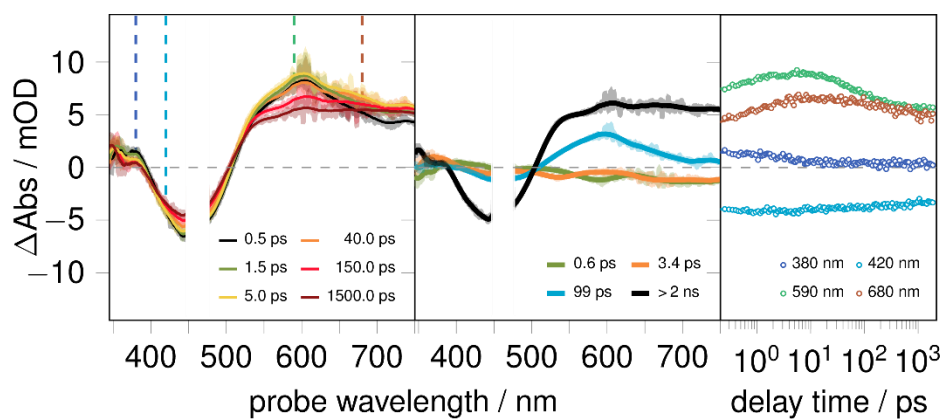


Figure S5.10. Ultrafast transient absorption spectra, decay associated spectra and kinetic traces at some selected probe wavelengths (as indicated by vertical lines in the transient spectra) of **Ru2** at 470 nm excitation (0.15 mW, OD at $\lambda_{\text{exc}} = 0.15$) in acetonitrile.

S5.3.3. Photoexcitation at 470 nm (fs-TA, ns-TA, ns-Em) in dichloromethane

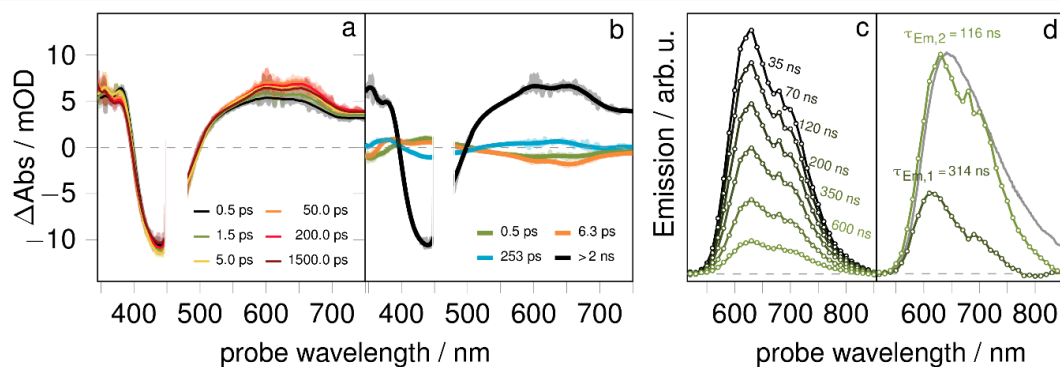


Figure S5.11. Time-resolved spectra of **Ru1** upon 470 nm excitation in dichloromethane: Ultrafast transient absorption spectra (a, 0.2 mW, OD at $\lambda_{exc} = 0.30$) and the corresponding decay associated spectra (b) and transient emission spectra (c, 3.5 mW, OD at $\lambda_{exc} = 0.3$) and corresponding decay associated spectra (d). The solid grey line in figure d shows the steady-state emission spectrum of **Ru0**.

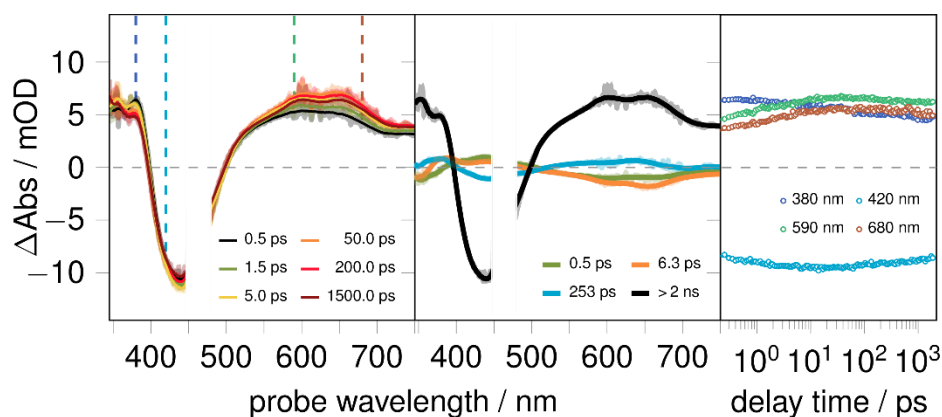


Figure S5.12. Ultrafast transient absorption spectra, decay associated spectra and kinetic traces at some selected probe wavelengths (as indicated by vertical lines in the transient spectra) of **Ru1** at 470 nm excitation (0.15 mW, OD at $\lambda_{exc} = 0.30$) in DCM.

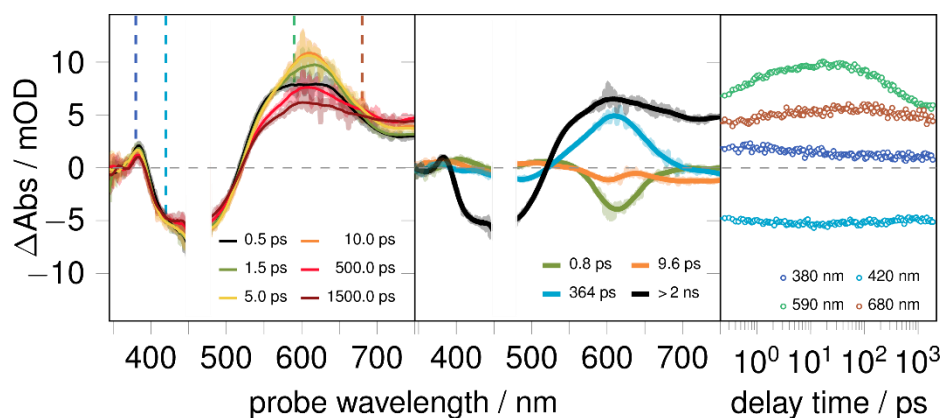


Figure S5.13. Ultrafast transient absorption spectra, decay associated spectra and kinetic traces at some selected probe wavelengths (as indicated by vertical lines in the transient spectra) of **Ru2** at 470 nm excitation (0.15 mW, OD at $\lambda_{exc} = 0.15$) in DCM.

S5.4. NMR spectra

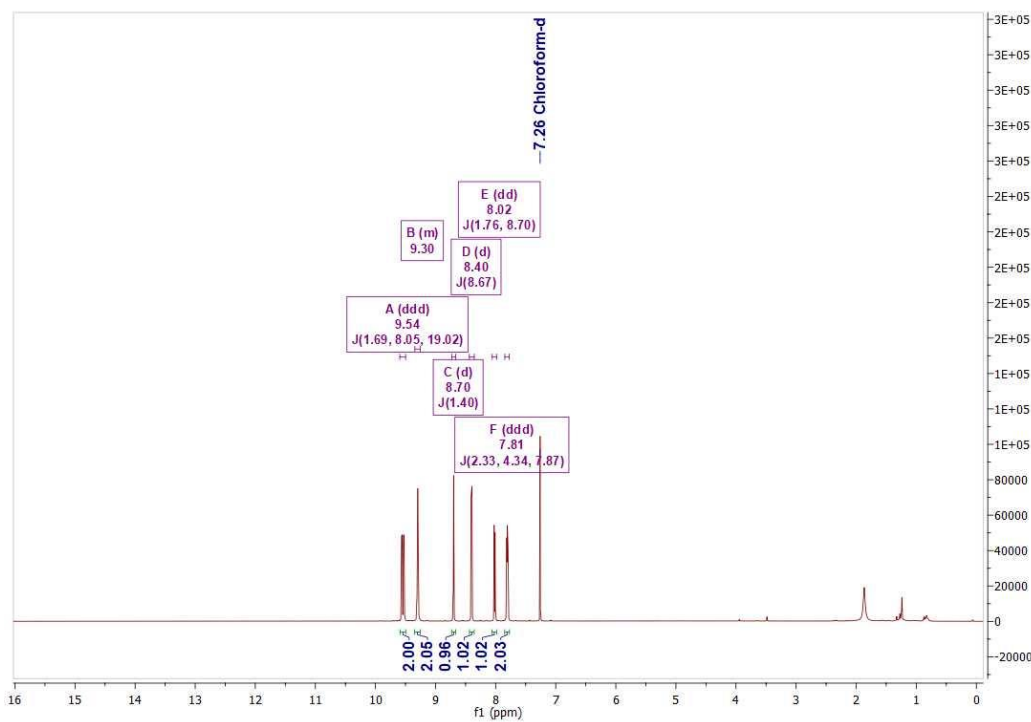


Figure S5.14. ^1H NMR spectrum of **2** in CDCl_3 .

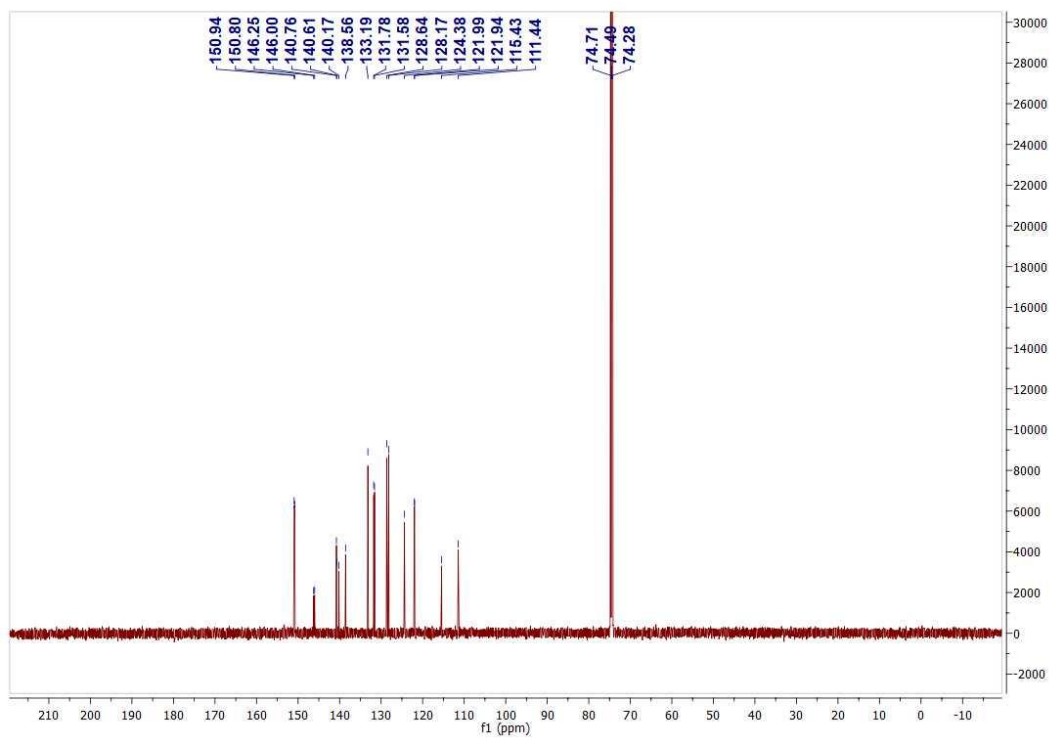


Figure S5.15. ^{13}C NMR spectrum of **2** in CDCl_3 .

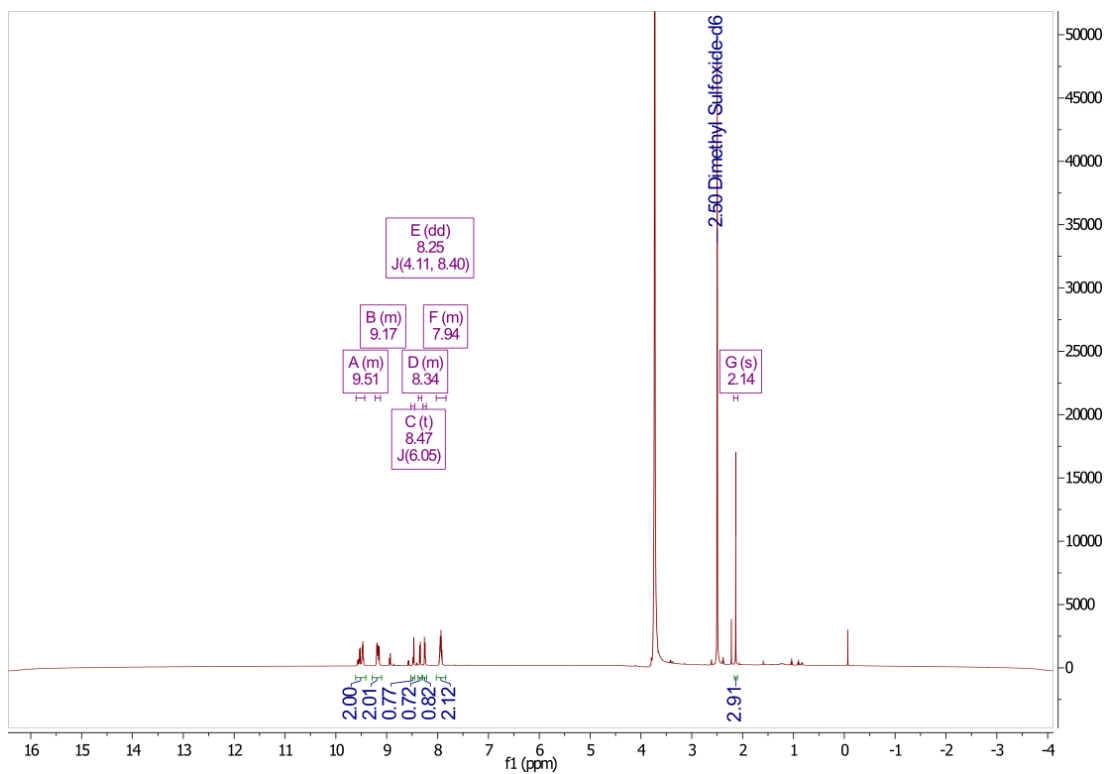


Figure S5.16. ^1H NMR spectrum of **3** in $\text{d}_6\text{-DMSO}$.

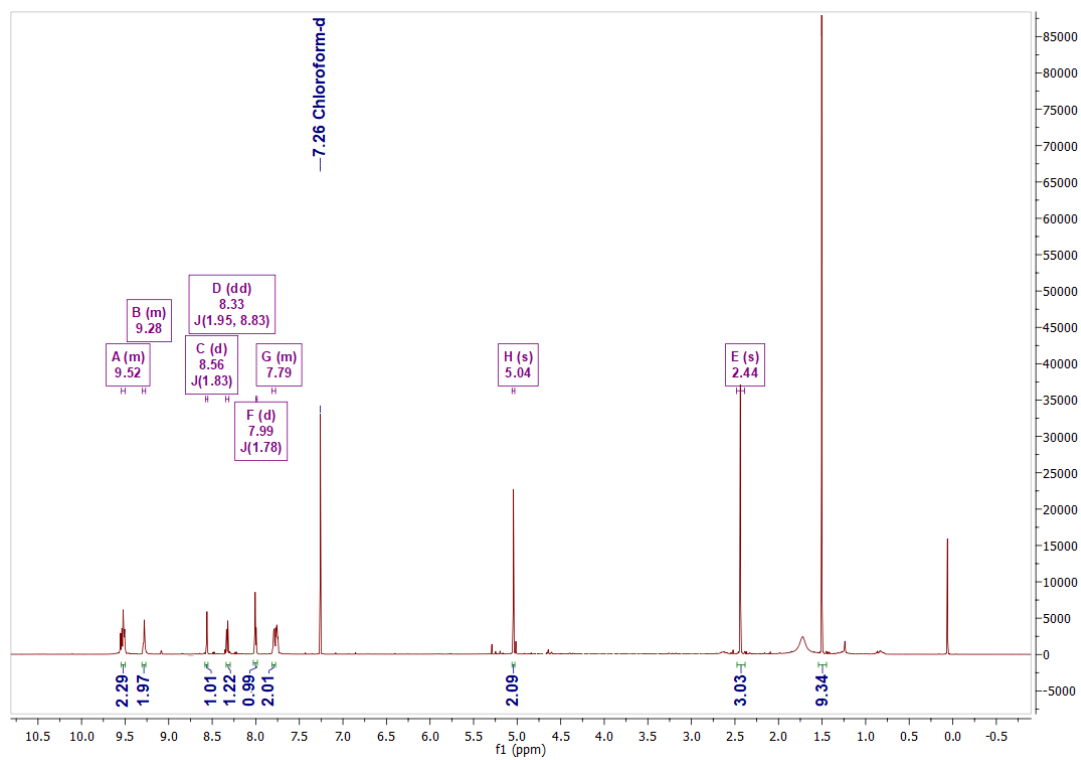


Figure S5.17. ^1H NMR spectrum of **L1** in CDCl_3 .

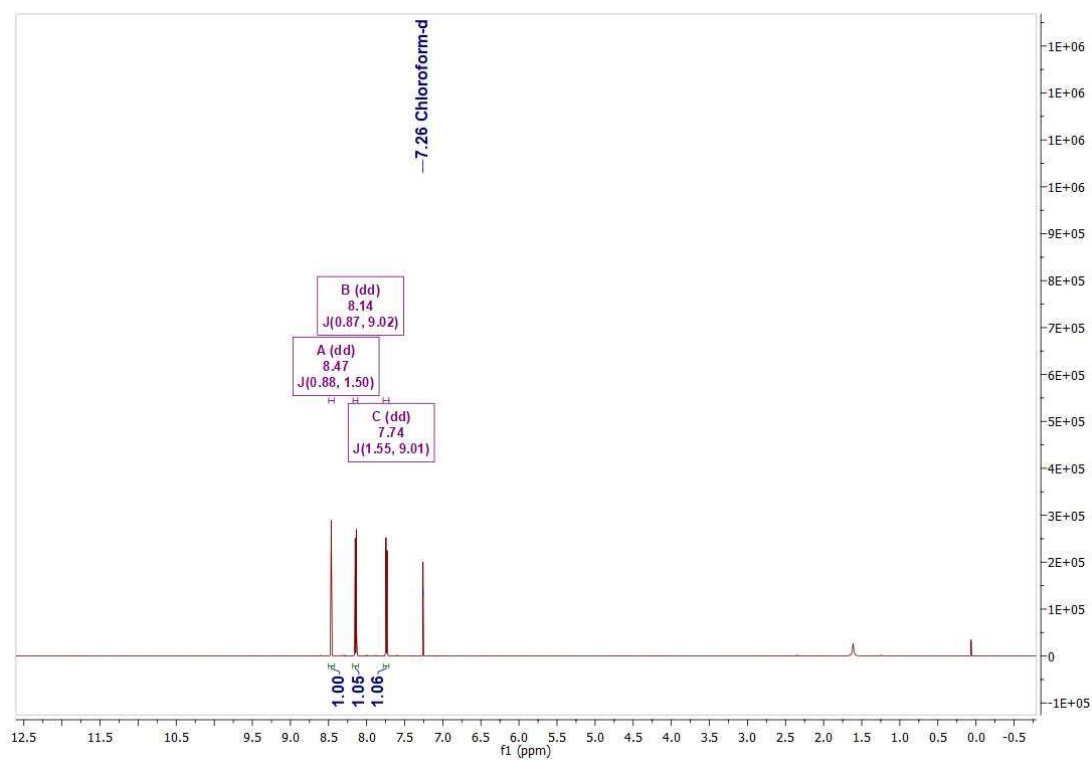


Figure S5.18. ^1H NMR spectrum of **4** in CDCl_3 .

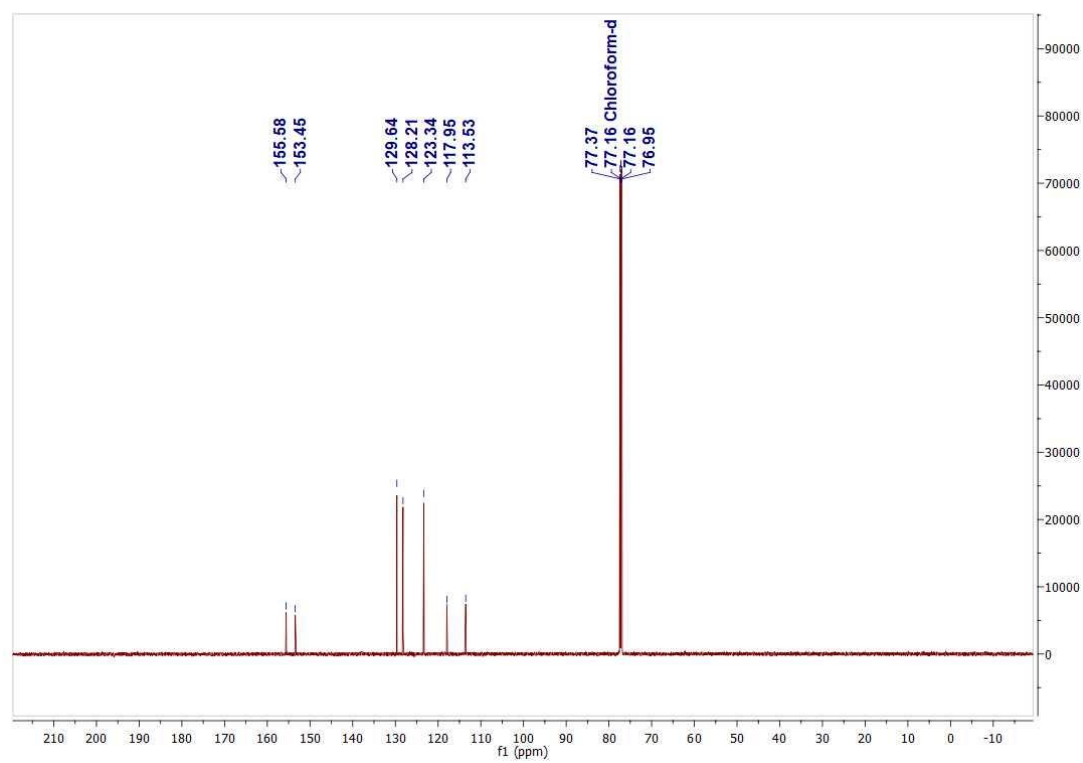


Figure S5.19. ^{13}C NMR spectrum of **4** in CDCl_3 .

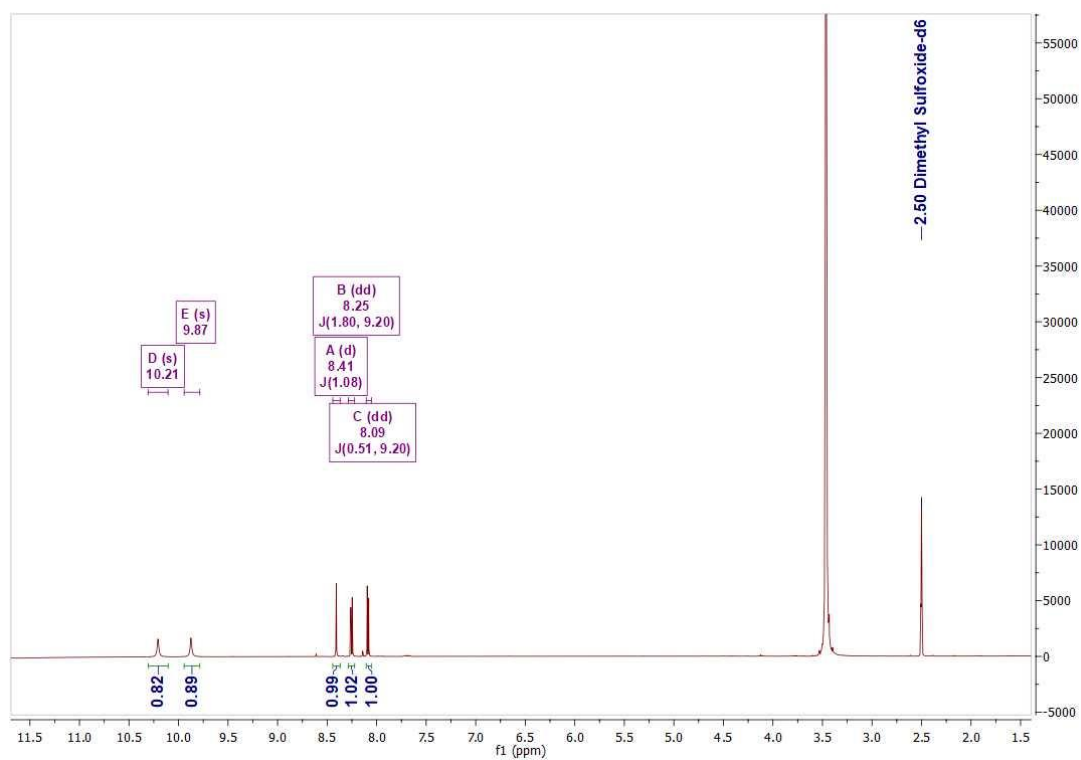


Figure S5.20. ^1H NMR spectrum of **5** in d_6 -DMSO.

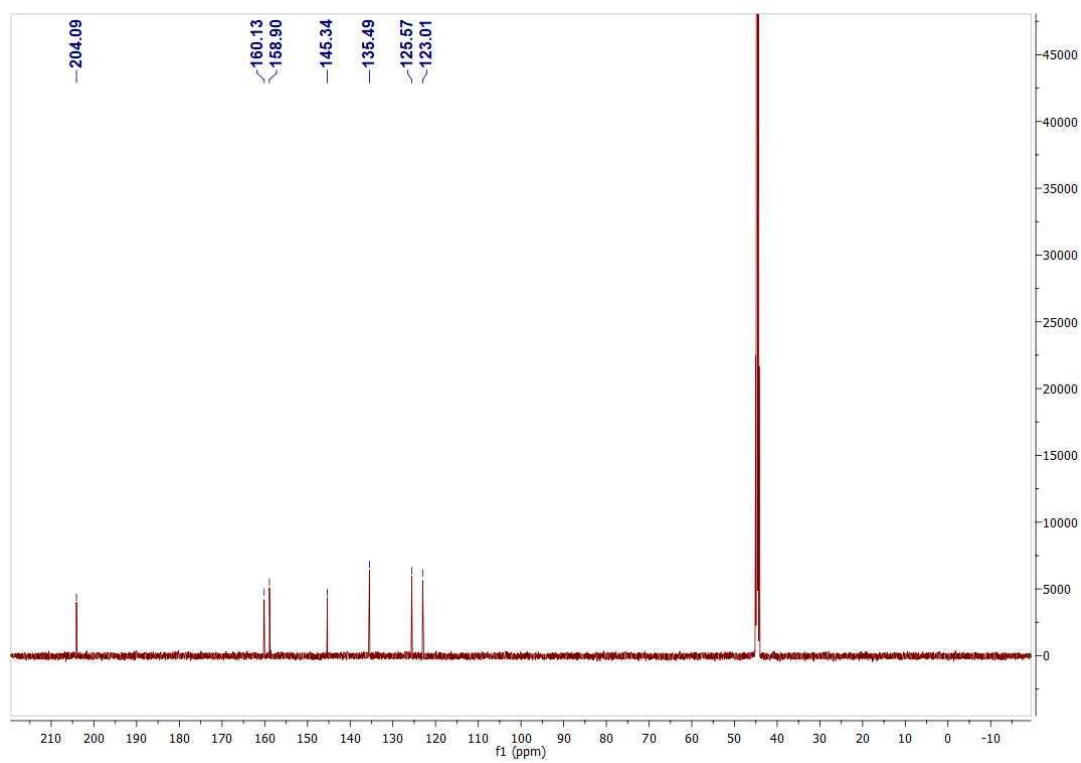


Figure S5.21. ^{13}C NMR spectrum of **5** in d_6 -DMSO.

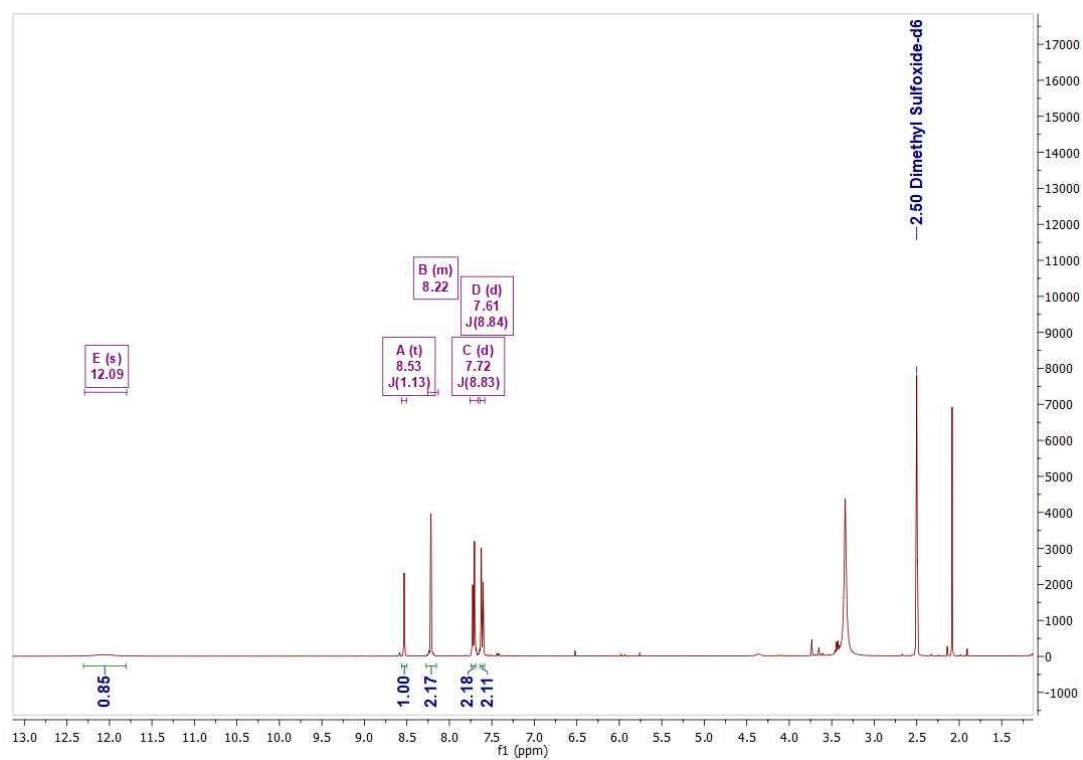


Figure S5.22. ^1H NMR spectrum of **6** in $\text{d}_6\text{-DMSO}$.

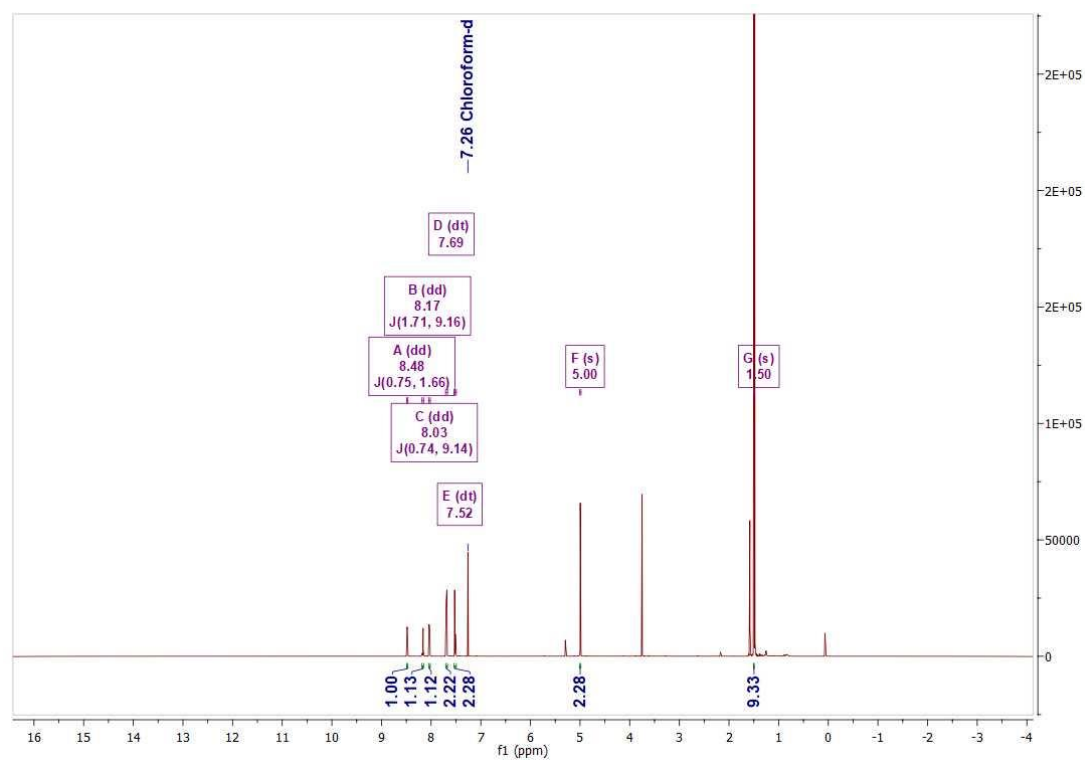


Figure S5.23. ^1H NMR spectrum of **7** in CDCl_3 .

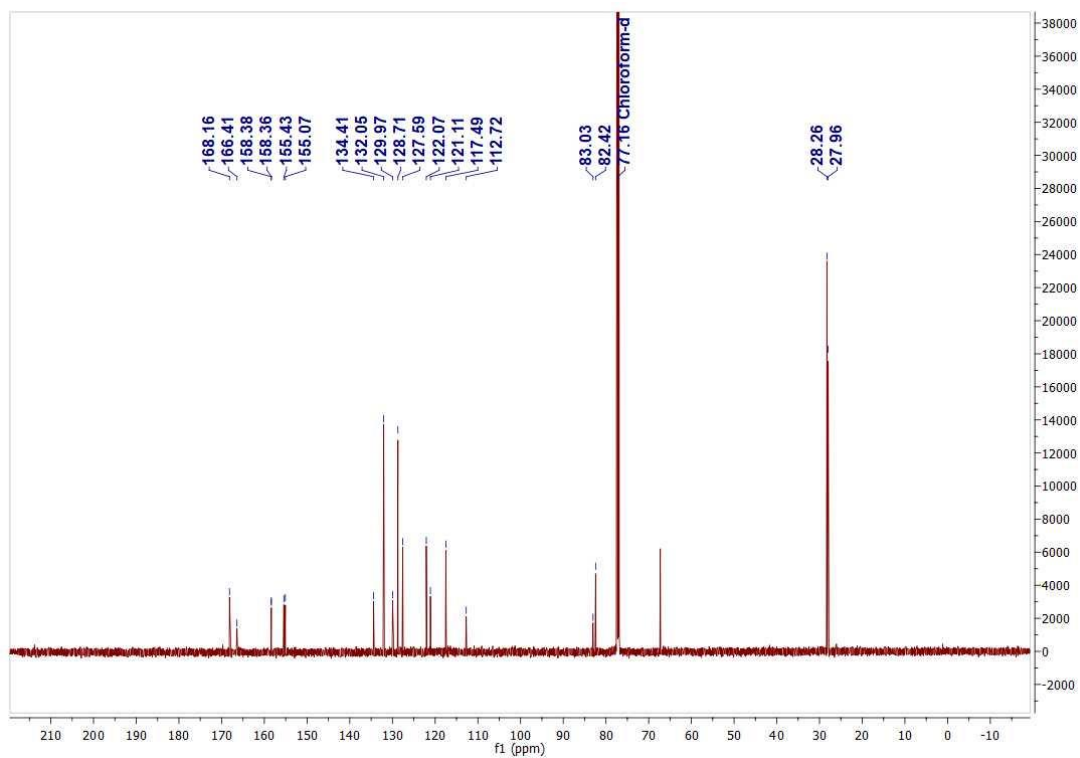


Figure S5.24. ^{13}C NMR spectrum of **7** in CDCl_3 .

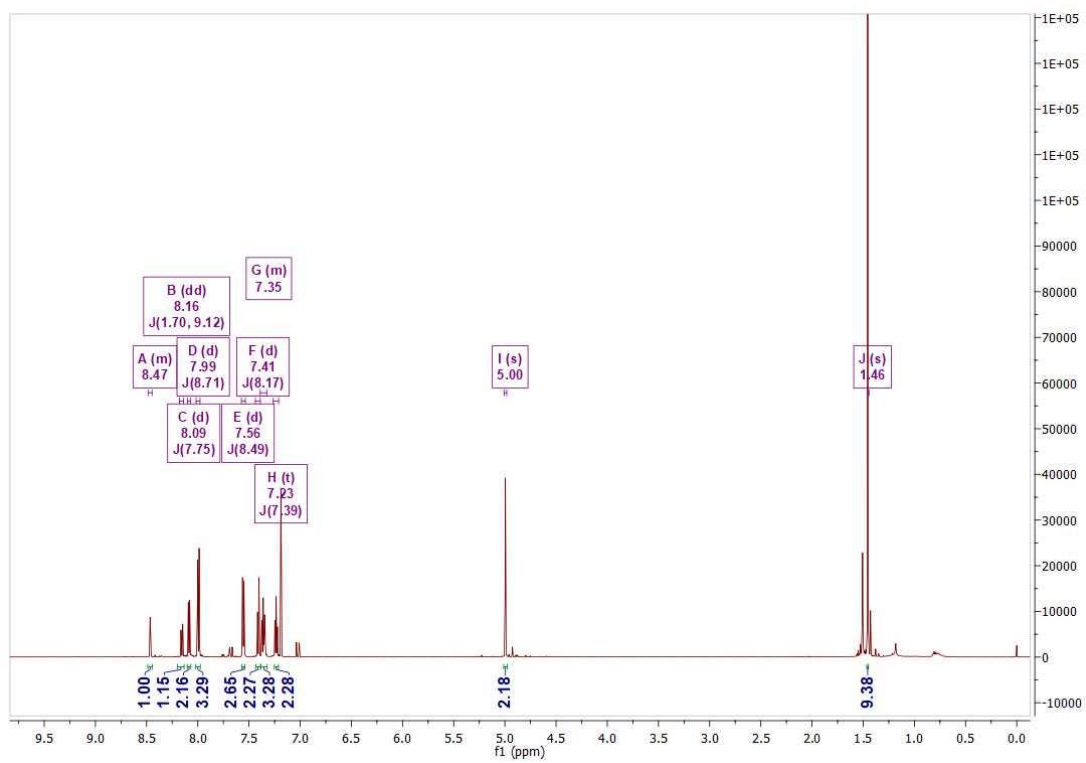


Figure S5.25. ^1H NMR spectrum of **8** in CDCl_3 .

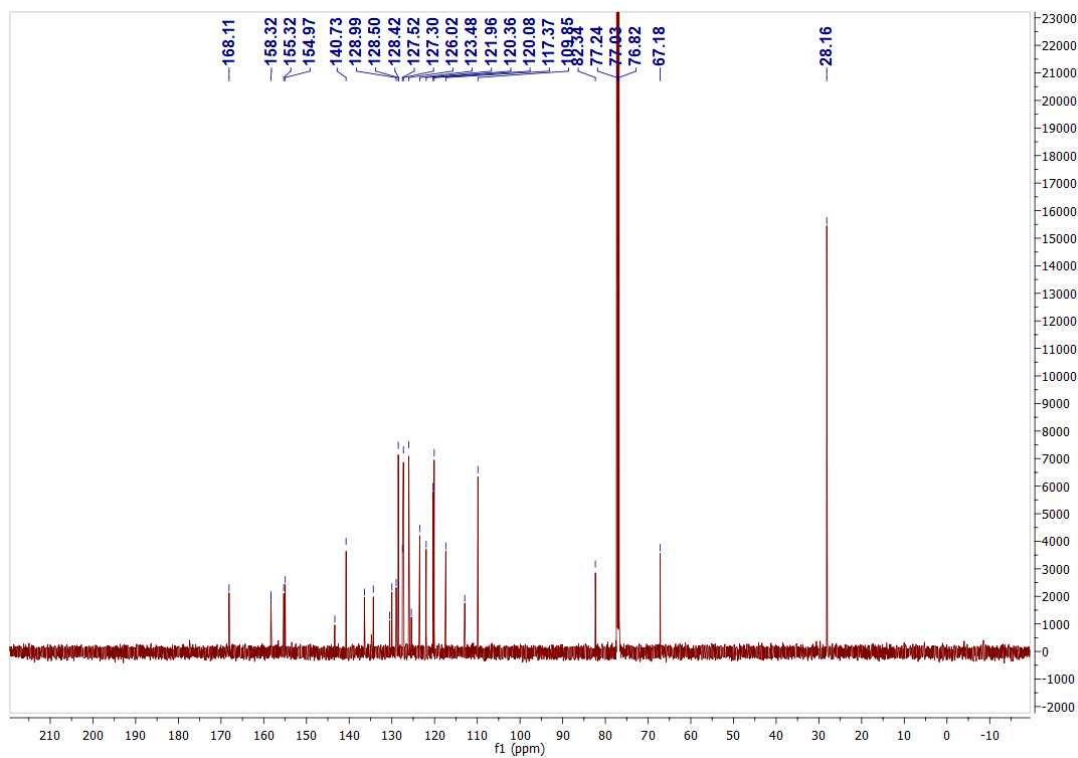


Figure S5.26. ^{13}C NMR spectrum of **8** in CDCl_3 .

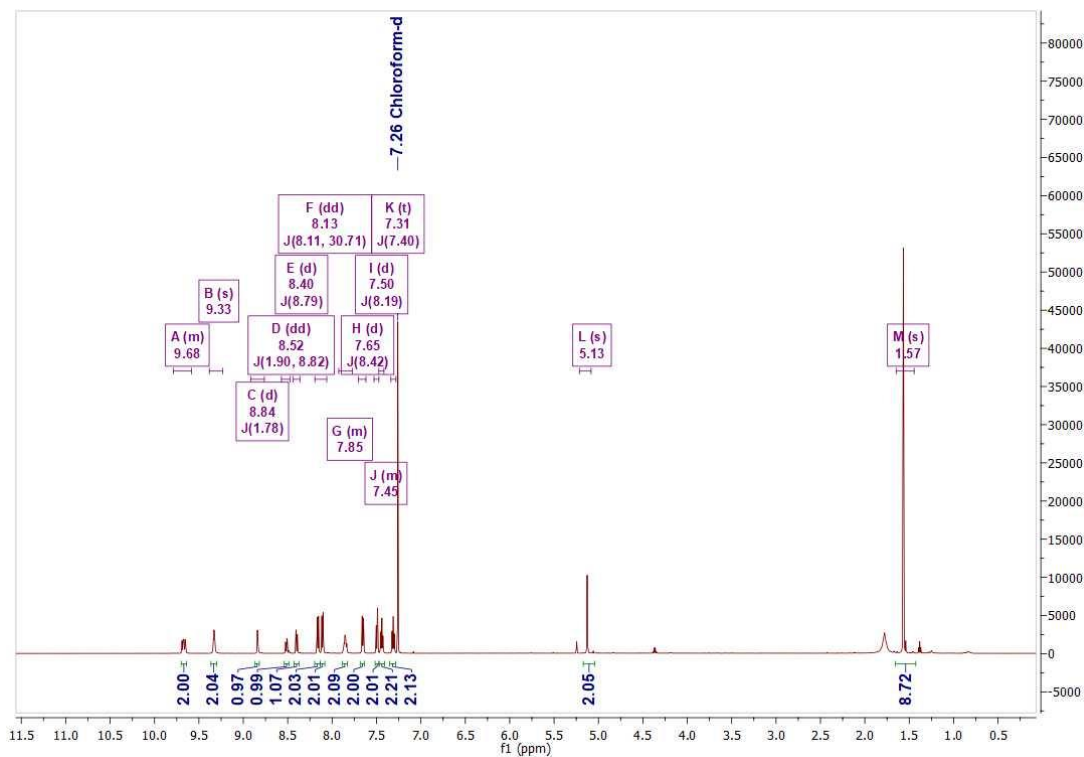


Figure S5.27. ^1H NMR spectrum of **L2** in CDCl_3 .

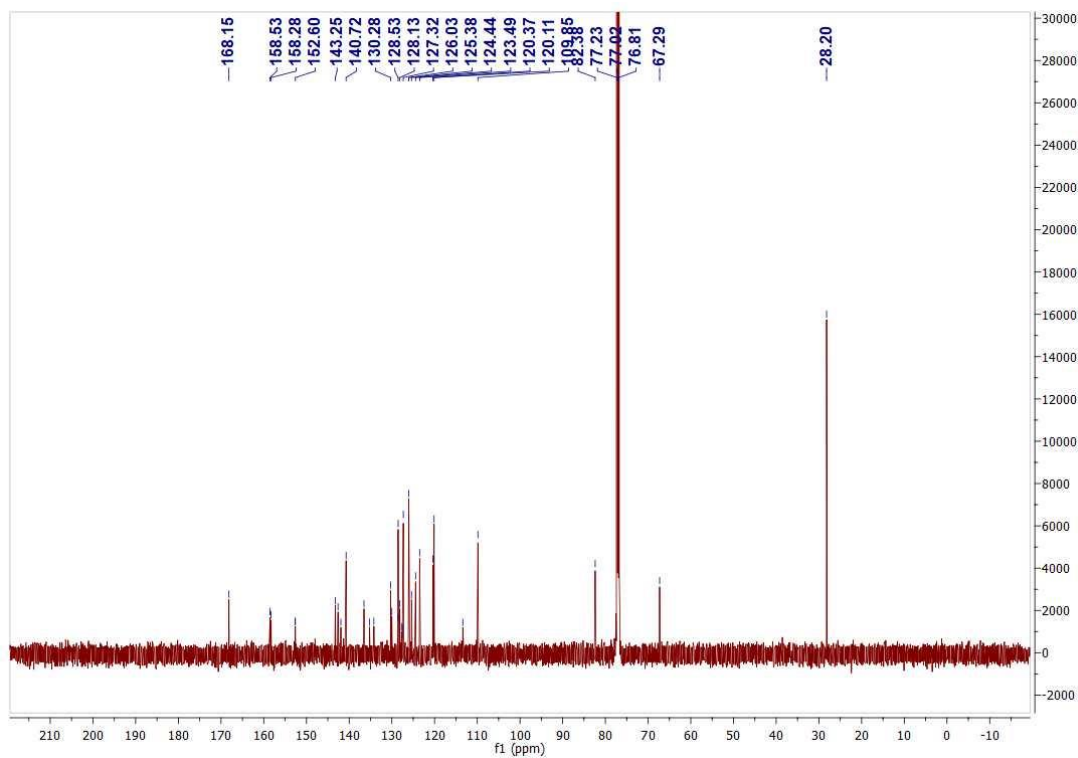


Figure S5.28. ^{13}C NMR spectrum of **L2** in CDCl_3 .

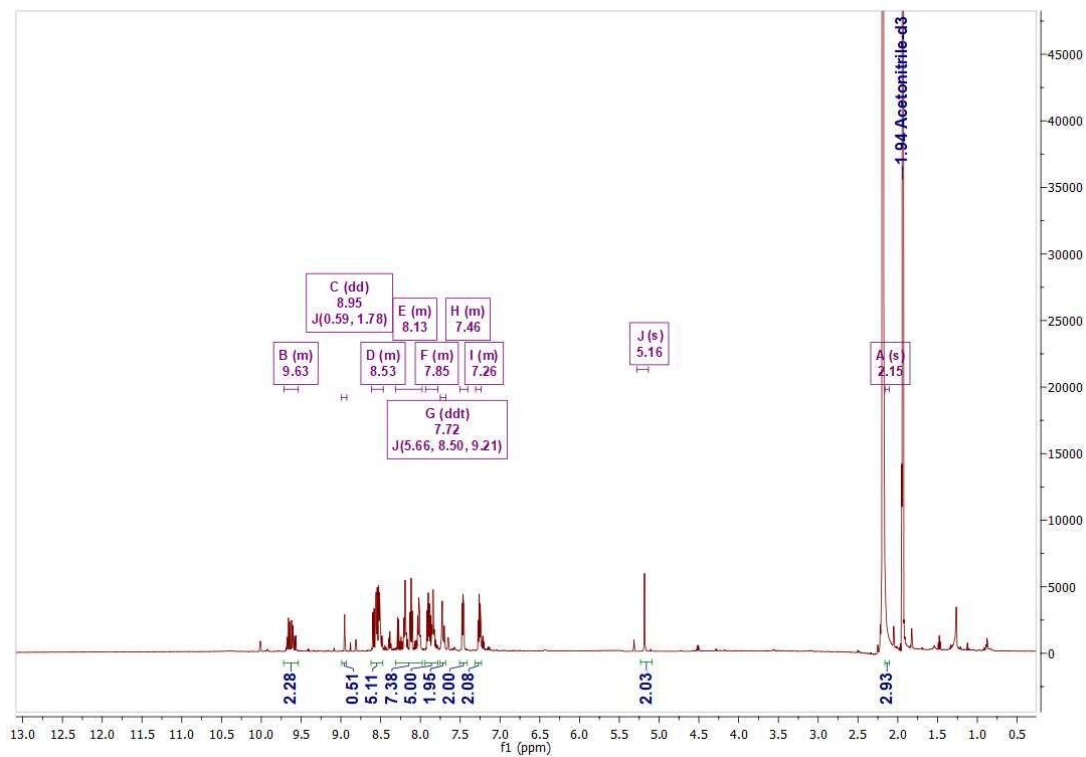


Figure S5.29. ^1H NMR spectrum of **Ru1** in $\text{d}_3\text{-ACN}$.

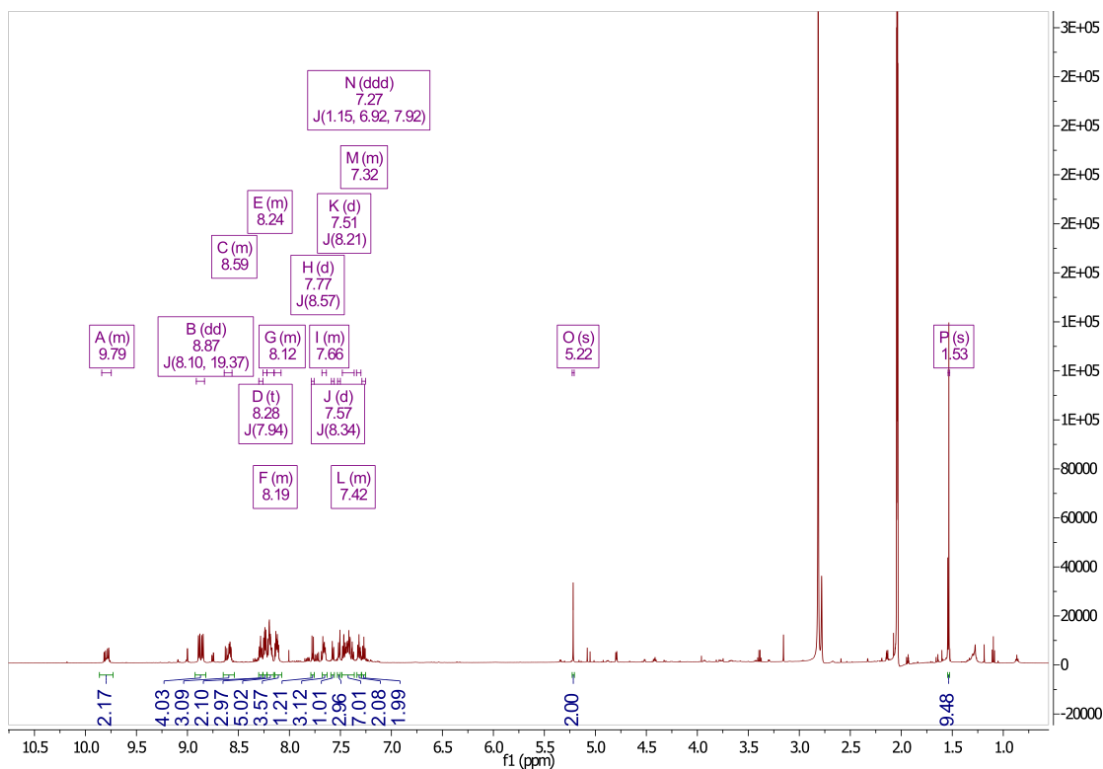


Figure S5.30. ^1H NMR spectrum of **Ru2** in d_6 -acetone.

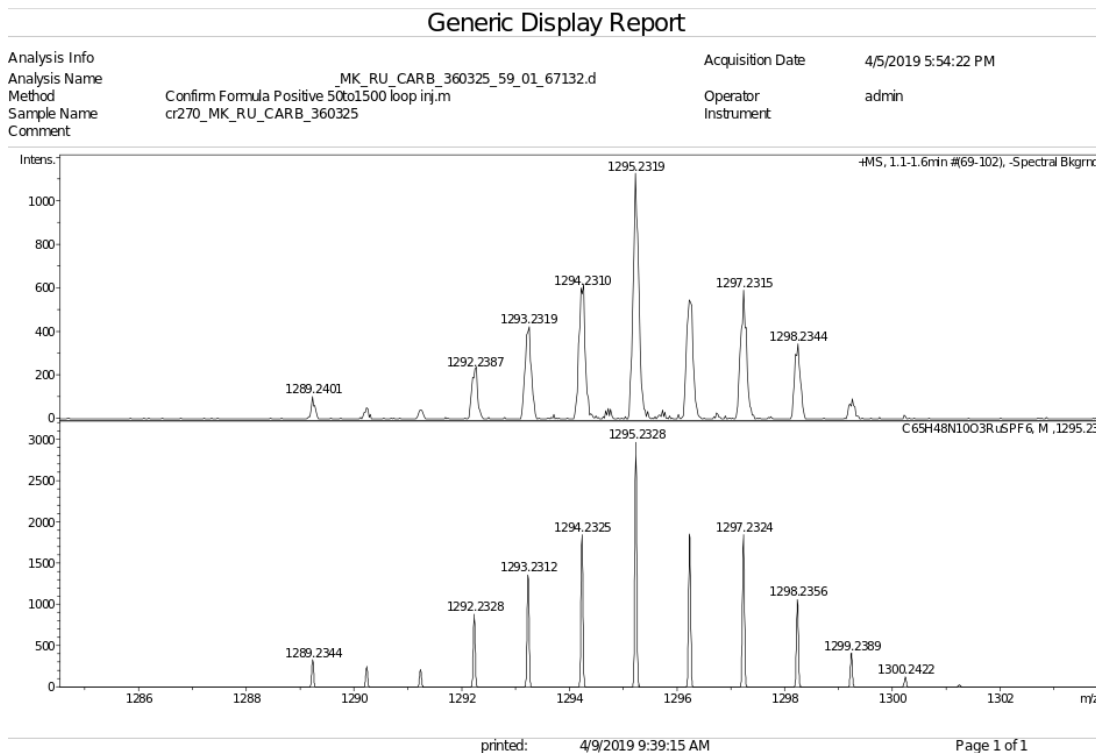
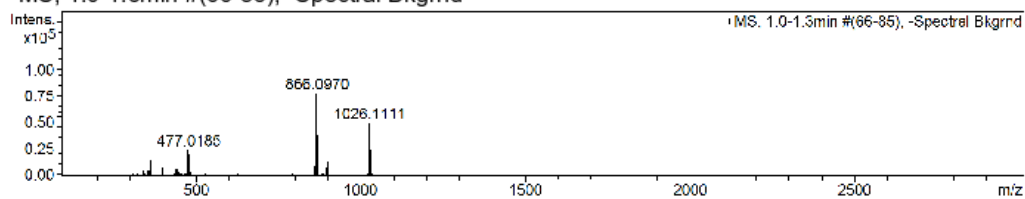


Figure S5.31. High resolution MS of **Ru2**.

Confirmation of Expected Formula

Sample-ID cr270_MK_RU_ME	Submitter cr270 [REDACTED]
Analysis Name cr270_MK_RU_ME_360328_62_01_67138.d	Supervisor atl21 [REDACTED]
Method used Confirm Formula Positive 50to1500 loop inj.m	Acquisition Date 05/04/2019 18:16:03
Ionisation Mode positive electrospray (ESI)	

+MS, 1.0-1.3min #(66-85), -Spectral Bkgnd



#	m/z	I	I%	Area	S/N
1	477.0185	23595	30.6	1100	3707.6
2	864.1094	32831	42.6	1820	2975.7
3	865.0937	39054	50.7	2649	3527.4
4	866.0970	77001	100.0	5208	6930.1
5	868.0977	37810	49.1	2288	3379.0
6	1024.1118	23306	30.3	2137	2150.0
7	1025.1169	33280	43.2	2844	3092.0
8	1026.1111	48877	63.5	4334	4573.2
9	1027.1187	26356	34.2	2630	2483.9
10	1028.1183	24098	31.3	1741	2287.5

Generate Molecular Formula Parameters

Charge	Tolerance	SearchRadius	H/C Ratio min.	H/C Ratio max.	Electron Conf.	Nitrogen Rule	sigma limit
positive	10 ppm	0.05 m/z	0	3	both	true	0.05
Expected Formula		C45H33N9O3RuS			Adduct(s):		H, Na

Figure S5.32. High resolution MS of Ru1.

S5.5. Bibliography

- (1) Beltrán-Leiva, M. J.; Páez-Hernández, D.; Arratia-Pérez, R. Theoretical Determination of Energy Transfer Processes and Influence of Symmetry in Lanthanide(III) Complexes: Methodological Considerations. *Inorg. Chem.* **2018**, *57* (9), 5120–5132. <https://doi.org/10.1021/acs.inorgchem.8b00159>.
- (2) Gieren, A.; Betz, H.; Hübner, T.; Lamm, V.; Neidlein, R.; Droste, D. Die Kristallstrukturen Des Benzo[1,2-c:3,4-C']Bis[1,2,5]Thiadiazols Und Des Semihomologen [1,2,5]Selenadiazolo[3,4-e]-2,1,3-Benzothiadiazols [1]/The Crystal Structures of the Benzo [1,2-c: 3,4-C']Bis[1,2,5]Thiadiazole and of the Semihomologous [1,2,5]Selenadiazolo[3,4-e]-2,1,3-Benzothiadiazole [1]. *Z. Für Naturforschung B* **1984**, *39* (4), 485–496. <https://doi.org/10.1515/znb-1984-0413>.
- (4) Gampe, D. M.; Hänsch, V. G.; Schramm, S.; Menzel, R.; Weiß, D.; Beckert, R. Mixing Chromophores: Donor–Acceptor Dyes with Low-Lying LUMOs and Narrow Band Gaps by Connecting 4-Alkoxythiazoles and Azaacenes. *Eur. J. Org. Chem.* **2017**, *2017* (10), 1369–1379. <https://doi.org/10.1002/ejoc.201601521>.

Appendix E

Supporting information associated with Chapter 6.

Table S6.1. The valence and low-lying singlet virtual orbitals, principle transitions for $[\text{Ru}(\text{phen})_2(\text{dppz})]^{2+}$ calculated in vacuo, with their energies (photon equivalent) and oscillator strengths with fragment contributions (Ru, dppz, and phen)); red highlighting represents dppz-based transitions, blue phen-based and yellow transitions with both phen and dppz contributions (L3 = all three ligands).

Label	HOMO-3	HOMO-2	HOMO-1	HOMO	LUMO	LUMO+1	LUMO+2	LUMO+3	LUMO+4	LUMO+5
MO	171	172	173	174	175	176	177	178	179	180
Energy	-10.89	-10.88	-10.81	-10.78	-7.35	-7.26	-7.25	-7.16	-7.11	-7.05
λ (f)	Predominant Origin and Destination Orbitals for Each Vertical Transition indicated by Coloured Bars									
451 nm (0.010)		Ru(dppz)			L3					
442 nm (0.023)	Ru(phen)				L3					
435 nm (0.016)				Ru				phen		
432 nm (0.046)	Ru(phen)					dppz				
426 nm (0.164)		Ru(dppz)				dppz				
416 nm (0.035)				Ru				phen		
406 nm (0.024)	Ru(phen)							phen		
404 nm (0.010)		Ru(dppz)						phen		
396 nm (0.013)				Ru						dppz
393 nm (0.022)	Ru(phen)							phen		
392 nm (0.003)			dppz		L3					
388 nm (0.062)		Ru(dppz)				dppz				
Fragment	% contribution of Fragment to orbital									
dppz	4.01	18.09	99.97	5.99	21.67	77.06	0.34	0.98	6.34	89.58
Ru	70.92	69.27	0.01	82.81	0.50	3.16	6.36	1.26	0.06	3.23
phen1	12.54	6.32	0.01	5.60	38.92	9.89	46.64	48.88	46.80	3.59
phen2	12.53	6.32	0.01	5.60	38.92	9.88	46.65	48.88	46.80	3.59

Table S6.2. The valence and low-lying virtual orbitals, principle transitions for [Ru(phen)₂(dppz)]²⁺•2H₂O calculated in vacuo, with their energies (photon equivalent) and oscillator strengths with fragment contributions (Ru, dppz, phen, and water); red highlighting represents dppz-based transitions, blue phen-based and yellow transitions with both phen and dppz contributions (L3 = all three ligands).

Label	HOMO -3	HOMO- 2	HOMO -1	HOM O	LUM O	LUMO+ 1	LUMO+ 2	LUMO+ 3	LUMO+ 4	LUMO+ 5
MO	181	182	183	184	185	186	187	188	189	190
Energy (-11.16	-10.77	-10.77	-10.66	-7.44	-7.25	-7.16	-7.07	-7.02	-6.96
λ (f)	Predominant Origin and Destination Orbitals for Each Vertical Transition indicated by arrows									
455nm (0.017)			RuL3			phen				
448nm (0.009)		Ru(phen)			dppz					
445nm (0.096)			RuL3		dppz					
438nm (0.052)		Ru(phen)				phen				
420nm (0.033)				Ru					phen	
413nm (0.096)		Ru(phen)						phen		
410nm (0.018)			RuL3						phen	
407nm (0.094)			RuL3					phen		
404nm (0.120)		Ru(phen)						phen		
400nm (0.022)			RuL3						phen	
396nm (0.024)		Ru(phen)							phen	
388nm (0.014)	π				π^*					
Fragment	% contribution of Fragment to orbital									
dppz	99.83	3.89	15.62	6.39	98.78	4.81	0.35	1.34	0.74	90.57
water	0.14	0.04	0.17	0.05	0.10	0.01	0.00	0.00	0.00	0.14
Ru	0.00	71.35	71.24	82.65	0.19	1.43	6.50	1.27	0.41	4.82
phen1	0.01	11.14	7.71	5.44	0.47	45.31	48.07	45.22	52.84	2.34
phen2	0.01	13.58	5.25	5.46	0.46	48.44	45.08	52.17	46.00	2.14

Atomic Coordinates for [Ru(phen)₂(dppz)]²⁺ UB3LYP LanL2DZ

Created by GaussView 6.0.16

77 84 0 0 0 0 0 0 0 0 0 0 0 0 0 0															
1.5861	-2.1870	2.7135	C	0	0	0	0	0	0	0	0	0	0	0	0
2.8405	-1.8008	2.2289	C	0	0	0	0	0	0	0	0	0	0	0	0
2.9076	-0.9124	1.1289	C	0	0	0	0	0	0	0	0	0	0	0	0
1.6947	-0.4531	0.5657	C	0	0	0	0	0	0	0	0	0	0	0	0
0.4169	-1.6871	2.1040	C	0	0	0	0	0	0	0	0	0	0	0	0
1.6947	0.4531	-0.5657	C	0	0	0	0	0	0	0	0	0	0	0	0
2.9076	0.9123	-1.1289	C	0	0	0	0	0	0	0	0	0	0	0	0
2.8405	1.8008	-2.2290	C	0	0	0	0	0	0	0	0	0	0	0	0
3.7639	2.1606	-2.6691	H	0	0	0	0	0	0	0	0	0	0	0	0
1.5861	2.1870	-2.7136	C	0	0	0	0	0	0	0	0	0	0	0	0
0.4169	1.6871	-2.1040	C	0	0	0	0	0	0	0	0	0	0	0	0
1.4963	-2.8675	3.5535	H	0	0	0	0	0	0	0	0	0	0	0	0
3.7639	-2.1607	2.6691	H	0	0	0	0	0	0	0	0	0	0	0	0
-0.5651	1.9693	-2.4633	H	0	0	0	0	0	0	0	0	0	0	0	0
0.4621	0.8338	-1.0521	N	0	0	0	0	0	0	0	0	0	0	0	0
-2.2107	2.6623	0.6775	C	0	0	0	0	0	0	0	0	0	0	0	0
-0.5552	2.0973	2.2435	C	0	0	0	0	0	0	0	0	0	0	0	0
-2.9547	2.2792	-0.4871	C	0	0	0	0	0	0	0	0	0	0	0	0
-2.4461	3.9221	1.2947	C	0	0	0	0	0	0	0	0	0	0	0	0
-0.7287	3.3333	2.9116	C	0	0	0	0	0	0	0	0	0	0	0	0
0.1707	1.3742	2.5954	H	0	0	0	0	0	0	0	0	0	0	0	0
-3.9424	3.1507	-1.0241	C	0	0	0	0	0	0	0	0	0	0	0	0
-1.6720	4.2487	2.4435	C	0	0	0	0	0	0	0	0	0	0	0	0
-0.1208	3.5509	3.7832	H	0	0	0	0	0	0	0	0	0	0	0	0
-4.6526	2.7123	-2.1769	C	0	0	0	0	0	0	0	0	0	0	0	0
-3.3549	0.6557	-2.1351	C	0	0	0	0	0	0	0	0	0	0	0	0
-1.8185	5.2010	2.9451	H	0	0	0	0	0	0	0	0	0	0	0	0
-4.3552	1.4645	-2.7261	C	0	0	0	0	0	0	0	0	0	0	0	0
-5.4160	3.3461	-2.6191	H	0	0	0	0	0	0	0	0	0	0	0	0
-3.1088	-0.3141	-2.5508	H	0	0	0	0	0	0	0	0	0	0	0	0
-4.8783	1.0990	-3.6032	H	0	0	0	0	0	0	0	0	0	0	0	0
-1.2770	1.7591	1.1529	N	0	0	0	0	0	0	0	0	0	0	0	0
-2.2107	-2.6623	-0.6775	C	0	0	0	0	0	0	0	0	0	0	0	0
-0.5553	-2.0973	-2.2435	C	0	0	0	0	0	0	0	0	0	0	0	0
-2.9548	-2.2792	0.4871	C	0	0	0	0	0	0	0	0	0	0	0	0
-2.4462	-3.9220	-1.2947	C	0	0	0	0	0	0	0	0	0	0	0	0
-0.7288	-3.3333	-2.9116	C	0	0	0	0	0	0	0	0	0	0	0	0
0.1707	-1.3742	-2.5954	H	0	0	0	0	0	0	0	0	0	0	0	0
-3.9425	-3.1507	1.0241	C	0	0	0	0	0	0	0	0	0	0	0	0
-1.6722	-4.2487	-2.4435	C	0	0	0	0	0	0	0	0	0	0	0	0
-0.1209	-3.5509	-3.7832	H	0	0	0	0	0	0	0	0	0	0	0	0
-4.6526	-2.7122	2.1769	C	0	0	0	0	0	0	0	0	0	0	0	0
-3.3549	-0.6557	2.1351	C	0	0	0	0	0	0	0	0	0	0	0	0
-1.8186	-5.2010	-2.9452	H	0	0	0	0	0	0	0	0	0	0	0	0
-4.3552	-1.4644	2.7261	C	0	0	0	0	0	0	0	0	0	0	0	0
-5.4160	-3.3460	2.6191	H	0	0	0	0	0	0	0	0	0	0	0	0
-3.1088	0.3141	2.5508	H	0	0	0	0	0	0	0	0	0	0	0	0
-4.8783	-1.0989	3.6032	H	0	0	0	0	0	0	0	0	0	0	0	0
-2.6626	-1.0467	1.0431	N	0	0	0	0	0	0	0	0	0	0	0	0
-1.2771	-1.7591	-1.1529	N	0	0	0	0	0	0	0	0	0	0	0	0
-2.6626	1.0467	-1.0430	N	0	0	0	0	0	0	0	0	0	0	0	0
0.4621	-0.8338	1.0521	N	0	0	0	0	0	0	0	0	0	0	0	0
1.4963	2.8674	-3.5535	H	0	0	0	0	0	0	0	0	0	0	0	0
-1.1602	-0.0000	-0.0000	Ru	0	0	0	0	0	0	0	0	0	0	0	0
-3.4499	4.7960	0.7317	C	0	0	0	0	0	0	0	0	0	0	0	0
-4.1704	4.4245	-0.3806	C	0	0	0	0	0	0	0	0	0	0	0	0
-4.9247	5.0884	-0.7940	H	0	0	0	0	0	0	0	0	0	0	0	0
-3.6277	5.7574	1.2059	H	0	0	0	0	0	0	0	0	0	0	0	0
-4.1705	-4.4244	0.3806	C	0	0	0	0	0	0	0	0	0	0	0	0
-3.4500	-4.7960	-0.7317	C	0	0	0	0	0	0	0	0	0	0	0	0
-4.9248	-5.0884	0.7941	H	0	0	0	0	0	0	0	0	0	0	0	0
-3.6278	-5.7573	-1.2059	H	0	0	0	0	0	0	0	0	0	0	0	0
-0.5652	-1.9694	2.4633	H	0	0	0	0	0	0	0	0	0	0	0	0

4.1796	-0.4547	0.5612	C	0	0	0	0	0	0	0	0	0	0	0	0
4.1796	0.4546	-0.5612	C	0	0	0	0	0	0	0	0	0	0	0	0
5.3285	0.8960	-1.1061	N	0	0	0	0	0	0	0	0	0	0	0	0
5.3285	-0.8960	1.1061	N	0	0	0	0	0	0	0	0	0	0	0	0
6.5078	0.4584	-0.5658	C	0	0	0	0	0	0	0	0	0	0	0	0
6.5078	-0.4584	0.5658	C	0	0	0	0	0	0	0	0	0	0	0	0
7.7498	-0.9004	1.1113	C	0	0	0	0	0	0	0	0	0	0	0	0
7.7498	0.9004	-1.1113	C	0	0	0	0	0	0	0	0	0	0	0	0
8.9398	0.4518	-0.5576	C	0	0	0	0	0	0	0	0	0	0	0	0
8.9398	-0.4519	0.5576	C	0	0	0	0	0	0	0	0	0	0	0	0
7.7295	1.5835	-1.9541	H	0	0	0	0	0	0	0	0	0	0	0	0
9.8892	0.7841	-0.9676	H	0	0	0	0	0	0	0	0	0	0	0	0
9.8892	-0.7842	0.9676	H	0	0	0	0	0	0	0	0	0	0	0	0
7.7295	-1.5835	1.9541	H	0	0	0	0	0	0	0	0	0	0	0	0
1	2	4	0	0	0	0									
1	5	4	0	0	0	0									
1	12	1	0	0	0	0									
2	3	4	0	0	0	0									
2	13	1	0	0	0	0									
3	4	4	0	0	0	0									
3	64	1	0	0	0	0									
4	6	1	0	0	0	0									
4	52	4	0	0	0	0									
5	52	4	0	0	0	0									
5	63	1	0	0	0	0									
6	7	4	0	0	0	0									
6	15	4	0	0	0	0									
7	8	4	0	0	0	0									
7	65	1	0	0	0	0									
8	9	1	0	0	0	0									
8	10	4	0	0	0	0									
10	11	4	0	0	0	0									
10	53	1	0	0	0	0									
11	14	1	0	0	0	0									
11	15	4	0	0	0	0									
16	18	4	0	0	0	0									
16	19	4	0	0	0	0									
16	32	1	0	0	0	0									
17	20	4	0	0	0	0									
17	21	1	0	0	0	0									
17	32	4	0	0	0	0									
18	22	4	0	0	0	0									
18	51	1	0	0	0	0									
19	23	4	0	0	0	0									
19	55	4	0	0	0	0									
20	23	4	0	0	0	0									
20	24	1	0	0	0	0									
22	25	4	0	0	0	0									
22	56	4	0	0	0	0									
23	27	1	0	0	0	0									
25	28	4	0	0	0	0									
25	29	1	0	0	0	0									
26	28	4	0	0	0	0									
26	30	1	0	0	0	0									
26	51	4	0	0	0	0									
28	31	1	0	0	0	0									
33	35	4	0	0	0	0									
33	36	4	0	0	0	0									
33	50	1	0	0	0	0									
34	37	4	0	0	0	0									
34	38	1	0	0	0	0									
34	50	4	0	0	0	0									
35	39	4	0	0	0	0									
35	49	1	0	0	0	0									
36	40	4	0	0	0	0									
36	60	4	0	0	0	0									
37	40	4	0	0	0	0									

37	41	1	0	0	0	0
39	42	4	0	0	0	0
39	59	4	0	0	0	0
40	44	1	0	0	0	0
42	45	4	0	0	0	0
42	46	1	0	0	0	0
43	45	4	0	0	0	0
43	47	1	0	0	0	0
43	49	4	0	0	0	0
45	48	1	0	0	0	0
55	56	2	0	0	0	0
55	58	1	0	0	0	0
56	57	1	0	0	0	0
59	60	2	0	0	0	0
59	61	1	0	0	0	0
60	62	1	0	0	0	0
64	65	4	0	0	0	0
64	67	4	0	0	0	0
65	66	4	0	0	0	0
66	68	4	0	0	0	0
67	69	4	0	0	0	0
68	69	1	0	0	0	0
68	71	4	0	0	0	0
69	70	4	0	0	0	0
70	73	4	0	0	0	0
70	77	1	0	0	0	0
71	72	4	0	0	0	0
71	74	1	0	0	0	0
72	73	4	0	0	0	0
72	75	1	0	0	0	0
73	76	1	0	0	0	0

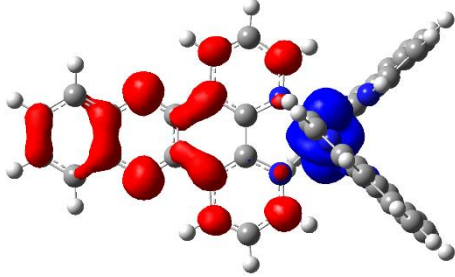
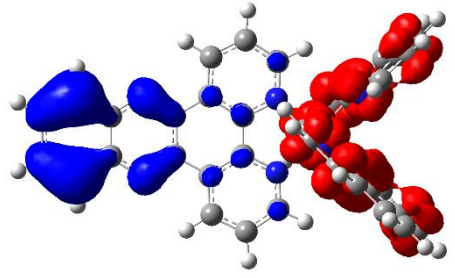
M END

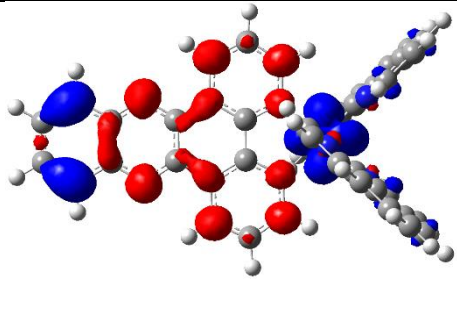
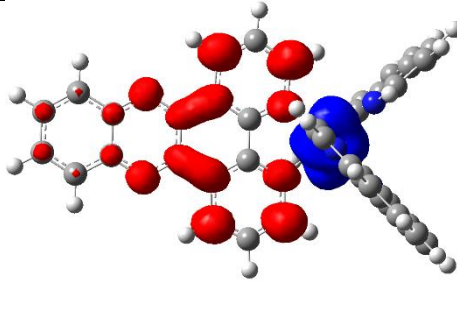
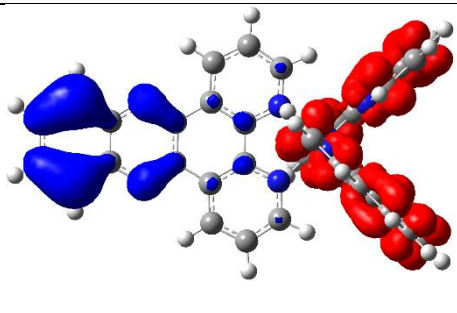
3.9099	-0.5347	0.4865	C	0	0	0	0	0	0	0	0	0	0	0	0
3.9081	0.5619	-0.4680	C	0	0	0	0	0	0	0	0	0	0	0	0
5.0689	1.0725	-0.9267	N	0	0	0	0	0	0	0	0	0	0	0	0
5.0725	-1.0575	0.9269	N	0	0	0	0	0	0	0	0	0	0	0	0
6.2543	0.5296	-0.5053	C	0	0	0	0	0	0	0	0	0	0	0	0
6.2561	-0.5621	0.4458	C	0	0	0	0	0	0	0	0	0	0	0	0
7.4990	-1.1195	0.8728	C	0	0	0	0	0	0	0	0	0	0	0	0
7.4950	1.0302	-1.0034	C	0	0	0	0	0	0	0	0	0	0	0	0
8.6861	0.4698	-0.5688	C	0	0	0	0	0	0	0	0	0	0	0	0
8.6881	-0.6101	0.3745	C	0	0	0	0	0	0	0	0	0	0	0	0
7.4893	1.8347	-1.7314	H	0	0	0	0	0	0	0	0	0	0	0	0
9.6328	0.8432	-0.9477	H	0	0	0	0	0	0	0	0	0	0	0	0
9.6364	-1.0332	0.6926	H	0	0	0	0	0	0	0	0	0	0	0	0
7.4972	-1.9479	1.5734	H	0	0	0	0	0	0	0	0	0	0	0	0
5.4231	-2.3656	2.3142	H	0	0	0	0	0	0	0	0	0	0	0	0
5.1573	-3.0598	2.9629	O	0	0	0	0	0	0	0	0	0	0	0	0
5.8714	-3.3665	3.5487	H	0	0	0	0	0	0	0	0	0	0	0	0
5.4124	2.6278	-2.0197	H	0	0	0	0	0	0	0	0	0	0	0	0
5.1576	3.3553	-2.6360	O	0	0	0	0	0	0	0	0	0	0	0	0
5.8491	4.0239	-2.7850	H	0	0	0	0	0	0	0	0	0	0	0	0
1	2	4	0	0	0	0									
1	5	4	0	0	0	0									
1	12	1	0	0	0	0									
2	3	4	0	0	0	0									
2	13	1	0	0	0	0									
3	4	4	0	0	0	0									
3	64	1	0	0	0	0									
4	6	1	0	0	0	0									
4	52	4	0	0	0	0									
5	52	4	0	0	0	0									
5	63	1	0	0	0	0									
6	7	4	0	0	0	0									
6	15	4	0	0	0	0									
7	8	4	0	0	0	0									
7	65	1	0	0	0	0									
8	9	1	0	0	0	0									
8	10	4	0	0	0	0									
10	11	4	0	0	0	0									
10	53	1	0	0	0	0									
11	14	1	0	0	0	0									
11	15	4	0	0	0	0									
16	18	4	0	0	0	0									
16	19	4	0	0	0	0									
16	32	1	0	0	0	0									
17	20	4	0	0	0	0									
17	21	1	0	0	0	0									
17	32	4	0	0	0	0									
18	22	4	0	0	0	0									
18	51	1	0	0	0	0									
19	23	4	0	0	0	0									
19	55	4	0	0	0	0									
20	23	4	0	0	0	0									
20	24	1	0	0	0	0									
22	25	4	0	0	0	0									
22	56	4	0	0	0	0									
23	27	1	0	0	0	0									
25	28	4	0	0	0	0									
25	29	1	0	0	0	0									
26	28	4	0	0	0	0									
26	30	1	0	0	0	0									
26	51	4	0	0	0	0									
28	31	1	0	0	0	0									
33	35	4	0	0	0	0									
33	36	4	0	0	0	0									
33	50	1	0	0	0	0									
34	37	4	0	0	0	0									
34	38	1	0	0	0	0									

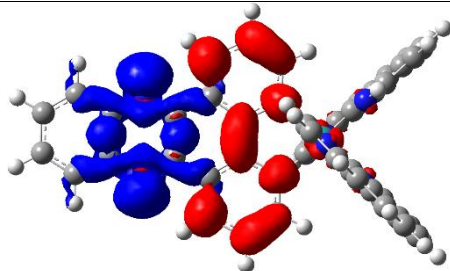
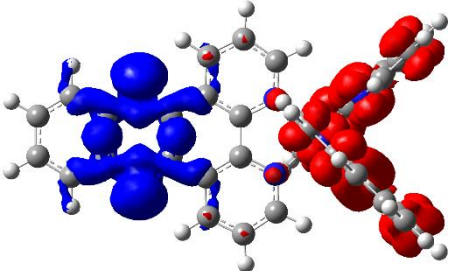
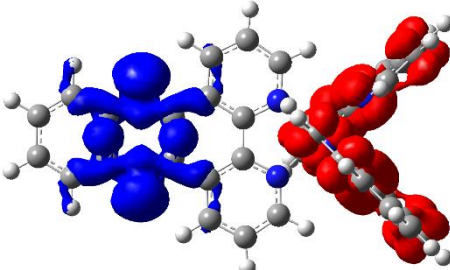
34	50	4	0	0	0	0
35	39	4	0	0	0	0
35	49	1	0	0	0	0
36	40	4	0	0	0	0
36	60	4	0	0	0	0
37	40	4	0	0	0	0
37	41	1	0	0	0	0
39	42	4	0	0	0	0
39	59	4	0	0	0	0
40	44	1	0	0	0	0
42	45	4	0	0	0	0
42	46	1	0	0	0	0
43	45	4	0	0	0	0
43	47	1	0	0	0	0
43	49	4	0	0	0	0
45	48	1	0	0	0	0
55	56	2	0	0	0	0
55	58	1	0	0	0	0
56	57	1	0	0	0	0
59	60	2	0	0	0	0
59	61	1	0	0	0	0
60	62	1	0	0	0	0
64	65	1	0	0	0	0
64	67	4	0	0	0	0
65	66	4	0	0	0	0
66	68	4	0	0	0	0
67	69	4	0	0	0	0
68	69	1	0	0	0	0
68	71	4	0	0	0	0
69	70	4	0	0	0	0
70	73	4	0	0	0	0
70	77	1	0	0	0	0
71	72	4	0	0	0	0
71	74	1	0	0	0	0
72	73	4	0	0	0	0
72	75	1	0	0	0	0
73	76	1	0	0	0	0
78	79	1	0	0	0	0
79	80	1	0	0	0	0
81	82	1	0	0	0	0
82	83	1	0	0	0	0

M END

Table S6.3. The orbital assignments of the optically accessible excited states of $[\text{Ru}(\text{phen})_2(\text{dppz})]^{2+}$ (in vacuo) UB3LYP/LanL2DZ.

Excited State #	nm	Oscillator Strength f	Assignment (contribution %)				E Density Map (iso 0.001)
16	451.1	0.0102	172- >175(39.5%)	172- >175B(39.5%)			
20	442.1	0.0227	171- >175(30.2%)	171- >175B(30.2%)			

21	435	0.0156	174- >178(32.3%)	174- >178B(32.3%)	171- >177B(15.3%)	171->177(15.3%)	
22	432.2	0.0457	171- >176(19.4%)	171- >176B(19.4%)	172->177(13.3%)	172- >177B(13.3%)	
24	426.2	0.1644	172- >176(25.1%)	172- >176B(25.1%)			

27	416.3	0.0353	174- >179(32.5%)	174- >179B(32.5%)	172- >178B(10.1%)	172->178(10.1%)	
32	406.3	0.0244	171- >178(33.5%)	171- >178B(33.5%)	172->179(11.3%)	172- >179B(11.3%)	
33	404.9	0.0995	172- >178(34.1%)	172- >178B(34.1%)			

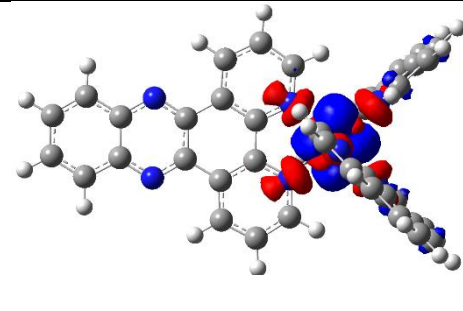
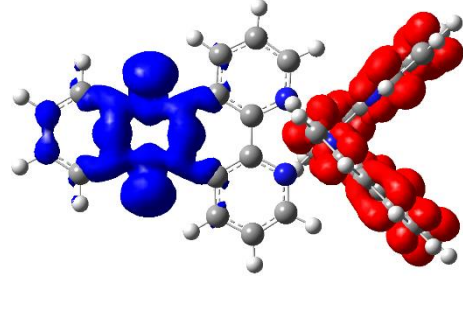
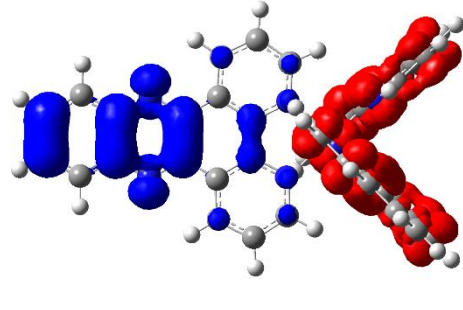
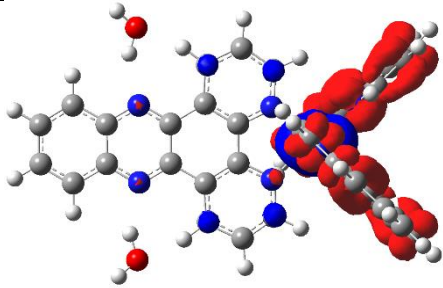
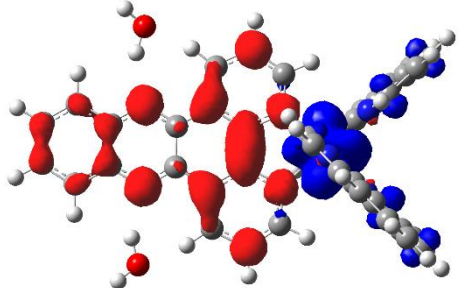
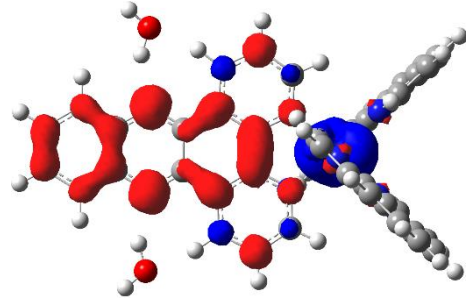
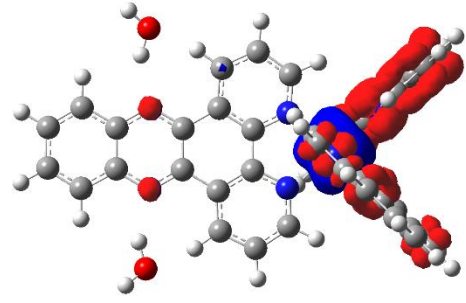
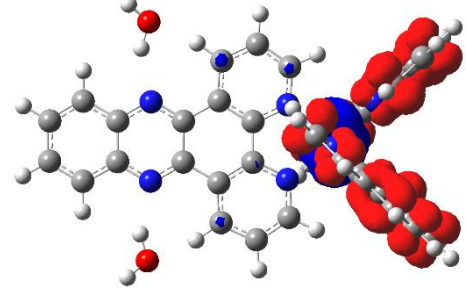
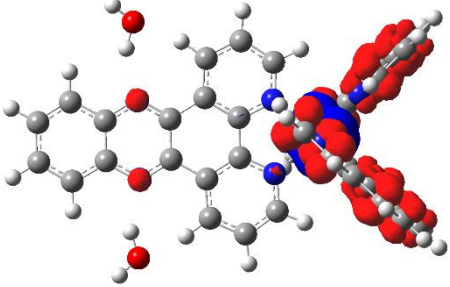
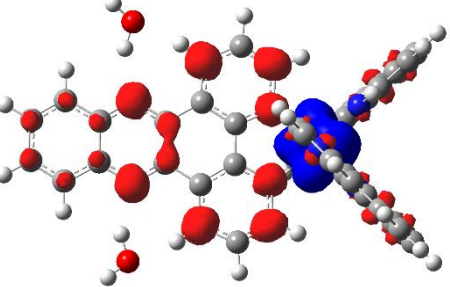
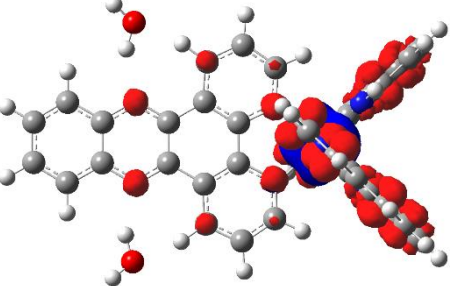
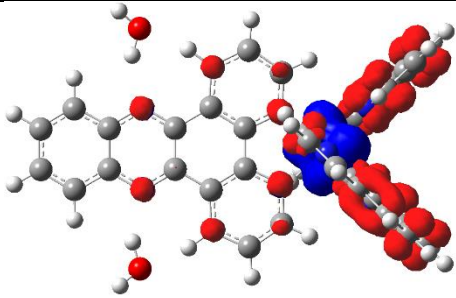
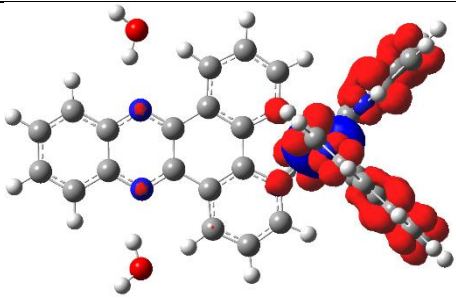
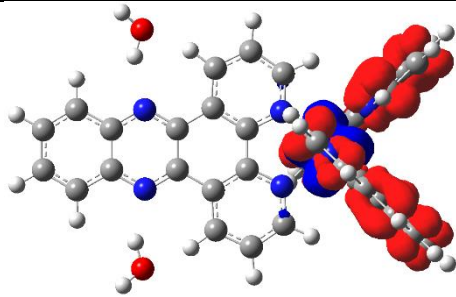
36	396.5	0.0132	174- >180(32.0%)	174- >180B(32.0%)			
39	393	0.0219	171- >179(39.1%)	171- >179B(39.1%)			
40	392.2	0.0033	173- >175(25.3%)	173- >175B(25.3%)	173->176(11.9%)	173- >176B(11.9%)	

Table S6.4. The Orbital Assignments of the Optically Accessible Excited States of $[\text{Ru}(\text{phen})_2(\text{dppz})]^{2+} \cdot 2\text{H}_2\text{O}$ (in vacuo) UB3LYP/LanL2DZ

Excited State #	nm	Oscillator Strength f	Assignment (contribution %)		e Density Map (iso value .001)
15	455.5	0.017	183->186(38.4%)	183->186B(38.4%)	
20	448.6	0.0092	182->185(35.0%)	182->185B(35.0%)	

23	445.3	0.0956	183->185(39.4%)	183->185B(39.4%)		
25	438.4	0.0523	182->186(18.3%)	182->186B(18.3%)	183->187(14.1%) 183->187B(14.1%)	
28	420.4	0.0332	184->189(33.0%)	184->189B(33.0%)	183->188B(10.6%) 183->188(10.6%)	

31	413.4	0.0096	182->188(20.4%)	182->188B(20.4%)	183->189(11.0%) 183->189B(11.0%)	
33	410	0.0185	183->189(33.6%)	183->189B(33.6%)	182-188B(11.0%) 182->188(11.0%)	
34	407.3	0.0935	183->188(23.0%)	183->188B(23.0%)	182->190B(13.3%) 182->190(13.3%)	

35	403.7	0.1198	182->188(24.7%)	182->188B(24.7%)		
36	400.3	0.0224	183->189(30.5%)	183->189B(30.5%)	183->190(11.8%) 183->190B(11.8%)	
38	396.1	0.0242	182->189(43.7%)	182->189B(43.7%)		

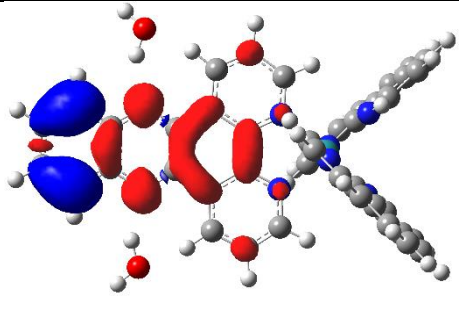
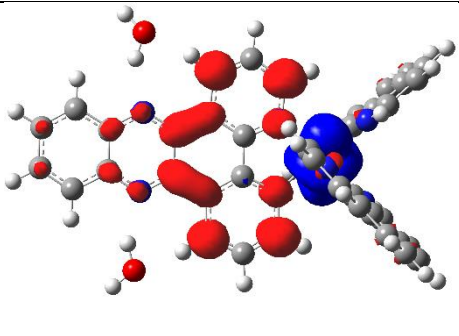
41	388.9	0.0137	181->185(47.4%)	181->185B(47.4%)	
44	384.9	0.0473	184->191(38.5%)	184->191B(38.5%)	

Table S6.5. Representations of the valence molecular orbitals of $[\text{Ru}(\text{Phen})_2(\text{dppz})]^{2+}$ and $[\text{Ru}(\text{phen})_2(\text{dppz})]^{2+} \cdot 2\text{H}_2\text{O}$ (iso value 0.02) with their energies (eV) and orbital designation number.

Label	HOMO-3	HOMO-2	HOMO-1	HOMO	LUMO	LUMO+1	LUMO+2
MO	171	172	173	174	175	176	177
Energy (eV)	-10.89	-10.88	-10.81	-10.78	-7.35	-7.26	-7.25
Label	HOMO-3	HOMO-2	HOMO-1	HOMO	LUMO	LUMO+1	LUMO+2
MO	181	182	183	184	185	186	187
Energy (eV)	-11.16	-10.77	-10.77	-10.66	-7.44	-7.25	-7.16

S6.1. Materials, Instrumental techniques, and methods

All reagents were purchased from Sigma Aldrich and were used without further purification. Synthesis was carried out using Schlenk techniques and under an inert atmosphere. ^1H and ^{13}C NMR spectroscopy was used to confirm complex formation and were consistent with published spectra. NMR spectra were recorded in deuterated solvents (d_6 -DMSO) on a Brüker AC600 NMR Spectrometer with residual solvent peaks as reference. Absorption spectra were measured on an Agilent 8453 UV-Vis 91 spectrophotometer in a 1 cm quartz cell using dry spectrophotometric grade solvents.

S6.1.1. Complex synthesis

Preparation of $[\text{Ru}(\text{phen})_2\text{Cl}_2]\cdot 2\text{H}_2\text{O}$

The synthetic method has been published previously.¹ Briefly, 60 mg (0.23 mmol) of $\text{RuCl}_3\cdot 3\text{H}_2\text{O}$, 82.9 mg (0.46 mmol) phen (1,10-phenanthroline) and 0.4 mg (0.01 mmol) LiCl were heated to reflux temperature in 10 mL anhydrous DMF for 8 hours under nitrogen atmosphere. The solution was then cooled to room temperature under nitrogen atmosphere. The volume of the reaction mixture was reduced by rotatory evaporation and 25 mL acetone was added. The reaction mixture was again brought to reflux temperature for 30 minutes and filtered immediately. The dark green literature was kept below 4 °C for 4 hours and the resulting dark green crystals were collected and washed with diethyl ether. NMR spectra agree with that previously reported.²

Preparation of $[\text{Ru}(\text{phen})_2\text{dppz}](\text{PF}_6)_2$

The synthetic method was carried out as per previously reported.¹ In brief, (266 mg, 0.50 mmol) $[\text{Ru}(\text{phen})_2\text{Cl}_2]\cdot 2\text{H}_2\text{O}$ was suspended in 30 mL 1:1 ethanol/water solution, followed by molar excess of dppz 211 mg (0.75 mmol) (dppz=dipyrido[3,2-*a*:2',3'-*c*]phenazine under a nitrogen atmosphere.. The reaction mixture was brought to reflux temperature for 6 hours. The reaction mixture turned dark red. The ethanol was completely removed by rotary evaporation and another 20 mL of water was added to the reaction mixture. The red aqueous reaction mixture was filtered and excess NH_4PF_6 was added producing a brick red precipitate. The product was washed with

water, followed by diethyl ether and then collected by filtration. The crude product was recrystallised from toluene/acetone solution before further purification using preparative scale HPLC to give a red crystalline complex. NMR spectra agree with that previously reported for the PF_6^- salt complex.³

S6.2. Bibliography

- (1) Sullivan, B. P.; Salmon, D. J.; Meyer, T. J. *Inorg. Chem.* **1978**, *17* (12), 3334–3341.
- (2) Zhang, L. Y.; Hou, Y. J.; Pan, M.; Chen, L.; Zhu, Y. X.; Yin, S. Y.; Shao, G.; Su, C. Y. *Dalt. Trans.* **2015**, *44* (34), 15212–15219.
- (3) Liao, G.; Ye, Z.; Liu, Y.; Fu, B.; Fu, C. *PeerJ* **2017**, *2017* (4).